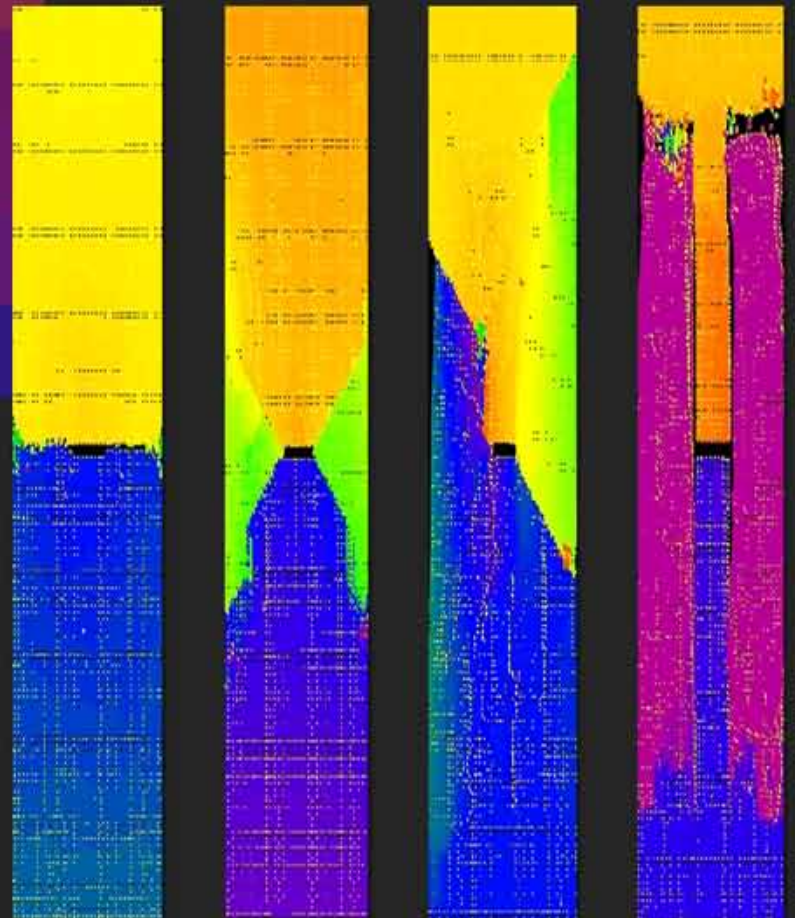


Advances in

MATERIALS SCIENCE

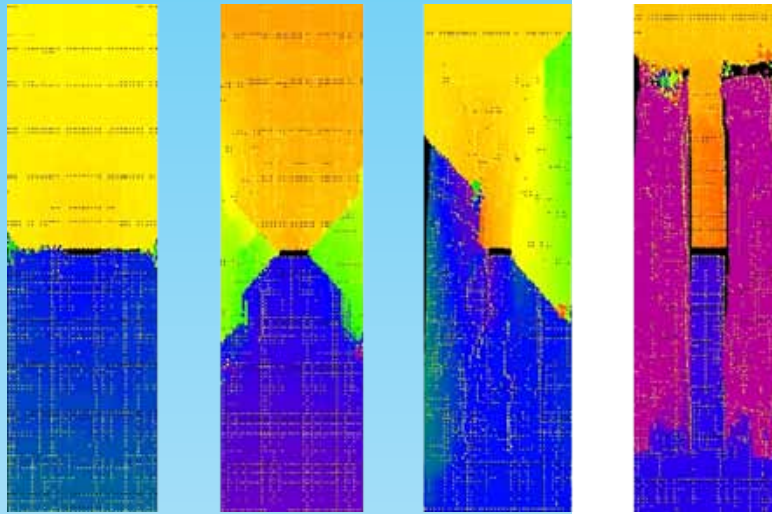


Editors:

Dimitri Kusnezov

Oleg Nikandrovich Shubin

$$m\ddot{\underline{r}}_k = \sum_{n=1}^N \frac{f(|\underline{r}_k - \underline{r}_n|)}{|\underline{r}_k - \underline{r}_n|} (\underline{r}_k - \underline{r}_n)$$



ON THE COVER:

Peridynamics simulation of uniaxial pull test of fiber-reinforced, laminate composite plates with initial central notches and having varying fiber orientations in the lamina (the "lay-ups"). The resulting damage and fracture emerge spontaneously in an unguided manner, and the cracking modes are consistent with those seen in laboratory tests. From left to right, the lay-ups are quasi-isotropic; all $\pm 45^\circ$ plies; $\pm 45^\circ$ plies and 0° plies; mostly 0° plies (along length of bar). Images are colored by vertical displacement. (See section 2, page: II-6.)



SAND 2009-4908 P

Issued by Sandia National Laboratories, Albuquerque, New Mexico, USA for the US National Nuclear Security Administration (NNSA) Office of Research & Development for National Security Science & Technology, NA-121.

Sandia is a multiprogram laboratory operated by Sandia Corporation, a Lockheed Martin Company, for the United States Department of Energy's National Nuclear Security Administration under contract DE-AC04-94AL85000.

Advances in **MATERIALS SCIENCE**

Dr. Dimitri Kusnezov

*Director of the Office of Research & Development for
National Security Science & Technology
National Nuclear Security Administration (NNSA), USA*

Dr. Oleg Nikandrovich Shubin

*Department for the Nuclear Munitions
Development & Testing and Defense Power Facilities
Rosatom, Russia*

August 2009

Foreword

Materials Science today is at a watershed. We have achieved remarkable computational capabilities, with the ability to simulate macroscopic samples of complex materials from inter-atomic interactions — trillions or more atoms with realistic potentials. Furthermore, experimental facilities are allowing remarkable visibility into dynamics at the quantum scale, such as femtosecond resolution through ultrafast optical techniques. Experimental, theoretical, and computational methods are evolving in such a manner that we are able to address novel issues in not only the understanding of materials, but more interestingly, the design of new materials that meet specific needs, and their responses in unusual environments or to phase transitions.

While research in materials properties is conducted worldwide, national scientific and research institutions still maintain unique roles in certain frontier areas that are tied to national missions such as energy or nuclear security. In that respect, the United States and the Russian Federation have been working together to define common interests and the opportunities that would ensue.

The articles in this volume represent ongoing cooperative research in materials science in both countries, as well as some new directions for future collaborative efforts. During their meetings in Spring 2009, U.S. President Barack Obama and Russian President Dmitry Medvedev expressed their desire in a joint statement¹ that cooperation of this nature continue: "...we also discussed the desire for greater cooperation not only between our governments, but also between our societies — more scientific cooperation..." This book represents a step towards these goals and lays the framework for the greater societal cooperation the presidents have discussed. It is our hope that this collection will be technically useful and serve as a milestone along the path of greater societal cooperation in a wide range of areas.

Dimitri Kusnezov

*Director of the Office of Research & Development for National Security Science & Technology
National Nuclear Security Administration (NNSA), USA*

Oleg Shubin

*Department for the Nuclear Munitions Development & Testing and Defense Power Facilities
Rosatom, Russia*

Prague, August 2009

¹See Appendix A for full text.

Acknowledgements

Like a well choreographed play, this document is an amalgam of international research representing diverse elements of materials science. It is both carefully structured and visually balanced. It reflects a variety of knowledge and effort expended by Russian and U.S. experts in materials sciences; simultaneously it is a credit to the managers who oversee such talent, sponsors who support such efforts with wisdom with diplomacy, and the ones who envision and produce a unified polished product. We applaud all for their skill, dedication and perseverance.

The tapestry of research represented in this volume has been performed at eight institutions within Russia and the U.S. The purpose and importance of research in each section is described by a leading expert. We acknowledge their insight as well as the results shared by the researchers and scientists.

Section I lead: Dr. Brandon Chung, Lawrence Livermore National Laboratory

Section II lead: Dr. A. V. Mirmilstein, VNIITF

Section III lead: Dr. Genri Norman, JIHT

Section IV lead: Dr. John Aidun, Sandia National Laboratories

Section V lead: Dr. Olga N. Ignatova, VNIIEF

Section VI lead: Dr. Alexander Belyaev, IPME

Section VII lead: Dr. Marvin (Tony) Zocher, Los Alamos National Laboratory

Supporting these individuals are the following whose commitment, support and patience also deserve special gratitude.

Russia – Dr. Oleg Shubin, Rosatom; Dr. V. P. Solovyev, VNIIEF; Dr. Olga Vorontsova, VNIIEF; Dr. Mikhail Avramenko, VNIITF; Dr. Lada Talantova, VNIITF; Dr. Andrey Sviridov, VNIIA; Dr. Alexey Sokovishin, VNIIA; Dr. Dimitri Indeitsev, IPME; Dr. Alexander Belyaev, IPME; Dr. Genri Norman, JIHT.

US – Dr. Dimitri Kusnezov, National Nuclear Security Administration (NNSA); Dr. Tom Bickel, Sandia; Dr. John Maenchen, Sandia; Dr. Stephen Folies, Sandia; Dr. Elizabeth Holm, Sandia; Dr. Robert Reinovsky, Los Alamos; Dr. M. Zocher, Los Alamos; Dr. Oleg Schilling, Lawrence Livermore.

And finally the envisioning and execution of this cohesive document is the product of the publishing team:

Reeta Garber, Managing Editor, Sandia National Laboratories

Phillip Brittenham, Copy Editor, Sandia National Laboratories

Barbara Haschke, Proofreading, KTech, Albuquerque, New Mexico, USA

Douglas Prout, Designer, Technically Write, Albuquerque, New Mexico, USA.

Contents

Section I: Aging of Materials

- I-2 Modeling of Plutonium Aging (VNIITF)
- I-7 Spectroscopic Signature of Aging in δ -Pu(Ga) (LLNL)
- I-10 Modeling the Aging and Reliability of Solder Joints (SNL)
- I-15 Polymer Material Thermal Decomposition Model with Intensive Decomposition Area (VNIIA)
- I-20 Experimental Characterization of Foams in Fire Environments (SNL)
- I-25 Numerical Modeling of Heat Transfer in Foams in Fire Environments (SNL)
- I-30 Study of Mineral Oil Aging Related to Design Materials of a Neutron Generator (VNIIA)

Section II: Computational Methods and Radiation Effects

- II-2 Accurate Prediction of Dynamic Fracture with Peridynamics (SNL)
- II-8 Molecular Dynamic Simulation of Thermodynamic and Mechanical Properties and Behavior of Materials at High Strain Rate (VNIITF)
- II-13 Challenges of, and Variations on, Coupled Atomistic-Continuum Simulation (SNL)
- II-19 Density and Nonideality Effects in Plasmas (JIHT)
- II-25 Self-Diffusion in Mo Using the AM05 Density Functional (SNL)
- II-30 Thermomechanical Effects in Perfect Crystals with Arbitrary Multibody Potential (IPME)
- II-35 Electrical Effects of Ionizing Radiation of Insulating Materials (SNL)
- II-39 Strongly Coupled Plasma Nanochannel Created by a Fast Single Ion in Condensed Matter (JIHT)
- II-45 Molecular Dynamics Simulations of Displacement Cascades in GaAs (SNL)

Section III: Materials Properties and Failure

- III-2 Modeling Coupled Interaction Between Crack Growth, Diffusion, and Chemical Reactions (IPME)
- III-7 Influence of Defects Type and Chemical Reaction on Fracture Initiation, Molecular Dynamics Study (IPME)
- III-12 Determination of the Small Hydrogen Traps as Nucleus of Fatigue and Destruction (IPME)
- III-17 First Principles Study of Site Occupation and Migration of Helium in β -phase Erbium Hydride (SNL)
- III-21 Theoretical Model for the Hydrogen-Material Interaction as a Basis for Prediction of the Material Mechanical Properties (IPME)
- III-26 Properties Research of Chemically Deposited Nickel Coatings Modified with Nano Diamonds (VNIIA)
- III-31 Evolving Metallurgical Behaviors in Plutonium from Self-Irradiation (LLNL)
- III-34 Isochronal Annealing of Radiation Damage in α - and δ -Pu Alloys (LLNL)

Section IV: Deformation and Computational Methods

- IV-2 Structural Changes in Metals Under High-Rate Deformation (VNIIEF)
- IV-6 Spall and Shear Fractures in the Spherically Converging Shells of Iron and Steels: Measurements of Energy and Residual Strains (VNIITF)
- IV-12 DFT Studies of Electronic Excitation Effects: Crystal Lattice Stability, Non-Adiabatic Transitions (JIHT)
- IV-16 Study of the Volume-Collapse Phase Transitions in F-Electron Materials (VNIITF)
- IV-21 Method of Cluster Dynamics for Simulation of Dynamic Processes of Continuum Mechanics (VNIIEF)
- IV-30 Spiked Alloy Production for Accelerated Aging of Plutonium (LLNL)

Contents

Section V: Materials Response to Dynamic Loading I

- V-2 Thermal Fluctuation Model of Plastic Flow (LANL)
- V-4 A Wide-Range Equation of State of Water (VNIITF)
- V-9 On the Universal Behavior of Some Organic Compounds Under Compression (VNIIEF)
- V-15 Shock-Induced Plasticity in Al, Cu, and Al-Cu Alloys (JIHT)
- V-20 Static Material Strength Determined Using a DAC (LLNL)
- V-24 Wide-Range High-Strain-Rate Shear Strength Model for Metals (VNIIEF)
- V-29 Measurement of Sound Velocities in Shock-Compressed Tin Under Pressures up to 150 GPa (VNIIEF)
- V-34 Determination of Longitudinal and Bulk Sound Velocities in Natural Uranium Under Shock-Wave Loading (VNIIEF)

Section VI: Materials Response to Dynamic Loading II

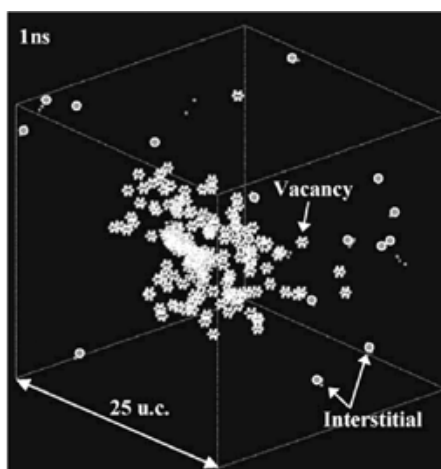
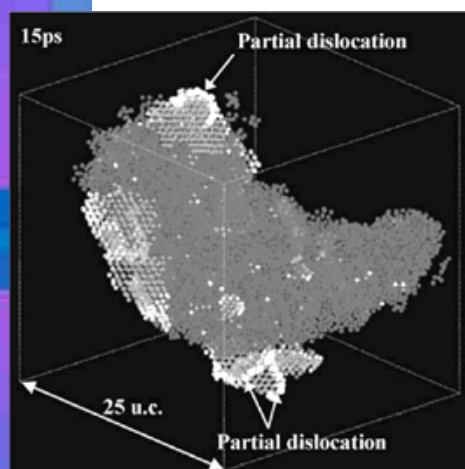
- VI-2 Models of Fracture from Atomistic Simulations (JIHT)
- VI-7 Modeling the Interconnections Between a Structural Transformation Front and a Growing Crack (IPME)
- VI-12 FEM Simulation of Fatigue Damage, Crack Nucleation, and Growth in a Pre-Damaged Material (IPME)
- VI-17 Solid-State Rayleigh-Taylor Experiments in Vanadium at Mbar Pressures at the Omega Laser (LLNL)
- VI-22 Influence of Dynamic Properties on Perturbation Growth in Tantalum (VNIIEF)
- VI-27 Calculation of Sound Speed behind the Shock Wave Front for Various Materials and Comparison with Experimental Data (VNIIEF)
- VI-34 Deviatoric Constitutive Model: Domain of Strain Rate Validity (LANL)
- VI-38 Modeling and Simulation of the Thermo-Acousto-Elastic Waves in Solids of Complex Rheology (IPME)
- VI-43 Accurate Direct Eulerian Simulation of Dynamic Elastic-Plastic Flow (LANL)

Section VII: Materials Response to Dynamic Loading III

- VII-2 Simulation of Ce Response to Dynamic Loading (VNIITF)
- VII-7 Predictions from the Equation of State of Cerium Yield Interesting Insights into Experimental Results (LANL)
- VII-11 Features of Cerium Compressibility and Spall Strength in the (γ - α) Phase—Transformation Region Under Explosive Loading (VNIITF)
- VII-16 Study of Phase Transitions in Cerium and Titanium by PVDF Gauge (VNIIEF)
- VII-20 Atomistic Modeling of Microstructure Influence on the Spall Strength (JIHT)
- VII-24 Effect of Shock Wave and Quasi-isentropic Loading on the Shear and Spalling Strength of Metals with Natural and Microcrystalline Structure (VNIIEF)
- VII-29 Spall Fracture and Compaction in Natural Uranium Under Shock-Wave Loading (VNIIEF)

Appendix A

Aging of MATERIALS



(Left) Melted region and plastic deformation in δ -Pu. Initial temperature 600 K. Dark grey is for the disordered structure (melted region), light grey is for stacking faults, and white is for partial dislocations. (Right) Residual point-like defects: white encircled spheres are interstitials and stars are vacancies.

A central theme of this section is the need to understand and predict the aging and stability of materials under diverse conditions that are of mutual interest to material scientists from the United States nuclear weapons laboratories and Russian Federation institutes. Linking how material ages and how the material performs is an enormous technical challenge. This section comprises seven articles that highlight recent advances in which experimental physical, chemical, and electronic properties of materials are directly linked to modeling or simulation. Articles by Dremov et al. and Tobin et al. discuss effects of aging upon plutonium properties. The article by Holm et al. discusses the unified creep plasticity and smeared crack models to predict the lifetime of solder joints. In their article, Sirenko and Egorova present the mathematical model capable of describing the PUF and fiberglass thermogravimetric behaviors. The next two articles, by Erikson et al. and Hogan et al., discuss the physical behavior and thermal response model of removable epoxy and hybrid foams in fire environments. The last article by Sokovishin et al. describes engineering approaches to estimate mineral oil compatibility with design materials of the neutron generator.

Brandon W. Chung, Lawrence Livermore National Laboratory, Livermore, CA, 94551 USA.

Section I:

- I-2 Modeling of Plutonium Aging (VNIITF)
- I-7 Spectroscopic Signature of Aging in δ -Pu(Ga) (LLNL)
- I-10 Modeling the Aging and Reliability of Solder Joints (SNL)
- I-15 Polymer Material Thermal Decomposition Model with Intensive Decomposition Area (VNIIA)
- I-20 Experimental Characterization of Foams in Fire Environments (SNL)
- I-25 Numerical Modeling of Heat Transfer in Foams in Fire Environments (SNL)
- I-30 Study of Mineral Oil Aging Related to Design Materials of a Neutron Generator (VNIIA)

MODELING OF PLUTONIUM AGING

V. Dremov,* A. Karavaev,* F. Sapozhnikov, M. Vorobyova,* G. Ionov,* V. Anisimov,† M. Korotin,†
A. Shorikov,† M. Zocher,†† D. Preston††

*Russian Federal Nuclear Center – Zababakhin Institute of Applied Physics, Snezhinsk 456770, Russia

† Institute of Metal Physics, Ural Division of RAS, Yekaterinburg 620219, Russia

††Los Alamos National Laboratory, Los Alamos, NM 87545 USA

We present a brief overview of results obtained in our MD and ab initio investigation focused on the problem of Pu aging. The investigation included modeling of the evolution of damage cascades in self-irradiated unalloyed and gallium-alloyed δ -Pu, the evaluation of helium atom interaction with Pu lattice, helium bubble properties, and mobility of defects, as well as possible effects of aging upon thermodynamic, mechanical, and magnetic properties of plutonium.

Introduction

The aging of actinides (i.e., the change of their properties with time due to self-irradiation) is caused by the accumulation of radiation defects and decay products in the bulk of the material. Investigation into this complicated problem may be addressed to molecular dynamics (MD) because this approach gives detailed information on the micro-scale structures and processes. Presenting this brief overview of theoretical results obtained in recent years, we should say that our investigation in this direction continues in close collaboration with our colleagues from LANL and LLNL through lab-to-lab contracts. The main issues for future consideration are phase stability and the effect of aging on it, construction of a potential for the low-symmetry monoclinic α -phase, peculiarities of radiation damages and their effects on the properties of α -phase, and updating the model of defects accumulation.

Radiation Damage

The radioactive decay of Pu generates high-energy particles of U (86 keV) and He (5 MeV), producing numerous damages when decelerating in the bulk of the material. We consider the process to consist of fast and slow stages. The fast stage lasts while particle energies are several times greater than the assumed displacement energy. This stage is simulated with the Monte Carlo (MC) method. The slow stage is characterized by the absence of new displacements caused by high-energy atoms, and the system evolves in the time scale of thermal relaxation. This stage is described by the MD technique. The Modified Embedded Atom Model (MEAM) developed for Pu and Pu-Ga alloys [1,2] was used to describe the interatomic interaction. Calculations were carried out for pure δ -Pu and a Ga (1 wt%) stabilized δ -Pu alloy. The combination of MC and MD techniques allows us, on the one hand, to take into account inelastic scattering and energy losses of high-energy particles and to eliminate shortcomings of the MEAM when interatomic distances are small and, on the other hand, to track the cascade evolution in time. Using MC instead of the full MD treatment with the adequate short range potential makes it much easier to gather statistics and to obtain the averaged characteristics of the cascades.

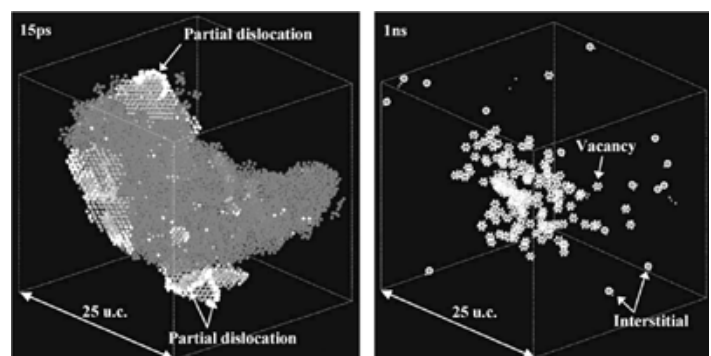


Figure 1. (Left) Melted region and plastic deformation in δ -Pu. Initial temperature 600 K. Dark gray is for the disordered structure (melted region), light gray is for stacking faults, and white is for partial dislocations. (Right) Residual point-like defects: white encircled spheres are interstitials and stars are vacancies (the figure was taken from [1]).

The simulations have shown [3,4] that the formation of the amorphous (melted) region is proper to the U cascade evolution in pure and alloyed Pu. Rapid recrystallization leaves point-like defects only (Figure1). The number of residual point defects (250 vacancies + 250 interstitials) is an order of magnitude smaller than the number of Frenkel pairs (~2500) formed during the fast (MC) stage.

It has been shown that accounting for only lattice heat conductivity leads to a melted region that measures ~25,000 and ~18,000 atoms for the initial temperatures of 600 K and 300 K, respectively. If electron-phonon coupling is taken into account, the corresponding numbers are ~17,000 and ~12,000. Assuming that the melted region includes ~12,000 atoms in the sample at initial temperature $T = 300$ K and the half-life period of Pu is 24,000 years, it is easy to estimate that it will take the whole sample about 2 to 3 years to completely melt and recrystallize.

Modeling Helium Bubbles

DFT and MD were used to investigate the dynamics of interaction between He and δ -Pu in a α -Pu lattice that has undergone self-irradiation damage. This effort included investigation into the dynamics of atomic He and the dynamics of an isolated He bubble [5]. Gaining a better understanding of these dynamical processes is of critical importance if we are to successfully predict the process of aging and the consequences thereof.

To do MD simulations, we needed three interatomic potentials: Pu-Pu, Pu-He, and He-He. The Pu-Pu and He-He interaction potentials were taken from the literature. A new potential (of the exp-6 variety) was developed for the Pu-He interaction. In order to develop the exp-6 Pu-He interaction potential, two sets of DFT calculations (one based on the generalized gradient approximation of the exchange-correlation potential and the other on the local density approximation) were carried out to assess the relief in the energy field associated with the presence of atomic He at various locations in an otherwise pristine δ -Pu lattice. The exp-6 potential was fit to the DFT-generated energy relief fields. It was observed that the exp-6 potential developed using the LDA results was stiffer and a better match to previously reported results. As a consequence, the exp-6 Pu-He potential ultimately selected for use in the MD simulations was the one based on the LDA results.

MD simulations investigating the dynamics of atomic He in a Pu lattice were carried out using the aforementioned interatomic potentials. Two sets of MD simulations were conducted. In the first set of calculations, atomic He was placed at a tetrahedral interstitial site, and MD was used to monitor the overall dynamics of the Pu-He system as it sought to minimize its aggregate energy state. It was observed that the dynamical process proceeds as follows. First, the He atom displaces the nearest Pu atom from its lattice site and takes up residence at this location. This sets up a chain reaction, wherein the displaced Pu atom displaces a neighboring Pu atom from its lattice site (and takes up residence at this location), and so on. The rate at which this process proceeds (split interstitial diffusion rate) has been calculated. In the second set of calculations, the dynamics of a cluster of He atoms (nine atoms) is investigated. The simulation commences with an He atom located at a lattice vacancy with the eight remaining He atoms situated at adjacent tetrahedral pores. A complex dynamical process ensues wherein four of the He atoms located at tetrahedral sites set up split interstitial chain reactions similar to the one just described, four of the He atoms remain in the vicinity of the original vacancy, and the ninth He atom migrates further into the lattice (where it too eventually sets up a split interstitial chain reaction).

MD simulations of an isolated He bubble were also carried out. The selection of bubble size and He-to-vacancy ratio was made with consideration given to experimental observations of actual bubbles in aged Pu. With respect to He-to-vacancy ratio, we chose to make the focus of our investigation the ratio of 3:1. This particular ratio is interesting for two reasons: (1) it is near the upper end of the observed range of this quantity in aged Pu and (2) previously reported MD simulations seemed to reveal an instability at this ratio. It is demonstrated herein that an He bubble with a 3:1 He-to-vacancy ratio is indeed stable (in keeping with experimental observations, but at

odds with the previously reported set of MD simulations). Our simulations show that an instability that is apparent at early time is in reality a transient phase, at the end of which spatial and temporal stability becomes manifest. We surmise that the previously reported instability was indeed erroneous and resulted naturally as a consequence of not continuing the calculation far enough in time. In addition to investigations concerning bubble size and stability, simulations were conducted to predict long-term bubble shape. Preliminary observations seem to indicate that a bubble that starts off roughly spherical in shape will over time take on a more tetrahedral character.

Mobility of Defects and Defects Accumulation Model

Characterization of thermodynamic and mechanical properties of materials as dependent upon alloying additions and defects concentration requires a model of defects accumulation due to self-irradiation. To construct the model one needs: (1) the data on types and the number of defects produced in collision cascades and (2) the data on the mobility of defects.

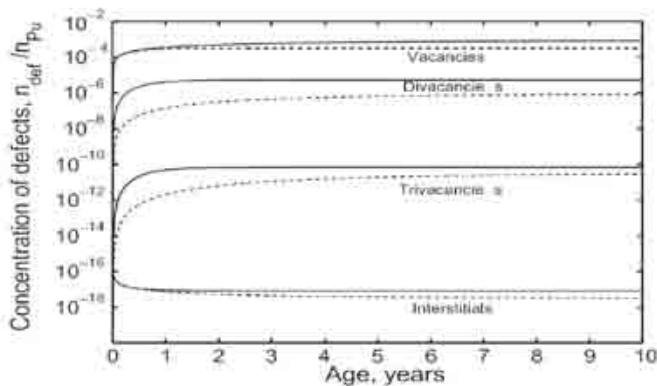


Figure 2. Evolution of primary radiation defects with time at $T = 300$ K. Solid and dashed lines correspond to different values of vacancy migration activation energy. The figure was taken from [7].

The results of damage cascade simulation (see Radiation Damage above) provide us with the rate of defects production or the source of primary radiation defects. To construct a model of defects evolution one needs data on defect mobility. Partially, this information is given in [6] regarding the vacancy, di-vacancy, and di-vacancy dissociation. In [7], we added the data on self-interstitial, tri-vacancy and the dissociation of the latter. In [7], a tentative radiation defect accumulation model that includes the above defects and accounts for grain size was constructed, and the evolution of defect concentrations with time was evaluated (Figure 2).

Plutonium Properties Affected by Aging

Theoretical data on the time evolution of primary radiation defects [7] agree with experimental data on changes in plutonium properties during the first years of storage [8]. Ref. [8] provides experimental results on changes in the volume of PuGa (2 at.% Ga) samples in aging. These results were obtained with the use of accelerated aging. Pu-238 (7.38 at.%) was added to the alloy and self-irradiation proceeded ~ 22 times faster. Figure 3 depicts dilatometry measurements from [8]. For all samples and measurement temperatures, the initial period of volume increasing is seen to be ~ 3 to 4 years; then the curve flattens out with a weak linear growth associated with the constant rate of helium accumulation. The dashed line in Figure 3 shows the relative change in volume evaluated in this work in the assumption that it equals the relative concentration of vacancies. It is, of course, an upper estimate because we assumed all interstitials that were absorbed by the grain boundary were built into the structure without changes in density. Figure 4 compares changes in density with time, obtained experimentally through dilatometry and immersion measurements for different plutonium samples and predicted by the model proposed.

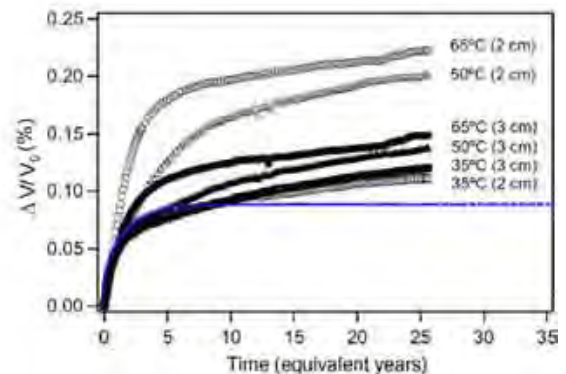


Figure 3. Relative change in the volume of Pu-238 enriched PuGa [8]. Time is measured in equivalent years. Measurements were done for two samples (2 and 3 cm) held at different temperatures. According to [8], data for 35°C are most reliable because surface effects at this temperature are weak and results for 2-cm and 3-cm samples coincide (see [8] for details). The dashed line shows calculations with the model proposed in [7].

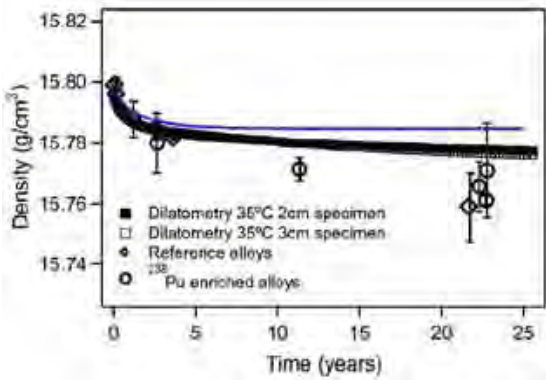


Figure 4. Density changes: dilatometry of the enriched plutonium sample (35°C), immersion of naturally aged and Pu-238 enriched samples (the data are taken from [8]). The dashed line shows calculations with the model proposed in [7].

This volumetric change is known as transient reverse expansion (i.e., it can be eliminated by annealing that reduces the equilibrium concentration of defects). The proposed model of defect accumulation is capable of simulating annealing using the constructed dependence of defect mobility on temperature. According to the model, it takes primary radiation defects about 2 h to anneal at $\sim 220^\circ\text{C}$. During this time, the concentration of defects reduces from $\sim 0.1\%$ to $\sim 0.00001\%$. This is also in agreement with the known experimental evidence that the density changes that occur in the first three years of storage can easily be recovered through annealing at 150 to 200°C .

In the near future, we plan to evaluate in direct MD simulations the effect of defects and helium bubbles on the thermodynamic and mechanical properties and phase stability of δ -Pu.

Defects also affect the magnetic properties of Pu. Results of magnetic properties investigation for pure metallic Pu published in the last years have promoted the idea of the nonmagnetic ground state of Pu in δ - and α -phases. However, it is difficult to accept the statement about the absence of magnetism in Pu, since available Pu samples always demonstrate the traces of magnetic interactions. The results of ab initio calculations [9] argue for formation of magnetism due to the presence of defects. For the investigation, the so called $LDA+U+SO$ band structure calculation method was used. It is based on the Local Density Approximation (LDA), including Coulomb (U) and Spin-Orbit coupling (SO) in generalized matrix form. This modification of the standard LDA is caused by the comparable strength of exchange and spin-orbit interactions in actinides. A supercell consisting of 32 Pu atoms originally arranged in FCC lattice plus interstitial Pu impurity in one of the octa-holes plus vacancy in

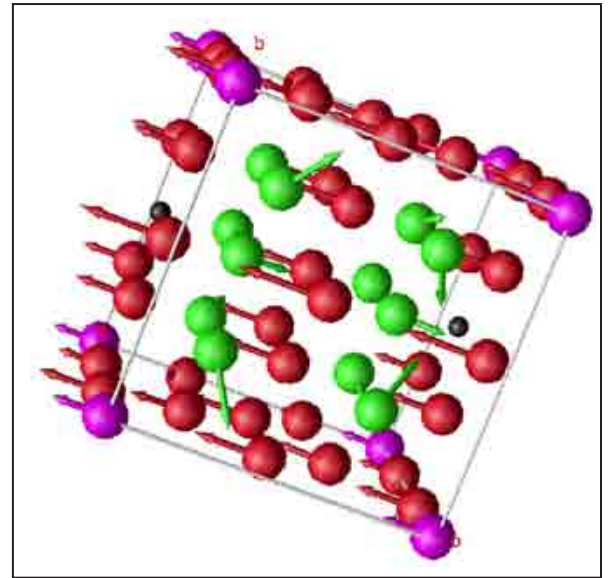


Figure 5. Calculated magnetic structure of Pu supercell with the interstitial atom (magenta balls) and the vacancy (black ball). Arrows show direction of J ; the greens and reds correspond to different signs of J_z component.

the third coordination sphere of the impurity was constructed and relaxed with the use of molecular dynamics technique with MEAM potential. The result is that the presence of the interstitial and the vacancy leads to the appearance of weak magnetism. This result agrees well with the experimental data [10] on magnetic moments in aged Pu, which disappear after annealing. An interstitial and a vacancy influence magnetic moments in different ways—the interstitial alone forms a ferromagnetic order close to AFM type A, but the vacancy alone forms the order of AFM type C. Acting simultaneously, they produce the noncollinear magnetic structure (Figure 5). Keeping in mind the structure of the primary radiation defect (see the previous section), one may predict that during the first 3 to 4 years of aging, Pu will gain magnetic properties proper to AFM type C.

References

- [1] M. I. Baskes, “Atomistic model of plutonium,” *Phys. Rev. B* **62** 15532 (2000).
- [2] M. I. Baskes, A. C. Lawson, S. M. Valone, “Lattice vibrations in δ -plutonium: Molecular dynamics calculation,” *Phys. Rev. B* **72** 014129 (2005).
- [3] V. V. Dremov, F. A. Sapozhnikov, S. I. Samarin, D. G. Modestov, N. E. Chizhkova, “Monte Carlo + molecular dynamics modeling of radiation damages in Pu,” *J. Alloys Comp.*, **444-445** 197-201 (2007).
- [4] V. V. Dremov and S. I. Samarin, “A hybrid model of primary radiation damage in crystals,” *J. Nuc. Mat.* **385**, Issue 1, 83–87 (2009).
- [5] V. V. Dremov, A. L. Kutevov, F. A. Sapozhnikov, V. I. Anisimov, M. A. Korotin, A. O. Shorikov, D.L. Preston, M.A. Zocher, “Atomistic simulations of helium dynamics in a plutonium lattice,” *Phys. Rev. B* **77** 224306 (2008).
- [6] B. P. Uberuaga, S. M. Valone, and M. I. Baskes, “Accelerated dynamics study of vacancy mobility in δ -plutonium,” *J. Alloys Comp.* **444-445** 314 (2007).
- [7] V. V. Dremov, A. V. Karvaev, S. I. Samarin, F. A. Sapozhnikov, M. A. Zocher, D. L. Preston, “Molecular dynamics characterization of thermodynamic and mechanical properties of Pu as dependent upon alloying additions and defects concentration. Part I,” *J. Nuc. Mat.* **385** 79-82 (2009).
- [8] B. W. Chung, S. R. Thompson, C. H. Woods, D. J. Hopkins, W. H. Gourdin, B. B. Ebbinghaus, “Density changes in plutonium observed from accelerated aging using Pu-238 enrichment,” *J. Nuc. Mat.* **355** 142 (2006).
- [9] M. A. Korotin, A. O. Shorikov, V. I. Anisimov, V. V. Dremov, P. A. Sapozhnikov, “Influence of interstitial impurity and vacancy on δ -Pu magnetic state: Ab-initio investigation,” *Proceedings of 6th US/Russian Workshop on Fundamentals of Pu Science* (2006) pp. 59-60.
- [10] S. K. McCall, M. J. Fluss, B. W. Chung, M. W. McElfresh, D. D. Jackson, G. F. Chapline, “Emergent magnetic moments produced by self-damage in plutonium,” *Proceedings of National Academy of Sciences* **103** (2006) pp. 17179–17183.

SPECTROSCOPIC SIGNATURE OF AGING IN δ -Pu(Ga)

J. G. Tobin, S.-W. Yu, B. W. Chung

Lawrence Livermore National Laboratory, Livermore, CA, USA 94550

The electronic structure of Pu is briefly discussed, with emphasis upon aging effects.

Introduction: Pu Electronic Structure

Photoelectron Spectroscopy [1,2] and X-ray Absorption Spectroscopy [2,3,4] have contributed greatly to our improved understanding of Pu electronic structure (Figure 1). From these and related measurements, the following have been determined:

1. The Pu 5f spin-orbit splitting is large.
2. The number of Pu 5f electrons is 5.
3. The Pu 5f spin-orbit splitting effect dominates 5f itinerancy.

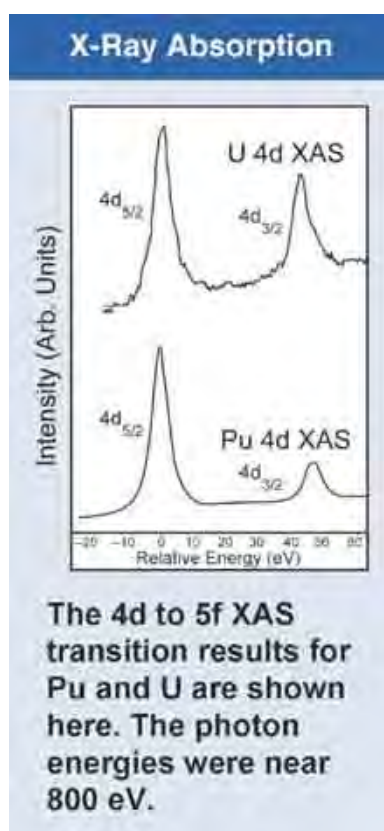


Figure 1. X-ray absorption spectra (XAS) of alpha-U and alpha-Pu

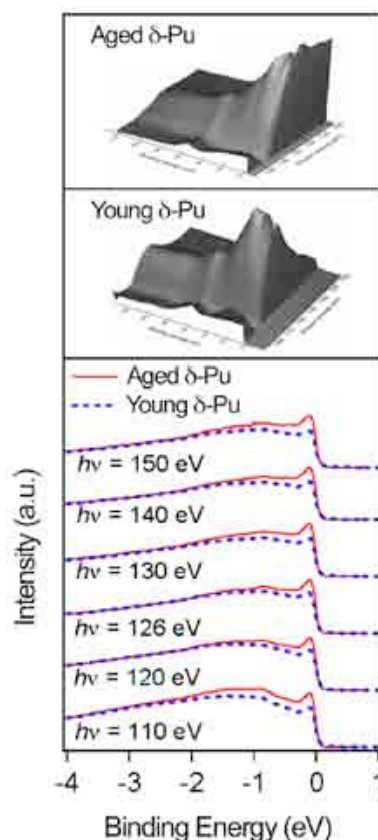


Figure 2. Resonant photoemission of young and aged delta-Pu

Past Method: Resonant Photoemission

Resonant Photoemission, a variant of Photoelectron Spectroscopy, has been demonstrated to have a sensitivity to aging in Pu samples (Figure 2). The spectroscopic results have been correlated with resistivity measurements and shown to be the fingerprint of mesoscopic or nanoscale internal damage in the Pu physical structure. This means that a spectroscopic signature of internal damage due to aging in Pu has been established [5].

Discussion: Present State

Significant questions remain concerning the nature of Pu electronic structure. Perhaps, the missing piece of the puzzle is the direct experimental determination of the unoccupied electronic structure using high-energy inverse photoelectron spectroscopy (Figure 3) or Bremsstrahlung Isochromat Spectroscopy (BIS) [6].

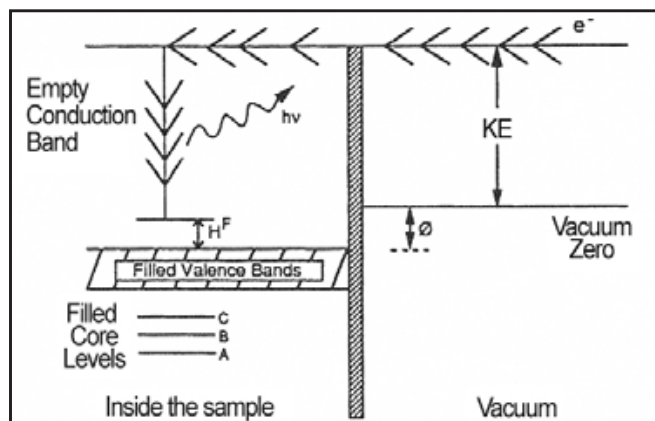


Figure 3. Schematic of the inverse photoelectron process. KE is kinetic energy of the incoming electron, ϕ is the work function, H^F is the energy of the state relative to the Fermi Level, and $h\nu$ is the energy of the emitted electron. A defining characteristic of IPES/BIS is that $h\nu \approx KE$.

Past BIS studies of Th and U indicate the feasibility and utility of Pu studies [7], as confirmed by our simulations shown in Figure 4 [6].

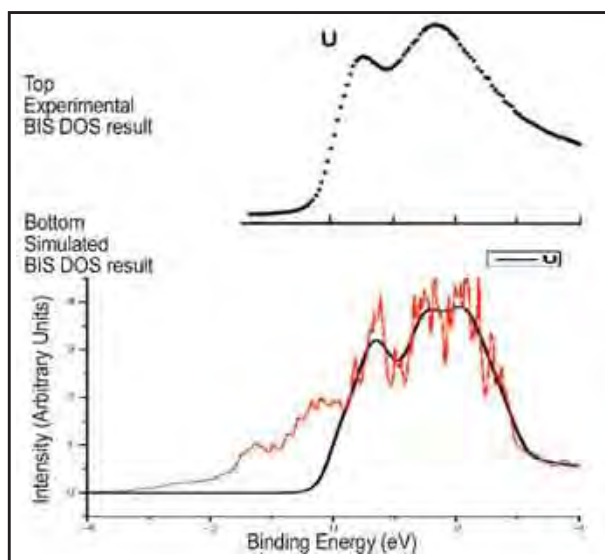


Figure 4. This is a comparison of an earlier BIS measurement by Baer and Lang [7] of uranium with a simulated Density of States generated by starting with a calculation by Kutepov (in red) [4], which is the truncated at the Fermi Energy (only unoccupied states can contribute to BIS) and then smoothed to reflect broadening from the instrumental band-pass (in black) [8]. Top: Experimental BIS result of Baer and Lang. Bottom: Red: DOS calculations by A. L. Kutepov; Black: DOS calculation times inverse Fermi function, with some instrumental broadening [8].

Conclusions: Future Directions

A new BIS capability has been developed in our laboratory [6] (Figure 5). Electron stimulated emission of photons has been carried out using the XES-350 monochromator and detector system.

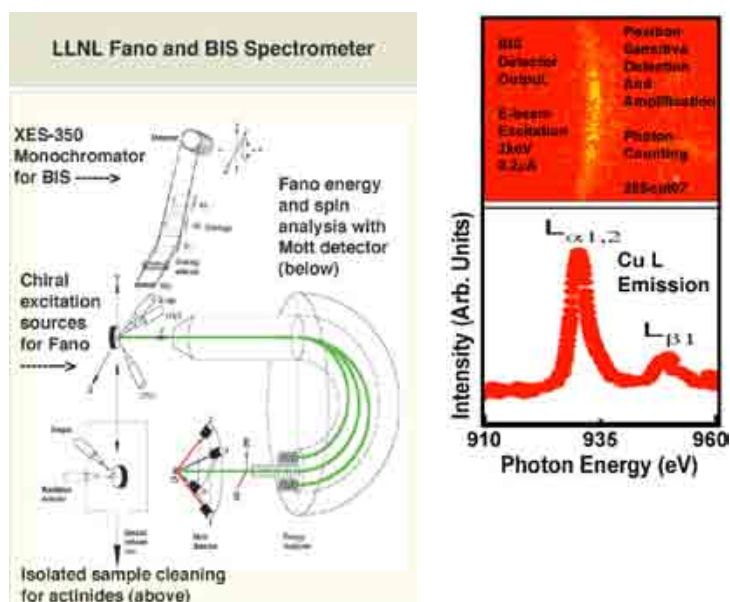


Figure 5. Left: Sketch for BIS and spin resolved photoelectron spectroscopy (SRPES) experimental setup installed recently at Lawrence Livermore National Laboratory for the electronic structure study of actinides. For BIS, the detection of the photons is performed with the XES-350 monochromator and multi-channel detector. For SRPES, unpolarized light hits sample at an angle of 45 degrees with respect to the surface normal. The energies and the spins of the normally emitted photoelectrons are analyzed by hemispherical electron energy analyzer and Mott detector, which has a thorium target operated at 25 keV with Sherman function of 0.16 ± 0.04 , respectively. Two transversal spin components P_X and P_Y can be measured in Mott detector simultaneously. Right: X-ray Emission Spectroscopy (XES) of Cu using an electron excitation beam of $E = 3000\text{eV}$.

Acknowledgements

This work was performed under the auspices of the U.S. Department of Energy by the University of California Lawrence Livermore National Laboratory under contract No. W-7405-Eng-48. Work that was performed by LLNL personnel was supported in part by the Office of Basic Energy Science at the U.S. Department of Energy and WCI.

This article was based upon UCRL-ABS-411058.

References

- [1] J. G. Tobin, B. W. Chung, R. K. Schulze, J. Terry, J. D. Farr, D. K. Shuh, K. Heinzelman, E. Rotenberg, G. D. Waddill, G. Van der Laan, "Resonant photoemission in f-electron systems: Pu and Gd," *Phys. Rev. B* **68** 155109 (2003).
- [2] J. G. Tobin, P. Söderlind, A. Landa, K. T. Moore, A. J. Schwartz, B. W. Chung, M. A. Wall, J. M. Wills, R. G. Haire, A. L. Kutepov, "On the electronic configuration in Pu: Spectroscopy and Theory," *J. Phys. Cond. Matter* **20** 125204 (2008); K. T. Moore, M. A. Wall, A. J. Schwartz, B. W. Chung, D. K. Shuh, R. K. Schulze, and J. G. Tobin, "The failure of Russell-Saunders coupling in the 5f states of Plutonium," *Phys. Rev. Lett.* **90** 196404 (2003).
- [3] G. van der Laan, K. T. Moore, J. G. Tobin, B. W. Chung, M. A. Wall, A. J. Schwartz, "Applicability of the spin-orbit sum rule for the actinide 5f states," *Phys. Rev. Lett.* **93** 097401 (2004).
- [4] J. G. Tobin, K. T. Moore, B. W. Chung, M. A. Wall, A. J. Schwartz, G. van der Laan, A. L. Kutepov, "Competition between delocalization and spin-orbit splitting in the actinide 5f states," *Phys. Rev. B* **72** 085109 (August 2005).
- [5] B. W. Chung, A. J. Schwartz, B. B. Ebbinghaus, M. J. Fluss, J. J. Haslam, K. J. M. Blobaum, J. G. Tobin, "Spectroscopic signature of aging in δ -Pu(Ga)," *J. Phys. Soc. Japan* **75** 5 054710 (2005).
- [6] J. G. Tobin, S. W. Yu, B. W. Chung, G. D. Waddill, A. L. Kutepov, "Soft X-ray Studies of Pu Electronic Structure: Past Lessons and Future Directions with BIS," *Proceedings of the XAS Actinides Meeting*, St. Aubin, France, July 2008, submitted to OECD Nuclear Energy Agency (NEA, France).
- [7] Y. Baer and J. K. Lang, *Phys. Rev B* **21** 2060 (1980).
- [8] M. T. Butterfield, J. G. Tobin, N. E. Teslich, Jr, R. A. Bliss, M. A. Wall, A. K. McMahan, B. W. Chung, A. J. Schwartz, A. L. Kutepov, "Utilizing nano-focussed Bremstrahlung Isochromat Spectroscopy (nBIS) to determine the unoccupied electronic structure of Pu," *Mater. Res. Soc. Symp. Proceedings* **893** 95 (2006).

MODELING THE AGING AND RELIABILITY OF SOLDER JOINTS

E. A. Holm, M. K. Neilsen, P. T. Vianco, A. C. Kilgo

Sandia National Laboratories, Albuquerque, NM 87185-1411 USA

Thermal-mechanical fatigue failure of solder joints is an important reliability issue for electronic circuit boards. In this article, we present a unified creep plasticity model for the cyclic deformation and failure of eutectic Pb-Sn solder joints; this model uniquely includes the effect of the coarsening microstructure on local softening and failure. After a crack initiates, we apply a smeared crack model to simulate crack propagation to an electrical open condition. Both the crack initiation and propagation models are validated using experiments on test vehicle circuit boards. The results of this work can be used in the design of new circuit boards and in the analysis of existing circuit boards.

Introduction

In the circuit boards that pervade modern electronic systems, low melting point solder materials provide the mechanical and electrical connections between the electronic components on the surface of the board and the board itself. Because solders perform at a significant fraction of their melting temperature, their microstructure may evolve during service. Furthermore, differential thermal expansion between the electronic components and the board substrate can place the solder materials under considerable mechanical strain. Finally, typical circuit boards undergo some form of thermal cycling, whether day/night, on/off, or seasonal, which results in the solder joints experiencing thermal-mechanical fatigue.

Typical solder joint failures entail a feedback loop between microstructural evolution and mechanical response. As local strain increases, the microstructure coarsens, which in turn weakens the material locally, driving strain up further. Thermal-mechanical fatigue leads to cracking and finally an open circuit. Typical circuit boards may contain thousands of solder joints, and even one failure can render a circuit board inoperable. Our internal estimates suggest that as many as 48% of electronics failures are due to solder joint failure. Clearly, solder joints are a significant reliability issue, particularly as systems are asked to serve beyond their initial design lifetime or in new, fine-pitch systems where less solder is asked to support more strain.

In order to predict the reliability of both new circuit board designs and existing components, we have developed a suite of models for the aging and failure of solder joints under thermal-mechanical fatigue conditions.

Thermal-Mechanical Fatigue Model

Unified Creep Plasticity Model

Typical approaches [e.g., 1,2,3] for modeling the response of eutectic Sn-Pb solder joints to thermal-mechanical fatigue involve developing finite element models of components with intact solder joints, subjecting these models to one or a few thermal cycles and making lifetime predictions based on some failure criterion. We use this basic framework, but develop our model and our failure criterion with the feedback loop between microstructural coarsening and mechanical response explicitly represented.

For objectivity, our solder model is written using the unrotated Cauchy stress, σ , and unrotated deformation rate, $\dot{\epsilon}$ [4,5]. For small elastic strains, the total strain rate, $\dot{\epsilon}$, can be additively decomposed into elastic, $\dot{\epsilon}^e$, and inelastic (creep + plastic), $\dot{\epsilon}^{in}$, parts as follows:

$$\dot{\boldsymbol{\varepsilon}} = \dot{\boldsymbol{\varepsilon}}^e + \dot{\boldsymbol{\varepsilon}}^{in} \quad (1)$$

We also assume that the elastic response is linear and isotropic such that the stress rate is given by

$$\dot{\boldsymbol{\sigma}} = \mathbf{E} : \dot{\boldsymbol{\varepsilon}}^e = \mathbf{E} : (\dot{\boldsymbol{\varepsilon}} - \dot{\boldsymbol{\varepsilon}}^{in}) \quad (2)$$

where \mathbf{E} is the fourth-order isotropic elasticity tensor. The inelastic strain rate is given by

$$\dot{\boldsymbol{\varepsilon}}^{in} = \frac{3}{2} \dot{\gamma} \mathbf{n} = \frac{3}{2} f(\theta) \left(\frac{\lambda_o}{\lambda} \right)^p \sinh^m \left(\frac{\tau}{\alpha(c + \hat{c})} \right) \mathbf{n} \quad (3)$$

where $\dot{\gamma}$ is a scalar measure of the inelastic strain rate, θ is the temperature in Kelvin. f , p , m , and α are material parameters. λ is a scalar measure of the microstructural coarsening [6] and represents the average diameter of the Pb-rich phase particles. λ_o is the initial lead-rich phase diameter. \mathbf{n} is the normalized stress difference tensor.

$$\mathbf{n} = \frac{\left(\mathbf{s} - \frac{2}{3} \mathbf{B} \right)}{\tau} \quad (4)$$

\mathbf{s} is the stress deviator, \mathbf{B} is the second-order back stress tensor, and τ , the vonMises effective stress difference, is given by

$$\tau = \sqrt{\frac{3}{2} \left(\mathbf{s} - \frac{2}{3} \mathbf{B} \right) : \left(\mathbf{s} - \frac{2}{3} \mathbf{B} \right)} \quad (5)$$

Evolution of the state variable c , which describes the isotropic hardening and recovery, is given by

$$\dot{c} = A_1 \dot{\gamma} - (A_2 \dot{\gamma} + A_3)(c - c_o)^2 \quad (6)$$

where A_1 , A_2 , and A_3 are material parameters. Evolution of the state tensor \mathbf{B} (back stress) is given by

$$\dot{\mathbf{B}} = A_4 \dot{\boldsymbol{\varepsilon}}^{in} - (A_5 \dot{\gamma} + A_6) \sqrt{\left(\frac{2}{3} \mathbf{B} : \mathbf{B} \right)} \mathbf{B} \quad (7)$$

where A_4 , A_5 , and A_6 are material parameters.

The effects of coarsening on the strength are given by the following Hall-Petch type relationship

$$\hat{c} = A_7 \left(\frac{\lambda_o}{\lambda} \right)^{A_8} \quad (8)$$

where A_7 , and A_8 are material parameters. Microstructural coarsening (evolution of the Pb-rich phase particle diameter) is given by [6]

$$\dot{\lambda} = \frac{(A_9 + A_{10} \dot{\gamma})}{(\lambda - \lambda_o)^{A_{11}}} \quad (9)$$

where A_9 , and A_{10} are Arrhenius functions of temperature and A_{11} is a material constant.

Table 1 lists the material parameters currently used for eutectic Sn-Pb solder. Note that flow rate, f , is not restricted to be an Arrhenius function of temperature, and instead the user is free to prescribe the variation in the natural log of f as a function of temperature.

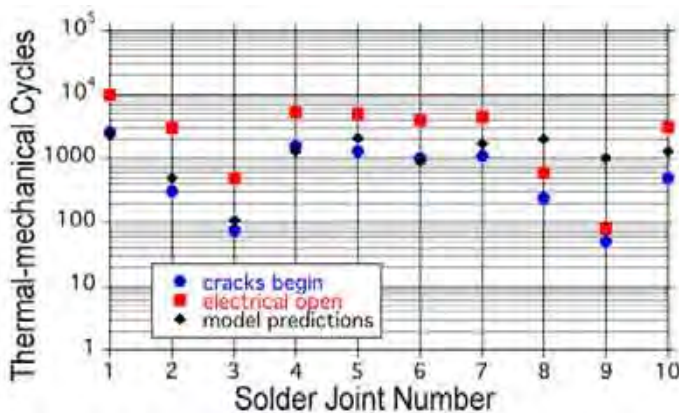
Table 1. Material parameters for Sn63-Pb37 solder

| Temperature (°C) | -55.0 | 20.0 | 125.0 | Temperature (°C) | -55.0 | 20.0 | 125.0 |
|-----------------------------|------------------------|---------|--------|-------------------|-----------------------|-----------------------|-----------------------|
| Shear Modulus (MPa) | 16,198 | 11,872 | 6,126 | A_1 (MPa) | 0.0 | | |
| Bulk Modulus (MPa) | 55,402 | 55,402 | 55,402 | A_2 (1/MPa) | 0.0 | | |
| Thermal Exp. Coef. (1/°C) | 25.0×10^{-6} | | | A_3 (1/MPa-sec) | 0.0 | | |
| Flow Rate * ($\ln(f)$) | -21.540 | -13.225 | -7.168 | A_4 (MPa) | 3351.0 | 2689.4 | 1769.2 |
| Sinh Exponent m | 3.04 | | | A_5 (1/MPa) | 6.385 | 11.788 | 19.587 |
| Grain Exponent p | 3.00 | | | A_6 (1/MPa-sec) | 3.96×10^{-6} | 51.1×10^{-6} | 8.15×10^{-3} |
| Alpha α | 1.00 | 1.00 | 1.00 | A_7 (MPa) | 5.6552 | | |
| Flow Stress c_0 (MPa) | 2.8276 | | | A_8 | 0.50 | | |
| Phase Size λ_0 (mm) | 2.257×10^{-3} | | | $\ln(A_9)$ | -62.1266 | -49.1624 | -39.2210 |
| | | | | $\ln(A_{10})$ | -31.4426 | -27.7545 | -24.9263 |
| | | | | A_{11} | 2.90625 | | |

* $\ln(f)$. f is in Equation 3.

Fatigue Lifetime Predictions

To generate a thermal-mechanical fatigue lifetime prediction, we subject an intact solder joint to one or a few thermal cycles, using the model described above implemented in Sandia's JAS3D finite element code. Because solder does not exhibit a significant amount of strain hardening or recovery, it quickly reaches a steady state in which the strain rate history is constant per cycle. This allows us to forward-integrate the microstructural coarsening rate in order to predict the coarsening parameter λ for the desired number of cycles [7]. We use the microstructural coarsening per cycle in the "worst" solder element to extrapolate the number of thermal cycles



required for the coarsening parameter λ to reach a critical value λ_c . When $\lambda = \lambda_c$, we predict crack initiation in the solder joint.

Figure 1. Comparison of solder lifetime model predictions (diamonds) with experimental results for crack initiation (circles) and electrical open (squares) in ten different solder joints on a test vehicle circuit board.

We validated this approach by comparing our predicted lifetimes (with $\lambda_c = 6 \mu\text{m}$) to an experimental data set of ten different solder joints (surface mount, flat pack, ball grid array, and column grid array) on a test vehicle circuit board subjected to thermal-mechanical fatigue conditions. Both crack initiation and electrical open were observed for each solder joint in the experimental system. Figure 1 shows that our model reproduces the experimental results for crack initiation with good fidelity. (The exceptions were components 8 and 9, where mesh issues were subsequently identified and corrected.) This is particularly impressive because this was a blind study; the experimental results were not known at the time the model predictions were made.

Fracture Model

The experimental results shown in Figure 1 clearly show that crack initiation precedes an electrical open failure, often by thousands of cycles. Because the circuit board generally performs properly until that higher limit is reached, a useful lifetime prediction is the number of cycles to electrical open, which requires modeling not only crack initiation (described above) but also the fracture process.

There are a number of approaches to modeling fatigue fracture [8,9,10]; we take a new strategy that combines our crack initiation model with a diffuse crack propagation model.

Crack Model

Fracture propagation is a challenge to capture in a finite element model due to stress singularities and nonlinear behavior. However, solder joint cracks are typically rather diffuse (not a single crack with a sharp crack tip). This allows us to attempt a smeared crack approach. In this model, when the microstructural parameter of an element reaches the critical value λ_c , the constitutive response of the solder material is changed to that of a weak (very flexible) elastic material, with a Young's modulus equal to 1/100 of the modulus of intact solder. Once the material is cracked, it is not allowed to change back. This dramatic change in element mechanical response changes boundary value problem; however, no remeshing is required because there is no numerical instability due to introduction of a discrete crack.

Figure 2 shows a crack propagation sequence for a surface mount solder joint. The crack initiates in the underfill at 600 thermal cycles. It then propagates across the underfill by 1200 cycles, bifurcates along the substrate and up the component at 2800 cycles, until an open circuit is reached at 7500 cycles. This example illustrates that a solder joint may have considerable useful service life remaining after cracking has begun.

Fracture models often have mesh dependence issues. We tested the effects of mesh refinement on cracking predictions and found that the cycles to generate an electrical open are sensitive to mesh refinement. For example, the predicted cycles to generate an electrical open decreased from 9100 cycles with the coarsest mesh to 7100 cycles when the solder element edge length was decreased by a factor of eight. Thus, lifetime predictions are somewhat sensitive to mesh refinement; in fact, crack initiation predictions are much more sensitive to mesh refinement than the predictions for cycles to generate an electrical open.

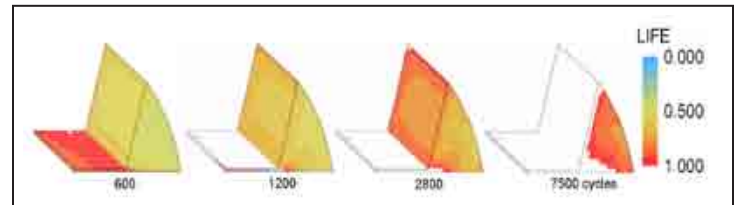
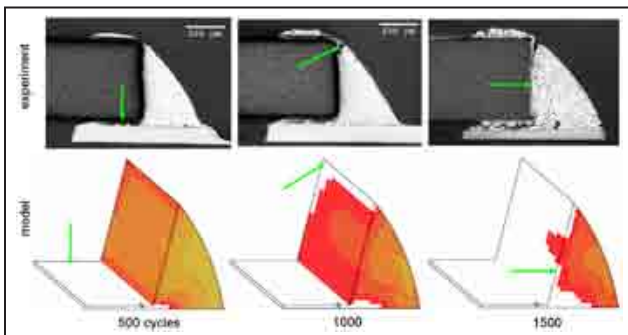


Figure 2. Crack propagation in a surface mount solder joint. The color scale shows the normalized microstructural parameter, with red indicating the critical (failure) value λ_c . White elements are cracked.

Experimental Validation

The fracture propagation model was validated against experimental observations of cracking in a surface mount solder joint on a test vehicle circuit board. As shown in Figure 3, the cracking simulations predicted cracks starting in the underfill after 500 cycles, followed by cracks starting near the upper outer corner after 1000 cycles (note that in the model images the front face is a symmetry plane, a mid-surface, and in the experimental images below the front face is an outer surface). Open circuit failure, which occurs



starting in the underfill after 500 cycles, followed by cracks starting near the upper outer corner after 1000 cycles (note that in the model images the front face is a symmetry plane, a mid-surface, and in the experimental images below the front face is an outer surface). Open circuit failure, which occurs

Figure 3. Model predictions for fracture of a surface mount solder joint compared with experimental observations. Arrows indicate crack comparison features.

when the two cracks link up in a continuous crack, is observed at 1500 cycles. These results are in good agreement with experimental observations, with respect to both crack location and temporal evolution.

Conclusions

We have developed a suite of models to predict the lifetime of solder joints subjected to thermal-mechanical fatigue in electronic circuit boards. The unified creep plasticity model predicts both mechanical response and thermal cycles to crack initiation. The smeared crack model predicts crack propagation and thermal cycles to an electrical open. Both models are in good agreement with validation experiments on test vehicle circuit boards. In concert, these models predict the lifetime of solder joints in a quantitative manner that may be used to design new circuit boards or to analyze existing components.

Acknowledgements

This work was supported by Sandia National Laboratories. Sandia is a multi-program laboratory operated by Sandia Corporation, a Lockheed Martin Company, for the United States Department of Energy under Contract DEAC04-94AL85000.

References

- [1] A. E. Perkins and S. K. Sitaraman, *Solder Joint Reliability Predictions for Multiple Environments* (New York, NY, Springer, 2008).
- [2] Q. Zhang, A. Dasgupta, D. Nelson, H. Pallavicini, "Systematic Study on Thermo-Mechanical Durability of Pb-Free Assemblies: Experiments and FE Analysis," *ASME J. Electron. Packag.* **127** 415 (2005).
- [3] R. Darveaux, "Effect of Simulation Methodology on Solder Joint Crack Growth Correlation and Fatigue Prediction," *ASME J. Electron. Packag.* **124** 147 (2002).
- [4] G. C. Johnson and D. J. Bammann, "A discussion of stress rates in finite deformation problems," *Intl. J. Solids Structures* **20** 725 (1984).
- [5] D. P. Flanagan and L. M. Taylor, "An accurate numerical algorithm for stress integration with finite rotations," *Comput. Meth. Appl. Mech. Engin.* **62** 305 (1987).
- [6] P. T. Vianco, S. N. Burchett, M. K. Neilsen, J. A. Rejent, D. R. Frear, "Coarsening of the Sn-Pb solder microstructure in constitutive model-based predictions of solder joint thermal mechanical fatigue," *J. Electron. Mater.* **28** 1290 (1999).
- [7] M. K. Neilsen, P. T. Vianco, A. C. Kilgo, E. A. Holm, "A capability to model crack initiation and growth in solder joints," to appear in *Proceedings of IPACK2009* IPACK2009-89230 (2009).
- [8] P. Towashiraporn, G. S. Subbarayan, C. S. Desai, "A hybrid model for computationally efficient fatigue fracture simulations at microelectronic assembly interfaces," *Int. J. Solids Struct.* **42** 4468 (2005).
- [9] D. Bhate, D. Chan, G. Subbarayan, L. Nguyen, "A nonlinear fracture mechanics approach to modeling fatigue crack growth in solder joints," *ASME J. Electron. Packag.* **130** 021003 (2008).
- [10] L. J. Ladani and A. Dasgupta, "A nonlinear fracture mechanics approach to modeling fatigue crack growth in solder joints," *ASME J. Electron. Packag.* **130** 011008 (2008).

POLYMER MATERIAL THERMAL DECOMPOSITION MODEL WITH INTENSIVE DECOMPOSITION AREA

V. S. Sirenko, E. A. Egorova

All-Russia Research Institute of Automatics (VNIIA),
22 Suschevskaya Str., Moscow, 127055, Russia
Author Contact: vniiia@vniiia.ru

The paper describes the mathematical model with the stable temporal attributes in the broad temperature range describes thermogravimetric curves for polyurethane polymers and fiber-glasses obtained at constant heating rates in the range 5-100 °C/min in inert atmosphere.

Introduction

In the design of protection structures applied in different areas of technology, including those in the extreme thermal environment, such polymer materials as polyurethane foams and glass-epoxy resins can be used. Experimental research of thermal decomposition for these materials in the dynamic heating mode and development of its mathematical model are very interesting from the standpoint of the “protection structure – hazardous cargo” system fire protection.

Polymer thermal decomposition at intensive heating is a complex physical and chemical process [1-4]. For its mathematical description, well-known relations of activation (Arrhenius) type are often applied. However, in this case, it is impossible to describe precisely the area of the material intensive thermal decomposition. For example, Z , E , n parameters of the thermal decomposition models for fiber-glass with epoxy matrix (FGEM), built at VNIIA based on experiments according to the traditional methods with two- ($n=1$) and three-parameter Arrhenius expressions, depending on the conversion degree, temperature, and heating rate, are instable:

Z (pre-exponent) – over five orders of magnitude;

E (activation energy) – over four times;

n (reaction order) – approximately twice.

To build a model precise enough to predict material behavior in the real operating environment, an approach is applied based on the application of the activation type relation set. The calculations related to the determination of the model parameters, to the increase of their number, are getting closer to the experimental data; however, they do not give any physically justified values of the activation energy and pre-exponent multiplier [1,2].

This paper demonstrates the possibility to build polymer and composite thermal decomposition models, including weight loss models, on principles that consider both chemical and physical nature of the process.

For this purpose, we used a complex of experimental methods: thermal gravimetric analysis (TGA), IR-spectroscopy (FTIR), gas chromatography (GC), and mass spectrometry (MS) in different combinations.

Material Thermal Decomposition Model

The analysis of the experimental data showed that the polyurethane foam (PUF) and FGEM thermal decomposition in the nitrogen atmosphere could be split into three areas. Each area can be identified as:

- Polymer activation decomposition;
- Polymer stability loss and quick char formation;
- Slow decomposition of the char residuum.

Each area according to its mechanism requires its own mathematical description. The content of solid residuum in the sample for each area has the following values:

- 100 % to 95 % – polymer decomposes according to the active mechanism;
- 95 % to 40 % – decomposition of instable organics;
- 40 % to 0 % – decomposition of char.

For the first area, the best correlation between the calculation and experimental data is observed in the case of the application of the activation processes mathematical description. The value of the activation energy for this area, calculated via the standard kinetic model, for the polyurethane foam lies below 100 kJ/mole. The presence of this area is especially important for describing processes with low heating rates (≤ 1 °C/min).

The area of the sharp sample weight loss is explained by the rapid decomposition of the organic polymer due to the loss of its thermodynamic stability. In this case, the value of the standard C-C and other bonds that break the barrier in the polymer is of the same order with the value of the molecular thermal motion energy, and the process occurs via the mechanism similar to the boiling mechanism [5]. This process occurs in a relatively narrow temperature band, and its rate depends on the deviation from some certain typical temperature (the temperature of stability complete loss) [1,5].

The loss of the condensed system weight during the heating is accompanied by the physical processes (evaporation and boiling of components that have appeared as the result of reaction) that do not change the chemical composition. We will determine the correlation between them at different heating modes.

The increase of decomposition product concentration at the assumption of no interaction between them can be expressed in the form of the total differential [5]:

$$dC = \left(\frac{\partial C}{\partial t}\right)_T dt + \left(\frac{\partial C}{\partial T}\right)_t dT.$$

The first item reflects the change of concentration as the result of kinetic processes—chemical reaction and evaporation from the surface of the condensed system; the second item reflects the change of concentration as the result of the phase transfer. When heating with constant rate $b = dT/dt$ (this mode is typical for thermo-analytical tests and occurs in the front processes of thermal decomposition near the heating surface), the concentration change rate is:

$$dC/dt = \left(\frac{\partial C}{\partial t}\right)_T + \left(\frac{\partial C}{\partial T}\right)_t b.$$

Thus, at a small heating rate, the second item that contains b as the factor is insignificant, and the weight loss in the condensed system depends mostly on the reaction kinetics and decomposition products' evaporation in the condensed system. On the other hand, at high heating rates, the second item is much greater than the first one, and the weight loss occurs mostly due to the phase transfer—the decomposition products' boil-off. This process is connected to the nucleation and filtration of the boil-off products through the condensed system [1].

The relation between the weight loss and temperature is derived using simple transformations from the following assumption. The polymer decomposition rate in the “diffused” phase transfer is proportional to the

relation $\left[\frac{T}{T_0}\right]^n$, where T_0 is characteristic temperature and T is the polymer current temperature. This relation is proportional both to the solid residuum weight loss and the vapor and gas products' weight gain, so:

$$\frac{m_0 - m_t}{m_t} = \left[\frac{T}{T_0}\right]^n,$$

where m_t - is the current sample weight, m_0 is the initial sample weight.

Since the max value of the process rate is achieved in the area of weight loss close to 50%, to describe the process we used the intensive thermal decomposition expression, where the temperature of the 50% sample weight loss is considered the typical temperature. In this case, the weight loss can be described as follows:

$$m = 1 / (1 + (T / T_0)^n), \quad (1)$$

where m - is the relative weight loss $m = m_t / m_0$, n is the constant for this material.

The process time relation is introduced indirectly through the heating rate:

$$T = T_{\text{нач}} + v \cdot \tau, \quad (2)$$

where T is the temperature;

$T_{\text{нач}}$ is the temperature at the beginning of the experiment;

τ is the experiment time;

v is the heating rate.

The analysis of the char residuum decomposition demonstrated that in the applied temperature range it does not show a clear activation nature. This process mostly depends on other factors (probably its rate is limited by the surface of the pore structure, diffusion controlled processes, etc.).

Processes like this with a complex interior nature are well described with an expression, the parameters of which depend on the fractal dimensions of the object [6]. The expression of the stretched exponent law (the Kohlrausch expression) or similar more general Erofeyev-Kolmogorov expression is as follows:

$$m = \exp(-C \cdot \tau^k), \quad (3)$$

where k is the constant for this material is the topological similarity coefficient of integral process to the elementary stages and C is the value on which the process rate depends, and generally has the form of an Arrhenius expression.

Parameters of the model that includes above-mentioned expressions were assessed using the experimental thermogravimetric cures with the linear regression method.

Thermal Decomposition Model Parameters

During the experiment result processing, we obtained the parameters of chemical kinetics expressions (according to Arrhenius) and also redeveloped the computer models of sample weight loss in thermal decomposition depending on the temperature; as the main parameter, we used the temperature corresponding to decomposition of 50% of fiberglass.

The results of parameter calculation according to the above model are summarized in Table 1.

Table 1. Parameters of the polyurethane foam and fiberglass thermal decomposition model.

| Sample | Heating rate, °C/min | Expression parameters | | | | | | Coefficient of correlation between calculated and experimental values | |
|--------|----------------------|-----------------------|------|-----------|-------|-------|-----------|-----------------------------------------------------------------------|----------------------|
| | | 1 | | | 3 | | | | |
| | | T_0 | n | \bar{n} | C | k | \bar{k} | $R(n,k)$ | $R(\bar{n},\bar{k})$ |
| PUF | 20 | 386 | 12.4 | 13.0 | 0.671 | 0.264 | 0.211 | 0.9980 | 0.9929 |
| PUF | 50 | 408 | 13.5 | | 0.943 | 0.160 | | 0.9974 | |
| PUF | 100 | 432 | 13.1 | | 1.225 | 0.268 | | 0.9846 | |
| FGEM | 20 | 476 | 10.8 | 13.2 | 0.652 | 0.171 | 0.194 | 0.9974 | 0.9852 |
| FGEM | 50 | 489 | 13.2 | | 0.827 | 0.165 | | 0.9976 | |
| FGEM | 100 | 506 | 15.5 | | 1.389 | 0.247 | | 0.9978 | |
| FGEM | 100 | 503 | 14.7 | | 1.361 | 0.334 | | 0.9953 | |

As shown in Table 1, parameters T_0 and C are the functions of the heating rate. In the ranges used in the research, these functions were close to linear. For n and k values, there is almost no relation with the conditions of their determination. Their values seem to depend on the chemical nature of the polymers.

The chemical nature of the polymers is reflected on the coefficient values. For example, the presence of nitrogen atoms in the polyurethane main chain leads to the reduction of the polymer thermal stability compared to epoxy resins, and that is reflected in the lower values of T_0 . Besides, higher values of n correspond to higher decomposition rate.

In the research, we developed a computer model with the SURTGM.EXE software that allows calculation of the model parameters and build calculated thermogravimetric relations. Besides, if the thermogravimetric curves are available obtained at different heating rates, it is possible to interpolate correctly the calculated relation in the rate range 5–100 °C/min. Extrapolation in this model can be correct for the higher heating rates.

As the indicator for adequate description of the experimental data with the nonlinear model, we used the multiple correlation coefficient. It was calculated as the correlation coefficient between the experimental and calculated values [7].

Figures 1 and 2 demonstrate the graphs of the fiberglass epoxy matrix weight loss calculated relations built according to expressions 1 and 3 compared with the experimental curves for heating rates 20 and 50 °C/min.

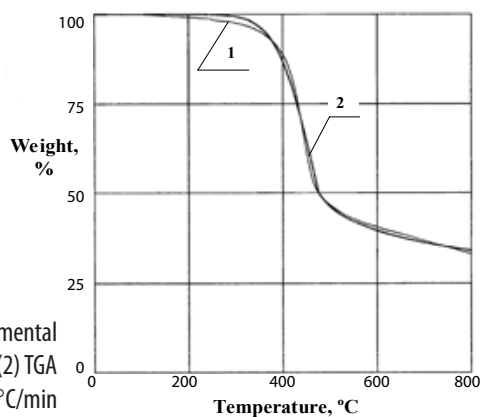


Figure 1. Experimental (1) and calculated (2) TGA curves at 20 °C/min heating rate.

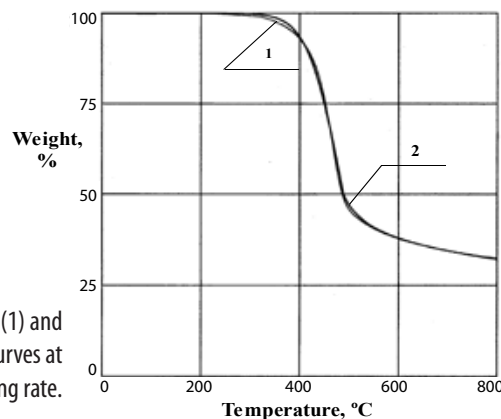


Figure 2. Experimental (1) and calculated (2) TGA curves at 50 °C/min heating rate.

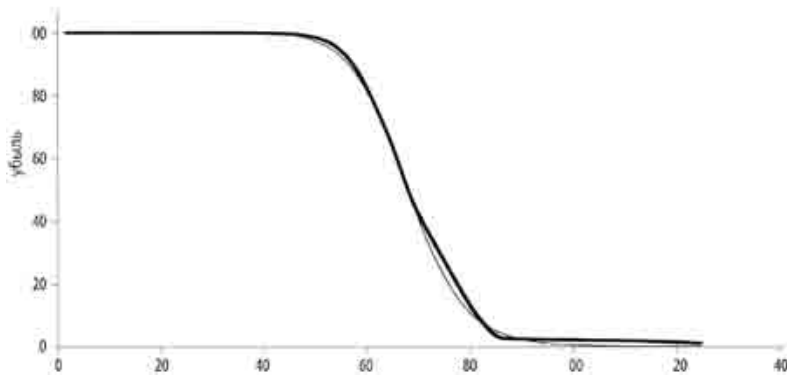


Figure 3. Experimental (thick) and calculated (thin) TGA curves for PU at 5 °C/min heating rate.

Also confirming the assumption of the physical nature of the process controlling the polymer thermal decomposition, Figure 3 demonstrates the TGA experiment curves and its model built according to expression 1 only.

The experiment was conducted on the thermoplastic polyurethane. During the experiment, the melt of the sample in the thermoanalytical system pan took an oval shape. Figure 3 demonstrates that the experimental and calculated (at $n = 25.5$) curves are almost identical in the whole range of weight loss in time at linear heating, and that proves the adequacy of expression 1 and the initial assumptions of the studied process.

Conclusion

The mathematical model was developed capable of describing the PUF and fiberglass thermogravimetric curves obtained at constant heating rates in the range 5-100 °C/min in inert atmosphere. The model reflects the physics and chemistry of the process in the polymer decomposition front in the small area of the temperature range, and the subsequent process of char decomposition. The model parameters reflect the chemical nature of the studied polymers.

The model is the result of the available data analysis and may require updating for the other heating rates.

The multiple correlation coefficient between the calculated and experimental values for weight-loss models is at least 0.985 for heating rates 5-100 °C/min, and that confirms the adequacy of the material thermal decomposition model.

References

- [1] O. F. Shlensky, N. V. Afanasyev, A. G. Shashkov, *Thermal Decomposition of Materials, Polymers and Composites during Intense Heating: College Tutorial* (M.: Energoatomizdat, 1996).
- [2] M. T. Bryk, *Destruction of Filled Polymers* (M.: Khimiya, 1989).
- [3] W. Wendland, *Thermal Methods of Analysis* (M.: Mir, 1978).
- [4] Ya. Shestak, *Theory of Thermal Analysis: Physical and Chemical Properties of Solid Inorganic Substances*, translated from English (M.: Mir, 1987).
- [5] V. S. Sirenko, O. F. Shlensky, "Modeling of thermal decomposition of polymer materials in intense heat fluxes," *Issues of Atomic Science and Technology. Series: Nuclear Instrumentation*, Issue 1, No. 23, 35-43 (2006).
- [6] M. Shlesinger and J. Klafter, "The nature of temporal hierarchies underlying relaxation in disordered systems, in fractals in physics," *Proceedings of the VI International Symposium on Fractals in Physics*, translated from English, eds. L. Pietronero, E. Tozati (M.: Mir, 1988).
- [7] P. V. Novitsky and I. A. Zograf. *Estimation of Error in Measurement Results*, (L.: Energoatomizdat, Leningrad Branch, 1985).

EXPERIMENTAL CHARACTERIZATION OF FOAMS IN FIRE ENVIRONMENTS

K. L. Erickson, R. E. Hogan, K. J. Dowding, V. F. Nicolette

Sandia National Laboratories, Albuquerque, NM 87185 USA

Contact Author: klerick@sandia.gov

The physical behavior of epoxy and hybrid epoxy-polyurethane-cyanate-ester foams during thermal decomposition in oxygen-deficient environments was examined experimentally. Experiments were done with foam samples in a variety of configurations that imposed different thermal and physical boundary conditions. Depending on the polymer and the physical boundary conditions, samples liquefied and flowed due to gravity, formed a two-phase (vapor-liquid) material that flowed due to a pressure gradient, or formed a large volume of relatively stable char. In closed containers, erosive channeling by hot fluids formed complicated three-dimensional foam decomposition zones. The physical behavior of the foam significantly impacted radiant heat transfer to foam-encapsulated objects and rates at which pressure developed in sealed containers.

Introduction

Organic polymer foams are used frequently to provide thermal, mechanical, and electrical isolation in engineered systems. Modeling the response of such systems in fire environments has important applications in safety and vulnerability analyses. Thermal damage, due to an incident heat flux, can be important to analyses involving foams in oxygen-deficient environments, such as sealed containers. The ability to predict heat transfer through thermally degrading foam materials, as well as the ability to predict pressurization of sealed containers, can depend strongly on the physical behavior of foam during degradation. Physical behavior depends on thermal and physical boundary conditions, initial polymer structure, and chemical mechanisms and kinetics controlling decomposition. This paper discusses results from radiant heat transfer experiments that examined heat transfer to objects encapsulated in a removable epoxy foam and in a hybrid epoxy-polyurethane-cyanate-ester foam. (Both foams were developed at Sandia National Laboratories.) Experiments were done with vented and sealed containers.

Experiments were done to provide data for evaluating numerical heat transfer models and to examine the physical behavior of the foams during decomposition. During decomposition, the removable epoxy foam liquefied and flowed due to gravity or a pressure gradient, and in closed containers, erosive channeling by hot fluids created complicated three-dimensional foam decomposition zones. The hybrid epoxy-polyurethane-cyanate-ester foam formed a large volume of relatively stable char that fractured in experiments with vented samples but remained intact during experiments with sealed samples. Those results had significant implications for modeling [1].

Experiment

To provide data for developing and evaluating numerical heat transfer models, two types of experiments were done: (1) Laboratory-scale experiments [2–5] such as TGA-FTIR, DSC, and pyrolysis-GC-FTIR were used to evaluate material and chemical properties in governing equations. (2) Separate radiant heat transfer experiments [2,3,4] with production-scale samples were done to examine physical behavior of foam during decomposition and to obtain data for model evaluation. Discussion of both laboratory-scale and radiant heat transfer experiments is beyond the scope of this paper.

This paper focuses on radiant heat transfer experiments done with both vented and sealed samples that were 8.8 cm in diameter and 6 or 8 cm in length and weighed about 40 g to 60 g. An exploded view of the sample configuration is shown in Figure 1a. The assembled unit and thermocouple (TC) locations are shown schematically in Figure 1b. The experiment setup and the three sample orientations (upright, prone, and inverted) that were used are shown schematically in Figures 2a and 2b, respectively.

In Figure 1a, a partially hollow foam cylinder was enclosed in a metal sleeve, which was sealed at both ends by metal plates electron-beam welded to the sleeve. The flat end plate, to be exposed to the heat lamp array, was adjacent to the SS316 vent tubes. The opposite unheated plate integrally incorporated a metal mass simulating an encapsulated object. The metal mass was inserted flush in the hollow region in the foam cylinder so that the foam filled the inside of the container. The sleeve was SS321 tubing, 8.89-cm (3.5-in.) outside diameter and 0.508-mm (0.020-in.) wall thickness. End plates were SS304L, 9.53 mm (0.375 in.) thick. The interior and exterior surfaces of heated plates and interior surfaces of unheated plates, including encapsulated mass, were painted with Pyromark™ 2500 series flat black paint. The encapsulated mass was SS304L, was 4.45-cm (1.75-in.) in diameter, and consisted of a solid end and a hollow end (Figure 1a). The hollow end fit snugly in the hole in the unheated plate and was set flush with (and welded to) the exterior surface of the plate. The encapsulated mass simulated a 2.54-cm (1-in.) thick solid mass mounted on a 1.27-cm (0.5-in.) hollow mass.

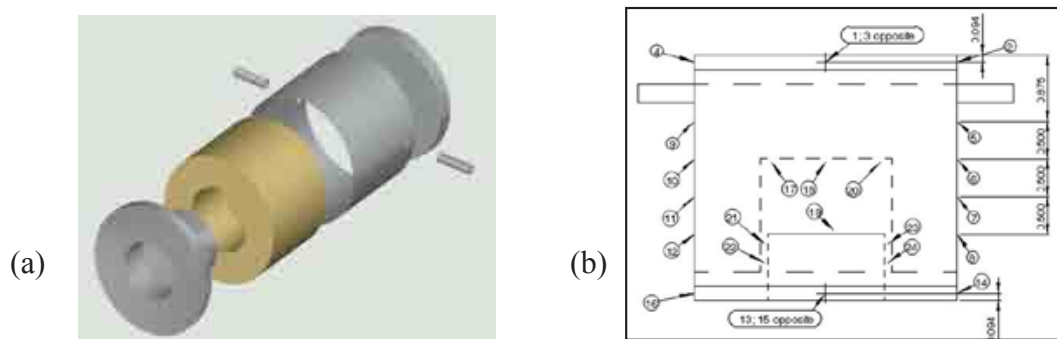


Figure 1. (a) Sample schematic and (b) thermocouple locations (in inches).

Between 19 and 24 thermocouples were used for temperature control, recording temperatures over the container's surface, and recording temperatures inside the encapsulated mass as shown in Figure 1b (note: dimensions are in inches). Generally, thermocouples 21 to 24 were omitted. Thermocouples 1–4, 13–16, and 17–20 were ungrounded, 1.62-mm (0.063-in.) diameter Inconel™-sheathed K-type thermocouples. Thermocouples 5–12 were ungrounded, 0.81-mm (0.032-in.) diameter Inconel™-sheathed K-type thermocouples. Pressure data were acquired using Setra model 206 transducers connected to a vent tube. A pneumatic valve was connected to the other vent tube. Temperature and pressure data were recorded at 0.5 Hz using a LabView™-based data acquisition system.

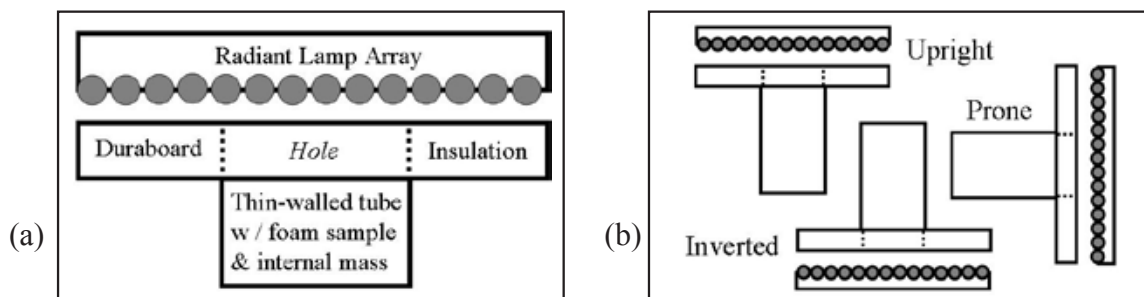


Figure 2. Schematic diagram of (a) experiment set up and (b) sample orientations.

Seventeen quartz lamps were used to heat samples. Each lamp was 9.53 mm (0.375 in.) in diameter and 25 cm (1.0 in.) in length. Each lamp had a maximum power rating of 6 kW. The 17 lamps were spaced 1.8 cm (0.72 in.) apart to form an array that was approximately 30 cm (11.8 in.) square. A board of rigid insulation, 2.54 cm (1 in.) thick, was placed 3.8 cm (1.5 in.) from the lamps. An 8.9-cm (3.5-in.) diameter hole was located in the center of the board. The sample container's heated plate was located 5.7 cm (2.25 in.) from the lamps, against the underside of the insulation board, and aligned with the hole in the board. The plate was heated at a constant rate of 3.33 K/s (200 K/min) to hold temperatures that were either 1023 K or 1173 K, after which the temperature of the plate was held constant for at least 35 minutes.

Results

Removable Epoxy Foam (REF) – Vented and Sealed Samples

Results from radiant heat transfer experiments with vented samples of REF are shown in Figure 3. For heated plate temperatures of 1023 K and 1173 K, Figure 3 shows temperature versus time data that were recorded from the thermocouple (TC 18) located 0.76 mm (0.030 in) below the center surface of the encapsulated metal mass (Figure 1b). Data are shown for samples in upright, inverted, and prone orientations.

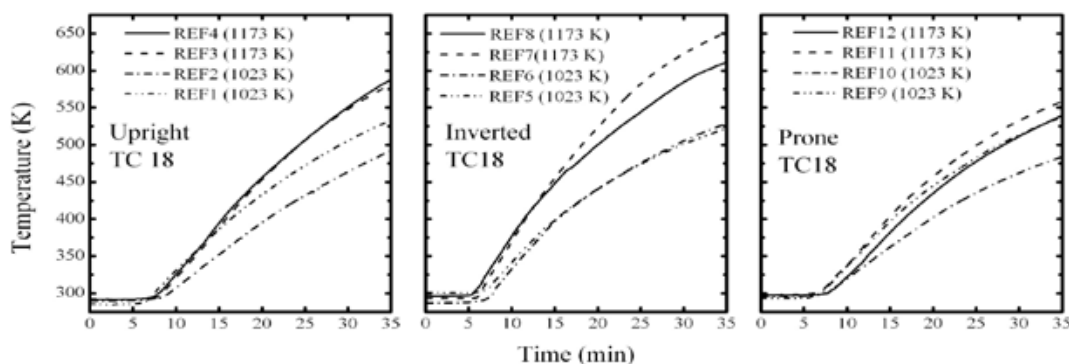


Figure 3. Results from radiant heat transfer experiments with vented samples of REF.

If the REF had behaved consistently, the results from TC 18 for all sample orientations should have been similar, including sample-to-sample variations. However, the temperature data showed substantial variation between sample orientations, and variations between replicate samples were more than desired. Data from samples in the prone orientation appeared anomalous since the heated plate temperature had little effect on the temperature at TC 18, which was significantly different from the results of the upright and inverted orientations. Postmortem examination indicated that samples liquefied and flowed during decomposition, which appeared to cause formation of bubble-like structures that varied in shape and volume depending on sample orientation [2]. The structures were a likely cause of sample-to-sample variations in the experimental data, as well as the apparently anomalous results from samples in the prone orientation.

Preliminary experiments with sealed samples of REF were done with shorter samples (about 6 cm in length), and the encapsulated mass was omitted. In these experiments, erosive channeling was observed and resulted from hot gases penetrating along the side of the sample container. Heat transfer between hot vapors and foam caused decomposition of the foam in contact with the vapor phase, as well as condensation of vapors. In the upright orientation, channeling appeared to promote movement of the condensed phase away from the heated plate (Figure 4a). In the inverted orientation, channeling appeared to cause the condensed phase to remain in close proximity to the heated plate (Figure 4b). The result was that the pressure increased much faster in the sample in the inverted orientation than in the sample in the upright orientation (Figure 4c).

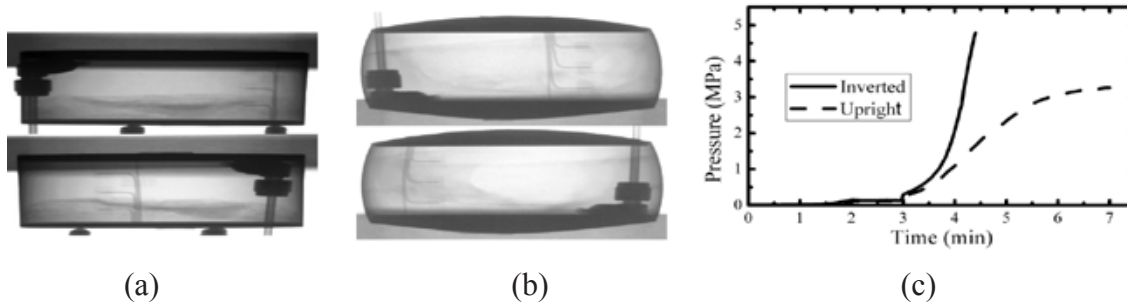


Figure 4. Sealed REF samples: (a) upright, (b) inverted, and (c) pressure comparison.

Hybrid Foam – Vented and Sealed Samples

The most relevant results from the heat transfer experiments with vented samples of hybrid foam are shown in Figure 5. For heated plate temperatures of 1023 K and 1173 K, Figure 5 shows temperatures recorded from the thermocouple (TC 18), located 0.76 mm (0.030 in.) below the center surface of the encapsulated mass (Figure 1b), for samples in upright, inverted, and prone orientations.

If the hybrid foam had maintained its original integrity, the results from TC 18 for all sample orientations should have been similar, including sample-to-sample variations. However, the temperature data showed substantial variation between sample orientations, and variations between replicate samples was more than desired. Postmortem examination of samples indicated that the samples fractured during three-dimensional decomposition. Between samples, the fractures varied significantly in size, number, and location. The temperatures measured by TC 18 appeared to be qualitatively consistent with the fracture patterns observed in the respective post mortem pictures, illustrated in Figure 6 (prone orientation) and discussed in detail by Erickson et al. [4].

A few experiments were done with sealed samples, in which the pressure increased rapidly (Figure 7a), and the containers failed or were vented before the temperature of the encapsulated object increased appreciably. However, the foam did not fracture, and the pressure results from upright, inverted, and prone orientations were

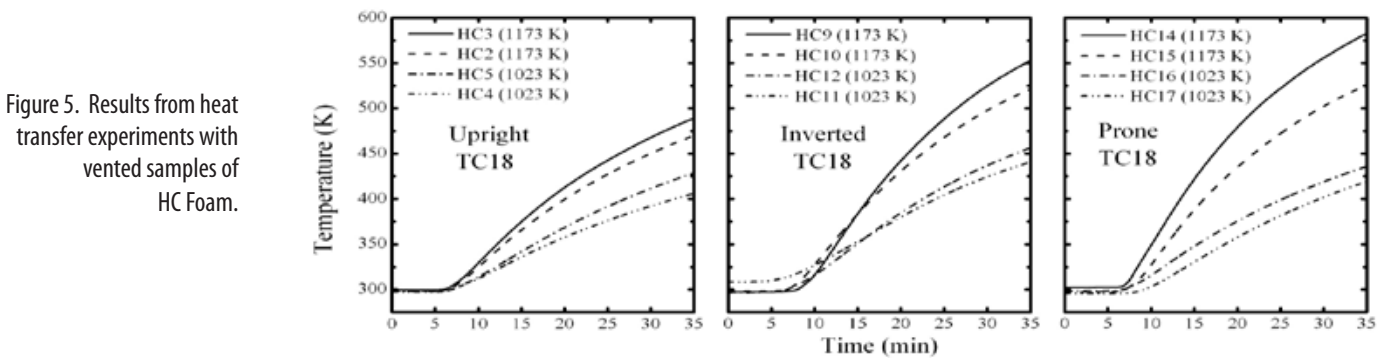


Figure 5. Results from heat transfer experiments with vented samples of HC Foam.

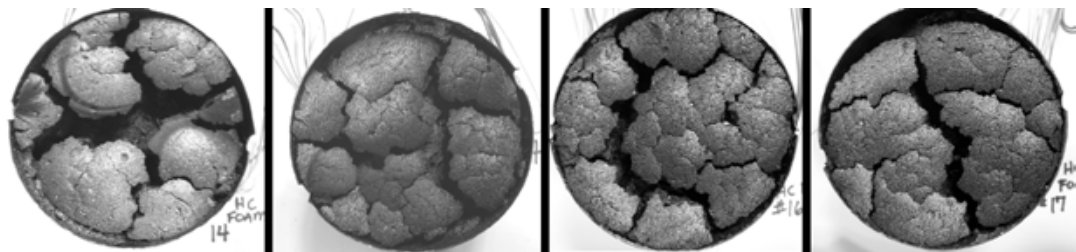


Figure 6. Postmortem pictures from vented samples in prone orientation.

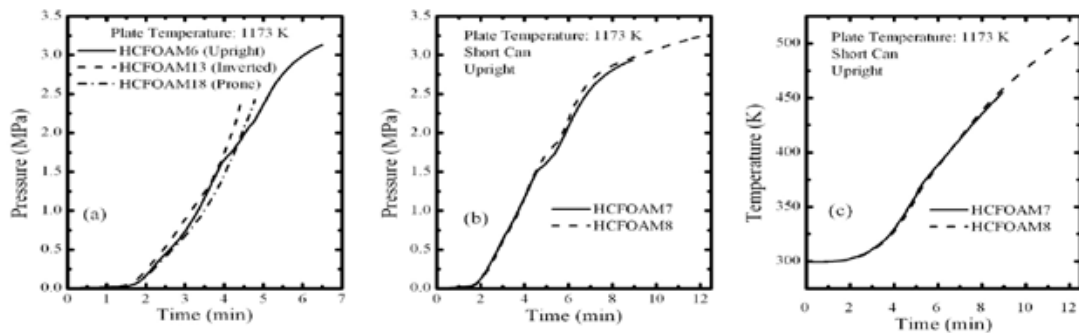
HC Foam 14

HC Foam 15

HC Foam 16

HC Foam 17

Figure 7. Pressure and temperature versus time from experiments with sealed samples.



very consistent [4]. To obtain additional data, experiments were done using samples made with a 1.9-cm shorter sleeve. Pressure and temperature results are shown in Figures 7b and 7c, respectively, for replicate samples in the upright orientation. Results were very consistent.

Conclusions

The physical behavior of removable epoxy and hybrid epoxy-polyurethane-cyanate-ester foams during thermal decomposition in oxygen-deficient environments was examined experimentally. Depending on the polymer and physical boundary conditions, samples liquefied and flowed due to gravity, formed a two-phase (vapor-liquid) material that flowed due to a pressure gradient, or formed a large volume of relatively stable char. In sealed containers, erosive channeling by hot fluids formed complicated three-dimensional foam decomposition zones. The physical behavior of the foam significantly impacted heat transfer to foam-encapsulated objects and the rate at which pressure developed in sealed containers. Current and future work will examine pressure generation in sealed systems containing TDI- and PMDI-based polyurethane foams, both of which liquefy and flow during decomposition. That work involves additional radiant heat transfer experiments, as well as collaborative work involving detailed examination of polymer decomposition mechanisms and evolved gas-phase products [6].

Acknowledgements

This work was supported by Sandia National Laboratories. Sandia is a multi-program laboratory operated by Sandia Corporation, a Lockheed Martin Company, for the United States Department of Energy under Contract DEAC04-94AL85000. The hybrid polyurethane cyanate ester epoxy foam was developed by M. Celina assisted by J. Aubert, A. Trujillo, N. Giron, and R. Ross.

References

- [1] R. E. Hogan, K. L. Erickson, V. F. Nicolette, K. J. Dowding, "Numerical Modeling of Heat Transfer in Foams in Fire Environments," in *Joint U.S. Russia Conference on Advances in Material Science* (Prague, Czech Republic, August 31-September 3, 2009).
- [2] K. L. Erickson, S. M. Trujillo, K. R. Thompson, A. C. Sun, M. L. Hobbs, K. J. Dowding, in *Computational Methods in Materials Characterization 2003* (Southampton, WIT Press,) pp. 217-242.
- [3] K. L. Erickson, in *Interflam 2007* (London, UK, Interscience Communications Ltd.) pp. 703-708.
- [4] K. L. Erickson, M. C. Celina, R. E. Hogan, V. F. Nicolette, J. H. Aubert, in *Fire and Materials 2009* (London, UK, Interscience Communications Ltd.) pp. 353-365.
- [5] K. L. Erickson, *J. Therm. Anal. Calor* **89** 427-440 (2007).
- [6] V. S. Sirenko, R. A. Kozlovskiy, Yu. K. Naganovsky, E. I. Popova, S. A. Mulyashov, K. L. Erickson, *Thermal Decomposition Mechanism of PMDI-Based Polyurethane Foam Studied by Multiple Methods*, manuscript in preparation.

NUMERICAL MODELING OF HEAT TRANSFER IN FOAMS IN FIRE ENVIRONMENTS

R. E. Hogan, K. L. Erickson, V. F. Nicolette, K. J. Dowding

Sandia National Laboratories, Albuquerque, NM, 87185 USA

Contact Author: rehogan@sandia.gov

A series of validation experiments and analyses has been performed to assess the predictive capability of thermal response models for objects embedded in Removable Epoxy Foam (REF) and in a newly developed hybrid epoxy-polyurethane-cyanate-ester foam. An overview of the mathematical model formulation and specific assumptions applicable to each of these foams is discussed. The modeling assumptions and simplifications are described and assessed in light of experimental data. Typical quantitative comparisons of model predictions and experimental data are presented.

Introduction

In many applications, foams are used to provide structural and thermal protection to components in systems. The thermal/chemical/mechanical response of these systems in fire environments is highly dependent on the decomposition behavior of these foams. Understanding the chemical decomposition, thermal response, and mechanical response of closed systems due to pressurization is important in assessing safety in these systems. An overview of the thermal response comparisons done to quantify the accuracy of numerical models for safety applications in abnormal thermal environments is presented. This validation assessment focuses on the heat transfer to an object embedded in thermally decomposing polymer foams. Future experiments are being designed to assess numerical models for pressurization and mechanical loading. An overview of the experimental setup is provided in a companion paper [1].

The thermal response of an embedded object depends on both the thermal conditions within the container and the physical behavior of the foam during decomposition. Several different formulations of foams have been considered in this program; removable epoxy foam (REF) and hybrid epoxy-polyurethane-cyanate-ester foams were two formulations. The physical behavior of these foams is strongly dependent on the thermal and physical conditions, the polymer composition, the decomposition kinetics, and the gas environment (vented or sealed). Previous studies have characterized the decomposition processes for these foams. Because the underlying decomposition processes are significantly different for these two foams, different physical models are needed to represent the underlying physics.

Numerical Model Description

Most of the calculations to support safety analyses are done with the Calore computer code, which deals with heat conduction, chemical reaction, and enclosure radiation [2]. It does not explicitly account for some of the differentiating physics observed in decomposing foams. An overview of the mathematical formulation of the numerical model, with particular implementation details for each of the different foams, follows.

The energy transport within the foam, container, and embedded component is dominated by conduction and is given by

$$\rho C_p \frac{\partial T}{\partial t} - \nabla(k \nabla T) + \nabla q_r = Q_c \quad (1)$$

where T is temperature, k is the thermal conductivity, ρ is the density, C_p is the specific heat, q_r is the participating media radiative flux, and t is time. The volumetric energy term \dot{Q}_c accounts for the energy associated with chemical kinetics of the decomposing foam. The energy transport due to radiation through transparent enclosures is coupled to thermal conduction through (flux) boundary conditions. Separate, coupled mathematical equations describe chemical kinetics and radiative transport. Convection and foam liquefaction and flow are both neglected in this model.

Chemical kinetics for both REF and hybrid foam were experimentally determined [3,4]. The kinetics for both are expressed in an Arrhenius form. The chemical reaction process is coupled to thermal conduction through a volumetric energy term represented by the product of the reaction rates and the overall heat of reaction for each reaction.

Thermal decomposition was experimentally shown to depend on whether the decomposition products remain local to the decomposing foam, Erickson [5]. This behavior was characterized using a “confinement” parameter to correlate the chemical kinetics to the measured behavior in TGA experiments with and without a vented cap. In the foam-in-can (FIC) experiments, the actual confinement conditions are not known, so its value was varied from unconfined to partially confined chemistry to bound this effect. The details and rationale for this approach are given by Hobbs [3,6].

Radiative Transfer in Decomposing Removable Epoxy Foam

In the conceptual model for decomposing REF, the foam is assumed to transition from a solid-phase directly to a gas-phase, leaving a void occupying the volume of the original solid-phase foam. Based on this concept, the energy transport was assumed to be dominated by radiation through the nonparticipating volume that evolved as the foam decomposed. Radiative transport between the surfaces bounding the void volume was computed using the net-radiation formulation for enclosures with diffuse and gray surfaces [7]. This procedure for evolving an enclosure is implemented in a finite element code by removing elements representing foam material from the thermal conduction equations once the solid mass-fraction computed from the chemical kinetics is below a specified lower-threshold value and is referred to as “element death.” Radiative fluxes are coupled to the conduction equation as boundary conditions [2].

Subsequent experiments provided additional insight into the physical behavior of decomposing REF [5,8]. Real-time x-ray diagnostics showed that the foam liquefied, flowed, and appeared to bubble or froth during decomposition. Post-test inspections revealed that several very thin, crust-like, layered structures had solidified within the void created by the foam decomposition [1,5]. It is unclear if these formed during the heating and decomposition process or if they formed during the post-test cool-down period. In either case, the presence of these structures (either the bubbles or the solidified structures) would impact the radiative heat transfer, and their presence is inconsistent with the modeling assumption of a transparent, nonparticipating void.

Radiative Transport in Decomposing Hybrid Foam

The development of the hybrid foam was motivated by the desire to improve the consistency and predictability of the physical behavior during decomposition, as well as to decompose in a way that is more amenable to analysis with Sandia conduction-based computer codes. The desired characteristics of this foam are to decompose predictably with minimal mass loss or overall shrinkage and leave a char structure occupying the entire volume. The foam analyzed in this work was developed with these objectives [4].

Experiments on the hybrid foam have shown that as it decomposes, it leaves a nearly-uniform char structure with minimal bulk shrinkage, but with some cracking. Based on these observations, the mathematical model for radiation transport within the foam treated the decomposing foam as a participating media. Optical measurements

of the unreacted foam determined that the foam behaved as an optically thick participating media. Consequently, radiative transport was modeled using a diffusion-based approach that easily integrated into the conduction equation. The effective conductivity can be expressed in terms of the radiative scattering coefficient and absorption coefficient [7]. The radiative properties were determined from transmittance and reflectance measurements over several wavelengths and a two-flux radiation model with isotropic scattering [9]. In principle, a highly charring foam has the advantage that material properties can be determined for both the initial, unreacted material and for the final char material, which permits interpolation of properties based on extent of reaction during the decomposition. Additional details regarding this approach can be found in Erickson [10].

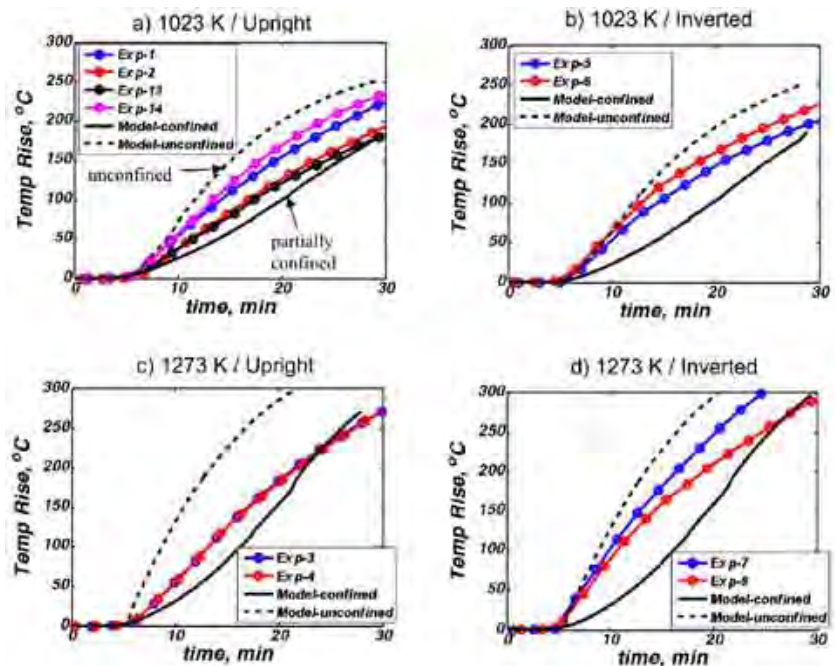
Results from Initial Radiant Heat Transfer Modeling

An overview of the comparisons of the initial numerical simulations with experiments follows. Detailed comparisons of model predictions and experimental data are beyond the scope of this paper, but can be found in [1,4,8,10]. In comparing the model predictions and the measured temperature response, it is important to recognize two primary modeling assumptions and simplifications. First, the tests were conducted with the FIC unit in three different orientations, which affect the foam response during decomposition. The numerical model has no dependence on orientation of the test device because it neglects convection and flowing liquids. Consequently, the model cannot be expected to predict or resolve any dependence on orientation. Secondly, no mass transfer of foam products of combustion is explicitly considered in the model. The effects of mass transfer on the chemical reaction rates were determined through TGA experiments and are included in the model using the “confinement” parameter previously mentioned. The effect of this simplifying modeling approach is evaluated by varying this parameter as part of comparing model predictions and measured data.

Comparison for Decomposing Removable Epoxy Foam

Figure 1 shows a comparison of model predictions and measured temperature responses of the thermocouple (TC 18) at the top center of the embedded component [1] for both partially confined and unconfined chemistry. The model predictions using the partially confined chemistry model responded more slowly than the response measured in the experiments. The predictions using the unconfined chemistry model responded more rapidly than the response measured in the experiments. For these predictions (both chemistry models), nominal values were used for all the other parameters. Consequently, the model predictions at the limits of unconfined and partially confined chemistry parameter basically bound the experimental data. This indicates that the model is sensitive to the confinement parameter, which is related to the mass transfer of decomposition products within the gas phase.

Figure 1. Thermal response for REF foam with 1023 K and 1173 K heated plate temperatures and upright and inverted orientations [4,7].



In some configurations, the temperature response of the model surpasses the temperature response of the experiment late in time. For the unconfined chemistry, there is also a different shape to the measured and predicted response curves. In particular, the measured temperature responses are concave downward, while the predicted temperatures are concave upward. These differences may be a result of modeling assumptions or relevant physics missing in the model. Recall that foam liquefaction, natural convection, participating media radiation, and the evolution of residue structures were not included in the numerical model. The applicability of enclosure radiation through a transparent void needs to be revisited in light of the solidified structures observed in post-test inspections. The uncertainty in the model due to chemistry will be accounted for in future analyses by varying the range of the confinement parameter.

Comparison for Decomposing Hybrid Foam

Experimental and initial modeling results for the hybrid foam are compared in Figure 2. For a heated plate temperature of 1023 K (Figure 2a), the data for samples labeled HC4 and HC12 represent the lowest and highest temperature responses from TC 18, respectively. Predicted results are shown for the case of conduction only and for the case of conduction and radiation (diffusive approximation). In the case of conduction only, the simulation under-predicts all of the experimental results. In the case of conduction and radiation, the simulation predicts results between the lowest and highest temperature responses from TC 18 for times after about 18 minutes. For a heated plate temperature of 1173 K (Figure 2b), the data for samples labeled HC2 and HC14 represent the lowest and highest temperature responses from TC 18, respectively. Again, predicted results are shown for the case of conduction only and for the case of conduction and radiation (diffusive approximation). In the case of conduction only, the simulation under-predicts all of the experimental results. In the case of conduction and radiation, the simulation predicts results that are between the experimental data for HC2 and HC14 for times after 11 minutes.

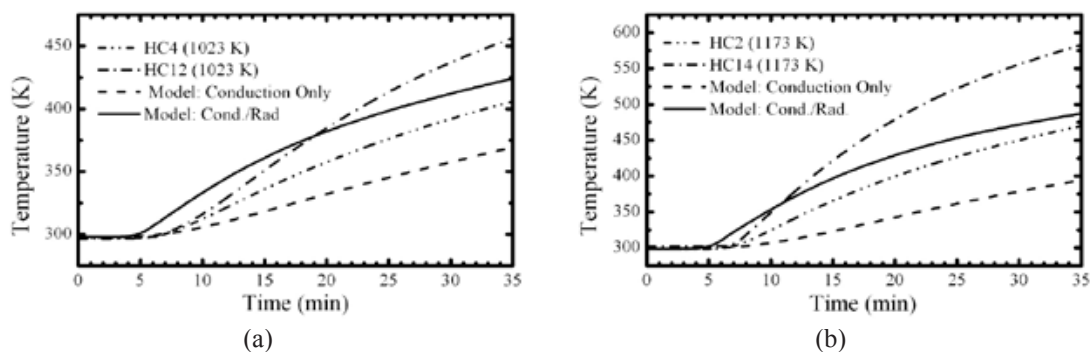


Figure 2. Thermal response for hybrid foam with heated plate temperature of (a) 1023 K and (b) 1173 K in upright (HC4) and inverted (HC12) orientations [10].

Conclusions

A brief overview of modeling capabilities for REF and hybrid foam decomposition has been presented. Mathematical models and simplifying assumptions for each of these foams have been discussed, and comparisons of predicted results with experimental data have been presented. Model developments for predicting pressure in sealed containers is on-going and deferred to a later publication. Activities to characterize these foams, as well as other candidate formulations are on-going in support of potential future applications. In addition to the heat transfer within decomposing foams; gas generation, pressurization, and mechanical response are topics of increasing attention in the future. Specifically, research is under way to quantify the uncertainty in pressure generation as a result of modeling assumptions/simplifications and numerical inaccuracies.

Acknowledgements

This work was supported by Sandia National Laboratories. Sandia is a multi-program laboratory operated by Sandia Corporation, a Lockheed Martin Company, for the United States Department of Energy under Contract DEAC04-94AL85000.

References

- [1] K. L. Erickson, R. E. Hogan, V. L. Nicolette, K. J. Dowding, "Experimental Characterization of Foams in Fire Environments," in *Joint U.S. Russia Conference on Advances in Material Science*, (Prague, Czech Republic, August 31- September 3, 2009).
- [2] S. W. Bova, K. D. Copps, C. K. Newman, *Calore, A Computational Heat Transfer Program, Volume 1: Theory Manual*, SAND2006-6083P (Albuquerque, NM, Sandia National Laboratories, 2006).
- [3] M. L. Hobbs, *SREF – A Simple Removable Epoxy Foam Decomposition Chemistry Model*, SAND2003-4550 (Albuquerque, NM, Sandia National Laboratories, 2003).
- [4] K. L. Erickson, M. C. Celina, R. E. Hogan, V. F. Nicolette, J. H. Aubert, "Hybrid Polyurethane Cyanate Ester Foam for Fire Environments," in *Fire and Materials 2009* (London, UK, Interscience Communications Ltd., San Francisco, CA, July 26-28, 2009) pp. 353-365.
- [5] K. L. Erickson, S. M. Trujillo, J. B. Oelfke, C. R. Hanks, B. Belone, D. M. Ramirez, *Component-Scale Removable Epoxy Foam (REF) Thermal Decomposition Experiments ("MFER" series, April 2003) Supporting the FY04/Q2 Level 1 V&V Milestone. Part 1: Temperature Data*, SAND Report in draft (Albuquerque, NM, Sandia National Laboratories, 2009).
- [6] M. L. Hobbs, "Modeling epoxy foams exposed to fire-like heat fluxes," *Polymer Degradation and Stability* **89** 353-372 (2005).
- [7] R. Siegel and J. R. Howell, *Thermal Radiation Heat Transfer*, 2nd ed. (Cambridge, Hemisphere Publishing Corp., 1982) pp. 497-501.
- [8] K. J. Dowding, R. E. Hogan, M. L. Hobbs, K. L. Erickson, S. M. Trujillo, *Validation Assessment for Modeling the Thermal Response of Components Embedded in Removable Epoxy Foam*, SAND2005-5754 (Albuquerque, NM, Sandia National Laboratories, 2005).
- [9] J. Reichman, *Applied Optics*, **12** (8) (August 1973).
- [10] K. L. Erickson, M. C. Celina, R. E. Hogan, V. F. Nicolette, J. H. Aubert, "Experimental-Modeling Approach for Predicting Radiation and Conduction Heat Transfer Through a Uniform, Highly-Charring Foam," in *20th Annual Recent Advances in Flame Retardancy of Polymeric Materials Conference* (Stamford, CT, June 1-3, 2009).

STUDY OF MINERAL OIL AGING RELATED TO DESIGN MATERIALS OF A NEUTRON GENERATOR

A. V. Sokovishin, G. N. Prokop'eva

All-Russia Research Institute of Automatics (VNIIA)

Moscow, 127055, Russia

Author Contact: sokovishin@vniia.ru

This paper represents presents an engineering method for estimation of mineral oil compatibility with the design materials of a neutron generator that was designed on the basis of previous experimental research, information on operational failures, and information received from scientific and technical literature.

Introduction

For many decades, mineral oil has been used for electrical insulation in high-voltage installations, mainly, in electrical transformers [1,2,3]. By now a great amount of experimental information has been devoted to research on mineral oil – transformer design materials system aging is accumulated all around the world. In neutron generators with oil insulation, designed by VNIIA, the set of design materials in contact with oil is significantly wider and differs from materials used in transformers. There is a considerable difference in working conditions – in contrast to power transformers, the average working life of generators constitutes, on the whole, just about 5 years, and the operating time is approximately from 100 to 200 hours. Permanent design improvements and materials substitution with parallel compatibility researches are necessary for new generators and generators with new properties development to meet the new customers' requirements. These improvements required development of an engineering method for estimation of mineral oil or some other dielectric liquid compatibility with neutron generators design materials and for fast estimation of permissibility of materials substitution.

Mineral Oil Aging

Among the influences that cause mineral oil aging in hermetically sealed equipment, like neutron generators, are electric and thermal fields, design materials (primarily copper, aluminum, cellulose, rubber, paints), and oxygen and oxidizing agents [1]. The transformer mineral oil aging produces gases, water, peroxides, dirt and acids, and the cellulose decomposition product—furfural [4,5]. It results in changes in mechanical, physical and chemical properties of oil.

In accordance with scope and standards for electrical equipment testing during power transformers operation are foreseen measurement of the following oil data: breakdown voltage, mechanical impurities content, dielectric loss tangent, flash temperature in closed crucible, acidity index, water-soluble acids and alkalis content, specific humidity, antioxidant additive content, gas content of oil and furan derivatives content, and to perform chromatographic analysis of gas dissolved in the oil.

Scope and standards for electrical equipment testing guidelines [6], in use for power transformer condition estimation, introduce the chromatographic analysis of gases, dissolved in oil (XAPT – hereafter referred to as DGCA, the dissolved gases chromatographic analysis). On the basis of DGCA, it is possible to disclose the two following groups of failures of the power transformers: the overheating of current-carrying connectors and design components and electrical discharges in oil. The concentration of seven gases can be determined: hydrogen (H_2),

methane (CH_4), acetylene (C_2H_2), ethylene (C_2H_4), ethane (C_2H_6), carbon oxide (CO), and carbon dioxide (CO_2). Measuring these gas concentration ratios provides a possible way to clear up the main processes resulting in aging—electrical and thermal.

Compatibility of design materials in a number of cases has a decisive importance for reliability of equipment during operation. On the one hand, design materials should not evolve substances that can influence in a negative way on the electric insulating properties of the oil or cause its accelerated aging. On the other hand, materials themselves should not decompose in contact with oil. The compatibility problem of power transformers using design materials with mineral oil insulation has been considered in multiple papers [7-11].

Research Method

The maximum scope of research, as a rule, takes place as a result of a new brand of oil or significant changes of generator operating conditions (max. operating temperature, shelf life, and operating period). In the most general case, all researches include the following stages:

- Initial information analysis (oils properties in accordance with available information sources and developer or manufacturer data; differences in technical specs in comparison to earlier tested brands of oil). At this, the information on generator operational failures, resulting from using of other brands of oil, is also a subject for consideration.
- Operating conditions analysis and determination of testing conditions based on the analysis results.
- Determination of design materials and units list to be tested in contact with oil, division into groups.
- Determination of oil and materials that are in a contact with oil controlled parameters list, determination of measurement methods (generally, standard methods are used).
- Carrying out an accelerated aging (on the basis of Arrhenius' law) of oil in contact with materials of all the groups separately and simultaneously. At this, testing vessels can be air-locked or allow oil air contact depending on generator design.
- Analysis of oil and design materials that were taken from a generator and had completely worked their lifetime (comparative analysis of nonstandard samples considering the limited set of parameters).
- Oil and materials controlled parameters determination. Aperiodicities revelation. Aperiodicities broadened research (if found). Compiling of recommendations for design improvements.
- Revelation of differences in oil properties and structural materials that were taken from a generator after lifetime end and underwent an accelerated aging. Interpretation of results.
- A final conclusion devoted to a possibility of a new oil brand implementation.

If generator design changes slightly with implementation, only one or several new materials, the scope of researches can be significantly reduced. In this case, we recommend performing an accelerated aging of oil in contact with new material(s) in testing vessels, accompanied by analysis of oil and material(s), taken from a generator at the end of the lifetime.

The scope of controlled parameters of both oil and materials that are in contact with it can differ in a greater degree depending on equipment reliability requirements and number of abnormalities that were revealed in the course of research.

Note that a typical quantity of materials subjected to research is about 50, the number of groups is from 4 up to 5, and the number of parameters determined for each material is from 3 to 10. Usually, aging simulation duration equals a triple generator lifetime (for revelation of slow going processes).

Method Application

The above-mentioned approach has found a successful application at VNIIA over many years. At least three types of mineral oils and about ten synthetic liquid dielectrics (including silicon and fluororganic) were subjected to research using the same methodology. For some types of equipment, design changes were proposed to eliminate potential sources of failure caused by incompatibility of insulating liquids with design materials. Absence of operational failures caused by incorrect application of materials proves the accuracy of the implemented approach.

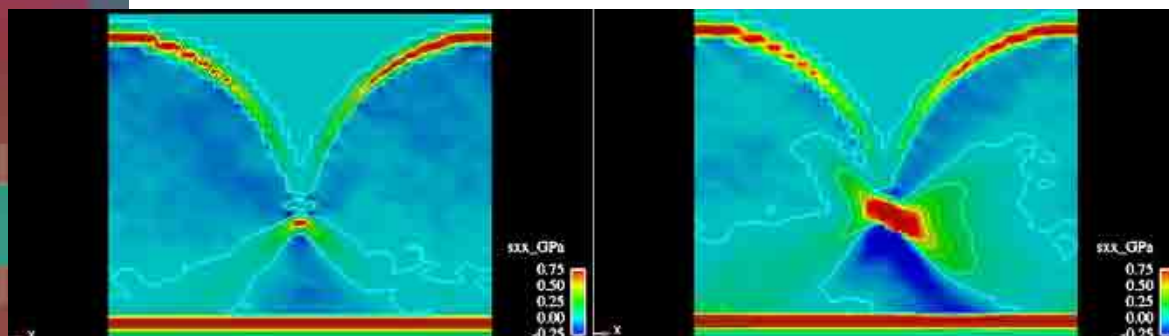
Conclusion

Providing reliable and complicated high-voltage electrophysical equipment, in general, and neutron generators in particular, requires proper selection of liquid dielectric and compatible generator design materials. A methodology was developed that guarantees a high level of equipment reliability and a very low probability of failure caused by improper application of materials.

References

- [1] Yu. V. Koritsky, ed. *Electrotechnical Materials Handbook in 3 vol., 1*, (M., Energoatomizdat, 1986) p. 368.
- [2] M. A. Grejsukh, G. S. Kuchinsky, A. A. Kaplan, G. T. Messerman, *Paper-Oil Isolation at High-Voltage Installations* (Gosenergoizdat, M.-L., 1963) p. 299.
- [3] R. A. Lipshtein, M. I. Shakhovich, *Dielectric Oil* (M., Energoatomizdat, 1983) p. 351.
- [4] M. Yu. Lvov and P. P. Kutler, *Physical and Chemical Methods for Mains Transformers Condition Estimation under Working Conditions: Teaching and Method Manual* (M.: IUE GUU, BIPK-energo, IPK of state services, 2003) p. 20.
- [5] *Scope and Standards for Electrical Equipment Testing Guidelines 34.45-51.300-97* (M., 1998).
- [6] *Method Guidelines in Diagnostics of Progressive Defects According to Results of Chromatographic Analysis of Gases Dissolved in Dielectric Oil (Guidelines PД 34.45-51.300-97. – M, 1989).*
- [7] M. R. Meshkatoddini and S. Abbaspour, “Aging study and lifetime estimation of transformer mineral oil” (*American J. of Engineering and Applied Sciences* **1** (4) 384-388 (2008).
- [8] J. Fabre and A. Pichon, *Deteriorating processes and products of paper in oil. Application to transformers*, CIGRÉ paper 137 (Paris, 1960).
- [9] T. K. Saha and D. J. T. Hill, “Electrical and chemical diagnostics of transformers insulation Part b: Accelerated aged insulation samples,” *IEEE Trans. Power Delivery* **12** 1555-1561 (1997).
- [10] W. J. McNutt, “Insulation thermal life consideration for transformer loading guide,” *IEEE Trans. Power Delivery* **7** 392-401 (1992).
- [11] B. Pahlavanpour, et al., “Copper dissolution and metal passivators in insulating oil,” *IEEE Elect. Insulat. Mag.* **23** 6-14 (2007).

Computational Methods and RADIATION EFFECTS



Time-averaged stress fields for cylindrical, thin-film islands before (left) and after (right) coalescence has occurred.

The papers in this section address the development of computational methods and their application in the study of a wide variety of technologically important phenomena, the understanding of which remain a grand challenge in materials physics and engineering mechanics. Molecular dynamics (MD) and the combination of MD and density functional theory (DFT) are used to simulate thermodynamic and mechanical properties of material as well as response to dynamic loading, vacancy diffusion in bcc metals, and radiation-induced displacement cascades in semiconductors. As a well-founded new theory of continuum mechanics, peridynamics enables unprecedented simulation of dynamic fracture in homogeneous and highly heterogeneous materials. Development of multi-scale modeling and coupled atomistic-continuum simulation (CACS) techniques favors further progress in predicting the deformation mechanisms leading to failure of a given material. The problem of coupling between atomistic and continuum-scale description of a system is also discussed in terms of an analytical approach based on averaging the equations of motion. This helps to define macroscopic thermo-mechanical parameters such as Piola and Cauchy stress tensors and heat flow via microscopic parameters. A time-dependent DFT method is successfully used to obtain the dielectric function of insulating materials and to predict the effects of high dose-rate ionizing irradiation. Remarkably, the MD method can be used to study not only condensed matter, but plasma as well. For example, it can be used to develop a self-consistent description of both free and weakly bound electron states in plasma. Taken as a whole, the section topics demonstrate significant progress in material simulation methods, and they provide useful comment on further challenges to be addressed.

A. V. Mirmelstein, All Russian Institute of Technical Physics (VNIITF), Snezhinsk, Russia

Section II:

- II-2 Accurate Prediction of Dynamic Fracture with Peridynamics (SNL)
- II-8 Molecular Dynamic Simulation of Thermodynamic and Mechanical Properties and Behavior of Materials at High Strain Rate (VNIITF)
- II-13 Challenges of, and Variations on, Coupled Atomistic-Continuum Simulation (SNL)
- II-19 Density and Nonideality Effects in Plasmas (JIHT)
- II-25 Self-Diffusion in Mo Using the AM05 Density Functional (SNL)
- II-30 Thermomechanical Effects in Perfect Crystals with Arbitrary Multibody Potential (IPME)
- II-35 Electrical Effects of Ionizing Radiation of Insulating Materials (SNL)
- II-39 Strongly Coupled Plasma Nanochannel Created by a Fast Single Ion in Condensed Matter (JIHT)
- II-45 Molecular Dynamics Simulations of Displacement Cascades in GaAs (SNL)

ACCURATE PREDICTION OF DYNAMIC FRACTURE WITH PERIDYNAMICS

John B. Aidun and Stewart A. Silling

Multiscale Dynamic Material Modeling Department
Sandia National Laboratories, Albuquerque, NM 87185-1322 USA
Contact Author: aidun@sandia.gov

*Dynamic fracture and fragmentation processes exhibit several striking characteristic phenomena. Numerical simulations, using any of a variety of methods, have had only limited success in replicating any of these characteristic phenomena. A fundamental impediment for numerical simulations of fracture that are based on traditional solid mechanics theory is that the governing equations are expressed as partial differential equations and the derivatives they entail **do not exist** at discontinuities. To remedy this inherent limitation, Silling proposed peridynamics as an enhancement of traditional solid mechanics theory. In the peridynamic continuum theory, momentum and energy conservation are expressed as integral equations that apply, without modification, to all types of material response; no auxiliary laws or rules are needed to treat crack initiation or growth. Hallmarks of the theory are nonlocal force interactions between material points; direct use of force and displacement in preference to stress and strain; representation of actual displacement rather than a local gradient approximation; and a numerical implementation that yields a mesh-free method. We show that the resulting simulation capability is able to accurately represent a wide variety of characteristic dynamic fracture phenomena, making peridynamics exceptional among numerical solid mechanics methods. Moreover, the method is **predictive** in that these phenomena are not “programmed” into the simulations in any way, but emerge from the combination of system geometry, initial and boundary conditions, and the chosen material force density constitutive model.*

Introduction

Material cracking and fracture are technologically important phenomena whose understanding remains a grand challenge in materials physics and engineering mechanics. The aims in managing cracking and fracture range from preventing them completely, to mitigating their effects on a body or structure, to guiding them to produce favorable fragmentation. The discipline of fracture mechanics can be partitioned into the study of quasi-static or stable cracking and dynamic fracture. The former includes fatigue cracking and slow crack growth; the latter encompasses situations where inertial effects influence cracking. The onset of defect or crack growth is the best understood aspect of fracture and can be accurately predicted by existing theories. In contrast, methods for predicting crack growth speed and direction, as well as whether and where branching occurs, are few and severely unreliable. In addition to predicting crack growth direction, a successful theory or simulation capability for dynamic fracture must be able to reproduce and provide insight into the following phenomena and experimental observations that are uniquely characteristic of dynamic fracture:

1. A steady, limiting crack speed;
2. Energy dissipation in dynamic crack growth (e.g., Charpy test);
3. The Mirror, Mist, Hackle sequence of textures on the fracture surface;
4. The transition from stable to unstable crack growth;
5. Arrest of unstable crack growth;
6. The specific angle of cracking the Kalthoff-Winkler notched plate impact experiment [1];
7. Transonic interface crack speeds [2];
8. Crack branching;
9. Fragment size distribution;

10. Membrane bursting;
11. The multiple, unstable cracking modes of fiber-reinforced composites;
12. Peeling and tearing of thin sheets.

Method

Until recently, no numerical simulation method was able to reproduce all these dynamic fracture phenomena, even qualitatively, let alone with quantitative accuracy. To address this deficiency, over the past decade, Silling and coworkers have developed peridynamics, which is a well-founded, new theory of continuum mechanics that is enabling unprecedented simulations of dynamic fracture in homogeneous and highly heterogeneous materials [3-7].

By representing the source terms of the conservation laws with integral equations, peridynamics avoids the problem inherent to traditional solid mechanics that the derivatives contained in the equations of motion, represented by partial differential equations, are not defined at material discontinuities. Instead, in peridynamics, fracture evolves from the deformation according to the equations of motion and the constitutive model. Consequently, simulation of fracture within peridynamics *does not require* supplemental kinetic relations that, in traditional fracture mechanics, would be needed to specify crack initiation, growth velocity, direction, arrest, and branching. In place of the traditional divergence of a stress field, peridynamics computes the force density that accelerates any material point using a functional of the displacement field within a spherical neighborhood of the point. The radius of the neighborhood is called the “horizon,” which is a material parameter. The resulting nonlocality of the interaction forces in peridynamics allows it to model complex material behavior possessing an intrinsic length-scale, which is represented by the horizon parameter.

An early version of peridynamics, called “bond-based” theory, was limited to the special case of forces, called “bonds,” between pairs of material points such that each bond responds independently of the others [3]. Damage and fracture are then easily treated at the bond level by allowing bonds between material points to break when they are stretched beyond some limit; a broken bond no longer contributes to the net force acting on its endpoints. The onset of bond breakage leads to local material softening, which can cause damage to accumulate, with broken bonds coalescing into a surface that becomes a fracture. Only bonds that exist in the initial state are considered during a simulation; no new bonds form as a result of deformation. Once a bond is broken, it does not heal. The result is a history dependent theory in which crack initiation and growth, and all associated phenomena, *emerge spontaneously*, in an unguided fashion, simply from the choice of system geometry, initial and boundary conditions, and the constitutive model.

While the bond-based peridynamic theory results in a mesh-free numerical implementation [6] that yields qualitatively accurate simulations of dynamic fracture in heterogeneous brittle materials, such as reinforced concrete and fiber-reinforced, laminated composites, it suffers two serious limitations. First, because peridynamics uses the more fundamental quantities of force and displacement in preference to the theoretical continuum quantities of stress and strain, the bond-based theory cannot apply material constitutive models of classical solid mechanics. Second, the elastic portion of a material’s response is restricted to that of a Cauchy solid, resulting in a Poisson’s ratio of 0.25 for any linear isotropic solid. These limitations of the bond-based theory were remedied with the “state-based” peridynamic theory [4]. The formal structure of the momentum conservation equation is unchanged; the force density remains an integral over the neighborhood of a material point of a difference in force states. However, the pairwise force function of the bond-based theory is replaced with a more general functional of the displacement field within the horizon. This effectively makes the bond forces on a material point additionally dependent on deformations of other bonds within the horizon.

Bond-based peridynamics is a special case of the state-based theory [4]. Another special case of this theory allows the force on a material point to be computed through a classical “stress-strain” constitutive model: Within the horizon, the strain tensor is approximated from the deformation and the resulting stress tensor is then mapped onto a distribution of bond forces.

A fundamental difference from classical solid mechanics theory is that the peridynamic functionals are formulated directly in terms of the displacement field, rather than the spatial derivatives of displacement. Since the classical assumption of smoothness is not required, an initially spherical volume can deform into a highly distorted, non-smooth region, not only into an ellipsoid. Constitutive models in peridynamics can, correspondingly, represent a wider range of material phenomena than can the stress-strain-based models of classical solid mechanics. Characterization of the range of material behaviors accessible in peridynamics and their usefulness are largely unexplored areas of investigation. In this regard, it is of interest that a formal mapping exists from interatomic potentials to peridynamic force density functions [9]. Indeed, peridynamic theory shares the same formal structure as molecular dynamics (MD) [10a] and can be regarded as a continuum version of MD [10b].

State-based peridynamic is consistent with classical elasticity in the range of applicability of the latter: It converges to classical elasticity in the appropriate limit as the horizon shrinks to zero, assuming that the underlying deformation is sufficiently smooth [5]. Additionally, because peridynamics avoids any assumption of smoothness of the deformation field and treats the exact kinematics, it is well aligned with the kinematic assumptions of molecular dynamics. These features illustrate ways in which peridynamics is a generalization of the classical theory.

Results and Discussion

Figure 1 illustrates that the peridynamic state theory enables use of traditional stress-strain based material models. Figure 1a shows well-behaved simulation results for a uniaxial tension test on an aluminum bar represented by a standard visco-plasticity constitutive model [8]. The calculation remains stable with decreasing load (Figure 1b). Figure 1c shows the results of a Taylor impact test using the same constitutive model for aluminum [8]. The final shape is seen to agree well with the experimental observation [11].

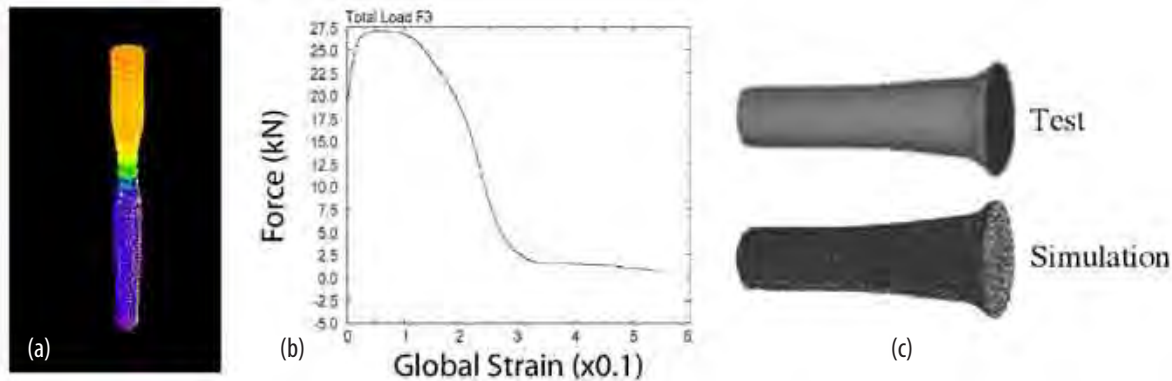


Figure 1. Employing conventional material models in state-based peridynamics. (a) Necking in a smooth bar loaded in uniaxial tension. Colors denote axial velocity. (b) Force-strain curve. (c) Experimental [11] and simulated images of a Taylor impact test on 6061 T-6 Aluminum [8].

Figure 2 shows that peridynamics recovers the characteristic structure of the “mirror, mist, hackle” surface produced by dynamic fracture. The fracture surface varies from being mirror-smooth near the onset of fracture, to cloudy further along the crack’s progression, until it becoming very rough. The roughening of the fracture surface

results from microscopic crack branching. Eventually, this can lead to macroscopic crack branching with further propagation of the fracture [12]. In the two-dimensional simulation shown, a crack is propagated from an initial notch at the left edge in a sheet of brittle material. The horizontal edges are initially displaced vertically and then held fixed, resulting in an initial tensile stress field. The fracture surface exhibits the characteristic progression from the smooth, mirror region, to the rougher mist region, to the very rough hackle region. Comparison of the damage (2a) with the fracture surface (2b) reveals that the roughening arises from arrested micro-branches along the fracture surface.



Figure 2. (a) Material damage (bond breaking) from dynamic cracking produced by lateral tension applied to an initially notched thin plate. (b) Fracture surface created by dynamic cracking simulation of Figure 2a.

Figure 3 shows the crack velocity history from this simulation. The initially unsteady speed is seen to reach a relatively stable limiting value that is substantially below the theoretical limiting wave speed. This result is in good agreement with experimental observations [12].

A simulation of the Kalthoff-Winkler experiment is shown in Figure 4. In this experiment a metal plate with two notches is struck on edge by an impactor [1]. The resulting cracks emanate from the notches at reproducible angles that depend on the impactor speed. For the chosen impactor speed, cracks are observed to make a 70° angle to the initial notch direction, which is well reproduced by the peridynamic simulation. Note, in addition, that the transition from mode II to mode I fracture naturally evolves without intervention by the analyst.

Under high stress intensity levels, branches can be emitted from a crack tip. With increasing stress level, the branching point moves closer to the starting defect. Figure 5 illustrates that both branching and the trend in branching point location can emerge from peridynamic simulations [13]. The cracks emanate from initial notches at the left edge. The only parameters specified for these simulations were constant values of density, Young's modulus, and energy release rate; no kinetic relation was used to guide the branching.

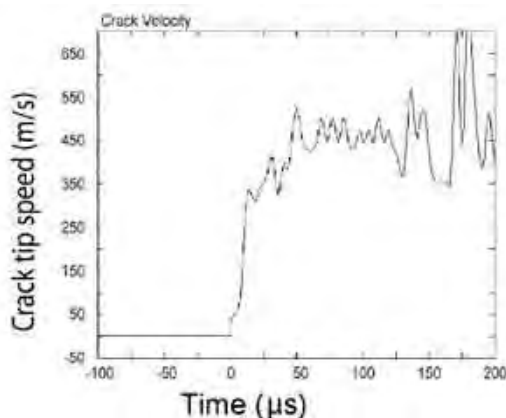


Figure 3. Crack velocity history for the simulation of Figure 2.

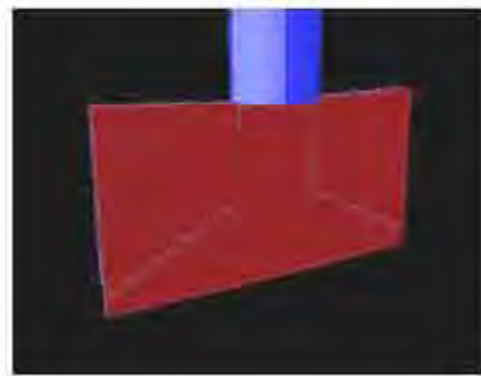


Figure 4. Kalthoff-Winkler Experiment. Peridynamics simulation of impact on a pre-notched plate.

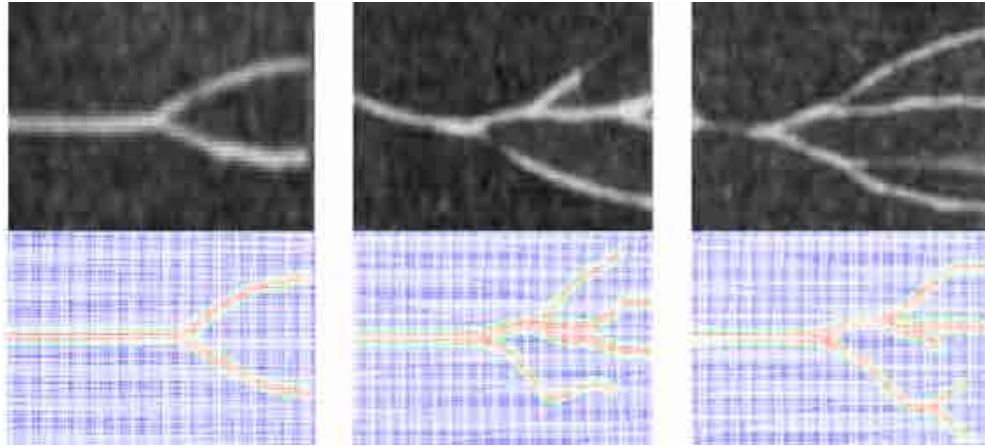


Figure 5. Cascading crack branching in glass under progressively higher applied stresses, left to right. Top row - Experimental results for soda-lime glass [14]. Bottom row - Simulations of Duran 50 glass [13]. Boundary conditions differed slightly in the experiment and simulation.

As a mesh-free method, peridynamics is well suited for simulating highly heterogeneous materials. Figure 6 shows the varying cracking modes that develop in laminated, fiber reinforced composites having differing lay-ups. All specimens have an initial horizontal center notch and are pulled in uniaxial tension. The figure illustrates variations of cracking mode with distribution of composite fiber directions that are comparable to those observed in laboratory tests.

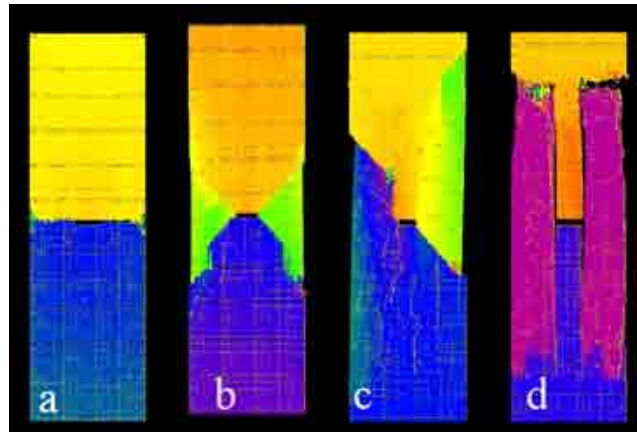


Figure 6. Variation in cracking modes in a notched laminate composite bar under vertically applied tension: (a) Quasi-isotropic sample; (b) All $\pm 45^\circ$ plies; (c) $\pm 45^\circ$ plies and 0° plies; (d) Mostly 0° plies (along length of bar). Images are colored by vertical displacement.

For the seven remaining characteristic phenomena of the 12 listed above, peridynamic simulation results for each agree very well with experiments, except for arrest of unstable crack growth, which has not yet been simulated.

Acknowledgement

We thank F. Bobaru and Y. D. Ha for early access to their branching simulations. Sandia is a multi-program laboratory operated by Sandia Corporation, a Lockheed Martin Company, for the United States Department of Energy under Contract DEAC04-94AL85000.

References

- [1] J. S. Kalthoff and S. Winkler, in *Impact Loading and Dynamic Behavior of Materials*, eds., C. Y. Chiem *et al.* (Germany, DGM Informationsgesellschaft, 1988) p. 185.
- [2] J. Lambros and A. J. Rosakis, “Shear dominated transonic interfacial crack growth in a bimaterial-I. Experimental observations,” *J. Mech. Phys. Solids* **43** 169-188 (1995).
- [3] S. A. Silling, “Reformulation of elasticity theory for discontinuities and long-range Forces,” *Journal of the Mechanics and Physics of Solids* **48** 175-209 (2000).
- [4] S. A. Silling, M. Epton, O. Weckner, J. Xu, E. Askari, “Peridynamic States and Constitutive Modeling,” *Journal of Elasticity* **88** 151-184 (2007).
- [5] S. A. Silling and R. B. Lehoucq, “Convergence of Peridynamics to Classical Elasticity Theory,” *Journal of Elasticity* **93** 13-37 (2008).
- [6] S. A. Silling and E. Askari, “A meshfree method based on the peridynamic model of solid mechanics,” *Computers and Structures* **83** 1526-1535 (2005). Also see <http://en.wikipedia.org/wiki/Peridynamics>.
- [7] E. Askari, F. Bobaru, R. B. Lehoucq, M. L. Parks, S. A. Silling, O. Weckner, “Peridynamics for multiscale materials modeling,” *SciDAC 2008, Journal of Physics: Conference Series* **125** (2008) pp. 012078.
- [8] J. T. Foster, S. A. Silling, W. W. Chen, *Viscoplasticity Using Peridynamics*, Sandia Report, SAND 2008-7835 (Albuquerque, NM, Sandia National Laboratories).
- [9] R. B. Lehoucq and S. A. Silling, *Statistical Coarse-Graining of Molecular Dynamics into Peridynamics*, Sandia Report, SAND2007-6410 (Albuquerque, NM, Sandia National Laboratories)..
- [10] (A) M. L. Parks, R. B. Lehoucq, S. Plimpton, S. Silling, “Implementing peridynamics within a molecular dynamics code,” *Computer Physics Communications* **179** 777-783 (2008). (B) P. Seleson, M. L. Parks, M. Gunzburger, R. B. Lehoucq, “Peridynamics as an upscaling of molecular dynamics,” accepted SIAM Multiscale Mod. Sim. (2009).
- [11] C. E. Anderson, Jr., A. E. Nicholls, I. S. Chocron, R. A. Ryckman, “Taylor Anvil Impact,” *AIP Conference Proceedings* **845** (Melville, NY, AIP, 2008) p. 1367.
- [12] J. Feinberg and M. Marder, “Instability in dynamic fracture,” *Physics Reports* **313** 1-108 (1999).
- [13] Y. D. Ha and F. Bobaru, *Crack Branching Analysis with Peridynamics*, Technical Report (Lincoln, NB, Department of Engineering Mechanics, University of Nebraska-Lincoln, May 2009).
- [14] F. P. Bowden, J. H. Brunton, J. E. Field, A. D. Heyes, “Controlled fracture of brittle solids and interruption of electrical current,” *Nature* **216** 38-42 (1967).

MOLECULAR DYNAMIC SIMULATION OF THERMODYNAMIC AND MECHANICAL PROPERTIES AND BEHAVIOR OF MATERIALS AT HIGH STRAIN RATE

V. Dremov,* A. Karavaev,* F. Sapozhnikov,* M. Vorobyova,* L. Soulard†

* Russian Federal Nuclear Center – Zababakhin Institute of Applied Physics, Russia

† CEA/DAM Ile-de-France, BP12, 91680 Bruyeres-le-Chatel

The classical MD approach was applied to model Be properties and response to dynamic loading. Special attention was paid to the calculation of the melting curve and physical properties during melting. The Hugoniot MD technique was applied to obtain the Hugoniot of beryllium taking melting into account. Results of calculations were compared with experimental data and the results of ab initio and quantum MD calculations. Results of the direct MD simulation of shock loading of nano-polycrystalline beryllium (hcp grains, average grain size ~10 nm) and data on dynamic yield stress as dependent on shock stress were obtained. Since the length of Be samples used was about 0.2 mm, only the ultra-fast stage (time-scale ~20 ps) of relaxation behind the shock front was investigated. Calculated results are discussed and analyzed in comparison with experimental data.

Introduction

In [1], parameters of the MEAM potential developed for HCP metals [2] were fitted for beryllium, and its mechanical, thermodynamic, and shock properties were investigated through MD simulations. Comparison of MD results with experimental data showed that the resulted potential adequately described the elastic properties of beryllium under static compression at normal temperature and the Hugoniot. However, further testing revealed an essential fault of the potential: it strongly underestimated the temperature of beryllium melting at $V=V_{300\text{ K}}$. Here we report modifications to some of the MEAM parameters, which helped bring this temperature into sync with experimental results. We did calculations for thermodynamic and mechanical properties of beryllium in a wide range of temperatures and pressures. Their results show that the new potential adequately describes melting versus pressure and sound velocity along the Hugoniot, including transition to liquid.

Static MD Calculations

In the macroscopic models, yield stress correlates with melting temperature through the temperature dependence of elastic moduli. That is why the correct description of the temperature dependence of elastic moduli and the melting curve in MD simulations is an implicit guarantee for the proper description of shear stress relaxation kinetics under dynamic loading.

Experimental data on the phase diagram of beryllium are limited to a pressure of 60 Kbar [3]. At $T=1530\text{ K}$ and ambient pressure, beryllium becomes body-centered cubic (BCC) structured and then melts at 1550 K. The HCP-BCC transition increases density which results in a negative slope of the phase boundary. This slope means that the transition may also occur at high pressures and room temperature, but in experiments up to the present, this transition has not been observed up to 2 Mbar [4].

MD simulations allow calculating the melting curve in a wide range of pressures. Here the curve was calculated for HCP beryllium because there is experimental evidence [5,6] that shocked beryllium melts just from this phase.

The start of the solid-to-liquid transition can be determined from the density jump on the isobar or the isotherm. Isobars and isotherms were calculated in pressure and temperature ranges up to 200 GPa and 4000 K, respectively.

The results suggest that

- the new potential gives a temperature of melting at $P=0$, which is close to the experimental 1550 K;
- the temperature of melting start on the Hugoniot is about 1500 K lower than that from quantum MD (see Figure 2)[5,8];
- the melting curves calculated with the equations of state from [7] and SESAME [9] and the Lindemann law agree well with results obtained in this work;
- all Hugoniot data agree well with each other in P-T coordinates (Figure 2).

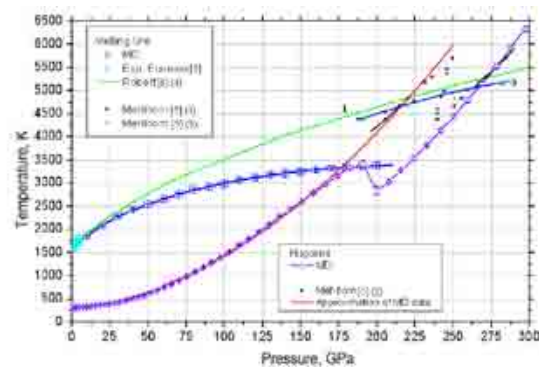


Figure 2. Melting curves and Hugoniot.

Calculations for the bulk and shear moduli in a wide range of pressures and temperatures are presented in Figures 3 and 4. The polymorphous HCP-BCC transition was not considered in MD calculations. Calculated HCP-BCC phase equilibrium boundaries [7,8] are provided in Figures 3 and 4 for reference.

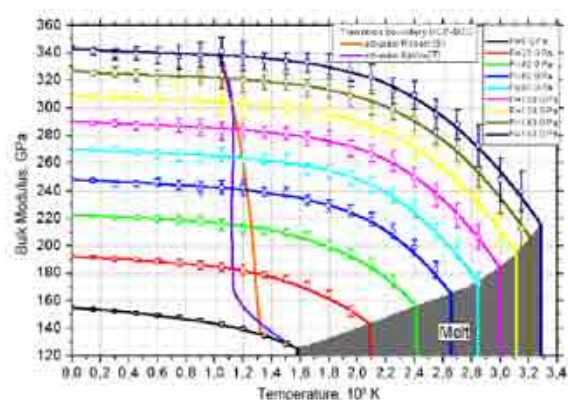


Figure 4. Shear modulus vs temperature for different pressures.

Bulk and longitudinal sound speeds along the Hugoniot were obtained in a wide pressure range with the use of (P-T) tabulated elastic moduli and the Hugoniot. Figure 5 shows sound speeds calculated in this work and in [8] by the method of *ab initio* molecular dynamics in comparison with experimental data from [13,14].

For $P < 50$ GPa, the bulk and longitudinal sound speeds are seen to agree well with *ab initio* molecular dynamics results [8] and with experimental data [13]. Data obtained at Sandia National Laboratories on Z [14] are the only available set of experimental results on beryllium shock compression, which covers the range of pressures on the Hugoniot including melting. According to these data (Figure 5), the start of melting on the Hugoniot can be placed at ~ 175 GPa, which agrees well with the position of the melting curve obtained in this work. As mentioned above, the point of melting on the Hugoniot obtained in *ab initio* MD calculations [8,10] is about 1500 K higher, which corresponds to a pressure of ~ 200 GPa.

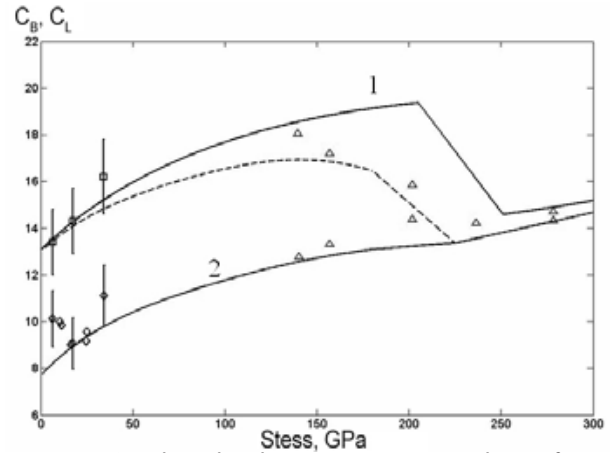


Figure 5. Sound speed on the Hugoniot: experimental points from [13] are black boxes (C_L) and rhombs (C_B); experimental points from [14] are triangles; *ab initio* MD results on C_L [8] are shown by solid line 1; longitudinal and bulk sound speeds from MD calculations are shown by dashed and solid (2) lines, respectively.

Direct MD Modeling of Beryllium Response to Shock

Plane wave shock loading was simulated with the use of Be monocrystalline and nano-polycrystalline samples having length ~ 0.18 μm and cross-section 70×70 rectangular unit cells (rectangular HCP u.c. contains four atoms). Figure 6 illustrates the process of shear stress relaxation behind the shock front. What draws attention are periodic perturbations in shear stress that are seen right behind the shock front. A likewise pattern with the solitary wave train was first observed in MD simulations where FCC copper was loaded in direction $[110]$ (see [17]). But those simulations were done for the cryogenic initial temperature (10 K), and as shown in [18], the pattern vanished as temperature increased to ~ 100 K. Our calculations for Be show the similar pattern for initial temperature 300 K. Given the high Debye temperature for Be ($\theta_D = 1460$ K), one can conclude that in Be at $T = 300$ K, thermal energy is actually lower than in the classical MD simulation and expect a stronger effect of the solitary wave train.

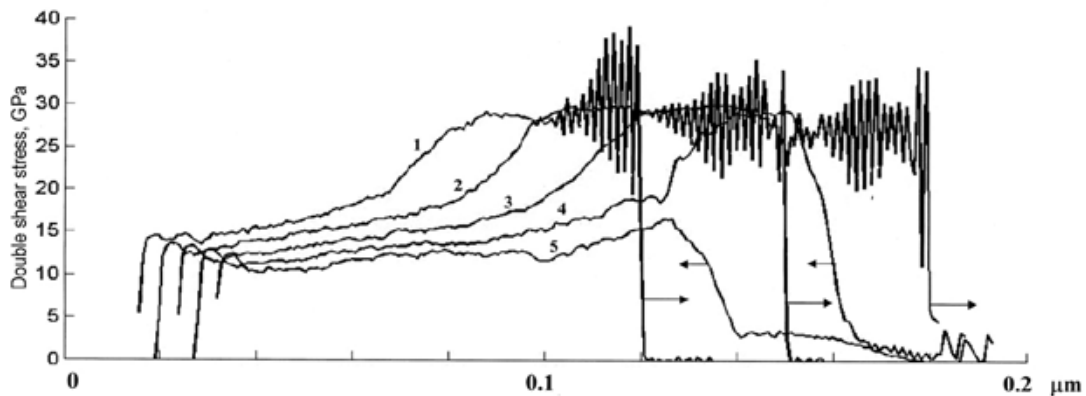


Figure 6. Evolution of the shear stress profile with time in single crystal Be loaded ($U_p = 2000$ m/s) in $[2110]$ direction. Curves 1–5 correspond to different times (8, 10, 12, 14, 16 ps). Arrows point to shock and rarefaction fronts and to the direction of wave propagation.

The typical shear stress profile is seen to be subdivided into three parts: (1) the maximum shear stress gained just behind the shock front and remaining constant for some time (relaxation delay); (2) the rapid decrease of the shear stress; and (3) the slow decrease of the shear stress.

Figure 7 generalizes data on the relaxation of shear stresses and their residual values resulted from MD simulations. The figure also provides comparison with experimental data on the dynamic yield stress of Be [13] and with the data calculated with the Steinberg model [15].

Figure 7 shows that both the longitudinal stress and the residual shear stress for polycrystalline samples are much closer to the experimental values. It is also seen that relaxation has not yet finished. One can see that relaxation in the single crystal sample being loaded in direction $_{[2\bar{1}10]}$ at $U_p=2000$ m/s is faster than at $U_p=1500$ m/s, and residual shear stresses are lower after one and the same time (20 ps). At $U_p=1000$ m/s, relaxation in the monocrystalline sample being loaded in direction $_{[2\bar{1}10]}$ does not start after 15 ps. Longitudinal stresses during relaxation also become closer to the values that were experimentally observed for the corresponding particle velocities.

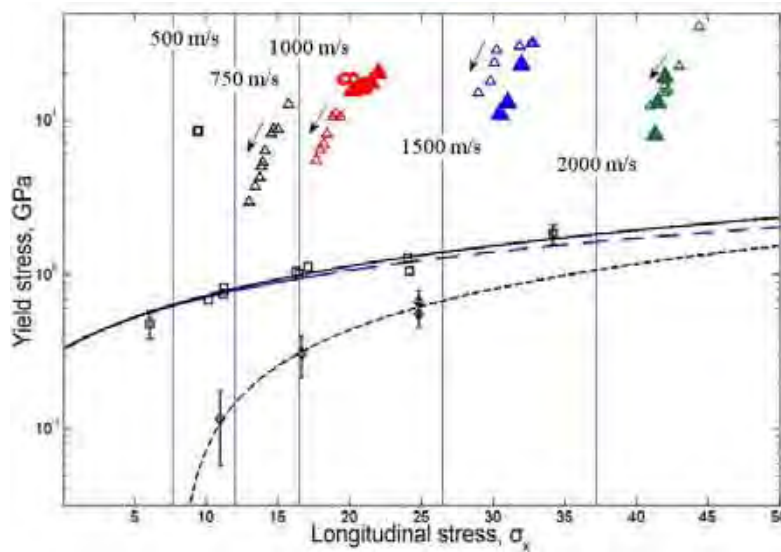


Figure 7. Yield stress versus longitudinal stress in shocks (color online). The solid line approximates experimental points from [13], which are shown by squares; the dashed line shows results obtained with the Steinberg model [15]; the dotted line approximates experimental points from [13] on shock recompression, which are shown by rhombs. The vertical thin lines with figures mark longitudinal stresses at $U_p=500, 750, 1000, 1500$ and 2000 m/s, determined from the experimental D-U relation ($D=7.99+1.13U$) [16]. Symbols show twice the shear stress versus longitudinal stress as shear stresses relax with time for different samples and stress levels: \triangle - single crystal $_{[2\bar{1}10]}$, $U_p=2000$ m/s; \triangle - single crystal $_{[2\bar{1}10]}$, $U_p=1500$ m/s; \circ - single crystal $_{[2\bar{1}10]}$, $U_p=1000$ m/s; \triangle - polycrystal, $U_p=1000$ m/s; \triangle - polycrystal, $U_p=750$ m/s; \square - single crystal $[0001]$, $U_p=500$ m/s. The arrows show direction from the earlier to the later time. Calculations with polycrystalline samples and MEAM(2) are marked by \triangle , \triangle , and \triangle .

Thus, our MD investigation into the elastic-plastic properties of Be suggests that at times typical for the MD simulation and the level of loading about 10–40 GPa, the yield stress for both monocrystalline and polycrystalline samples is much higher than in experiment. More properly, we should say about the effective yield stress whose value is defined by the relatively slow kinetics of elastic-plastic deformation.

References

- [1] V. V. Dremov, A. V. Karavaev, A. L. Kutepov, L. Soulard, "Molecular dynamics simulation of thermodynamic and mechanical properties of Be and Mg," *AIP Conference Proceedings* **955** (Melville, NY, AIP, 2008) pp. 305-308.
- [2] M. I. Baskes and R. A. Johnson, "Modified embedded atom potentials for HCP metals," *Modelling Simul. Mater. Sci. Eng.* **2** 147-163 (1994).
- [3] M. Francois and M. Contre, *Proceeding of the Conference Internationale sur la Metallurgie du Beryllium* (Paris, Universite de France, 1965). [Can't find more info.]
- [4] W. J. Evans, M. J. Lipp, H. Cynn, C. S. Yoo, M. Somayazulu, D. Häusermann, G. Shen, V. Prakapenka, X-ray diffraction and Raman studies of beryllium: Static and elastic properties at high pressures, *Phys. Rev. B* **72** 094113 (2005).
- [5] T. Mehlhorn, Presentation at Zababakhin Scientific Talks (2007).
- [6] L. X. Benedict, T. Ogitsu, A. Trave, C. J. Wu, P. A. Sterne, E. Schwegler, "Calculations of high-pressure properties of beryllium: Construction of a multiphase equation of state," *Phys. Rev. B* **79** 064106 (2009).
- [7] G. V. Sin'ko and N. A. Smirnov, "Relative stability and elastic properties of hcp, bcc, and fcc beryllium under pressure," *Phys. Rev. B* **71** 214108 (2005).
- [8] R. G., A. Sollier, and Ph. Legrand, "Multiphase equation of state and strength properties of beryllium from *Ab Initio* and quantum molecular dynamics calculations," *AIP Conference Proceedings* **955** (Melville, NY, AIP, 2008) pp. 97-100.
- [9] D. C. Swift, T. E. Tierney, S.-N. Luo, D. L. Paisley, G. A. Kyrala, A. Hauer, S. R. Greenfield, A. C. Koskelo, K. J. McClellan, H. E. Lorenzana, D. Kalantar, B. A. Remington, P. Peralta, E. Loomis, "Dynamic response of materials on subnanosecond time scales, and beryllium properties for inertial confinement fusion," *Physics of Plasmas* **12** 056308 (2005).
- [10] J. F. Smith and C. L. Arbogast, "Elastic constants of single crystal beryllium," *Journal Appl. Phys.* **31**, Issue 1, 99 (1960).
- [11] K. Nakano, Y. Akahama, H. Kawamura, "X-ray diffraction study of Be to megabar pressure," *J. Phys.: Condens. Matter* **14**, No. 44, 10569 (2002).
- [12] N. Velisavljevic, G. N. Chestnut, Y. K. Vohra, S. T. Weir, V. Malba, J. Akella, "Structural and electrical properties of beryllium metal to 66 GPa studied using designer diamond anvils," *Phys. Rev. B* **65** 172107 (2002).
- [13] L. C. Chhabildas, J. L. Wise, J. R. Asay, "Reshock and release behavior of beryllium," *Shock Waves in Condensed Matter; AIP Conference Proceedings* **78**, Issue 1, 422-426 (1982).
- [14] C. Deeney, Dynamic materials experiments on Z in support of Campaigns 2.1 and 2.2, CEGSNL Working Groups (2006).
- [15] D. J. Steinberg, *Equation of State and Strength Properties of Selected Materials*, UCRL-MA-106439 (Livermore, CA, Lawrence Livermore National Laboratory) (1991).
- [16] *LASL Shock Hugoniot Data*, ed. S. P. Marsch (Berkeley, CA, University of California Press 1980).
- [17] T. C. Germann, B. L. Holian, P. S. Lomdahl, "Orientation Dependence in Molecular Dynamics Simulations of Shocked Single Crystals," *Phys. Rev. Lett.* **84** 5351-5354 (2000).
- [18] V. V. Dremov, F. A. Sapozhnikov, M. S. Smirnova, "Molecular dynamics investigation into elastic-plastic properties of solids," *Proc. of 5th International Symp. on High Dynamic Pressures (HDP-5) I* (Sain-Malo, France, 2003) pp. 331-340.

CHALLENGES OF, AND VARIATIONS ON, COUPLED ATOMISTIC-CONTINUUM SIMULATION

J. A. Zimmerman

Sandia National Laboratories, Livermore, CA 94550 USA

Contact Author: jjzimmer@sandia.gov

A primary objective of materials modeling is to assess the mechanical reliability of components by predicting the deformation mechanisms leading to failure of a given material. As these mechanisms operate at length scales ranging from nanometers to microns, a variety of materials simulations methods and tools have been developed that couple these scales. This coupling is often accomplished by directly interfacing multiple analysis techniques (e.g., atomistic simulations with continuum-scale finite element analysis), but can also be instantiated through informational or hierarchical means such as by evaluating continuum variables within the framework of atomic-scale calculations. This paper reviews two different flavors of multi-scale coupling and comment on future challenges yet to be addressed.

Introduction

Recent technology advances have focused around the use of Micro-Electro-Mechanical Systems (MEMS) and their nanoscale counterpart, aptly named NEMS. Of particular concern is the performance and reliability of MEMS and NEMS under a range of thermomechanical operating conditions. In these systems, device dimensions are the same or smaller than the scales at which material failure mechanisms are known to operate. Such mechanisms include brittle and ductile fracture, dislocation activity, large plastic deformation, grain boundary sliding, stiction, friction, and wear.

While many models and simulation methods have been developed to study and predict the behavior of these failure mechanisms, they typically fall into two categories: continuum mechanics analysis [1] and atomistic simulation [2]. Continuum mechanical modeling and simulation methods include the finite element (FE) and boundary element methods, as well as more exotic techniques such as dislocation dynamics. The state of the art in continuum analysis has evolved to include cohesive approaches for surface separation and damage accumulation models for bulk material degradation. However, these techniques only capture anticipated deformation phenomena. Moreover, the relative strengths of competing mechanisms are not always well represented.

Atomistic simulation methods, such as molecular statics and dynamics (MD), use simple inter-atomic potentials, the relation between particle forces and energies, and Newton's 2nd law (for MD) to govern the basic physics of the system's response to an applied load. Atomistic simulation can display competing mechanisms of material deformation, such as fracture, dislocation nucleation and propagation, and void nucleation, growth, and coalescence. As with continuum analysis, atomistic simulation has its own limitations (e.g., current computational capabilities are insufficient for the analysis of micro-scale systems).

The advantages of both atomistic simulation and continuum analysis have given rise to the development of multi-scale modeling and coupled atomistic-continuum simulation (CACS) techniques. This paper reviews two different types of multi-scale coupling. In one technique, atomistic and continuum analyses directly interface. In the other, coupling occurs in an informational sense, as expressions are used to evaluate continuum mechanical variable fields within atomistic simulations. The paper concludes with comments on future challenges yet to be addressed by these methods.

CACS for Arbitrary Overlapping Domains

This section will briefly summarize the formulation by Klein and Zimmerman for coupled atomistic-continuum simulations for quasi-static analysis [3,4]. This technique enables the geometry of the continuum discretization and the atomic crystal to overlap arbitrarily. The coupling between the two regimes lies in the development of kinematic and thermodynamic expressions that connect energy and deformation, and not to the particular representation of atoms and nodes. Expanded details on both the theory and computational aspects of the method can be found in [3].

Kinematics

In this method, an FE mesh covers all parts of the computational domain, while only limited regions of interest, such as crack tips, are also represented with an atomic crystal. The mesh is defined through two groups of nodes, those that are free to be deformed according the continuum equations of motion (nodal displacement – \mathbf{U}) and those that have their motion prescribed via projection from the underlying atomic system ($\hat{\mathbf{U}}$). Likewise, the atomic system is composed of free atoms (atomic displacement – \mathbf{Q}) and atoms that have their displacement prescribed via interpolation from the overlapping continuum ($\hat{\mathbf{Q}}$). These fields are connected to each other in the following way:

$$\begin{Bmatrix} \mathbf{Q} \\ \hat{\mathbf{Q}} \end{Bmatrix} = \mathbf{N} \begin{Bmatrix} \mathbf{U} \\ \hat{\mathbf{U}} \end{Bmatrix} + \begin{Bmatrix} \mathbf{Q}' \\ \mathbf{0} \end{Bmatrix}, \quad \text{where} \quad \mathbf{N} = \begin{bmatrix} \mathbf{N}_{\mathbf{QU}} & \mathbf{N}_{\mathbf{Q}\hat{\mathbf{U}}} \\ \mathbf{N}_{\hat{\mathbf{Q}}\mathbf{U}} & \mathbf{N}_{\hat{\mathbf{Q}}\hat{\mathbf{U}}} \end{bmatrix} \quad (1)$$

The submatrices of \mathbf{N} contain defined interpolation or shape functions. \mathbf{Q}' is introduced since the FE shape functions $\mathbf{N}_{\mathbf{QU}}$ and $\mathbf{N}_{\hat{\mathbf{Q}}\mathbf{U}}$ are generally too coarse to represent the atomistic displacement exactly. The goal to minimize the error related to \mathbf{Q}' is achieved by defining $\hat{\mathbf{U}}$ and $\hat{\mathbf{Q}}$ as follows:

$$\hat{\mathbf{U}} = \mathbf{B}_{\hat{\mathbf{U}}\mathbf{Q}} \mathbf{Q} + \mathbf{B}_{\hat{\mathbf{U}}\mathbf{U}} \mathbf{U}, \quad \hat{\mathbf{Q}} = \mathbf{B}_{\hat{\mathbf{Q}}\mathbf{Q}} \mathbf{Q} + \mathbf{B}_{\hat{\mathbf{Q}}\mathbf{U}} \mathbf{U} \quad (2)$$

where

$$\mathbf{B}_{\hat{\mathbf{U}}\mathbf{Q}} = \mathbf{M}_{\hat{\mathbf{U}}\mathbf{U}}^{-1} \mathbf{N}_{\mathbf{Q}\hat{\mathbf{U}}}^T, \quad \mathbf{B}_{\hat{\mathbf{U}}\mathbf{U}} = -\mathbf{B}_{\hat{\mathbf{U}}\mathbf{Q}} \mathbf{N}_{\mathbf{QU}}, \quad \mathbf{B}_{\hat{\mathbf{Q}}\mathbf{Q}} = \mathbf{N}_{\hat{\mathbf{Q}}\hat{\mathbf{U}}} \mathbf{B}_{\hat{\mathbf{U}}\mathbf{Q}}, \quad \mathbf{B}_{\hat{\mathbf{Q}}\mathbf{U}} = \mathbf{N}_{\hat{\mathbf{Q}}\mathbf{U}} - \mathbf{B}_{\hat{\mathbf{Q}}\mathbf{Q}} \mathbf{N}_{\mathbf{QU}} \quad (3)$$

and $\mathbf{M}_{\hat{\mathbf{U}}\mathbf{U}} = \mathbf{N}_{\mathbf{Q}\hat{\mathbf{U}}}^T \mathbf{N}_{\mathbf{Q}\hat{\mathbf{U}}}$. Klein and Zimmerman have also shown that a moving least squares (MLS) interpolation can be substituted for the projection operation, thereby replacing the term $\mathbf{B}_{\hat{\mathbf{U}}\mathbf{Q}}$ with a matrix of shape functions possessing unique properties.

Coupled Equilibrium Equations

As stated succinctly in [4], the solution for the displacements \mathbf{Q} and \mathbf{U} can be determined using equilibrium equations derived by formulating the total potential energy of the coupled atomistic-continuum system:

$$\Pi(\mathbf{Q}, \mathbf{U}) = \Pi_{\mathbf{Q}}(\mathbf{Q}, \hat{\mathbf{Q}}(\mathbf{Q}, \mathbf{U})) + \Pi_{\mathbf{U}}(\mathbf{U}, \hat{\mathbf{U}}(\mathbf{Q}, \mathbf{U})) - \mathbf{F}_{\mathbf{Q}} \cdot \mathbf{Q} - \mathbf{F}_{\mathbf{U}} \cdot \mathbf{U} \quad (4)$$

In this equation, $\Pi_{\mathbf{Q}}$ represents the potential energy in the bonds of the crystal, $\Pi_{\mathbf{U}}$ is the strain energy density integrated over the continuum, and $\mathbf{F}_{\mathbf{Q}}$ and $\mathbf{F}_{\mathbf{U}}$ are external forces acting on the atoms and nodes, respectively.

The resulting static equilibrium equations are:

$$\mathbf{R}_Q = \frac{\partial \Pi_Q}{\partial \mathbf{Q}} + \mathbf{B}_{\hat{Q}Q}^T \frac{\partial \Pi_Q}{\partial \hat{\mathbf{Q}}} + \mathbf{B}_{\hat{U}Q}^T \frac{\partial \Pi_U}{\partial \hat{\mathbf{U}}} - \mathbf{F}_Q = 0 \quad (5)$$

$$\mathbf{R}_U = \frac{\partial \Pi_U}{\partial \mathbf{U}} + \mathbf{B}_{\hat{U}U}^T \frac{\partial \Pi_U}{\partial \hat{\mathbf{U}}} + \mathbf{B}_{\hat{Q}U}^T \frac{\partial \Pi_Q}{\partial \hat{\mathbf{Q}}} - \mathbf{F}_U = 0 \quad (6)$$

Correction to the Cauchy-Born Relation

The final element of this formulation is to prescribe the potential energy functions (constitutive models) for both the atomistic and continuum used in equation (4). Π_Q is computed from a sum of bond energies in the crystal directly using whichever inter-atomic potential is chosen to model the material of interest. Π_U is computed using the Cauchy-Born relation to connect the chosen inter-atomic potential to the strain energy density of a homogeneously deformed atomic crystal, $\Phi = \Phi(\mathbf{C}, \mathbf{X})$. An important concern is how to correct for the overlap of the continuum and the underlying crystal. This correction amounts to weighting the contributions to potential energy from elements containing both free nodes and ghost atoms. Spatially varying bond density functions are introduced so that the calculation of strain energy density accounts for only the “missing” energy that is not represented by actual bonds between atoms within the system. These functions are determined by enforcing a condition of homogeneous deformation given the appropriate boundary conditions, and by minimizing the fictitious forces on both free and prescribed nodes within the overlap region for the coupled system. Further details can be found in [3].

Example Simulation: Surface Relaxation of a Nanowire

This method can be used to examine surface relaxations in nanostructured materials with free surfaces. In general, materials with free surfaces possess atoms with different bond spacing than interior atoms. For a system created with a uniform bulk configuration, energy minimization produces an inward or outward surface relaxation, depending on the nature of the inter-atomic bonding. Figure 1 shows the cross-sectional view of a nanowire containing a face-centered-cubic crystal of about 96,000 atoms. Atoms interact via a fifth neighbor Lennard-Jones potential for gold. The crystal is oriented with the wire axis along a [100] direction.

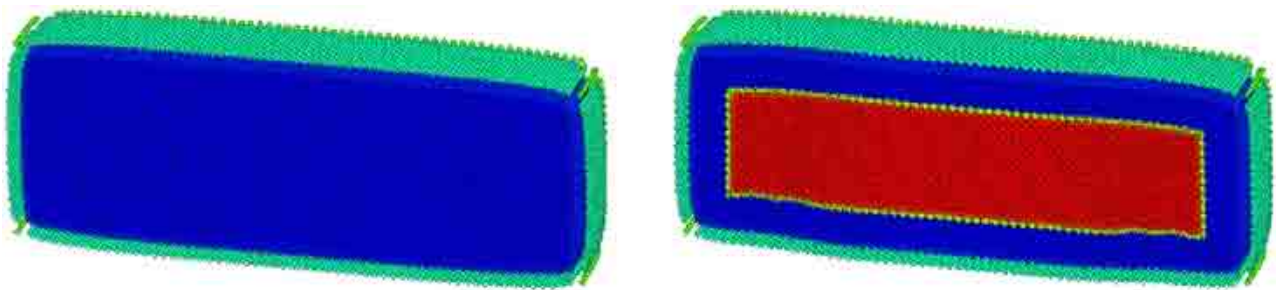


Figure 1. Cross-sectional view of surface relaxation of a nanowire. Displacements are magnified by a factor of 100. Left: Atomistic simulation. Right: Coupled atomistic-FE simulation using an underlying hexahedral mesh.

With displacements magnified by a factor of 100, the figure shows that atoms at or near the free surfaces displace significantly as compared with atoms just a few layers in. Moreover, Figure 1 shows that the coupled method produces a configuration very similar to that achieved by pure atomistic simulation. Here, atoms are colored according to how much bond energy they receive from the atomistic analysis. The interior of the coupled region, occupied only by ghost atoms, has nearly zero energy (colored red) while the free atoms near the surfaces assume energy values in agreement with the pure atomistic simulation (colored blue and green).

Extracting Continuum Variables from Atomistic Simulation

Atomistic-continuum coupling can also be done in an informational sense. Expressions for continuum thermomechanical variables such as stress, heat, and temperature have been developed that use atomistic simulation quantities (e.g., inter-atomic forces and atomic velocities). While a variety of approaches exist, the resulting expressions are usually similar in appearance. Here, we briefly review the method developed by R. J. Hardy [5]. In addition to references by Hardy and his co-authors, Hardy's formulation has also been extensively examined by Zimmerman and colleagues [4,6,7]. The reader is referred to these articles for more information.

Hardy's Formulation

Hardy's method consists of defining the continuum fields of mass (ρ), momentum (\mathbf{p}) and energy (e) density in terms of atomic positions (\mathbf{x}^α) and velocities (\mathbf{v}^α):

$$\rho(\mathbf{x}, t) = \sum_{\alpha=1}^N m^\alpha \psi(\mathbf{x}^\alpha - \mathbf{x}), \quad \mathbf{p}(\mathbf{x}, t) = \sum_{\alpha=1}^N m^\alpha \mathbf{v}^\alpha \psi(\mathbf{x}^\alpha - \mathbf{x}) \quad (7)$$

$$e(\mathbf{x}, t) = \sum_{\alpha=1}^N \left\{ \frac{1}{2} m^\alpha \mathbf{v}^\alpha \cdot \mathbf{v}^\alpha + \phi^\alpha \right\} \psi(\mathbf{x}^\alpha - \mathbf{x}) \quad (8)$$

where ϕ^α represents the potential energy attributed to atom α , m^α represents the atom's mass, and the localization function ψ is a weighting factor for averaging the properties of the atoms, allowing each atom to contribute to a continuum property at a fixed spatial point \mathbf{x} at time t . Detailed information regarding the use and properties of the localization function can be found in [4-7]. Using these density functions within the continuum balance equations for linear momentum and energy, Hardy developed expressions for stress (σ) and heat flux (q) at a spatial point. For example,

$$\sigma(\mathbf{x}, t) = - \left\{ \frac{1}{2} \sum_{\alpha=1}^N \sum_{\beta \neq \alpha}^N \mathbf{x}^{\alpha\beta} \otimes \mathbf{F}^{\alpha\beta} B^{\alpha\beta}(\mathbf{x}) + \sum_{\alpha=1}^N m^\alpha \mathbf{u}^\alpha \otimes \mathbf{u}^\alpha \psi(\mathbf{x}^\alpha - \mathbf{x}) \right\}. \quad (9)$$

Here, $\mathbf{x}^{\alpha\beta} = \mathbf{x}^\alpha - \mathbf{x}^\beta$, $x^{\alpha\beta} = |\mathbf{x}^{\alpha\beta}|$, $\mathbf{F}^{\alpha\beta}$ is the inter-atomic force exerted on atom α by atom, β , $\mathbf{u}^\alpha \equiv \mathbf{v}^\alpha - \mathbf{v}$ where $\mathbf{v} \equiv \mathbf{p}/\rho$, and $B^{\alpha\beta}$ is the bond function defined by the expression $B^{\alpha\beta}(\mathbf{x}) = \int_0^1 \psi(\lambda \mathbf{x}^{\alpha\beta} + \mathbf{x}^\beta - \mathbf{x}) d\lambda$.

Stress Field Evolution During Thin Film Island Coalescence

Hardy's expression for stress can be used to gain fundamental understanding of materials behavior: specifically stress evolution during metallic thin film growth. During such growth, isolated islands are first nucleated and then proceed to coalesce and form continuous planar films. While experiments have successfully quantified the average stress within a film during growth, little is known about the distribution of stress within a film or whether defects form as island coalescence occurs. MD simulations were used to examine the initial coalescence that occurs when neighboring cylindrical islands first join together. Figure 2 shows one component of the stress field within the islands before and after the coalescence process. It is observed that some variation of stress exists within the island, and that, upon coalescence, a dislocation defect is formed along with a concentration of tensile stress within the coalescence region.

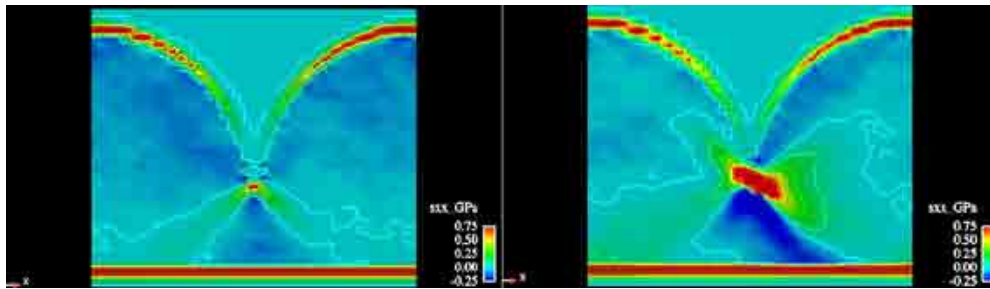


Figure 2. Time-averaged stress fields for cylindrical, thin-film islands before (left) and after (right) coalescence has occurred.

Conclusions

This paper has briefly discussed two methods for atomistic-continuum coupling, one that involves direct interfacing of multiple analysis methods and one that uses expressions for extracting continuum field information from atomistic simulation. Several researchers have done impressive work to extend what has been presented here. For example, Chen and her colleagues have done much to use expressions similar to Hardy's as the basis for a multiscale simulation framework [8]. While subsequent publications have analyzed materials governed by covalent and ionic bonding, more needs to be done to define the resolution limits where the validity of the produced fields becomes suspect. Another example is the recent attempt made by coworkers and myself to develop an approach similar to Hardy's for material frame continuum quantities such as the 1st Piola-Kirchhoff stress [9]. This effort included expressions for a micromorphic continuum, and further work needs to be pursued to apply these expressions to directionally bonded materials and to develop robust field expressions in both the spatial and material frames that accounts for the arbitrary distribution of atomic mass relative to continuum points.

Acknowledgements

The author gratefully acknowledges contributions and collaborations from the following individuals: D. J. Bammann, R. J. Hardy, J. J. Hoyt, R. E. Jones, P. A. Klein, S. C. Seel, E. B. Webb III, and N. S. Weingarten. Sandia is a multiprogram laboratory operated by Sandia Corporation, a Lockheed Martin Company, for the United States Department of Energy under Contract DEAC04-94AL85000.

References

- [1] L. E. Malvern, *Introduction to the Mechanics of a Continuous Medium* (New Jersey, Prentice-Hall, 1969).
- [2] M. P. Allen and D. J. Tildesley, *Computer Simulation of Liquids* (Oxford, Clarendon Press, 1987).
- [3] P. A. Klein and J. A. Zimmerman, "Coupled Atomistic-Continuum Simulation using Arbitrary Overlapping Domains, *Journal of Computational Physics* **213** 86-116 (2006).
- [4] J. A. Zimmerman, P. A. Klein, E. B. Webb III, "Coupling and communicating between atomistic and continuum simulation methodologies," in *Multiscale Modeling in Molecular and Continuum Mechanics: Interaction of Time and Size from Macro to Nano* (The Netherlands, Springer, 2007) pp. 439-455.
- [5] R. J. Hardy, "Formulas for determining local properties in molecular-dynamics simulations: Shock waves," *Journal of Chemical Physics* **76** 1 622-628 (1982).
- [6] J. A. Zimmerman, E. B. Webb III, J. J. Hoyt, R. E. Jones, P. A. Klein, D. J. Bammann, "Calculation of stress in atomistic simulation," *Modelling and Simulation in Materials Science and Engineering* **12** S319-S332 (2004).
- [7] E. B. Webb III, J. A. Zimmerman, S. C. Seel, "Reconsideration of continuum thermomechanical quantities in atomic scale simulations," *Mathematics and Mechanics of Solids* **13** 221-266 (2008).
- [8] Y. Chen and J. Lee, "Atomistic formulation of a multiscale field theory for nano/micro solids," *Philosophical Magazine* **85** [33-35] 4095-4126 (2005).
- [9] J. A. Zimmerman, R. E. Jones, J. A. Templeton, "A material frame approach for evaluating continuum variables in atomistic simulations," *Journal of Computational Physics*, Submitted (2009).

DENSITY AND NONIDEALITY EFFECTS IN PLASMAS

A. V. Lankin, G. E. Norman

Joint Institute for High Temperatures (JIHT), Russian Academy of Sciences, Moscow, 125412, Russia

Author Contact: norman@ihed.ras.ru

Self-consistent joint description of free and weakly bound electron states in plasmas is presented. Existence of two problems is emphasized: restriction of the number of atomic excited states and description of the smooth crossover from bound pair electron-ion excited states to collective excitations of free electrons. The fluctuation approach is developed to study the spectrum domain intermediate between low-lying excited atoms and free electron continuous energy levels. Density and nonideality effects are separated. The density effects are predominant for the shape of the curve the energy spectrum near the ionization limit. Collisional recombination rate is studied. A strong suppression of recombination in strongly coupled plasmas is found. It is determined by the plasma nonideality. The suppression agrees with the measurements for the ultracold plasma.

Introduction

Adequate treatment of highly excited atoms is one of the most complicated problems in the theory of strongly coupled plasmas (SCP) [1]. $E_s = -Ry/s^2$ is the expression for the energy levels, s is the principal quantum number, and Ry is the ionization potential. The statistical weight of the level $g_s = 2s^2$ diverges for large s . Since $2Ry/s^3$ is the energy distance between levels, the Coulomb density of states $g(s)$ diverges as $g(s) = s^5/Ry$ or

$$g_{Coul}(E_s) = Ry^{3/2} |E_s|^{-5/2} \quad (1)$$

The partition function Z of the hydrogen atom diverges as well

$$Z = \sum_{s=1}^{s_{max}} 2s^2 \exp\left[-\frac{Ry}{kT} \left(1 - \frac{1}{s^2}\right)\right] \approx 2 + \int_{-Ry/4}^0 dE g(E) \exp\left(-\frac{E}{kT}\right) \quad (2)$$

where s_{max} is the maximum principal quantum number, T is temperature, k is Boltzman constant, $g(E)$ is the smoothed density of states, and subscript s is omitted at the transition to integration. The population distribution dZ/dE is related to $g(E)$

$$dZ/dE = g(E) \exp(-E/kT) \quad (3)$$

for highly excited states. The argument E is used for both negative and positive energies.

The *first problem* appeared rather long ago—*restriction of the number of excited states of atoms*. The problem was treated by Bohr, Planck, Fermi, Larkin, Ebeling, Starostin, and other authors. The Planck-Larkin recipe is to include into consideration free electron-proton states as well. Mutual compensation of the divergences in bound and free spectrum of the two-body (electron and proton) system results in the convergent expression for Z and the integrable divergence $|E|^{-1/2}$ of the effective density of bound states. The function $g(E)$ becomes temperature dependent in this case. However, the two-body problem is not sufficient to describe plasma, which is a many-body system, because a break arises at the zero energy: divergent density of states at negative energies and starting from zero density at positive energies. The break between two branches of the spectrum seems to be artificial.

So the *second problem* arises—description of the *crossover from bound pair* electron-ion excited states to collective excitations of free electrons. Contrary to the very old first problem, the second problem was not almost touched upon earlier. Planck-Larkin approach does not take into account collective excitations of free electrons and does not treat a region of highly excited states adjacent to the ionization limit. These states cannot be treated in pair approximation in any plasma, since they are strongly disturbed by the neighboring particles.

Our work is devoted to the removal of the second problem and development of a reasonable description of the spectrum domain intermediate between discrete and continuous electron energy levels. The objective is to bridge the break by the smooth transition from negative to positive energies for SCP. So the approach should be a many-body one in the whole spectrum domain and comprise both bound and free electron states collective excitations included. As collective excitations have fluctuation nature, our idea of the crossover is to bridge collective fluctuations or excitations (plasma waves) to multiple fluctuations, then to triple fluctuations, then to pair fluctuations, and finally to excited atoms, which could be considered as stabilized pair fluctuations.

Dispersion of frequency and damping decrement of plasma waves are studied in SCP by the method of molecular dynamics (MD) using analysis of space-time fluctuations of charge density. MD method presents the universal approach for the study of all kinds of fluctuations. The problem is to develop the adequate measurement procedure for any kind of fluctuations. For diagnostics of pairs, the algorithm [2] of identifying pair fluctuations is employed.

The crossover between from bound to free states is coincided in the next section. It is shown the crossover is defined mostly by the density effects. The collisional recombination is coincided in the third section. It is shown that deviation of free body recombination rate is defined by the plasma nonideality.

Density Effects: Crossover from Bound to Free States

Distribution of Pair Fluctuations over Their Energies

Energy distributions dZ/dE of the pair fluctuation population are calculated by MD for a number of temperatures, densities and cut-off values of Coulomb potential [2]. Results of MD modeling are presented in Figure 1. We proceed from dZ/dE to $g(E)$ using (3). There are no pairs in a certain interval below the ionization limit. Since the distribution above the cutoff level does not depend on its value, both smooth but steep decrease of $g(E)$ and a gap ΔE below the ionization limit have a physical sense.

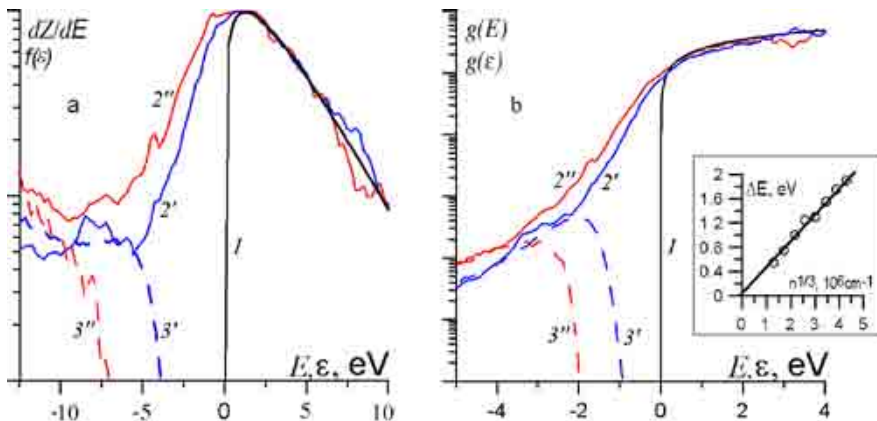


Figure 1. Relative population distributions (a) and density of states (b) for $n = 2.7 \cdot 10^{20} \text{ cm}^{-3}$ (2', 3') and $n = 1.25 \cdot 10^{21} \text{ cm}^{-3}$ (2'', 3''). Free electrons (1), total for $T = 2.5 \text{ eV}$ (2), pairs (3). Dependence of ΔE on $n^{1/3}$ is shown in the insertion.

The values of $g(E)$ are normalized in Figure 1 at the large negative energies by the Coulomb density of states where relative behavior of $g(E)$ for both Coulomb and MD cases coincide with each other. Coincidence points to the correctness of our approach. There is a drastic deviation of Coulomb and Planck-Larkin $g(E)$ from the MD results near the ionization limit [2]. Moreover Planck-Larkin $g(E)$ contradicts to the MD data in the whole energy interval studied.

Densities of the pair states are presented in Figure 1b for different values of electron number density n . The dependence of ΔE on $n^{1/3}$ is given in the insertion. It is close to the linear one $\Delta E \approx 2n^{1/3}$. The result can be related to the Unsold formula. However relation of the gap to the plasma frequency is not excluded as well. Rotation frequency of an electron in the pair is $\omega \sim E^{3/2}$, plasma frequency is $\omega_0 \sim n^{1/2}$, the border of the pair stability could be defined as $\omega = \omega_0$ and we obtain $\Delta E \sim n^{1/3}$.

Note that not only ΔE value but also the shape of $g(E)$ depends mostly on n . It is seen from Figure 2a where the results for different temperatures at the constant electron number density are shown. Since the scatter between the curves corresponding to the different temperatures is slow Figure 2a is given in a linear scale.

Diagram of typical plasma areas is shown in Figure 2b. The line 1 presents the border between excited atoms and pair fluctuations. The line 2 corresponds to the gap $\Delta E \approx 2n^{1/3}$. Both lines do not depend on T . Three typical areas of electron states can be separated out in

Figure 2b. Area I is the area of excited atom existence with the discrete broadened levels. The spectrum is a pseudocontinuous one in the area II. It is the area of pair fluctuations. The new result is that there exists the area III where there are neither atoms nor pairs. The area III exists not only for hydrogen but for other atoms as well and can be compared with experimental data [1]. It is evident from the Figure 2b that even the first excited Cs level is transformed into a pair fluctuation in the range studied and completely disappears in the right part of the range. The higher excited levels do not exist even as pairs in the whole range.

Disappearances of excited states are observed experimentally in multicharge laser impulse induced plasma [3]. A significant contribution of the C VI Ly $_{\beta}$ line was observed with 8 ns pulses. The lack of the lines in the sub-10-fs spectra is considered in [3] as indication that the plasma is at high density where pressure ionization has removed the upper levels. It agrees with our estimations of ΔE for the experimental values of the ion charge $Z = 4.5$ and $n \sim 5 \cdot 10^{23}$. It is a density effect since $T = 190$ eV, which gives $\Gamma \sim 0.1$.

Distribution of Electrons over Total Energy

Besides the energy E of an electron in the pair, its total energy ε can be calculated, which includes not only the interaction of the electron with the nearest ion and the kinetic energy of the relative motion but also the interaction of the electron with all the neighboring charges. Two examples of the population distribution $f(\varepsilon)$ obtained are given in Figure 1a. Both curves 2' and 2'' are normalized to the asymptotic of the Maxwellian distribution 1 for large ε . The distribution of free electrons for energies greater than the interaction energy turns out to be Maxwellian one that is a trivial result since we used the classical MD. The

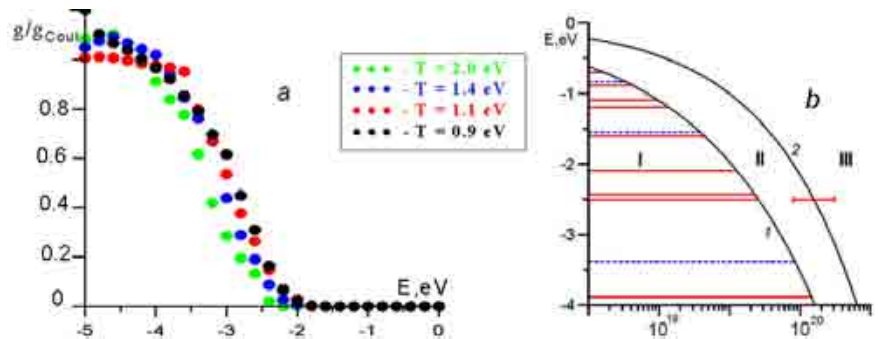


Figure 2. (a) – The ratio of MD-results for $g(E)$ to the density of states (1) for different temperatures at $n = 8 \cdot 10^{19} \text{ cm}^{-3}$. (b) – Diagram energy levels - free ion number density. I is the area of discrete spectrum of Cs (solid horizontal lines) and H (dotted horizontal lines), II is the area of pairs, III is the area without either excited atoms or pairs. The horizontal bar indicates data [1] that correspond to the first excited state of Cs.

interesting result is that it seems to be nonshifted with respect to the ionization limit of the isolated atom. The result does not depend on the density or Γ .

The distributions $f(\epsilon)$ (2',2'') and dZ/dE (3',3'') coincide with each other in the region of large negative energies to the scatter of numerical data in Figure 1a, so pair interactions predominate here over all other interactions $\epsilon \approx E$. There is a minimum in $f(\epsilon)$ in the intermediate region below the ionization limit where the electron population drops its value by more than order of magnitude. To elucidate the situation we proceed from $f(\epsilon)$ to the effective total density of states $g(\epsilon)$

$$f(\epsilon) = g(\epsilon) \exp(-\epsilon / kT) \quad (4)$$

Figure 1 reveals that there is no gap in $g(\epsilon)$, but a real gap ΔE does exist between pairs (curve 3) and collective states of free electrons (curve 1) and expands with the increase of density. One is able to guess that the crossover between curves 3 and 1 is filled by many-particle fluctuations.

Nonideality Effects: Rate of Recombination

To study the recombination process in SCP the approach [4] is used. It is found that dependents of collision recombination rate on nonideality is not a monotonous one. It increases according to the ideal plasma three-body recombination rate $K = C \cdot Z^3 e^{10} m^{-1/2} \cdot n^2 T^{-9/2}$ at small with increase of Γ . The value $C = 1.4$ is chosen to fit the MD data. Then K passes a maximum and decreases at larger Γ . The maximum value of $K\tau_e$ is about 0.03 for all Z , τ_e is plasma oscillation period.

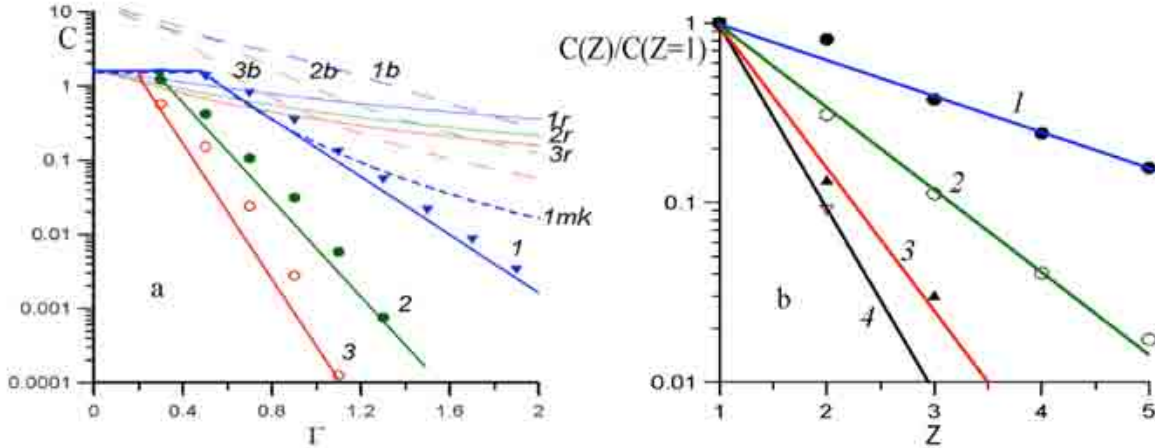


Figure 3. Different projections of the function $C(\Gamma, Z)$. a - dependencies on Γ at the different values of the ion charge:

1 - $Z=1$, 2 - $Z=2$, 3 - $Z=3$; the line $C = \text{const}$ and exponential fit used in (5) are drawn through the MD points;

the letter "b" – Biberman, 87, the letter "r" - Romanovsky, 98, the letter "h" – original Hahn, 97, the letter "mh" - modified Hahn, 97

[4]; b - dependencies on the ion charge at the different values of nonideality: 1 - $\Gamma=0.3$, 2 - $\Gamma=0.5$, 3 - $\Gamma=0.7$, 4 - $\Gamma=0.9$.

If we allow the coefficient C to become a function $C(\Gamma, Z)$, and use that freedom to fit the calculated recombination rates for a SCP, we can reveal the influence of nonideality in a more apparent way. The results are presented in Figure 3a. The constant value $C(\Gamma, Z) = 1.4$ remains valid for $\Gamma < 0.5$ at $Z=1$. The Γ interval of the constant $C = 1.4$ reduces with increase of Z . The drop of C at the larger nonidealities can

be approximated by $C = A(Z)\exp[-\lambda(Z)\Gamma]$. Introduction of functions $A(Z)$ and $\lambda(Z)$ permits to separate Z and Γ dependences. The Z dependences of $C(\Gamma, Z)$ for a number of Γ values (Figure 3b) is approximated by $C = B(\Gamma)\exp[-\mu(\Gamma)Z]$, where Z and Γ dependences are separated again. The result is

$$K_e \tau_e = K_0 Z^3 \Gamma^{9/2} e^{a_1 Z} e^{-\lambda_0 \Gamma} e^{-\lambda_1 Z \Gamma} \quad (5)$$

where $K_0 = 2.7$, $a_1 = 0$, $\lambda_0 = 1.5$, $\lambda_1 = 3$. We see that $K\tau_e$ depends only from Γ . It is related to the fact that collisional recombination rate is defined by the ratio of ΔE to Γ .

Killian-Rolston measurements [5] show that only about 20% of ions recombined for $10^2 \mu s$ in ultracold plasma with the electron number density 10^{10}cm^{-3} . They give the estimation of the recombination rate as $2.3 \cdot 10^{-6} \tau_e^{-1}$ in agreement with the value $2.6 \cdot 10^{-6} \tau_e^{-1}$, which follows from (5) for the temperature 1 K. The latter value is pointed out as the lower border in [5]. The comparison is only of qualitative value, since some subsequent theoretical and experimental papers on ultracold plasmas have shown that the electron temperature varies during the evolution of the plasma because of disorder induced heating, and the electron Coulomb coupling parameter rapidly (within the first microsecond) goes to about $\Gamma = 0.2$. However, if the traditional expression for the recombination rate was valid for plasma obtained in [3], the recombination time would not exceed few nanoseconds (six orders of magnitude faster) for it. So recombination should be dramatically suppressed in order disorder induced heating would become the fastest relaxation process.

Another indirect relevance of the MD data obtained can be derived from the experimental study of the initial stage of the latent track formation. The plasma model developed in [6] can give the self-consistent explanation of the transient X-ray emission observed only under the assumption that the recombination rate is much slower than predicted by the formula for three-body recombination in ideal plasma.

Conclusions

The self-consistent fluctuation approach is developed to bridge the smooth crossover from the plasma waves to pair fluctuations, and finally to excited atoms (stabilized pair fluctuations) in the electron spectrum.

Following density effects are discovered with the help of the MD method. The smooth but steep restriction of pair fluctuation density is obtained which could explain the restriction of excited atom contribution to the atomic partition function. The energy domain adjoining to the ionization limit (a “gap”) is found where the pair fluctuation density is close to zero, contrary to the Coulomb and Planck-Larkin approximations for the excited atom density. The area of plasma nonidealities is discovered where there are neither excited atoms nor pair fluctuations. Maxwellian energy distribution of free electrons turns out to be nonshifted with respect to the ionization limit of the isolated atom.

A drastic suppression of the recombination rate is discovered with respect to the extrapolation of the conventional expression for the three-body recombination. The absolute value of the rate passes through a maximum with an increase of nonideality and then decreases exponentially. The suppression is shifted to lower electron nonidealities with the increase of the multiplicity of ionization.

Acknowledgements

The authors acknowledge fruitful discussions with V. P. Krainov, M.Yu. Romanovsky, I. V. Morozov and I. Yu. Skobelev. This work is partially supported by the RAS program 12, the RFBR grant 07-08-00738 and Sandia National Laboratories under the DOE/NNSA Advanced Simulation and Computing Program. A. V. L. acknowledges the support of the Dynasty Foundation. The calculations were performed using the cluster of FMBP of MIPT and the cluster MFTI-60.

References

- [1] V. E. Fortov, I. T. Iakubov, A. G. Khrapak, *Physics of Strongly Coupled Plasma* (Oxford, Oxford University Press, 2006).
- [2] A. V. Lankin and G. E. Norman, “Crossover from bound to free states in plasmas,” *J. Phys. A: Math. Theor.* **42** [21] 214032 (2009).
- [3] J. Osterholz, F. Brandl, T. Fischer, D. Hemmers, M. Cerchez, G. Pretzler, O. Willi, S. J. Rose, “Production of dense plasmas with sub-10-fs laser pulses,” *Phys. Rev. Letters* **96** [8] 085002 (2006).
- [4] A. V. Lankin and G. E. Norman, “Collisional recombination in strongly coupled plasmas,” *J. Phys. A: Math. Theor.* **42** [21] 214042 (2009).
- [5] T. C. Killian, M. J. Lim, S. Kulin, R. Dumke, S. D. Bergeson, S. L. Rolston, “Formation of Rydberg atoms in an expanding ultracold neutral plasma,” *Phys. Rev. Letters* **86** [17] 3759-3762 (2001).
- [6] A. V. Lankin, I. V. Morozov, G. E. Norman, S. A. Pikuz, Jr., I. Y. Skobelev, “Solid-density plasma nanochannel generated by a fast single ion in condensed matter,” *Phys. Rev. E* **79** 3 036407 (2009).

SELF-DIFFUSION IN Mo USING THE AM05 DENSITY FUNCTIONAL

T. R. Mattsson,^{*} N. Sandberg,[†] R. Armiento,[‡] A. E. Mattsson^{*}

^{*}Sandia National Laboratories, Albuquerque, NM 87185 USA

[†]Royal Institute of Technology, Stockholm, SE-100 44, SWEDEN

[‡]University of Bayreuth, Bayreuth, D-95440, GERMANY

Contact Author: trmatts@sandia.gov

Vacancy diffusion is the most important microscopic mechanism for mass-transport in solids. While vacancy diffusion in fcc metals is relatively well understood from a microscopic perspective, the same does not hold true for bcc metals. We present first-principles simulations using the AM05 density functional of vacancy diffusion in Mo. The calculated self-diffusion coefficient is in quantitative agreement with available experimental data. We also discuss the excellent performance of AM05 for lattice constants and bulk moduli.

Introduction

Real solids are never perfect crystals, and the importance of defects like vacancies, interstitials, and dislocations to the properties of materials can hardly be overstated. Mass transport in solids is dominated by vacancy motion, radiation creates vacancies that can nucleate and grow voids, and the motion of dislocations is important for material strength. There are thus ample reasons to, from a microscopic perspective, understand and ultimately predict properties of defects in solids, for example, vacancies.

Early work applying density functional theory [1, 2] (DFT) to study transition metal vacancies [3] used the LDA exchange correlation functional, was computationally restricted to relatively small unit cells, and structural relaxation was beyond reach. In retrospect, somewhat surprisingly, these pioneering calculations came out in very good agreement with experimental data for the vacancy formation energy. However, it turned out to be difficult to improve upon them. For example, when using larger super cells and including structural relaxation, the calculated vacancy formation energies were lowered, away from experimental data. In addition, although generalized gradient exchange-correlation functionals as in Perdew and Wang-91 (PW91) [4] and Perdew, Burke, and Ernzerhof (PBE) [5] improve upon LDA for lattice constants and cohesive energies, they lower vacancy formation energies even further, worsening the DFT calculations.

We solved this paradox in references [6] and [7] by post-processing the DFT calculations. The confusion regarding DFT calculations of vacancy formation energies was due to different intrinsic surface error of LDA and PW91. By correcting for it [7], we were able to reconcile the different results and quantify the contributions from structural relaxation, large super cells, and exchange-correlation functional [7]. The post-processing correction method, however, has limitations, and most importantly, it cannot be used to correct molecular dynamics (MD) calculations. For MD to work in the context of vacancies, the surface intrinsic error correction has to be incorporated into the exchange-correlation (xc) functional itself [8].

In this paper, we have studied vacancy formation and diffusion in Mo as an example of a bcc metal with strongly non-Arrhenius behavior for self-diffusion. We find that DFT based MD simulations reach quantitative agreement with available experimental data on the self-diffusion coefficient.

Method

Density Functional Theory

Density functional theory [1,2] is a formally exact reformulation of the Schrödinger equation. In DFT, the fundamental property is the density of electrons in three-dimensional real space, $\rho(x,y,z)$, *regardless of how many electrons are in the system*. In contrast, for N electrons, the Schrödinger equation is $3N$ dimensional. The key term in the Kohn-Sham equations is the approximation of the many-body interaction, the so-called exchange-correlation functional. The first approximation, the local density approximation (LDA) was put forward already in the pioneering work [1,2]. LDA works excellently for many systems, in particular metals, but rather poorly for molecules. Functionals taking the gradient of the density into account were developed later by many: Becke, Lee, Yang, and Parr (BLYP) [9,10], PW91 [4], PBE [5], and revised PBE (RPBE) [11]. Gradient corrected functionals improved significantly upon LDA for molecular systems. However, only PW91 and PBE are widely used for solid-state problems. At the time, PW91 and PBE were considered equivalent and are often referred to as the generalized gradient approximation (GGA). Only recently was it discovered that PW91 and PBE can, and do, yield different results [12]. As computers became faster and codes more efficient, it became possible to apply DFT also to problems that require several tens of atoms in the super-cell: surfaces, defects, interfaces, and alloys. As this development accelerated, there were only two semi-local xc-functionals in widespread use for solids state applications: LDA or GGA (PW91/PBE). This changed in 2005.

The AM05 Functional

Development of an exchange-correlation functional based on a surface model system was discussed by Kohn and Mattsson [13]. The approach was later formalized and generalized in the subsystem functional scheme [15] and implemented in the AM05 functional [8]. AM05 involves two model systems: the uniform electron gas is used in regions that are locally bulk-like and a surface functional (derived from the Airy gas [11] and jellium surfaces) for regions that are locally surface-like. By including two different exact reference systems, AM05 constitutes a systematic improvement over LDA. In the first paper, it was demonstrated that AM05 gives lattice constants and bulk moduli to high accuracy for Al (simple metal), Pt (transition metal), and Si (semi conductor) [8]. More recently, by comparing results for 20 solids (Al, Ag, Pd, Rh, Cu, GaAs, GaP, Na, NaF, NaCl, MgO, SiC, Si, C, GaN, BN, BP, Li, LiF, and LiCl), it was confirmed that AM05 yields lattice constants that on average are significantly better than LDA, PBE, RPBE, and BLYP [16], mean absolute errors are shown in Figure 1. The functional employed in this work, AM05, performs on average as well as computationally significantly more expensive hybrids.

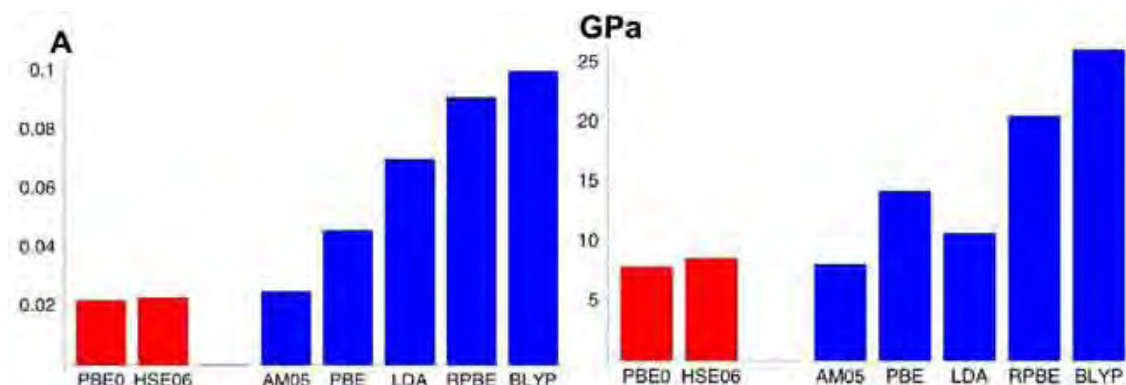


Figure 1. Mean absolute errors for lattice constant and bulk modulus for 20 solids with seven functionals: PBE0 and HSE06 [17] and AM05, PBE, LDA, RPBE, and BLYP [16].

Code and Computational Details

The MD simulations were performed with a massively parallel version of the projector augmented wave [18,19] (PAW) core-potential code VASP 5.1.40 [20,21,22] on a CRAY-XT [23] using stringent convergence settings [24]. The PAW implementation in VASP 5.1 allows use of multiple XC functionals on the same set of core potentials while retaining high precision [16]. We used the six valence electron Mo PAW PBE core function of 08Apr2002. While it has a nominal plane-wave cutoff (ENMAX) of 224.584 eV, we used 400 eV to converge the pressure to a few percent. The electronic structure is minimized to 10^{-5} eV convergence criterion. Real-space projections were not applied. Convergence with respect to kpoints was investigated by comparing energies for gamma point (0,0,0), mean-value point (1/4,1/4,1/4), and Monkhorst-Pack grids with a 2^3 and 4^3 sampling. The mean-value point has proven to yield results that are significantly improved compared to gamma-only calculations.

The DFT-MD simulations are the most computationally demanding parts of the present work, but are necessary for the study of the an-harmonic contributions to the formation and migration energies. We use velocity Verlet time-integration with a time-step of 2.0 fs, resulting in about five electronic iterations being required per ionic step at 2800 K. The simulations are kept in the NVT ensemble with a nose thermostat (80 fs time-constant). The electronic states are distributed according to the finite-temperature formulation of DFT [25], the use of which is very important for obtaining accurate thermodynamic properties [26]. Structural optimization was used to find the low-temperature limit of the vacancy formation energy and the migration activation energy in 128 atom supercells. The corresponding prefactors for vacancy formation and migration were obtained by calculating the force-constant matrix via finite displacements [27]. This was done in 54 atom unit cells. Static calculations for LDA and PBE were done with VASP 4.6. All AM05 calculations were done using VASP 5.1.40.

Vacancy Formation Enthalpy and Vacancy Hopping from MD

The vacancy formation energy was obtained by comparing thermally averaged energies in a system containing a vacancy, with that in a bulk system, using DFT-MD. In order to unambiguously locate the vacancy at each time step, we use a model potential [28] to quench a copy of each atomic configuration, and associate the empty lattice site with the position of the vacancy [29] to obtain a trajectory in time of the vacancy migration. By comparing long model potential simulations in 127, 1023, and 3455 atom systems, we conclude that the jump-rate in a 127-atom system is representative of that in larger systems to within 5%.

Results

Vacancy Formation Enthalpy

The result for vacancy formation enthalpy calculated from long DFT-MD simulations is shown in Figure 2. The strong temperature dependence is well described by a quadratic form [30]. Figure 2 also demonstrates the importance of including finite electronic temperature.

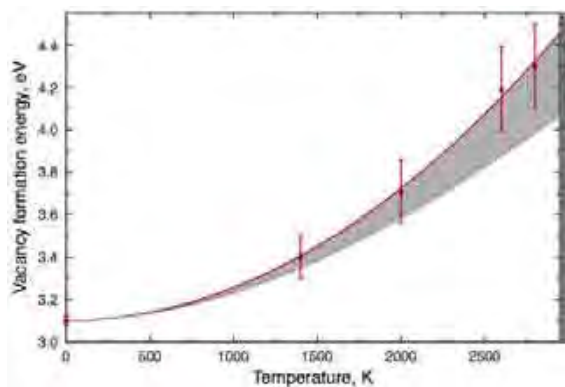


Figure 2. Mo vacancy formation energy as function of temperature [24]. The shaded contribution is from the electronic entropy, and error bars are 2σ statistical uncertainty calculated by block-averaging.

Self-Diffusion

Based on the hopping rates obtained in the MD simulations, we estimate the vacancy diffusion coefficient. Since the formation energy is known as a function of temperature (Figure 2), we use it to find the migration energy as a function of temperature to match self-diffusion from room temperature to melting. The calculated self-diffusion is shown in Figure 3. The AM05 results are in quantitative agreement with experimental data when considering the difficulties involved in accurate calculations of point defects and point-defect kinetics in transition metals [7]. There is a significant difference between using PBE and AM05, confirming the central importance of the exchange-correlation functional also for solid-state systems.

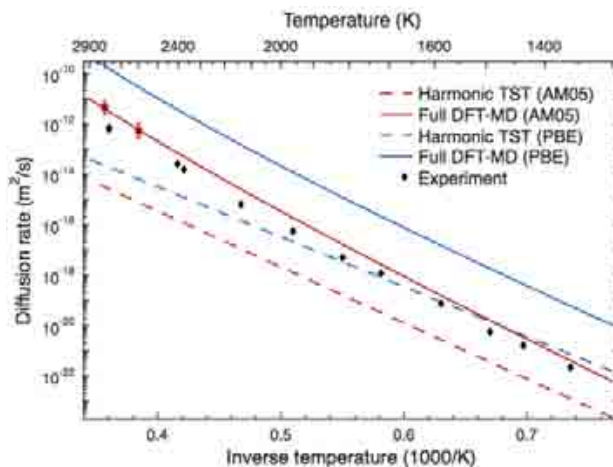


Figure 3. Calculated Mo self-diffusion rate as a function of temperature [30], with experimental data by Maier, Mehrer, and Rein [31]. Red squares are from the long direct MD simulations of hopping, the red line is from vacancy formation energy in Figure 2 combined with a vacancy migration energy to fit the MD diffusion.

Conclusions

We have shown that a quantitative microscopic model of vacancy diffusion in bcc metals can be founded on DFT simulations given that the xc-functional is of high fidelity and MD simulations are performed close to the melting point. Given the large change in vacancy formation energy as a function of temperature as well as the importance of including finite temperature treatment of the electronic states, we infer that the use of a classical model potential over the entire interval in temperature is an approach that faces formidable challenges to correctly describe defects in Mo, and likely other bcc metals.

Acknowledgements

We thank Göran Grimvall for discussions and Odd Runevall for performing some of the verification calculations. We also thank Georg Kresse for the early opportunity to employ VASP 5.1 and Paul Kent for sharing Cray XT4 code modifications. The MD calculations were run on Red Storm at Sandia High Performance Computing, and we thank Dennis Dinger for technical support on the machine. R. A. gratefully acknowledges support from the Alexander von Humboldt Foundation.

Sandia is a multiprogram laboratory operated by Sandia Corporation, a Lockheed Martin Company, for the United States Department of Energy's National Nuclear Security Administration under contract DE-AC04-94AL85000.

References

- [1] P. Hohenberg and W. Kohn, "Inhomogeneous electron gas," *Phys. Rev.* **136** B864 (1964).
- [2] W. Kohn and L. J. Sham, "Self-consistent equations including exchange and correlation effects," *Phys. Rev.* **140** A1133 (1965).
- [3] T. Korhonen, M. J. Puska, R. M. Nieminen, "Vacancy-formation energies for fcc and bcc transition metals," *Phys. Rev. B* **51**, Issue 15, 9526 (1995).
- [4] J. P. Perdew and Y. Wang, "Accurate and simple analytic representation of the electron-gas correlation energy," *Phys. Rev. B* **45**, Issue 23, 13244 (1992).
- [5] J. P. Perdew, K. Burke, M. Ernzerhof, "Generalized gradient approximation made simple," *Phys. Rev. Lett.* **77** 3865 (1996).
- [6] K. Carling, G. Wahnström, T. R. Mattsson, A. E. Mattsson, N. Sandberg, G. Grimvall, "Vacancies in metals: From first-principles calculations to experimental data," *Phys. Rev. Lett.* **85** 3862 (2000).
- [7] T. R. Mattsson and A. E. Mattsson, "Calculating the vacancy formation energy in metals: Pt, Pd, and Mo," *Phys. Rev. B* **66**, Issue 21, 214110 (2002).
- [8] R. Armiento and A. E. Mattsson, "Functional designed to include surface effects in self-consistent density functional theory," *Phys. Rev. B* **72** 085108 (2005).
- [9] A. D. Becke, "Density-functional exchange-energy approximation with correct asymptotic behavior," *Phys. Rev. A* **38** 3098 (1988);
- [10] C. Lee, W. Yang, and R. G. Parr, "Development of the Colle-Salvetti correlation-energy formula into a functional of the electron density," *Phys. Rev. B* **37** 785 (1988).
- [11] B. Hammer, L. B. Hansen, J. K. Nørskov, "Improved adsorption energetics within density-functional theory using revised Perdew-Burke-Ernzerhof functionals," *Phys. Rev. B* **59** 7413 (1999).
- [12] A. E. Mattsson, R. Armiento, P. A. Schultz, T. R. Mattsson, "Nonequivalence of the generalized gradient approximations PBE and PW91," *Phys. Rev. B* **73** 195123 (2006).
- [13] W. Kohn and A. E. Mattsson, "Edge electron gas," *Phys. Rev. Lett.* **81** 3487 (1998).
- [14] A. E. Mattsson and W. Kohn, "An energy functional for surfaces," *J. Chem. Phys.* **115**, Issue 8, 3441 (2001).
- [15] R. Armiento and A. E. Mattsson, "Subsystem functionals in density-functional theory: Investigating the exchange energy per particle," *Phys. Rev. B* **66** 165117 (2002).
- [16] A. E. Mattsson, R. Armiento, J. Paier, G. Kresse, J. M. Wills, T. R. Mattsson, "The AM05 density functional applied to solids," *J. Chem. Phys.* **128** 084714 (2008).
- [17] J. Paier, M. Marsman, K. Hummer, G. Kresse, I. C. Gerber, J. Ángyán, "Screened hybrid density functionals applied to solids," *J. Chem. Phys.* **124** 154709 (2006), **125** 249901 (2006).
- [18] P. E. Blöchl, "Projector augmented-wave method," *Phys. Rev. B* **50**, Issue 24, 17953 (1994).
- [19] G. Kresse and D. Joubert, "From ultrasoft pseudopotentials to the projector augmented-wave method," *Phys. Rev. B* **59**, Issue 3, 1758 (1999).
- [20] G. Kresse and J. Hafner, "Ab initio molecular dynamics for liquid metals," *Phys. Rev. B* **47** 558 (1993).
- [21] G. Kresse and J. Hafner, "Ab initio molecular-dynamics simulation of the liquid-metal-amorphous-semiconductor transition in germanium," *Phys. Rev. B* **49** 14251 (1994).
- [22] G. Kresse and J. Furthmüller, "Efficient iterative schemes for ab initio total-energy calculations using a plane-wave basis set," *Phys. Rev. B* **54** 11169 (1996).
- [23] P. R. C. Kent, "Computational challenges of large-scale, long-time, first-principles molecular dynamics," *J. Phys.: Conf. Ser.* **125** 012058 (2008).
- [24] A. E. Mattsson, P. A. Schultz, M. P. Desjarlais, T. R. Mattsson, K. Leung, "Designing meaningful density functional theory calculations in materials science—a primer," *Modell. Simul. Mater. Sci. Eng.* **13** R1 (2005).
- [25] N. D. Mermin, "Thermal properties of the inhomogeneous gas," *Phys. Rev.* **137** A1441 (1965).
- [26] T. R. Mattsson and M. P. Desjarlais, "Phase diagram and electrical Conductivity of high energy-density water from density functional theory," *Phys. Rev. Lett.* **97** 017801 (2006).
- [27] M. Mantina, Y. Wang, R. Arroyave, L. Q. Chen, Z. K. Liu, C. Wolverton, "First-principles calculation of self-diffusion coefficients," *Phys. Rev. Lett.* **100** 215901 (2008).
- [28] M. W. Finnis and J. E. Sinclair, "A simple empirical N-body potential for transition metals," *Phil. Mag. A* **50**, Issue 1, 45 (1984).
- [29] N. Sandberg, B. Magyari-Köpe, and T. R. Mattsson, "Self-diffusion rates in Al from combined first-principles and model-potential calculations," *Phys. Rev. Lett.* **89** 065901 (2002).
- [30] Thomas R. Mattsson et al., submitted to *Phys. Rev. Lett.* (2009).
- [31] K. Maier, H. Mehrer, G. Rein: *Zeitschrift fuer Metallkunde*, "Self-diffusion in molybdenum," *Inst. für Theoretische und Angewandte Phys.* **70** (Univ. Stuttgart, Stuttgart, West Germany, 1979) p. 271.

THERMOMECHANICAL EFFECTS IN PERFECT CRYSTALS WITH ARBITRARY MULTIBODY POTENTIAL

V. A. Kuzkin, A. M. Krivtsov

Institute for Problems in Mechanical Engineering, Russian Academy of Sciences

Saint Petersburg, 197198, Russia

Contact Authors: kuzkinva@gmail.com

akrivtsov@bk.ru.

Derivation of equivalent thermo-mechanical parameters for perfect crystals in the case of arbitrary interatomic potential is conducted. The approach based on the averaging of equations of motion is considered. Long wave approximation is used to make link between the discrete system and equivalent continuum. Macroscopic thermo-mechanical parameters such as Piola and Cauchy stress tensors, heat flux are represented via microscopic parameters.

Introduction

Determination of the connection between parameters of discrete and continual systems is one of the challenging problems for modern physics. Various methods of transition from discrete system to equivalent continual exist. Long wave assumption is used in [1]. The concept of quasi-continuum is proposed in [2]. Localization functions are used in [3,4]. These approaches give the opportunity to spread mechanical parameters determined in lattice nodes on all volume of the body. Decomposition of motions on slow macroscopic and fast thermal is used for description of thermal properties. In papers [3,4] the decomposition of particles' velocities is conducted by the use of localization functions. As a result, the dependencies of stress tensor and heat flux on parameters of the discrete system were obtained and analyzed. Fourier transformation was used in [5] for decomposition of displacements and velocities of particles. Different methods of decompositions were discussed. It was noted that the result of the decomposition is not unique. It should depend on characteristic time and spatial scales of the problem.

The approach based on averaging of equations of motions and application of long wave assumption [1] was proposed in papers [6,7,8]. In [6], it was used for derivation of expressions for stress tensors for ideal crystals with pair interactions. Thermal motion was neglected. The influence of thermal oscillations on mechanical properties was considered in [6,7] for a one-dimensional case and generalized for a three-dimensional case in [8].

Different assumptions about interatomic potentials were used in all papers mentioned above. This fact decreases the range of applications of results of these papers. In the present paper, derivations are conducted for arbitrary multibody potential. It is assumed that the energy per one particle depends on all vectors connecting this particle with its neighbors. The approach proposed in works [6,7] is used for transition from discrete system to equivalent continual. Equations of motion of particles are derived. The connection of Cauchy and Piola stress tensors and heat flux with parameters of discrete systems is determined. The symmetry of obtained Cauchy stress tensor is proved. Relation with known expressions for Cauchy stress tensors is discussed.

Method

Hypotheses and Designations

Let us consider the discrete system of interacting particles that form perfect a simple crystal lattice in $d = 1, 2$, or 3 dimensions. Two main principles are used for transition from discrete system to equivalent continual: decomposition of motions of particles on slow macroscopic and fast thermal [5,7], and long wave assumption [1].

First let us focus on decomposition. In practice, different types of averaging, such as time averaging and spatial averaging, are used for decomposition. In [5], it was noted that unique decomposition is impossible because there are no rules for the choice of the period of averaging, size of representative volume, etc. These parameters should depend somehow on time and spatial scales of the considered problem. According to the opinion of the author of the present paper, derivations should not be based on the particular method of decomposition. In addition, results should not change qualitatively with replacement of the method of averaging. Therefore, let us consider average component $\langle f \rangle$ and thermal component \tilde{f} of physical value f that are connected by the following expression

$$f = \langle f \rangle + \tilde{f}. \quad (1)$$

The second important statement is the long-wave assumption [1]. The idea of the assumption is as follows: the average component of any physical value is assumed to be slowly changing in space on distances of order of interatomic distance. Then the average component can be considered as continual function of space variable and can be expanded into a power series with respect to interatomic distance. Resulting series should converge rapidly. Exactly this assumption allows a transition from a discrete system to a continuum.

Let us use a Lagrangian (material) description of equivalent continuum and consider the reference and actual configurations of discrete and continual systems. Let us take an unstrained configuration of crystal lattice as the reference one for discrete system. Let us denote radius-vectors of material points of equivalent continuum in reference and actual configurations as \underline{r} and \underline{R} , respectively. Two ways for identification of the particles will be used. On the one hand, the position of the particle is determined by its radius-vector. On the other hand, let us use local numbering. Starting with one reference particle, let us mark all its neighbors by index α . Let us denote vector connecting the reference particle with its neighbor number α as \underline{a}_α . The numbering will be conducted in such a manner that \underline{a}_α has the following property: $\underline{a}_\alpha = -\underline{a}_{-\alpha}$. The same vectors in actual configuration \underline{A}_α will be represented as a sum of averaged component \underline{A}_α and thermal component $\tilde{\underline{A}}_\alpha$.

Let us assume that potential energy per one particle is represented by the following expression

$$\Pi = \Pi(\{\underline{A}_\alpha\}_{\alpha \in \Lambda}). \quad (2)$$

Here $\{\underline{A}_\alpha\}_{\alpha \in \Lambda}$ is the set of all vectors for \underline{A}_α the given particle; Λ is the set of all numbers of particles that interact with the given particle. Potential energy per particle can be represented in the form (2) for the majority of commonly used potentials. In particular, equation (2) is satisfied for pair potentials, embedded atom potential [9], Stillinger-Weber potential [10], Tersoff potential [11].

Derivation of Expressions for Thermomechanical Parameters

Let us derive the equation of motion of the particle with radius-vector \underline{r} in the reference configuration. For the sake of simplicity, let us consider the case when volumetrical forces are absent. Let us denote potential energy

per particle α as Π_α , $\Pi_\alpha \stackrel{\text{def}}{=} \Pi(\{\underline{A}_\beta(\underline{r} + \underline{a}_\alpha)\}_{\beta \in \Lambda})$. Using Lagrange approach one can obtain the equation of motion of the reference particle

$$m \ddot{\underline{u}}_t = - \frac{\partial \Pi}{\partial \underline{u}_t} - \sum_\alpha \frac{\partial \Pi_\alpha}{\partial \underline{u}_t}, \quad (3)$$

where \underline{u}_t is the current displacement of the particle, summation is conducted on the set Λ . Calculating derivatives in equation (3) one can obtain

$$m\ddot{\underline{u}}_t = \sum_{\alpha} \underline{F}_{\alpha}, \quad \underline{F}_{\alpha} \stackrel{\text{def}}{=} \frac{1}{2} (\underline{\mathcal{F}}_{\alpha}(\underline{r}) - \underline{\mathcal{F}}_{-\alpha}(\underline{r} + \underline{a}_{\alpha})), \quad \underline{\mathcal{F}}_{\alpha} \stackrel{\text{def}}{=} 2 \frac{\partial \Pi}{\partial \underline{A}_{\alpha}}. \quad (4)$$

Here \underline{F}_{α} is the force acting between the given particle and particle α . One can prove that the third Newton's law is satisfied for; \underline{F}_{α} i.e., $\underline{F}_{\alpha}(\underline{r}) = -\underline{F}_{-\alpha}(\underline{r} + \underline{a}_{\alpha})$. In the case of pair interactions, one has $\underline{F}_{\alpha} = \underline{\mathcal{F}}_{\alpha}$. Note that $\underline{\mathcal{F}}_{\alpha}$ can be considered as a force only in this particular case. One can verify this statement on the example of embedded-atom potential [9].

Now let us obtain equation of balance of momentum for equivalent continuum. Let us average equation (4) and apply long-wave assumption. Also, let us use the following expression:

$$\langle \underline{\mathcal{F}}_{\alpha} \rangle(\underline{r} + \underline{a}_{\alpha}) \approx \langle \underline{\mathcal{F}}_{\alpha} \rangle(\underline{r}) + \underline{a}_{\alpha} \cdot \overset{0}{\nabla} \langle \underline{\mathcal{F}}_{\alpha} \rangle(\underline{r}). \quad (5)$$

Here long wave assumption was used. Substituting (5) into averaged equation (4) and comparing the result with equation of motion of continual media in Piola form, one can obtain the expression for Piola stress tensor $\underline{\underline{P}}$. Similarly, one can obtain the expression for Cauchy stress tensor $\underline{\underline{\tau}}$. As a result, one has the following formulae:

$$\underline{\underline{P}} = \frac{1}{2V_0} \sum_{\alpha} \underline{a}_{\alpha} \langle \underline{\mathcal{F}}_{\alpha} \rangle, \quad \underline{\underline{\tau}} = \frac{1}{2V} \sum_{\alpha} \underline{A}_{\alpha} \langle \underline{\mathcal{F}}_{\alpha} \rangle. \quad (6)$$

One can see that tensor $\underline{\underline{\tau}}$ is not symmetrical in the general case. Necessary conditions of the symmetry will be discussed later.

Let us derive the expression for heat flux. For the sake of simplicity, let us consider the case, when volumetrical forces and volumetrical heat sources are equal to zero. Derivations will be conducted in the reference configuration. In this case, averaged specific total energy per volume V_0 has the following form:

$$\rho_0 E = \rho_0 K + \rho_0 U, \quad \rho_0 K = \frac{1}{2} \rho_0 \dot{\underline{u}}^2, \quad \rho_0 U = \frac{1}{2} \rho_0 \langle \dot{\underline{u}}^2 \rangle + \frac{1}{2V_0} \sum_{\alpha} \langle \Pi_{\alpha}(\{\underline{\mathcal{F}}_{\alpha}\}_{\alpha \in \Lambda}) \rangle \quad (7)$$

Here E , K , U are mass densities of the total, kinetic and internal energies respectively. Differentiating K and U with respect to time, one can obtain the following expression for $\rho_0 \dot{U}$:

$$\rho_0 \dot{U} = \underline{\underline{P}} \cdot \left(\underline{u} \overset{0}{\nabla} \right)^{\cdot} + \overset{0}{\nabla} \cdot \left(\frac{1}{2V_0} \sum_{\alpha} \underline{a}_{\alpha} \langle \underline{\mathcal{F}}_{\alpha} \cdot \dot{\underline{u}}_{\alpha} \rangle \right) \quad (8)$$

Comparing equation (9) with equation of balance of energy for continuum one obtains the expression for heat flux in the reference configuration \underline{h} . Using the known connection between fluxes in different configurations one can obtain the expression for heat flux in the actual configuration \underline{H} . The results are as follows:

$$\underline{h} = -\frac{1}{2V_0} \sum_{\alpha} \underline{a}_{\alpha} \langle \underline{\mathcal{F}}_{\alpha} \cdot \dot{\underline{u}}_{\alpha} \rangle, \quad \underline{H} = -\frac{1}{2V} \sum_{\alpha} \underline{A}_{\alpha} \langle \underline{\mathcal{F}}_{\alpha} \cdot \dot{\underline{u}}_{\alpha} \rangle. \quad (9)$$

Results and Discussion

Different expressions connecting Cauchy stress tensor with parameters of discrete systems are proposed in literature. Full reviews on this topic can be found in papers [4, 5]. In [5], it was shown that the majority of known expressions can be represented in the form proposed in paper [3]. Let us find the relation between this expression and the second of the formulae (6). The equation of thermal motion of the reference particle has the following form:

$$m\ddot{\underline{u}} = \frac{1}{2} \sum_{\alpha} \left(\underline{\tilde{\mathcal{F}}}_{\alpha}(\underline{r}) - \underline{\tilde{\mathcal{F}}}_{-\alpha}(\underline{r} + \underline{a}_{\alpha}) \right), \quad (10)$$

Multiplying both part of the given equation by $\underline{\tilde{u}}$, averaging it and using long wave assumption one obtains

$$\rho \langle \underline{\tilde{u}} \dot{\underline{u}} \rangle^* - \rho \langle \dot{\underline{u}} \underline{\tilde{u}} \rangle = \underline{\tau} - \frac{1}{2V} \sum_{\alpha} \langle \underline{A}_{\alpha} \underline{\mathcal{F}}_{\alpha} \rangle + \frac{1}{2V} \overset{0}{\nabla} \cdot \left(\sum_{\alpha} \underline{a}_{\alpha} \langle \underline{\mathcal{F}}_{\alpha} \underline{\tilde{u}}_{\alpha} \rangle \right) \quad (11)$$

On the one hand this expression can be used for the proof of symmetry of Cauchy stress. Thereto one can calculate vector invariant of both parts of equation (11).

$$\underline{\underline{E}} \cdot \underline{\tau} = \rho \langle \underline{\tilde{u}} \times \dot{\underline{u}} \rangle^* + \frac{1}{2V} \sum_{\alpha} \langle \underline{A}_{\alpha} \times \underline{\mathcal{F}}_{\alpha} \rangle - \frac{1}{2V} \overset{0}{\nabla} \cdot \left(\sum_{\alpha} \underline{a}_{\alpha} \langle \underline{\mathcal{F}}_{\alpha} \times \underline{\tilde{u}}_{\alpha} \rangle \right) \quad (12)$$

The first expression in the right side of this equation is equal to the derivative of moment of momentum, which corresponds to thermal motion. Let the averaging operator includes spatial averaging over significantly big volume and let us assume that thermal motion does not lead to macroscopic rotation of the volume. Then the first term in (12) is equal to zero. One can show that the second term is equal to zero as well in the case, when

potential energy has form $\Pi = \Pi \left(\{ \underline{A}_{\alpha} \}_{\alpha \in \Lambda}, \{ \underline{A}_{\beta} \cdot \underline{A}_{\gamma} \}_{\beta, \gamma \in \Lambda} \right)$. Therefore, one can conclude that in this particular case $\| \underline{\tau}^A \| \ll \| \underline{\tau}^S \|$. Thus spatial averaging is necessary for symmetry of the stress tensor.

On the other hand, one can consider stationary state.¹ In this case, one obtains

$$\underline{\tau} = \frac{1}{2V} \sum_{\alpha} \underline{A}_{\alpha} \langle \underline{\mathcal{F}}_{\alpha} \rangle = \frac{1}{2V} \sum_{\alpha} \langle \underline{A}_{\alpha} \underline{\mathcal{F}}_{\alpha} \rangle - \rho \langle \dot{\underline{u}} \underline{\tilde{u}} \rangle. \quad (13)$$

Thus, in the particular case, formula (6) is similar with the expression used in [3,4].

Conclusions

Generalization of approach for transition from discrete system to equivalent continuum proposed in [6] was conducted. Two main principles were used for transition: decomposition of motions into continual and thermal parts and long-wave assumption [1]. The decomposition was conducted by means of averaging operator of general type. It was proposed to represent potential energy per particle as function of all vectors connecting the given particle with its neighbors. Transition from the equation of motion of discrete system to equation of motion for continuum was conducted. Expressions connecting Cauchy and Piola stress tensor with parameters of a discrete system were obtained. It was shown that in the general case the discrete analog of Cauchy stress tensor can be

¹ In the stationary state, the average components of all physical values are constant in time and space.

unsymmetrical. The symmetry was proven in the case when potential energy per particle depends on distances between the particle and its neighbors and angles between bonds created by the particle. Also, it was shown that spatial averaging is required for symmetry of the stress tensor. Thus, it was proven that averaging operator cannot be taken arbitrary. It was shown that expression for Cauchy stress tensor is similar with expression proposed in [3,4]. Equation of balance of energy was considered. The expression for connection between heat flux and parameters of discrete system was obtained.

References

- [1] M. Born and K. Huang, *Dynamical Theory of Crystal Lattices* (Oxford, Clarendon Press, 1988).
- [2] I. A. Kunin, *Theory of Elastic Media with Microstructures* (Springer-Verlag, 1982).
- [3] R. J. Hardy, "Formulae for determining local properties in molecular-dynamics simulations: shock waves," *J. Chem. Phys.* **76** 622-628 (1982).
- [4] E. B. Webb, J. A. Zimmerman, S. C. Seel, "Reconsideration of continuum thermomechanical quantities in atomic scale simulations," *Mathematics and Mechanics of Solids*. **13** 221-266 (2008).
- [5] M. Zhou, "Thermomechanical continuum representation of atomistic deformation at arbitrary size scales," *Proc. R. Soc. A*. **461** 3437-3472 (2005).
- [6] A. M. Krivtsov, *Deformation and Fracture of Bodies with Microstructure* (Moscow, FIZMATLIT, 2007) p. 302 [in Russian].
- [7] A. M. Krivtsov, "From nonlinear oscillations to equation of state for simple discrete systems," *Chaos, Solutions & Fractals* **17** 79 (2003).
- [8] A. M. Krivtsov and V.A. Kuzkin, "Derivation of equations of state for perfect crystals with simple structure," *Mechanics of Solids* [paper in press].
- [9] S. M. Foiles, M. S. Daw, and M. I. Baskes, "Embedded-atom-method functions for fcc metals Cu, Ag, Au, Ni, Pd, Pt, and their alloys," *Phys. Rev. B*. **33** 12 (1986).
- [10] F. H. Stillinger and T. A. Weber, "Computer simulation of local order in condensed phases of silicon," *Phys. Rev. B*. **31** 8 (1985).
- [11] J. Tersoff, "New empirical model for structural properties of silicon," *Phys. Rev. Lett.* **56** 6 (1986).

ELECTRICAL EFFECTS OF IONIZING RADIATION OF INSULATING MATERIALS

H. P. Hjalmarson, K. E. Kambour, R. J. Magyar

Sandia National Laboratories, Albuquerque, NM 87185 USA

Author Contact: hphjalm@sandia.gov

The effects of high dose-rate ionizing irradiation of insulators are discussed.

Introduction

Research on the effects of ionizing radiation has led to many advances in materials science during the last several decades. Much of this effort has focused on materials issues such as defects and their effects on electrical properties [1-4]. In the research described in this paper, the effects of high dose rates of energetic radiation are considered as a function of time during and after the irradiation. To make these problems tractable, the phenomena at different time scales are studied with different computational methods. These efforts are unified by their focus on radiation-induced conductivity measured at times long compared with the underlying atomic phenomena.

The physical phenomena in ionizing radiation effects on an insulator are illustrated in Figure 1. This schematic shows the valence and conduction bands of an insulator with a large bandgap sandwiched between two heavily-doped semiconductors. The heavy doping causes these semiconductors to have metallic conductivity. Thus, this metal-insulator-metal structure behaves as a capacitor.

At very short times, an initial hot electron-hole pair is shown. It is assumed that these particles have energies much greater than the bandgap of the insulator. In the subsequent snapshots, the initial energetic particle generates electron-hole pairs by impact ionization. This process is also assumed to create lattice defects.

A key objective is the transient electrical current created in this capacitor for a given radiation pulse as a function of voltage applied to the capacitor. This voltage is applied before the irradiation pulse starts. Thus, the calculations show the transient current induced by irradiation of an initially charged capacitor.

The three snapshot images of this capacitor structure are intended to show the events as a function of time. These times can be taken as femtoseconds, picoseconds, and nanoseconds for the three cases, respectively.

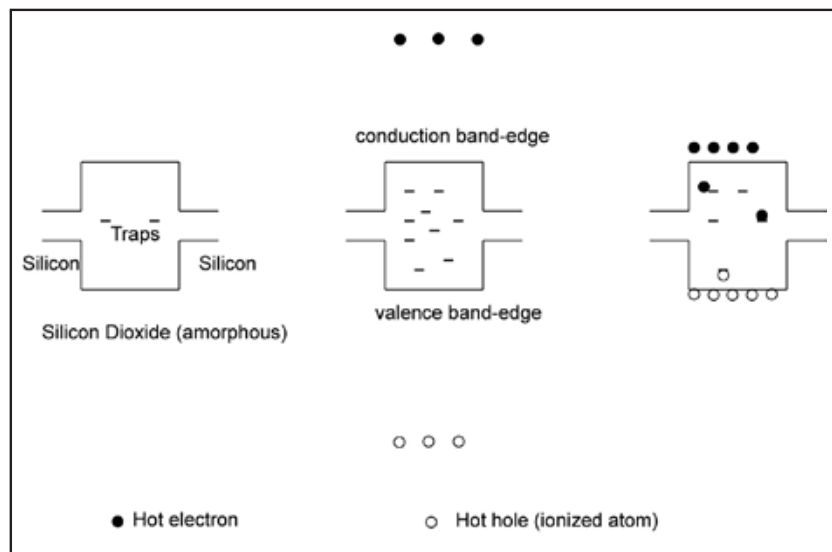


Figure 1. Shows radiation effects as a function of time. The filled circles are electrons, open circles are holes, and short lines are defect energy levels.

The electrical effects of defects are often important in controlling this transient current [1-5]. Such defects introduce additional energy states in the bandgap of a material. The figure shows an existing set of defects, but the density of defects is assumed to vary during the irradiation events depicted in the figure.

In the intermediate snapshot, the density of electrons and holes has increased because each hot electron or hole can generate another electron-hole pair. This generation of electron-hole pairs cools the electrons and holes. In contrast, Auger recombination of an electron-hole pair heats either an electron or a hole. Eventually, the competition between these processes produces a quasi-equilibrium distribution characterized by a carrier temperature that is large compared with the lattice temperature.

The electrons and holes also cool by emitting phonons, thereby heating the lattice. Eventually, the carrier temperature cools to the lattice temperature. The electrons and holes can also create neutral electron-hole pairs called excitons that may persist until they release their energy by emitting a photon or by recombining at a lattice site. This latter process can displace an atom [6]. This displacement of an atom creates two defects, the interstitial atom and the vacancy. These defects, schematically depicted in the figure, can also act as carrier recombination centers. In principle, the emitted photons can create more electron-hole pairs, but this effect is ignored.

In the final snapshot, the carriers have cooled to the lattice temperature. The density of defects has been increased but some defects have healed in the sense that interstitials and vacancies have recombined to place the atom back on a lattice site again.

Theory

As stated above, a particular focus of this study is the electrical and optical responses of this material. At long times, this response can be stated as the low-frequency portion of the optical conductivity $\sigma(\omega, \kappa)$. This response can also be expressed as the dielectric function $\epsilon(\omega, \kappa)$ of the material. These two tensor quantities are related:

$$\epsilon(\omega, k) = 1 + \frac{i\sigma(\omega, k)}{4\pi\epsilon_0\omega}. \quad (1)$$

To be more specific, the electrical effects are associated with the longitudinal portion and the optical effects are associated with the transverse portion of these functions.

The phenomena at very short times can be computed using a time-dependent density functional theory (TDDFT) method to obtain the dielectric function [7-11]. In this method, the many-body quantum density is propagated in time, and the resulting quantities can be analyzed to determine the dielectric function. This calculation involves the simultaneous evolution of two objects, an auxiliary wave-function and a polarization vector potential. The dielectric function is directly related to the ratio of the polarization vector potential and the perturbing vector potential. To include the ionizing events, the simulations are perturbed from a nonequilibrium state that can be arbitrarily constructed from the auxiliary wave-functions or achieved through a perturbing time-dependent field. Some of these contributions to the conductivity, such as carrier-carrier scattering, will also be computed by solving the Boltzmann equation in which these effects are included in an approximate way.

The phenomena at intermediate times are computed using a molecular dynamics method in which the effects of the hot carriers are included as a heating term. The phenomena at long times are computed using a continuum method to solve for the transport of electrical current in the presence of defects that can trap and recombine the electrons and holes. This method also allows for the inclusion of defect reactions to include the effects of the interstitial-vacancy pairs, and it also includes the effects of carrier heating.

Results and Discussion

The electrical effects of defects in a capacitor structure under irradiation are discussed in this section. These defects are assumed to be present in the insulator prior to the irradiation. In other words, the creation of new defects by the radiation is ignored in these calculations. The effects of carrier heating are not included in these calculations, and carrier-carrier scattering effects on carrier mobility are not included.

The silicon dioxide insulator layer is assumed to be 1 micron thick and the silicon semiconductor layers are also 1 micron thick.

Figure 2 shows the transient current following ionizing radiation of three different dose rates. Each family of current-voltage curves shows the current as the voltage is increased by factors of ten. To be specific, the voltages are 0.01, 0.1, 1.0, 10.0, and 100.0 V. The irradiation at the dose rate of 10^4 rd/s produces a current that reaches a steady-state condition. For the three lowest voltages, each of the current-versus-time curves has a linear dependence on voltage. This can be seen as a displacement up by a factor of ten as the voltage increases by a factor of ten. However, the two current-time curves for the two largest voltages reveal that a saturation is approached at high voltages. By inspection, the current for the largest voltage is nearly unchanged by increasing the voltage. In this case, the voltage is high enough that all the electrons and holes are extracted.

The second family of curves, for an irradiation at 10^8 rd/s, looks similar. The increase in dose rate shifts the entire family of five current-voltage curves up by approximately $1e4$ corresponding to a linear dependence on radiation dose rate. In this case also, the currents become saturated at the highest voltages.

The irradiation at the highest dose rate, 10^{12} rd/s, produces a qualitatively different effect. For each voltage, the current reaches a quasi-steady state at very short times, but then it falls to a lower value by a factor of 20. This effect is caused by a polarization of the electron-hole plasma by the electric field. The creation of this charge dipole contributes to the current at short times. However, once the polarization has been created, the current drops to a new steady-state value and it then remains nearly constant.

Finally, the current does not saturate at high voltages for the irradiation at this highest dose rate. The absence of saturation is not understood at this time, but it appears to be caused by the fact that the current is controlled by intrinsic plasma effects rather than the defects as in the lower dose-rate calculations.

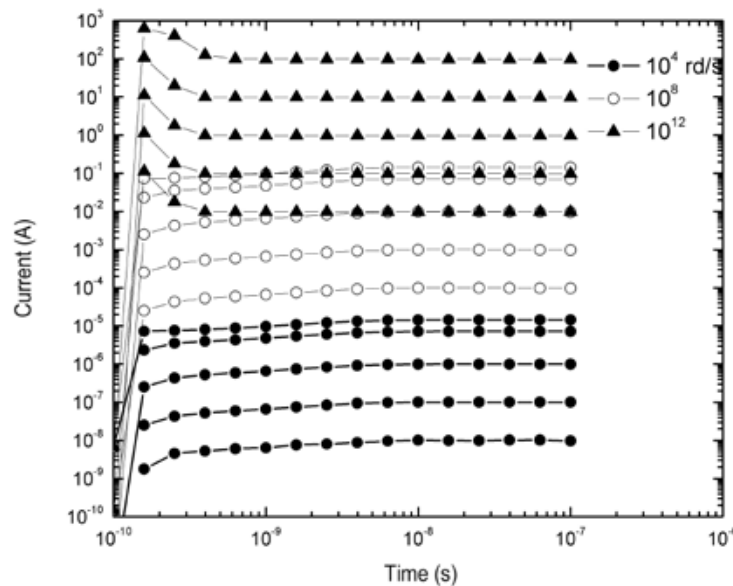


Figure 2. Transient current as a function of time.

Conclusions

The electrical effects of ionizing radiation depend on defects and radiation dose-rates. These effects have been demonstrated by discussing a simple transient electrical calculation for a capacitor structure.

Acknowledgements

This work was supported by Sandia National Laboratories. Sandia is a multi-program laboratory operated by Sandia Corporation, a Lockheed Martin Company, for the United States Department of Energy under Contract DEAC04-94AL85000.

References

- [1] G. J. Dienes, "Radiation Effects in Solids," *Annual Review of Nuclear Science*, **2** 187-220 (1953).
- [2] T. P. Ma and P. V. Dressendorfer, *Ionizing Radiation Effects in MOS Devices and Circuits* (John Wiley and Sons, New York, 1989).
- [2] C. Claeys and E. Simoen, *Radiation Effects in Advanced Semiconductor Materials and Devices* (Springer, NY, 2002).
- [4] A. Holmes-Siedle and L. Adams, *Handbook of Radiation Effects* (Oxford, Oxford University Press, 2002).
- [5] R. F. Fowler, "X-ray induced conductivity in insulating materials," *Proc. Royal Soc. London A*, **236** 1207 (1956).
- [6] N. Itoh and A. M. Stoneham, *Material Modification by Electronic Excitation* (Cambridge, University Press, 2000).
- [7] E. Runge and E. K. U. Gross, "Density-functional theory for time-dependent systems," *Phys. Rev. Lett.* **52** 997 (1984).
- [8] G. G. Bertsch, J. I. Iwata, A. Rubio, K. Yabana, "Real-space, real-time method for the dielectric function," *Phys. Rev. B* **62**, 7998 (2000).
- [9] T. Otake, K. Yabana, J. I. Iwata, "First-principles calculation of the electron dynamics in crystalline SiO₂," *J. Phys. Condens. Matter* **21** 064224 (2009).
- [10] K. Yabana, T. Nakatsukasa, J. I. Iwata, G.F. Bertsch, "Real-time, real-space implementation of the linear response time-dependent density functional theory," *Phys. Stat. Sol. B* **243** 1121 (2006).
- [11] T. Otake, M. Yamagiwa, J. I. Iwata, K. Yabana, T. Nakatsukasa, G. F. Bertsch, "First-principles electron dynamics simulation for optical breakdown of dielectrics under intense laser field," *Phys. Rev. B* **77** 165104-1 (2008).

STRONGLY COUPLED PLASMA NANOCHANNEL CREATED BY A FAST SINGLE ION IN CONDENSED MATTER

A. V. Lankin, I. V. Morozov, G. E. Norman,
S. A. Pikuz, Jr., I. Yu. Skobelev

Joint Institute for High Temperatures (JIHT), Russian Academy of Sciences, Moscow, 125412, Russia
Contact Author: spikuz@gmail.com

A plasma model of relaxation of a medium in heavy ion tracks in condensed matter is proposed. The model is based on three assumptions: the Maxwell distribution of plasma electrons, localization of plasma inside the track nanochannel and constant values of the plasma electron density and temperature during the X-ray irradiation. It is demonstrated that the plasma relaxation model adequately describes the X-ray spectra observed upon interaction of a fast ion with condensed target. Assumptions of plasma relaxation model are validated by the molecular dynamics modeling and simulation.

Introduction

Beams of fast heavy ions can be obtained from electro-magnetic accelerator as well as from plasma of short laser pulses. Due to beam absorption features in condensed matter, these beams are widely used for a number of important technical and medical applications. The interaction of single fast heavy ion with condensed matter leads to the formation of a track. On the initial stage of track formation, the excited channel is created with transverse size of about 1 nm as it is illustrated in Figure 1a. Due to ionization of the target atoms by the Coulomb field of a projectile ion a number of multicharged ions appears in the channel. The following relaxation of the channel can be studied experimentally by measuring X-ray spectra generated by radiative decay of autoionizing states of these ions [1,2,3].

The conventional model to interpret X-ray spectra is based on the assumption that the relaxation of different ions is independent of each other, and the excitation of surrounding target medium is not taken into account [4]. In this case, the intensity of the X-ray spectral line is proportional to the corresponding multiple ionization cross sections of ion Z multiplied by the branching factor $A^Z/(A^Z + \Gamma^Z)$, where A^Z is the radiative transition probability and Γ^Z is the autoionization probability. In what follows, we recall this model as an “atomic relaxation” one [1]. But it is well known that the plasma-like environment arising after the initial ionization enables a wider range of relaxation processes for the excited ions. For example, owing to the collisions with free electrons, the initially excited Z ion can either be ionized or recombine before filling the K vacancy upon the radiative transition. It means that the initial excitation of the Z ion could actually result in formation of ions with different charge states with K vacancies and, hence, could lead to emission of spectral lines of ions with $Z' \neq Z$. In this case, the observed X-ray spectrum should reflect not only the characteristics of the interaction of the projectile ion with the target atoms but also the parameters (temperature and density) of the plasma formed.

The conclusion about generation of plasma inside the track of a fast heavy ion was drawn quite long time ago. Moreover, it was noted there that the plasma was strongly coupled (nonideal). The model to describe the relaxation of plasma created by single fast ions with total energies of 0.1 – 1.0 GeV is proposed in this paper. This model is based on (1) the conclusion that the solid-density nanosize plasma in the area of projectile-target atom interaction is created; (2) the solution of the time-dependent equations of the collisional-radiative kinetics to describe the evolution of an initially created excited state.

Three time stages of the formation of a nonequilibrium strongly coupled solid-state nanoplasma in the region of the track are considered.

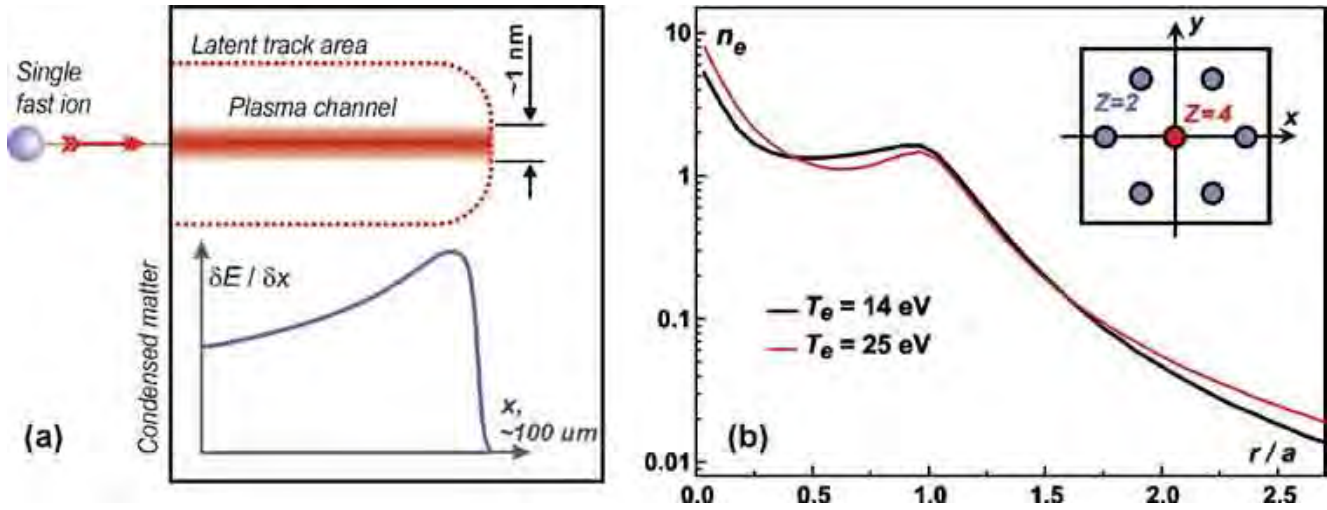


Figure 1. (a) Plasma channel created by a single fast ion slowing down in condensed matter. (b) Steady-state radial profile of the electron number density in the electric double layer for electron temperatures of 14 and 25 eV. The distance from the track axis r is in units of the interatomic distance a . The arrangement of ions in the track cross-section is given on the insertion.

Plasma Relaxation Model

At the initial stage ($\sim 10^{-2}$ fs) the state of the medium is described by the conventional atomic relaxation model [4] (i.e., is defined by the multiple ionization of target atoms by a projectile). The initial channel of ionized matter is produced with the transversal diameter of several nanometers and electron density of $n_e \sim 10^{23} \text{ cm}^{-3}$ (for ion charges $Z = 2 - 6$). Ions with K-shell vacancies are localized in the vicinity of the channel axis. Although their fraction is relatively low, they are responsible for the appearance of X-ray emission spectra. To clarify, we will consider a solid target consisting of atoms having fully populated K and L shells and several electrons in M-shell. Initially, both free electrons and different multicharged ions with single K-shell vacancy, n L-shell vacancies and fully ionized M-shell are produced in the area of a single fast ion track. The populations N_n of the states with n vacancies in the L shell are proportional to the cross sections σ_n of the multiple ionization of the target atom by the field of the projectile ion. According to atomic relaxation model, σ_n depends on the probability $p_L(0)$ of ionization of the L -electron at collision with the zero impact parameter (see, for example, [4]). This probability is the function of the projectile ion charge, target atom nuclear charge, and the projectile ion velocity. Unfortunately, the exact calculation of this quantity is a very complex problem, so $p_L(0)$ is considered as the first free parameter of our model.

The second stage of track relaxation process was studied by nonequilibrium molecular dynamics (MD) simulations [1]. The initial structure of ions in the cylinder cross-section is shown in the insertion to Figure 1b. This cell is periodically extended along Z -axis with the period a equal to the edge of hexahedron. Although this is a relatively rough approach to the real ion structure in SiO_2 , it is appropriate to estimate the required relaxation times and describe the evolution of free electron density and velocities in the central track area.

As the plasma is largely neutral, spreading of the electron cloud produces a positive charge in the track center and a double electric layer on the track surface. The ion motion can be neglected when studying the dynamics of electrons. The steady-state radial density profiles of electrons obtained by MD simulations for two cases of 25 and 14 eV are shown in Figure 1b. The first peak at $r = a$ corresponds to the outer ion shell. It follows from

our calculations that the number of electrons remaining in area $r < 1.5a$ decreases not more than below 85% of initial density. These electrons form the plasma around radiating ions, which is dense enough for the collisional relaxation of ions. For both cases, Maxwell distribution of free electron temperature is established on the timescale less than 1 fs. Since this time is an order of magnitude lower than the time of K-shell spectra emission, one can assume that the electron subsystem is in a stationary state during the whole time of spectroscopy data acquisition.

Further evolution (tens of fs) of initially created charge state distribution for the ions with K-shell vacancies (see ion level scheme in Figure 2) is described by the system of time-depended equations of collisional-radiation kinetics. For ion Z with $(n+1)$ electrons, see Figure 3.

We use the following assumptions to decrease the number of equations and correspondingly simplify the problem. First, only ground configurations of the ions and their lowest-lying autoionized configurations are included. Second, it is assumed that the populations of neighboring ion levels are proportional to their total statistical weights. It is related to the fact that the probabilities of collisional transitions between these levels in a solid-state plasma exceed the probabilities of the radiative and autoionized transitions. As a result only one level (e.g., $1s2l^{(n+m)}$) is introduced in calculations instead of the great number of terms related to the configurations $1s2s^n2p^m(2S+1)L_{(2J+1)}$.

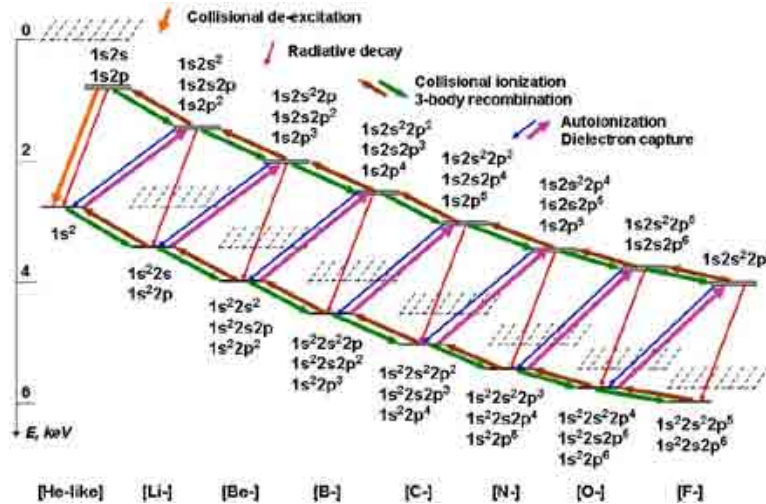
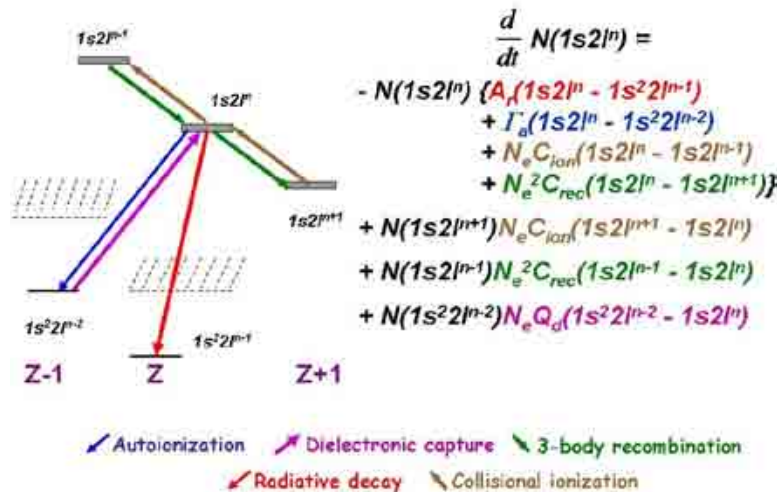


Figure 2. The scheme of Si ion levels and processes taking into account in the plasma model of track relaxation.



The solution of the system of kinetic equations with the initial population values defined from atomic relaxation model makes it possible also to calculate the emission spectrum of fast ion track plasma channel. Total intensity

I^Z of an array of unresolved satellite transitions in the ion Z is determined by the expression,
$$I^Z = \int_0^{\tau_{\text{plasma}}} N^Z(t) A^Z dt$$

where A^Z is the probability of the radiative decay of the autoionizing state and τ_{plasma} is plasma lifetime. The relaxation for the most abundant ions is completed in 10-20 fs, and then the populations of their autoionizing states become relatively low. Thus, the main contribution to X-ray radiation of plasma results from the times when the plasma is not only extremely nonequilibrium but also strongly nonstationary. Accordingly, the value of $\tau_{\text{plasma}} = 20$ fs is used in our spectra simulations. The group of dielectronic satellite lines for every ion charge state Z consists of a number of radiation transitions inside a narrow spectral range of about 0.05 Å. Usually, these transitions are unresolved and registered as a spectral peculiarity with the overall profile width defined by the distribution $g^Z A^Z(\lambda)$ rather than by broadening of individual lines. For spectra simulation, the spectral functions describing the shape for satellite groups were taken out of the experiment [2,3].

Determination of Plasma Nanochannel Parameters Using X-ray Spectra

The most detailed experimental studies of the X-ray spectra emitted under interaction of fast heavy ions with condensed targets were done recently in the linear heavy ion accelerator facility UNILAC (GSI, Germany) [3,4]. Among others, the interaction of Ni(58) and Mg(26) fast ions with low (0.15 g/cc) bulk density quartz aerogel and solid Al targets was investigated, correspondingly. The use of the aerogel target allowed the track length to be expanded up to 2 mm and provided the spatial resolution of the spectra along the track. Ions with the energy of 11.4 and 5.9 MeV/amu were focused into the 2 mm spot at the edge of a target. The target was exposed to a beam current of ~ 0.1 μA for 2 to 3 hours. Such a low current provided the average time interval of 10 ps between single ion propagation. Therefore, the measured spectrum can be considered as an average over the independent acts of a single heavy ion interaction with the cold target matter.

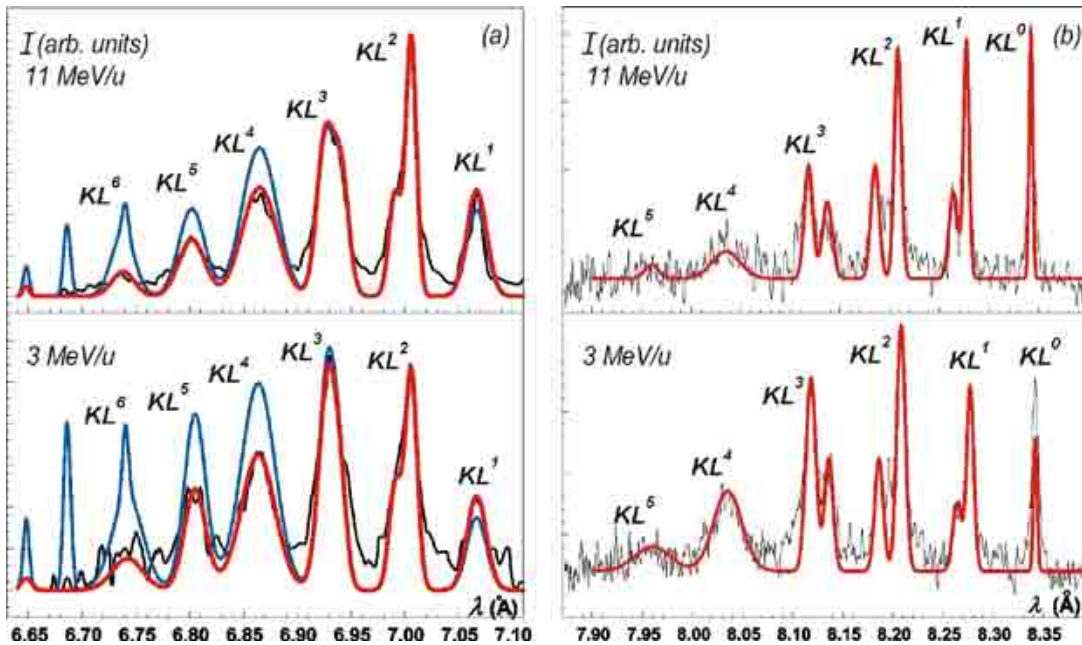


Figure 4. X-ray spectra of Si (a) and Al (b) multicharged ions excited by single fast ions with energy of 11 and 3 MeV/amu: black lines are spectra measured in [2,3]; blue lines are spectra modeled according the atomic relaxation model, and red lines correspond to the plasma relaxation model.

The dielectronic satellites to the He_α resonance line for every charge state of the Si and Al target ion were registered. The experimental data are compared with modeling ones. Although only two fitting parameters $p_L(0)$ and T_e are used, a good agreement for all 6 to 8 satellite groups is obvious (see Figure 4). Whereas even the best fit for the former atomic relaxation model as it is seen from the left part of this figure (blue lines) fails to describe the experimental results, it confirms the validity and self-consistency of the plasma relaxation model and allows us to propose the X-ray spectroscopy method to measure the plasma temperature inside the fast heavy ion track.

Table 1 represents the values of $p_L(0)$ and T_e obtained by the simulation of the experimental data considered. As seen, the value of $p_L(0)$ depends very weakly on the projectile ion energy in the range of $E \sim 3\text{--}11$ MeV/amu. The values of $p_L(0)$ and their energy dependence for the interaction of Ni^{+14} ions with Si targets have not been described before. In contrast to $p_L(0)$, the plasma temperature increases significantly with projectile ion slowing down to $E \sim 3$ MeV/amu. The latter reflects the fact that the linear energy loss of the projectile ion is increasing along with the stopping process from 11 to 3 MeV/amu.

The last three columns in Table 1 contain the values of the electron-electron nonideality parameter Γ_{ee} , the formal number of electrons in the Debye sphere N_D and the degeneracy parameter θ . It follows from Table 1 that the electron gas in heavy ion track in solids is nondegenerate and essentially strongly coupled. Note that recently it was shown also by X-ray spectroscopy methods that strongly coupled plasma is created in laser-driven shock-compressed targets [5].

Table 1. The plasma parameters determined from spectra simulation according the plasma model for the experimental conditions and data obtained in [3,4].

| Projectile - Target | Projectile energy (MeV/amu) | Electron density (10^{23}cm^{-3}) | Measured parameters | | N_D | Γ_{ee} | θ |
|----------------------------------|-----------------------------|----------------------------------------------|---------------------|------------|-------|---------------|----------|
| | | | $p_L(0)$ | T_e (eV) | | | |
| $\text{Ni}^{+14} - \text{SiO}_2$ | 11 | 4.5 | 0.33 | 14 | 0.13 | 1.3 | 0.18 |
| $\text{Ni}^{+14} - \text{SiO}_2$ | 6 | 4.5 | 0.335 | 15 | 0.15 | 1.2 | 0.16 |
| $\text{Ni}^{+14} - \text{SiO}_2$ | 3 | 4.5 | 0.34 | 25 | 0.32 | 0.71 | 0.076 |
| $\text{Mg}^{+7} - \text{Al}$ | 11 | 4.0 | 0.235 | 25 | 0.34 | 0.68 | 0.067 |
| $\text{Mg}^{+7} - \text{Al}$ | 3 | 4.0 | 0.285 | 40 | 0.69 | 0.43 | 0.033 |

Conclusions

The plasma relaxation model is considered to describe the excitation of solids by single fast ions with energies of 0.1–1.0 GeV. Three time stages of the formation of nonequilibrium strongly coupled (nonideal) solid-state nanoplasma are studied in the region of the track. The creation of initial ionized channel at timescale of 10^{-2} fs with nanometer transversal diameter and electron density of $\sim 10^{23}\text{cm}^{-3}$ ($Z = 2 - 6$) is described by the conventional atomic relaxation model. At second stage (≤ 1 fs), Maxwell distribution of free electrons is established with the temperature of tens of eV. The electric double layer with thickness of about interatomic distance is formed around the initial channel. The next relaxation stage (tens of fs) is described by the time-dependent equations of collisional-radiation kinetics. The ions are stable in the crystal lattice so that the band structure is retained while the matter is still deeply ionized. The nanoplasma lifetime is defined by recombination rates and amounts of several hundreds fs.

X-ray K-shell spectra of solid quartz and Al targets excited by 100–600 MeV single ions [2,3] are explained with a good agreement between the proposed model simulation and the experimental data. Both the agreement and MD modeling confirm the validity and self-consistency of the plasma relaxation model. Plasma parameters were found that allow us to conclude that the strongly coupled plasma nanochannel is created on the timescale of tens of fs after single fast ion propagates through solid media. The X-ray spectroscopy method is proposed to measure plasma temperature within the nanochannel. The obtained results can be used to study further stages of heavy ion track evolution up to, finally, a change in the material properties with accumulation of tracks.

Acknowledgements

The authors appreciate A. Faenov for developing the X-ray spectroscopy methods and techniques allowed to obtain the experimental data used to check the validity of the plasma relaxation model. The authors appreciate B. Doyle, H. Hjalmarson, J. Aidun, M. M. Basko, B. M. Smirnov, and V. S. Vorobyev for prolific discussions and suggestions. The work was partly supported by ISTC Grant No. 3504, Programs of Fundamental Research No. 12 and No. 27 of the Presidium of RAS, Grant of RF President MK-4375.2008.8. I. V. Morozov and A. V. Lankin acknowledge the "Dynasty" foundation. Simulations were performed on MIPT-60 cluster.

References

- [1] A. V. Lankin, I. V. Morozov, G. E. Norman, S. A. Pikuz Jr., I. Yu. Skobelev, "Solid-density plasma nanochannel generated by a fast single ion in condensed matter," *Phys. Rev. E* **79** 036407 (2009).
- [2] S. A. Pikuz, Jr., V. P. Efremov, O. Rosmej, A. Blazevic, S. Korostiy, A. Fertman, A. V. Shutov, G. E. Norman, D. H. H. Hoffmann, "Investigations of heavy-ion tracks' energy deposition inside solid media by methods of x-ray spectroscopy," *J. Phys. A* **39** 17 4765-4769 (2006).
- [3] O. N. Rosmej, A. Blazevic, S. Korostiy, R. Bock, D. H. H. Hoffmann, S. A. Pikuz, V. P. Efremov, V. E. Fortov, A. Fertman, T. Mutin, T. A. Pikuz, A. Ya. Faenov, "Charge state and stopping dynamics of fast heavy ions in dense matter," *Phys. Rev. A* **72**, 052901 (2005).
- [4] A. Schmiedekamp, T. J. Gray, B. L. Doyle, U. Schiebel, "Target and projectile cross sections for F ions on Ti, V, Cr, Fe, and Co: 1.7 MeV/amu," *Phys. Rev. A* **19** 6 2167-2172 (1979).
- [5] A. Ravasio, G. Gregori, A. Benuzzi-Mounaix, J. Daligault, A. Delserieys, A. Ya. Faenov, B. Loupiau, N. Ozaki, M. Rabec le Gloahec, T. A. Pikuz, D. Riley, M. Koenig, "Direct observation of strong ion coupling in laser-driven shock-compressed targets," *Phys. Rev. Letters* **99** 135006 (2007).

MOLECULAR DYNAMICS SIMULATIONS OF DISPLACEMENT CASCADES IN GaAs

Stephen M. Foiles

Sandia National Laboratories, Albuquerque, NM 87185 USA

Contact Author: foiles@sandia.gov

The quantification of the production of primary defects via displacement cascades is an important ingredient in the prediction of the influence of radiation on the performance of electronic components in radiation environments. Molecular dynamics simulations of displacement cascades are performed for GaAs. The interatomic interactions are described using a recently proposed Bond Order Potential, and a simple model of electronic stopping is incorporated. The production of point defects is quantified as a function of recoil energy and recoil species. Correlations in the point defects are examined. There are a large number of anti-site defects nearest-neighbor pairs as well as di-vacancies and larger order vacancy clusters.

Introduction

Radiation damage and ion implantation in materials have been studied via molecular dynamics for many years [1,2,3]. A significant challenge in these simulations is the detailed identification and quantification of the primary defect production. For the present case of a compound semiconductor, GaAs, there are a larger number of possible point defects compared to elemental materials; two types of vacancies, two types of interstitials and anti-site defects. This is further complicated by the fact that, in addition to the formation of point defects, amorphous zones may also be created [4].

The goal of the current work is to quantify the production of primary defects in GaAs due to radiation exposures. This information will be used as part of an effort to predict the influence of radiation environments on the performance of electronic components and circuits. The data provide the initial state for continuum-level analysis of the temporal evolution of defect populations. For this initial state, it is important to know both the number of the various point defects that may be produced as well as the initial spatial correlations between the primary defects. The molecular dynamics simulations employ a recently developed Bond Order Potential (BOP) for GaAs [5]. The analysis of the resulting atomic configurations follows a generalization of methods presented previously for elemental Si [6]. The number of point defects of various types, exclusive of the amorphous zones, is predicted as a function of recoil energy. It is also shown that certain primary point defects are initially formed in binary or larger clusters.

Method

Interatomic Potentials

Development of an interatomic potential for GaAs is more challenging than for the elemental semiconductors due to the increased number of required interactions, the larger space of properties and the increased complexity of the bonding. Three of the existing potentials for GaAs are based on an extension of the functional form proposed by Tersoff for the modeling of Si and other covalent systems [7]. The first such potential was developed by Smith [8]. The parameterization of this potential was later modified by Sayed [9]. Studies with these potentials showed that they have significant shortcomings with regard to surfaces, melting behavior, point defect properties, and relative energies of alternate crystal structures [10]. For these reasons, the potentials are not viewed as reliable for defect simulations. More recently, a new parameterization of the Tersoff approach was performed by Albe, Nordlund, Nord, and Kuronen (ANNK) [11]. The strengths and weaknesses of these potentials for GaAs have been discussed in the context of vapor phase deposition by Murdick, Zhou, and Wadley [12].

Recently, a new interatomic potential model for GaAs has been proposed [5], which is based on the analytic Bond-Order-Potentials (BOP) formalism that has been pioneered by Pettifor and coworkers [13-18]. The bond-order potentials are based on a tight-binding description of the electronic bonding in sp-valent systems. The analytic forms are developed to describe both the σ - and π -type bonding for systems that form open phases, close-packed structures, and compounds. While the physical motivation behind the BOP potentials is superior to the Tersoff potentials, the computational effort associated with these potentials is also substantially greater.

Molecular Dynamics Simulations

The molecular dynamics simulations of recoil cascades are performed via molecular dynamics using the following protocol. An ideal GaAs lattice is equilibrated at 300 K to provide the initial atomic positions and velocities. The cell has periodic boundary conditions in all three directions with a size dependent on the energy of the recoil to be considered. Some representative size and recoil energy combinations used are 64 000 atoms for 100 eV recoils, 216 000 atoms for 1 keV recoils and 4 096 000 atoms for 25 keV recoils. Note that for these sizes in the absence of any thermostat, the equilibrium temperature rise due to the added energy will be less than 24 K. Further, the net drift of the cell due to the momentum introduced will be less than, or on the order of, 5×10^{-3} nm/ps. For most of the computational cell, no thermostat is applied. However, there is a 2 nm thick layer on the faces of the cubic periodic cell where a Langevin thermostat is applied. This thermostat acts both to control the temperature of the system and to partially disrupt the propagation of waves passing through the periodic boundaries. An atom is selected in the initial cell and given a velocity appropriate to the desired recoil energy. The atom is located near the edge of the central, unthermostatted region of the cell such that its velocity is toward the center of the cell. In this way, the cascade will occur in the unthermostatted region of the cell.

The dynamics are also modified to incorporate a simple model of electronic stopping. A frictional force is added to the dynamics to mimic the transfer of energy to the electronic system. For atoms with kinetic energy greater than 10 eV, the Lindhard-Scharf model gives this drag force. For atoms with kinetic energies less than 5 eV, the drag force is zero. For atoms with intermediate kinetic energies, the drag force ramps up from 0 at 5 eV to the Lindhard-Scharf value at 10 eV. Note that for the majority of the atoms in the system, this electronic stopping model does not alter the dynamics.

The molecular dynamic simulations are performed using the LAMMPS molecular dynamics program modified to implement the BOP interatomic interaction and the electronic stopping model. The calculations are performed using a variable time step determined from the maximum atomic velocity such that all displacements in a single time step are less than 10^{-3} nm, and in no case will the time step be longer than 1 fs.

A major challenge in MD simulations of radiation cascades is the quantitative analysis of the defect production. The strategy used in the current work is similar in approach to earlier analysis of the damage in Si [6]. A computationally convenient method is to consider Wigner-Seitz cells located around each site of the ideal lattice and to compare the actual occupation of that site with the occupation in the ideal lattice. If they are the same, it is assumed that there is no defect. If the cell is empty, the site is a vacancy; if it is multiply occupied, it is an interstitial, and if it is singly occupied but with the wrong chemical species, it is an anti-site defect. The problem with this approach is that it implicitly assumes that the system is a near-perfect crystal with localized point defects. However, it is known that locally amorphous regions can be formed in radiation cascades. In such an amorphous region, the above criteria no longer make physical sense. In this work, the amorphous regions are identified by an analysis of the ring structures in the crystal (i.e., closed loops along nearest neighbor steps). In the diamond structure, the smallest rings involve six steps. In the case of amorphous Si, it is known that there are a significant number of five- and seven-member rings that are absent in the ideal crystal structure. Following our

earlier work in Si [6], we identify amorphous regions as those where the density of five- and seven-member rings is above a threshold determined by the analysis of amorphous structures. The Wigner-Seitz cell analysis is then used to identify and count the number of defects of various types in the remaining nearly crystalline regions.

Results and Discussion

Threshold Displacement Energies

The threshold displacement energy is the minimum recoil energy required to produce defects and is a key parameter to validate interatomic potentials for displacement damage calculations. There have been several experimental studies of the threshold displacement energy in GaAs as reviewed by Pons and Bourgoïn [19]. A recent compilation of displacement energies lists 10 eV [20] for GaAs. Based on the anisotropy of the defect production with the direction of electron irradiation, it is concluded that the defects formed at low energies are on the As sublattice. In comparing with the MD simulations, it is important to consider whether this means that defects are not formed on the Ga sublattice. Pons and Bourgoïn [19] argue that very short-lived Frenkel pairs are formed on the Ga sublattice but they recombine quickly even at cryogenic temperatures.

The computed threshold displacement energies for the BOP potential are in reasonable agreement with experiment, especially considering that the potentials are not fit to this quantity. The threshold for the formation of Frenkel pairs on the As sublattice is determined to be about 12 eV. This is close to, though somewhat higher than, the experimental value of 10 eV. The threshold for forming Frenkel pairs on the Ga sublattice is found to be somewhat lower than for the As sublattice, about 9 eV. As discussed above, Frenkel pairs on the Ga sublattice are expected to be very short-lived experimentally. Therefore, one cannot determine the threshold energy for the transient formation of these defects. By comparison, the ANNK potential shows a threshold for the production of Ga Frenkel pairs of between 10 and 15 eV for Ga PKAs and less than 10 eV for As PKAs. The threshold for the production of As Frenkel pairs is greater than 25 eV. This result is in sharp disagreement with the experimental observation that As Frenkel pairs are formed with a threshold of about 10 eV. The poor prediction of the threshold energy by the ANNK potential motivated the use of the more computationally expensive BOP potential.

Quantification of Defect Production

A primary goal of this research is to quantify the number of defects produced in a displacement cascade. Figure 1 shows the results for the number of defects produced, *excluding amorphous zones*, as a function of recoil energy. The curves represent the average of ten simulations at each set of conditions with recoil directions chosen at random. Note that the difference in the defect production between recoils initiating on the Ga or As sublattices is small. Given the nature of a displacement cascade, this is not surprising. Somewhat more surprising is that there is only a small difference in the number of vacancies and interstitials produced between the two sublattices. Over the range of energies studied here, we observe that the number of vacancies and interstitials produced is approximately linear in the recoil energy. One also sees that the number of isolated anti-site defects produced is comparable to the number of vacancies and interstitials.

An important consideration for the subsequent evolution of the defect populations is correlations in the initial defect locations. One strong correlation observed is the tendency to form nearest-neighbor pairs of anti-site defects of the opposite character. The paired anti-site defects are not included in the sums for Figure 1c. Figure 1d shows the number of such anti-site defect pairs as a function of recoil energy. Note that the number of anti-site defects in these pairs is somewhat larger than the number of isolated anti-site defects. Another observation concerns the concentration of di-vacancies. Our studies of defect production in Si revealed that the initial number of vacancies associated with di-vacancies and larger vacancy clusters is comparable to the number of mono-vacancies. The

large number of initial di-vacancies has a strong impact on the evolution of the defect populations. In the current study, we find a similar conclusion that a large fraction of the vacancies are located in di-vacancy and larger clusters. The details of these initial vacancy clustering will be presented in a later publication.

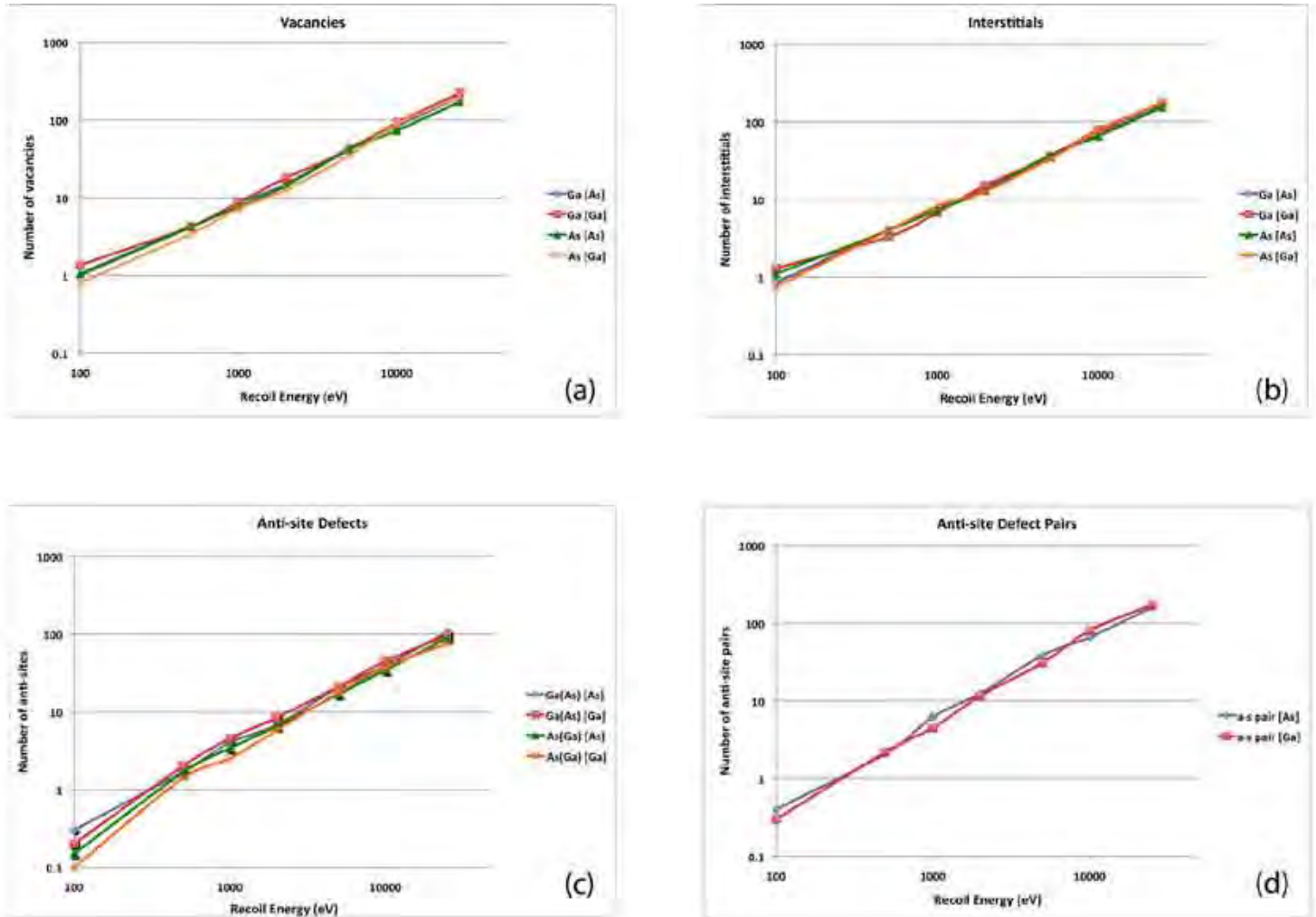


Figure 1. The number of point defects exclusive of amorphous regions as a function of recoil energy: (a) vacancies, (b) interstitials, (c) anti-site-defects where A(B) indicates an A atom on a B site, (d) pairs of anti-site defects. The element in brackets denotes the sublattice of the initial recoil.

Conclusions

Molecular dynamics simulations of displacement cascades in GaAs are performed using the BOP potentials. Amorphous zones are identified in the resultant structures by the presence of 5- and 7-member rings. The defects in the crystalline regions are identified via the occupation of Wigner-Seitz cells. The number of point defects is then determined for recoil energies up to 25 keV. It is found that many anti-site defects occur in nearest neighbor pairs and that there are significant numbers of di-vacancies in the primary damage state.

Acknowledgements

This work was supported by Sandia National Laboratories. Sandia is a multiprogram laboratory operated by Sandia Corporation, a Lockheed Martin Company, for the United States Department of Energy's National Nuclear Security Administration under Contract DEAC04-94AL85000.

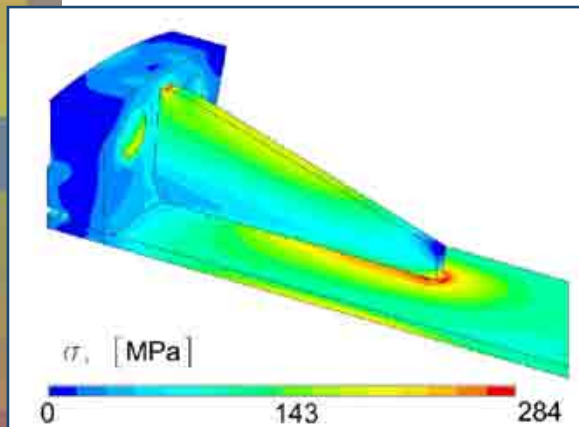
References

- [1] R. S. Averback and T. Diaz de la Rubia, "Displacement Damage in Irradiated Metals and Semiconductors," in *Solid State Physics: Advances in Research and Applications*, eds. H. Ehrenreich and F. Spaepen (San Diego, Academic Press, 1998) p. 281-403.
- [2] T. Diaz de la Rubia, "Irradiation-induced defect production in elemental metals and semiconductors: a review of recent molecular dynamics studies," *Ann. Rev. of Mat. Sci.* **26** 613-649 (1996).
- [3] G. Hobler and G. Betz, "On the useful range of application of molecular dynamics simulations in the recoil interaction approximation," *Nucl. Instr. and Meth. B* **180** 203-208 (2001).
- [4] M. W. Bench et al., "Production of amorphous zones in GaAs by the direct impact of energetic heavy ions," *Journal of Applied Physics* **87** 49-56 (2000).
- [5] D. A. Murdick et al., "Analytic bond-order potential for the gallium arsenide system," *Physical Review B* **73** 045206 (2006).
- [6] S. M. Foiles, "Detailed characterization of defect production in molecular dynamics simulations of cascades in Si," *Nuclear Instruments and Methods in Physics Research B* **255** 101 (2007).
- [7] J. Tersoff, "Empirical interatomic potential for silicon with improved elastic constants," *Physical Review B* **38** 9902 (1988).
- [8] R. Smith, "A semi-empirical many-body interatomic potential for modelling dynamical processes in gallium arsenide," *Nuclear Instruments and Methods in Physics Research B* **67** 335-339 (1992).
- [9] M. Sayed et al., "Computer simulation of atomic displacements in Si, GaAs, and AlAs," *Nuclear Instruments and Methods in Physics Research B* **102** 232-235 (1995).
- [10] K. Nordlund and A. Kuronen, "Non-equilibrium properties of GaAs interatomic potentials," *Nuclear Instruments and Methods in Physics Research B* **159** 183-186 (1999).
- [11] K. Albe et al., "Modeling of compound semiconductors: analytic bond-order potential for Ga, As and GaAs," *Physical Review B* **66** 035205 (2002).
- [12] D. A. Murdick, X. W. Zhou, H. N. G. Wadley, "Assessment of interatomic potentials for molecular dynamics simulations of GaAs deposition," *Physical Review B* **72** 205340 (2005).
- [13] R. Drautz et al., "Analytic bond-order potential for predicting structural trends across the sp-valent elements," *Physical Review B* **72** 144105 (2005).
- [14] D. G. Pettifor, "New many-body potential for the bond order," *Physical Review Letters* **63** 2480-2483 (1989).
- [15] D. G. Pettifor et al., "Analytic bond-order potentials for multicomponent systems," *Materials Science and Engineering A* **365** 2-13 (2004).
- [16] D. G. Pettifor and I. I. Oleinik, "Analytic bond-order potentials beyond Tersoff-Brenner: theory," *Physical Review B* **59** 8487-8499 (1999).

- [17] D. G. Pettifor and I. I. Oleinik, “Bounded analytic bond-order potentials for sigma and pi bonds,” *Physical Review Letters* **84** 4124-4127 (2000).
- [18] D. G. Pettifor and I. I. Oleinik, “Analytic bond-order potentials for open and close-packed phases,” *Physical Review B* **65** 172103 (2002).
- [19] D. Pons and J. C. Bourgoin, “Irradiation-induced defects in GaAs,” *Journal of Physics C: Solid State Physics* **18** 3839-3871 (1985).
- [20] R. S. Averback and M. Ghal, “Fundamental aspects of defect production in solids,” *Nucl. Instr. and Meth. B* **127/128** 1-11 (1997).

MATERIALS

Properties and Failure



The distribution of the von Mises stress in the flange connection of the steel pipe line.

The section considers different aspects of the effect of chemical reactions, defects, and impurities of all kinds on materials properties and failure. IPME RAS demonstrates a many-sided approach to the problem. Vilchevskaya and Freidin treat the oxidation zone formation in front of a crack and the interconnection between the zone and the crack growth in a polycrystalline silicon film. Continuum approximation is used. Krivtsov solves a similar problem

by a molecular dynamics method. Vacancies, holes, and predefined cracks are considered. The oxidation of the initial and new specimen surfaces during the fracture process is taken into account. Indeitsev et al. describe the relaxation of stresses and degradation of material properties under the mechanical loading in a hydrogen-contained environment. The effect is demonstrated in gas pipeline modeling. Polyanskiy et al. analyze the influence of small hydrogen concentration on materials properties, and material fatigue and destruction are treated. Snow et al. use first principles density functional methods to investigate the atomistic behavior of helium in β -phase erbium hydride. Migration barriers are calculated; a concerted-motion mechanism is described. The age-related changes in plutonium physical properties that are induced by alpha-decay are considered by Chung et al. The ultimate goal of the work is to develop capabilities to predict metallurgical evolution driven by aging effects. Magnetic isochronal annealing curves are measured by McCall et al. for self-damaged α -Pu and several δ -Pu alloys. Distinct differences are observed between the magnetic and resistive annealing for δ -Pu; the onset of vacancy migration is strongly reflected in the magnetization signal. Fedotov et al. represent research on depositing properties of chemical nickel coatings modified with nanodiamonds or carbon content. A comparative analysis of microstructure, physical, and mechanical properties is carried out.

Genri Norman, Joint Institute of High Temperatures (JIHT), Moscow, Russia

Section III:

- III-2 Modeling Coupled Interaction Between Crack Growth, Diffusion, and Chemical Reactions (IPME)
- III-7 Influence of Defects Type and Chemical Reaction on Fracture Initiation, Molecular Dynamics Study (IPME)
- III-12 Determination of the Small Hydrogen Traps as Nucleus of Fatigue and Destruction (IPME)
- III-17 First Principles Study of Site Occupation and Migration of Helium in β -phase Erbium Hydride (SNL)
- III-21 Theoretical Model for the Hydrogen-Material Interaction as a Basis for Prediction of the Material Mechanical Properties (IPME)
- III-26 Properties Research of Chemically Deposited Nickel Coatings Modified with Nano Diamonds (VNIIA)
- III-31 Evolving Metallurgical Behaviors in Plutonium from Self-Irradiation (LLNL)
- III-34 Isochronal Annealing of Radiation Damage in α - and δ -Pu Alloys (LLNL)

MODELING COUPLED INTERACTION BETWEEN CRACK GROWTH, DIFFUSION, AND CHEMICAL REACTIONS

E. N. Vilchevskaya, A. B. Freidin

Institute of Problems in Mechanical Engineering (IPME)
Russian Academy of Sciences (RAS), Saint Petersburg, 199178, Russia

The model is suggested to describe the oxidation zone formation in front of a crack and the interconnection between the zone and the crack growth in a polycrystalline silicon film. The simplest realization of the model within the framework of Barenblatt-Dugdale cohesive zone approach is suggested. The crack growth description is based on the critical crack opening criterion. It is shown that the crack will not grow until the oxide size reaches a certain value. Then the crack begins to grow and reaches the oxide boundary after some time. If there is a gap between critical crack opening values in polysilicon and silicon-oxide, then the further crack growth rate is determined by the velocity of the chemical reaction front until the critical crack opening for polysilicon is reached.

Introduction

Micron-scale polycrystalline silicon thin films as used in microelectromechanical systems (MEMS) are known to fail in cyclic fatigue in ambient atmospheres [1,2]. The mechanisms associated with such fatigue failures involves sequential oxidation and environmentally assisted crack growth solely within the SiO₂ layer (Figure 1).

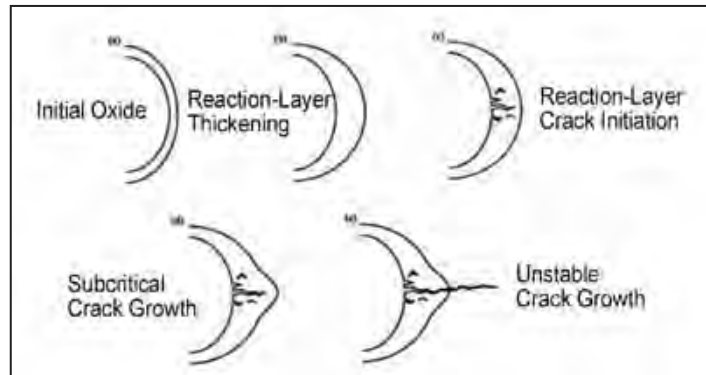


Figure 1. Oxide formation at the root of the notch [1].

In this paper, we consider a polycrystalline silicon film with a small crack and develop a model directed to the description of crack growth due to the oxidation of silicon. Following Muhlstein et al. [1], we divide a body into three zones: a fracture zone (a crack itself), a diffusion (transport) zone of oxide through which chemically active components are delivered, and a chemical reactions zone near the interface between polysilicon Si and silicon-oxide SiO₂ (the chemical reactions front).

We consider a straight line crack in a thin specimen. A plastic zone near the crack tip is represented by the Dugdale model [3]. We assume that chemical reactions and diffusion are also localized in a thin layer in front of crack. The motivation is increasing the chemical activity of a plastically deformed material. As a result, the diffusion problems become a one-dimensional problem. The diffusion equation takes the form

$$\frac{\partial c}{\partial t} = -\frac{\partial J}{\partial x} - qc^\alpha, \quad J = -\beta c \frac{\partial \mu}{\partial x} \quad (1)$$

where c is the partial molar concentration of oxidizing species, J is the flux, μ is a chemical potential, β is the molar mobility, the term qc^α represents the sink (recombination) of oxidizing component, α is the order of the bulk recombination, q is the rate coefficient of the recombination.

We assume that the oxidizing component concentration is given at the external oxide surface and coincides with the concentration at the crack tip, that is,

$$c = c_0 \quad \text{at} \quad x = l(t) \quad (2)$$

The oxidizing component concentration on the interface $x = x_*(t)$ between SiO_2 and Si is controlled by the balance of the diffusion influx and the deflux due to oxidation reaction. The last is accepted to be proportional to the concentration. Then neglecting recombination processes, we have

$$\beta c \frac{\partial \mu}{\partial x} = -kc \quad \text{at} \quad x = x_*(t) \quad (3)$$

where k is a parameter of the reaction.

The velocity V of the chemical reactions front is determined by the mass balance

$$\beta c \frac{\partial \mu}{\partial x} \Big|_{x_*} = -nVg \quad (4)$$

where g is the concentration of soluble components (i.e., the concentration of Si that participates in the reaction equal to the concentration of SiO_2). Note that silica formation first of all takes place in the inter-crystallite space. The multiplier n is equal to the number of oxidizing units for forming one SiO_2 unit. In a case of the oxidation by radicals OH or ions OH $n = 2$.

In the steady-state approximation

$$\frac{\partial c}{\partial t} = -i \frac{\partial c}{\partial x} \equiv -i \frac{\partial c}{\partial \xi}, \quad \xi = x - l \quad (5)$$

where $l = l(t)$ is the crack length, i is the crack growth rate.

If the problem (1) - (5) is solved, then, given l , we know the lengths $\xi_* = x_* - l$ of the oxide zone.

Since the oxide formation is accompanied by the volume increase, the oxide zone is under the action of compression acting from the side of a surrounding material. This compression is proportional to g and volume mismatch of Si and SiO_2 . On the other hand, oxide formation produces tension stresses in front of the diffusion zone. We do not have experimental evidence of crack initiation in front of oxide zone. This motivates that oxide induced stresses relax in front of the oxide zone because of plastic deformations.

To complete the statement, we have to formulate the fracture criterion. Various local fracture criteria, including the entropy criterion and energy balance/release criteria can be examined. The demonstration presented below is based on widely used critical crack opening criterion [3].

Results

To simplify the consideration we assume that the stress acting on the oxide segment is a known constant t_* in the absence of external stress. This means that we relate these stresses only with the concentration of the oxide

and do not discuss how elasticity moduli changes due to chemical reactions affect the stress state. The distribution of the oxidant concentration $c(\xi)$ affects only the size ξ_* of the oxide zone.

The next simplification is related with the chemical potential. One of the opportunities would be to take μ as the trace of the partial Eshelby stress tensor. Suspending this opportunity, we accept now Fick's first law of diffusion:

$$J = -D \frac{\partial c}{\partial x} \quad (6)$$

where D is the diffusion coefficient. Then the problem (1) - (5) takes the form

$$D \frac{\partial^2 c}{\partial \xi^2} - qc^a = -l \frac{\partial c}{\partial \xi} \quad \xi \in [0, \xi_*] \quad (7)$$

$$c = c_0 \quad \text{at} \quad \xi = 0, \quad D \frac{\partial c}{\partial \xi} = -kc \quad \text{at} \quad \xi = \xi_*$$

$$-D \frac{\partial c}{\partial \xi} \Big|_{\xi_*} = kc \Big|_{\xi_*} = nVg$$

To calculate stresses and the crack opening we use Barenblatt-Dugdale cohesive zone model (Figure 2). In the case of a crack $(-l, l)$ under external uniform tension σ_0 , the stress is calculated as the superposition of uniform tension σ_0 and stresses in a body with a crack $x \in (-l-a, l+a)$ loaded at $y = 0, x \in (-l-a, l+a)$ by normal stress $-p(x)$,

$$p(x) = \begin{cases} \sigma_0, & x \in (-l, l), \\ \sigma_0 + t_*, & |x| \in (l, l + \xi_*), \\ \sigma_0 - \sigma_s, & |x| \in (l + \xi_*, l + a) \end{cases} \quad (8)$$

where σ_s is the yield limit of polysilicon and $\pm(l+a)$ are coordinates of the plastic zone ends. The size a depends on l and ξ_* . The dependence is to be found from the condition that stress is not infinite [stress intensity factor for the segment $x \in (-l-a, l+a)$ equals zero], ξ_* is found from the solution of (7).

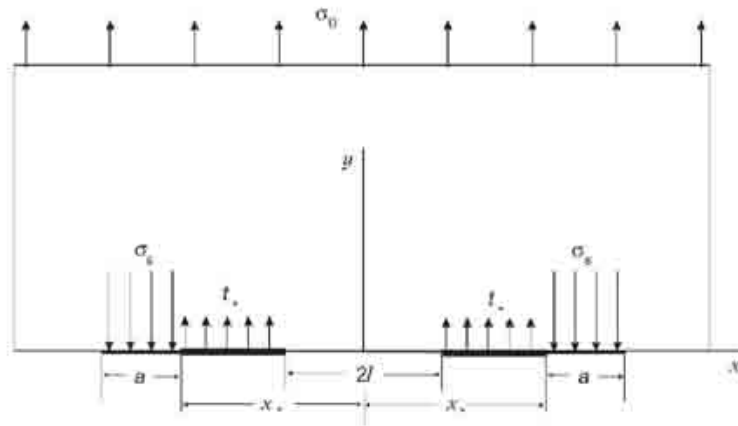


Figure 2. A crack with oxide and plastic zones in Barenblatt-Dugdale model.

The crack growth description is based on the critical crack opening criterion. The opening $\delta(x) = 2v(x)$, $x \in (-l+a, l+a)$, where v is a vertical displacement, is given by known formulae. We assume that

$$\delta(x=l) = \delta_c \quad (9)$$

where δ_c is a critical opening for SiO_2 . We also believe that $\delta_c < \delta_c^0$ where δ_c^0 is the crack-critical opening for polysilicon Si. Note that oxide layer is compressed by stresses induced by chemical reactions. Then the crack propagation in oxide is a result of competition between external and internal stresses.

The stress nonsingularity condition

$$\int_{-(l+a)}^{l+a} p(x) \sqrt{\frac{l+a+x}{l+a-x}} dx = 0 \quad (10)$$

with $p(x)$ given by (8) takes the form of the equation

$$\psi(l, a | \xi_*, \sigma_0) = 0 \quad (11)$$

where σ_0 is given by boundary conditions, and can be considered as a time parameter. The dependence of ξ_* on time is found independently from the solution of the diffusion problem (7)

The criterion (9) takes the form of the equation

$$\delta(l | l+a, \xi_*, \sigma_0) = \delta_c \quad (12)$$

The solution of the system of two equations (11) and (12) gives the dependencies $l(x_*)$ and $a(x_*)$ where the position x_* of the chemical reaction front act as time.

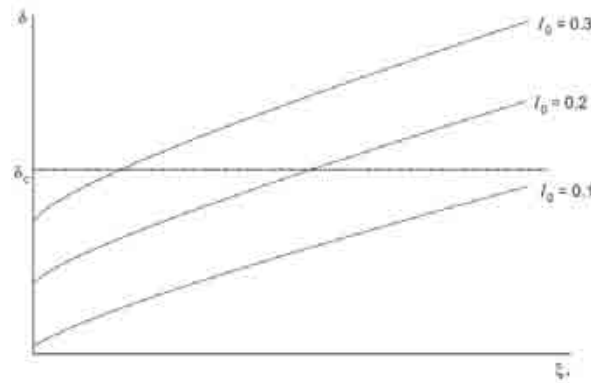


Figure 3. Crack opening $\delta (x = l_0)$ in dependence on the oxide zone size at various crack lengths l_0 . Given δ_c and l_0 , the incubation time corresponds to ξ_* at which the dotted line crosses the solid line.

The model predicts that the crack will not grow until the oxide size reaches a certain value. Indeed, Figure 3 represents the dependencies of the opening $\delta (x = l_0)$ at the crack tip on the size of the diffusion zone ξ_* at various initial crack lengths l_0 . One can see that if $\delta (x = l_0) < \delta_c$ then incubation time t_{in} must pass before the crack starts. Oxide size must reach a value such that the opening at $x = l_0$ will reach the critical value δ_c .

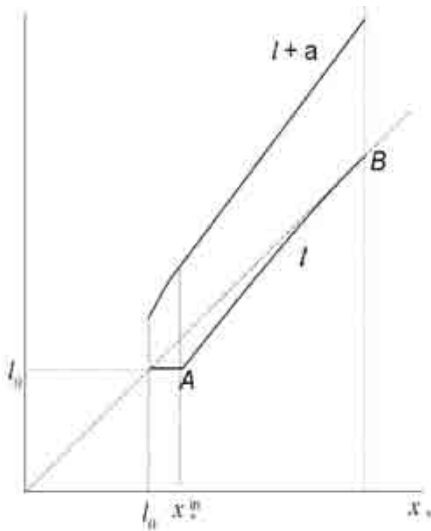


Figure 4 represents the dependencies of the crack length and the position of the plastic deformation front on x_* . The point A corresponds to $x_* = x_*^{in}$ at $t = t_{in}$. The critical state (point B) corresponds to $l = x_*$ when the line of the solution $l = l(x_*)$ crosses the straight line $l = x_*$. Then $\delta(x = l) > \delta_c$ if the crack grows. If there is a gap between δ_c and $\delta_c^0 > \delta_c$, then the crack growth rate is determined by the velocity V of the chemical reaction front until the final instability moment $\delta(x = l) = \delta_c$.

The above calculations have been made at the stresses:

$$t_* = \sigma_s / 4, \sigma_0 = \sigma_s / 2$$

Figure 4. Crack and plastic zone growth due to the oxidation process.

Conclusion

The model presented is developed as the simplest one that takes into account diffusion, chemistry, and stresses in the crack growth. The diffusion and stress problems remain to be uncoupled unless the dependencies of chemical potential and diffusion parameters on stress/strain are taken into account. Further progress is expected by considering stress assisted chemical chemical reactions and diffusion and developing numerical procedures for 2D-modelling.

Acknowledgements

This work is supported by the Sandia National Laboratories (USA) and the Program for Fundamental Research (RAS). Sandia is a multi-program laboratory operated by Sandia Corporation, a Lockheed Martin Company, for the United States Department of Energy under Contract DEAC04-94AL85000.

References

- [1] C. L. Muhlstein, S. B. Brown, R. O. Ritchie, "High-cycle fatigue and durability of polycrystalline silicon thin films in ambient air," *Sensors and Actuators A* **94** 177-188 (2001).
- [2] H. Kahn, R. Ballarini, R. L. Mullen, A. H. Heuer, "Electrostatically actuated failure of microfabricated fracture mechanics specimens," in *Proceedings of the Royal Society of London A* **455** 3807-3823 (1999).
- [3] L. M. Kachanov, *Fundamentals of Fracture Mechanics* (Nauka, 1974) p. 312.

INFLUENCE OF DEFECTS TYPE AND CHEMICAL REACTION ON FRACTURE INITIATION, MOLECULAR DYNAMICS STUDY

A. M. Krivtsov

Laboratory Discrete Models in Mechanics,
Institute of Problems in Mechanical Engineering (IPME)
Russian Academy of Sciences (RAS), Saint Petersburg, 199178, Russia

A molecular dynamics model for fracture in a material with defects is presented. Crack initiation and development in specimens subjected to a uniaxial loading is investigated. Different types of defects (vacancy, hole, predefined crack) are considered. The oxidation of the initial and new specimen surfaces during the fracture process are taken into account. It is postulated that the material properties such as density, stiffness, and strength are changing due to the oxidation. Influence of the chemical reaction (oxidation) on the fracture scenario is investigated. The fracture process for specimens of different shape, with and without predefined defects, is studied.

Introduction

Molecular dynamics is powerful tool for modeling of fracture in material with various internal structure and defects distribution. In most of these models, only single-phase material is considered. However, in real applications, the fracture is closely connected with chemical reactions. In particular, for MEMS made from silicon, the oxidation process accompanying the fracture is essential, since the mechanical properties of the silicon dioxide differ essentially from those of the pure silicon [1].

The following model is suggested. The properties of particles adjusting to the surfaces are changed mimicking the difference between the silicon and its dioxide: the size of the particles became slightly bigger; the elastic and strength properties became substantially lower then for the initial particles. This change takes place immediately and involves the particles surrounding the original surfaces of the specimen and the particles near the new surfaces provided by the fracture and crack development. Since the size of the particles increases, this can provide separation of the pieces of material — the oxidization induced fracture. In this case, fracture and chemical reaction can stimulate each other, resulting in a self-generating process. Although mainly we will be studying situations when the fracture is induced by an external load, the possibility and conditions of such self-generation will be considered.

Computational Model

The simulation procedure applied in this work is similar to that used in [2,3]. It is described in more detail in [4,5]. The material is represented by a set of particles interacting through a pair potential $\Pi(r)$.

The equations of particle motion have the form

$$m\ddot{\underline{r}}_k = \sum_{n=1}^N \frac{f(|\underline{r}_k - \underline{r}_n|)}{|\underline{r}_k - \underline{r}_n|} (\underline{r}_k - \underline{r}_n) \quad (1)$$

where \underline{r}_k is the radius vector of the k -th particle, m is the particle mass, N is the total number of particles, and $f(r) = -\Pi'(r)$ is the interparticle interaction force. We use the following notation: a is the equilibrium distance between two particles ($f(a) = 0$), $D = |\Pi(a)|$ is binding energy, C is the stiffness of the interatomic bond in equilibrium, and T_0 is the period of vibrations of the mass m under the action of a linear force with stiffness C

$$C = -P''(a) \equiv -f(a), \quad T_0 = 2\pi\sqrt{m/C}. \quad (2)$$

We will use the quantities a and T_0 as microscopic distance and time scales. For a particle of mass m that is in equilibrium in the potential field $\Pi(r)$, its minimum velocity to reach infinity is $v_d = \sqrt{2D/m}$ — so called dissociation velocity. We will use this quantity as a velocity scale. To measure the level of thermal motion in material the velocities deviation, Δv (mean-square value of random velocities) will be used. Let us consider the classical Lennard-Jones potential:

$$P_{LJ}(r) = D \left[\left(\frac{a}{r} \right)^{12} - 2 \left(\frac{a}{r} \right)^6 \right], \quad (3)$$

where D and a are the binding energy and the equilibrium interatomic distances, introduced earlier. The corresponding interaction force $f(r) = -\Pi'(r)$ has the form

$$f_{LJ}(r) = Q \left[\left(\frac{a}{r} \right)^{13} - \left(\frac{a}{r} \right)^7 \right], \quad Q \stackrel{\text{def}}{=} \frac{12D}{a}, \quad (4)$$

where Q is the interparticle force magnitude. In the case of the Lennard–Jones potential, the stiffness C and the binding energy D obey the relation $C = 72D/a^2$; the force (4) reaches its minimum value (the bond strength) at $r = b = \sqrt[6]{13/7}$, where b is the break distance. The corresponding break deformation of the Lennard-Jones bond is $\varepsilon_* = b - a \approx 0.109$. To speed up the computations, the shortened Lennard-Jones interaction is used [2] with the cut-off distance $a_{\text{cut}} = 1.4a$.

In case of oxidation, it is postulated that the properties of the particle are changing. The diameter and force magnitude for the oxidized particles will be denoted as \tilde{a} and \tilde{Q} . For the silicon dioxide, it approximately fulfills

$$\tilde{a}/a = 1.1, \quad \tilde{Q}/Q = 1/3. \quad (7)$$

The vector of interaction force between two original particles can be represented as following:

$$\underline{f} = \Phi(r^2)\underline{r}, \quad \Phi(r^2) \stackrel{\text{def}}{=} f(r)/r. \quad (8)$$

When one or both of the interacting particles are oxidized, then the interaction law takes the form

$$\underline{f} = \Phi(\lambda(r^2 - \bar{a}^2) + a^2)\underline{r}, \quad \lambda \stackrel{\text{def}}{=} a^2/\bar{a}^2, \quad (9)$$

where function Φ is calculated using average values for the particle diameter and force magnitude:

$$\bar{a} \stackrel{\text{def}}{=} (a_1 + a_2)/2, \quad \bar{Q} \stackrel{\text{def}}{=} (Q_1 + Q_2)/2; \quad (10)$$

indexes 1 and 2 correspond to the first and the second interacting particle. The law (10) independently of the particle sizes preserves the same width of the potential well.

For simulation, a two-dimensional material will be used, where particles are packed to form an ideal 2D close-packed (triangular) crystal lattice. This is a simplified lattice; however, its symmetry is the same as the symmetry of surfaces of 3D crystal lattices, such as FCC and diamond (the last one is the lattice of silicon crystals). For the computations, periodic boundary conditions are applied at all boundaries. All specimens are subjected to uniaxial

loading by applying a small uniform deformation to positions of all particles and to the periodic boundaries. After each step of deformation, a step of MD computation is used. The deformation is changing according the formula

$$e(t) = e_{\max} \frac{t}{t_{\max}} \quad (11)$$

where ε_{\max} is the maximum value of strain and t_{\max} is the time of computation. The strain is directed along one of the sides of triangles, forming the lattice. The computation parameters are given in Table 1.

Table 1. Computation parameters.

| Parameter | Symbol | Value |
|----------------------------|-------------------------------|------------------|
| Number of particles | N | 10^5 |
| Cut-off radius | a_{cut} | $1.4a$ |
| Initial velocity deviation | Δv | $0.005v_d$ |
| Integration step | Δt | $0.02T_0$ |
| Maximum strain | ε_{\max} | 0.15 |
| Strain rate | $\varepsilon_{\max}/t_{\max}$ | $0.002T_0^{-1}$ |
| Chemical inflation | \tilde{a}/a | $1.10 \div 1.15$ |
| Chemical strengthening | \tilde{Q}/Q | 1/3 |

Results of Computations

The results of the computer experiment are presented in Figure 1. A single vacancy placed in the center of specimen is used to initiate a crack. In Figure 1a, no chemical reaction is taken into account. In this case, four straight cracks are propagating in crystallographical directions. In Figure 1b, c, the particles adjusting to the crack surfaces are subjected to oxidation that results in change of particle size (chemical inflation) and bond strength. The bond strength for the oxidized material in all experiments is taken three times lower than for the original material. The chemical inflation is 10% for Figure 1b and it is 15% for Figure 1c (e.g., $\tilde{a}/a = 1.10$ and $\tilde{a}/a = 1.15$ respectively). In the figures, the original material is shown by blue color, the oxide—by cyan, the empty space is white. From Figure 1b, it follows that oxidation stimulates the fracture: initial fracture zone appears in the vicinity of the initial vacancy where the oxidized material forms an elliptical area; the cracks are producing branches, substantially complicating the crack shape.

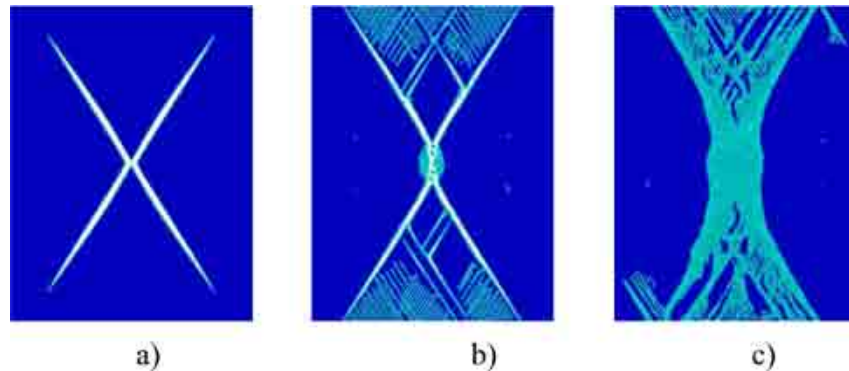


Figure 1. Comparison of the computational results for different rate of chemical inflation: (a) no chemical reaction, (b) 10% chemical inflation, (c) 15% chemical inflation.

In Figure 1c, it is visible that when the chemical inflation is increased from 10% to 15%, then the amount of the oxidized material is greatly increased. The explanation of this phenomenon is that the break extension of the interatomic bond for the considered interaction potential is 11%. If the chemical inflation rate is greater than this value, then the chemical reactions produce a fracture in the material. The fracture creates new surfaces, where oxidation takes place, again producing the fracture, and so on. Thus, we have a self-developing process, wherein the chemical reaction and fracture stimulate each other. If the greater values of the chemical inflation are used, then this process can take place without external loading at all, resulting in very fast oxidation of the whole specimen. Also, the high chemical inflation can result in the crack closing, since the oxidized material requires more space than the original one.

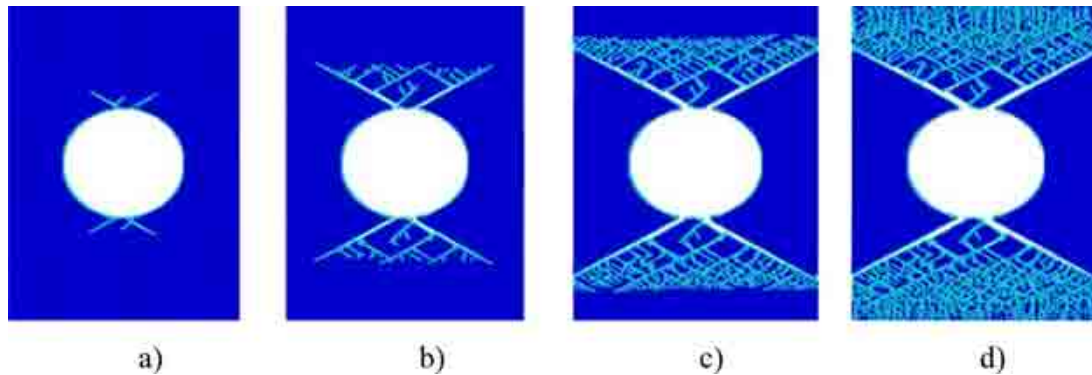


Figure 2. Sequential stages of extension for the specimen with circular hole: (a) $\varepsilon = 7\%$, (b) $\varepsilon = 10\%$, (c) $\varepsilon = 13\%$, (d) $\varepsilon = 15\%$.

Figure 2 shows the sequential stages of the fracture process for the specimen with a circular hole. The chemical inflation is 10%. No predefined crack is used, and the fracture starts just from the inner boundaries of the specimen. From the beginning, several cracks appear, and then the branching process produces a very complicated, fractal structure of the cracks. Comparison with extension of the specimen with a predefined crack is shown in Figure 3, which shows, that the predefined crack localizes the beginning of the fracture in the specified area. However, the developed crack due to its branching does not depend much on whether the predefined crack was introduced or not.

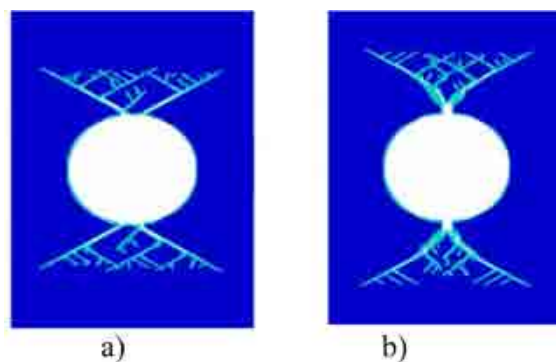


Figure 3. Comparison of 10% extension for the specimen: (a) without predefined crack, (b) with predefined crack.

Comparison of the results for the different rate of the chemical inflation is shown in Figure 4. The specimen with a circular hole and predefined crack is used. As for the case of the fracture starting from a single vacancy, increasing the rate of the chemical inflation over the critical value of 11% results in abrupt increase of the oxidized area. The oxide is located not only in the vicinity of the crack, but also is forming a wide belt around the hole, forming a zone of plastic deformation.

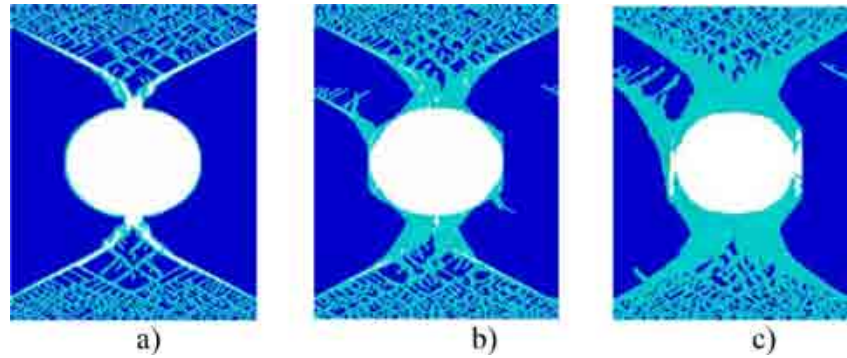


Figure 4. Comparison of results for different chemical inflation: (a) 10%, (b) 12%, c) 15%.

Conclusions

A molecular dynamics model for the fracture accompanied by a chemical reaction was suggested. Crack initiation and development in specimens subjected to an uniaxial loading were considered. The oxidation of the initial and new specimen surfaces during the fracture process was taken into account. The material properties such as density, stiffness, and strength are changing due to the oxidation. The results of the computer experiments show that oxidation stimulates the fracture. The cracks are producing branches, substantially complicating the crack shape. The branching of the cracks forms fractal-like structures. If the rate of the chemical inflation is over the break extension of the interatomic bond, then an abrupt increase of the oxidized area can be observed. The explanation of this fact is that in this case, the chemical reactions produces fracture in the material. Thus, a self-generating process is realized, where the chemical reaction and fracture stimulate each other. For the greater values of the chemical inflation, this process can take place without external loading at all, resulting in a very fast oxidation of the whole specimen.

Acknowledgements

This work was supported by Sandia National Laboratories. Sandia is a multi-program laboratory operated by Sandia Corporation, a Lockheed Martin Company, for the United States Department of Energy under Contract DEAC04-94AL85000.

References

- [1] C. L. Muhlstein, S. B. Brown, and R. O. Ritchie, "High-cycle fatigue and durability of polycrystalline silicon thin films in ambient air," *Sensors and Actuators A* **94** 177-188 (Elsevier, 2001).
- [2] A. M. Krivtsov, "MD modeling of low-cycle high-amplitude loading of monocrystal material with defects," *Proc. of XXXIII Summer School, Advanced Problems in Mechanics 2005* (St. Petersburg, Russia, 2006) 341-346.
- [3] A. M. Krivtsov, "Molecular dynamics simulation of plastic effects upon spalling," *Phys. Solid State* **46** 6 (2004).
- [4] M. P. Allen and A. K. Tildesley, *Computer Simulation of Liquids* (Oxford: Clarendon Press, 1987) 385.
- [5] A. M. Krivtsov, "Deformation and Fracture of Solids with Microstructure" (Moscow, Fismatlit, 2007). [in Russian]

DETERMINATION OF THE SMALL HYDROGEN TRAPS AS NUCLEUS OF FATIGUE AND DESTRUCTION

V. A. Polyanskiy,^{*} A. M. Polyanskiy,[†] A. K. Belyaev,[‡] Yu. A. Yakovlev^{*}

^{*}St.-Petersburg State Polytechnic University, Polytekhnicheskaya, 29,
St.-Petersburg, 195251, Russia

[†]RDC Electronbeamtech,
St.-Petersburg, Bronevaya 6, 198188, Russia

[‡]Institute of Problems in Mechanical Engineering (IPME)
Russian Academy of Sciences (RAS), Saint Petersburg, 199178, Russia
Author Contact: vapol@electronbeamtech.com

A method for investigation of materials fatigue and destruction is suggested. This method is based on the influence of the small hydrogen concentration on materials properties. The measurement of the hydrogen concentration and its binding energy enables one to determine the fatigue and destruction zones in the materials after the mechanical, fatigue and thermomechanical loading.

Introduction

Considerable concentrations of hydrogen contained in metals and nonmetals are often one of the causes of destruction. Saturation with hydrogen from the outside ultimately leads to hydrogen brittleness.

Accumulation of hydrogen in the destruction zone occurs both by the influx from outside and redistribution of natural hydrogen inside the material. For practically all the structural materials, the concentration of natural hydrogen is from decimal ppm to several ppm, and there have been very few works on its influence on the mechanical properties.

It is known that the hydrogen in materials is found in the traps with different binding energies. In steels, the total hydrogen content is 0.1–6 n.cm³/100g, while it is only hydrogen with a low binding energy that affects the strength (i.e., diffusive hydrogen). In the aluminum alloys, the entire hydrogen diluted in the metal has a low binding energy, which is about 0.2–0.8 eV. The concentrations that are critical for the mechanical strength of weakly bound hydrogen in steels and aluminum alloys are also about decimal ppm. In the aluminum alloys, it includes the entire diluted hydrogen, while in steels it is up to 5% to 10% of the total amount of diluted hydrogen. Thus, the volume of the hydrogen traps with low binding energy is very small.

Measuring such a low hydrogen concentration in the specimens of the mass of 1 g to 3 g presents a challenging scientific and engineering problem. Therefore, as a rule, any information on the relation between the hydrogen concentrations and the mechanical state of the metals was obtained after a preliminary saturation of the specimens by hydrogen. Such a saturation results in a distortion of the natural picture of hydrogen distribution over the traps with different binding energies, and thus the experimentally established laws do not always work in the case of pure mechanical loading.

We have developed a precision analyzer (AV-1) that makes possible an accurate measurement of low natural concentrations. The analyzer is so sensitive that we can measure the amount of hydrogen in the traps whose volume is thousands times smaller than the total amount of hydrogen extracted from the specimen. The method of high-temperature vacuum extraction by analyzer AV-1 was applied for investigating the defective structure of materials for fatigue failure and destruction under the uniaxial tension. The method developed for analysis of the

dynamic curves of vacuum extraction enables us to determine the binding energy and the volumes of traps of the various nature, as well as the constants of hydrogen diffusion in the specimen under examination.

Method of Investigation

Measurement

The precision hydrogen analyzer AV-1 was developed for determining the hydrogen content in metals and alloys under the laboratory conditions and is used for output control of alloy castings. The analyzer utilizes the mass-spectrometric principle. The specimen preparation requires a vacuum extractor and an oven. The specimen inside the metal extractor is heated gradually up to an extraction temperature of 400°C to 900°C. The temperature needed for analysis is below the melting temperature of the specimen. The gases released at heating in vacuum are analyzed by means of the mass-spectrometer. The time-dependence of the hydrogen flux $q(t)$ registered by means of the data acquisition system yields the so-called extraction curve. The extraction curve for specimen of AMg-5 aluminum-magnesium alloy is displayed in Figure 1.

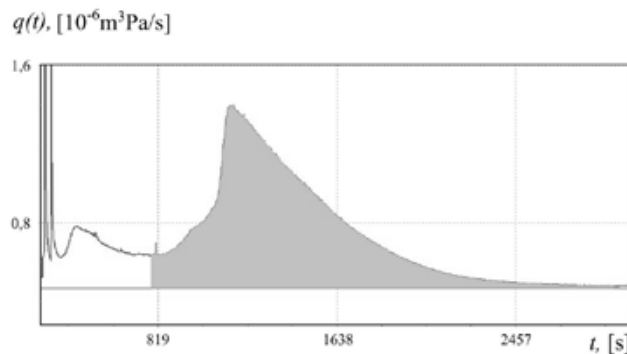


Figure 1. The extraction curve for aluminum magnesium alloy AMg-5.

Estimation of the Hydrogen Binding Energy in Metal and the Diffusion Constants

The high sensitivity of AV-1 enables observing a number of maxima on the extraction curve. Analysing the position of the maximum and its shape, one can determine the binding energy, diffusion constants, and cumulative volume of the flow with the corresponding separate peaks, cf. [1].

Figure 2 shows the experimental curve for the monocrystal silicon. The hydrogen binding energy is indicated near the corresponding peak.

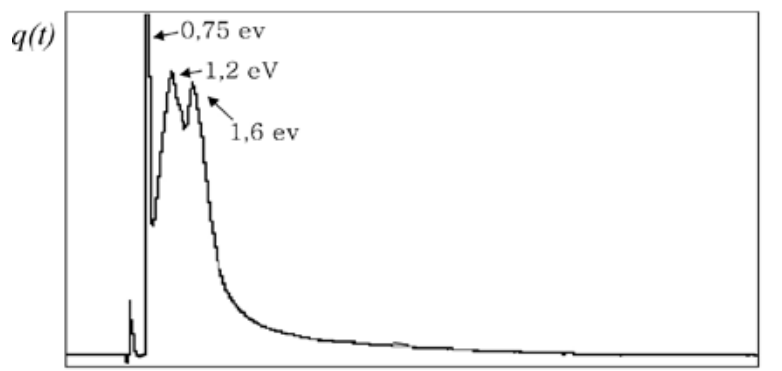


Figure 2. Extraction curve for the monocrystal silicon, indicating the binding energies that correspond to the certain peaks of the curve.

The result of many tests confirms that the hydrogen inside metals and semiconductor materials has discrete energy levels (e.g., for the aluminum alloys, two to four levels are observed within the range 0.2 to 0.8 eV).

Results and Discussion

For our analysis, we took the titanium tubes of a steam generator (diameter 22 mm, thickness 2.6 mm), which had been subjected to cyclic nonuniform heating. The temperature of the cold part of the tube was 100°C and that of the hot part was 300°C. The temperature drop within the 15 cm length was about 200°C. The ends of the tube were fixed which results in the thermal strains. After approximately 15,000 loading cycles, the fatigue cracks formed at the point with minimum temperature.

To analyze the hydrogen content, the tube was cut into small specimens. The schematic of the specimens' positions relative to the crack is shown in Figure 3.

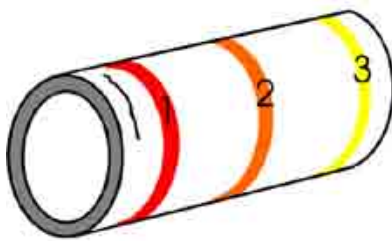


Figure 3. Schematic of the titanium tube with the crack and the specimens' positions relative to the crack. The red denotes the hydrogen concentration values of 498 [ppm] while the orange and yellow ones stand for 329 [ppm] and 186 [ppm], respectively.

The hydrogen content in the tubes was controlled before the steam generator started. The initial content was 20 [ppm]. In the process of operation, the hydrogen content in the tube went up by more than 10 times, while that in the destruction zone increased by 25 times. In the destruction zone, the hydrogen concentration is 2.5 times higher than that in the other parts of the tube. Therefore, one observes the absorption of hydrogen from the outside and its redistribution into the fatigue destruction zone.

The full concentration of hydrogen is not the only indicator of accumulation of the defects. The shape of the extraction curve on the fatigue crack zone is of special interest. The experimental curves in Figures 4 and 5 show that the last peak area in the specimens after loading is the largest one if we compare it with the unloaded specimen.

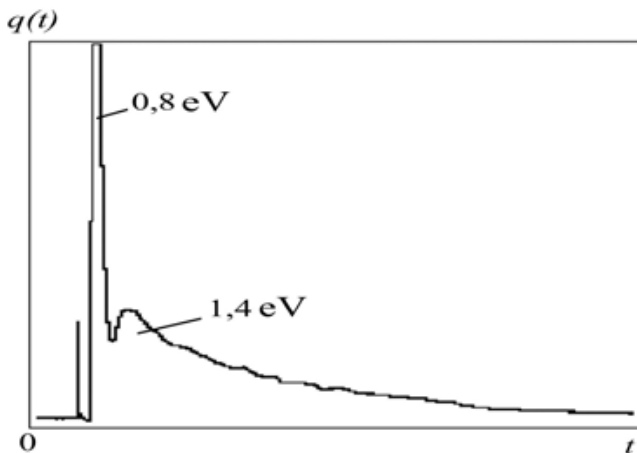


Figure 4. Experimental extraction curve of the unloaded specimen.

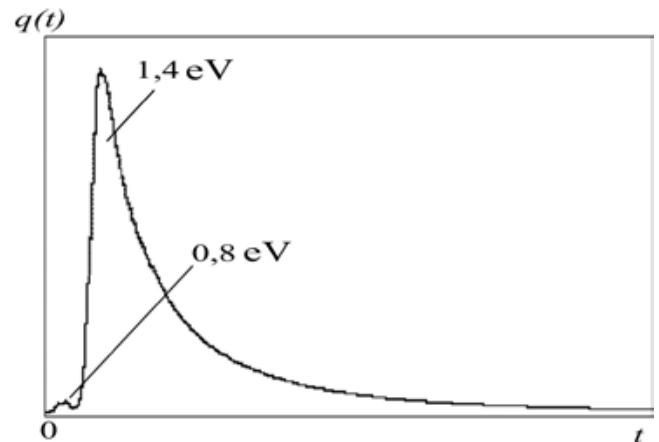


Figure 5. Experimental extraction curve of the specimen after loading.

The gases are known to dilute in metals [2]. In many cases, the gases that do not form stable chemical compounds with the alloy components are accumulated on the grain boundaries in the traps of various natures.

There exists a method of examining the dislocation structure of solids by low-temperature saturation of metals with inert gases (helium, argon, etc.). Upon subsequent heating of the specimens, the dynamics of gas release is studied. The dynamic curves of the gas release—extraction curves—are used for determining the dislocation density and the rate of change in the dislocation density. It was experimentally discovered that the adsorption of gas molecules with a very high binding energy was possible in the micro-defects on the free surface of the crystal. For example, the binding energy for chemically inert helium is about 1 eV, which is close to the chemical bond energy [3].

In many cases, it is impossible to explain the increased concentrations by hydrogen diffusion from the environment as the natural hydrogen concentration in the air is 0.5 ppmv. The literature provides descriptions of two mechanisms of hydrogen accumulation, which are the transfer by micro-defects inside the material and the release of hydrogen from water under corrosion.

In our experiments, we managed to study the fine structure of hydrogen bonds in metal. We studied natural concentrations and discovered that the fatigue phenomenon is accompanied by accumulation of the bound hydrogen. The accumulation itself can be explained by the processes of hydrogen transfer at formation of new structural micro-defects in the destruction zone. It is most probable that due to the strains, the hydrogen is bound with free surfaces and it causes weakening of the material due to a reduction of the free energy and fixation of the defects. After rupture, the tensile stresses disappear, and the hydrogen is squeezed out into a weakly bound state.

We are of the opinion that the hydrogen has the discrete character of the energy levels in the solid body. Therefore, each peak of the extraction curves corresponds to a different character of the hydrogen bond with the crystal lattice of the material.

If our hypotheses are correct, then the prevention of hydrogen diffusion in materials serves to substantially increase in its fatigue strength and the maximum deformations. The same effect can be obtained by decreasing the gas permeability of the material surface (e.g., by designing parts with an increased surface tension or by using special coatings). The absence of hydrogen inflow from the outside will increase the service life of the part.

This fact makes it possible to use the measurement results for hydrogen concentration distribution according to binding energies not only for analysis of the causes of destruction and material quality control, but also for the development of new materials with enhanced mechanical characteristics.

Application of the methods developed to nonmetallic material opens yet another application area of hydrogen diagnostics.

Conclusions

- We have developed the equipment that makes it possible to obtain information on the structure of hydrogen bonds within the material according to the hydrogen extraction curve at heating a specimen in a vacuum. The accuracy of determination of the extraction curve makes it possible to obtain information on both the hydrogen binding energy in the metal and on the concentration of mechanical flaws.
- The experiments we conducted have confirmed that the fatigue phenomena and the destruction of structural materials are accompanied by increased concentration of bound hydrogen in the destruction zone.
- It was detected for the first time that the mechanical loads result in a substantial redistribution of hydrogen according to the binding energies inside metals.
- The energy activation values obtained as a result of processing the experimental data for aluminum alloys are within the 0.2 to 0.8 eV range, which enables us to conclude that there is no chemically bound hydrogen in these alloys.

- This approach to investigation of the properties of materials does not require preliminary saturation of the specimens. The natural hydrogen in the metals contains the information on the past history of the material, which, once the methods have been developed, will make it possible to obtain more detailed information from the measured extraction curves.
- The metrological setup consisting of a hydrogen analyzer and the calibration standards enables implementing the principle of a single measurement utility for analysis of various metals and alloys and obtaining additional information on the volume and structure of the internal and surface mechanical defects.

Acknowledgements

The financial support of the Sandia Corporation, contract 891092, and the Russian Foundation for Basic Research, grants 08-08-00737 and 08-01-12017, is acknowledged. Sandia is a multi-program laboratory operated by Sandia Corporation, a Lockheed Martin Company, for the United States Department of Energy under Contract DEAC04-94AL85000.

References

- [1] A. M. Polyanskiy, V. A. Polyanskiy, D. B. Popov-Diumin, "Diagnostics of mechanical condition of materials by method of high-temperature hydrogen vacuum-extraction," in *Proceedings of the Sixth International Congress on Thermal Stresses*, vol. 2 (Vienna, Austria, 2005) 589-592.
- [2] B. A. Kolachev, "Hydrogen brittleness of metals," *Metallurgy* (Moscow, 1985). [in Russian]
- [3] O. V. Klyavin, "Dislocation dynamic diffusion in crystal bodies," *FTT* **35** 3 513-541 (1993). [in Russian]

FIRST PRINCIPLES STUDY OF SITE OCCUPATION AND MIGRATION OF HELIUM IN β -PHASE ERBIUM HYDRIDE

C. S. Snow, R. R. Wixom, P. A. Schultz

Sandia National Laboratories, Albuquerque, NM, 87185 USA

Author Contact: cssnow@email.com

First principles density functional methods were used to investigate the atomistic behavior of helium in β -phase ErT_2 . The barrier to helium migration between two unoccupied neighboring tetrahedral sites is 0.49 eV, where the path maximum corresponds to the octahedral site. If an extended network of two neighboring vacancies exists, the relatively small barrier provides that helium may move throughout that network at room temperature. Given enough energy to escape the tetrahedral site(s), 1.31 eV, helium may continue to migrate by a 0.88 eV concerted-motion mechanism—temporarily displacing hydrogen as it moves between empty octahedral sites and filled tetrahedral sites.

Introduction

Rare earth metal hydrides readily absorb hydrogen, and for this reason they are obvious candidate materials for neutron generators that utilize either deuterium-deuterium (D+D) or deuterium-tritium (D+T) reactions to produce neutrons. For tritium containing designs, the relatively short half-life of tritium (12.3 years) introduces very interesting materials science challenges due to the resulting production of helium via the reaction $\text{T} \rightarrow {}^3\text{He} + \beta^- + \bar{\nu}$, where β^- is a beta particle and $\bar{\nu}$ is an anti-neutrino. Early in the life of erbium tritide, small amounts of helium escape from the near surface regions [1]. Later, when the helium concentration becomes large enough, platelike helium bubbles form, which are observable in transmission electron micrographs (TEM) [1]. Eventually, the concentration of helium reaches the point of “critical release,” where wholesale escape of helium occurs. Beyond these empirical observations, our understanding of the behavior of helium in this material is in its infancy. As such, intriguing questions remain regarding the atomistic nature of the material itself, helium bubble nucleation and growth, and the consequences of impurities. Experimental studies of the transient material properties resulting from tritium decay are extremely time consuming, expensive, and difficult. The allure of theoretical investigations is to mitigate these difficulties while gaining quantitative insight into the fundamental physical processes that drive the macroscopic behavior. In this study, we investigate migration helium in erbium tritide, using first principles calculations within density functional theory (DFT).

Method

The exchange-correlation functional we used for this DFT study was the generalized gradient approximation (GGA) of Perdew, Burke, and Ernzerhof (PBE) [2]. The calculations were performed with SeqQuest [3], using standard (semi-local) normconserving pseudopotentials, and well-optimized double-zeta plus polarization contracted Gaussian basis sets. The helium and erbium atoms used the generalized norm-conserving pseudopotentials of Hamann [4], all using the fhi98PP code [5]. The H pseudopotential was generated using a new method by Hamann. Additional calculations, as noted in the text, were performed with the Vienna *ab initio* Simulation Package (VASP) [6]. These involved the projector augmented wave (PAW) method, where the PAW potentials were taken from the VASP database [7], and used a plane wave basis with a kinetic energy cutoff of 400 eV.

The computed equilibrium lattice parameters for $\beta\text{-ErH}_2$ were 5.115 Å with SeqQuest and 5.129 Å with VASP, both in good agreement with each other and with the experimental value 5.126 Å [8]. The agreement between

SeqQuest and VASP results continues throughout the numerical results presented in this paper. In the calculations repeated by both codes, a typical difference in the results was 0.02 eV. Given that these are very different codes, using different basis sets and atomic potentials, this lends confidence to the construction of the computational models for Er and, in particular, verifies the construction of the pseudopotentials.

The barrier energies (E_a) obtained by CINEB were used to make qualitative estimates of diffusion lengths L , where $L = (6Dt)^{1/2}$, and $D = D_0 \exp(-E_a/kT)$. In these equations, t is the time, T is temperature, k is the Boltzmann constant, and D_0 is a frequency factor. In the absence of first principles values for D_0 , we have used representative values for similar systems taken from the literature, 1×10^{-4} for both hydrogen and helium [9].

Results and Discussion

In material containing helium from tritium decay, there is initially a tetrahedral vacancy (V_{Tet}) associated with every helium atom produced. The newly created helium atom could occupy the tetrahedral site vacated by a decayed tritium, or it could prefer one of the neighboring octahedral sites. Our calculations predict that helium will occupy the tetrahedral site (He_{Tet}) rather than the octahedral site (He_{Oct}) and is not locally stable in an octahedral site neighboring an empty tetrahedral site. The helium atom is bound to the tetrahedral vacancy by 0.49 eV, with a prohibitive 1.31 eV dissociation energy. The NEB results for helium in erbium hydride are shown in Figure 1 and illustrated in Figure 2 and Figure 3. The energy barrier for motion between two tetrahedral sites (unoccupied by hydrogen) is only 0.49 eV (indicated as (c) in the figures), and as such, even at room temperature, helium should move freely between vacant tetrahedral sites. In material where tritium decay continuously produces tetrahedral vacancies, neighboring vacancies are not unlikely, and even an extended network of neighboring vacancies could exist. Such a network would greatly enhance the range of helium migration.

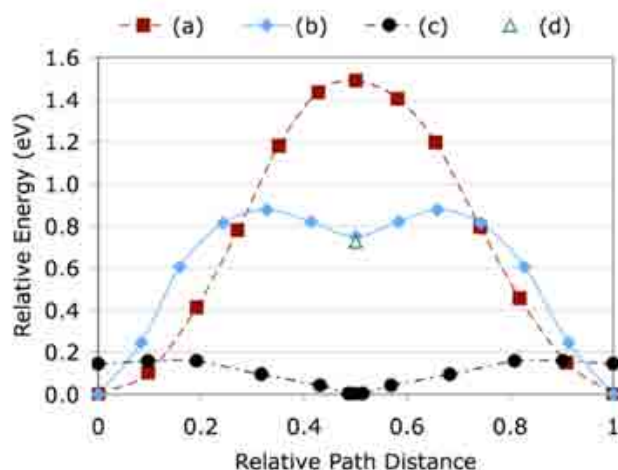


Figure 1. Climbing image nudged elastic band data for helium migration in ErH_2 . (a) Direct octahedral to octahedral migration. (b) Concerted-motion from empty octahedral to a filled tetrahedral position (path distance of 0.5) and on to another empty octahedral site. The energy of the tetrahedral site, 0.75 eV, was also calculated with VASP as 0.73 eV. (c) Migration between octahedral and vacant tetrahedral sites. All the data are arranged such that a path distance of 0 or 1 is an octahedral site. For paths (b) and (c) 0.5 is in the tetrahedral site, while for (a) it is the direct mid-point between two octahedral sites. The corresponding mechanisms and schematic potential energy are illustrated in Figure 2 and Figure 3 respectively.

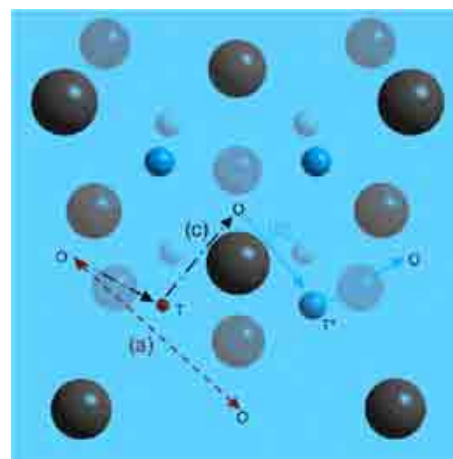


Figure 2. Illustration of helium migration mechanisms corresponding to the data in Figure 1. The lower part of the figure is a diagram of the potential energy. (a) The red dashed line indicates direct octahedral (O) to octahedral migration. (b) The blue solid lines shows the motion of helium from octahedral to octahedral through the intermediate filled tetrahedral site T^* . (c) The black dash-dot line shows motion of helium from octahedral to octahedral through an intermediate tetrahedral site T (the ground state). The blue atoms are hydrogen, the smaller red atom is helium, and the larger grey atoms are erbium.

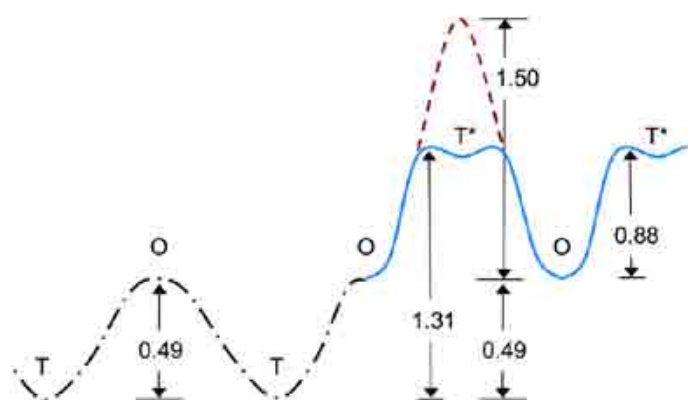


Figure 3. Schematic illustration and alignment of the helium NEB data from Figure 1. The red dashed line is the barrier for direct octahedral (O) to octahedral migration. The blue solid lines shows the motion of helium from octahedral to octahedral through the intermediate filled tetrahedral site T^* , as in stoichiometric β -phase. The black dash-dot line, corresponding to path (c) in Figures 4 and 5, shows the barrier for motion of helium from a tetrahedral site to a neighboring tetrahedral vacancy. The alignment of the left (black dash-dot) and right (blue solid) portions of the diagram was calculated by an additional VASP NEB calculation starting from site T and ending in site T^* , providing the barrier of 1.31 eV for dissociation of helium from $VTet$. The shoulder in this barrier, at 0.40 eV, does not represent a metastable state, but configurationally is near the octahedral position

The NEB data for paths (a) and (b) in Figure 1 resulted from the SeqQuest code, while the data for path (c) results from VASP. The energies of the initial, final, and transition configurations were confirmed in each case with the alternate code (better than 0.025 eV agreement). In Figures 2 and 3, tetrahedral sites not occupied by hydrogen are labeled as T, while those occupied by hydrogen are labeled T^* .

The alignment of potential energy, including the shoulder shown in Figure 3, between helium trapped in a vacancy and dissociation to a region of stoichiometric ErH_2 was confirmed by an NEB calculation between the site T and a neighboring site T^* in the figure. The shoulder in this barrier for dissociation, which is spatially near an octahedral site, has an energy of 0.40 eV.

If helium impurities exist that are not associated with the decay of a tritium atom, or if helium migrates to a region where the material is stoichiometrically ideal, the energetics of helium site occupation are very different. In this case, the tetrahedral sites are occupied, requiring helium to either reside in an empty octahedral site or displace hydrogen. The energetic price of displacing hydrogen is 0.75 eV (0.73 calculated with VASP), making it much more favorable for helium to occupy the octahedral sites. Energetics, obtained with the NEB method, of the migration path and barrier for displacement of tetrahedral hydrogen by helium are shown in Figure 1(b). After making such a transition, diffusion of helium can proceed by transition to a tetrahedral site different from the initial configuration and continuing to make transitions between empty octahedral and filled tetrahedral sites. As can be seen in Figures 1 and 2, migration by this mechanism has a lower rate-limiting barrier ((b) 0.88 eV) than the conceptually straight forward mechanism of direct octahedral-to-octahedral transitions ((a) 1.50 eV), and will be the more dominant mechanism for helium diffusion through ErH_2 where V_{Tet} is not present. We note that this barrier is also relevant to the previous discussion of helium being trapped in a tetrahedral vacancy, since once helium dissociates from the vacancy (or network of vacancies), it must diffuse through material where the tetrahedral sites are occupied.

The Arrhenius equation was used to estimate diffusion lengths for helium in ErH_2 . Diffusion of helium in the hydride or tritide will depend on stoichiometry and/or the amount of tritium decay because the number and distribution of tetrahedral vacancies will determine the rate-limiting mechanism. In the case where helium is diffusing through a material with few or no V_{Tet} , the dominant mechanism will involve transitions between empty octahedral sites and filled tetrahedral sites, a process requiring a temporary displacement of H_{Tet} . This process has a rate-limiting barrier of 0.88 eV. Using this barrier, an estimate of the diffusion length for a time of 60 minutes at 300°C is 2.04 μm . Another interesting estimate for analysis of aging tritide films would be 25°C and 10 years, which gives a helium diffusion length of 0.17 μm . These estimates are only valid for a uniform material, and actual diffusion lengths may vary drastically from this prediction due to the presence of traps (V_{Tet}), impurities, or variations in stoichiometry. In the tritide, the number of V_{Tet} will be continuously increasing over time as the tritium decays into helium, vacating the tetrahedral sites. After a long time, it is possible that large extended networks of near neighbor V_{Tet} will allow for wholesale room temperature migration of helium throughout the

film. This simple exercise also neglects the presence of other helium traps, the interactions of multiple helium atoms, and the formation of helium bubbles. A future computational analysis will take all of these factors into consideration simultaneously. Nevertheless, our present calculations will serve as a basis for interpretation of future results and serve as a first look into the atomistic processes governing aging of tritium loaded erbium.

Conclusions

Helium created by tritium decay will seek its ground-state in a vacant tetrahedral site where it will likely be trapped, bound by 0.49 eV. If a connected network of vacant tetrahedral sites exists, helium migration throughout the network will occur at room temperature. Dissociation from this trap has a barrier of 1.31 eV, and the rate limiting barrier for migration beyond this volume is predicted to be 0.88 eV. In order to migrate through the stoichiometric β -phase, helium must move into an empty octahedral site and diffuse by octahedral-tetrahedral-octahedral jumps, forcing H_{Tet} temporarily out of the way as it proceeds. At this point, our calculations do not provide a clear mechanism for helium bubble formation, but future calculations are designed to provide insight.

A natural extension of this work will be to make calculations of several helium atoms clustered and arranged in various directions inside the ErH_2 lattice. For example, can DFT calculations shed more light on the fundamental reason why helium bubbles in some materials form plate-like bubbles while others are more spherical. In ErH_2 the predominant impurity is oxygen, which is at 2 to 3 atomic percent in some films. We would like to use DFT to answer the question of the impact of these oxygen impurities on atomic helium clustering and eventual helium bubble growth. Finally, these DFT results may be fed into larger scale computational methods like Kinetic Monte-Carlo (KMC) where helium bubble evolution and interaction may be studied.

Acknowledgements

We would like to thank Thomas Mattsson at SNL for his expert advice in performing these calculations and Jim Browning help with the experimental data. A more complete version of this paper, including discussions of hydrogen and oxygen site occupancies and migration paths can be found in R. R. Wixom, et al., *Journal of Applied Physics*, Vol. 103, 123708 (2008). Sandia is a multi-program laboratory operated by Sandia Corporation, a Lockheed Martin Company, for the United States Department of Energy under Contract DEAC04-94AL85000.

References

- [1] C. S. Snow, L. N. Brewer, D. S. Gelles, M. A. Rodriguez, P. G. Kotula, J. C. Banks, M.A. Mangan, J.F. Browning, "Helium release and microstructural changes in $Er(D,T)_{2-x}^3He_x$," *J. Nucl. Mater.* **374**, 147 (2007).
- [2] J. P. Perdew, K. Burke, M. Ernzerhof, "Generalized gradient approximation made simple," *Phys. Rev. Lett.* **77**, 3865 (1996).
- [3] P. A. Schultz, unpublished; For additional information, see <http://dft.sandia.gov/Quest/>
- [4] D. R. Hamann, "Generalized norm-conserving pseudopotentials," *Phys. Rev. B* **40**, 2980 (1989).
- [5] M. Fuchs and M. Scheffler, "Ab initio pseudopotentials for electronic structure calculations of poly-atomic systems using density-functional theory," *Comput. Phys. Commun.* **119**, 67 (1999).
- [6] G. Kresse and J. Hafner, "Ab initio molecular dynamics for liquid metals," *Phys. Rev. B* **47**, 558 (1993).
- [7] G. Kresse, and J. Joubert, "From ultrasoft pseudopotentials to the projector augmented-wave method," *Phys. Rev. B* **59**, 1758 (1999).
- [8] J. A. Grimshaw, F. J. Spooner, C. G. Wilson, A. D. McQuillan, "The growth of crystals of erbium hydride," *J. Mater. Sci.* **16**, 2855 (1981).
- [9] Chad M. Parish, C. S. Snow, L. N. Brewer, "The manifestation of oxygen contamination in ErD_2 thin films," *J. Mater. Res.* **24**, 1868 (2009).

THEORETICAL MODEL FOR THE HYDROGEN-MATERIAL INTERACTION AS A BASIS FOR PREDICTION OF THE MATERIAL MECHANICAL PROPERTIES

D. A. Indeitsev,* V. A. Polyanskiy,† A. K. Belyaev,* A. A. Sukhanov†

* Institute of Problems in Mechanical Engineering of Russian Academy of Sciences,
St. Petersburg, 199178, Russia

† St. Petersburg State Polytechnic University, Polytekhnicheskaya, 29,
St. Petersburg, 195294, Russia

Author Contact: ind@director.ipme.ru

A two-continuum model of the hydrogen-solid body interaction is suggested. This model describes the relaxation of the stresses and degradation of the material properties under the mechanical loading in a hydrogen-contained environment. The application of this model provides one with the instrument for prediction of the time resource and the mechanical properties of the aggregates of machines and mechanisms. The effect of the hydrogen-material interaction in the gas pipeline modeling is demonstrated.

Introduction

Hydrogen is contained in any metal. The hydrogen concentration is very low (about 1 atom of hydrogen in 100,000 atoms of the metal matrix); nevertheless, its influence on the mechanical properties of the metals is of crucial importance. As a rule, hydrogen is accumulated in metals during their exploitation. The main source for the hydrogen appearance in metals is water; however, the hydrogen diffusion for the gas and other hydrogen-containing substances is feasible.

In metals, the hydrogen is contained in the traps with various bounding energies. It has been established, cf. [1], that thermomechanical loading results in the hydrogen redistribution over the traps. Diffuse hydrogen accumulates mostly in the aluminum alloys while strongly bounded hydrogen accumulates mostly in the titanium alloys.

A number of papers were concerned with the influence of hydrogen on the mechanical properties of metals (see, e.g., [2]). Nearly all the papers use phenomenological models, and the redistribution of hydrogen over the traps is not described. The degradation of mechanical properties is carried out by means of empirical dependences.

The two-continuum model of solid [3] allows one to describe the influence of small concentration of hydrogen on the mechanical properties of materials in terms of changing the bonding energy of the second continuum, the latter being responsible for the hydrogen concentration. The results obtained with the help of simple models should be generalized in order to make the account of small hydrogen concentration on the mechanical properties of materials available for the engineering practice.

Method of Analysis

A Two Continuum Model

Basic principles of the above-mentioned hypothesis can be illustrated on an example of analysis of the one-dimensional chain consisting of identical particles, which are the point mass m_0 (the atom mass in the crystal lattice of a material). They are connected to each other by the identical nonlinear springs of the length a , cf. Figure 1.

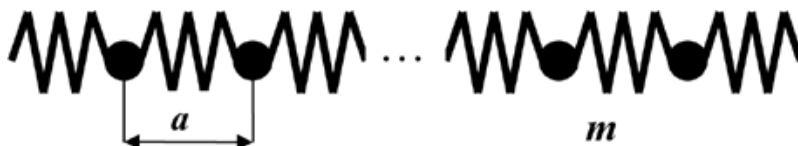


Figure 1. The schematics of the material model.

The basic equation of the motion in the long-wave approximation is given by (cf. [2])

$$m_0 \ddot{u} = -a[f(a(1+u'))]' \quad (1)$$

where a dot denotes the time derivative. As for small deformations $\varepsilon = \partial u / \partial x$, we arrive at the following equation:

$$\ddot{u} - \mathcal{G}_0^2 u'' = 0, \quad \mathcal{G}_0 = a\sqrt{c/m} \quad (2)$$

since $f[a(1+\varepsilon)] \approx -Ca\varepsilon = -Ca\partial u / \partial x$.

The weakening of the internuclear bonds caused by “landing” of the hydrogen particles (or other mobile internal elements of structure) can produce the chain formations of new internuclear bonds, see Figure 2, as the consecutive connections of elastic bonds of the basic lattice and the introduced elastic bonds of new elements (e.g. hydrogen particles). Obviously, such chain is possible under the assumption that the mass of particles of a mobile structure is small, i.e., $m_0 \gg m_H$.

Equivalent rigidity of the new bond can be obtained from the equation

$$\frac{N_\Sigma}{C_\Sigma} = \frac{N_0}{C_0} + \frac{N_H^+}{C_H} \quad N_\Sigma = N_0 + N_H^+ \quad (3)$$

The constitutive equation for this medium is as follows:

$$\sigma^{(1)} = E_\Sigma \varepsilon, \quad E_\Sigma = \frac{E_0 E_H}{n_0 E_H + n^+ E_0}, \quad n_0 = \frac{N_0}{N_\Sigma}, \quad n^+ = \frac{N_H^+}{N_\Sigma}, \quad n_0 + n^+ = 1. \quad (4)$$

Here N_Σ denotes the total number of the particles in the elementary volume, and N_H^+ is the number of hydrogen particles attached to the lattice with the bonds of rigidity C_H . Finally, n_0 , n^+ are the concentrations of the corresponding particles (Figure 2).

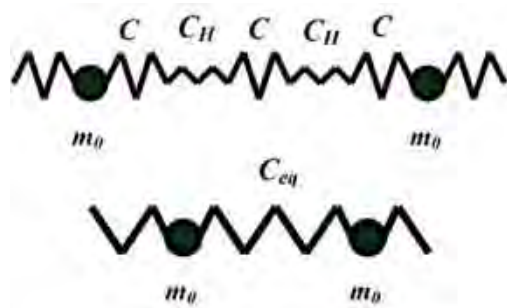


Figure 2. The model of the material with hydrogen particles

For small deformations the nonlinear force f in Eq. (1) can be introduced as

$$f = -C_\Sigma a\varepsilon = -E_\Sigma \varepsilon \quad (5)$$

The equivalent modulus of the lattice E_Σ , see (4), can be decreased essentially, since $E_H \ll E_0$ ($C_H \ll C_0$), and has a strong dependence on the concentration of the attached particles n^+ .

The number of the lattice settled by the hydrogen particles depends on the stress state of the lattice at every point and, in general, on time. The unknown functional dependence of E_{Ξ} on $n^+(\varepsilon, x, t)$ should be determined with the help of the model of two-component continuum.

The details of the theory of two-component continuum can be found in [3]; therefore, we are presenting here only the final results with some necessary explanation of the processes.

From the state equation, we have $\sigma = \sigma(\varepsilon, n^+(\varepsilon, x, t))$; thus,

$$\sigma = E_0 \varepsilon \left[1 - \frac{n^+}{n^+ + n^{(0)} E_H / E_0} \right], \quad (6)$$

and the essential dependence of the stress state on concentration of the bonded hydrogen becomes evident.

The hydrogen concentration is described by the equation for n^+

$$\frac{\partial^2 n_H^+}{\partial t^2} + (\alpha + \beta) \frac{\partial n_H^+}{\partial t} - A \cdot D(\varepsilon_{st}) \left[\beta \frac{\partial^2 n_H^+}{\partial x^2} + \frac{\partial^3 n_H^+}{\partial t \partial^2 x} \right] = 0 \quad (7)$$

Here $A = c_H^2 k j$, α and β are some constants, and $D(\varepsilon_{st})$ denotes the hydrogen diffusion constant.

Equations (6) and (7) form a system for modeling the hydrogen influence on the dependence $\sigma(\varepsilon)$ for the material.

The stress-strain curve for steel is changing due to the hydrogen saturation, which is displayed in Figure 3. Figure 4 demonstrates the relaxation of the yield stress in steel with time in the presence of hydrogen. It is easy to see that the yield stress decreases, which leads to the exponential weakening of the material strength as time progresses [3].

Hydrogen saturation time depends strongly on the temperature and varies in the range of tens of minutes at temperatures about 900°C up to several months at a temperature near 20°C.

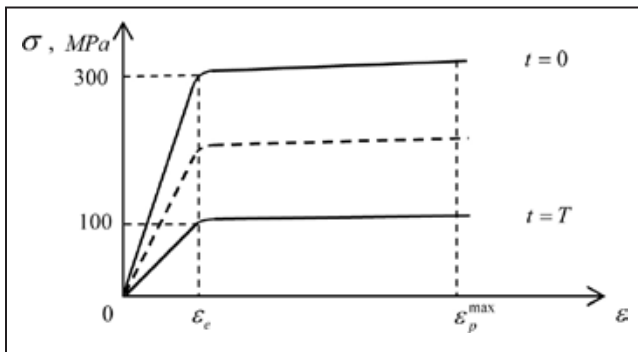


Figure 3. The stress-strain curve for steel.

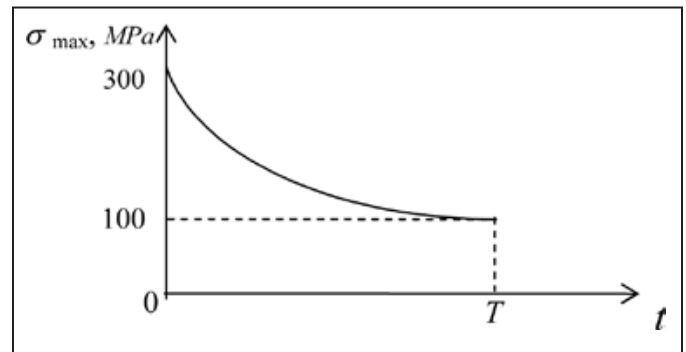


Figure 4. The relaxation of the yield stress in steel with time in the presence of hydrogen.

Results and Discussion

The mechanism of the gradual hydrogen embrittlement is demonstrated on the example of the flange connection of the pipeline part under high gas with hydrogen pressure. The analysis of pipeline hydrogen saturation is made by means of the three-dimensional finite element code.

The flanges on the high diameter pipe (up to 2 meters) are very often supported with the stiffening ribs. The von Mises stress distribution in the fragment of the flange connection with the stiffening ribs after is shown on Figure 5.

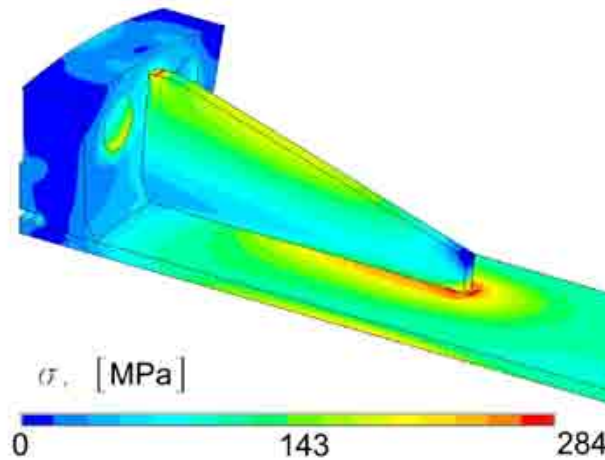


Figure 5. The distribution of the von Mises stress in the flange connection of the steel pipe line.

The stress concentration is easily seen; however, the maximum stress 284 MPa is under the yield stress 300 MPa. The stress field is redistributed after the relaxation time T . The hydrogen is accumulated in the zones of the tensile stress. After several successive calculations of the stress and hydrogen's accumulation, we can calculate the final picture of the stress and the strain. The strain field is shown in Figure 6. A very high strain level $\epsilon = 33\%$ is observed at the place of welding of the support to the pipe. This means that the welding will be totally destroyed, so the hydrogen redistribution inside the steel leads to destruction of the flange connection.

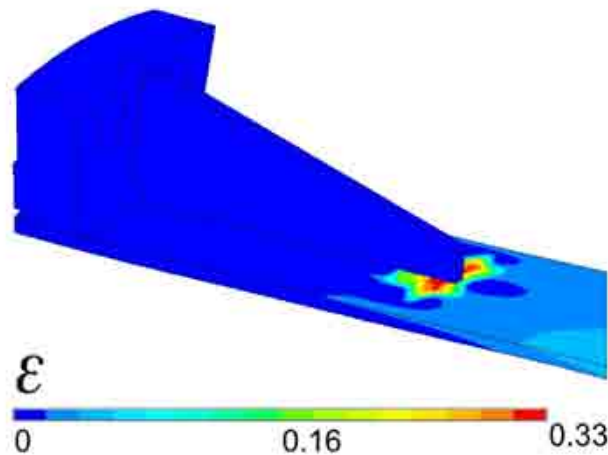


Figure 6. The strain distribution in the flange connection after the hydrogen saturation.

The relaxation time constant T can be rather high; that is, the saturation process is rather slow. The hydrogen saturation depends on the initial concentration of the hydrogen, diffusion constants temperatures, environment hydrogen concentration, etc. In this paper, we made only a first calculation of the effects of hydrogen influence. Such calculation can be carried out by means of the empirical models of the material properties [2]. The present approach provides us with the possibility of developing an adequate multiple-factor model.

Conclusions

A model is suggested that allows one to describe the kinetics of hydrogen in metals. The model is also appropriate for estimating the hydrogen transition from the mobile state to the bonded state depending upon the stresses and describing the localization of the bounded hydrogen. The result is destruction of the material at the localization places.

The constructed models enables describing very different effects of the hydrogen embrittlement such as the hydrogen concentration, diffusion rate, material temperature, and the stress character in the framework of the same approach. This result allows one to predict the lifetime of the material in the hydrogen-containing environment.

The calculation of the stress field of the pipeline flange has clearly demonstrated that the two-component model can be successfully applied for engineering estimations of metal structures.

Acknowledgements

The financial support of the Sandia Corporation, contract 891092, and the Russian Foundation for Basic Research, grants 08-08-00737 and 08-01-12017, is acknowledged. Sandia is a multi-program laboratory operated by Sandia Corporation, a Lockheed Martin Company, for the United States Department of Energy under Contract DEAC04-94AL85000.

References

- [1] A. M. Polyanskiy, V. A. Polyanskiy, D. B. Popov-Diumin, "Diagnostics of mechanical condition of tructural material by method of high-temperature hydrogen vacuum-extraction," in *Proceedings of the Sixth International Congress on Thermal Stresses* vol. 2 589-592 (Vienna, Austria, May 2005) pp. 589-592.
- [2] D. C. Ahn, P. Sofronis, R. Dodds, Jr. "Modeling of hydrogen-assisted ductile crack propagation in metals and alloys," *Int. J. Fract.* **145** 135-157 (2007).
- [3] D. A. Indeitsev, B. N. Semenov, "About a model of structural-phase transformations under hydrogen influence" *Acta Mechanica* **195** 295-304 (2008).

PROPERTIES RESEARCH OF CHEMICALLY DEPOSITED NICKEL COATINGS MODIFIED WITH NANO DIAMONDS

S. A. Fedotov, L. P. Ryabchikova, N. S. Fedotova

All-Russian Research Institute of Automatics,
Moscow, Russia

This work represents research on the depositing properties of chemical nickel coatings modified with nano diamonds. Those were obtained from the knocking synthesis method with further activation. Research of dependency on the carbon content in coating on depositing properties and modes was made too. A comparison research of microstructure, physical and mechanical properties of chemically deposited nickel coatings with/without nano diamonds was also carried out.

Introduction

Composite galvanic and chemical coatings provide a wide range of improved physical and mechanical properties and are of a great interest for scientific researches and industrial use.

Composite coatings with dispersed particles that contain salt of depositing metal and a dispersed phase get through use of deposition method from electrolyte. The electrolyte content and the disperse phase properties, such as dimensions, nature, tolerance to sedimentation, and coagulation, determine the quality of the received coating. Electrolytes that contain superdispersed diamonds of knocking synthesis (hereafter referred to as SD, nano diamonds) have a great stability that is conditioned by the small size of SD particles, their chemical stability, and surface hydrophilic properties that arise from oxygen-containing groups on the surface. The SD particles are introduced in the surface during metal deposition and influence onto the surface structure and properties [1,2].

Experiment

A water suspension of superdispersed diamonds (SD) was used as an addition, means chemical nickel-plating, into the electrolyte. The solution content of chemical nickel-plating follows:

- $\text{NiSO}_4 \cdot 7\text{H}_2\text{O}$ – 20–30 g/l
- Sodium hypophosphite – 10–25 g/l
- Acetous sodium – 10–15 g/l
- Acetic acid – 4–6 g/l
- Thiourea – 0,001–0,003 g/l
- Temperature – 82–87°C.

Samples from the aluminum alloy were coated.

Both the initial SD suspension before introduction into the electrolyte and the electrolyte after the correspondent introduction underwent the ultrasonic dispersion.

Particles distribution in accordance with their dimensions was made using the laser particles analyzer—analyzette 22 (the FRTSCH company). Considering a diffused light and complex math was made a calculation—distribution for dimension groups. The volumetric parts are gained as a result of calculations and those correspond to equivalent diameters at laser diffraction.

The CS-200 analyzer (the LECO company) was used to determine the carbon content in the coating. This analyzer is designed for the carbon content determination in inorganic materials. When samples burn up in the inductive furnace in the oxygen current, the carbon contained in the sample oxidizes to CO_2 that absorbs the infrared radiation. Going down energy level on the infrared detector of analyzer, it is possible to determine the generated CO_2 concentration and the carbon content, respectively.

Coating structures with different carbon content were examined by the electron microscopy method (the Hitachi TM-1000 electron microscope). Hardness measurement (H) and module of elasticity (E) of received coatings before and after thermal treatment were carried out using the microhardness measurement unit—Micro-Hardness Tester (MHT).

Microhardness measurement was carried out at the following parameters:

- Indenter – Vickers pyramid
- Max. indicator load – 300 mN
- Load/unload rate – 600 mN/min
- Exposure time at max. load – 15 sec.

During the research process from 12 to 15 measurements of microhardness of each coating sample were made.

Researches in the wear resisting property and in the friction coefficient, when sliding in accordance with the “rod-disk” scheme, were carried out using the Tribometer, CSM Instr. unit. The Axiovert 25 optical microscope was used to determine the wear spot diameter of ride (a little steel ball) and the wear groove width.

Testing conditions:

- Rider – the little ball with the 3 mm diameter,
- Rider material – 400C (the analog 95X18III),
- Normal load – 1H,
- Linear speed – 10 cm/sec,
- Relative humidity – 49%.

Results Discussion

When adding the SD electrolyte, generates the electrolyte-suspension instead the homophase one. In that one (means the electrolyte-suspension) the disperse phase is the particulate matter with dimensions of micro- and nano- order.

Polydisperse that is the content of received electrolyte-suspension.

Data on particle dimensions and their distribution in the electrolyte are necessary for the structure analysis of received coatings.

Particle dimensions spectrum of electrolyte and the amount of parts of particles divided into groups in accordance with their dimensions were achieved using laser particles analyzer—analyzette 22 (the FRITSCH company) and are shown in Figure 1.

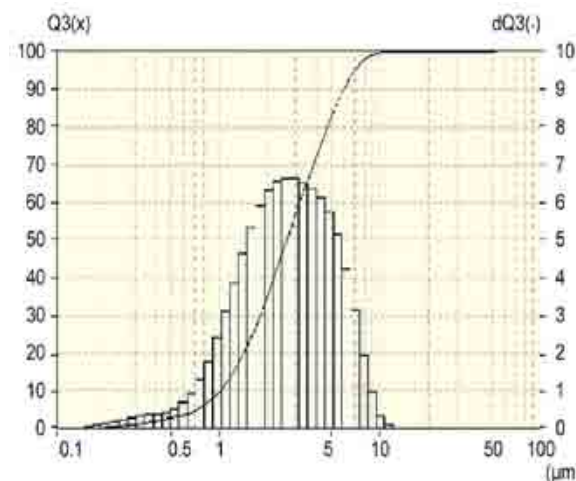


Figure 1. Particles distribution in accordance with their dimensions in the electrolyte (chemically deposited nickel).

From data, it is clear that the presence of particles with dimensions from 100 up to 500 nm is approximately ~10%, and the great part, about 70%, constitute particles with dimensions from 1 up to 5 μm .

Turbidimetric method and the KFK-2MP unit were also used for the particles content determination in the electrolyte, proceeding from the known concentration of initial SD suspension.

After an hour of settling, the content of particles in the electrolyte remains permanent. This provides a necessary basis to make a suppose that the largest particles under the gravity influence settle, and the small ones are distributed in the electrolyte and directly take part in the settling of coating.

In order to confirm the supposition, three volumes of electrolyte were prepared with the SD addition in the amount of 2 g/l. Those were left for settling for 1, 2, and 3 hours after the SD introduction and supersonic dispersion.

Then coats on the surface of samples were applied from the aluminum alloy. The operation took 1 hour. The thickness of coat constituted ~7 μm .

The carbon content in coatings made from the three volumes of electrolyte constituted ~0,4–0,5%.

Thus, only particles with then determined dimensions were in the process of chemical settling of nickel.

The carbon content in the coating depends on the SD concentration in the electrolyte. When the SD concentration in the electrolyte is 1 and 2 g/l, the carbon content will be 0,4–0,5%, and 0,8% under the concentration of 5 g/l.

The structure of coatings with different carbon content was examined using the optical electron microscopy.

As it can be seen from Figure 2, the coating of chemically deposited nickel without the SD is composed from accrete hemispheres.

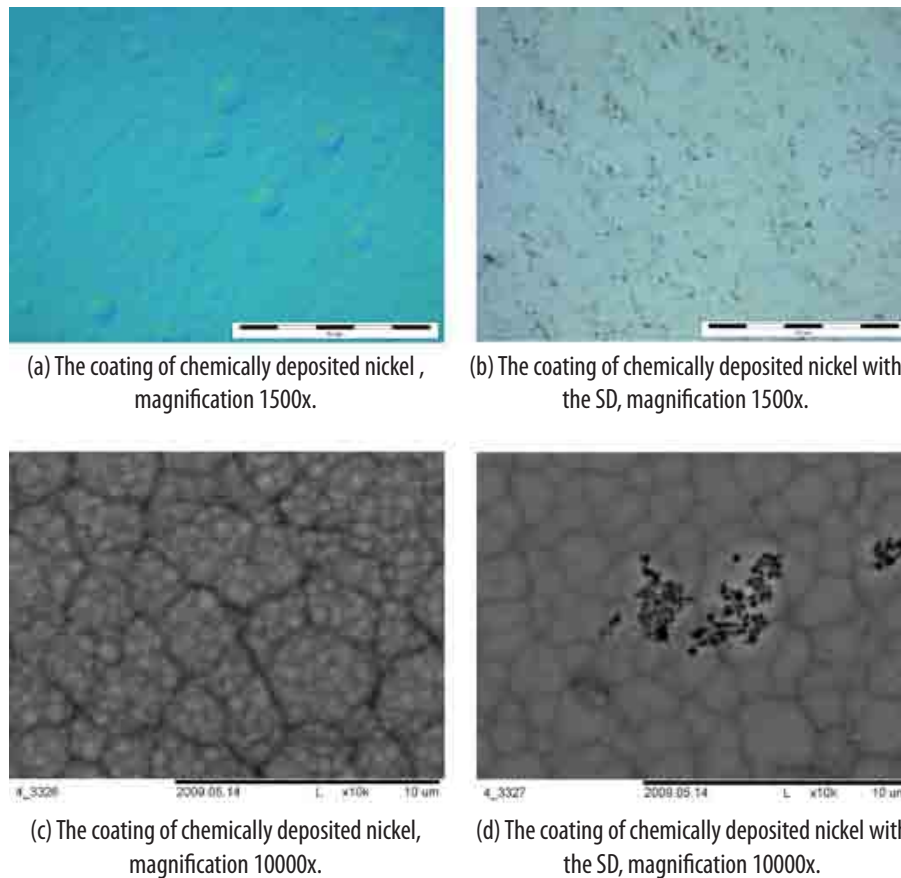


Figure 2. The morphology or structure of coating surface of chemically deposited nickel with the SD and without it.

The morphology analysis of coatings surfaces with the SD showed that besides small hemispheres with dimensions that equal approximately ~ 250 nm (that correspond to dimensions of particles distributed in the volume of electrolyte), there are larger cluster structures with the SD dimensions of ~ 2 μ m. Clusters with the SD are disoriented towards each other.

Samples with nickel coating with different amount of carbon were made for researches in physical and mechanical properties.

It is known that the heating of nickel coatings up to the temperature of $\sim 400^\circ\text{C}$ for 2 hours leads to a microhardness increase that is related with structure changes in coatings.

Microhardness measurement results and module of elasticity of coatings before and after thermal treatment are represented in Table 1.

Table 1. Microhardness measurement results.

| Sample | Before treatment | | After treatment | |
|--------|----------------------|---------------------|-----------------------|----------------------|
| | HV | E(GPa) | HV | E(GPa) |
| N0 | 676,370 \pm 19,261 | 137,534 \pm 6,246 | 1165 \pm 99,824 | 183,502 \pm 12,626 |
| N1 | 538,558 \pm 27,275 | 116,945 \pm 7,074 | 999,304 \pm 93,040 | 144,299 \pm 10,156 |
| N2 | 455,361 \pm 26,058 | 97,927 \pm 3,937 | 973,550 \pm 45,788 | 146,527 \pm 7,725 |
| N3 | 554,339 \pm 25,796 | 110,654 \pm 7,164 | 202,538 \pm 13,416 | 58,915 \pm 1,264 |
| N4 | 394,729 \pm 27,364 | 93,143 \pm 2,800 | 1046,480 \pm 77,674 | 150,037 \pm 7,127 |

Samples: N0 – coating without SD and with 20 μ m thickness; N1 – coating, got from the SD solution with a 2 g/l content and 10 μ m thickness; N2 – coating, got from the SD solution with a 2 g/l content and 20 μ m thickness; N3 – coating, got from the SD solution with a 5 g/l content and 20 μ m thickness; N4 – coating, got from the SD solution with a 1 g/l content and 20 μ m thickness.

Microhardness comparison researches of coatings containing SD, cannot provide a necessary basis in order to determine the coating hardness dependency on the SD concentration in initial solutions.

Thermal treatment of coatings without SD and with a less presence of SD in the coating (0,4–0,5%) leads to increase of their microhardness nearly in two times.

When increasing the SD content in the coating up to 0,8%, the microhardness will decrease. This might be related with the presence of some part of carbon as a separate (amorphous) phase that was not entered into the nickel matrix structure and imparted a fragility for the coating.

Received values for hardness of thermal treated coatings correspond to the hardness of galvanic chromium.

Measurement results of wear resistant properties and friction coefficient are given in Table 2.

Table 2. Measurement results of wear resistant properties and friction coefficient.

| Sample N. | Wear of sample, $10^{-5}\text{mm}^3/\text{N/m}$ | Wear of rider, $10^{-7}\text{mm}^3/\text{N/m}$ | Friction coefficient | | | | Running, min^{-1} |
|-----------|-------------------------------------------------|------------------------------------------------|----------------------|------|-------|------|----------------------------|
| | | | Start. | Max. | Aver. | Fin. | |
| 0 | 1,51 | 9,69 | 0,13 | 0,87 | 0,80 | 0,86 | 4045/203 |
| 1 | 1,67 | 3,46 | 0,16 | 0,73 | 0,61 | 0,63 | 3956/200 |
| 2 | 2,02 | 16,01 | 0,17 | 1,01 | 0,86 | 0,89 | 3957/200 |
| 3 | 3,03 | 7,17 | 0,13 | 0,89 | 0,79 | 0,87 | 3956/200 |
| 4 | 2,27 | 8,90 | 0,15 | 0,92 | 0,85 | 0,88 | 3958/200 |

In the process of friction and wear goes an interaction of surfaces, formation of the contact spot, changes in the surface layer, destruction of friction surface. Multifactor influence on the process of wearing troubles the dependency revelation between wearing and mechanical properties (particularly coating hardness).

In accordance with the received data, the surface with 0,4–0,5% of carbon presence and 10 μm thickness has the lowest friction coefficient and provides high level of operation efficacy between details.

Conclusions

1. In the process of nickel chemical deposition with superdispersed diamonds (SD) take part particles with micro- and nano- meter dimensions.
2. The SD entered the nickel coating matrix, forming cluster structures.
3. Microhardness practically did not depend on the SD content. Thermal treatment under 400°C during 2 hours leads to microhardness increase of nearly twice. Received values for coatings hardness after thermal treatment correspond to galvanic chrome hardness.
4. The lowest friction coefficient has a coating with 0,4–0,5% of the carbon content and 10 μm thickness.
5. The coating from the electrolyte that has 10 μm thickness and the SD content that equals 2 g/l, can be recommended for wear-resisting property improvement of details that operate in friction conditions.

References

- [1] Yu. Dolmatov, “Superdispersed diamonds of knocking synthesis. Receipt, conditions, application” (St. Petersburg, 2003) 344.
- [2] J. N. Balaraju and K. S. Rajam, “Preparation and characterization of autocatalytic low phosphorus nickel coating submicron silicon nitride particles,” *Journal of Alloys and Compounds* **459** 311-319 (2008).

EVOLVING METALLURGICAL BEHAVIORS IN PLUTONIUM FROM SELF-IRRADIATION

B. W. Chung, K. E. Lema, D. S. Hiromoto

Lawrence Livermore National Laboratory, Livermore, CA 94551 USA

Author Contact: Chung7@llnl.gov

The plutonium alpha-decay leads to the age-related changes in physical properties. We review our experimental approaches including analytical techniques to assess the effects of extended aging on plutonium alloys, together with our recent results on age-related changes in physical and static mechanical properties. The ultimate goal of this work is to develop capabilities to predict metallurgical evolution driven by aging effects.

Introduction

Plutonium exhibits notoriously complicated metallurgical behaviors, depending sensitively on phase as well as on chemical content and microstructure [1,2]. Current studies in plutonium metallurgy are motivated by the need to better understand the influence of the metallurgical phenomena on the physical and mechanical properties for stockpile stewardship, nonproliferation, environmental issues, and nuclear power. One of the key areas of research is developing capabilities to predict metallurgical evolution driven by the radioactive decay of plutonium that incessantly creates lattice damage and in-growth of radiogenic helium. Because these integrated aging effects would normally require decades to measure, studies are under way to assess the effects of extended aging on the physical and static mechanical properties of plutonium alloys by incorporating roughly 7.3 atomic % of highly specific activity isotope ^{238}Pu into the ^{239}Pu metal to accelerate the aging process. By monitoring the properties of the ^{238}Pu enriched alloy and naturally aged plutonium alloys, the aging properties of plutonium from the self-irradiation damage can be predicted.

Method

Sample Preparation

Radiation damage from alpha decay in plutonium occurs at a rate of ~ 0.1 dpa (displacement per atom) per year. Because the effects of interest occur over decades, our approach is to accelerate the effects of radiation damage in plutonium metal by incorporating 7.3 atomic % of the higher specific activity isotope ^{238}Pu into the ^{239}Pu lattice. The rate of α -decay of ^{238}Pu is nearly 300 times that of ^{239}Pu , so the rate of radiation damage accumulation can be increased. Using this method, the radiation damage in plutonium equivalent to 60 years of natural aging can be simulated in only a few years. Additional details of sample preparation are presented elsewhere [3]. In addition, plutonium alloys of various ages are characterized.

Measurement Techniques

Details of operation of the dilatometer system, immersion density, and static tensile and compression test techniques are presented elsewhere [3], so only a brief description is provided here. Specifically designed dilatometers, immersion density equipment, static tensile and compression tester were set up inside a nitrogen atmosphere glovebox. The dilatometer is designed to monitor long-term growth resulting from the lattice damage and helium in-growth in plutonium alloys. The immersion density equipment closely matches a design used by Bowen et al. [4] and uses about 200 ml of Fluorinert Electronic Liquid FC-43 as the immersion fluid. The static

tensile and compression tester has a specially designed fixture for testing plutonium samples. With a 0.24 inch GL extensometer for the strain measurement, typical testing was performed at crosshead speed of 0.05 inch/min so that the ultimate strain rate was about $3.5 \times 10^{-3}/\text{sec}$.

Results and Discussion

Significant questions remain concerning the metallurgical evolution driven by aging effects. Three principal aging mechanisms have been identified as a result of the self-irradiation of plutonium that would cause metallurgical changes: the initial transient, accumulation of radiogenic helium and actinide daughter products, and void swelling. The initial transient saturates after a short time and results mainly from the increase in lattice parameter. The second contributor to metallurgical changes is the build-up helium and actinide daughters from the radioactive decay of plutonium. The void swelling is another phenomenon, but has not yet been observed in aged plutonium alloys. In addition to these three major mechanisms, a hypothesis suggests that small precipitates of the higher density $\zeta\text{-Pu}_3\text{Ga}$ phase form in the matrix [5].

Results from dilatometry, immersion density, and static tensile measurements show effects from the first two mechanisms on plutonium alloys with ~ 2 atomic % Ga (see Figures 1 and 2). These techniques are well suited in measuring small property changes produced by aging mechanisms. Results indicate that these plutonium alloys undergo small changes in properties with time, without any signs of void swelling. Aged plutonium alloys exhibit a drop in strength when annealed to 300°C , indicating the annealing out of the accumulated lattice damage. Current annealing experiments show reduction in the yield strength by ~ 30 MPa from ~ 170 MPa on enriched alloys doped with ~ 3 atomic % Ga (and aged to ~ 90 equivalent years). This reduction appears to be related to the annealing out the accumulated lattice damage from aged plutonium alloys. We estimate the in-growth of helium contributes ~ 60 MPa for this alloy aged to ~ 90 equivalent years.

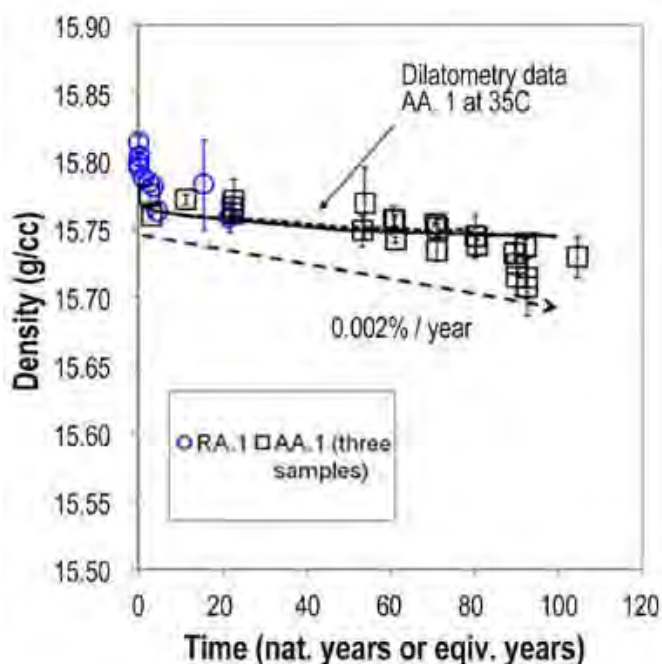


Figure 1. Immersion densities of both enriched (^{238}Pu doped) and reference alloys. The decrease in density is less than 0.002% per year. Circles are reference alloys (RA) and squares are enriched alloys (AA.1). The length change measured by dilatometry is converted to a relative change in density for comparison.

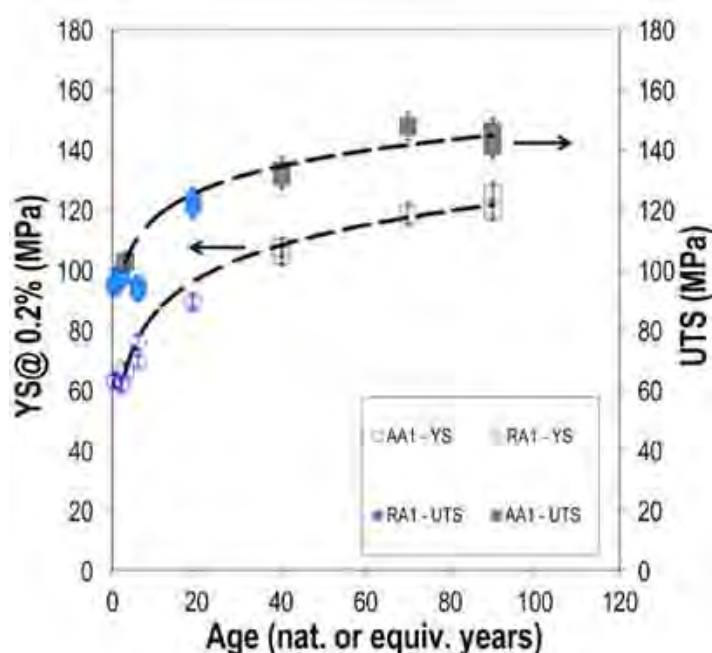


Figure 2. Engineering yield strength (YS) and ultimate tensile strength (UTS) of plutonium alloys from aging [6]. Circles are reference alloys and squares are enriched alloys.

Conclusions

We have developed analytical techniques to measure small changes in plutonium properties by aging. Results of measurements show evolving metallurgical properties of plutonium alloys from incessant self-irradiation damage. So far, however, void swelling has not been observed. Annealing recovery experiments are also under way to better understand aging mechanisms responsible of evolving metallurgical properties with age.

Acknowledgements

This work was performed under the auspices of the U.S. Department of Energy by the University of California Lawrence Livermore National Laboratory under contract No. W-7405-Eng-48.

References

- [1] W. G. Wolfer, "Radiation effects in plutonium. What is known? Where should we go from here," in *Los Alamos Science*, ed. N. G. Cooper (Los Alamos, Los Alamos National Laboratory, 2000) **26** 274-285.
- [2] S. S. Hecker and J. C. Martz, "Aging of plutonium and its alloys," in *Los Alamos Science*, ed. N. G. Cooper (Los Alamos, Los Alamos National Laboratory, 2000) **26** 238-243.
- [3] B. W. Chung, S. R. Thompson, C. H. Woods, D. J. Hopkins, W. H. Gourdin, B. B. Ebbinghaus, "Density changes in plutonium observed from accelerated aging using Pu-238 enrichment," *Journal of Nuclear Materials* **335** 142-149 (2006).
- [4] H. A. Bowen and R. M. Schoonover, "Procedure for high precision density determination by hydrostatic weighing," *Journal of Research of the National Bureau of Standards – C* **71C**[3] 179-198 (1967).
- [5] W. G. Wolfer, A. Kubota, P. Soderlind, A. I. Landa, B. Oudot, B. Sadigh, J. B. Sturgeon, M. P. Surh, "Density changes in Ga-stabilized delta-Pu, and what they mean," *Journal of Alloys and Compounds* **444-445** 72-79 (2007).
- [6] B. W. Chung, S. R. Thompson, K. E. Lema, D. S. Hiromoto, B. B. Ebbinghaus, "Evolving density and static mechanical properties in plutonium from self-irradiation," *Journal of Nuclear Materials* **385** 91-94 (2009).

ISOCHRONAL ANNEALING OF RADIATION DAMAGE IN α - AND δ -PU ALLOYS

S. K. McCall*, M. J. Fluss*, B. W. Chung*, and R. G. Haire†

*Lawrence Livermore National Laboratory, Livermore, CA 94550 USA

† Oak Ridge National Laboratory, Oak Ridge, TN 37830 USA

Magnetic isochronal annealing curves were measured on specimens of self-damaged α -Pu and several δ -Pu alloys stabilized by Ga and Am. These results are compared to one another and to isochronal resistivity annealing curves, where distinct differences are observed between the magnetic and resistive annealing for the case of δ -Pu. The first stage of annealing observed in the resistivity measurements is largely missing from the magnetic measurements, indicating that interstitials contribute little if any signal to the magnetization, while the onset of vacancy migration is strongly reflected in the magnetization signal.

Introduction

Radiation damage is a naturally occurring process in all of the actinides, wherein the actinide atom spontaneously decays, creating a cascade of vacancies and interstitials that disorder the atomic lattice. In the case of Pu, the predominant route of decay is via a 5.16 MeV α -particle, which travels about 10 microns through the lattice, losing about 99.9% of its energy through electronic excitations and atomic ionizations. Near the end of its travel, it begins to collide with atoms in the lattice and creates a cascade of about 800 nm in size with roughly 265 Frenkel pairs (an interstitial and a vacancy). Perhaps more interestingly, the resulting U ion recoils with 86 KeV of energy, travels about 12 nm, and initiates a dense cascade of vacancies and interstitials most of which anneal out over the succeeding few hundred picoseconds, leaving a cloud of approximately 2300 vacancies, interstitials, and their aggregates. Preliminary theoretical calculations suggested that these defects existed within a sphere of about 7.5 nm [1] diameter, while more recent calculations suggest a diameter closer to 30 nm [2]. This later value is consistent with estimations from experimental measurement of the saturation in the excess magnetic susceptibility arising from radiation damage [3]. Like Pu, Am also decays by α -emission, albeit with a slightly more energetic 5.28 MeV particle, which behaves in a manner substantially equivalent to the Pu case. The recoiling Np ion, with about 89 KeV of energy will also generate a damage cascade that to a first approximation mirrors that of the U ion for Pu. In the case of ^{243}Am , used in these experiments, the resulting ^{239}Np decays by a 720 KeV β^- emission, with a half-life of 2.35 days, to ^{239}Pu . The recoiling ^{239}Pu of the β^- emission has only a few eV of energy and thus is unlikely to generate even one Frenkel pair, and the β^- lacks the momentum to create vacancy-interstitial pairs on its own.

At cryogenic temperatures, after the initial generation, the damage cascades are frozen in the lattice, and the effects of these defects can be observed indirectly through the measurement of many physical properties. The most frequently monitored physical property is resistivity because of the relative ease of the measurement, but similar observations can be made using heat capacity, dilatometry, thermal conductivity, or magnetization. Isochronal annealing studies of radiation damage map the change in a physical property as the radiation damage is thermally annealed by soaking for a fixed period at progressively higher temperatures, and then monitoring the physical property at a fixed low temperature. The basic protocol for a self-damaging specimen is to accumulate damage at a low temperature for a period of time and then measure the property of interest at that temperature, T_M . Then the specimen is heated to a higher temperature, held for a fixed period, and returned to T_M , where the property is measured again. This process of heating, soaking, and returning to the base temperature is repeated at progressively higher annealing temperatures until the property of interest returns to its initial value, indicating that all the radiation damage has been annealed away. Because these measurements are made on a self-damaging

specimen, a first-order correction to the annealing curve is made by repeating the above prescription on the same sample immediately after annealing. This allows for subtraction of the damage accumulated while the measurement is being performed. Further details of this process are described by Fluss et al. elsewhere [4].

Method

Magnetization

Magnetization measurements reported were performed using a commercial magnetometer (Quantum Design MPMS 5) in an applied magnetic field of 3T. Small samples (15–90 mg) of the alloys were coated with a 5-micron layer of polyimide to contain spall and act as a layer of encapsulation. The samples were then mounted in the center of a 20 cm long brass sample tube and hermetically sealed with a gold O-ring under an inert atmosphere. The tube acts as a second level of encapsulation as well as helping to ensure that the temperature of the sample is in equilibrium with the system thermometer. The magnetometer makes measurements using a second order gradiometer by moving the sample through a set of detection coils. Because the sample holder is much longer than the separation between the detection coils, its contribution to the magnetization is very small ($< 1\%$) and unaffected by radiation damage. Prior to loading a specimen, a background curve is run on the sample holder, and this is subtracted from the sample measurement. An example of an uncorrected isochronal annealing curve and the first order correction curve are presented in Figure 1 for a $\text{Pu}_{1-x}\text{Am}_x$ ($x=0.19$) alloy where the measured physical property was magnetization. The radiation damage was allowed to accumulate for 45 days at $T < 20$ K, over which time the magnetization increased by about 6.5%. Magnetization measurements were made at 5K, and each annealing curve took approximately 6 days to complete, with soaks at each annealing temperature of 20 minutes.

Resistivity (Figures 1 and 2)

Resistivity measurements were made on the same specimens measured via magnetization. The initial roughly spherical samples were rolled, with repeated intermediate annealing, to remove strain until a thickness of ~ 75 microns was obtained. Then the samples were cut into a cloverleaf pattern and hermetically sealed inside a copper sample holder. Spring-loaded pins inside the holder make contact with the sample, with two leads on each leaf of the pattern, totaling eight leads. In this configuration, both co-linear resistivity measurements and Van der Pauw configurations were available, as was the ability to make Hall measurements when placed in a magnetic field. The

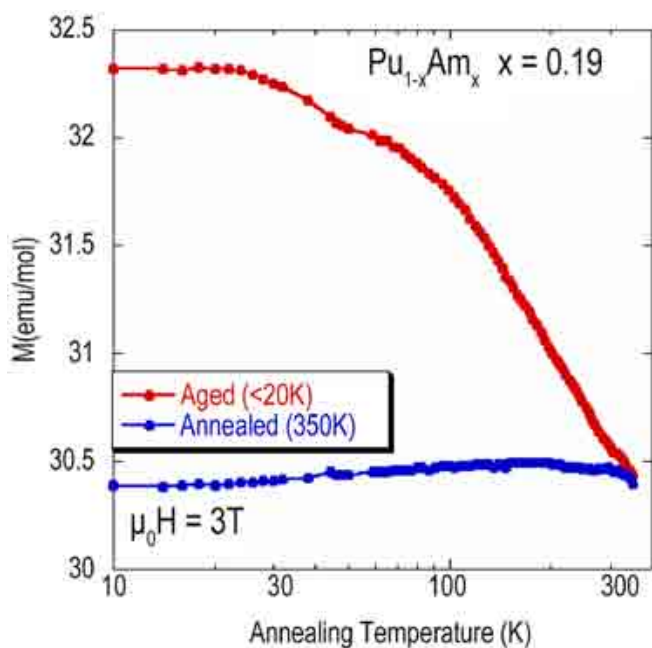


Figure 1. Uncorrected isochronal annealing data (red) and first order correction (blue) curve for a PuAm alloy. Radiation damage was accumulated for ~ 45 days on this specimen resulting in a 6.3% increase in the magnetization due to self-damage.

sample holder was then coated with polyimide to form a second layer of encapsulation. A thermometer (Cernox) was mounted inside the sample holder, approximately 1–2 mm from the specimen. Measurements were made using a commercial system with a resistance bridge (Quantum Design PPMS).

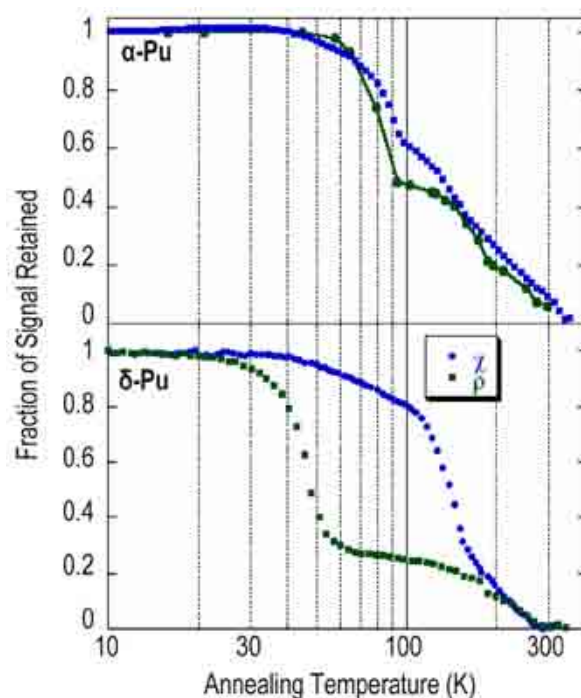


Figure 2. Isochronal annealing curves for α -Pu and δ -Pu(4.3at%Ga) measured with magnetization (blue data) and resistivity (green data). The α -Pu resistivity data are from the work of Wigley [5] and track well with the magnetization data. For δ -Pu(4.3at%Ga), the first annealing stage observed in the resistivity is missing in the magnetization measurement, illustrating the different sensitivities of distinct measurement techniques to radiation damage.

Results and Discussion

While the effects of radiation damage are observable through the measurement of many different physical properties, the sensitivity of each property to such damage and the specific type of damage may vary. This is very effectively demonstrated in Figure 2, where isochronal annealing curves for α -Pu and δ -Pu(4.3at%Ga) are shown for both resistivity and magnetization measurements. In the case of α -Pu, the two measurements track one another quite closely, both in terms of features and in terms of the signal retained. However, for the δ -Pu specimen, the magnetization annealing curve is largely insensitive to the first annealing stage, which is revealed quite clearly in the resistivity data, where roughly three-quarters of the damage signal is annealed away. This is where interstitials become mobile, and close vacancy-interstitial pairs annihilate.

Isothermal resistivity measurements near 50 K are second order as expected for a feature dominated by vacancy interstitial recombination as opposed to single impurity channels such as interstitials becoming trapped by an impurity, or reaching a grain boundary. The relative insensitivity of the magnetic measurement in this temperature range suggests that interstitials are largely invisible to the magnetic measurement in the case of δ -Pu. The magnetic annealing curve does show a strong reduction in signal at Stage III, which occurs around 150 K in δ -Pu(4.3at%Ga) and is normally associated with vacancy migration. Here, roughly 60% of the magnetic signal is removed, while the impact on the resistivity is slight, indicating that the magnetic properties are strongly influenced by the vacancy concentration. Above this temperature, near 200 K, the fraction of the signal retained for both measurements overlaps again and follows a similar pattern to 300 K, which is where the damage signal in this specimen anneals away. This overlap comprises stages IV and V of radiation damage recovery, typically involving release of vacancies from traps and finally the dissolution of vacancy clusters.

Figure 3 shows the isochronal magnetic annealing curves for two stabilized δ -Pu alloys: the Ga stabilized specimen described above and a 19% Am disordered alloy, which remains FCC but has an expanded lattice relative to the Ga-stabilized alloy. In the dilute limit, the observed signal per α -decay is comparable in each specimen at 30–40 μ_B per α -particle. While the general features of the two annealing curves are similar, the onset of the first annealing stage occurs at a lower temperature in the Am alloy, suggesting that the interstitial migration energy decreases as the lattice expands. Similarly, the onset of stage III is considerably broadened relative to the δ -Pu(4.3at%Ga) specimen, becoming almost continuous with stage IV. This suggests that the migration energy of the vacancies varies with the local environment. Finally, full annealing in the PuAm alloy is about 50 K higher than in the δ -Pu(4.3at%Ga) case. This may be a reflection of the higher melting point of PuAm alloys and suggests that an isochronal annealing study of americium will accumulate significantly more radiation damage at room temperature than plutonium.

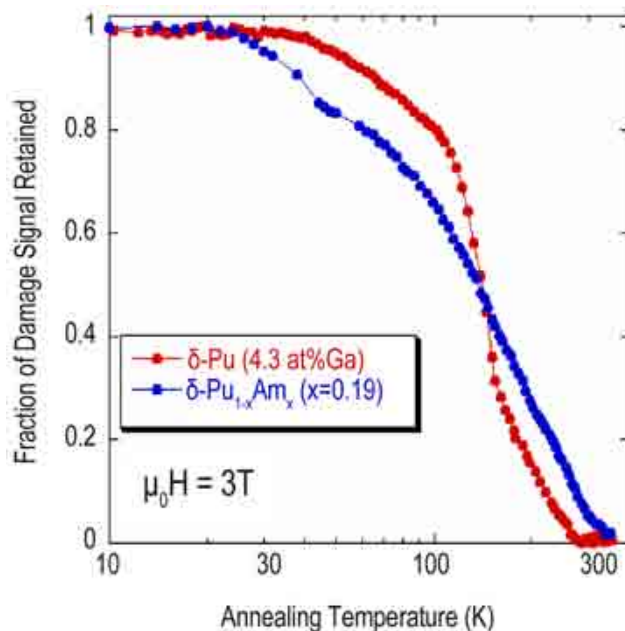


Figure 3. Isochronal magnetic annealing curves for two δ -Pu alloys. The general features are similar, although it appears that recovery begins at a slightly lower temperature for the expanded PuAm lattice and finishes at a slightly higher temperature.

Conclusions

Isochronal annealing studies of self-damage in Pu and Pu alloys show that different measurement techniques are sensitive to different damage products. Isothermal annealing measurements can extract the order and activation energies of the annealing stage. Because magnetization is very sensitive to stage III annealing, while resistivity is relatively insensitive, isothermal magnetic annealing may present an opportunity to obtain the vacancy migration energies in Ga stabilized δ -Pu. A comparison of isochronal annealing curves for δ -Pu alloys with different deltagens may provide further insight into the mechanisms underlying radiation damage in these materials.

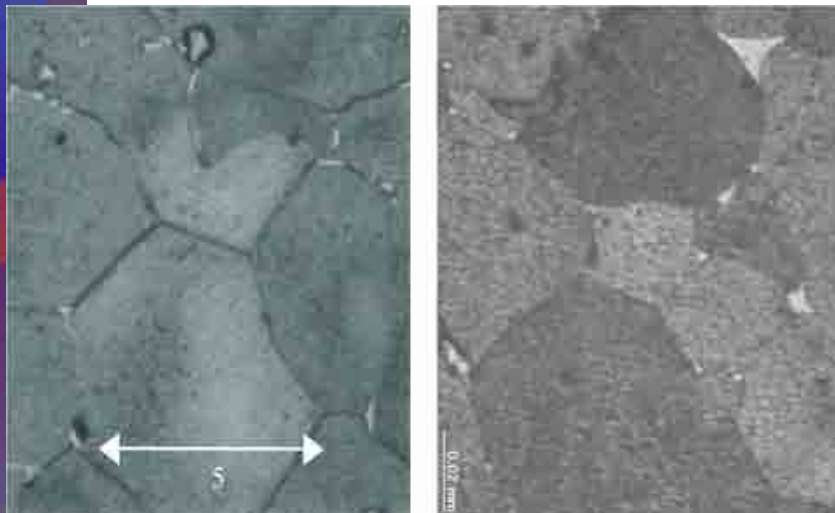
Acknowledgements

This work was performed under the auspices of the U.S. Department of Energy by Lawrence Livermore National Laboratory under Contract DE-AC52-07NA27344.

References

- [1] W. G. Wolfer, "Radiation Effects in Plutonium," in *Los Alamos Science*, ed. N. G. Cooper (Los Alamos, Los Alamos National Laboratory, 2000) **26**(1) 274 (2000).
- [2] A. Kubota, W. Wolfer, S. Valone, M. Baskes, "Collision cascades in pure δ -plutonium," *Journal of Computer-Aided Materials Design* **14**(3) 367 (2007).
- [3] S. K. McCall, M. J. Fluss, B. W. Chung, M. W. McElfresh, D. D. Jackson, G. F. Chapline, "Emergent magnetic moments produced by self-damage in plutonium," *Proceedings of the National Academy of Sciences of the United States of America* **103**(46) 17179 (2006).
- [4] M. J. Fluss, B. D. Wirth, M. Wall, T. E. Felter, M. J. Caturla, A. Kubota, T. D. de la Rubia, "Temperature-dependent defect properties from ion-irradiation in Pu(Ga)," *Journal of Alloys & Compounds*. **368** 62 (2004).
- [5] D. A. Wigley, "Effect of annealing on the resistivity of self damaged plutonium," *Proceedings of the Royal Society of London, Series A: Mathematical and Physical Sciences* **284** 344 (1964).

Deformation and Computational METHODS



Metallographic images are shown at ~700X of reference alloy and spiked alloy.

Dynamic loading can produce a wide variety of material responses, depending on both the type of materials and the intensity and rate of the loading. Three papers in this section report on observed deformation characteristics in metals and the pressure response of an f-electron compound. The other two present computational methods that enable investigation of electronic excitations, and damage and fracture resulting from dynamic loading. Podurets and coworkers compare crystal dislocation and microstructure in Cu resulting from quasi-isentropic loading with that of shock-wave loading. Kozlov and coworkers assess spall and shear fractures resulting from converging shock loading on spherical shells of iron and steel. Stegailov applies finite temperature density functional theory calculations to evaluate how electronic excitations would change interatomic bonding in a LiF crystal irradiated by a high-powered femtosecond laser. Mirmelstein and coworkers present pressure effects in the intermediate-valence compound CeNi, with implications for understanding actinide materials. Finally, Davydov and Piskunov present their cluster dynamics method, which describes the molecular dynamics of coarse grains, making it applicable to simulating continuum behaviors. Its capabilities are demonstrated with simulations of impact on, and penetration of, thick and thin aluminum plates.

John Aidun, Sandia National Laboratories, Albuquerque, New Mexico, USA

Section IV:

- IV-2 Structural Changes in Metals Under High-Rate Deformation (VNIIEF)
- IV-6 Spall and Shear Fractures in the Spherically Converging Shells of Iron and Steels: Measurements of Energy and Residual Strains (VNIITF)
- IV-12 DFT Studies of Electronic Excitation Effects: Crystal Lattice Stability, Non-Adiabatic Transitions (JIHT)
- IV-16 Study of the Volume-Collapse Phase Transitions in F-Electron Materials (VNIITF)
- IV-21 Method of Cluster Dynamics for Simulation of Dynamic Processes of Continuum Mechanics (VNIIEF)
- IV-30 Spiked Alloy Production for Accelerated Aging of Plutonium (LLNL)

STRUCTURAL CHANGES IN METALS UNDER HIGH-RATE DEFORMATION

A. M. Podurets, V. A. Raevsky,* M. I. Tkachenko,* A. N. Balandina,* I. N. Kondrokhina,* O. N. Ignatova,* A. I. Lebedev,* V. G. Khanzhin,[†] J. Petit,[‡] M. A. Zocher[◇]

*All-Russia Research Institute of Experimental Physics (VNIIEF),
Sarov, 607190, Russia

[†] Moscow Steel and Alloys Institute, Russia

[‡] CEG, Gramat, France

[◇] LANL, Los Alamos, NM, USA

Author Contact: am.podurets@gmail.com

Dislocation and twin structure parameters in Cu are studied in samples with different grain sizes after dynamic loading by quasi-isentropic and shock waves with use of optical and transmission electron microscopy and X-ray diffraction analysis.

Introduction

The most well-founded physical models, which describe the deformation of solids, should consider the deformation mechanism at the microlevel. In the strain rate and microstructure area of our interest, there are two such mechanisms, namely, dislocation slip and twinning.

Microstructure at shock loading of metals is determined by the processes that determine any deformation, including competition of both main plastic deformation mechanisms. The general tendency during dynamic deformation of metals having different crystal lattices is the increase in number of slip systems and initiation of twinning as a competitive process. Each of two mechanisms has particular features; therefore, each mechanism works at certain conditions. First of all, the mechanisms have different velocities. Twins spread at sound velocity; the dislocation velocities at quasi-static deformation are lower. Hence, the twinning mechanism has an a priori advantage at high-strain-rate phenomena.

The distinctive feature of metal microstructures after high-rate deformation is the presence of bands of localized deformation (BLD) inside the grains. During the optical microscope study, these bands are the system of parallel lines with an interval of several microns (Figure 1a). Though these bands have often been observed, the effect has not been not studied properly.

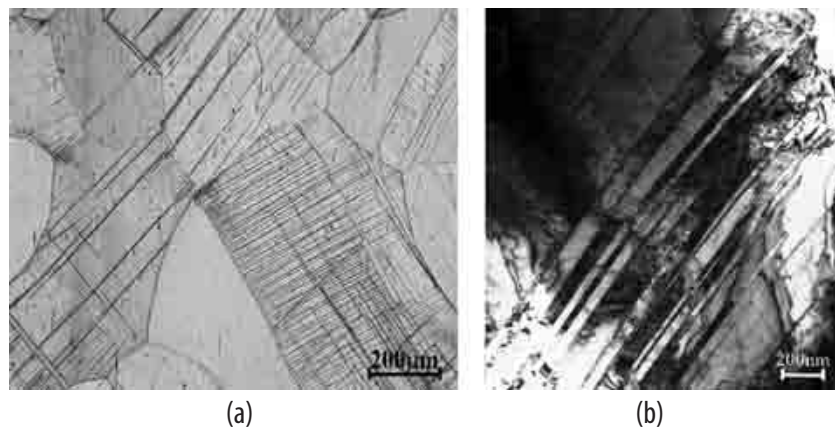


Figure 1. Bands of localized deformation in copper (a) $d \sim 200 \mu\text{m}$, optical microscope; (b) $d \sim 20 \mu\text{m}$, transmission electron microscope.

Experimental Results and Discussion

Samples of Cu M1 with different initial grain sizes ($d \approx 200$, 100, and 15 μm) were loaded by shock wave with decaying intensity (at entry into the sample, the shock amplitude was $P \approx 80$ GPa; at exit, 20 GPa) and recovered. Experiments were conducted at different initial temperatures of the samples, namely, $T \approx 20^\circ\text{C}$ and $T \approx 190^\circ\text{C}$.

The BLD were observed in all recovered samples at optical microscopic study, but the number of the bands depends on the experimental conditions. A parameter that characterizes BLD in the structure concentration of grains with BLD was used. Dependencies of grains with BLD concentration on pressure, initial temperature, and grain size are presented in Figure 2.

Looking at the curves in Figure 2, we can conclude that a grain size influences strongly on the probability of BLD formation. Also, we see the influence that temperature, namely, cooling, contributes to the increase of the BLD number. As for the interval between the bands, we see the tendency of its decreasing while pressure increases.

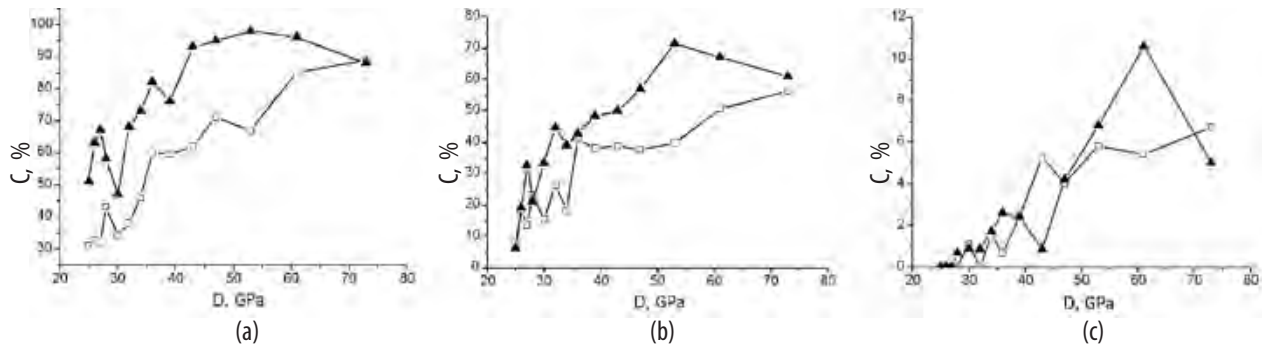


Figure 2. Dependence of grains with BLD concentration (C) on pressure in samples with different initial grain size (a – $d \approx 200 \mu\text{m}$, b – $100 \mu\text{m}$, c – $15 \mu\text{m}$). (□) – data for $T \approx 20^\circ\text{C}$, (▲) – for $T \approx 190^\circ\text{C}$.

Other experiments were done to clarify the influence of strain rate on BLD formation. A quasi-isentropic (shockless) wave was initiated in the sample. As far as it moved through the sample, the wave transformed into a shock wave, and the strain rate changed from $\sim 10^5 \text{ s}^{-1}$ at the surface to $\sim 10^8 \div 10^9 \text{ s}^{-1}$. The level of maximum pressure remained constant. Pressure amplitudes in these experiments were 20, 35, and 50 GPa. Using such a setup, fine-grain copper was studied ($d \approx 20 \mu\text{m}$).

Heterogeneous deformation (BLD) was revealed in the samples loaded to $P = 35$ and 50 GPa. Distribution of BLD-containing grains along depth of the samples is shown in Figure 3.

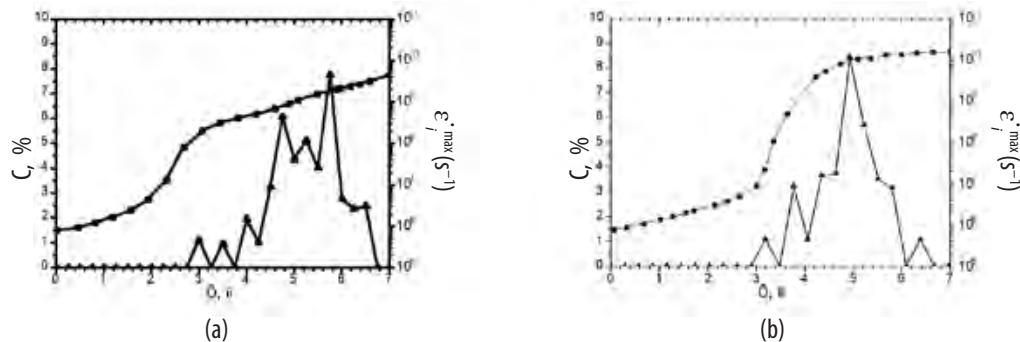


Figure 3. Dependence of grains with BLD concentration C (▲) and strain rate $\dot{\epsilon}_i^{\max}$ (●) on depth in samples with $d \approx 20 \mu\text{m}$, loaded to 35 GPa (a) and 50 GPa (b).

As shown in the figure, the BLD in both samples appears at depth about 3 mm (i.e., where the quasi-isentropic wave begins to transform to a shock wave). Close to the rare surfaces of the samples, the BLD number decreases to zero. Obviously, it is caused by the unloading effect.

Maximum concentration of grains with BLD in these experiments with 20 μm copper is almost the same as for 15 μm (Figure 2c) at the same pressures and significantly lower than for coarse grain (Figure 2a, b).

Thus, we can note following features of BLD formation in copper with different grain size:

- BLD are formed mainly in coarse grain copper.
- There is a threshold value for BLD formation of pressure and strain rate as well.
- When pressure grows (up to recrystallization effects), the number of BLD increases, and the interval decreases.
- When strain rate increases, the number of BLD increases.
- Lowering of temperature leads to an increase of BLD formation.

Considering the peculiarity of twin formation at high-rate deformation, the features mentioned above allow us to state that twinning is the mechanism that controls the BLD formation during shock loading.

Morphology of twin structure was studied using transmission electron microscopy. We can mark “thin” ($< 10\text{ nm}$) and “thick” ($\sim 100\text{ nm}$) twins. Thick twins with noncoherent boundaries can be “inherited” from the initial state of material. Another possibility is the model of amalgamation of twins for a long enough loading pulse suggested in [1].

Typical configuration is the grouping of twins into bands having width of several microns (Figure 1b). Obviously, these twin bands form the surface relief that we observe as BLD.

In the same samples, we measured dislocation density using the X-ray technique. Results are shown in Figure 4 in comparison with the twin density data. We see that with increasing of strain rate, both the dislocation density and twin density increase.

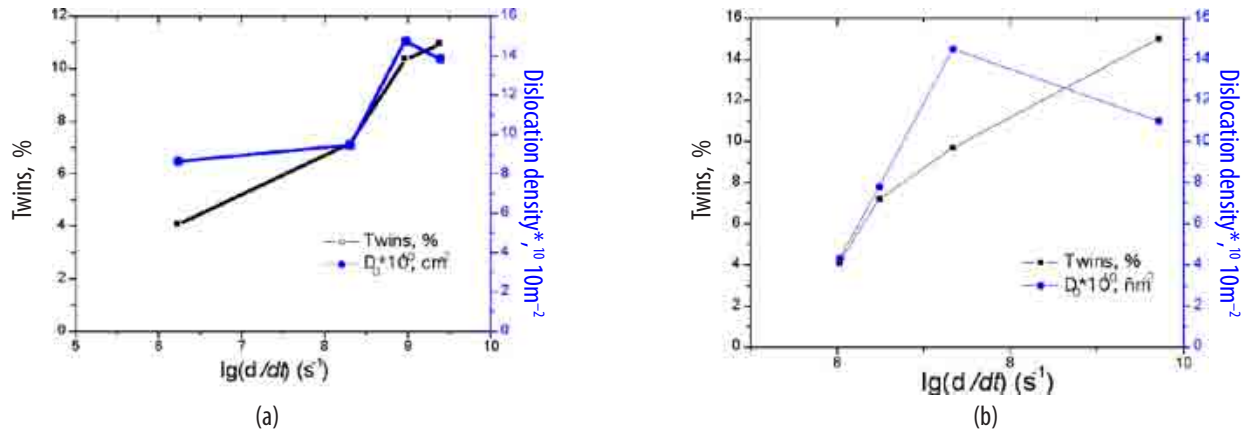


Figure 4. Dislocation and twin density vs. strain rate for Cu at 35 GPa (a) and 50 GPa (b).

Dislocation density was measured in copper with a grain size of 0.5 (ultra-fine grain) and 3 μm (Figure 5) at $P=30\text{-}60\text{ GPa}$. Results are shown in comparison with the quasi-static data in the strain-density coordinates.

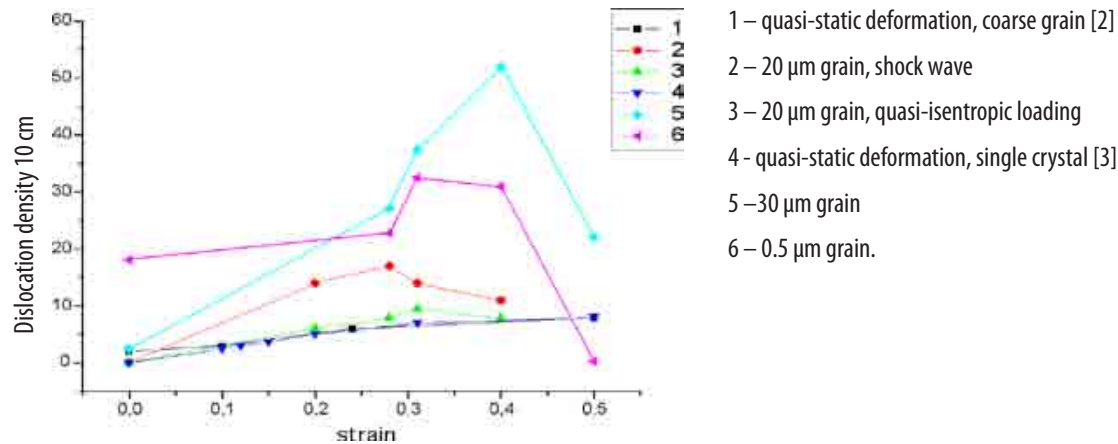


Figure 5. Dependence of dislocation density on strain in Cu with different grain sizes.

Obviously, the high-rate loading generates higher dislocation density in Cu than quasi-static deformation. The largest growth of dislocation density is demonstrated by fine grain 30 μm copper. The UFG copper, having the highest initial dislocation density, shows relatively low growth (less than two times). In all dynamically loaded samples, we see the maximum at $\varepsilon \sim 0.3\text{--}0.4$ (which corresponds to pressure of 30–50 GPa) followed by drop. We explain such a drop by dislocation annealing during the adiabatic compression. We obtain the most sharp decrease for UFG copper, since it has the most deformed and nonequilibrium structure. Thus, after $\varepsilon \sim 0.5$ ($P=60$ GPa), the dislocation density value decreases it almost to the value of annealed metal.

Conclusions

In pressure range of 20–50 GPa, twin formation in 20 μm copper occurs during both shock wave and quasi-isentropic loading at strain rate of $10^6\text{--}10^{10} \text{ s}^{-1}$. Above the certain pressure (> 20 GPa) and strain rate ($> 10^6 \text{ s}^{-1}$) threshold, deformation twins are grouping into bands, which, during the optical microscopic study, are observed like bands of localized deformation (BLD) with the typical interval of 2–15 μm . Below this threshold, deformation twins are spreading more uniformly in the metal. BLD formation depends on grain size, pressure, strain rate, temperature of the experiment.

Dislocation density in Cu with different grain size increases with pressure and strain rate increasing. Maximum value of dislocation density is reached in the range of 30–50 GPa followed by aging of defects during adiabatic heating.

Cu strengthening after the shock loading is defined by presence of twins in its structure (both grouped into BLD and spread uniformly) and by increasing of dislocation density as well.

References

- [1] S. Larouche, E. T. Marsh, D. E. Mikkola, "Strengthening effects of deformation twins and dislocations introduced by short duration shock pulses in Cu-8.7Ge," *Met. Trans.* **A12** 10 1777-1785 (1981).
- [2] M. Zehetbauer, T. Ungar et al. "Scanning X-ray diffraction peak profile analysis in deformed Cu-polycrystals by synchrotron radiation," *Acta Materialia* **47** 1053-1061 (1999).
- [3] M. Habermann, P. Klimanek, M. Motylenko, "Substructure development in cold rolled copper single crystals," *Materials Science and Engineering* **A324** 196-199 (2002).

SPALL AND SHEAR FRACTURES IN THE SPHERICALLY CONVERGING SHELLS OF IRON AND STEELS: MEASUREMENTS OF ENERGY AND RESIDUAL STRAINS

E. A. Kozlov, S. A. Brichikov, V. G. Vildanov, D. M. Gorbachev, D. T. Yusupov

All Russian Research Institute of Technical Physics (VNIITF)
456770 Snezhinsk, Chelyabinsk Region, Russia
Author Contact: E.A.Kozlov@vniitf.ru

Results of comparative explosive experiments on compression of recovered spherical shells of unalloyed iron and 30KhGSA and 12Kh18N10T steels with spall and shear fractures of different completeness are presented. Experimental results are of interest for verification and certification of modern strength models and multi-phase equations of state and also can be used to estimate the influence of rheological properties of the shell material both on dynamics of shell convergence and recompaction of the fractured material.

Introduction

Systematic experimental data are important (i) to verify and certify modern kinetic strength models of shear and spall strength of materials, multi-phase equations of state describing polymorphous, electron, and phase transformations in the shock and rarefaction waves, and (ii) to estimate how the explosion-products energy transform to the shells, as well as to analyze the character of recompaction of the shell material in the process.

Note that in the assumption of incompressibility of shell materials, dynamics of shells convergence is independent of rheological properties of materials and depends only on the relationship between the mass of the shell surface unit and the high explosive (HE) layer accelerating this shell. In the experiments under consideration, the steel shells cannot be taken as incompressible. Single spall or even multiple spall fractures occur in them under explosive loading. These fractures result from interaction of two groups of rarefaction waves. One group arises when the shock wave arrives at the free (internal) surface of the test shell. The second group propagates from the external surface of the shell on the side of the scattering explosion products. Interference of these rarefaction waves in the shell results in tensile stresses. If the material of the shell cannot withstand tensile stresses having certain amplitude and duration, then the spall layer separation or spall separation takes place in the shell (on the side of its internal surface).

The first spall is formed in the shell when the converging shock wave is reflected from its internal boundary for the first time (i.e., when the shell is still at the “high” radius). Being formed, the spall layer begins to move towards the center, thus spending its kinetic energy for the work of plastic deformation and heating. In shells of brittle materials in the process of convergence, the spall can fracture into individual fragments but already by the shear mechanism. Explosion products have no influence on the separated layer, since it is shielded by the nonfractured part of the shell. If the thickness of the HE spherical layer used for shell loading is not great enough, then explosion products quickly get unloaded in the free scatter, and the shell would stop in the course of convergence. If the scatter of explosion products from a thin HE layer is confined by a heavy casing with a small gap, which is installed above this HE layer, then one can ensure that the main part of the shell would catch up with the spall layer and can observe specifics and character of material recompaction for the shell fractured at the high radius in the process of its convergence to a smaller radius. Intense explosive loading of the shell or small spall strength of its material can lead to several subsequent spall fractures.

Reliable statement of the fact that spall fracture took place in the material of the spherically converging shell and, moreover, determination of the amount and actual thickness of spalled layers, as well as radii at which their external boundaries stop is a rather difficult methodical problem. Even the first setup of comparative explosive

experiments without confinement of explosion products scatter [1,2,3] is rather informative and useful both to verify calculation models of the spall and shear fractures, and to extend capabilities of systematic metallographic and electron-microscopic analysis of specifics in incipience and development of spall fractures in the material of recovered shells that stopped prior to focusing. These investigations at different structural levels allow better understanding of how structural and phase transformations and different design features of explosive devices influence incipience and development of fractures in the shell.

Comparative experiments with confined scatter of explosion products is an innovative experimental setup, since it allows (with a small gap between HE and the casing) one (i) to have in the shell, during the first reflection of the shock wave from the internal free surface, just the same spall fractures as in the first experimental setup and (ii) to further follow peculiarities in recompaction of the fractured shell material in the process of shell convergence to smaller radii. This experimental setup permits recovery of converged shells, measurements of their energy and residual strain, as well as systematic material science investigations.

The purpose of this work was to obtain comparative experimental data on specifics in spall and shear fractures of shells made of iron and some steels having almost similar densities under normal conditions but different equations of state, as well as strength characteristics under low- and high-rate deformation.

Results and Discussion

Consideration was given to spherical shells (49-mm nominal external diameter, 10-mm initial thickness, 380 g mass at density of 7.85 g/cm³) of unalloyed high-purity armco-Fe (215–300 μm grain size), steel 30KhGSA as received and after hardening to 35–40 HR_c hardness, austenitic steel 12Kh18N10T.

Note that unalloyed iron was chosen that has noticeable mechanical hardening and retains the capability for homogeneous deformation without localization to the highest critical deformations, in contrast to hardened steel 30KhGSA, which is prone to thermal softening and formation of adiabatic shear bands under high strain and high-rate deformation. It was selected because the behavior of this material is most studied in plane and spherically converging intense stress waves [1-7, 9-10]. Austenitic viscous steel has almost similar initial density and has no well-known α - ϵ -phase transformation observed in iron and steel 30KhGSA but has the γ - α' -martensite transformation in case of tensile stress occurrence [4,8].

The test spherical layer consisted of two parts connected with the help of a threaded joint. This layer was installed in turn into two sealing shells of steel 12Kh18N10T with the nominal thickness 4 and 7 mm, respectively. Then these shells were joined by means of electron-beam welding in vacuum and argon arc welding. Mutual orientation of equatorial joints in the test shell and the first (nearest to the test shell, internal) hermetically sealed casing was parallel. Joints of the internal and external sealing shells were mutually orthogonal. Orientation of joints, size of micro-gaps between shells (0.03–0.05 mm), and depth of weld penetration were thoroughly controlled.

Two types of spherical explosive devices were used for explosive loading of prepared mechanical assemblies having identical initial geometry, almost the same mass, and only one difference (i.e., the material of the internal spherical layer). The size, type of HE in the spherical layer, and the system of HE initiation were identical in all explosive experiments. The equatorial joint of HE was orthogonal to the equatorial joint of the external hermetically sealed casing. The only difference in these experiments was presence or absence of the external casing that confines the scatter of explosion products.

Size and type of HE, its initiation depended on the condition that developed spall and shear fractures shall be guaranteed in the material of investigated shells at high radii and that the spall layer (layers) shall stop in these shells prior to its focusing. Parameters of the external casing confining explosion products scatter were taken on the condition that the basic part of the shell will obviously catch up with the spall layer (layers) separated from the shell at high radii prior to or after focusing and that the compacted assembly will obviously be recovered under the second mode of loading. Cast iron was used as the material of the external casing.

Prior to and after explosive loading, weight and volume of the assembly being the test shell sealed in two jackets of steel 12Kh18N10T were determined by weighing in the air and in the distilled water with the help of analytic balance. The specially developed solid-state calorimeter was used to determine energy the explosion products imparted to the compressed assembly [2]. The compressed assemblies got into the calorimeter 25–30 sec after the explosion.

Quantitative data on the experimental setup of spherical explosive experiments and their basic results are given in Table 1. Note significant difference in residual energies of test assemblies after identical loading. Significant increase of residual energies is observed in the second experimental setup with explosion products scatter confined by the external casing. This is due to dynamic compaction of the material in the internal shell fractured at high radii in the process of shell convergence to the deep radius.

Table 1. Experiment results for explosive loading of shells of different materials with unconfined (I) and confined (II) explosion products scatter.

| Parameter | I | II | I | II | I | II |
|-----------------------------------------------------------------------------------|-------------------------|-----------------|------------------------------------|-----------------|----------------------------------|-----------------|
| Weight of plastic HE, g | 181.8 | 182.8 | 181.8 | 182.8 | 181.8 | 182.8 |
| in: | | | | | | |
| 5-mm thick spherical layer with $R_{HE}=40$ mm | 133.6 | 133.6 | 133.6 | 133.6 | 133.6 | 133.6 |
| in the initiating device | 48 | 48 | 48 | 48 | 48 | 48 |
| in detonation-transfer units | 0.2 | 1.2 | 0.2 | 1.2 | 0.2 | 1.2 |
| Assembly (shell in two hermitically sealed jackets) | | | | | | |
| Weight in the air and water (numerator / denominator), g: | | | | | | |
| prior to explosion | 1274.48 / 1097.89 | 1280.34/1103.79 | 1278.01/1101.34 | 1278.56/1101.68 | 1276.98/1100.08 | 1278.70/1101.85 |
| after explosion | 1274.23/1101.84 | 1280.05/1116.32 | 1277.70/1102.66 | 1278.27/1113.84 | 1276.92/1101.94 | 1278.35/1113.62 |
| External hermetically sealed jacket (steel 12Kh18N10T) | | | | | | |
| Dimensions, mm: | | | | | | |
| prior to explosion (diameter / thickness) | 69.65 / 6.7 | 69.65 / 6.7 | 69.69 / 6.8 | 69.65 / 6.78 | 69.69 / 6.79 | 69.65 / 6.7 |
| after explosion (diameter) | 69.10 | 67.93 | 68.02 | 69.45 | 68.06 | 67.93 |
| Relative change of diameter ($\Delta D/D_0$), % | 0.79 | 2.47 | 0.30 | 2.40 | 0.36 | 2.33 |
| Internal hermetically sealed jacket (steel 12Kh18N10T) with the test shell | | | | | | |
| Weight (in the air and water), g: | | | | | | |
| prior to explosion | 609.81 / 522.69 | 618.06 / 538.44 | 613.39 / 522.27 | 613.04 / 522.04 | 611.55 / 520.65 | 613.80 / 522.77 |
| after explosion | No data | No data | 613.36 / 525.04 | 612.90 / 533.26 | 611.55 / 523.23 | 613.80 / 533.58 |
| External diameter of the jacket / thickness, mm: | | | | | | |
| prior to explosion | No data | No data | 55.87 / 3.44 | 55.84 / 3.43 | 55.80 / 3.42 | 55.85 / 3.43 |
| after explosion | 55.04 | 53.43 | 55.29 | 53.42 | 55.42 | 53.55 |
| The test shell, material | Steel 12Kh18N10T | | Steel 30KhGSA (as received) | | Steel 30 KhGSA (hardened) | |
| Weight (in the air and water), g: | | | | | | |
| prior to explosion | 379.5 / – | 389.95 / 328.65 | 382.81 / 321.72 | 382.55 / 321.47 | 382.23 / 321.15 | 383.30 / 322.16 |
| after explosion | 379.5 / 324.48 | 389.90 / 339.66 | 382.81 / 324.45 | 382.54 / 332.52 | 382.23 / 324.57 | 383.30 / 332.58 |
| External diameter of the shell / thickness, mm: | | | | | | |
| prior to explosion | 48.77 / 10.2 | 48.95 / 10.5 | 48.90 / 10.45 | 48.89 / 10.44 | 48.89 / 10.45 | 48.89 / 10.44 |
| after explosion | 47.35 | 45.81 | 48.16 | 45.57 | 47.96 | 45.96 |
| Relative change of diameter ($\Delta D/D_0$), % | 2.91 | 6.41 | 1.51 | 6.44 | 1.90 | 6.04 |
| Energy accumulated by the assembly, kJ | 65.6 | No data | 72.9 | 85.5 | 78.0 | 93.7 |
| Relative values of energies | 0.70 | – | 0.78 | 0.91 | 0.83 | 1 |

After removal of two jackets of steel 12Kh18N10T, shells recovered during spherical compaction were cut by electrosparking along the meridional plane going through the poles (south and north) and through the shell's top point found from above in the gravity field during cooling (Figure 1 and 2).

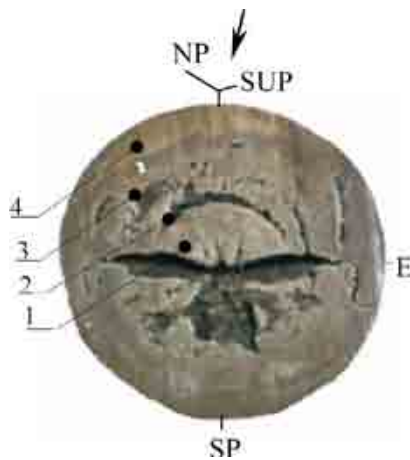


Figure 1. Meridional section of the armco-Fe shell after spherical explosive compression without the external casing that confines explosion products scatter NP, SP – north and south poles of the test spherical shell; E – equator or equatorial joint of spherical layer members; SUP – upper point of the shell when cooling in the gravity field. Arrow shows the direction of gravity field acceleration. 1 – first spall; 2 – second spall; 3 – third spall; 4 – peripheral part of the shell, which remained unfractured.

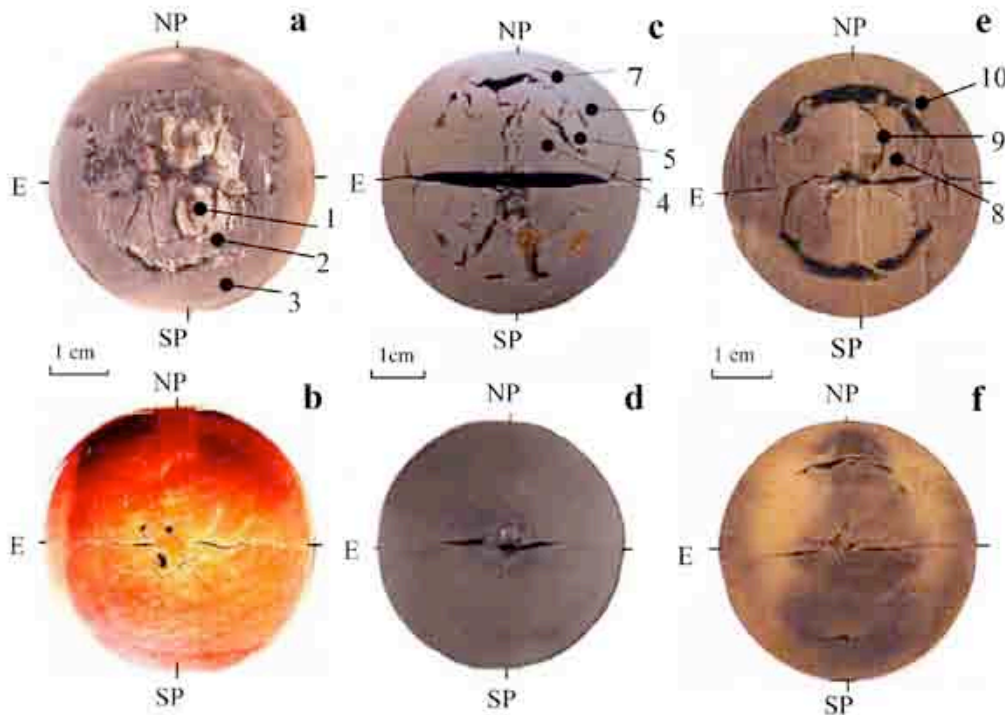


Figure 2. Meridional section of shells for austenitic steel 12Kh18N10T (a, b), as-received 30KhGSA steel (c, d) and 30KhGSA 35-40 HRc 35-40 steel (e, f) after spherical explosive compression in loading modes I and II with unconfined (a, c, e) and confined (b, d, f) explosion products scatter.

1 – first spall; 2 – second spall; 3 – unfractured peripheral part of the shell; 4 – first spall; 5 – second spall; 6 – peripheral part of the shell with the local spall fracture 7; 8 – spall layer formed under explosive loading; 9 – a trajectory of maximum shear stress locations, along which the spall layer gets fractured; 10 – unfractured peripheral part of the shell.

The viscous character of spall fracture was observed in the shell of Armco-Fe (Figure 1) and austenite steel 12Kh18N10T (Figure 2). Shells of the steels fractured at high radii are well compacted into the sphere in conditions of explosive compaction with confined free scatter of explosion products in contrast to shells of as-received steel 30KhGSA and especially in the hardened state (Figure 2). Areas with incomplete compression are revealed in

polar zones of the shell made of prehardened steel 30KhGSA. All test shells are noted to have a different character of the spall and shear fractures in polar zones and in the area of equatorial joint of members forming the spherical layer being investigated. This is associated both with the initial structure present in the material of test ingots, and with small gaps in the threaded joint, which though cause transformation of the shape and parameters of the stress pulse that approaches the internal boundary of the shell in this zone. In its turn, this causes changes of spall fracture, right up to vanishing, in the area beneath the thread. After chemical or ion etching of the meridional section, measurements of distribution of hardness $H_v(r, \theta)$ and microhardness $H_\mu(r, \theta)$ along radius r and by polar angle θ in shells of armco-Fe and steel 30KhGSA revealed occurrence of three concentrically arranged zones and the following:

- Zone of high-rate deformation of ferrite in the initial α -phase; this zone is adjacent to the external boundary of the compressed shell.
- Zone of high-rate deformation of ferrite in the range of the reversible α - ϵ -phase transformation; this zone is found in layers at the deeper radius.
- Zone of the recrystallized structure for the first mode of explosive loading with unconfined scatter of explosion products or zone of local melting for the second mode of explosive loading with explosion products scatter confined by the external casing; this zone is close to the center.
- Detail results of the metallographic, as well as SEM and TEM examinations of each iron and steel shell after their explosive loading will be presented in the follow-on work.

Conclusion

Experiments on spherical explosive compression and follow-on recovery of hermetically sealed shells with the different-extent spall and shear fractures are proposed and implemented. Different character of spall and shear fractures, as well as of the material compaction of shells fractured at high radii, was demonstrated by the example of shells of unalloyed high-purity iron, steel 30KhGSA as received and hardened up to 35–40 HR_c, as well as austenite steel 12Kh18N10T.

Spherical explosive experiments with the guaranteed recovery of loaded shells and their calorimetric measurements directly after loading with the follow-on measurement of residual strain and metallographic and electron-microscopic analysis are of interest from the standpoint of monitoring constancy of dynamic mechanical properties and characteristics, that is, shear and spall strength of materials in case of changes in the technologies of their fabrication or in the process of long-term storage after their fabrication.

Similar experiments on the spherical explosive compression of even thinner shells in systems with $R_{HE}=40$ and 110 mm are of interest for verification and certification of kinetic strength models and multi-phase equations of state used in modern 1-D, 2-D, and 3-D program complexes.

References

- [1] E. A. Kozlov, V. I. Tarzhanov, V. G. Vildanov, V. M. El'kin, "Explosive experiments for studying dynamic properties of transition metals, some actinides, and alloys on their basis," in *6th US-Russian Workshop on Fundamentals of Pu Science* (Livermore, CA, University of California, July 14-15, 2006) pp. 26-30.
- [2] E. A. Kozlov, S. A. Brichikov, V. G. Vildanov, D. M. Gorbachev, D. T. Yusupov, "Spall and shear fractures in the spherically converging shells of iron and steels. Measurements of energy and residual strains," *Russ. J. Deformation and Fracture of Materials* **11** 2-10 (2008).
- [3] L. M. Barker and R. E. Hollenbach, "Shock wave study of the α - ϵ phase transition in iron," *J. Appl. Phys.* **45** [11] 4872-4887 (1974).
- [4] E. A. Kozlov, "Shock adiabat features, phase transition macrokinetics, and spall fracture of iron in different phase states," *High Pressure Research* **10** 541-582 (1992).
- [5] J. C. Boettger, D. C. Wallace, "Metastability and dynamics of the shock-induced phase transition in iron," *Phys. Rev.* **B55** [5] 2840-2849 (1997).
- [6] E. A. Kozlov, I. V. Telichko, D. M. Gorbachev, D. G. Pankratov, A. V. Dobromyslov, N. I. Taluts, "On the metastability and incompleteness of the α - ϵ phase transformation in unalloyed iron under the effect of threshold loading pulses: Specific features of the deformation behavior and structure of armco iron," *Phys. Met. & Metall. (Engl transl.)* **99** 3 300-313 (2005).
- [7] L. C. Chhabildas, W. D. Reimhart, "Dynamic properties of AerMet 100 steel to 25 GPa," in *Proc. 7th Int. Conf. Mechanical and Physical Behaviour of Materials under Dynamic Loading* (Porto, Portugal, 2003) pp. 76-771.
- [8] A. N. Dremin, A. M. Molodets, A. I. Melkumov, A. V. Kolesnikov, "On anomalous increase of steel spall strength and relationship to martensitic transformation," in *Shock-Wave and High-Strain-Rate Phenomena in Metals (EXPLOMET-1990)* (New York–Basel–Hong Kong, Marcel Dekker, Inc., 1992) pp. 751-757.
- [9] E. A. Kozlov, A. V. Zhukov, "Phase transitions in spherical stress waves," in *High Pressure Science and Technology* (Colorado Springs, Colorado 1993, Proc. Conf. – New York: American Institute of Physics, 1994) pp. 977-980.
- [10] G. V. Kovalenko, E. A. Kozlov, A. V. Petrovtsev, "On energy cumulation and completeness of explosive product energy transference at explosive compression of spheres made of unalloyed iron and steels 30KhGSA and 12Kh18N10T," in *Int. Conf. SWCM* (St. Petersburg, Russia, 2002) pp. 236-237; in *Proceedings of VIII Khariton Sci. Talks* (Sarov, RFNC–VNIIEF, 2007) pp. 129-136.

DFT STUDIES OF ELECTRONIC EXCITATION EFFECTS: CRYSTAL LATTICE STABILITY, NON-ADIABATIC TRANSITIONS

V. V. Stegailov

Joint Institute for High Temperatures (JIHT)
Russian Academy of Sciences, Moscow, 125412 Russia
Author Contact: stegailov@ihed.ras.ru

The density functional theory (DFT) is used for modeling of two different cases of electronic excitation. The finite temperature DFT approach is deployed for description of the two-temperature system of hot electrons and cold lattice that is formed after ultrafast energy deposition. The lattice stability and the interatomic bonding at elevated electronic temperatures are studied for LiF crystal. The restricted open-shell Kohn-Sham DFT method is deployed for description of the molecular dynamics in the first excited singlet state. The radiationless decay of the N-methylformamide is simulated using the semiclassical approach of Tully for surface hopping.

Introduction

This paper presents the ab initio computational studies based on the DFT method that has been recently started in our group (the results of the electrical double layer DFT simulations targeted at perspective supercapacitors remain beyond the scope of this paper).

Crystal Lattice Stability of LiF with “Hot” Electron Subsystem

Modern technology allows unprecedentedly ultrafast energy depositions into condensed matter, posing new challenges for theory and computer simulation. For example, the terawatt femtosecond laser facilities produce powerful laser pulses of a much shorter duration than phonon periods. The electromagnetic field generates strong excitations in the electron subsystem of solids that quickly thermalize and result in a two temperature system. The change of the electron distribution can be nearly instantaneous in comparison with the nuclear motion times. Thus, the crystal lattice experiences a rapid change in the effective potential energy landscape. The possible result can be the loss of crystal lattice stability and its amorphization (so called *nonthermal melting*) before the energy is actually transferred into the lattice due to the electron-phonon scattering (Figures 1 and 2).

Figure 1. Electron density of states for fcc LiF crystal at different electron temperatures: $T_e=0$ (black) and $T_e=3.2\text{eV}$ (blue). The corresponding Fermi-Dirac distributions of occupancies are shown as well.

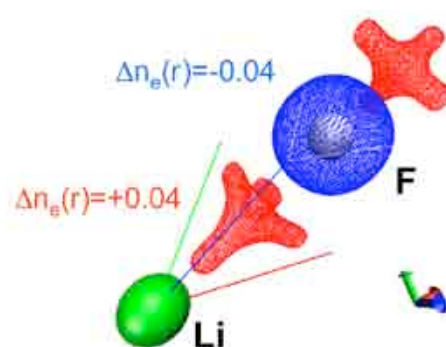
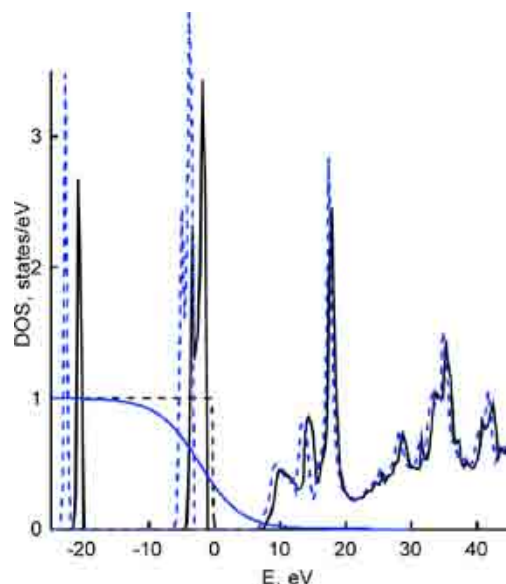


Figure 2. The unit cell of the LiF fcc lattice is shown (the green sphere is Li atom, the grey sphere is F atom). The wireframe surfaces show the surfaces of the constant value for the difference in the electron density at $\Delta n_e = n_e(r)|_{3.2\text{eV}} - n_e(r)|_{0.0\text{eV}}$: $\Delta n_e = -0.04$ (blue) and $\Delta n_e = +0.04$ (red).

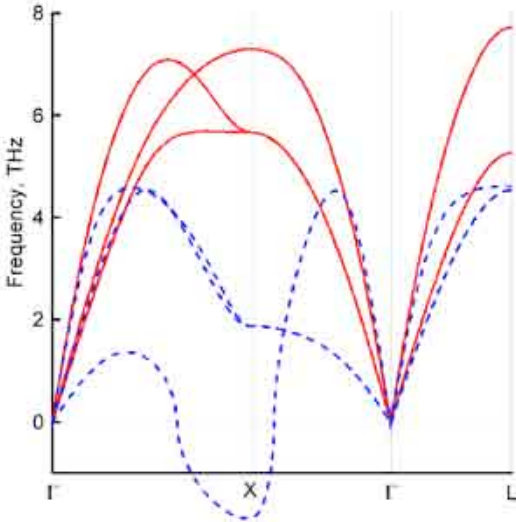


Figure 3. The acoustic branches of the phonon dispersion dependencies in fcc LiF lattice at different electron temperatures: $T_e = 2.0$ (red) and $T_e = 3.2$ eV (blue).

The theoretical framework deployed for this work is based on the finite temperature density functional theory (FT-DFT). The original DFT approach to finding the ground state of a many-electron system in the external potential was extended to finite temperatures treating the electronic excitations in the averaged statistical fashion (Mermin, 1965). This approach was applied in the work of Alavi et al. [1] for ab initio molecular dynamics (MD) calculations. The influence of the finite temperature electron distribution on dynamics of nuclei is manifested in the fact that the effective potential energy landscape along with the Hellmann-Feynman forces is determined by the dependence of the free energy of electron subsystem on nuclei positions, rather than on its ground state energy. The accompanying use of the (free energy) Born-Oppenheimer approximation for nuclear motion means that the electronic state evolves with time at a given temperature under the inclusion of incoherent electronic transitions. This model is quite reasonable if the relaxation time scale of the electron subsystem is much shorter than the electron-phonon relaxation times.

This approach, sometimes referred to as the free energy molecular dynamics (FEMD), was applied to study different aspects of the elevated electron temperature on lattice stability. The FEMD simulation of laser heated Si [2] showed that the presence of a large concentration of excited electrons weakens the covalent bonds of the crystal, so that under the action of this modified interaction the system melts. A more subtle analysis in the same theoretical framework was applied to the study of the specific phonon mode softening in laser-excited tellurium [3]. Two different regimes of electronic relaxation and hence band structure filling, corresponding to two different time scales of the electron-hole recombination rate, were considered: (i) where the conduction-band electrons and valence-band holes are in chemical equilibrium (i.e., rapid electron-hole recombination) and hence share a single chemical potential; (ii) where chemical equilibrium between valence and conduction-band carriers is not established (i.e., slow electron-hole recombination), and so they have two separate chemical potentials.

To rigorously quantify the effect of the electronic excitation on the potential energy surface, the evolution of the phonon spectrum as a function of the electronic temperature up to 6 eV was studied for three representative systems: a semiconductor, Si; a free-electron-like metal, Al; and a noble metal, Au [4]. The phonon spectra analysis showed that whereas for silicon the lattice becomes unstable through a transverse acoustic phonon instability when electron temperature is increased, metals tend to become more stable, with an increasing of the Debye temperature, elastic constants, and a higher melting temperature. This effect was shown to be small for free-electron-like metals such as aluminum, but appears to become large for a noble metal like gold. This fact is attributed in [4] to the influence of the localized electrons that participate in bonding.

In this section, we use FT-DFT for the study of LiF crystal stability after excitation of the electronic subsystem. This study is motivated by the recent results [5] concerning small ablation threshold caused by picosecond X-ray laser irradiation.

Description of the Model and Results

FT-DFT calculations were performed using the VASP package [6] based on plane wave basis set representation. The 2s and the 2p electrons were treated as valence electrons for Li and F respectively. Projector augmented-wave method pseudopotentials were used for effective description of the nuclei and core electrons [7]. The general gradient approximation (GGA) was used for the exchange and correlation contribution to the total energy. The small displacement method [8] was used for the calculation of the acoustical branches of the phonon dispersion dependencies.

The rise of the electronic temperature results in the prominent changes in the electronic band structure of the crystal (see Figure 1). The electron density is redistributed in a way that impose the covalent features to the ionic bonding in the fcc LiF crystal (see Figure 2). The change of the effective interatomic potential is manifested in the decrease of the mechanical stability of lattice. Figure 3 shows that the lattice remains stability at electronic temperature of 2.0 eV. However, at 3.2 eV, the soft acoustical phonon mode is present that implies the loss of mechanical stability of the fcc structure and the possibility of nonthermal melting. The GGA DFT description of LiF is known to underestimate the large band gap of this insulator. That is why the values of electronic temperature have more qualitative than quantitative meaning.

These calculations were performed under the assumption that the electrons in the conduction band and the holes in the valence band are characterized by the same chemical potential. However, the rate of recombination in LiF may be sufficiently slow, and the more adequate description should include different two chemical potentials for the electrons and the holes [3]. The effects of electronic excitation on mechanical stability in this case are the aim of future investigations.

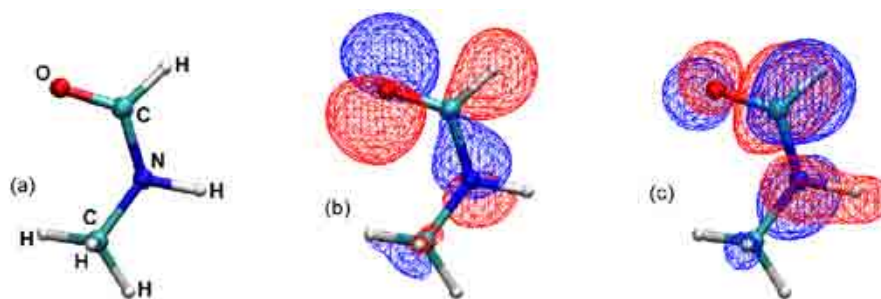


Figure 4. The visualization of the molecular orbitals of N-methylformamide molecule: a – molecular structure, b – highest occupied molecular orbital for S_0 , c – single electron orbital for S_1 .

Molecular Dynamics with Nonadiabatic Transitions: Radiationless Decay of N-methylformamide

The successful deployment of the DFT method for the description of the ground state of various molecular systems stimulated the attempts for using the same methodology for modeling of excited states. Photochemical reactions are of the most important relevant applications. The wide class of photoreactions of organic molecules occurs in the first excited singlet (S_1) or the lower triplet (T_1) states. Other energy levels usually have much smaller lifetime. For the DFT calculations of the S_1 potential energy surface, the restricted open-shell Kohn-Sham method (ROKS) was developed [9]. It is emphasized in [9] that this approach is heuristic, and its deployment is based on the successful description of experimental data for molecules in S_1 excited states.

The calculation of the energy of the vertical excitation into the S_1 state for the N-methylformamide molecule gives the value ~ 7.8 eV that is close to the experimental data 7.1–7.2 eV [10]. Figure 4 illustrates the one-electron orbitals of the ground and S_1 states. Figure 2 illustrates the molecular dynamics trajectory of the radiationless decay of the S_1 excited state that is calculated using the semiclassical surface hopping approach of Tully [11] implemented using the ROKS method [12] in the CPMD package (CPMD V3.13 Copyright IBM Corp 1990–2008, Copyright MPI fuer Festkoerperforschung Stuttgart 1997–2001).

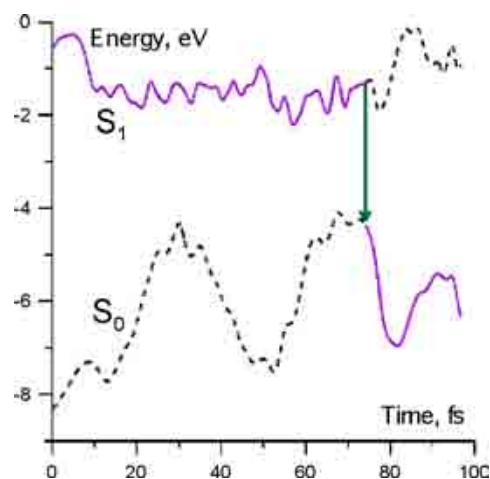


Figure 5. System energy as a function of time for a single molecular-dynamics trajectory of the radiationless decay process of the N-methylformamide molecule.

Conclusions

The excitation of the electronic subsystem results in the loss of mechanical stability of the fcc LiF lattice that is manifested as an appearance of the soft acoustic phonon mode. The corresponding redistribution of the electronic density implies that the originally strongly ionic interatomic interaction becomes more of covalent character with the rise of electronic temperature.

DFT based approaches allow the description of the first excited singlet state. The S1 excitation energy for the N-methylformamide molecule is in good agreement with experimental data. The corresponding model of the radiationless decay is built using the semiclassical surface-hopping approach implemented the CPMD package.

Acknowledgements

This work is partially supported by the RFBR grant 09-08-01116, RAS programs #5, 12 and Sandia National Laboratories under the U.S. DOW/NNSA Advances Simulation and Computing program. I am indebted to Nikos Doltsinis for his advices concerning nonadiabatic molecular dynamics and the CPMD package. Sandia is a multi-program laboratory operated by Sandia Corporation, a Lockheed Martin Company, for the United States Department of Energy under Contract DEAC04-94AL85000.

References

- [1] A. Alavi, J. Kohanoff, M. Parrinello, D. Frenkel, "Ab initio molecular dynamics with excited electrons," *Phys. Rev. Lett.* **73** 2599-2602 (1994).
- [2] P. L. Silvestrelli, A. Alavi, M. Parrinello, D. Frenkel, "Ab initio molecular dynamics simulation of laser melting of silicon," *Phys. Rev. Lett.* **77** 3149-3152 (1996).
- [3] P. Tangney, S. Fahy, "Density-functional theory approach to ultrafast laser excitation of semiconductors: Application to the A1 phonon in tellurium," *Phys. Rev. B* **65** 54302 (2002).
- [4] V. Recoules, J. Cl  rouin, G. Z  rah, P. M. Anglade, S. Mazevet, "Effect of intense laser irradiation on the lattice stability of semiconductors and metals," *Phys. Rev. Lett.* **96** 55503 (2006).
- [5] N. A. Inogamov, A. Ya. Faenov, V. A. Khokhlov, V. V. Zhakhovskii, Yu. V. Petrov, I. Yu. Skobelev, K. Nishihara, Y. Kato, M. Tanaka, T. A. Pikuz, M. Kishimoto, M. Ishino, M. Nishikino, Y. Fukuda, S. V. Bulanov, T. Kawachi, "Spallative ablation of metals and dielectrics," *Contrib. Plasma Phys.* (submitted)
- [6] G. Kresse, J. Furthm  ller, "Efficient iterative schemes for ab initio total-energy calculations using a plane-wave basis set," *Phys. Rev. B* **54** 11169 (1996).
- [7] G. Kresse, D. Joubert, "From ultrasoft pseudopotentials to the projector augmented-wave method," *Phys. Rev. B* **59** 1758 (1999).
- [8] D. Alf  , "PHON: A program to calculate phonons using the small displacement method," *Comp. Phys. Comm.* in press (2009).
- [9] I. Frank, J. Hutter, D. Marx, M. Parrinello, "Molecular dynamics in low-spin excited states," *J. Chem. Phys.* **108** 4060 (1998).
- [10] K. Kaya and S. Nagakura, "Vacuum ultraviolet absorption spectra of simple amides," *Theor. Chim. Acta.* **7** 117 (1967).
- [11] J. C. Tully, "Molecular dynamics with electronic transitions," *J. Chem. Phys.* **93** 1061 (1990).
- [12] P. R. L. Markwick, N. L. Doltsinis, "Ultrafast repair of irradiated DNA: Nonadiabatic ab initio simulations of the guanine-cytosine photocycle," *J. Chem. Phys.* **126** 175102 (2007).

STUDY OF THE VOLUME-COLLAPSE PHASE TRANSITIONS IN F-ELECTRON MATERIALS**A. V. Mirmelstein,* E. S. Clementyev,† O. V. Kerbel**** All Russian Research Institute of Technicial Physics (NIITF)
456770, Snezhinsk, Chelyabinsk Region, Russia

† ISSSP, Russian Research Center “Kurchatov Institute,” Moscow 123182 Russia

Author Contact: mirmelstein@mail.ru

We present recent results of the study of pressure effects in the intermediate-valence CeNi compound and demonstrate that the approaches developed to analyze the behavior of CeNi as a function of either chemical or external pressure can be applied for better understanding of actinides including plutonium. In particular, we briefly discuss the concept of multiple intermediate valence in plutonium to explain sharp variation of the Pu atomic volume as compared to the volumes of its neighbors in the actinide series and Pu magnetic properties. Possible directions of further investigations of basic properties of actinide materials are also discussed that could be of interest for Russia-US collaboration in this scientific field.

Introduction

In spite of rather long investigation, the nature and mechanisms of volume-collapse first-order phase transitions in *f*-electronic materials are still widely debated. The $\gamma \rightarrow \alpha$ transition in Ce metal is an excellent example. According to Manley et al. [1], the dominant contribution to the transition entropy in $\text{Ce}_{0.9}\text{Th}_{0.1}$ comes from magnetic excitations (spin fluctuations and crystal field). However, according to [2], in pure Ce metal about a half of transition entropy is related to lattice vibrations. A similar situation is reported for Pu metal [3], in which only a quarter of the transition entropy between α - and δ -phases can be associated with phonons. The origin of the rest of the entropy remains hypothetical. Obviously, the physics of *f*-electronic materials cannot be completely understood until such transitions are comprehensive explained.

This paper presents the results of a study of pressure effects in CeNi. This compound was chosen for several reasons. First, CeNi is well known as a typical intermediate-valence (IV) system. Second, the phonon spectrum and the spectrum of magnetic excitations in CeNi are known from inelastic neutron scattering experiments. Third, the pressure-induced first-order phase transition was found in CeNi, which is accompanied by a volume jump of $\sim 6\%$. The features of this transition are studied rather weakly. Finally, due to such an important parameter as the electronic specific heat coefficient, CeNi resembles the stabilized δ -phase of Pu.

We show that analysis of CeNi properties as a function of pressure proved to be useful not only to demonstrate its similarity to δ -Pu, but to emphasize the difference that leads to the idea of multiple intermediate valence (MIV) in plutonium. We show that using the MIV model, it is possible to quantitatively describe some important parameters both of α - and δ -Pu. We end with a discussion of possible directions of further investigations of the actinide basic properties.

Results and Discussion**Pressure Effects in CeNi**

We performed a series of experiments to study effects of chemical and external pressure on the properties of CeNi [4,5]. In 1985, Gignoux and Voiron found pressure-induced first-order structural phase transition in CeNi and determined its phase *P-T* diagram up to 0.5 GPa and 150 K [6]. Using neutron diffraction and magnetic measurements, we extended the phase diagram up to ~ 2 GPa and 300 K and showed that only two CeNi phases

exist within this pressure-temperature domain (i.e., the orthorhombic ambient-pressure and the tetragonal high-pressure ones [5]). The volume jump due to transition at $T = 300$ K is as high as $\Delta V/V = [V_{300\text{ K}}(P=0) - V_{300\text{ K}}(P=5\text{ GPa})]/V_{300\text{ K}}(P=0) = 6.5\%$.

Measurements of specific heat and magnetic susceptibility are very informative for quantitative analysis of pressure effects in the IV systems. The IV regime is characterized by a significant degree of the f electrons delocalization and by a significant deviation of the f -shell valence from an integer value. To describe the IV states one can introduce a parameter ϵ_f ($-1 \leq \epsilon_f \leq 1$) that characterizes a fraction of the electron passed from the f shell to the conduction band ($\epsilon_f > 0$), or a fraction of the electron passed from the conduction band to the f shell ($\epsilon_f < 0$) [7]. "Electronic" configuration ($\epsilon_f > 0$) realizes in Ce, which corresponds to fluctuations between the magnetic Ce^{3+} state and the "empty" Ce^{4+} state. "Hole" configurations ($\epsilon_f < 0$) are realized in such valence-unstable ions as Sm and Yb fluctuating between the 3+ and 2+ states. $|\epsilon_f|$ measures deviation of the ion valence from the integer value corresponding to magnetic configuration of the ion. The ion valence v can be expressed as $v = 3 + \epsilon_f$. Fractional population of magnetic configuration $\langle n_f \rangle = 1 - |\epsilon_f|$ is an important parameter that determines the state of the IV system and characterizes its magnetic properties.

For quantitative analysis of specific heat and magnetic susceptibility data, one can use Fermi-liquid expressions for electronic specific heat coefficient and low-temperature magnetic susceptibility $\chi(0)$ for Kondo-systems [7]:

$$\gamma = N_A \pi^2 k_B^2 \langle n_f \rangle \frac{1}{3E_0} \frac{N-1}{N} \quad (1)$$

$$\chi(0) = N_A \mu_{\text{eff}}^2 \langle n_f \rangle \frac{1}{3E_0}, \quad \mu_{\text{eff}}^2 = g^2 \mu_B^2 J(J+1). \quad (2)$$

Parameters of this simple model are the typical energy scale (Kondo energy) E_0 , the fractional occupation of the magnetic f -shell configuration $\langle n_f \rangle$, and the magnetic degeneracy of the ground state f -multiplet N . For the Ce^{3+} ion the total angular momentum $J = 5/2$, and N , as an effective parameter, can take any value between 2 and 6.

Besides, note that the energy scale E_0 and fractional occupation $\langle n_f \rangle$ are not independent. For an almost integer valence of the f ion, close to 3+, the regime of heavy fermions with small Kondo energies is implemented in the system. In the IV regime, the valence differs from an integer corresponding to increasing $|\epsilon_f|$ and decreasing $\langle n_f \rangle$. There exists a simple empirical relation between $\langle n_f \rangle$ and E_0 that holds with reasonable accuracy for the Ce- and Yb based Kondo-systems at $0.95 > \langle n_f \rangle > 0.7$ [7]:

$$\langle n_f \rangle = 1 - 0.00523(\text{meV}^{-1})E_0 \quad (3)$$

Figure 1 shows that Sommerfeld coefficient γ as a function of E_0 , which increases with increasing chemical pressure in CeNi, varies in accordance with relations (1) and (3). Moreover, the values of γ , recalculated from the values of $\chi(0)$ according to (1) and (2), are found to be close to the experimental ones for the same compositions. Thus, we conclude that relations (1) to (3) are valid for CeNi under chemical pressure. Figure 1 shows that the behavior of CeNi under chemical pressure is dominated by "Kondo physics." Therefore, assuming the values of γ and $\chi(0)$ to be known from the experiment, we can estimate variation of Kondo energy E_0 , fractional occupation $\langle n_f \rangle$, and valence of the Ce ions $v = 3 + \epsilon_f$ as a function of pressure or variation of chemical composition.

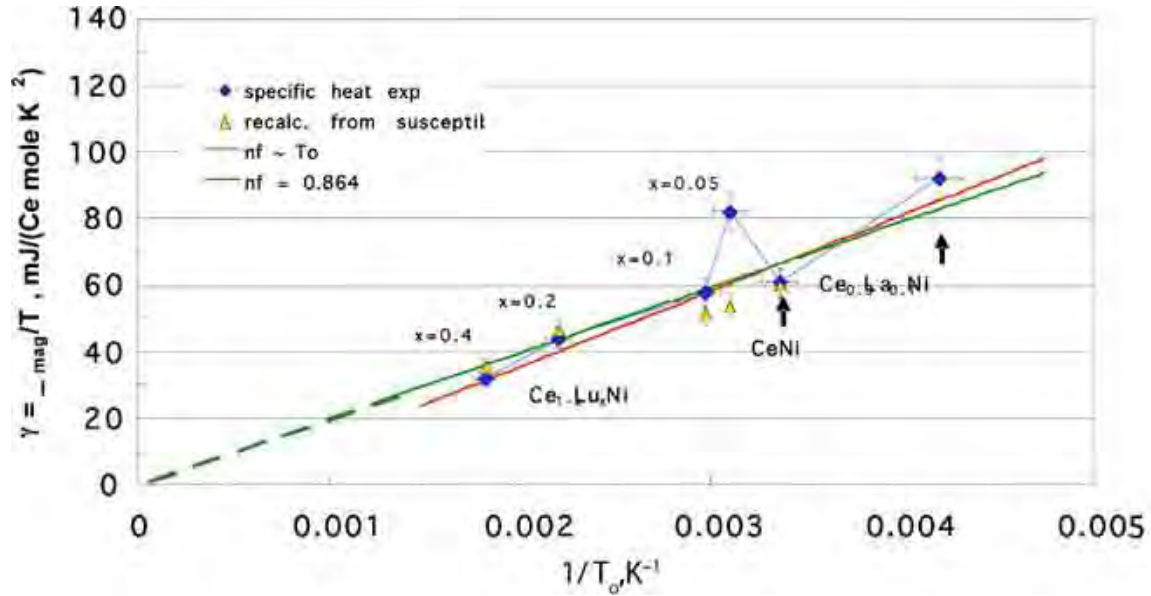


Figure 1. Sommerfeld coefficient γ as a function of the inverse Kondo temperature $T_0 = E_0/k_B$ for CeNi, chemically compressed compositions $\text{Ce}_{1-x}\text{Lu}_x\text{Ni}$ ($x=0.05, 0.1, 0.2, 0.4$) and $\text{Ce}_{0.9}\text{La}_{0.1}\text{Ni}$ (blue circles). Yellow triangles correspond to the values of γ recalculated from the values of $\chi(0)$ using relations (1) and (2). The lines show variation of γ vs. T_0^{-1} , calculated with relation (1) for the fixed value of $\langle n_f \rangle = 0.86$ (green) and $\langle n_f \rangle = f(E_0)$ (3) (red).

Multiple Intermediate Valence in Plutonium

In [7] we show that at low temperatures δ -Pu can be classified as an intermediate-valence system, while experimentally observed values of $\gamma \sim 65 \text{ mJ}/(\text{K}^2 \text{ mole})$ and $\chi(0) \sim 550 \text{ } \mu\text{emu}/\text{mole}$ are well reproduced by relations (1) to (3). However, neither the observed temperature dependence of magnetic susceptibility of δ -Pu nor the properties of α -Pu can be described in terms of the same approach. We assume that organization principles of the $5f$ electrons in plutonium are more complicated than in $4f$ -based IV systems. We assume that in the former fluctuation occurs not between two but minimum between three electronic configurations with valence states $|3+\rangle$, $|2+\rangle$, and $|4+\rangle$. Such a regime can be called multiple intermediate valence (MIV) [7]. By analogy to relation (1) from [7], the wave function of the MIV state, which reflects the quantum-mechanical superposition of integer-valence states, can be schematically represented as:

$$|\psi\rangle = (1 - \varepsilon_{2+} - \varepsilon_{4+})|5f^n k\rangle + \varepsilon_{2+}|5f^{n+1}\rangle + \varepsilon_{4+}|5f^{n-1} k k\rangle. \quad (4)$$

Assuming the Kondo-singlet to be the ground-state of the MIV-system (in spite of two magnetic configurations involved) and Fermi-liquid relations (1) and (2) to be still valid in this case,¹ one can calculate magnetic susceptibility, Sommerfeld coefficient, and Pu atomic volume for δ - and α -phases (Figure 2). It is seen that our model well reproduces the experimental data. According to the MIV-model α -phase differs from δ -phase by higher values of E_0 and higher admixture of the $|4+\rangle$ electronic configuration.

¹Support of these assumptions is out of the limits of the present paper and will be reported elsewhere.

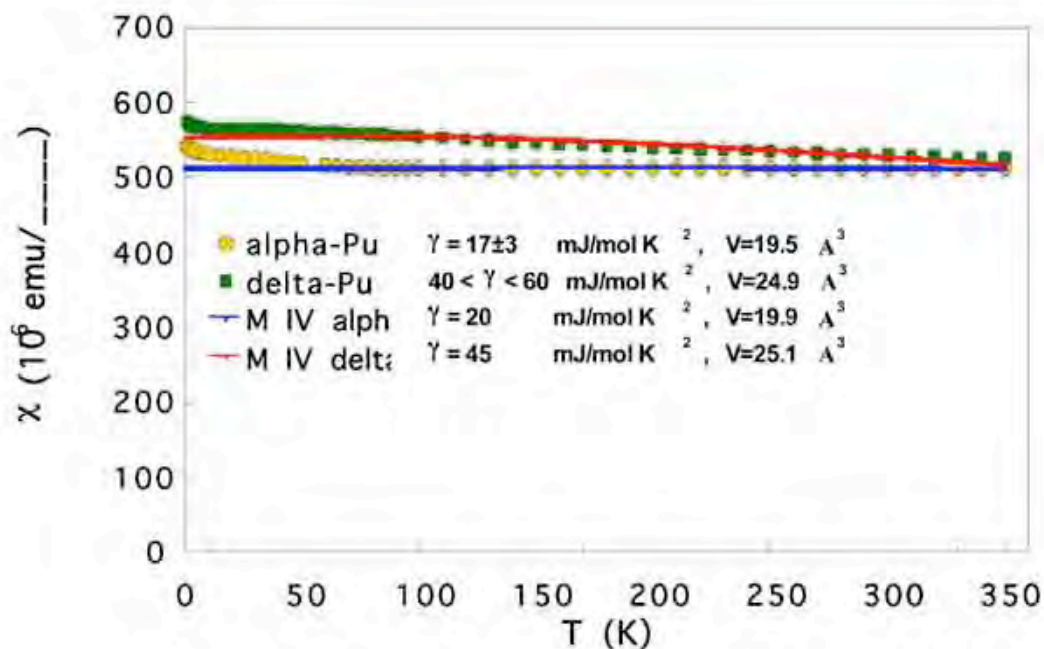


Figure 2. Temperature dependence of magnetic susceptibility for δ - and α -Pu. Signs show the experimental data from [8], lines correspond to the calculated behavior in terms of the MIV model. The experimental and calculated values of Sommerfeld coefficients and equilibrium atomic volumes are also shown.

Further Studies

In spite of simplicity and rather empirical character the MIV concept seems to serve as a convenient instrument for further studies of the peculiarities of the $5f$ -electronic states balancing between localized and delocalized behavior. Firstly, we believe that this model reflects some important organization principles of these electronic systems and can be useful for further development of microscopic quantum-mechanical theory of strongly correlated $5f$ -based materials. Secondly, the MIV concept can serve as a guide to analyze new experimental data.

Our future plan includes as follows:

- Further study of pressure-induced structural phase transition in CeNi to refine the structure of high-pressure phases, to determine the effective Ce ion valence as a function of pressure by independent spectroscopic experiments, and to understand the effect of chemical pressure on parameters of the pressure-induced transition.
- Investigation of the diluted Pu alloys to study the peculiarities of the plutonium ground-state formation in metals.
- Study of PuNi_n compounds to establish the role of the Pu nearest surrounding on the magnetic properties of Pu.
- Study of plutonium metal samples prepared from the Pu-242 isotope.

Conclusions

The paper presents some investigation results of pressure effect on the properties of the IV CeNi intermetallic compound. In particular, we show that increasing chemical or external pressure strengthens hybridization of f -electrons Ce with the conduction band electrons. We consider f -electronic system of Pu to be more complicated (i.e., hybridization of the conduction electrons involves more than two $5f$ -electron configurations). The simplest model of this multiple intermediate valence regime allows consistent description of magnetic susceptibility (both its absolute value and temperature dependence), Sommerfeld coefficient, and Pu atomic volume for δ - and α -phases. Though MIV model requires further examination and serious elaboration, we assume it to be useful for analysis of experimental data including mechanisms of phase transitions in materials with unstable f -shells. For example, according to this model, the α -phase of Pu differs from δ -phase first of all by stronger hybridization of $5f$ and conduction electrons.

Acknowledgements

This work has been performed under the auspices of the Russian State Corporation "Rosatom."

References

- [1] M. E. Manley, R. J. McQueeney, D. Fultz et al., "No role for phonon entropy in the fcc→fcc volume collapse transition in $\text{Ce}_{0.9}\text{Th}_{0.1}$ at ambient pressure," *Phys. Rev. B* **67** 014103 (2003).
- [2] I.-K. Jeong, T. W. Darling, M. I. Graf et al., "Role of the lattice in the $\gamma \rightarrow \alpha$ phase transition of Ce: a high-pressure neutron and X-ray diffraction study," *Phys. Rev. Lett.* **92** 105702 (2004).
- [3] M. E. Manley, A. H. Said, M. J. Fluss et al., "Phonon density of states of α - and δ -plutonium by inelastic x-ray scattering," *Phys. Rev. B* **79** 052301 (2009).
- [4] A. Mirmelstein, E. Clementyev, V. Voronin et al., "Effect of chemical and external pressure on the structure of intermetallic compound CeNi," *J. Alloys. Comp.* **444&445** 281-284 (2007).
- [5] A. Mirmelstein, E. Clementyev, O. Kerbel et al., "Pressure effects in CeNi," *J. Nucl. Mater.* **385** 57-59 (2009)
- [6] D. Gignoux and J. Voiron, "Pressure-induced first-order transition associated with $4f$ instability in CeNi," *Phys. Rev. B* **32** 4822-4824 (1985).
- [7] E. S. Clementyev and A. V. Mirmelstein, "Kondo universality, energy scales, and intermediate valence in plutonium," *JETP* **136** 148 (2009).
- [8] R. H. Heffner, K. Ohishi, M. J. Fluss et al., "The search for magnetic order in δ -Pu metal using muon spin relaxation," *J. Alloys. Comp.* **444&445** 80-83 (2007).

METHOD OF CLUSTER DYNAMICS FOR SIMULATION OF DYNAMIC PROCESSES OF CONTINUUM MECHANICS

I. A. Davydov, V. N. Piskunov

All-Russia Research Institute of Experimental Physics (VNIIEF),
Sarov 607190, Russia

Author Contact: I.A.Davydov@vniief.ru

Described here is the cluster dynamics method (CDM), which is one of the variants of the particle method intended for simulation of the processes associated with large deformations and continuity violation of the material. The basic advantage of CDM is the possibility to choose the base cluster; and it allows the simulation of the processes in a wide range of spatial scales (from micrometer to tens of centimeters). Described here is the construction procedure for cluster interaction potentials corresponding to real equations of state of material by the example of typical metals. Numerical simulation of a shock wave arrival at the profiled plate surface and high-velocity target penetration was carried out using CDM. The computational results are compared with experimental data and other computational results. The results show that CDM can be used for full-scale simulation of large deformation and dynamic fracture of materials at impulse loading at characteristic rates of relative deformation of 10^3 - 10^6 s⁻¹.

Introduction

A special class of continuum mechanics problems is the description of large deformation and material fracture at impulse loading when considerable change of geometry takes place up to the continuity violation (connectivity) of the considered range. Based on the continuity equation of continuum mechanics, these problems are extremely difficult for computer simulation. The application of the particle method [1] is in fact the only approach based on representation of the continuous medium as a set of finite number of interacting elements (particles). As the particle method assumes the discrete structure of the medium, there are no essential difficulties in describing the fracture, continuity violation, structure change, and others.

The particles are used as the numerical technique to integrate the continuum dynamics equations in a number of implementations of the approach: particle-in-cell method, large particle method; smoothed particle hydrodynamics (SPH); and others [1,2,3]. The molecular dynamics method (MD) [4,5] is one of the discrete simulation methods in which the equations of particle motion defined by the interaction potential are used as the basis. This method has been developed considerably for the last ten years and used to simulate the physical, chemical, and biological properties of the objects of hundreds of nanometers.

It impossible to use MD directly to describe macroscopic objects. In this case, the advancement is possible if the elements of larger scale are chosen instead of the molecules—for example, grains of the material (see the description of moving cellular automations [6] and particle dynamics technique [7]). It is remarkable to see that the use of the elementary interaction potential (e.g., Morse or Lenard-Jones) allows the simulation of the most complex effects, such as plasticity, cracking, and fracture [6–8]. Consider also the mesh-free approach called peridynamic by the authors of [9,10] and strongly exemplified in [11].

The present paper considers the developed cluster dynamics methods (CDM) [12], which are based on the methods listed above and take the advantages of these methods. At the same time, many assumptions of [4-11] required the refinement, improvement, and complication described here.

Cluster Dynamics Method

Basic Assumptions

The following assumptions serve as the basis of the cluster dynamics method:

- continuum representation as a set of distinguished units (point base cluster);
- substitution of continuum mechanics equations for equations of motion of interacting clusters;
- application of molecular dynamics method to describe the dynamics of cluster motion;
- selection of cluster interaction potential based on the real equation of state of the simulated material.

For simplicity, accept the classical equations of cluster motion in Newton form, the interactions are considered to be pair:

$$m\ddot{\vec{r}}_k = \sum_{n=1}^N \vec{f}(|\vec{r}_k - \vec{r}_n|) \quad (1)$$

where \vec{r}_k – radius vector of k particle, m – particle mass, N – the total quantity of particles, $\vec{f} = -\nabla U$ – interaction force between the particles corresponding to the interaction potential U.

Base cluster quantities (mass m, equilibrium distance between the clusters) are chosen to reproduce the matter density and region geometry. Here, the peculiarities of the initial geometry problems should be reproduced in detail on the one hand, and the computations for the real size of the region should be fulfilled for the reasonable time. The freedom in choosing the cluster dimension (conserving medium density and region size) means that the initial equations should be of certain scale invariance. Thus, for the sake of self-consistency the interaction potential transformation law should be defined at changing cluster parameters.

Postulate the following transformation law of pair particle interaction U changing base cluster dimension:

$$U(r; a, m) = \frac{m}{m_0} U_0 \left(r \frac{a_0}{a} \right), \quad m \sim a^3 \quad (2)$$

where index 0 denotes certain initial values of base cluster parameter. Transformation (2) provides one and the same behavior of particle velocities. It is shown in energy conservation law:

$$\left[\frac{v_i^2(r_i)}{2} + \sum_k U_0 \left((r_i - r_k) \frac{a_0}{a} \right) \right] = const$$

The dynamic of the process does not depend on base cluster size and the force stress is determined only by the relative deformation when fulfilling (2). Thus, the form (2) provides the independence of the basic mechanical characteristics of deformable material on cluster dimensions, it also allows one to obtain one and the same field of medium mass velocity in calculations.

Note that the clusters introduced above should not be associated with physical particles; it is rather mathematical simulation objects used for the further averaging and serve as medium marker similarly to SPH method. According to the form (2), the range of potential action will increase with the growth of base cluster dimensions. Moreover, thermal velocity of cluster is independent of its dimensions (mass). Both of these properties do not agree with real particle behavior (e.g., cluster volume integration potential is still short-range). However, it is important that cluster dimension does not influence the obtained macroscopic flow pattern as well as the distribution of averaged quantities (energy, pressure, velocity, density), which allows one to use CDM for numerical simulation of continuum mechanics dynamic processes.

Cluster Interaction Potential

It is very important to choose the functional dependence for $U(r)$ potential for CDM implementation. We shall find this dependence using experimental data for shock compression in a large number of points by the density. Cluster interaction potentials found like that will allow for the behavior of dynamic compression and external loading extension of the metals. It is obvious that the accuracy of the simulation of real construction dynamic loading with 2-D, 3-D effects with such potential will be higher as compared with potential fitting by two or three mechanical characteristics [7].

One should use the reliable experimental data to reproduce the particle interaction pair potential by cold compression curve. There are data of great number of works [13-15] which are in good agreement in compression. The most reasonable is the four-parametric equation of material state [15] in the region of extension which properly reproduces the density, cohesion energy, isothermal bulk modulus of compression and its first pressure derivative. Moreover, frequently used in practice is dependence of cold matter pressure on compression called the Mie-Grüneisen equation:

$$p_c(\delta) = \frac{\rho_0 c_0^2}{n-k} (\delta^n - \delta^k) \quad (3)$$

where c_0 – velocity of sound, ρ – density, $\delta = \rho/\rho_0$, n and k – matched parameters.

MD [16] parameters will be used for numerical simulation of cluster motion dynamics, therefore the approximations commonly assumed as Morse potential were used:

$$U_M(r) = D [\exp(-2\alpha(r-a)) - 2\exp(-\alpha(r-a))] \quad (4)$$

and as Mie-Grüneisen and Lenard-Jones potentials

$$U_{MG}(r, n, k) = \frac{D}{n-k} \left[k \left(\frac{a}{r} \right)^n - n \left(\frac{a}{r} \right)^k \right], \quad U_{LD}(r) = U_{MG}(r, 12, 6) \quad (5)$$

Here D has the dimension of energy and defines the depth of potential well, and α which has the dimension of inverse length defines the range of action of Morse potential.

The procedure of choosing potential parameters by cold compression curve is described in [12] in detail; also given are the calculation results for aluminum. The normal parameters have been chosen for starting calculations in (4) (cluster mass is aluminum atomic mass). Then the calculations were carried out for the cluster of arbitrary dimension (mass) using the form (2). Moreover, MD program [16] was used to carry out the calculations for NTV thermodynamic ensemble at different temperatures and densities to find the equation of state with thermal components. The calculations showed [12], that for temperature ranges of $300 \text{ K} < T < 2000 \text{ K}$ and pressure $0,0001 \text{ GPa} < P < 20 \text{ GPa}$, the result error is not more than $\sim 5 \%$ in comparison with aluminum equation of state obtained in [17]. The given ranges of temperature and pressure changes are quite sufficient for the further shock loading problems of aluminum samples.

The problem of interaction potential between different clusters (e.g., between the particles of different materials 1 and 2) is important for practical application. To demonstrate this, the particles are presented as elastic small balls separated by the hard wall. The wall position is easily estimated by the condition of the equilibrium of forces acting on particles 1 and 2 in compression. The sum of elastic energy of particles 1 and 2 in equilibrium position gives the required interaction potential between multi-type particles U . The given procedure was used for Morse potential for multi-type material, which allowed, for example, the simulation of titanium and aluminum plate collision.

Methodological Problems

If U potential depends only on the distance between r clusters, then \vec{f} force in (1) is central and the analytical solution of equation of particle motion can be defined. Consider one-dimensional motion $r = x$ of two identical particles with m mass, the interaction of these particles is defined by Morse potential (4). Let them be in equilibrium position $x \equiv (x_2 - x_1)|_{t=0} = x_0 = a$ at the initial time and scatter at initial velocities $v_2|_{t=0} = V_0$; $v_1|_{t=0} = -V_0$. Introduce $\beta = \sqrt{mV_0^2/D}$ parameter. At $\beta \geq 1$, the particles are infinitely scattered, but at $\beta < 1$, they will be oscillated about the equilibrium position. For $\beta = 1$, the equation (1) is written as :

$$\frac{dx}{dt} = 2v(t) = V_0 \frac{4[1 + 2\alpha V_0]}{[1 + (1 + 2\alpha V_0)^2]} ; \quad x(t) = a + \frac{1}{\alpha} \ln \frac{[1 + (1 + 2\alpha V_0)^2]}{2} ; \quad (6)$$

Fulfilling the $V_0 = \sqrt{D/m}$ condition, the potential well depth— D is exactly equal to kinetic energy of particles; therefore Equation (6) corresponds to the most long-term process of particle motion. Thus, the given solution is the most suitable for gauging and debugging of numerical schemes and computational methods.

The interaction force between two particles \vec{f} for θ angular-variable-dependent potential will not be \vec{r} radius-vector-directed:

$$\vec{f} = -\text{grad}U = -\frac{\partial U}{\partial r} \vec{e}_r - \frac{1}{r} \frac{\partial U}{\partial \theta} \vec{e}_\theta \quad (7)$$

In this case, the particle motion is more complicated. The series of semi-analytic solutions for the motion of two and three particles in a noncentral field was obtained. These solutions can be used for gauging the numerical calculation schemes and will be published separately.

The Hamiltonian difference scheme RKN4 of the forth order of approximation was suggested as the new numerical scheme for equations (1). The suggested scheme stability and accuracy were studied. It is shown that there is actually no phase error for the scheme RKN4 at considerable change of Courant number. Thus, the calculations can be done with a step large enough without loss of accuracy. All the test calculations for two interaction particles using RKN4 schemes show that the amplitude error and total energy unbalance are reduced by approximately 3 or 4 orders in comparison with usual schemes [18, 19].

There are only translational degrees of freedom in the interacting cluster system used in CDM. Therefore, the Grüneisen coefficient G is equal to $2/3$ for any simulated matter. In principle, the plasticity effects cannot be described in Equation (1) without dissipative components on the right side of the equation. These problems may be solved by introducing the cluster rotational degrees of freedom and formulating the equations in addition to (1) similarly to [20,21]. MD-code LAMMPS update version [28] for numerical implementation of these models should be mentioned in this connection. At present, LAMMPS code [28] is used for numerical computations and can be stated as suitable and applicable to mesoscale simulation using CDM without any modifications and changes.

Examples of CDM Application in Dynamical Problems

The CDM method has been verified using the following problems with experimental data provided:

1. Aluminum projectile penetration of thick aluminum plate at initial velocity $\sim 7,4$ km/s;
2. Aluminum projectile penetration of thin aluminum plate at initial velocity $\sim 6,7$ km/s;
3. Collision of plates moving at relative velocities $1 \div 3$ km/s;
4. Shock wave arrival at amplitude ~ 30 GPa at profiled free surface of aluminum samples.

In a number of problems, the cutoff potential parameter $b > 1$ has been introduced to reproduce correctly the destruction effects of the given material. The potential was used to reduce the real range of action by fulfilling the condition: $U = 0$ при $r/a \geq b$.

The computation results for the problems 1, 2, and 4 are detailed in [12]. Here only main results are given.

Thick Target Penetration Problem

The calculation definition suits the experiments from [22]. The computational pattern (Figure 1) is in qualitative agreement with the experiment, only calculations in [12] show considerably more damage of the back side of the plate (experiments connected with target penetration of the 14 mm thick pattern showed a slipping off of the part of the back side of the plate and ~7 mm deep cratering).

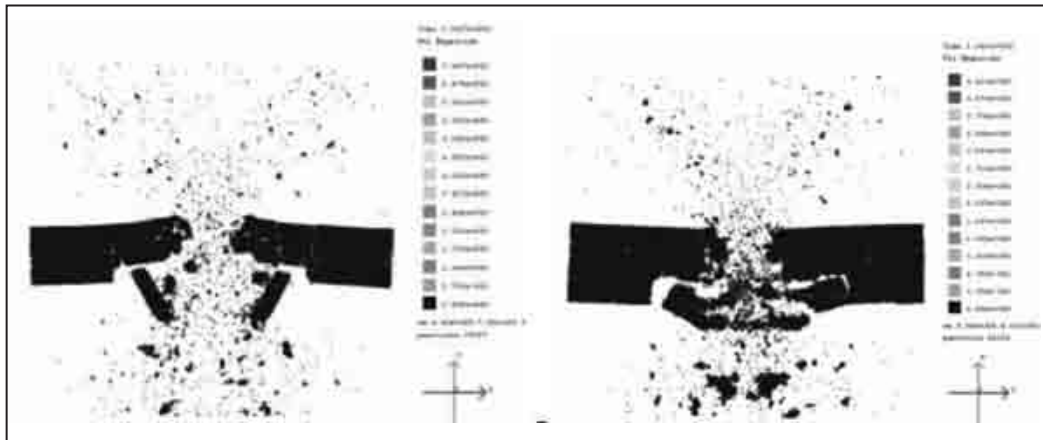


Figure 1. Calculation results of cluster dynamics: (a) – pattern thickness 10 mm; (b) – pattern thickness 14 mm [12]. Time point $t = 25 \mu s$ from collision moment.

Thin Target Penetration Problem

The problem of “thin” hyper-velocity spherical target penetration with through hole and secondary fragment cloud formation is frequently used to test elasto-plastic numerical techniques. In this case, a large through hole is formed in the target; the forming fragment field is under principal consideration. The experimental data for the given test computation are obtained from [23].

Comparison of computational results with experimental X-ray patterns given in [23] shows that the overall picture of the process is accurately reproduced [12]. SPH and CDM computational results differ from experimental data no more than ~10 %. Hole diameter d in the target is better reproduced in the CDM method in comparison to the SPH method, but the CDM method gives worse reproduction of the inverse fragment separation angle θ (Table 1).

Table 1. Comparison of computational results [12] with experiment [23].

| | d , mm | θ , deg |
|--------------------|----------|----------------|
| X-ray pattern [23] | 17,3 | 20,67 |
| SPH computation | 18,0 | 27,08 |
| CDM computation | 17 | 39 |

Plate Collision

The problems of two plates collision have been solved: 0,5 cm thick projectile and 1 cm thick target. Target and projectile materials (aluminum and titanium) as well as projectile initial velocity ($U_0 = 1.0, 1.5, 2.0, 3.0$

km/s) varied. The initial parameters of shock waves in projectile and target as well as fracture pattern at $\sim 10 \mu\text{s}$ were obtained. Figure 2 shows the computational results.

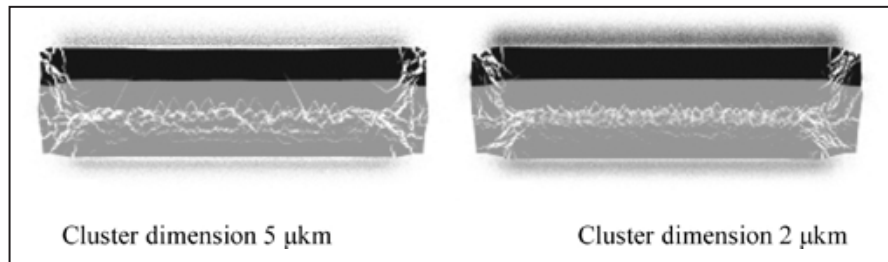


Figure 2. Calculation results of different cluster dimensions at $9.7 \mu\text{s}$.

Calculations of shock wave initial parameters (pressure P , material mass velocity in projectile and target— u_1 and u_2 , respectively), obtained with CDM, were compared with numerical solutions obtained in MASTER 1D gas-dynamic simulation [25] (see Table 2). Table 2 shows CDM values in brackets.

Table 2. Shock wave initial computation parameters (projectile – titanium).

| u_0 , km/s | Target - titanium | | | Target - aluminum | | |
|-----------------|-------------------|--------------|--------------|-------------------|---------------|---------------|
| | P , GPa | u_2 , km/s | u_1 , km/s | P , GPa | u_2 , km/s | u_1 , km/s |
| 1.0 | 11.9 (11.6) | 0.5 (0.5) | 0.5 (0.5) | 9.95 (9.7) | 0.575 (0.570) | 0.425 (0.430) |
| 1.5 | 18.9 (19.0) | 0.75 (0.749) | 0.75 (0.751) | 15.8 (15.4) | 0.859 (0.852) | 0.640 (0.649) |
| 2.0 | 26.6 (27.5) | 1.0 (1.0) | 1.0 (1.0) | 22.2 (22.9) | 1.143 (1.130) | 0.857 (0.869) |
| 3.0 | 44.2 (47.8) | 1.5 (1.5) | 1.5 (1.5) | 36.6 (39.6) | 1.75 (1.70) | 1.295 (1.31) |

The computational results of two plates collision problems show:

- Fracture visual pattern depends on cluster dimensions, but the reduction of cluster dimensions shows the result convergence—the slipping-off position is not changed, only changed is the morphology and small parts of fracture area. Interface particle dusting is observed when cluster dimensions are 20 micrometers and less.
- A good agreement was obtained for the computational results for projectile and target pressure and mass velocity with gas-dynamic computational results (including collision of bodies widely differing in mechanical properties.)

Computational results show that CDM can be successfully used in dynamic fracture problems.

Cumulation Problem

Experimental results on shock wave arrival at a profiled free surface of aluminum alloy pattern are given in [24]. The profiled free surface pattern was subject to explosive shock-wave load. As a result, the arriving shock wave was formed with a frontal surface amplitude of ~ 30 GPa. Jet flows at velocity of ~ 3.7 km/s were formed on the free surface for the surface profile characterized by 1 mm amplitude, 10 mm wavelength, and continuous mass velocity ~ 3.2 km/s. X-ray results of the process are given in [24,12].

A considerable number of 2D computations was carried out. Computational results are given in [12]. Computational results for the selected plate fragment and for three typical time points are given in Figure 3. They are in good agreement with experimentally fixed process pattern. Surface profiling time as well as typical motion velocities of the material in the pattern and cumulative jet correspond to the experimental data.

It should be noted that numerical implementation of CDM allows not only a space distribution of crumbled material density, but also size distribution of crumbled particles. The particle spectrum recovery (size distribution) algorithm has been developed by the enumeration of connections between single clusters. The clusters are considered to be in one particle if cluster distance does not exceed interaction radius $r \leq b \cdot a$. A particle is a set of clusters with at least one link with other clusters. From a mathematical point of view, this procedure is undirected graph construction. Here each particle corresponds to graph connectivity component (wood, cycle, edge). Enumeration of the connectivity components allows spectrum reconstruction of particles by constructing $N(g)$ dependence, where N is the particle number in a system consisting of g clusters.

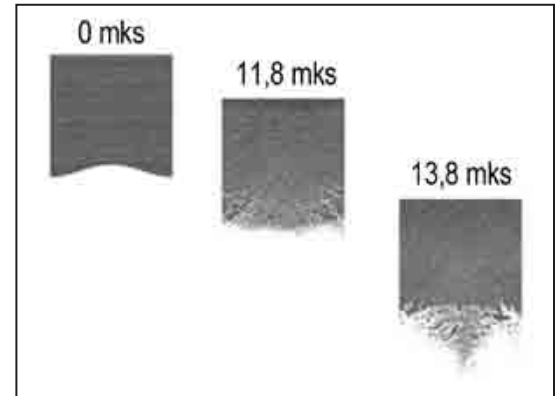


Figure 3. Pattern state at different initiation times [12].

Spectrum gauging can be made by using modern methods of disperse microparticle registration. Microparticle visualization technique in gas-dynamic flows has been developed in VNIIEF using laser illumination. The visualization experiments of microparticles ejected from material surface differing in properties and internal microstructure (including lead, aluminum, ceramic materials) have been carried out. The experimental results are used for CDM gauging; we hope they will be published in the nearest future.

Conclusions

The simulation results of high-velocity shock loading of solids using CDM and their comparison with experimental data show that CDM allows the results of sufficiently different in dynamic experiments formulation to be described. The processes include cumulative jet formation at shock wave arrival at a free surface, target penetration, and fission field formation due to high-velocity collision of the projectile and target.

The sufficient advantage of CDM is the possibility to choose the base cluster dimension that allows mesoscale simulation of dynamic processes in a wide range of spatial scale (from micrometer to tens of centimeters). CDM is highly reliable, has computational stability, and does not require interference in computation. The possibility of numerical implementation in standard MD programs (e.g., VNIIEF MD [16] or LAMMPS code [26]) is the other advantage. At present, LAMMPS code [28] is used for numerical computations and would be suitable and applicable to mesoscale simulation using CDM without any modifications and changes.

A challenge is the possibility to combine CDM with the existing grid gas-dynamic techniques to develop hybrid simulation methods similar to the peridynamic in [27].

Important problems for further CDM development are accounting for real material structure, plasticity effect, and cluster rotational degree of freedom.

References

- [1] R. Hockney and J. Eastwood, Numerical Simulation Using Particle Method,” (M.: Mir 1987) 640.
- [2] O. M. Belotserkovsky, Yu M. Davydov, “Large Particle Method in Gas-Dynamics,” (M.: Nauka, 1982) p. 392.
- [3] J. J. Monaghan, “Introduction to SPH,” *Comp. Phys. Comm.* **48** (1987).
- [4] B. J. Alder, T. E. Wainwright, “Studies in molecular dynamics. I. General method,” *J. Chem. Phys.* **27** 1208. (1957).
- [5] B. L. Holian, R. Ravelo, “Fracture simulations using large-scale molecular dynamics,” *Phys. Rev. V.* **B51** N 17 11275 (1995).
- [6] V. L. Popov, S. G. Psakhie, “Theoretical simulation fundamentals of elasto-plastic media using moving cellular automation method,” *Physical Mesomechanics* **4** 1 17 (2001).
- [7] A. M. Krivtsov, H. B. Krivtsova, “Particle method and its application in deformable solid mechanics,” *Dalnevostochny Matematichesky Zhurnal DVO RAS* **3** 2 254 (2002).
- [8] A. M. Krivtsov, “Plasticity effects description at molecular-dynamic simulation of slipping-off fracture,” *FTT* **46** 6 1025 (2004).
- [9] S. A. Silling, “Reformulation of elasticity theory for discontinuities and long-range forces,” *J. Mech. Phys. Sol.* **48**, 1 175 (2000).
- [10] S. A. Silling, E. A. Askari, “Meshfree method based on the peridynamic model of solid mechanics,” *Computers and Structures* **83** 1526 (2005).
- [11] S. A. Silling, F. Bobaru, “Peridynamic modeling of membranes and fibers,” *International Journal of Non-Linear Mechanics*, **40** 395 (2005).
- [12] V. N. Piskuniv, I. A. Davydov, “Cluster dynamics method and its application to pulse loading of solids,” *Deformation and Destruction of Materials* №1 3. (2008).
- [13] F. A. Baum, L. P. Orlenko, K. P. Stanyukovich, et al., *Explosion Physics*, ed. K. P. Stanyukovich (M.: Nauka, 1975) p. 704.
- [14] *Physical Quantities*, ed. I. S. Grigor’ev, E. Z. Meilikhov, (M.: Energoatomizdat 1991) p. 1232.
- [15] J. H. Li, S. H. Liang, H. B. Guo, B. X. Liu, “Four-parameter equation of state of solids,” *App. Phys. Lett.* **87** 194111 (2005).
- [16] A. Yu. Aleinikov, R. A. Barabanov, O. I. Butnev et al., “MDP-SOVS code for molecular dynamics problems using shared memory parallel computers,” *VANT. Ser. Methods and Programs for Mathematical Physics Numerical Problems* № 1. 3. (2001).
- [17] D. G. Gordeev, L. F. Gudarenko, V. G. Kudel’kin, “State equation model with specific heat of nuclei and electrons with Debye temperature. State equations of beryllium and aluminum,” *Voprosy atomnoi nauki i tekhniki. Ser. Theoretical and Applied Physics*. Issue1-2 51 (2005).
- [18] L. Verlet, “Computer 'experiments' on classical fluids. I. Thermodynamical properties of Lennard-Jones molecules,” *Phys. Rev. V* **159** 98 (1967).
- [19] E. Rougier, A. Munjiza, N. W. M. John, “Numerical comparison of some explicit time integration schemes used in DEM, FEM/DEM and molecular dynamics,” *International Journal for Numerical Methods in Engineering* **61** 856 (2004).
- [20] S. G. Psakh’e, A. Yu. Smolin, E. V. Shil’ko, S. Yu. Korostelev et al., “On the features of the steady-state conditions of solids deformation,” *GTF* **67** № 9 34 (1997).
- [21] S. Ioshida, “Plastic deformation dynamics by energy regeneration and dissipation with plasticity,” *Physical Mesomechanics* **11** No. 231 (2008).
- [22] J. Gering, “High-velocity impact from the engineering point of view, in *High-Velocity Impact Effects*, (M.: Mir, 1973) p. 468.
- [23] A. J. Piekutowski, “Characteristics of debris clouds produced by hypervelocity impact of aluminum spheres with thin aluminum plates,” *Int. J. Impact Engng.* **14** 573 (1993).

- [24] V. A. Ogorodnikov, A. L. Mikhailov, A. V. Romanov et al., “Jet simulation at shock wave arrival at the profiled free surface,” *PMTF* **48** 1 16 (2006).
- [25] E. Tchekhounov, V. Roudenko, M. Chabourov, “Tutorial and research package MASTER on continuum mechanics,” in *Proc. Second European Conference "Physics Teaching in Engineering Education"* (Budapest, Hungary 2000).
- [26] J. Plimpton, “Fast parallel algorithms for short-range molecular dynamics,” *J. Comp. Phys.*, 117 1-19 (1995).
- [27] W. Gerstle, N. Sau, S. Silling, “Peridynamic modeling of concrete structures,” *Nuclear Engineering and Design*, No. 237 1250 (2007).
- [28] M. L. Parks, R. B. Lehoucq, S. J. Plimpton, S. A. Silling, “Implementing peridynamics within a molecular dynamics code,” *Computer Physics Communications* **179** 777 (2008).

SPIKED ALLOY PRODUCTION FOR ACCELERATED AGING OF PLUTONIUM

P. A. Wilk, J. A. McNeese, K. E. Dodson, W. L. Williams, O. H. Krikorian, M. S. Blau, J. E. Schmitz, F. G. Bajao, D. A. Mew, T. E. Matz, R. A. Torres, D. M. Holck, K. J. Moody, J. M. Kenneally

Lawrence Livermore National Laboratory, Livermore, CA 94551 USA

Author Contact: wilk2@llnl.gov

The accelerated aging effects on weapons grade plutonium alloys are being studied using ^{238}Pu -enriched plutonium metal to increase the rate of formation of defect structures. Pyrochemical processing methods have been used to produce two ^{238}Pu -spiked plutonium alloys with nominal compositions of 7.5 wt% ^{238}Pu . Processes used in the preparation of the alloys include direct oxide reduction of PuO_2 with calcium and electrorefining. Rolled disks were prepared from the spiked alloys for sampling. Test specimens were cut out of the disks for physical property measurements.

Introduction

While metals in general have been studied for thousands of years, plutonium occupies a rather unique place among the metals as it has only been studied as a metal for less than a century. The pit of a nuclear weapon is subject to the constant self-irradiation from the radioactive plutonium that it contains, and this radiation could produce a significant amount of damage over the lifetime of the pit. The aging effects most of concern are thought to be helium bubble formation and void swelling. Since it is assumed that the damage produced should scale with the radiation dose received, replacing a portion of the ^{239}Pu with a much more radioactive isotope of plutonium would allow experiments to be conducted over a period of a few years that should reflect the aging behavior of plutonium in a weapon in excess of 50 years.

Spiked Alloy Production

The plutonium starting materials for the spiked alloy production were weapons grade (WG) plutonium, either as the oxide or the metal, and ^{238}Pu -enriched PuO_2 . The ^{238}Pu -enriched oxide contains approximately 70 wt% $^{238}\text{PuO}_2$, 15 wt% WG PuO_2 , 14 wt% $^{234}\text{UO}_2$, and 0.3 wt% $^{241}\text{AmO}_2$. The ^{238}Pu -enriched oxide will be referred to henceforth as $^{238}\text{PuO}_2$. Pyrochemical processing methods were used to produce ^{238}Pu -spiked alloys with 7.5 wt% ^{238}Pu and 1 wt% gallium nominal composition. The aging in a 7.5% ^{238}Pu -spiked plutonium alloy is about 16 times faster than in weapons grade plutonium.

All the plutonium used for the alloy had to be first reduced to the metal; for this, a direct oxide reduction (DOR) [1] process was used in which calcium metal reduces the $^{238}\text{PuO}_2$ and WG PuO_2 to ^{238}Pu -spiked metal. The reduction was carried out in a MgO crucible and dry CaCl_2 salt at $\sim 900^\circ\text{C}$. All the reagents, plutonium, calcium and CaCl_2 , are molten at this temperature. The reduction of plutonium oxides by calcium produces plutonium metal and CaO which is soluble in the molten CaCl_2 . The molten ^{238}Pu -spiked metal from the reduction is insoluble in the molten CaCl_2 , and forms droplets in the salt. These droplets coalesce in the stirred salt and eventually settle to the bottom of the crucible, which is later recovered as an ingot (Figure 1). Each DOR reaction produced approximately 1 kg of ^{238}Pu -spiked Pu metal.

Following the reduction, the metal must be purified by electrorefining [1]. Electrorefining is used to remove metallic impurities from the plutonium, such as iron,



Figure 1. DOR button.

nickel, aluminum, gallium, americium and uranium. Electrorefining is a low yield process because it retains a significant amount of plutonium in the electrolyte and impure plutonium containing all the impurities in the anode heel. About three DOR runs were needed to provide enough plutonium for one electrorefining run. The electrorefiner uses a cast plutonium ingot for the anode and dry CaCl_2 salt as the electrolyte. Either PuCl_3 or Cs_2PuCl_6 (dicesiumhexachloroplutonate, DCHP) is added to the salt to provide the initial plutonium ions in the electrolyte. The electrorefining is carried out at $\sim 850^\circ\text{C}$ and 1 to 2 volts DC for about six days duration. See Figure 2 and Figure 3. The electrolytic reactions are:

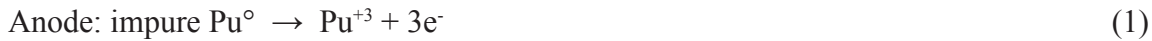


Figure 2 . Cast anode for electrorefining feed.



Figure 3. Electrorefined ring.



Figure 4. Cast cookies.

The electrorefined plutonium (Figure 3) is next cast into cookies. Cookies are solid cylinders 1.5" in diameter by 3/8" high (Figure 4). Gallium and a small amount of iron are added at this point. After being poured into the molds, the castings are annealed at $\sim 450^\circ\text{C}$ to stabilize the plutonium δ -phase. The cookie castings are then cooled and removed from the molds and the cookies are machined to obtain clean surfaces and flat parallel top and bottom faces (Figure 5). After machining, the cookies are rolled into 1/8" thick stock in the shape of disks (Figure 6). The disks are annealed at $\sim 450^\circ\text{C}$ to remove cold work, and test specimens are machined out of the disks. Test specimens are machined into special shapes for measurement and testing (Figure 7).



Figure 5 . Machined cookies.



Figure 6. Rolled and annealed disk.



Figure 7. Specimens are rough cut from the disk.

Unspiked WG Pu material with a similar composition to the spiked alloy was also produced, and test specimens were machined for physical property measurements. This material is referred to as reference alloy.

Isotopic and elemental analyses were carried out by Induction Coupled Mass Spectrometry on the spiked materials and compared with the reference alloy. The analyses on the individual disks showed very small variations from the values.

Spiked Alloy Characterization and Physical Property Measurements

Metallographic images are shown in Figure 8 of the reference and spiked alloy. The microstructures appear to be similar. The average grain size between the alloys show good agreement in grain size. TEM was carried out on the reference and spiked alloys. A few bubbles are found in the spiked alloy, but none are seen in the reference alloy. The reference alloy was also characterized by X-ray diffraction, which verified that the material is delta phase plutonium.

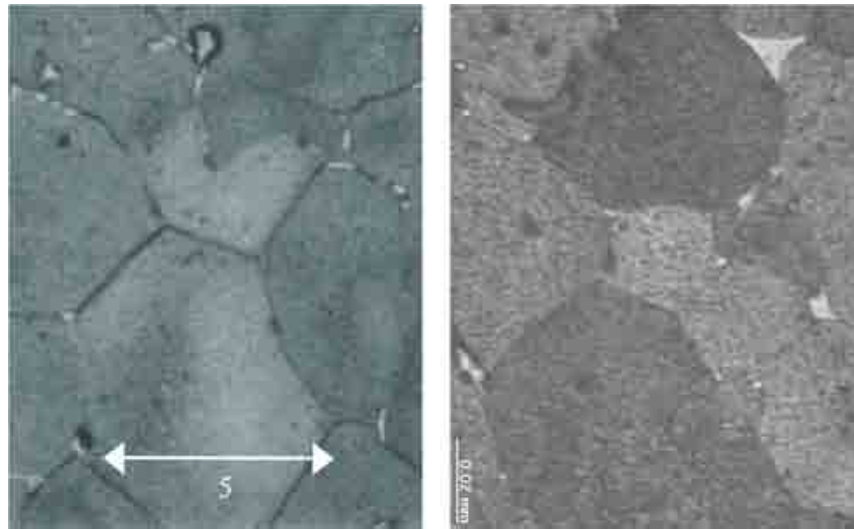


Figure 8. Metallographic images are shown at ~700X of reference alloy and spiked alloy.

Conclusions

The ^{238}Pu -spiked alloys were successfully prepared by pyrochemical processing. Comparison of chemical analyses on the spiked alloys with that of the reference alloy showed similar impurity levels. The ^{238}Pu contents, 7.38 wt% and 7.16 wt%, were found to be somewhat lower than the goal of 7.5 wt%, but were sufficiently close as to allow aging determinations to be made within a reasonable time.

Characterization by metallography, grain size, Vickers hardness, and TEM of the spiked alloy showed excellent consistency with the reference alloy. Tensile testing generally showed good consistency between the spiked alloy and the reference alloy.

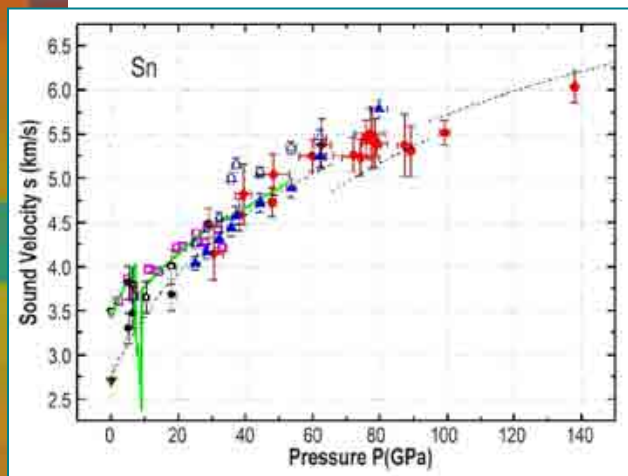
Acknowledgements

This work was performed under the auspices of the U.S. Department of Energy by Lawrence Livermore National Laboratory in part under Contract W-7405-Eng-48 and in part under Contract DE-AC52-07NA27344.

Reference

- [1] K. E. Dodson, "Pyrochemical Treatment of Salts," in *Separation Techniques in Nuclear Waste Management*, eds. T. E. Carlson, N. A. Chipman, C. M. Wai, (CRC Press, 1996).

Materials Response to DYNAMIC LOADING I



Experimental dependence of sound velocities in tin on pressure of shock compression.

The fifth session includes papers devoted to numerical and experimental researches on material behavior under the effect of dynamic loading. The process of material deformation under high-rate loading has a complicated, ambiguous character. Therefore, it cannot be predicted a priori, and to formulate adequate wide-range constitutive relations for materials, a large scope of experimental data is required.

In this session, several works are devoted to experimental measurements of sound velocities (elastic and volume) for metals (uranium, tin) under the effect of shock waves. Knowing dependences of sound velocities on pressure, it is possible to get information on phase transitions, which occur under shock-wave loading, testing of shear modulus, and, as a consequence, strength of a studied material. Besides, organic compounds are considered. Under the effect of shock waves, their behaviors are similar and can be described by a unified equation of state. Using the method of diamond anvil cell (DAC), yield strengths of polycrystalline tantalum and iron were studied. It was revealed that yield strength increases linearly as pressure grows in tantalum but that the behavior of iron is complicated by the presence of a phase transformation. Also, the fifth session presents kinetics of phase transition based on the Landau-Ginsburg model for martensite transformations, which can be used to calculate system behavior at various stresses and temperatures. Application of the methods of molecular dynamics (MD) allows getting a new and advanced understanding of the processes that occur in metals during deformation by shock waves. The model was tested using coarse-grain copper, and the calculational results are compared to available experimental data.

Olga N. Ignatova, All Russian Scientific Research Institute of Experimental Physics, Sarov, Russia

Section V:

- V-2 Thermal Fluctuation Model of Plastic Flow (LANL)
- V-4 A Wide-Range Equation of State of Water (VNIITF)
- V-9 On the Universal Behavior of Some Organic Compounds Under Compression (VNIIEF)
- V-15 Shock-Induced Plasticity in Al, Cu, and Al-Cu Alloys (JIHT)
- V-20 Static Material Strength Determined Using a DAC (LLNL)
- V-24 Wide-Range High-Strain-Rate Shear Strength Model for Metals (VNIIEF)
- V-29 Measurement of Sound Velocities in Shock-Compressed Tin Under Pressures up to 150 Gpa (VNIIEF)
- V-34 Determination of Longitudinal and Bulk Sound Velocities in Natural Uranium Under Shock-Wave Loading (VNIIEF)

THERMAL FLUCTUATION MODEL OF PLASTIC FLOW

Dean L. Preston

Physics Division, Los Alamos National Laboratory

Landau theory is a phenomenological framework that originated as a description of second-order (continuous) phase transformations. Although the conventional Landau approach is strictly valid only for second-order phase transformations, Landau theory has been generalized to encompass first-order phase transformations, in particular, displacive reconstructive transitions, which include martensitic transformations.

The basic ingredients of a Landau model are a set of order parameters, η_k , which encode the atomic configurations through the transformation, and the thermodynamic potential, G , which is a function of the order parameters.

In Landau-Ginzburg theory, a gradient term is added to the total energy to account for interface surface energy

$$G_{GL} = G + \frac{1}{2} \sum_{k=1}^n \beta_k (\nabla \eta_k)^2 \quad (1)$$

where the β_k are gradient energy coefficients. Since the driving force to change η_k equals $-\delta G_{GL} / \delta \eta_k$, the coupled kinetic equations for the η_k are

$$\frac{\partial \eta_k}{\partial t} = - \sum_{p=1}^n L_{kp} \frac{\delta G_{GL}}{\delta \eta_p} + \xi_k = - \sum_{p=1}^n L_{kp} \left(\frac{\partial G}{\partial \eta_p} - \beta_p \nabla^2 \eta_p \right) + \xi_k. \quad (2)$$

Here ξ_k is the noise due to thermal fluctuations, and the L_{kp} are kinetic coefficients.

We have constructed a Landau free energy, G , that describes martensitic phase transformations (PTs) in steels and shape memory alloys for an arbitrary number, n , of martensitic variants [1, 2]. Hence, the transformation strain is temperature independent, the stress hysteresis is weakly temperature dependent, and the tangent elastic moduli at the PT point are nonzero. Finally, the theory accommodates all the thermomechanical properties of both phases. For the simplest case of a single variant, the free energy is of the form

$$G = -\sigma : \lambda : \sigma / 2 - \sigma : \varepsilon_t \phi(\eta) + f(\theta, \eta), \quad (3)$$

where θ is the temperature, σ is the stress tensor, λ is the elastic compliance tensor, and ε_t is the transformation strain in going from austenite ($\eta = 0$) to martensite ($\eta = 1$); ϕ and f , the thermal energy, are 2-3-4 (quartic) or 2-4-6 (sixth degree) polynomials in the order parameter. An additional term is required for two or more variants. We note in passing that this is a small strain theory, though we have extended it to account for large transformation strains and lattice rotations [3].

One of the most fundamental and challenging topics in the theory of first-order phase transformations is that of kinetics, the progress of the transformation. The specific issue addressed here is nucleation, the process by which the system evolves when quenched into a metastable state. Equation (2) with (3) possesses a localized time-independent solution with the property that larger profiles grow while smaller profiles shrink away; hence, such a solution is a critical martensitic nucleus [4]. The focus here is not on finding such solutions, but rather on determining the *rate* at which critical nuclei are formed.

The calculation of the nucleation rate hinges on a key observation, namely, that the Landau-Ginzburg equations with (thermal) noise, (2), are the equations of motion of a reaction-diffusion system. In the absence of noise, the action that yields (2) is trivially obtained by left multiplying (2) by a conjugate field, $\bar{\eta}$; the functional derivative of the action with respect to $\bar{\eta}$ then returns (2). However, to yield an equation of motion with noise, it is necessary to add a term of the form $(\bar{\eta} \eta)^2$ to the action. The action is then linearized in the conjugate field by means of a Hubbard-Stratonovich transformation, which adds a term $\eta(x,t) \dot{W}(t)$, with $W(t)$ a Wiener process, to the equations of motion. Thus, the action for the Landau-Ginzburg system with noise for one martensitic variant in d dimensions may be written

$$S = \int d^d x dt \left\{ \bar{\eta} \left[\frac{\partial \eta}{\partial t} - L \left(\beta \nabla^2 \eta - \frac{\partial G}{\partial \eta} \right) \right] + \lambda (\bar{\eta} \eta)^2 \right\} . \quad (4)$$

This action can be regarded as that for a field theory obtained, using a procedure developed by M. Doi [5], from a continuous-time master equation for the distribution of interacting particles diffusing over a lattice. Expressing the Hamiltonian, H , corresponding to (4) in terms of creation and annihilation operators, time-dependent densities and correlation functions may be put in the interaction picture, where the time dependence of any operator is induced by the diffusive term in H , and then evaluated (for weak coupling) by expanding exponentials and using Wick's theorem, yielding Feynman diagrams. Alternatively, the densities and correlators can be given coherent state path integral representations, which can again be expanded into sums of Feynman diagrams.

Conclusions

In summary, our Landau-Ginzburg theory for martensitic phase transformations is mapped into a field theory. The powerful methods of quantum field theory can then be exploited to calculate the evolution of the system as the stress and temperature are varied. Progress toward evaluating the homogeneous martensite nucleation rate for our 2-3-4 polynomial potential, G , in a single order parameter will be presented.

References

- [1] V. I. Levitas, D. L. Preston, "Three-dimensional Landau theory for multivariant stress-induced martensitic phase transformations. I. Austenite \leftrightarrow martensite," *Phys. Rev. B* **66** 134206 (2002).
- [2] V. I. Levitas, D. L. Preston, "Three-dimensional Landau theory for multivariant stress-induced martensitic phase transformations. II. Multivariant phase transformations and stress space analysis," *Phys. Rev. B* **66** 134207 (2002).
- [3] V. I. Levitas and D. L. Preston, "Thermomechanical lattice instability and phase field theory of martensitic phase transformations, twinning, and dislocations at large strain," *Phys. Lett. A* **343** 32 (2005).
- [4] V. I. Levitas, D. L. Preston, D.-W. Lee, "Three-dimensional Landau theory for multivariant stress-induced martensitic phase transformations. III. Alternative potentials, critical nuclei, kink solutions, and dislocation theory," *Phys. Rev. B* **68** 134201 (2003).
- [5] M. Doi, "Second quantization representation for classical many-particle system," *J. Phys. A* **9** 1465, 1479 (1976).

A WIDE-RANGE EQUATION OF STATE OF WATER

V. V. Dremov, A. T. Sapozhnikov, M. A. Smirnova, E. E. Mironova

Russian Federal Nuclear Center – Zababakhin Institute of Applied Physics, Snezhinsk,
Chelyabinsk Region, 456770 Russia

Here we present a new wide-range equation of state for water. It was constructed by sewing together a number of local models describing the matter in different regions of the phase diagram. At temperatures below dissociation and moderate densities, the semi-empirical equations of state describing water with high accuracy and taking evaporation into account were used. To construct a thermodynamic model describing properties of water in the region covered by shock data, Variational Perturbation Theory was applied. Dissociation reactions were also included in the model. In this region, water is considered as a mixture of molecular fluids. Some peculiarities of the intermolecular potential for water and their effect upon shock compression parameters were investigated. Results of the calculation were compared with experimental data on shock compression of porous ice and snow. At high densities, the matter is considered as a homogeneous mixture of atoms, and the Thomas-Fermi model with quantum corrections and nuclei treatment by Kopyshchev is applied. At low densities and high temperatures, the model of weakly nonperfect dissociating gas and the Saha model of ionized gas were used. The EOS was converted into tabular form to make it efficient in hydrodynamic codes.

Introduction

Water is abundant in nature and is often used as a working fluid in technology. That is why experimental and theoretical investigations in many fields of physics, including the physics of shock waves, require an equation of state of water capable of precise calculation of its thermodynamic properties in a wide range of temperatures and densities.

In the past 25 years, a number of wide-range water EOSs have been constructed. The tabular EOS proposed in [1] describes water at densities $10^{-6} < \rho (\text{g/cm}^3) < 6$ and energies $0 < E (\text{kJ/g}) < 10^6$. It uses precise approximations of experimental data on water and vapor [2] and approximations [3] of calculation data [4] at high temperatures and densities obtained with the Thomas-Fermi model. In the region covered by shock experiments, EOS [1] uses a modified EOS [5] and a semiempirical approach from [3] to describe dissociation.

The wide range EOS from [6] gives analytical forms for pressure and energy as functions of density and temperature. It takes into account evaporation, oscillation excitations, dissociation (semi-empirical approach), and hydrogen bonding. At high temperatures and pressures, this EOS approximates calculation data [4]. The EOS [6] satisfactorily describes experimental data [2] at $\rho > 0.01 \text{ g/cm}^3$ and experimental data on shock compression of water, but inadequately describes experimental data on shock compression of porous ice and snow [7,8].

The EOS from [9] also has an analytical form and uses specific volume and entropy as independent thermodynamic variables. This EOS is in satisfactory agreement with experimental data on shock compression of water and porous ice, but at pressures below 10 GPa and temperatures below 1000 K, it fails to describe the precise experimental data on static compression [2]. Also, entropy as an independent variable hampers the use of the EOS in hydrocodes.

The experimental data on shock compression of water into Megabar range (0.5–31.5 Mbar) [10–13] and new theoretical data on the thermodynamic properties of water as a homogeneous mixture of oxygen and hydrogen obtained with the Thomas-Fermi model with quantum corrections [9] were used to construct the tabular EOS GLOBUS [14]. The EOS works in the ranges $10^{-3} \leq \rho (\text{g/cm}^3) \leq 64$, $300 \leq T (\text{K}) \leq 1.6 \cdot 10^8$ and has a more sophisticated mathematical form compared to the EOS [1]. Potential pressure at densities lower and higher than density at

ambient conditions is presented on uniform and logarithmic grids, respectively. Potential energy is found from the equation of thermodynamic compatibility. The EOS domain of definition is subdivided into a number of rectangular subdomains corresponding to the models valid in these ranges of density and temperature. Thermal pressure and energy are presented within the subdomains on logarithmic grids. Bi-cubic interpolation is used between their nodes. Beyond the EOS's domain of definition, a simple extrapolation is applied.

GLOBUS-3 Equation of State

Here we present the GLOBUS-3 EOS for water, which is a modification of GLOBUS EOS [14]. The main difference of the new EOS is that the subdomains corresponding to different physical models are no longer rectangular (Figure 1).

When tabulating this EOS, we used a more comprehensive set of models and local EOSs compared [14]:

- The model of weakly nonperfect dissociating gas;
- Variational perturbation theory;
- Calculation data on ionized gas of low density – Saha model [15];
- Calculation data obtained with Thomas-Fermi model with quantum corrections [16] and nuclei treatment by Kopyshchev [17] for the homogeneous mixture of oxygen and hydrogen.

Compared to the earlier EOSs, the GLOBUS-3 EOS better describes the regions of dissociation and ionization, experimental data on shock compression of porous ice and snow [7,8], and water properties at extremely high pressures on the Hugoniot [13]. The ranges of its applicability are $10^{-4} \leq \rho \text{ (g/cm}^3\text{)} \leq 100$; $273 \leq T \text{ (K)} \leq 6 \cdot 10^7$.

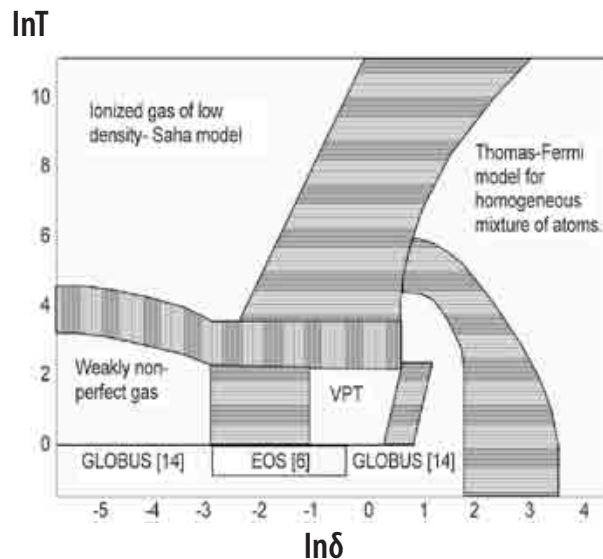


Figure 1. Layout of models sewed together in the wide range GLOBUS-3 EOS of water. Shading denotes interpolation regions between models.

Application of Variational Perturbation Theory

To construct the thermodynamic model describing water properties in the region covered by the shock data obtained in experiments with porous ice and snow [7,8], we used variational perturbation theory (VPT) [18]. Dissociation reactions were also introduced in the model in accord with [19].

We have found that at densities corresponding to condensed matter the main reaction affecting the parameters of water shock compression is



This reaction is responsible for water conduction under shock compression [21].

In the paper by Ree [20], the following form of the intermolecular potential for water was proposed (exp-6):

$$\varphi(r) = \varepsilon(T) \left\{ \left(\frac{6}{\alpha - 6} \right) \exp \left[\alpha \left(1 - r/r_0^* \right) \right] - \left(\frac{\alpha}{\alpha - 6} \right) \left(\frac{r_0^*}{r} \right)^6 \right\}, \quad (2)$$

where the parameter ε depends upon temperature (due to the dipole moment of water molecules). This formula, being a simple approximation of ab initio calculations [21], gives excellent agreement with experimental data on the Hugoniot of water.

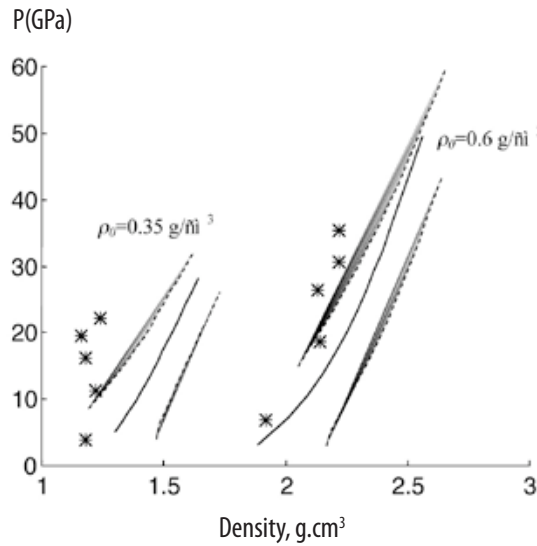


Figure 2. Hugoniot of porous ice. Stars: experimental data [7]; solid lines: calculation with the potential [20]; the dashed lines bound the region of Hugoniot from different possible approximations of the ab initio data [21].

However, calculations carried out for porous ice (Figure 2) showed strong disagreement with the experimental data. Dissociation at pressures $P < 20$ GPa for these Hugoniot is $< 1\%$ and hence does not affect their positions. The conclusion is that the approximation (2) is unsatisfactory. Indeed, not only the minimum depth, but also the minimum position is temperature dependent: it shifts to the right as temperature increases [21]. This leads to a decrease of compressibility. Since at the given pressure on the Hugoniot, the temperature increases with initial porosity, the increase of compressibility reveals itself stronger as the initial porosity grows.

Calculations carried out with limiting approximations corresponding to the lower (1000 K) and the upper curve (10000 K) from [21] bound the region of Hugoniot from different possible approximations of the ab initio data [21] (Figure 2). The experimental data go out of this region as pressure grows. Therefore, the matter is not only in successful approximation. We suppose the following reasons for the disagreement between the calculation and the experiment. Ab initio calculations [21] do not take into account multiparticle interactions; the multipolar and other interactions dependent upon mutual orientations were taken into account indirectly, namely, via averaging over the orientations at the given temperature.

Two simple steps were done to improve the model. As already mentioned above, a more accurate approximation of the ab initio data [21] requires a temperature dependence of r'_0 (characteristic radius), which was taken in the form

$$r'_0 = r'_{00}((1.0 + \xi \exp(-T_0/T))) \quad (3)$$

Then we tried to effectively account for the multiparticle effects. Remaining in the frame of the pair potential, we suppose that the growth of the characteristic radius with temperature (i.e., the spherical symmetrization of the interaction) is suppressed as density increases (i.e., assume that T_0 in (3) is a function of density):

$$T_0 = T_{00}(1 + \nu\rho) \quad (4)$$

Our calculations with the modified potential and experimental data on shock compression of water, porous ice, and snow [7,8] are compared in Figure 3. One can see a very good agreement.

A similar approach to water EOS was applied in [22] where intermolecular interaction is described by a spherically symmetric exp-6 potential and an angular dependent multipolar contribution. Unfortunately, in [22], there is no comparison with experimental data for porous ice and snow.

The principal Hugoniot of water calculated with the GLOBUS-3 EOS in which different physical models were sewed together is presented in Figure 4.

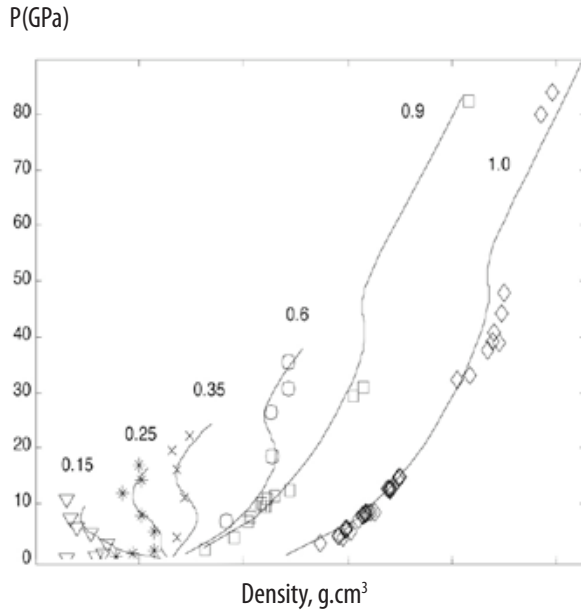


Figure 3. Hugoniot of water and porous ice and snow. Solid lines: calculation with the modified potential; markers: experimental data [7,8,10-13,23]. The digits near the curves are initial densities. Data on densities for $\rho_0 = 1.0 \text{ g/cm}^3$ were increased by $+0.5 \text{ g/cm}^3$.

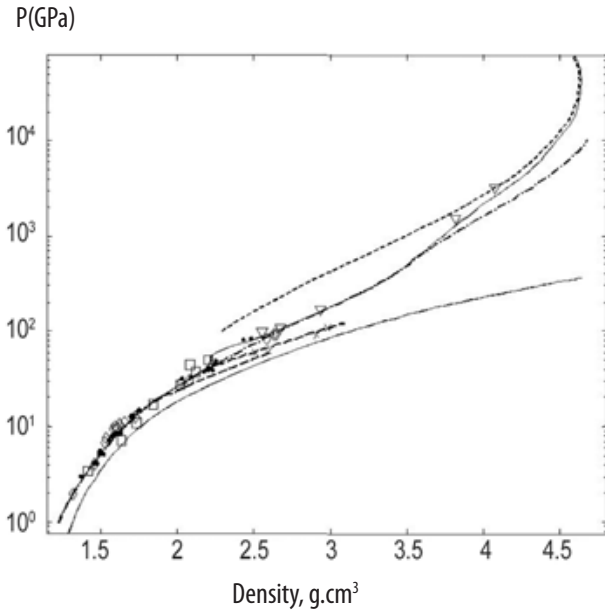


Figure 4. Hugoniot of water. Solid line: GLOBUS-3 EOS; dashed and dotted line: GLOBUS EOS [14]; markers: experimental data [7-8,10-13,23]; dashed line: Thomas-Fermi model with quantum corrections for the homogeneous mixture of atoms; long dashed line: double compression calculated by GLOBUS-3; x: experimental data on double compression [7]; lower solid line: potential pressure.

References

- [1] G. V. Kovalenko, A. T. Sapozhnikov, *Meth. & Codes for Num. Sol.* **4** 6 40-46 (Vopr. Atom, Nauki I Tech., 1979, in Russian).
- [2] M. P. Vukalovich, S. L. Ryvkin, A. A. Alexandrov, *Tables of Thermodynamic Properties of Water and Water Vapour* (in Russian) (1969).
- [3] B. V. Zamyshlyayev and M. G. Menzhulin, Interpolational equation of state of water and water vapor,” *Zh. Prikl. Mekh. Tekh. Fiz.* **3** 113-118 (1971).
- [4] R. Latter, “Temperature Behavior of the Thomas-Fermi Statistical Model for Atoms,” *Phys. Rev.* **99** 1854-1859 (1955).
- [5] A. T. Sapozhnikov and A. V. Pershina, *Meth. & Codes for Num. Sol.* **4** 6 47-52 (Vopr. Atom, Nauki I Tech., 1979, in Russian).
- [6] S. V. Bobrovskii, V. M. Gogolev, M. G. Menzhulin, R. V. Shilova, “Interpolyatsionnaya termodinamicheskaya model' dlya vody v oblasti odnorodnykh i dvukhfaznykh sostoyanii,” *Zh. Prikl. Mekh. Tekhn. Phys.* **5** 130-139 (1978).
- [7] A. A. Bakanova, V. N. Zubarev, Yu. N. Sutulov, R. F. Trunin, “Thermodynamic properties of water at high pressures and temperature,” *Zh. Eksp. Teor. Fiz.* **68** 1099-1107 (1975).
- [8] R. F. Trunin, G. V. Simakov, M. V. Zhernokletov, V. V. Dorokhin, *Teplofizika Vysokih Temperatur*, **37** 732-737 (1999).
- [9] N. N. Kalitkin, L. V. Kuzmina, I. I. Sharipjanov, “Constraction of equations of state for chemical compounds,” Preprint No. 43 (Moscow: Institute of Applied Mathematics of the USSR Academy of Sciences, 1976).
- [10] L. P. Volkov, N. P. Voloshin, P. A. Mangasarov, *Pis'ma v Zh. Eksp. Teor. Fiz.* **31** 564-548 (1980).
- [11] A. C. Mitchell and W. J. Nellis, “Equation of state and electrical conductivity of water and ammonia shocked to the 100 GPa (1 Mbar) pressure range,” *J. Chem. Phys.* **76** 6273-6281 (1982).
- [12] M. A. Podurets, G. V. Simakov, R. F. Trunin, L. V. Popov, B. N. Moiseev, “Compression of water by strong shock waves,” *Zh. Eksp. Teor. Fiz.* **62** 710-712 (1972).
- [13] E. N. Avrorin, B. K. Vodolaga, N. P. Voloshin, G. V. Kovalenko, V. F. Kuropatenko, V. A. Simonenko, B. T. Chernovoluyuk, “Experimental study of the shell effects on the shock adiabats of condensed substances,” *Zh. Eksp. Teor. Fiz.* **93** 613-626 (1987). [*Sov. Phys. JETP* **66** 347 (1987)].
- [14] A. T. Sapozhnikov, G. V. Kovalenko, P. D. Gershchuk, E. E. Mironova, *Mat. Mod. Fiz. Protsessov* **2** 15-19 (Vopr. Atom., Nauki I Tech., 1991).
- [15] N. N. Kalitkin, I. V. Ritus, A. M. Mironov, “Ionization equilibrium taking into account degeneration of electrons,” Peprint 46 (Moscow, Institute of Applied Mathematics of the USSR Academy of Sciences, 1983).
- [16] N. N. Kalitkin, L. V. Kuz'min, “Tables of thermodynamic functions at high energy concentration,” Preprint 35 (Moscow, Institute of Applied Mathematics of the USSR Academy of Sciences, 1975).
- [17] V. P. Kopyshev, “Numerical techniques of continuous medium mechanics,” *Rus. Chisl. Metody. Mekh. Splosh. Sred.* **8** 54-67 (1977).
- [18] M. Ross, “A high-density fluid-perturbation theory based on an inverse 12th-power hard-sphere reference system,” *J. Chem. Phys.* **71**, Issue 4, 1567 (1979).
- [19] V. V. Dremov and D. G. Modestov, “Calculation of shock compression parameters for chloriated methane,” *Chem. Phys. Reports* **17** 781-790 (1998).
- [20] F. H. Ree, “A statistical mechanical theory of chemically reacting multiphase mixtures: Application to the detonation properties of PE,” *J. Chem. Phys.* **81** 1251-1262 (1984).
- [21] F. H. Ree, “Molecular interaction of dense water at high temperature,” *J. Chem. Phys.* **76** 6287 (1982).
- [22] H. D. Jones, “Theoretical equation of state for water at high pressures,” *Shock Compression of Condensed Matter-2001: 12th APS Topical Conference*, ed. M. D. Furnish, N. N. Thadhani, and Y. Horie, *AIP Conference Proceedings* **620**, Issue 1, 103-106 (Melville, NY, AIP, 2001) pp. 103-106.
- [23] J. M. Walsh and M. H. Rice, “Equation of state and electrical conductivity of water and ammonia shocked to the 100 GPa (1 Mbar) pressure range,” *J. Chem. Phys.* **76** 6273 (1982).

ON THE UNIVERSAL BEHAVIOR OF SOME ORGANIC COMPOUNDS UNDER COMPRESSION

B.A. Nadykto

All-Russia Research Institute of Experimental Physics (VNIIEF),
Sarov 607190, Russia

Such materials as polyethylene, polypropylene, polyisobutylene have about the same initial density and the same elemental composition (CH_2); only the structures of the initial molecules differ. As the analysis shows, the behaviors of polyethylene and polypropylene under compression are similar and described with one and the same equation of state (with the same parameters). The correlation behavior of compressibility of hydrocarbon and fluorocarbon compounds of CF_2 type is shown. This may be because of identical electron configuration of oxygen-like carbon ion in these compounds.

Introduction

In his papers, P. Bridgman demonstrated that many crystals undergo crystalline structure change under static pressure [1]. Pressure-induced phase transitions were observed later in shock-wave experiments too [2,3,4]. They proceed under these conditions in very short times (up to a few nanoseconds).

In the late 1940s, the concept of electron phases of solids appeared; it was found then from X-ray diffraction measurements in samples under pressure [5] that different cerium phases that had been discovered previously by P. Bridgman had the same crystalline lattice type.

Such transformations are also observed in hydrocarbon and fluorocarbon materials. Plastic materials on the base of hydrocarbons and fluorocarbons are extensively used in practice, including their application in devices that can be subjected to impulsive loads. Some organic fluids, such as hexane, are used in shock-wave experiments as a transparent shield. To develop models of the behavior of these materials, knowledge of their equations of state is required. Currently, the main data on the equation of state (EOS) for these materials can be obtained from a D-u diagram, which is constructed during shock-wave experiments (6,7).

Method of Calculation

To calculate material compressibility, we use the method described in detail in [8-12]. The model of [8-12] provides approximate analytical expressions describing elastic energy and pressure in compression and allows estimation of outer electron energy state as $E_n = 9AB_0/2N_A\rho_n$. Here, energy and pressure are written as a sum of their cold (elastic, potential) and thermal components:

$$E = E_C + E_T; \quad P = P_C + P_T. \quad (1)$$

The elastic components of energy and pressure are given by the following expressions:

$$E(\sigma) = \frac{9B_0}{\rho_n} \left(\frac{\sigma^{2/3}}{2} - \sigma^{1/3} \right); \quad P(\sigma) = 3B_0 (\sigma^{5/3} - \sigma^{4/3}), \quad (2)$$

where $\sigma = \rho/\rho_n$ is the compression ratio, ρ_n is the equilibrium density of material with $P=0$, $T=0$.

The thermal component of pressure in Mie-Grueneisen form is $P_T = \Gamma \rho E_T$. The Grueneisen coefficient, Γ , can be calculated based on (2). In the Dugdale-MacDonald approximation, $\Gamma = (2\sigma^{1/3} - 1)/(3\sigma^{1/3} - 2)$. The EOS given above can be used to calculate the shock-wave compression of material.

Results and Discussion

There are two different procedures of manufacturing polyethylene, and hence, it has somewhat different density at normal pressure and temperature. The density of polyethylene manufactured under high-pressure (HP) is 0.92 g/cm^3 , and the low-pressure (LP) technology gives polyethylene density 0.95 g/cm^3 . Ref. [7] contains the main experimental data on the shock-wave compression of polyethylene up to 50 GPa for HP polyethylene and up to 60 GPa for LP polyethylene, and [6] contains data on the polyethylene compression up to 44 GPa for HP polyethylene and up to 55 GPa for LP polyethylene.

We obtained the polyethylene EOS of the form (1, 2). The experimental data in D-u, P- ρ and P-u coordinates clearly show the changed slope of the experimental curves near $u=1.97 \text{ km/s}$, $D=5.7 \text{ km/s}$, $P=10 \text{ GPa}$, and $\rho=1.4 \text{ g/cm}^3$. The slope changes can be attributed to changes in the electron structure of polyethylene under compression. Therefore, the polyethylene EOS was fitted in the form of two sections with different parameters for each phase:

I $\rho_0 = 1.07 \text{ g/cm}^3$; $B_0 = 17.0 \text{ GPa}$.

II $\rho_0 = 1.325 \text{ g/cm}^3$; $B_0 = 50 \text{ GPa}$.

Figure 1(a) gives a comparison between the calculated P(ρ) curves and the experimental data from [6,7] for HP polyethylene ($\rho_{00} = 0.92 \text{ g/cm}^3$). Calculations of Hugoniot for LP polyethylene ($\rho_{00} = 0.95 \text{ g/cm}^3$) using the same EOS as for HP polyethylene demonstrate a noticeable difference in Hugoniot for various initial densities of polyethylene (7–10% in pressure). Comparison of the calculated dependences P(ρ) with the experimental data from [6,7] for polypropylene is shown in Figure 1(b). The calculation for polypropylene was performed under the assumption that its EOS was the same as the polyethylene EOS. Each of the D-u, P- ρ , and P-u curves is described well by this EOS. The data of [6] are significantly fuller than those of [7]. The clearly seen difference between the two experimental points from [7] and the data from [6] can be attributed (besides a measurement error) to the metastable state of the previous phase implemented, for one reason or another, in [7].

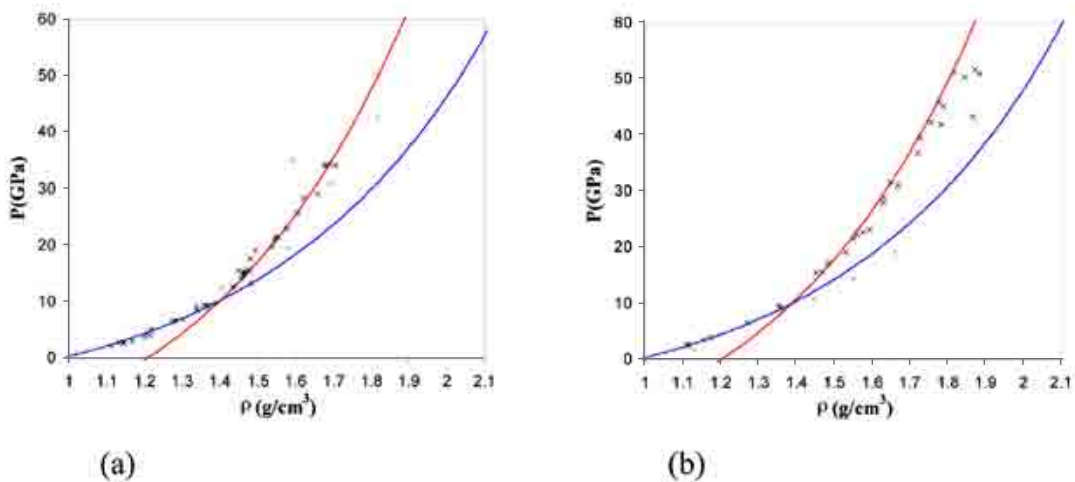


Figure 1. The P(ρ) curves for (a) HP polyethylene ($\rho_{00} = 0.92 \text{ g/cm}^3$); (b) polypropylene ($\rho_{00} = 0.90 \text{ g/cm}^3$). Experimental data: \square - from [7], \times - from [6]. The curves were calculated by us for two different polyethylene phases.

Polytetrafluoroethylene is a polymer with linear chain CF_2 , which is similar to polyethylene with linear chain CH_2 . There is a common known trademark “Teflon” with density of $2.15\text{--}2.19\text{ g/cm}^3$ under normal conditions. Experimental data for polytetrafluoroethylene under shock compression with pressures higher than $1.4\text{--}4\text{ GPa}$ are given in [6] (for pressures up to 86 GPa) and [7] (for pressures up to 174 GPa). Data on the shock-wave experiments with pressures lower than 3 GPa (see [15,16]) and data on the static experiments (see [13,14]) are also available. Static experiments [13,14] show that Teflon demonstrates its phase transition under hydrostatic pressure $0.54 \pm 0.01\text{ GPa}$. The phase transition results in 2.3% volume changes. The shock-wave experiments described in [15,16] prove that Teflon demonstrates its phase transition under pressure 0.5 GPa [15], or 0.7 GPa [16], which can be found from the intersection of $P(\rho)$ curves. As for high pressures, the $P(\rho)$ curves also intersect at $P \approx 4, 15$, and 30 GPa , and such intersections can be treated as changes in the electron structure of material under compression. The available experimental data make it possible to construct the equation of state for polytetrafluoroethylene with pressures up to 200 GPa . Each of the five sections of the $P(\rho)$ curve corresponding to different phase states parameters for EOS (2) is given below:

- I $\rho_0 = 2.3\text{ g/cm}^3$, $B_0 = 5.7\text{ GPa}$. II $\rho_0 = 2.43\text{ g/cm}^3$, $B_0 = 18.4\text{ GPa}$.
 III $\rho_0 = 2.62\text{ g/cm}^3$, $B_0 = 37\text{ GPa}$. IV $\rho_0 = 2.93\text{ g/cm}^3$, $B_0 = 85\text{ GPa}$.
 V $\rho_0 = 3.365\text{ g/cm}^3$, $B_0 = 217\text{ GPa}$.

Under normal conditions (atmospheric pressure, $T=293\text{ K}$), the estimated equilibrium density of Teflon is $\rho_{00} = 2.165\text{ g/cm}^3$, and the bulk modulus is $B = 4.73\text{ GPa}$. Comparison between the calculated $P(\rho)$ and $D(u)$ curves and the experimental data is given in Figure 2. Use of the values of parameters for five different phases allows the experimental data within the whole range of measurements to be described quite well.

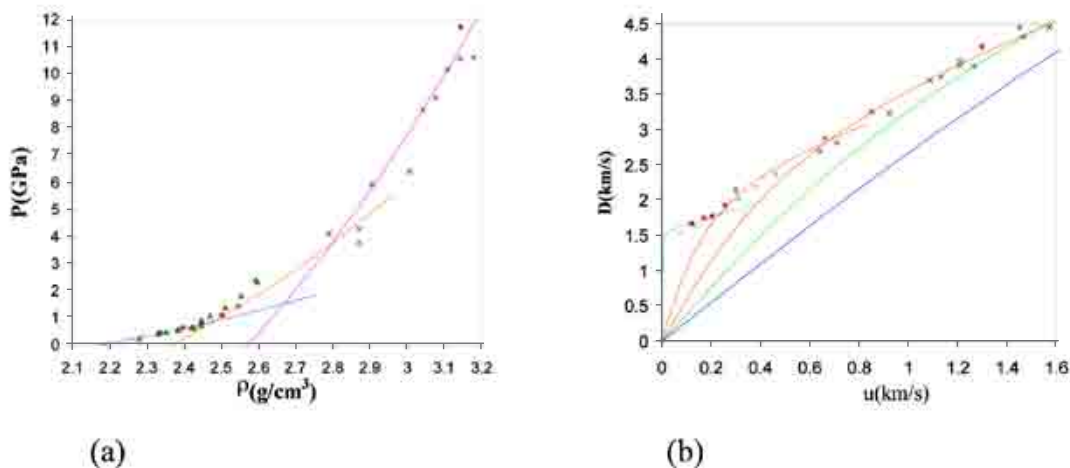


Figure 2. The dependence of parameters on the Hugoniot for polytetrafluoroethylene: a) $P(\rho)$; b) $D(u)$. Experimental data: \square – from [16], Δ – from [15], \times – from [6], \diamond – from [7]. The curves are the results of our calculations for various polytetrafluoroethylene's phases.

The fluoropolymer modification— $\text{C}_2\text{F}_3\text{Cl}$ —in which one atom of fluorine is replaced by chlorine, is widespread in practice. In spite of an essentially large atomic weight of chlorine, as compared to fluorine, the polychlorotrifluoroethylene density is even slightly lower than the polytetrafluoroethylene density. This indicates that a chlorine ion in this compound has a large volume in comparison with that of a fluorine ion (if the fluorine and chlorine ions' volumes were the same, the density of $\text{C}_2\text{F}_3\text{Cl}$ would be higher than the density of CF_2 by a factor of 1.165). Ref. [6] gives detailed experimental data on the shock compression of polychlorotrifluoroethylene

with pressure 0.3-75 GPa. For each section of the $P(\rho)$ curve for polychlorotrifluoroethylene corresponding to its different phase states the parameters selected for EOS (2) are given below:

- I $\rho_0 = 2.1998 \text{ g/cm}^3$, $B_0 = 9.8 \text{ GPa}$. II $\rho_0 = 2.37 \text{ g/cm}^3$, $B_0 = 18.2 \text{ GPa}$.
 III $\rho_0 = 2.604 \text{ g/cm}^3$, $B_0 = 38.1 \text{ GPa}$. IV $\rho_0 = 3.03 \text{ g/cm}^3$, $B_0 = 85 \text{ GPa}$.
 V $\rho_0 = 3.6 \text{ g/cm}^3$, $B_0 = 170 \text{ GPa}$.

Under normal conditions (atmospheric pressure, $T=293 \text{ K}$), the estimated equilibrium density of polychlorotrifluoroethylene is $\rho_{00} = 2.14 \text{ g/cm}^3$, the bulk modulus is $B = 9 \text{ GPa}$ under these conditions. Figure 3 illustrates comparison between the calculated $P(\rho)$, $D(u)$ curves, and experimental data.

Figure 3. The curves for polychlorotrifluoroethylene: a) $P(\rho)$, b) $D(u)$. Experimental data: x – from [6]. The curves are the results of our calculations for various polychlorotrifluoroethylene's phases.

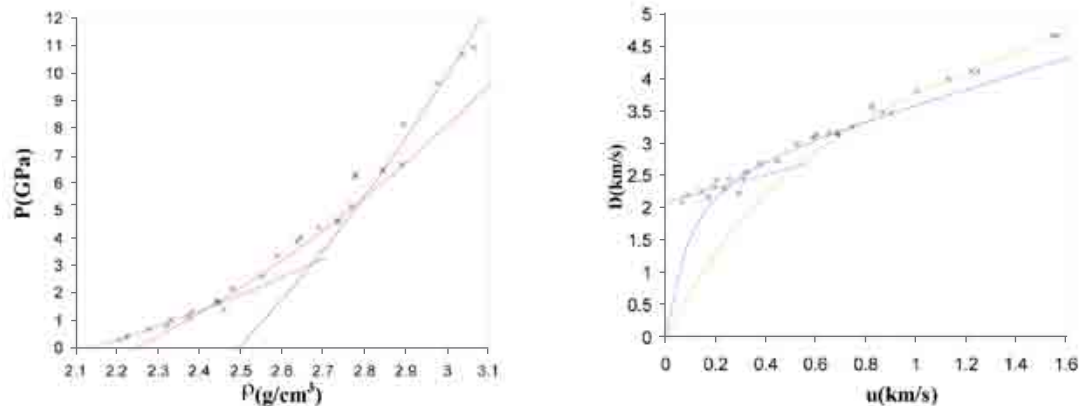
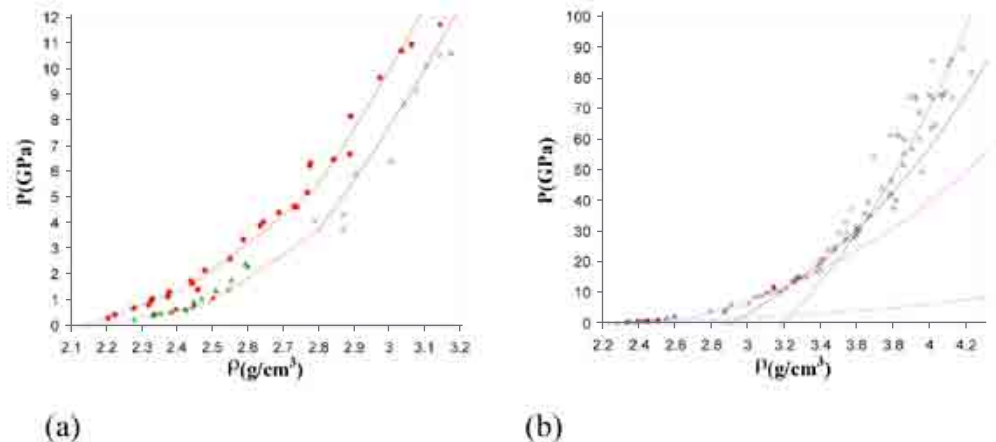


Figure 4(a) illustrates for comparison the $P(\rho)$ curves for polytetrafluoroethylene and polychlorotrifluoroethylene. One can see that these fluorocarbons of different elemental compositions have almost the same slopes of their $P(\rho)$ curves in sections with appropriate pressure values (i.e., close values of bulk modulus). Possibly, this can be attributed to the same compressibility of electron shell of a carbon atom (ion) in various fluorocarbons. Figure 4(b) shows pressure points [7] on the Hugoniot (triangles) for liquid (carbogal), which has the same elemental composition (CF_2) as Teflon. Under high pressures, the experimental points for carbogal of initial density 1.89 g/cm^3 are located in parallel to the curve for Teflon and close to it. Two points under lower pressures are located close to the curve for the previous phase. This indicates that with the same elemental composition, the behavior of atoms is almost the same in solid and liquid phases.

Figure 4. (a) Comparison between the $P(\rho)$ curves for polytetrafluoroethylene (curves and experimental data on the right) and polychlorotrifluoroethylene (curves and experimental data on the left). It is evident that these materials demonstrate similar behavior in compression. (b) The $P(\rho)$ curve for polytetrafluoroethylene. Triangles (Δ) show the pressure points [7] on the Hugoniot for liquid (carbogal) of the same elemental composition (CF_2) as Teflon.



Polyvinylidene fluoride (PVDF) is a polymer structure of the form $[\text{CH}_2-\text{CF}_2]_n$. There are experimental data [6] within the range of pressures from 4 to 75 GPa. Several experimental points are given in [17] for pressures below 4 GPa. Under pressure, PVDF similar to polytetrafluorethylene and polychlorotrifluorethylene demonstrates intersections of the $P(\rho)$ curves, which can be treated as changes in the electron structure of PVDF under compression. For each section of the $P(\rho)$ curve for PVDF corresponding to various phase states of this material the following parameters were selected for EOS (2):

- I $\rho_0 = 1.882 \text{ g/cm}^3$, $B_0 = 6.9 \text{ GPa}$. II $\rho_0 = 1.856 \text{ g/cm}^3$, $B_0 = 18.6 \text{ GPa}$.
 III $\rho_0 = 2.10 \text{ g/cm}^3$, $B_0 = 45.5 \text{ GPa}$. IV $\rho_0 = 2.93 \text{ g/cm}^3$, $B_0 = 85 \text{ GPa}$.

Under normal conditions (atmospheric pressure, $T=293 \text{ K}$), the estimated equilibrium density of PVDF is $\rho_{00} = 1.767 \text{ g/cm}^3$, and the bulk modulus is $B = 5.7 \text{ GPa}$ under the same conditions. Comparison between the calculated $P(\rho)$, $D(u)$ curves, and experimental data is given in Figure 5.

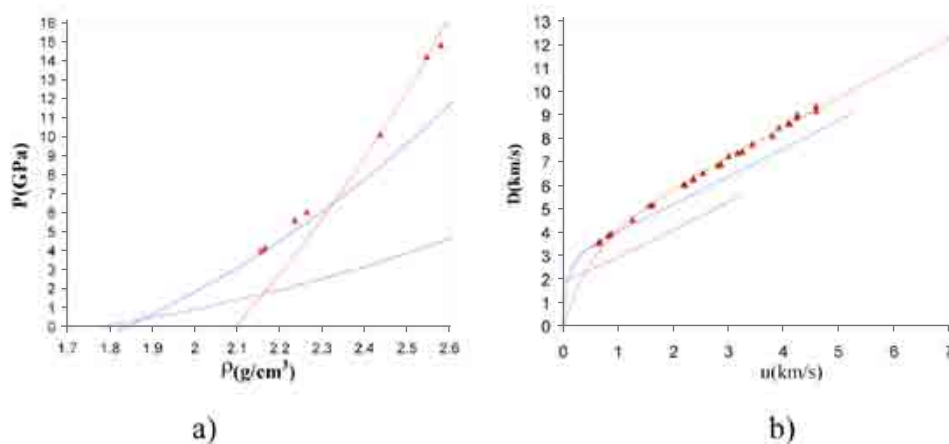


Figure 5. Curves a) $P(\rho)$, b) $D(u)$ for polyvinylidene fluoride (PVDF). Experimental data: Δ – from [6], \square – from [17]. The curves are the result of our calculations for various PVDF phases.

Conclusions

It has been shown that hydrocarbons of the same elemental composition, CH_2 , demonstrate the same behavior under compression. Apparently, the volume and compressibility of a compound is determined by a carbon ion, and hydrogen makes no contribution to its volume.

It is noted that fluorocarbons of different elemental compositions have almost the same slopes of the $P(\rho)$ curves in sections with appropriate pressures (close values of bulk modulus). This can be attributed to the fact of the same compressibility of the electron shell of a carbon atom (ion) in various fluorocarbons.

The calculated $D(u)$ curves clearly demonstrate non-linear and non-monotone behavior within a wide range of parameters. Such non-monotone behavior is demonstrated to the highest extent by the $P(\rho)$ curves. The non-monotone behavior is proved by comparison with available experimental data.

References

- [1] P. W. Bridgman, *Collected Experimental Papers*, 7 vols. (Cambridge, MA, Harvard University Press, 1964).
- [2] J. M. Walsh, "Metal equation of state from shock wave studies," *Bull. Am. Phys. Soc.* **29** 28 (1954).
- [3] D. Bancroft, E. L. Peterson, S. Minshall, "Polymorphism of iron at high pressure," *J. Appl. Phys.* **27**, Issue 3, 291 (1956).
- [4] L. V. Altshuler, "Use of shock waves in high-pressure physics," *USP FIZ NAUK* **85**, No. 2, 197 (1965). [*Sov. Phys. Usp.* **8** 52 (1965) – in Russian]
- [5] A. W. Lawson and T. Y. Tang, "Concerning the high pressure allotropic modification of cerium," *Phys. Rev.* **76** 301 (1949).
- [6] S. P. Marsch, ed., *LASL Shock Hugoniot Data* (Berkeley, CA, University of California Press, 1980).
- [7] R. F. Trunin (ed.), *Experimental Data on Shock-Wave Compression and Adiabatic Expansion of Condensed Matters*, (Sarov, Russian Federal Nuclear Center Academic Publication, 2006).
- [8] B. A. Nadykto, *Doklady Akademii Nauk SSSR*. **316** 6 1389 (1991).
- [9] B. A. Nadykto, "A semiempirical model for calculation of the energies of states of multielectron ions," *Physics-Uspokhi* **36** 794 (1993).
- [10] B. A. Nadykto, *Theor. i Prikl. Fizika*, Issue 3, 58 (Vopr. Atom. Nauki i Tech. 1996).
- [11] B. A. Nadykto, "Calculation of Electron Phase Parameters of Elements and Compounds Using Compressibility Data," in *New Models and Numerical Codes for Shock Wave Processes in Condensed Media*, ed. I. G. Cameron (Oxford: AWE Hunting BRAE, 1998) p. 205.
- [12] B. A. Nadykto *Khimicheskaya Fizika* **18** 11 87 (1999).
- [13] G. C. Kennedy and P. N. LaMori, "The pressures of some solid-solid transitions," *J. Geophys. Res.* **67** (Institute of Geophysics and Planetary Physics, University of California, Los Angeles, CA, 1962) p. 851.
- [14] C. E. Weir, "Transitions and phases of polytetrafluoroethylene (Teflon)," *J. Res. Natl. Bur. Std.* **50** 95 (1953).
- [15] A. R. Champion, "Shock compression of teflon from 2.5 to 25 kbar-evidence for a shock-induced transition," *J. Appl. Phys.* **42**, Issue 13, 5546-5550 (1971).
- [16] D. L. Robbins, S. A. Sheffield, R. R. Alcon, "Magnetic particle velocity measurements of shocked teflon," *Shock Compression of Condensed Matter 2003, AIP Conference Proceedings*, eds. M. D. Furnish, Y. M. Gupta, and J. W. Forbes (Melville, NY, AIP, 2004) pp. 675-678.
- [17] J. C. F. Millett and N. K. Bourne, "The shock induced equation of state and shear strength of polyvinylidene difluoride," *J. Phys. IV France* **134** 719-724 (2006).

SHOCK INDUCED PLASTICITY IN AL, CU, AND AL-CU ALLOYS

A. V. Yanilkin, A. Yu. Kuksin, G. E. Norman, V. V. Stegailov

Joint Institute for High Temperatures (JIHT), Russian Academy of Sciences, Moscow, 125412, Russia

Author Contact: aleyanilkin@gmail.com

The molecular dynamic (MD) simulations presented are devoted to the study of mechanisms and kinetics of shock-induced plasticity of Al and its alloy with Cu. Dislocation velocities as functions of applied shear stress are calculated in a wide temperature range up to melting point. Dislocation interaction with nanosize obstacles (voids, precipitates) is considered. The critical resolved shear stress necessary for a dislocation to penetrate through an obstacle is determined. The results are used to characterize the effect of temperature on the dynamic yield stress in perfect crystals and crystals with nano-sized obstacles.

Introduction

The ability of a crystal to exhibit plastic deformation is related to the presence of dislocations in the crystal lattice. The motion of dislocations provides for the formation of a real atomic structure in crystalline solids and the kinetics of deformation of crystals under load; it underlies the control of many important physical properties of solids [1].

It is known that the dependence of the yield stress on deformation rate in many metals increases sharply when the deformation rate exceeds 10^3 - 10^4 s⁻¹. This phenomenon can be interpreted as the consequence of a change in the mechanism of dislocation motion. Moving at low velocities, dislocations overcome obstacles as a result of the joint action of the applied stress and thermal fluctuations. Due to this, an increase in the temperature is accompanied by a decrease in the yield stress of the material. For a high-rate deformation, it is necessary to apply higher stresses. At a deformation rate exceeding a certain threshold (10^4 s⁻¹ for pure metals), the acting stresses prove to be sufficient for the dynamic overcoming of obstacles without an additional contribution from thermal fluctuations. In this case, the pumping of the dislocation energy to the crystal lattice vibrations or, depending on temperature, to the electron subsystem becomes the dominating mechanism of the retardation of dislocations. In contrast to the region of thermofluctuational mobility, the dislocation velocity in the dynamic region decreases with temperature in accordance with an increase in the density of the gas of elementary excitations. For this reason, an anomalous increase in the yield stress with increasing temperature is observed for some materials at very high rates of deformation [1].

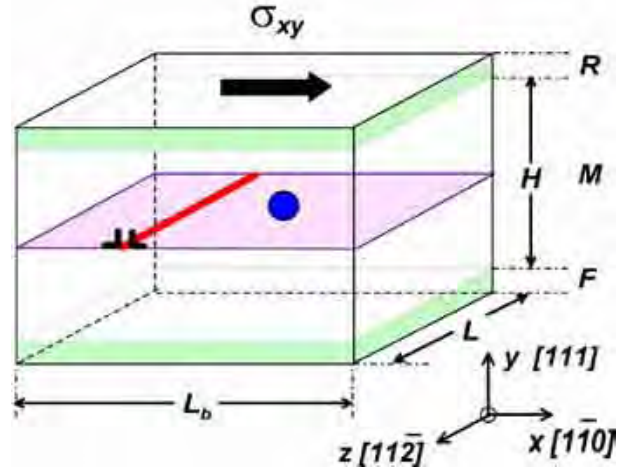
In the present paper, mechanisms and kinetics of plasticity of Al and its alloys are studied under strain rates 10^5 s⁻¹ and more. The mobility of dislocations is evaluated from nonequilibrium MD simulations. The influence of temperature, Cu precipitates, and voids on dislocation motion is analyzed. The results of simulation are compared with the values of the dynamic yield stress for single crystalline aluminum in the shock-wave experiments [1].

Model

Three types of MD models (with different boundary conditions) are used to study the mobility of single dislocations. Our calculations are based on a variant of the model proposed by Daw et al.[2], where the periodic boundary conditions are set not only along the dislocation axis, but also along the direction of the Burgers vector **b** of the dislocation. In this case, the system can be represented as an array of dislocations periodically repeating in space.

Figure 1 shows a schematic diagram of the calculation cell used in this model. The axes are oriented so as to correspond to one of the glide systems typical of the fcc lattice of aluminum, namely, $[1-10](111)$. The Burgers vector of the pure edge dislocation providing such a glide is $\mathbf{b} = a/2[1-10]$ (the direction coincides with the X axis). The dislocation glides in the XZ plane that coincides with the (111) plane. The edge-dislocation line coincides with the Z axis. The periodic boundary conditions are set along the X and Z axes. The mobile particles of the calculation cell form the M unit.

Figure 1. Schematic diagram of the model used for calculating the behavior of a dislocation in the fcc crystal under the action of shear: (M) mobile atoms, (F) fixed atoms, (R) the rigid block where individual atoms are displaced in the direction of axis X .



For generating shear stresses σ_{xy} , we used several border atomic layers, each consisting of particles fixed relative to one another. The positions of three atomic layers near the lower boundary F are fixed, while the layers near the upper boundary R move along the axis X either under the action of a preset external force F_x or at a constant preset velocity v_x . Thus, in the first case, the shear stress is directly controlled, while, in the second case, the shear strain is controlled. It is necessary to emphasize that the pure dislocation, which is energetically less favorable for the fcc lattice, splits into two partial edge dislocations. The modeling has used EAM potential [2], parameterized by Liu et al., and the LAMMPS package [3].

Results and Discussion

Dislocation Motion in Single Crystal/Phonon Drag Coefficient

It is convenient to study the mobility of dislocations as a function of the shear stress. The shearing force F_x is determined by a preset value of the stress σ_{xy} and the surface area S_{xz} to which it is applied: $F_x = \sigma_{xy} S_{xz}$. As a result, the crystal is subjected to elastic deformation. For small stresses, the dislocation can be immobile or make irregular motions in arbitrary directions on a glide plane. As the stress reaches a critical level, the displacements of the dislocation become ordered, and it moves at a constant velocity, depending on the applied shearing force and the temperature. Figure 2 shows the dependences of the dislocation velocity v on the shear stress σ measured at various temperatures up to the melting temperature. Two regimes can be distinguished (especially at low temperatures): a linear regime in the region of low stresses and the asymptotic approach of the dislocation velocity to the transverse sound velocity. In the entire range under consideration, an increase in the temperature results in decreasing dislocation velocity. Thus, the motion of dislocations requires no thermal activation; on the contrary, a dynamic regime with a phonon drag of dislocations takes place. The motion is controlled by the energy pumping from a dislocation to elementary excitations in the crystal. The linear portion of the dependence is conventionally characterized by the (drag) coefficient B of dislocations:

$$\sigma b = Bv \quad (1)$$

where b (2.9 Å) is the value of the Burgers vector of a dislocation.

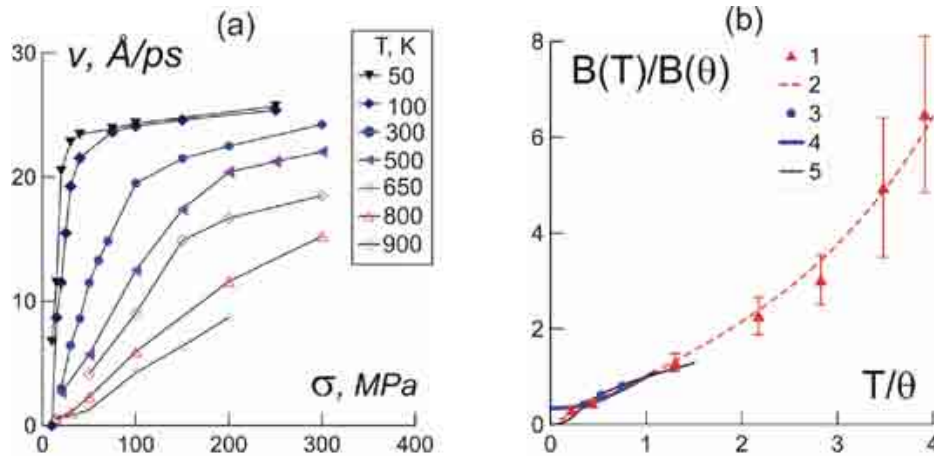


Figure 2. (a) Dependences of the dislocation velocity v on the applied shear stress σ_{xy} . (b) The temperature dependence of the phonon drag coefficient normalized to the temperature $\theta = 230$ K and the value of $B(\theta)$: (1) MD; (2) approximation of MD data using Equation 1; (3), (4) experiments; (5) theoretical estimation.

On the basis of data obtained by MD method, we determined the temperature dependence of the dislocation drag coefficient $B(T)$ [4]. The dependence $B(T)$ is shown in Figure 2 in the dimensionless form, where $\theta = 230$ K (it is close to Debye temperature). For comparison, we also present the experimental data taken from review [1]. The absolute value of the drag coefficient at 300 K found from the MD simulations amounted to approximately $1.4 \cdot 10^{-5}$ Pa*s, which is close to the experimental values. In the region of moderate temperatures, the dependence is virtually linear. Such a behavior of $B(T)$ is described within the framework of the existing theories of the phonon drag. With increasing temperature, deviations from the linear law are observed, which are described well by a polynomial of the third or fourth order [4].

Dislocation Interaction with Obstacles

Dislocation interaction in Al with the nanosize obstacle (precipitate or void) is considered under the dynamic regime of dislocation motion. The MD scheme used is the same as in part of a single Al crystal. The difference is the loading conditions. In this scheme, the shear stress is increased linearly with time. It results in the bending of dislocation line, and then depinning from the obstacle [5]. Critical resolved shear stresses required for dislocation to penetrate through the obstacle are calculated as a maximum stress.

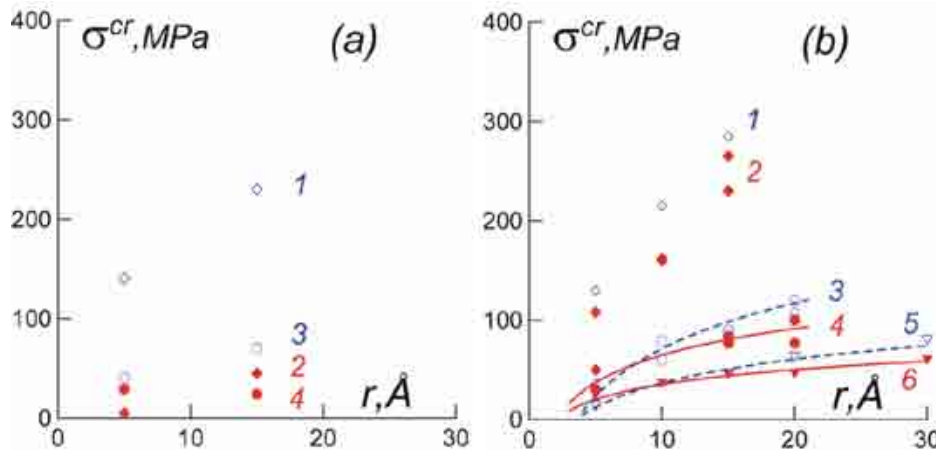


Figure 3. The dependence of the depinning stress on the radius of obstacle: (a) void and (b) copper cluster. The distance L between the obstacles is the following: 1,2 - 10 nm; 3,4 - 30 nm; 5,6 - 60 nm. Two temperatures are shown: the open symbols 1,3,5 - 300 K; the solid symbols 2,4,6 - 800 K. The solids line are the approximations by dependence obtained from the continuum model of Orowan mechanism.

Dynamic Yield Strength

The yield stress value under high-rate loading conditions can be determined by assuming that the plastic deformation rate $\dot{\epsilon}$ is determined by the mobility of dislocations as $\dot{\epsilon} = \rho_m b v$ [6]. We also assume that the density of mobile dislocations ρ_m remains constant in various experiments and is independent of the temperature and the deformation conditions. Then, the value of the dynamic yield stress as a function of the temperature is determined by the temperature dependence of the phonon drag coefficient $B(T)$ according to the following formula:

$$\sigma_Y(T) = \dot{\epsilon} B(T) / (\rho b^2) \quad (2)$$

The values thus obtained can be compared to the data on the dynamic yield stress of single crystalline aluminum obtained from the shock-wave experiment [1], where the deformation rates amounted to approximately $\dot{\epsilon} = 10^6 \text{ s}^{-1}$ (Figure 4). Exact values of the dislocation density under the conditions of shock-wave compression are not known; however, it can be seen that the temperature dependence obtained in the experiment is described well by the temperature dependence of the phonon drag coefficient $B(T)$ obtained by simulations assuming the dislocation density to be $\rho_m = 7 \cdot 10^8 \text{ cm}^{-2}$. The difference of one or two orders of magnitude in comparison to the characteristic density of mobile dislocations in single-crystalline aluminum under normal conditions ($10^6 - 10^7 \text{ cm}^{-2}$ according to the experimental data) can be explained by an increase in the dislocation density as a result of material compression in the shock wave.

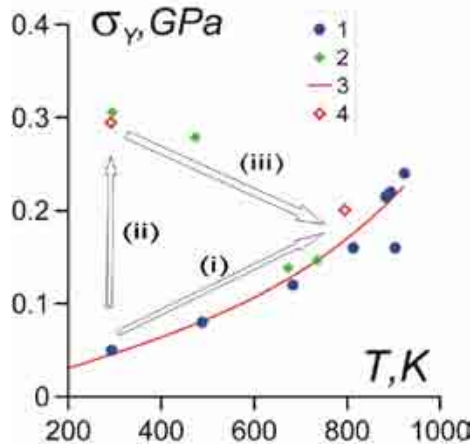


Figure 4. Temperature dependence of dynamic yield strength. (1) experimental data on the Al single crystal [1]; (2) experimental data on the Al alloy D16T [7]; (3) estimation from equation 2; (4) critical shear stress from MD for Al alloy with Cu (4%); the cluster size is 1.5 nm.

Based on MD results for critical resolved shear stress (Figure 3), one can estimate the yield strength of Al-Cu alloy. The temperature dependence of the yield strength of Al with Cu precipitates (4%) is in a good agreement with the experimental one for unannealed alloy of the similar composition D16T [7] (points 2 and 4 on Figure 4). The diffusion increases with increasing temperature, and the precipitates grow. It results in the decrease of the yield strength with temperature, and the magnitude depends on the duration thermal treatment. Therefore, the yield strength of annealed D16T is lower than for unannealed alloy. The arrows on Figure 4 demonstrate three effects: (i) the increase of the dynamic yield stress of single crystal due to increasing of the phonon drag, (ii) the hardening by dislocation-cluster interaction, and (iii) the thermal activation of dislocation depinning.

Conclusions

Motion of the edge dissociated dislocation is considered under the shear stress at various temperatures. With increasing applied shear stress, the ultimate velocity of dislocations close to the rate of propagation of elastic shear perturbations is achieved. The obtained temperature dependence of the phonon drag coefficient agrees at low temperatures with the available experimental data and with the present theoretical notions. On approaching the melting temperature, the dependence of the drag coefficient of dislocations significantly deviates from linear.

The influence of Cu precipitates and voids on dislocation motion is considered. The critical resolved shear stresses are obtained for different distances and sizes of obstacles. The MD results are in good agreement with the continuum model of the Orowan mechanism. The temperature influence is analyzed.

Based on MD results, the dynamic yield strength is estimated for single Al and Al-Cu alloy. The temperature dependence of estimated yield strength agrees with the experimental one.

Acknowledgements

We thank G. I. Kanel, V. E. Fortov, and J. B. Aidun for their interest in this study and useful discussion. This work was partially supported by the RFBR09-08-01116-a grant, RAS programs #11, 12 and Sandia National Laboratories under the U.S. DOE/NNSA Advanced Simulation and Computing program.

References

- [1] G. I. Kanel, V. E. Fortov, and S. V. Razorenov. "Shock waves in condensed-state physics," *Phys. Usp.* **50**, No. 8, 771-793 (2007).
- [2] M. S. Daw, S. M. Foiles, M. I. Baskes. "The embedded-atom method: a review of theory and application" *Mater. Sci. Rep.* **9** 251 (1993).
- [3] S. J. Plimpton. "Fast parallel algorithms for short-range molecular dynamics," *J. Comp. Phys.* **117** 1–19 (1995).
- [4] A. Yu. Kuksin, V. V. Stegailov, A. V. Yanilkin. "Molecular-dynamics simulation of edge-dislocation dynamics in aluminum," *Doklady Physics* **53**, No. 6, 287-291 (2008).
- [5] V. V. Stegailov, A. Yu. Kuksin, G. E. Norman, A. V. Yanilkin, "Atomistic study of nanoprecipitates influence on plasticity and fracture of crystalline metals," in *Shock Compression of Condensed Matter*, **955**, eds. M. D. Furnish et al. (New York, American Institute of Physics, 2007) pp. 339-342.
- [6] A. Yu. Kuksin, G.E. Norman, V. V. Stegailov, A. V. Yanilkin. "The influence of temperature on plasticity of Al alloys: molecular dynamics study," in *Multiscale Materials Modeling* (Florida State University, Department of Scientific Computing, 2008) pp. 442-445.
- [7] G. V. Garkushin, S. V. Razorenov, G. I. Kanel. "Submicrosecond strength of the d16t aluminum alloy at room and elevated temperatures," *Physics of the Solid State* **50**, No. 5, 839-843 (2008).

STATIC MATERIAL STRENGTH DETERMINED USING A DAC

H. Cynn,* W. J. Evans,* J. P. Klepeis,* M. J. Lipp,*
P. Liermann,^{1†} W. Yang[†]

*Lawrence Livermore National Laboratory, Livermore, CA 94550 USA

[†] HPCAT, Advanced Photon Source Argonne National Laboratory, Argonne, IL 60439 USA

¹ Currently at DESY, HASYLAB, Petra III, P02 Notkestr. 22607 Hamburg, Germany

By measuring sample thickness and pressure gradient using X-ray absorption and X-ray diffraction, respectively, the accurate static yield strengths of Ta and Fe were determined at high pressure. This improved method has several advantages over other similar methods to quantitatively determine static material strength.

Introduction

There have been continuous efforts to understand material strength at high pressure under static and dynamic conditions. Most static strength measurements are based on X-ray diffraction data, which easily connect to high-pressure measurements using a diamond anvil cell (DAC). By simplifying the stress conditions of a sample compressed uniaxially in a DAC, the deviatoric stress, $\sigma_3 - \sigma_1$, is approximated as yield strength of the sample [1]. Due to the symmetry along the axial compression of the diamond anvil cell (DAC) and the sample, the determined yield strength is represented at a pressure that equals the mean normal stress.

According to Singh and others [2,3,4], the lattice parameter, $a(hkl)$, of the cubic system calculated from the measured d-spacings can be represented by the following relation:

$$a(hkl) = M_o + M_l[3(1-3\sin^2\theta_{hkl})\Gamma(hkl)], \quad (1)$$

where,

$$\Gamma(hkl) = (h^2k^2 + k^2l^2 + l^2h^2)/(h^2 + k^2 + l^2)^2. \quad (2)$$

The intercept, M_o , and the slope, M_l , of the equation (1) with knowledge of elastic compliances, S_{ij} , of the sample, and the structure factor, $\Gamma(hkl)$, in equation (3) are used to calculate the deviatoric stress represented by the following relation:

$$\sigma_3 - \sigma_1 = -3M_l/\alpha M_o(S_{11} - S_{12} - S_{44}/2). \quad (3)$$

The term α is introduced to approximate the stress and strain conditions at the grain boundary. The Reuss approximation approximates iso-stress conditions across the grain boundary, $\alpha = 1$. If the strain across the grain boundary is approximated the same under the Voigt condition, α approaches zero.

Dewaele et al. [5] proposed a single crystal strain measurement using X-ray diffraction to estimate material strength with the knowledge of elastic constants of the sample. A laser interference pattern was used to estimate the plastic strain of the sample.

Meade and Jeanloz [6] approximated the difference between the axial and the radial stress under uniaxial compression of a nonhydrostatically compressed sample inside a gasket. In the Tresca approximation, they evaluated the deviatoric stress through the following relation:

$$\sigma_3 - \sigma_1 = h(dP/dr) \quad (4)$$

where h represents the thickness of the sample and dP/dr is the pressure gradient of the sample. Meade and

Jeanloz [6] used the ruby fluorescence method to determine the pressure gradient, measured the thickness of the recovered gasket, and applied the equation of state to back-calculate the thickness during the compression.

We decided to compare these methods to outline their advantages and weaknesses and to propose an improved methodology to determine the static material strength at high pressure using a DAC.

Method

Polycrystalline Ta and Fe powders (99.99% purity with a nominal grain size of 1.5 μm) were commercially available from Alfa Aesar. The samples were packed in a hole (300 μm in diameter and 10 ~ 40 μm thick) prepared in a Be gasket without a pressure medium. The size of the anvil was 400 μm . Hardened Be gaskets (3 mm in diameter and 1.5 mm thick) were pre-indented to 100 μm and provides the maximum X-ray transmission with a material strength sufficient for achieving high pressures [7]. The volume across the sample was determined via energy-dispersive X-ray diffraction and the pressure was calculated using the equation of state of the sample [8,9]. To measure thickness changes during compression, the x-ray transmission was recorded across the sample. The measured X-ray transmission through the diamond anvils and sample under compression was normalized against the transmission through the X-ray transparent Be gasket plus the anvils. The sample thickness, h , was calculated using the following relation:

$$I = I_0 \exp(-\mu_l h), \quad (5)$$

where I_0 and I , respectively, represent the initial and attenuated X-ray beam intensities. μ_l denotes the linear X-ray absorption coefficient. The mass absorption coefficient, μ_m , is equal to μ_l/ρ . ρ is the density of the sample.

Results and Conclusion

The X-ray transmission of Ta at 52 GPa is shown in Figure 1. Using equation (5), the thickness of the Ta sample at 52 GPa was estimated (Figure 2).

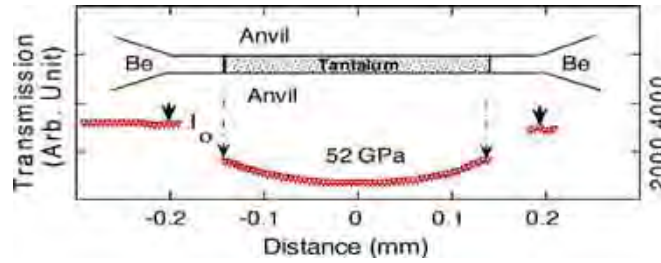


Figure 1. Transmission of Ta at 52 GPa across the 0.3 mm opening of the Be gasket. I_0 is the X-ray transmission intensity through the Be gasket and diamond anvils.

The sample thickness at the center is about 8.7 μm at 52 GPa with a measurable cupping by about 3 μm over 150 μm to the diamond culet edge.

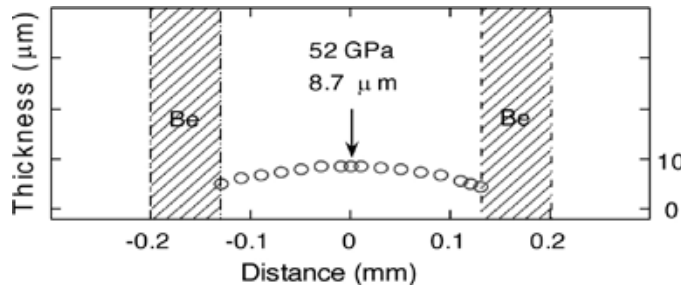


Figure 2. The thickness of a Ta sample at 52 GPa as obtained by using (5) is plotted as a function of the distance from the center. The size of the open circle represents the uncertainty in thickness determination.

To obtain the pressure gradient of Ta, the lattice strain was measured at every 5 to 20 μm steps using X-ray diffraction along the compression direction. Figure 3 shows spatially resolved pressure distribution at three pressures whose maximum values at the centers are 52, 27, and 13 GPa.

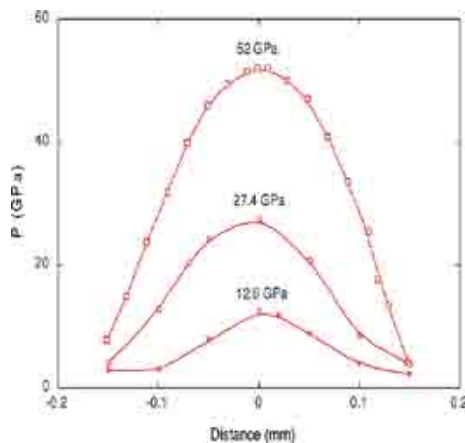


Figure 3. Spatially resolved pressure distribution with the maximum pressure at the center of the sample. For visual aid solid lines are used to connect the data points.

Based on the above-mentioned methods to measure sample thickness and pressure gradient, the deviatoric stresses of uniaxially compressed Ta powder were determined. The resulting deviatoric stress of Ta is plotted as a function of pressure in Figure 4, superimposed with the stresses estimated by Weir et al. [10] and Dewaele and Loubeyre [5]. Linear relation is apparent in this study and in Dewaele and Loubeyre [5].

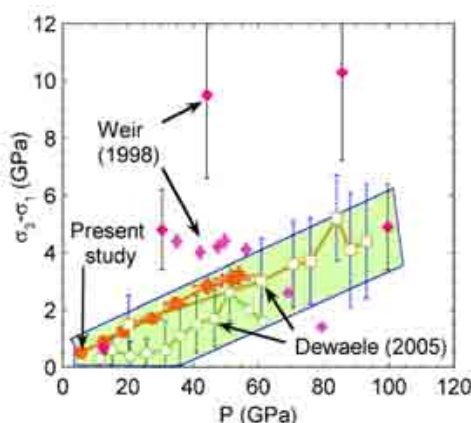


Figure 4. Deviatoric stress, $\sigma_3 - \sigma_1$, of Ta as a function of pressure. Present results are shown as solid orange circles. Two sets of data by Weir et al. [10] are shown as red and pink diamonds. Another two sets of data by Dewaele and Loubeyre [5] are shown as open circle and square.

Deviatoric stress of Fe was also determined using the same methods as in Ta (Figure 4) and compared with the stress determined by Singh et al. [11]. Below 20 GPa, the deviatoric stress of Fe appears decreasing as pressure increases. The stress increases rapidly after 20 GPa up to 50 GPa.

High-pressure static deviatoric stresses of Ta and Fe were determined using pressure gradient and absorption measurement. The methods employed in the present study have been modified compared to previous methods [6,10]. The pressure was measured using the EOS of the sample itself unlike the ruby method used by Meade and Jeanloz [6]. One of the disadvantages of the ruby method is the peak broadening at high pressure, especially at nonhydrostatic conditions, which may lower the resolution of the peak position and accordingly result in a less accurate pressure determination. To measure sample thickness, this study used X-ray absorption, Weir et al. [10] measured the recovered gasket thickness and applied the equation of state of the gasket material to estimate the thickness during compression. This can be rather uncertain, since plastic deformation and rebound after the recovery are not known. The single crystal strain method by Dewaele and Loubeyre [5] yields the deviatoric stress of Ta in good agreement with the present study. A linear fit to the present data yields the following relation: $\sigma_3 - \sigma_1$ (GPa) = $0.0564 \cdot P$ (GPa) + 0.2006 GPa. The uncertainty in the deviatoric stress increases with increasing pressure because of a less accurate estimation of the sample thickness at high pressure due to thinning of sample and cupping of anvils.

The present modified method seems to yield deviatoric stress results that agree very well with those determined using different methods. As shown in Figure 5, a comparison of deviatoric stress of Fe at high pressure suggests that the deviatoric stress determined by Singh et al. [11] agrees well with the values obtained by the present methods. Recent phonon measurements using near-edge resonant inelastic X-ray scattering of Fe show indeed average velocity decreases from ambient conditions to 6 GPa at 300 K [12], which suggest that the α -Fe instability may be related to the softening of the mechanical properties.

The modified methods to measure sample thickness and pressure gradient are essentially in situ methods unlike others [6,10]. Moreover, this newly established method does not depend on knowledge of the elastic constants of the sample. Last but not least, this new and improved method is easy to adapt at high pressure using a DAC.

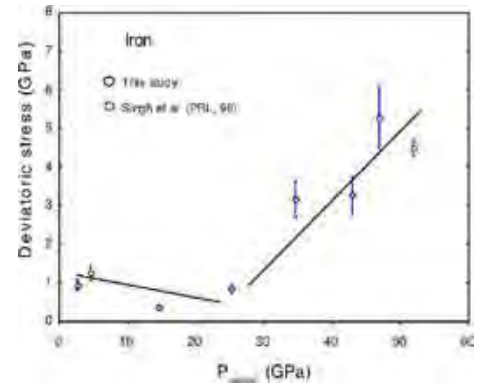


Figure 5. Deviatoric stress, $\sigma_3 - \sigma_1$, of Fe as a function of pressure. Singh et al. [11] used (3) based on Au elastic compliances.

Acknowledgements

This work was performed under the auspices of the U.S. Department of Energy by Lawrence Livermore National Laboratory in part under contract W-7405-Eng-48 and in part under Contract DE-AC52-07NA27344. We also acknowledge support from the LLNL LDRD office (07-ERD-029). The synchrotron radiation experiments were performed at NSLS, SSRL, and HP-CAT.

References

- [1] A. L. Ruoff, "Stress anisotropy in opposed anvil high-pressure cells," *J. Appl. Phys.* **46** 3 1389-1392 (1975).
- [2] A. K. Singh and G. C. Kennedy, "Uniaxial stress component in tungsten carbide anvil high-pressure x-ray cameras," *J. Appl. Phys.* **45** 11 4686-4691 (1974).
- [3] A. K. Singh, C. Balasingh, H. K. Mao, R. J. Hemley, J. Shu, "Analysis of lattice strains measured under non-hydrostatic pressure," *J. Appl. Phys.* **83** 12 7567-7575 (1998).
- [4] A. K. Singh and K. Takemura, "Measurement and analysis of nonhydrostatic lattice strain component in niobium to 145 GPa under various fluid pressure-transmitting media," *J. Appl. Phys.* **90** 7 3269-3275 (2001).
- [5] A. Dewaele, P. Loubeyre, "Mechanical properties of tantalum under high pressure," *Phys. Rev. B* **72** 13 134106 1-9 (2005).
- [6] C. Meade, R. Jeanloz, "Yield strength of the B1 and B2 phases of NaCl," *J. Geophys. Res.* **93** B4 3261-3269 (1988).
- [7] H. K. Mao, J. Shu, G. Shen, R. J. Hemley, B. Li, A. K. Singh, "Elasticity and rheology of iron above 220 GPa and the nature of the Earth's inner core," *Nature* **396** 741-743 (1999).
- [8] H. Cynn, C.-S. Yoo, "Equation of state of tantalum to 174 GPa," *Phys. Rev. B* **59** 13 8526-8529 (1999).
- [9] A. P. Jephcoat, H. K. Mao, P. Bell, "Static compression of iron to 78 GPa with rare gas solids as pressure-transmitting media," *J. Geophys. Res.* **91** B5 4677-4684 (1987).
- [10] S. T. Weir, J. Akella, C. Ruddle, T. Goodwin, L. Hsiung, "Static strengths of Ta and U under ultrahigh pressure," *Phys. Rev. B* **58** 17 11258-11265 (1998).
- [11] A. Singh, H. K. Mao, J. Shu, and R. J. Hemley, "Estimation of single-crystal elastic moduli from polycrystalline x-ray diffraction at high pressure: application to FeO and iron," *Phys. Rev. Lett.* **80** 2157-2160 (1998).
- [12] G. Shen, W. Sturhahn, E. E. Alp, J. Zao, T. S. Toellner, V. B. Prakapenka, Y. Meng, H. K. Mao, "Phonon density of states in iron at high pressures and high temperatures," *Phys. Chem. Minerals* **31** 6 353-359 (2004).

WIDE-RANGE HIGH-STRAIN-RATE SHEAR STRENGTH MODEL FOR METALS

S. S. Nadezhin, O. N. Ignatova, V. A. Rayevsky, V. P. Soloviev

All-Russia Research Institute of Experimental Physics (VNIIEF), Sarov 607190, Russia

Author Contact: NSS@vniief.ru

The behavior of media possessing shear strength under dynamic loading is an actual problem. There are a lot of models describing the dependence of shear stresses on pressure, temperature, strain, and strain rate, etc. However, it does not always work to describe both high-strain-rate and quasi-static deformation processes. At this point, one perspective is to develop wide-range models allowing description of experimental regularities under wide intervals of changing the deformation characteristics in one manner. This work presents the relaxation model of shear strength of copper, which takes into account such phenomena as temperature effect and strain hardening depending on strain rate. The model of heterogeneous deformation of metals, which describes the phenomenon of temporal softening of a medium under high-intensity shock waves, has been developed along with a homogeneous model of strength. The results of numerical simulation are compared with experimental data.

Introduction

The material resistance to shear strain under high-strain-rate depends in a complicated manner on the stress-strain state in a medium. It is a difficult task, at the present time, to describe ab initio the elementary event of plastic deformation. For this reason, the use of phenomenological models of various types—functional, relaxation, etc.—is preferable to describe the behavior of continuum under intense loading. The applicability range of such models is limited by the time and amplitude characteristics of stress-strain state implemented during numerical experiments. The larger the number of tests described using a phenomenological model (and the range of variations of the loading intensity values), the higher is the degree of belief in adequacy of computation results obtained using the given model.

Relaxation Model

From recent times, the relaxation model of shear strength has been developed and successfully used at VNIIEF for a set of structural materials. The major component of this model is used in the Glushak-Steinberg representation. The model is based on the adequate description of various experiments conducted to investigate material shear strength.

Dynamic yield strength is determined from a differential equation [1]

$$\frac{dY_d}{dt} = 3 \cdot G \cdot \dot{\epsilon}_i - \frac{Y_d - Y_s}{\tau} \quad (1)$$

where G – is the shear modulus, $\dot{\epsilon}_i$ – is the strain rate, Y_s – is the stationary yield strength under $\dot{\epsilon}_i=0$, τ – is the elastic stress relaxation time. The stationary part in the yield strength expression is presented as follows:

$$Y_s = Y_0 \cdot (1 + f(t)) \cdot \frac{G}{G_0} \quad (2)$$

where G_0 – is the shear modulus in initial state, Y_0 – is the yield strength in the initial state, $f(t)$ – is the function, which takes into account the deformation hardening:

$$\dot{f}(t) = \frac{1}{\varepsilon_{il}} \cdot \varphi(\dot{\varepsilon}_i) \cdot \dot{\varepsilon}_i \cdot (f_m(0) - f) - \frac{f - f_m(T)}{\tau_{An}} \cdot \Theta(f - f_m(T)) \quad (3)$$

where $\Theta(f - f_m(T))$ – is the unit function.

$$f_m(T) = a_1 \cdot e^{-\left(\frac{T}{n_1}\right)^{n_2}}, \quad \varphi = \frac{1 + \varphi_{max} \cdot \left(\frac{\dot{\varepsilon}_i}{\dot{\varepsilon}_{0S}}\right)^p}{1 + \left(\frac{\dot{\varepsilon}_i}{\dot{\varepsilon}_{0S}}\right)^p}, \quad \tau_{An} = a_2 \cdot e^{\frac{n_2}{T}},$$

where ε_{il} , $f_m(0)$, φ_{max} , p , $\dot{\varepsilon}_{0S}$, $\dot{\varepsilon}_0$, $n_{1,2}$, $a_{1,2}$ are constants, determined from experiment,

$\bar{O} = \frac{\dot{O}}{\dot{O}_m}$, T , and T_m are temperature and melting temperature, correspondingly.

Figure 1 presents the dependence of conventional yield strength on strain under quasi-static deformation of annealed copper in the initial state and after preliminary shock wave loading of different amplitude. As one can see from the graph, the model presented describes the medium strength fall, when shock-wave intensity exceeds a specific (critical) value, correctly. Therefore, the acceleration of dislocation generation under strain rate increasing above the critical value $\dot{\varepsilon}_i > \dot{\varepsilon}_{il}$ is taken into account, as well as temperature effect.

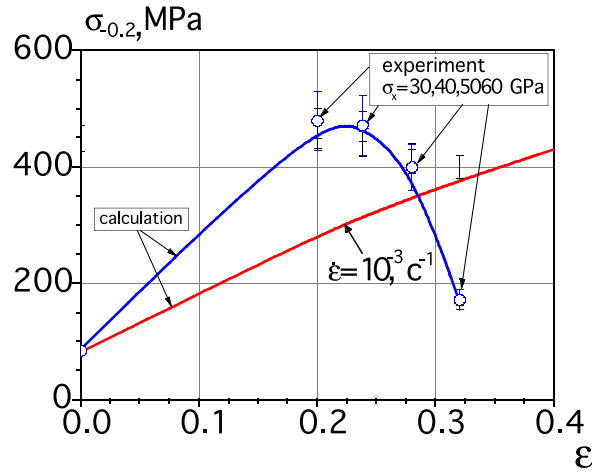


Figure 1. The conventional yield strength vs strain under quasi-static deformation for annealed copper in initial state (red curve) and after preliminary shock wave loading of different amplitude (blue curve).

Study of Dynamic Shear Strength of Copper by “Perturbations’ Growth” Method

The “perturbations’ growth” method is the most sensitive one to determine the value of shear strength of the material under high-strain-rate among others. It has recommended itself by both information retrieved and test simplicity in studying the shear strength of the whole series of metals. Central to the method is the X-ray recording of growth of the periodic perturbations, applied on the surface of a liner made of material under study and accelerated by HE explosion products. The perturbations grow in Raleigh-Taylor instability conditions, so this method possesses high sensitivity to the material shear strength, which realizes during the experiment, under specific initial parameters of perturbations.

One of the problems, arising under numerical simulation of tests on the shear strength study, was the systematic nonsatisfactory description of shock-wave loading data while quasi-isentropic loading data (with the same loading intensity) are described adequately. Figure 2(a), (b) presents loading pressure pulses for shock-wave and quasi-isentropic regimes of loading the liners. Having similar amplitude of pressure, the strain rate differs more than by an order of two. Relative amplitude of the perturbations vs liner's path, which corresponds to these two regimes of loading, are presented in Figure 3(a), (b). As one can see from the graphs, there is good agreement between numerical simulation made with phenomenological model of shear strength (1)-(3), and experimental data, obtained under quasi-isentropic loading. At that time, the results of shock-wave tests were not described by this model: the calculated strength is approximately three times higher than that observed in experiment.

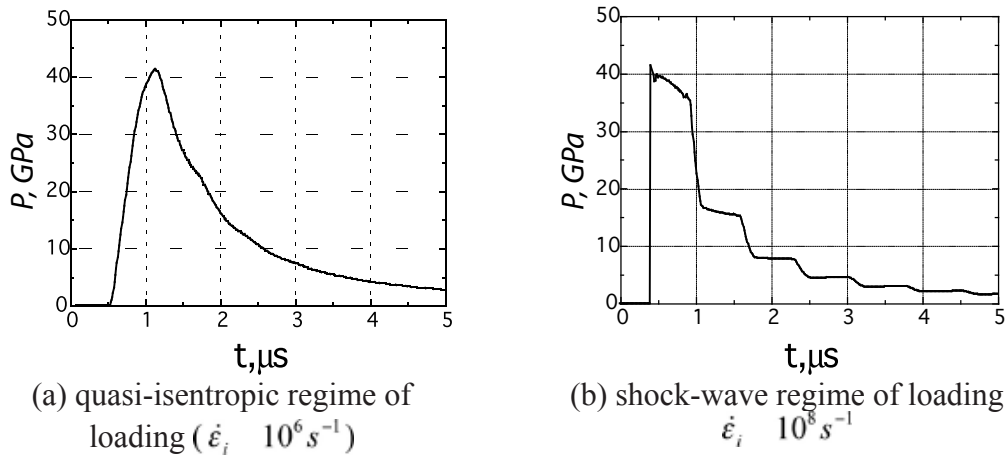


Figure 2. Loading pressure pulses for two regimes of loading.

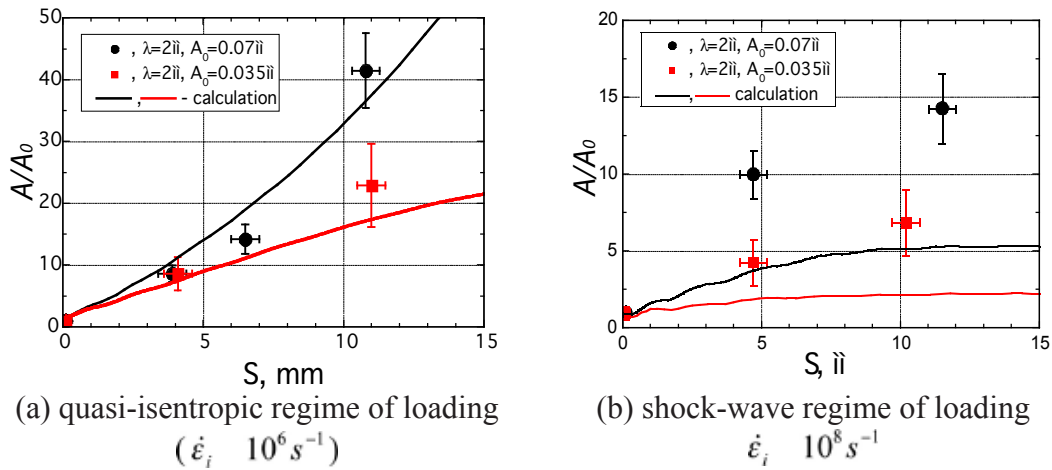


Figure 3. Relative amplitude of perturbations vs liner's path.

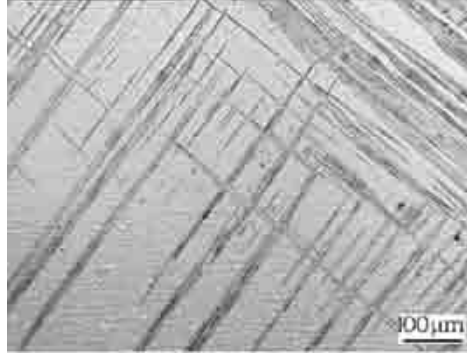


Figure 4. Metallographic section of copper, subjected to shock wave loading with $\dot{\epsilon}_i = 10^8 \text{ s}^{-1}$.

In addition to the numerical and experimental study of dynamic shear strength of copper, the results of metallographic analysis of the recovered liners, subjected to shock-wave loading, have been involved. Figure 4 presents the typical view of such metallographic section—a pattern of localized strain bands, intercrossing at the angle of 45° , is observed.

Along with the homogeneous model of shear strength (1)-(3), which makes it possible to describe the experiments in pressure range of 10–40 GPa and strain rate $\dot{\epsilon}_i = 10^2 \div 10^6 \text{ s}^{-1}$ correctly. The strength model, which accounts for the heterogeneous deformation, is developed to describe the phenomenon of temporal softening of a medium in a shock wave. The basic assumptions on the forming the periodic structures in a medium under shock wave and their influence on shear strength were discussed earlier. Below, the basic equations of a heterogeneous model are presented [2]:

$$\begin{cases} \dot{Y}_d = 3G\dot{\epsilon}_i - \frac{Y_d - Y_s}{\tau} & Y_d \geq Y_s \\ \sigma'_{ij} = 2G\epsilon'_{ij} & Y_d < Y_s \end{cases} \quad \text{is the equation for dynamic yield strength} \quad (4)$$

$$Y_s(\epsilon_i^p, P, T) = Y_0 \cdot f(\epsilon_i^p, T) \cdot f(P) \cdot f(\bar{T}) \quad (5)$$

is the stationary part of the yield strength, depending on strain, pressure, and temperature.

$$\tau = \frac{\tau_0}{\left(1 + \frac{\dot{\epsilon}_i}{\dot{\epsilon}_0}\right)^{0.5} \left(1 + \frac{l}{L}(\bar{G} - 1)\right)} \quad (6)$$

is the time of elastic stresses' relaxation, where l is the thickness of localized strain band, L is the period of localized strain bands;

$$\Delta \dot{E} = \frac{(L/l - 1)\dot{A}_{pl}}{\rho} - \alpha \frac{\Delta E \chi}{l^2} \quad (7)$$

is the differential equation for additional thermal energy ΔE , emitted in a band with thickness l due to plastic deformation work A_{pl} and taking into account the heat conductivity (χ), α is a constant.

$$\frac{L}{l} = 1 + \bar{\epsilon} \cdot \frac{\dot{A}_{pl} / \rho}{\Delta E_m} \quad (8)$$

is the geometric ratio between the band thickness and its period.

However, using this model revealed a high sensitivity of the numerical results to the strain rate, which depends, in its own turn, on the number of numerical cells. Due to this fact, a modification has been proposed supposing that if the whole work on plastic strains is transformed into heat, then one can write:

$$\dot{T} = \frac{\dot{E}}{Cv} = \frac{\dot{A}_{pl}}{\rho Cv} = \frac{Y \cdot \dot{\epsilon}_i}{\rho Cv}, \text{ where } \rho \text{ is the density, } Cv \text{ is the heat capacity, } Y \text{ is the yield strength, } \dot{\epsilon}_i \text{ is the plastic strain intensity, } \dot{A}_{pl} \text{ is the work on plastic strains.}$$

Making such an assumption, one can obtain more stable solutions from the mathematical convergence viewpoint in view of the fact that thermodynamic values (such as temperature) do not practically depend on the computing grid changing. This improved model has been used for numerical analysis of “perturbation method” tests with shock-wave loading of copper liners. Results of numerical simulations using a homogeneous model (1)-(3) and heterogeneous model (4)-(8) are compared with experimental data in Figure 5. As one can see, the heterogeneous model allows describing of experimental points position determined by the effect of temporal softening of the material. At present, these two models are modified to be combined into one approach to simulate quasi-isentropic and shock-wave deformation of metals.

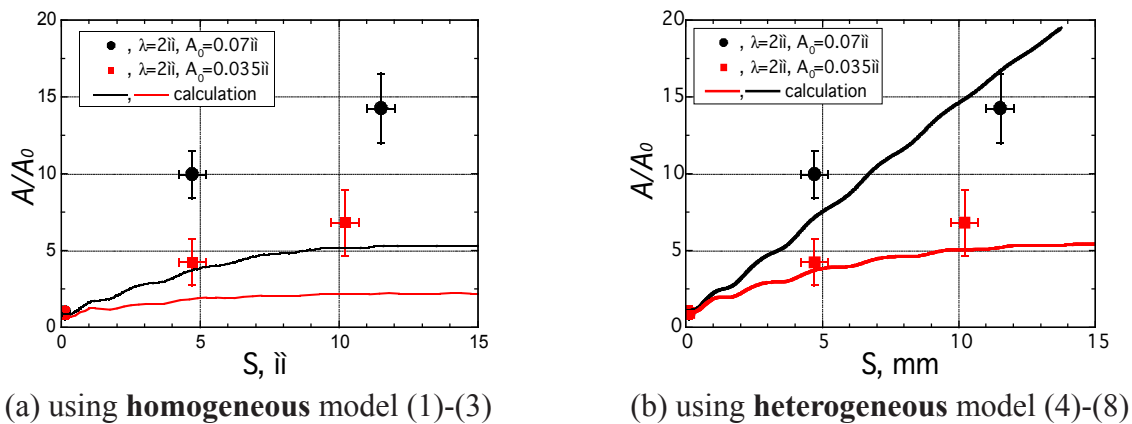


Figure 5. Relative amplitude of perturbations vs liner's path under shock-wave loading.

Conclusions

The homogeneous model of copper deformation is presented, which describes the copper behavior under static and dynamic (quasi-isentropic) loading in the range of strain rate $\dot{\epsilon}_i = 10^2 \div 10^6 s^{-1}$ and pressure $10 \div 40$ GPa correctly. Equations of heterogeneous model of shear strength are also presented. The last model allows simulating the effect of temporal softening in metals (under typical strain rates $\dot{\epsilon}_i = 10^8 s^{-1}$), as opposed to the homogeneous model.

References

- [1] B. L. Glushak, O. N. Ignatova, S. S. Nadezhin, P. N. Nizovtsev, A. M. Podurets, V. A. Raevsky, Marvin A. Zocher, Dean L. Preston, “A phenomenological visco-elastic-plastic model for dynamic yield of m1 cu account for grain size,” *SCCM*, (2007) p. 649.
- [2] G. A. Salishew, V. A. Raevskiy, O. N. Ignatova, M. Zocher et al., “Influence of intensive plastic strain and shock-wave loading on copper strength,” International Conference “*New Models and Hydrocodes for Shock Wave Processes in Condensed Matter*” Dijon, France 9-14 April (2006) p. 17.

MEASUREMENT OF SOUND VELOCITIES IN SHOCK-COMPRESSED TIN UNDER PRESSURES UP TO 150 GPa

M. V. Zhernokletov,* A. E. Kovalev,* V. V. Komissarov,* M. A. Zocher† and F. J. Cherne†

*All-Russia Research Institute of Experimental Physics (VNIIEF), Sarov 607190, Russia

†Los Alamos National Laboratory, Los Alamos, NM, 87545 USA

Sound velocity in shock-compressed tin was measured in a pressure range of 31÷138 GPa by the method of overtaking release with use of indicator liquids. Photodiode-based optical gauges were used to record luminescence of the liquid indicators. Under pressures of shock compression of 5÷18 GPa, sound velocity in tin was measured by the method of oncoming release employing manganin gauges. The experimental data were compared to calculation results and data of the other authors. According to data obtained in this work, the range of tin melting at shock adiabat is ~63÷90 GPa.

Introduction

It is now of significant interest to investigate tin by both the theoretical [1,2] and the experimental methods [3-7]. Tin has a complicated phase diagram [1,2], which can be explained by the presence of structural phase transitions.

Sound velocity is an important parameter, which has high sensitivity to change in substance compressibility. The kink in the “sound velocity – pressure” relation is caused by structural transitions in a shock-compressed substance. Therefore, by measurement of longitudinal elastic sound velocity C_L and volume sound velocity C_B , it is possible to reveal phase transitions of a substance along shock adiabat, including its melting.

Results of various authors testify to very prominent differences in melting ranges for tin pressures in SW, and in total, the melting range covers approximately from 35 to 93 GPa. For this reason, it is necessary to measure sound velocities in tin and to revise the melting range of this metal in shock waves.

Optical Method

Optical measurements of sound velocities were performed by the method of overtaking release with the use of indicator liquids that was described in detail in [8].

Tin samples of different thicknesses (1.5÷6 mm) were placed in the through hole (a “well” in a thick disk made of aluminum (AD 1) or steel (St.3) having a thickness of 10 mm, which was fastened to a baseplate made of aluminum or steel of the same types [8]).

The “well” was filled with indicator liquid. In testing, after the impact of a fast-flying thin plate against the baseplate, where the tin sample was placed, a rarefaction wave was formed at the back side of the impactor. The rarefaction wave passes sequentially through layers of the impactor, the baseplate, and investigated sample, and then it enters the indicator liquid. The objective is to determine the sample thickness X_{MAX} , where the rarefaction wave overtakes the front of shock wave. To generate shock waves in tin samples, generators of shock waves based on acceleration of thin impactors by products of explosion of cylindrical HE charges of different powers were used.

Preliminary evaluations were made for shock-compressed states of samples caused by these devices. Basing on these evaluations, particular geometry was selected for an experimental cell to measure sound velocity by the method of indicator liquid.

Carbogal (perfluorine-1.3-dimethyl cyclohexane, $\rho_0=1.856 \text{ g/cm}^3$), tetrachlormethane ($\rho_0=1.585 \text{ g/cm}^3$), and tribromomethane (bromoform, $\rho_0=2.886 \text{ g/cm}^3$) were used as the indicator liquids.

Sound velocity in tin was calculated by the formula:

$$C_{\text{sound}} = \frac{X_{\text{MAX}}}{\sigma \cdot (t_{\text{SW}} - t_{\text{RW}} + \frac{X_{\text{MAX}}}{D})}, \quad (1)$$

where σ is the compression; t_{SW} is the time of shock wave entering the sample; t_{RW} is the time of rarefaction wave entering the sample (times are determined from the Xt -diagrams); D is the velocity of shock wave in tin; X_{MAX} is the step thickness, when overtaking occurs at the “tin – indicator” interface.

Typical oscillograms of the test with measurement of sound velocity in a four-step sample of tin are presented in Figure 1. The arrows point to the time of shock wave arrival to the indicator liquid (carbogal) (t_1) and “overtaking” (t_2) of the shock wave front by the rarefaction wave.

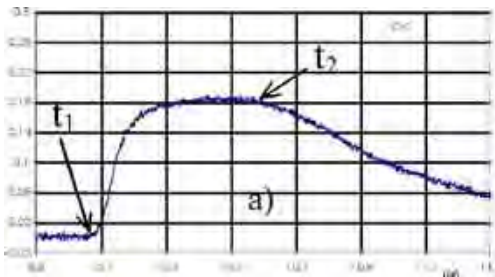


Figure 1. Radiation of shock-wave front in CHBr_3 at $P_{\text{sn}} = 72 \text{ GPa}$ behind tin steps: (a) 2.95 mm.

At pressures less 30 GPa in the studied samples, the illumination temperature of a shock-compressed liquid indicator is close to the sensitivity limit of the recording photodiodes FD 256 (about 1500 K).

For this reason, tests using a manganin gauge were performed for determination of sound velocities in tin in the low pressure area (up to 30 GPa).

Manganin Pressure Gauge Method

The detail structure of shock front of loading and rarefaction wave in tin samples was revealed by the method of manganin gauge of pressure [5,9].

Gauges having shapes of bifilar spirals with thickness of 0.03 and diameter of $\sim 4.5 \text{ mm}$ were glued by epoxy resin between two tin samples, and they were isolated by mica having a thickness from 0.05 to 0.15 mm (depending on value of loading pressure) against the studied material.

Joint processing of oscillograms recorded by pressure gauges and electrocontact gauge determined the elastic and volume sound velocities. During the calculations, small corrections were made to account for thickness of the pressure gauge and its insulation. Precision of the pressure measurements is $\sim 5\%$.

Experimental Results

Parameters of the tin states and the experimental values of sound velocities in shock-compressed tin, which were obtained by the optical method and by the method of manganin gauge, are presented in Tables 1 and 2.

Table 1. Parameters of states in tin (optical method)

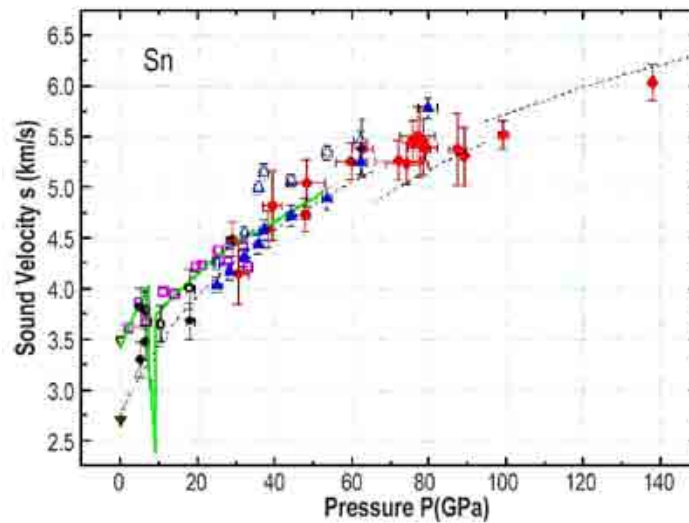
| N | Parameters of states in tin | | | |
|----|-----------------------------|------------|-----------|--------------------|
| | D , km/s | u , km/s | P , GPa | C_{sound} , km/s |
| 1 | 4,05 | 0,98 | 29±3 | 4,49±0,17 |
| 2 | 4,38 | 1,19 | 38±1 | 4,59±0,18 |
| 3 | 4,43 | 1,22 | 39±2 | 4,82±0,34 |
| 4 | 4,71 | 1,40 | 48±5 | 5,05±0,23 |
| 5 | 5,05 | 1,62 | 60±4 | 5,26±0,18 |
| 6 | 5,13 | 1,67 | 63±3 | 5,39±0,29 |
| 7 | 5,38 | 1,84 | 72±6 | 5,27±0,20 |
| 8 | 5,44 | 1,87 | 74±5 | 5,24±0,20 |
| 9 | 5,48 | 1,90 | 76±1 | 5,46±0,20 |
| 10 | 5,50 | 1,92 | 77±5 | 5,51±0,29 |
| 11 | 5,52 | 1,93 | 77±2 | 5,45±0,34 |
| 12 | 5,54 | 1,94 | 78±4 | 5,40±0,27 |
| 13 | 5,59 | 1,95 | 79±1 | 5,39±0,13 |
| 14 | 5,75 | 2,08 | 87±2 | 5,38±0,35 |
| 15 | 5,79 | 2,11 | 89±2 | 5,31±0,22 |
| 16 | 6,02 | 2,26 | 99±1 | 5,52±0,14 |
| 17 | 6,78 | 2,79 | 138±1 | 6,04±0,18 |

Table 2. Parameters of states in tin (method of manganin gauge)

| N | D , km/s | u , km/s | P , GPa | C_L , km/s | C_B , km/s |
|---|------------|------------|-----------|--------------|--------------|
| 1 | 2,85 | 0,25 | 5,09±0,15 | 3,82±0,19 | 3,30±0,17 |
| 2 | 2,94 | 0,30 | 6,48±0,19 | 3,79±0,19 | 3,47±0,17 |
| 3 | 3,18 | 0,45 | 10,4±0,31 | 3,65±0,18 | - |
| 4 | 3,58 | 0,69 | 18,0±0,54 | 4,00±0,20 | 3,68±0,18 |

Figure 2 presents data from the tables concerning dependence of sound velocity on pressure, together with data of the other authors. Under atmospheric pressure, the value of longitudinal sound velocity $C_L = 3.49$ km/s was measured in VNIIEF by the ultrasonic method, and the value of the isentropic sound velocity $C_B = 2.71$ km/s at the same pressure was taken from the reference book [10]. Figure 2 presents results of the experiments with measurement of sound velocity in tin in the pressure range from 2.4 to 33 GPa with use of a Doppler laser interferometer from work [6] and data [7] for longitudinal and bulk sound velocities in pressure range from ~25 to ~80 GPa, which were measured using a direct reverse-impact method and VISAR technique.

Multiphase equations of state of tin were considered in [1,2]. The dependences of sound velocity on pressure, which were calculated by these equations of state, are also presented in Figure 2.



□ - calculation by EOS [1]; — - calculation by EOS [2]; ▽ - sound velocity from [6]; 8, 7 - sound velocity from [7]; ▼ - plastic (volume) sound velocity from [10]; X - elastic (longitudinal) sound velocity (ultrasonic method); ▲ - present work (optical method); •, - - present work (manganin)

Figure 2. Experimental dependence of sound velocities in tin on pressure of shock compression.

As shown in Figure 2, data obtained with use of the manganin gauge within the measurement error are in good agreement with the results of work [6] and the calculations from [1,2]. The experimental data, which were obtained by the optical method under the pressures from 40 to 80 GPa, are located slightly higher than the both calculated dependences. Under pressures higher 63 GPa, sound velocity values stop actually growing in tin up to the pressure of ~90 GPa. Based on that, the conclusion can be made that tin undergoes a phase transition, which is probably associated with melting in the pressure range of ~63 ÷ 90 GPa.

Conclusions

We have performed experiments on tin to measure sound velocities using optical techniques and the manganin gauge method. The accuracy of the sound velocity measurements is approximately 5%. We observed a break in the sound velocity versus pressure in the (60–90) GPa, which is, in our opinion, caused by melting.

To determine the upper boundary of the melting range, it is required to perform additional tests under pressures higher 90 GPa.

Acknowledgments

This work was performed under the auspices of the U.S. Department of Energy by the University of California Los Alamos National Laboratory under contract #37713-000-02-35 (#035).

References

- [1] K. V. Khishenko, "Extreme states of substance. Detonation shock waves," *Proceedings of the International Conference IX Khariton's Topical Scientific Readings* (Sarov, Russia, VNIIEF, 2007) pp. 316-318.
- [2] G. A. Cox, "A multiphase equation of state and strength model for tin," *Shock Compression of Condensed Matter-2005*, eds. M. D. Furnish, M. Elert, T. P. Russel, and C. T. White, *AIP Conference Proceedings* (Melville, New York, AIP, 2006) pp. 208-211.
- [3] M. Liu and L. Liu, "Compressions and phase transitions of tin to half a megabar," *High. Temp. – High. Press.* **18** 79-85 (1986).
- [4] S. Desgreniers, Y. K. Vohra, A. L. Ruoff, "Tin at high pressure: An energy-dispersive x-ray-diffraction study to 120 GPa," *Phys. Rev. B* **39** 10359-10361 (1989).
- [5] V. V. Komissarov and M. N. Pavlovskii, *Zh. Eksp. Teor. Fiz.* **98**, Issue 5, No. 11, 1748 (1990). [Sov. Phys. JETP **71**, [sic] (1990)]
- [6] E. Martinez and J. M. Servas, "Sound velocity Doppler laser interferometry measurements on TiN," *Shock Compression of Condensed Matter-2001*, eds. M. D. Furnish, N. N. Thadhani, and Y. Horie (Melville, New York, AIP, 2002) pp. 1200-1203.
- [7] H. Jianbo, Z. Xianming, H. Tan, J. Li, C. Dai, "Successive phase transitions of tin under shock compression," *Applied Physics Letters*. **92** 111905 (2008).
- [8] R. G. McQueen, J. W. Hopson, J. N. Fritz, "Optical technique for determining rarefaction wave velocities at very high pressures," *Rev. Sci. Instrum.* **53** 2 245-250 (1982).
- [9] M. N. Pavlovskii and V. V. Komissarov, "Features of the phase transition of bismuth in a rarefaction wave," *Zh. Eksp. Teor. Fiz.* **83**, Issue 6, No. 12, 2146-2151 (1982).
- [10] *Handbook of Rare Metals* [Russian translation], ed. Izd. Plyushchev (Mir, Moscow, 1965).

DETERMINATION OF LONGITUDINAL AND BULK SOUND VELOCITIES IN NATURAL URANIUM UNDER SHOCK-WAVE LOADING

**A. V. Fedorov,* A. L. Mikhaylov, S. A. Finyushin, D. V. Nazarov,
T. A. Govorunova, D. A. Kalashnikov, E. A. Mikhaylov, V. N. Knyazev**

*All-Russia Research Institute of Experimental Physics (VNIIEF), Sarov 607190, Russia

Author Contact: fedorovsarov@mail.ru

The authors determined longitudinal and bulk sound velocities, values of Poisson's ratio and shear strength of natural uranium under shock-wave loading.

Introduction

When formulating equations of state, investigating dynamic strength, elastic-plastic properties and the processes of destruction and deformation of structural materials, it is necessary to take account for influence of resistance of plastic deformation (influence of shear strength). For this purpose, it is necessary to know the values of longitudinal and bulk sound velocities, amplitude of elastic release wave [1-4]. There are various experimental methods for determining these values. Continuous recording of the velocity of the free surface by laser interferometer [5-7] is one of the most informative methods for recording the parameters of an elastic-plastic wave. The laser interferometric Fabry-Perot method was chosen for the investigation. This method has high resolution for measuring the velocity (10–20 m/s), and it allows the recording of the velocity of the free surface and contact surface (with transparent material) of a test specimen.

It is possible to determine longitudinal and volume sound velocities, compression modulus, Poisson's ratio, modulus of elasticity, and shear strength by knowing thicknesses of a test specimen and an impactor and after having measured parameters of elastic and plastic unloading waves as well as their times of arrival on the interface under study.

Experimental Results

Coarse-grained (100-200 μm) natural uranium ($\rho=18.91 \text{ g/cm}^3$) was studied in the paper. A set of 12 experiments was performed, in which a uranium impactor was accelerated through a vacuum gap by the help of an HE charge, and it loaded the sample made of the same material. Loading amplitude of uranium samples in experiments amounted to 40...72 GPa.

The velocity of the U–LiF interface was recorded in experiments. Mirror coating made of aluminum 1 μm thick was applied to LiF.

There were two or three channels for velocity measurement in each experiment. The authors used Fabry-Perot interferometers having baseline distances (a distance between mirrors) from 50 to 150 mm with errors in measurement from $\pm 35 \text{ m/s}$ to $\pm 12 \text{ m/s}$.

The values of mass velocity and arrival times at the U–LiF interface of elastic and plastic release waves were recorded on profiles. The values recorded in LiF on the known shock adiabats were converted to states in uranium.

Figure 1 presents interferograms and a velocity curve showing the determination of elastic C_l and bulk C_b velocities of sound.

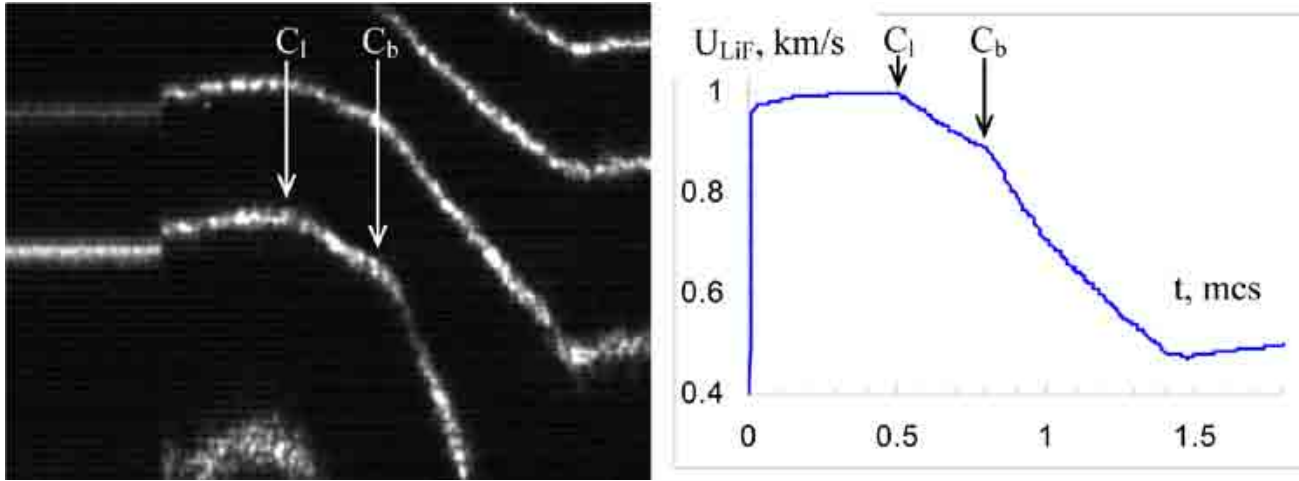


Figure 1. Interferogram and velocity curve illustrating determination of longitudinal and volume velocities of sound.

The values of uranium longitudinal and bulk velocities of sound beyond shock-wave front were calculated from the following formulas:

$$c_l = \frac{U_{LiF} \cdot t_1 + L + (D - W) \cdot \frac{L}{D}}{\frac{L}{D} + t_1 - \frac{L}{D}} \cdot U \quad (1)$$

$$c_b = \frac{U_{LiF} \cdot t_2 + L + (D - W) \cdot \frac{L}{D} + U_{LiF}^2 \cdot (t_2 - t_1)}{\frac{L}{D} + t_2 - \frac{L}{D}} \cdot U \quad (2)$$

where U_{LiF} is particle velocity at exit to the U-LiF interface of elastic release wave; U is uranium particle velocity; W is impactor velocity; D is shock wave velocity; L is target thickness, l is impactor thickness. t_1 , t_2 are time from the instant of exit of a shock wave at the interface up to the instant of arrival of elastic (t_1) and plastic (t_2) release waves.

The present formulas define the values of velocities of sound without regard for a change of uranium state in a counter-propagating release wave (propagating from the U-LiF interface). Below are presented the results of accounting of the influence of the counter-propagating release wave on the recording of a sound speed.

Table 1 shows the results of the experiments, where D , P_1 , U_1 are shock wave velocity, pressure, and particle velocity in uranium at the instant of arrival of an elastic release wave; P_2 is pressure of a plastic release wave; $\Delta\sigma_{elastic}$ is amplitude of an elastic release wave; Y_g is value of shear strength, and μ is Poisson's ratio. Other designations are analogous to formulas (1), (2).

Table 1. Results of experiments.

| Nº | Liner l, mm | Sample L, mm | U_1 , km/s | P_1 , GPa | P_2 , GPa | D , km/s | C_L , km/s | C_b , km/s | μ | $\Delta\sigma$, GPa | Y_g , GPa |
|------|----------------|-----------------|-----------------|----------------|----------------|---------------|-----------------|-----------------|-------|-------------------------|----------------|
| 1903 | 2 | 3.97 | 0.963 | 71.88 | - | 3.96 | 5.03 | - | - | - | - |
| 1904 | 2 | 3.92 | 0.964 | 72.05 | - | 3.96 | 4.88 | - | - | - | - |
| 1905 | 1.99 | 3.9 | 0.956 | 71.2 | - | 3.95 | 4.81 | - | - | - | - |
| 1911 | 1.98 | 3.85 | 0.963 | 71.85 | - | 3.96 | 5.01 | - | - | - | - |
| 1913 | 1.98 | 3.96 | 0.943 | 70 | - | 3.93 | 5.11 | - | - | - | - |
| 1954 | 4 | 4 | 0.850 | 61 | 54.53 | 3.79 | 4.76 | 4.04 | 0.37 | 6.47 | 1.36 |
| 1962 | 3.95 | 3.95 | 0.874 | 63.27 | - | 3.83 | 4.79 | - | - | - | - |
| 1965 | 3.96 | 3.98 | 0.890 | 64.89 | 58.09 | 3.85 | 4.46 | 3.92 | 0.40 | 6.8 | 1.15 |
| 1987 | 2 | 3.95 | 0.647 | 42.59 | 37.27 | 3.49 | 4.44 | 3.86 | 0.39 | 5.32 | 0.97 |
| 1997 | 4 | 6 | 0.656 | 43.46 | - | 3.50 | 4.48 | - | - | - | - |
| 1998 | 2 | 6 | 0.622 | 40.62 | - | 3.45 | 4.53 | - | - | - | - |
| 2200 | 2 | 3.9 | 0.650 | 43 | 37.75 | 3.49 | 4.66 | 3.84 | 0.34 | 5.25 | 1.26 |

Figure 2 presents a curve of longitudinal (c_l) and volume (c_b) velocities of sound versus pressure.

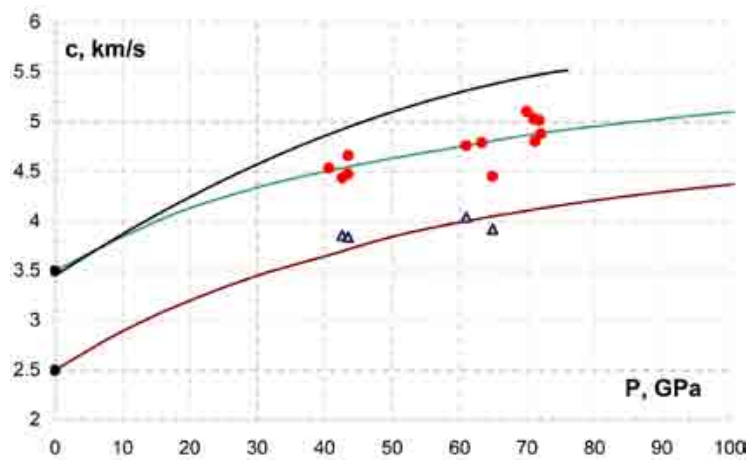


Figure 2. Measurement data of dependence of longitudinal (c_l) and volume (c_b) velocities of sound upon pressure.

Good reproducibility of results was noted. A spread of the measured values of the longitudinal velocity of sound did not exceed 3% (4.96 ± 0.15 km/s) in five tests at a pressure of 71 ± 1 GPa. Figure 2 also presents the data on sound speed in uranium obtained in static tests at zero pressure [8]. All the recorded values of the velocity lay on two dependencies for longitudinal and bulk velocities of sound.

It is necessary to take into account the influence of a counter-propagating release wave for the exact determination of a velocity of sound. Figure 2 shows the results of gas dynamic calculations for real studies, where the effect of the counter-propagating release wave was considered (curve c_l^+).

It is evident from the figure that a real value of a sound speed (curve c_l^+) was on the average higher by 380–520 m/s than without regard for an unloading wave (curve c_l) in a pressure range at hand (40–72 GPa) and the real value accounted for 4.9–5.5 km/s.

Discussion of Results

In contrast to a model of an elasto-plastic body in the majority of presented tests, there is no clearly marked boundary between elastic and plastic waves (breakpoints) in a rarefaction wave. If the break (kink) connected with the arrival of an elastic wave at the U–LiF interface is clearly marked on interferograms (it was recorded in all 12 tests), the break connected with the onset of a plastic release wave is expressed slightly and is not recorded on many interferograms. Such a break was recorded only in three tests on a resolution limit of a method (only in the most sensitive first or second interference rings). The breaks tied to the arrival of elastic and plastic release waves were clearly recorded on the profile in test 2200 (see Figure 1). Ultra-fine-grained (UFG) uranium, with a grain size of 100–200 nm [3,4], was selected as a material to study in the test. When studying elasto-plastic properties of various materials, we noted that parameters of a break (kink) due to an arrival of a plastic release wave are recorded rather clearly if an elastic precursor has a near-rectangular shape (steel, aluminum, UFG uranium, UFG copper) on a shock wave front. Reliable recording of a break depends on mechanical properties and a structure of a material in the initial state. In the first place, it depends on grain sizes of a basic material. For example, the tests with ultra-fine-grained materials (grain size 0.1–1 μm) enable one to reveal a clear elasto-plastic behavior both in a loading wave and in a release wave.

The values of Poisson's ratio and dynamic yield strength were determined by means of the formulas:

$$\mu = \frac{3c_b^2 - c_l^2}{3c_b^2 + c_l^2} \quad (3)$$

$$Y_g = \frac{(1 - 2\mu) \cdot (\Delta\sigma_{\text{elast}})}{2(1 - \mu)} \quad (4)$$

For the whole region of the pressures under study, the amplitude of an elastic wave amounted to $\Delta\sigma_{\text{elast}} = 5.2\text{--}6.8$ GPa, the value of Poisson's ratio amounted to $\mu = 0.37\text{--}0.40$ for coarse-grained uranium and $\mu = 0.34$ for UFG uranium; the value of shear strength amounted to 1.16 ± 0.2 GPa for coarse-grained uranium and for UFG uranium – 1.26 GPa.

A previously complicated elasto-plastic behavior was recorded in an elastic loading wave for coarse-grained uranium [5]. The authors recorded a smooth growth of strains and sound velocity dispersion on an elastic precursor in an elastic region instead of a sharply expressed initial front.

Unfortunately, a volume velocity of sound was determined only in four of twelve experiments in the present paper. The data on a volume velocity of sound, Poisson's ratio, and shear strength are preliminary in this account and call for additional investigations, including investigations in a wider region of pressures.

It should be noted that the value of a longitudinal sound velocity measured in the present paper is higher by $\approx 700\text{--}800$ m/s than the values obtained in paper [2]. This difference, to our mind, is because a manganin-based gauge records the time of exit of an elastic wave with low accuracy in paper [2].

Conclusions

The authors obtained experimental dependencies of longitudinal (c_l) and bulk (c_b) sound velocities of natural uranium upon pressure using a method of recording of mass velocity profile by the help of a Fabry-Perot laser interferometer in the region of pressures $40 \div 72$ GPa. The value of a longitudinal sound velocity was 4.9...5.5 km/s, amplitude of elastic unloading wave was 5.2...6.8 GPa. Poisson's ratio was defined for coarse-grained uranium ($\mu = 0.37...0.40$) and for UFG uranium ($\mu = 0.34$). Dynamic yield stress was determined for coarse-grained uranium $Y_g = 1.16 \pm 0.2$ GPa and for UFG uranium $Y_g = 1.26$ GPa.

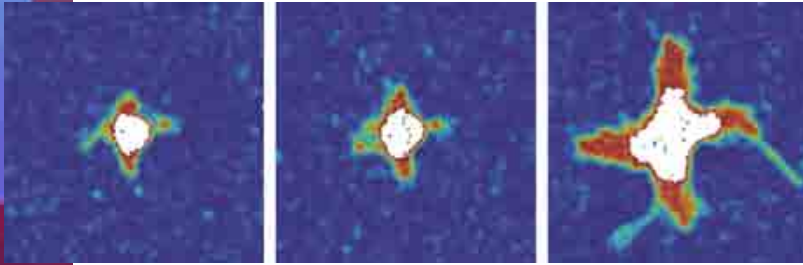
Acknowledgments

The work was fulfilled under the aegis of Scientific School No. NSH-1307.2008.1.

References

- [1] M. V. Zhernokletov, ed., *Investigating Techniques of Properties of Materials at Intensive Dynamic Loads* (Sarov, 2003).
- [2] V. G. Vildanov, A. O. Borshchevskiy et al., "Measurement of longitudinal velocity of sound in shock-compressed uranium," VIII International Workshop – Fundamental Properties of Plutonium (Snezhinsk, 2008).
- [3] E. A. Kozlov, D. G. Pankratov et al. "Elastic precursor relaxation at explosive loading of preliminary quasi-statically extruded fine-grained unalloyed uranium," volume **421**, no. 3 (Doklady Akademiy Nauk (Rus), 2008).
- [4] E. A. Kozlov, D. G. Pankratov et al. "Dynamic shear and spall strengths of preliminary quasi-statically extruded fine-grained uranium and alloy U–0,3%Mo," *Proceedings of Conference Shock Waves in Condensed Matter* (Saint-Petersburg, 2008) pp. 208-215.
- [5] A. V. Fedorov, A. L. Mikhailov, S. A. Finyushin et al., *Proceedings of SCCM – 2005* (Baltimore) pp. 713-716.
- [6] A. V. Fedorov, A. L. Mikhailov, S. A. Finyushin et al., *Proceedings of SCCM – 2005* (Baltimore), pp. 717-720.
- [7] A. V. Fedorov, A. L. Mikhailov, S. A. Finyushin et al., *Chemical Physics (Rus)*, (2005), **24** 10 66-70 (2005).
- [8] S. P. Marsh, ed., *LASL Shock Hugoniot Data* (University of California Press, Berkeley, 1980).

Materials Response to DYNAMIC LOADING II



Void growth in Al single crystal via emission of dislocation loops and amorphization. $T = 300$ K, $60 \times 60 \times 60$ unit cells, $R_0 = 1.0$ nm.

The section consists of nine papers and is concerned with the various aspect of dynamic behavior of structural materials.

The contribution by A. Kuksin et al. (JIHT RAS) is devoted to the study of fracture kinetics in ductile solids and liquids by applying the molecular dynamics approach. The result obtained is compared with the shock-wave experimental data on the spall. A. Freidin (IPME RAS) reports on problems of modeling the coupled interaction between different processes accompanying crack growth: inelastic deformations, phase transformations, and chemical reactions. To this end, the Eshelby stress concept and thermodynamic considerations are utilized to study how a crack growth interconnects with an advancing transformation front. This subject continues in the next paper (I. Korolev) of IPME RAS, which addresses the problem of FEM simulation of fatigue damage, crack nucleation, and growth in predamaged materials. The report by B. Remington et al. (LLNL) on the solid-state Rayleigh-Taylor experiments in vanadium at Mbar pressures at the Omega laser presents the results of tests on the Rayleigh-Taylor instability in the plastic flow regime of the solid-state vanadium. The presentation by V. Igonin et al. (RFNC-VNIIEF) reports the results of experimental and numerical-theoretical study of peculiarities of plastic deformation of tantalum, the study being carried out by Russian (VNIIEF) and American (LANL) teams. The calculation of sound speed behind the shock-wave front for various materials and comparison with the experimental data are the subject of the report by B. Nadykto (RFNC-VNIIEF). The equation-of-state parameters for a number of materials are obtained on the basis of experimental data on the shock-wave and static compression, and the results are compared with published experimental data. Another result of the cooperation of VNIIEF and LANL teams on the deviatoric constitutive model is reported by M. Zocher. The objective of the presentation is an enhanced methodology in determining the parameters of the deviatoric constitutive model. The paper by D. Indeitsev et al. (IPME RAS) is concerned with modeling and simulation of the thermo-acousto-elastic waves in solids of complex rheology. The approach suggested is applied to the problem of change of mechanical properties of metals as a result of inflow of hydrogen. The report by Kamm et al. (LANL) suggests an accurate, direct Eulerian simulation of the dynamic elastoplastic flow. The authors develop a new scheme for solving the equations of the elastoplasticity in the framework of the Eulerian description.

Alexander K. Belyaev, Institute of Problems in Mechanical Engineering, St. Petersburg, Russia

Section VI:

- VI-2 Models of Fracture from Atomistic Simulations (JIHT)
- VI-7 Modeling the Interconnections Between a Structural Transformation Front and a Growing Crack (IPME)
- VI-12 FEM Simulation of Fatigue Damage, Crack Nucleation, and Growth in a Pre-Damaged Material (IPME)
- VI-17 Solid-State Rayleigh-Taylor Experiments in Vanadium at Mbar Pressures at the Omega Laser (LLNL)
- VI-22 Influence of Dynamic Properties on Perturbation Growth in Tantalum (VNIIEF)
- VI-27 Calculation of Sound Speed behind the Shock Wave Front for Various Materials and Comparison with Experimental Data (VNIIEF)
- VI-34 Deviatoric Constitutive Model: Domain of Strain Rate Validity (LANL)
- VI-38 Modeling and Simulation of the Thermo-Acousto-Elastic Waves in Solids of Complex Rheology (IPME)
- VI-43 Accurate Direct Eulerian Simulation of Dynamic Elastic-Plastic Flow (LANL)

MODELS OF FRACTURE FROM ATOMISTIC SIMULATIONS

A. Yu. Kuksin, G. E. Norman, V. V. Pisarev, V. V. Stegailov, A. V. Yanilkin

Joint Institute for High Temperatures (JIHT), Russian Academy of Sciences, Moscow, 125412, Russia

Author Contact: alexey.kuksin@gmail.com

The work is devoted to the study of fracture kinetics in ductile solids and liquids. An attempt is made to present the results of molecular dynamics (MD) calculations as kinetic constitutive relations for description of the elementary processes of fracture: nucleation and growth of voids. The results are used for description of spall under high strain-rate ($> 10^6 \text{ s}^{-1}$) tension. The comparison with the shock wave experimental data on the spall strength [1,2] is discussed.

Introduction

Kinetic models for the nucleation and growth theory of material damage are widely used in hydrocodes for description of fracture under extremely high strain rates ($\sim 10^8 - 10^{10} \text{ s}^{-1}$) whereas they were established and experimentally verified for the moderate range of strain rates up to $10^5 - 10^7 \text{ s}^{-1}$. Owing to the typical timescale of the classical MD and system sizes available on current computational facilities, MD simulations may be used for modification of the kinetic models of fracture at such high strain rates. Examples of fracture models for ductile metal and simple liquid are presented in this paper. Rates of nucleation and growth of voids are evaluated for a range of pressures and temperatures and compared with the predictions of theoretical models. Some properties used in the models (such as surface tension, viscosity) are calculated from independent MD simulations, which makes it possible to compare theoretical predictions with the simulations of nucleation and growth kinetics within the scope of one model system.

The modeling was done using the LAMMPS [3] package. The embedded atom method is used to describe interatomic interactions in ductile metal (aluminum), namely, interatomic potential from [4]. It reproduces the elastic constants, the stacking fault energies, and the surface energies. The fracture in simple liquid (hexan) is studied within the model with paired Lennard Jones (LJ) potential with the cutoff radius $r_c = 4.0 \sigma$. In the latter case, it is convenient to use universal LJ units, which are for a hexane: $\sigma = 0.59 \text{ nm}$, $\varepsilon = 413 \text{ K}$, $\tau \approx 2.96 \text{ ps}$, $\varepsilon/\sigma^3 \approx 28 \text{ MPa}$.

Void Nucleation Rate

The rate of the spontaneous phase transition can be characterized by a number of critical nuclei of a new phase formed in a unit volume of a metastable phase in a unit time. The latter value is called nucleation rate J . It is calculated by means of the statistical averaging technique applied to the lifetimes of a metastable phase [5]. The lifetime of a metastable macrostate before the decay (first appearance of the void or the supercritical nucleus of a liquid phase) is averaged over the ensemble of the initial microstates corresponding to a homogeneous phase at the same fixed strain and temperature. Nucleation is manifested by the instantaneous drop of temperature or pressure. Thus, the lifetime at a single MD run is defined by the duration of the trajectory stationary part. The nucleation rate is obtained as $J = 1/(N\tau)$, where N is the number of particles in the simulation box (or a volume of the box) and τ is the average lifetime.

Single Crystal Aluminum

Various mechanisms of void nucleation are observed, depending on temperature. At low temperatures, the liquid phase is less stable than the crystalline one. Hence local disordering of crystal lattice results in void nucleation in the crystal. Typical size of the initial void observed is just a few lattice constants. A certain tensile

stress is needed for further void growth. The threshold value increases with the decrease of void size; hence, nucleation of the critical voids is observed at relatively high negative pressure. But the melting line can be achieved at negative pressures, so the other scenario for crystal decay under tension is melting. When approaching the melting point, a small pressure may initiate amorphization. Tensile strength of the liquid is comparable to that of the crystal at elevated temperatures, and local crystal melting is possible. Then the void formation takes place in the melt formed.

The procedure for evaluation of nucleation rate described above results in the nucleation rate in homogeneous crystal with the fixed temperature T and strain (tension) characterized by a density ρ , or a lattice constant a , or a pressure P . Figure 1a shows the nucleation rate $J(a, T)$ in logarithmic scale as a function of the lattice constant a for several temperatures considered $T = 935, 800, 700$, and 300 K. Typical magnitude of a lifetime until melting ranges from 100 to 10^3 ps. The step of the numerical integration used was 10^{-3} ps. The number of particles in a simulation box N varies from 500 (for large J , corresponding to the upper part of the plot) to $32,000$ (lower J). The region considered is quit close to the kinetic stability limit of the crystalline aluminum. It reveals the linear dependence of $\log J$ on the lattice constant along isotherm. The resulting fitting formula used in the kinetic model [6] is follows:

$$\lg(J/J_0) = A(a - a_{\text{lim}}) \quad (1)$$

One can see that both the slope of the isotherms $A(T)$ and a shift of the kinetic stability limit $a_{\text{lim}}(T)$ depend on temperature.

Simple Liquid

Pressure dependence of nucleation rate for three isotherms of LJ liquid are presented in Figure 1(b). The number of particles in the simulations N was varied from $8,000$ at high nucleation rates to $216,000$ in the region with small J . The change of nucleation rate J along an isotherm T can be approximated in the form of the classical nucleation theory:

$$J = J_0 \exp(-16\pi\gamma^3 / 3P^2kT) \quad (2)$$

where γ is surface tension and P is pressure in liquid phase. It is assumed to be equal to a mean pressure along the stationary part of the MD trajectory, while pressure of vapor in the cavity is negligible compared to the pressure in liquid phase. The values of the surface tension evaluated from fitting of the curves are close to one calculated from the size of void in equilibrium. Theoretical predictions of the pre-exponent J_0 are not satisfactory, so the values evaluated from MD simulations are used in the kinetic model.

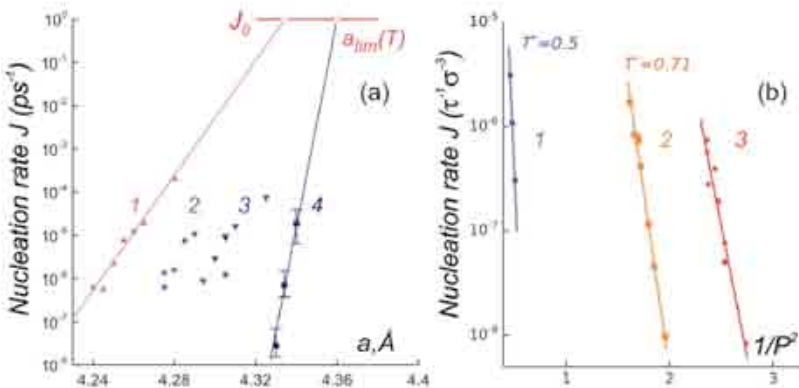


Figure 1. Isotherms of void nucleation rate: a) in single crystal aluminum (1 – 935 K; 2 – 800 K; 3 – 700 K; 4 – 300 K); b) in simple liquid (1 – 0.50 ϵ ; 2 – 0.71 ϵ ; 3 – 0.75 ϵ).

Kinetics of Void Growth

The void growth rate is evaluated from the nonequilibrium MD simulations. The system without cavities is equilibrated to a given pressure and temperature at the preparatory stage. Then a spherical void is cut off and the evolution of the system is observed. While the void volume increases the pressure and temperature relaxation occur, which affect the growth rate noticeably. It constrains the time where void grows into unbounded media. The system volume under consideration should be large enough.

Single Crystal Aluminum

Two competitive mechanisms of the void growth in crystal under tensile load are observed: lattice amorphization around the growing pore and local shear via formation of dislocation loops. Anisotropic distribution of stresses is observed around the void, and regions with large shear stresses are formed near the void surface even in case of the hydrostatic loading. Thus, the spontaneous growth starts with the emission of shear dislocation loops. The pure dislocation mechanism is observed at small growth rates and small temperatures. Amorphization starts at the junctions of dislocation loops in the case of strong metastability (one can see the process in Figure 2), when void growth rate is high. The critical stress for a void growth is determined for several temperatures, it decreases with the increase of the void size and temperature. While pores are not spherical, an effective radius can be introduced. The void growth rate is evaluated as a function of pressure and temperature and used in the kinetic model for crystalline Al.

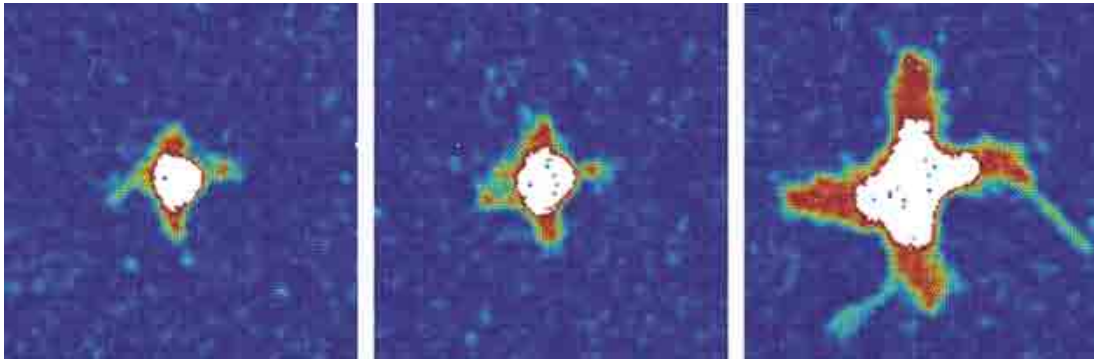


Figure 2. Void growth in Al single crystal via emission of dislocation loops and amorphization. $T = 300$ K, $60 \times 60 \times 60$ unit cells, $R_0 = 1.0$ nm.

Simple Liquid

Contrary to the crystalline case the shape of the void in liquid is spherical at all the stages of the void growth. The evolution of the void radius in time for LJ liquid is presented in Figure 3 for various pressures and temperature $T=0.75 \epsilon$. The dependence of void radius is not linear, and growth rate changes. The results of MD simulations are shown by solid lines, while dashed lines correspond to the solution of the Rayleigh-Plesset equation:

$$R\ddot{R} + \left(3\dot{R}^2/2\right) + (4\eta\dot{R}/\rho R) + (2\gamma/\rho R) = -P(t)/\rho \quad (3)$$

It describes the evolution of the void radius R in an incompressible liquid with density ρ , surface tension γ and viscosity η under the action of the external pressure $P(t)$. The surface tension and the viscosity are not free parameters for a fitting and are calculated independently for the LJ liquid in the given state (Figure 3). One can see that the kinetics of void growth in liquid is described well by the hydrodynamic Rayleigh-Plesset equation.

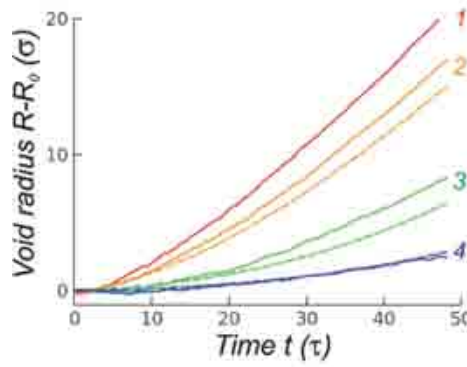


Figure 3. Evolution of void radius in LJ liquid at $T = 0.75 \epsilon$ and pressure ($R_0 = 4.9 \sigma$): 1 – $P = -0.56 \epsilon/\sigma^3$; 2 – $P = -0.535 \epsilon/\sigma^3$; 3 – $P = -0.41 \epsilon/\sigma^3$; 4 – $P = -0.33 \epsilon/\sigma^3$.

Results and Discussion

The data obtained from a set of MD simulations are incorporated as constitutive relations within the kinetic model of fracture based on the nucleation and growth (NAG) approach [7]. It allows us to proceed from MD to kinetics of fracture at mesoscale and to estimate the spall strength σ_{sp} . The dynamic deformation of a sample at the constant stretching rate is considered in mesoscale modeling. The net volume of voids V_v in an arbitrary volume V_0 at the time moment t could be found from the nucleation rate $dn/d\tau = J[a(\tau)]$ and evolution of volume of a single void described by (1, 2, 3):

$$V_v(t) = \int_0^t v_v(t-\tau) \dot{n}(\tau) d\tau \quad (4)$$

We assume the moment of spallation t_{sp} as the moment when the net volume of voids V_v becomes equal to the initial volume V_0 or when the void growth rate is equal to the strain rate $\dot{\epsilon}$. Given the time dependence $a(t)$ or $\rho(t)$ for the regime concerned and equation of state $P(\rho, T)$, one obtains the pressure value at the moment of spallation (i.e., the spall strength $\sigma_{sp} = -P_{sp}$). Figure 4 presents the estimated values of spall strength for deformation in a dynamic regime in dependence on the strain rate $\dot{\epsilon}$. The results are in good agreement with experimental ones at low strain rates and direct MD simulation at high strain rates. Direct MD simulations are represented by uniform stretching of single crystal Al or LJ liquid at the constant temperature.

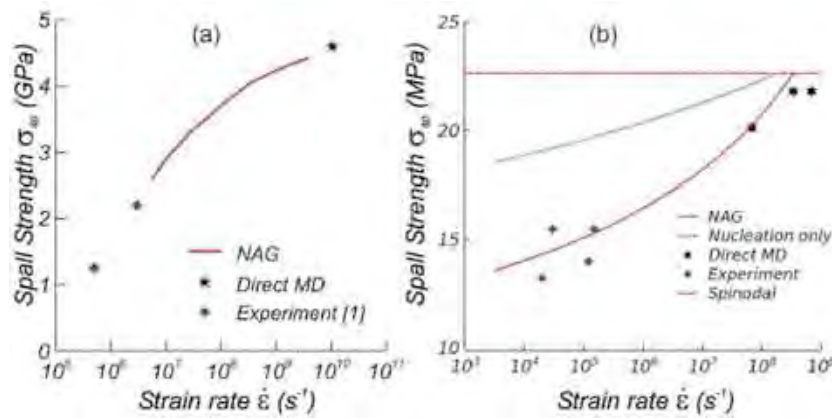


Figure 4. Dependence of the spall strength on the strain rate. Comparison of the NAG kinetic model with the results of direct MD simulations and shock-wave experiments.

The comparison with the results from shock-wave tests [1] on Al at elevated temperature ($T \sim 900$ K) and [2] on hexane (the initial temperature $T_0 \sim 290$ K corresponds to $T_0 \sim 0.71\epsilon$ in LJ units for hexane) is also shown in Figure 4. With the decrease of temperature, the agreement becomes worse for Al. The reason is connected

with the increasing role of defects in the fracture process at the strain rates considered. At lower temperature, the significant rate of homogeneous nucleation is achieved at very high stresses. Hence, lattice defects act as nucleation sites, and fracture starts at lower stress.

Conclusions

MD data obtained are incorporated within a “nucleation and growth” model. The dependence of the dynamic spall strength on the strain rate is estimated with the help of the kinetic model developed. The results are in a good agreement with the experiments at low strain rates and direct MD simulation at high strain rates.

Acknowledgements

We are grateful to J. B. Aidun, E. M. Bringa, and G. I. Kanel for stimulating discussions. This work was partially supported by the RFBR09-08-01116-a grant, RAS programs #11, 12, and Sandia National Laboratories under the U.S. DOE/NNSA Advanced Simulation and Computing program. Sandia is a multi-program laboratory operated by Sandia Corporation, a Lockheed Martin Company, for the United States Department of Energy under Contract DEAC04-94AL85000.

References

- [1] G. I. Kanel, S. V. Razorenov, K. Baumung, J. Singer, “Dynamic yield and tensile strength of aluminum single crystals at temperatures up to the melting point,” *J. of Applied Physics* **90** 136-143 (2001).
- [2] A. V. Utkin, V. A. Sosikov, A. A. Bogach, V. E. Fortov, “Tension of liquids by shock waves,” in *Shock Compression of Condensed Matter-2003*, eds. M. D. Furnish et al. (Melville, New York, American Institute of Physics 2004) pp. 765-768.
- [3] S. J. Plimpton, “Fast parallel algorithms for short-range molecular dynamics,” *J. Comp. Phys.* **117** 1-19 (1995).
- [4] Y. Mishin, D. Farkas, M. J. Mehl, D. A. Papaconstatopoulos, “Interatomic potentials for monoatomic metals from experimental data and ab initio calculations,” *Phys. Rev. B* **59** 5 3393-3407 (1999).
- [5] G. E. Norman, V. V. Stegailov, “Simulation of Ideal Crystal Superheating and Decay,” *Mol. Simul.* **30** 9 397-406 (2004).
- [6] A. Y. Kuksin, G. E. Norman, V. V. Stegailov, A. V. Yanilkin, “Modeling of Al crystal fracture under high-rate strain based on atomistic simulations” in *Shock Compression of Condensed Matter-2007*, ed. M. D. Furnish et al. (Melville, New York, American Institute of Physics, 2007) pp. 317-320.
- [7] T. W. Barbee, L. Seaman, R. Crewdson, D. R. Curran, “Dynamic Fracture Criteria for Ductile and Brittle Metals” *J. of Materials* **7** 393-401 (1972).

MODELING THE INTERCONNECTIONS BETWEEN A STRUCTURAL TRANSFORMATION FRONT AND A GROWING CRACK

A. B. Freidin

Institute of Problems in Mechanical Engineering, St. Petersburg, 199178 Russia

We discuss problems of modeling the coupled interaction between different processes accompanying and preceding a crack growth: inelastic deformations, phase transformations, and chemical reactions. Based on the Eshelby stress concept and thermodynamic considerations, we focus on how a crack growth interconnects with an advancing transformation front.

Energy Release Due to Simultaneous Propagation of a Crack and a Phase Boundary

We consider a quasi-static crack growth in a case of small strains. We suppose that a material in front of the crack undergoes phase transformations. Two-dimension model is shown in Figure 1. A crack is a traction free surface Σ in a body \mathfrak{v} bounded by the surface $\Omega = \Omega_\sigma \cup \Omega_u$. The traction \mathbf{t}_0 and \mathbf{u} displacement are given at Ω_σ and Ω_u , respectively.

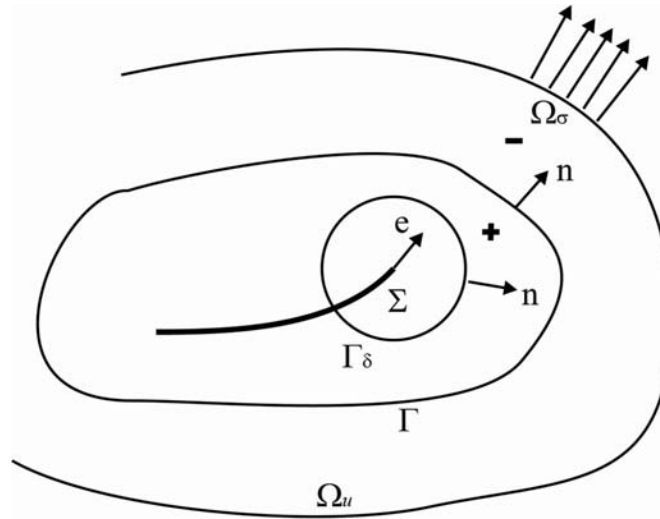


Figure 1. Crack in a two-phase body.

The unit vector \mathbf{e} at the crack tip is tangent to the crack trajectory and gives the direction of crack growth. The crack tip velocity $\mathbf{v}_l = \dot{l}\mathbf{e}$ where l is a crack length, a dot denotes a time derivative.

A small neighborhood \mathfrak{v}_δ of a crack tip is bounded by a circle Γ_δ of the radius δ . It is included into the consideration to isolate the singularity (we follow [4] here). Volume integrals are calculated as a limit of integrals taken over the volume $\mathfrak{v} \setminus \mathfrak{v}_\delta$ at $\delta \rightarrow 0$. Additional conditions [4] provide the convergence. The disk \mathfrak{v}_δ moves with a crack tip.

The moving interface Γ divides a body without the disk \mathfrak{v}_δ into two domains \mathfrak{v}_+ and \mathfrak{v}_- , $\mathfrak{v}_- \cup \mathfrak{v}_+ = \mathfrak{v} \setminus \mathfrak{v}_\delta$, superscripts or subscripts “-” and “+” will identify the values being taken for a material in the “-” and “+” domains, respectively. The displacement is continuous across the interface, but some components of the strain tensor may have a jump.

Assume that the strain tensor $\boldsymbol{\varepsilon}$ can be decomposed as $\boldsymbol{\varepsilon} = \boldsymbol{\varepsilon}^e + \boldsymbol{\varepsilon}^p$ where $\boldsymbol{\varepsilon}^e$ and $\boldsymbol{\varepsilon}^p$ are elastic and inelastic strains, respectively. Assume that free energy density

$$f = f(\boldsymbol{\varepsilon}^e, \alpha, T)$$

where T is the temperature, α represents a set of state variables responsible for inelastic strains. The simplest constitutive relationship between α and $\boldsymbol{\varepsilon}^p$ is $\dot{\alpha} = \mathbf{g} : \dot{\boldsymbol{\varepsilon}}^p$ [8].

From the dissipation inequality known as the Clausius-Duhem inequality it follows that

$$\boldsymbol{\sigma} = \frac{\partial f}{\partial \boldsymbol{\varepsilon}^e}, \quad s = -\frac{\partial f}{\partial T}, \quad \left(\boldsymbol{\sigma} - \frac{\partial f}{\partial \alpha} \mathbf{g} \right) : \dot{\boldsymbol{\varepsilon}}^p \geq 0 \quad (1)$$

where $\boldsymbol{\sigma}$ is Cauchy stress, s is the entropy density. Further we assume that the thermodynamic force

$$\boldsymbol{\psi} = \boldsymbol{\sigma} - \frac{\partial f}{\partial \alpha} \mathbf{g} \quad (2)$$

is a known function of the thermodynamic flux: $\dot{\boldsymbol{\varepsilon}}^p : \boldsymbol{\psi} = \boldsymbol{\psi}(\dot{\boldsymbol{\varepsilon}}^p)$ [8].

Using above relationships, finally, we obtain the following expression of the entropy production in a case of a straight line crack

$$TP[S] = (J - 2\gamma_\Sigma) \dot{l} - \int_\Gamma [\mu_n] v_n^* d\Gamma + D \geq 0 \quad (3)$$

where γ_Σ is the surface free energy density,

$$\mu_n = \mathbf{n} \cdot \mathbf{M} \cdot \mathbf{n}, \quad \mathbf{M} = J\mathbf{E} - \nabla \mathbf{u} \cdot \boldsymbol{\sigma} \quad (4)$$

is the Eshelby stress tensor (see, e.g., [1] and reference therein), \mathbf{E} is the unit tensor, \mathbf{u} is a displacement, \mathbf{n} is a normal, square brackets denote a jump across the interface, J is the Rice integral,

$$J = \lim_{\delta \rightarrow 0} J(\delta), \quad J(\delta) = \mathbf{e} \cdot \int_{\Gamma_\delta} \mathbf{M}_+ \cdot \mathbf{n} d\Gamma, \quad D = \lim_{\delta \rightarrow 0} \int_{v_- \cup v_+} \boldsymbol{\psi} : \dot{\boldsymbol{\varepsilon}}^p dv$$

J - integral can be calculated along an arbitrary path taken inside the domain occupied by the phase “+”, and a material must be uniform inside the path. Note the necessity to take into account the fact that the evolution of the parameters α may produce material heterogeneity.

From (3) one can see that a moving interface as well as dissipation due to inelastic deformations can provide an opportunity of subcritical crack growth, when $J(l) < 2\gamma_\Sigma$. Even if a crack does not grow, it affects the value $[\mu_n]$ at the moving interface through a stress concentration.

Two Linear Elastic Phases

Now we specify the free energy dependence as

$$f^\pm(\boldsymbol{\varepsilon}, T) = f_0^\pm(T) + \frac{1}{2}(\boldsymbol{\varepsilon} - \boldsymbol{\varepsilon}_\pm^p) : \mathbf{C}_\pm : (\boldsymbol{\varepsilon} - \boldsymbol{\varepsilon}_\pm^p) \quad (5)$$

Upper and lower scripts “+” and “-” in relationships correspond to each other. The parameters \mathbf{C}_\pm , $f_0^\pm(T)$ and $\boldsymbol{\varepsilon}_\pm^p$ are the elasticity tensors, free energy densities and strain tensors in unstressed phases “ \pm ”, respectively, $[\boldsymbol{\varepsilon}^p]$ is the transformation strain.

The constitutive relations take the form:

$$\boldsymbol{\sigma}_\pm(\boldsymbol{\varepsilon}) = \mathbf{C}_\pm : (\boldsymbol{\varepsilon} - \boldsymbol{\varepsilon}_\pm^p) \quad (6)$$

The jumps in strain or in stress across the interface can be express through the strain or stress on one side of the interface (“+” or “-”) [6,5]. It can be shown that

$$\begin{aligned} [\boldsymbol{\varepsilon}] &= \mathbf{K}_\mp(\mathbf{n}) : \mathbf{q}_\pm, \quad [\boldsymbol{\sigma}] = \mathbf{S}_\mp(\mathbf{n}) : \mathbf{m}_\pm \\ \mathbf{q} &\triangleq -\mathbf{C}_1 : \boldsymbol{\varepsilon} + [\mathbf{C} : \boldsymbol{\varepsilon}^p], \quad \mathbf{m} \triangleq \mathbf{B}_1 : \boldsymbol{\sigma} + [\boldsymbol{\varepsilon}^p] \\ \mathbf{K}_\mp(\mathbf{n}) &= \{\mathbf{n} \otimes \mathbf{G}_\mp(\mathbf{n}) \otimes \mathbf{n}\}^s, \quad \mathbf{G}_\mp(\mathbf{n}) = (\mathbf{n} \cdot \mathbf{C}_\mp \cdot \mathbf{n})^{-1}, \\ \mathbf{S}_\mp(\mathbf{n}) &= \mathbf{C}_\mp : \mathbf{K}_\mp(\mathbf{n}) : \mathbf{C}_\mp - \mathbf{C}_\mp \\ \mathbf{B}_\pm &= \mathbf{C}_\pm^{-1}, \quad \mathbf{C}_1 = \mathbf{C}_+ - \mathbf{C}_-, \quad \mathbf{B}_1 = \mathbf{B}_+ - \mathbf{B}_- \end{aligned} \quad (7)$$

where $\mathbf{G}(\mathbf{n})$ is the Fourier transform of Green's tensor, the inverse of the acoustic tensor, s means the symmetrization: $K_{ijkl} = n_{(i} G_{j)(k} n_{l)}$. If the phase “-” is isotropic, then

$$\begin{aligned} \mathbf{C}_- &= \lambda_- \mathbf{E} \otimes \mathbf{E} + 2\mu_- \mathbf{I}, \\ \mathbf{K}_-(\mathbf{n}) &= \frac{1}{\mu_-} (\mathbf{n} \otimes \mathbf{E} \otimes \mathbf{n})^s - \frac{1}{2\mu_-(1-\nu_-)} \mathbf{n} \otimes \mathbf{n} \otimes \mathbf{n} \otimes \mathbf{n} \end{aligned}$$

where, $(\mathbf{E} \otimes \mathbf{E})_{ijkl} = \delta_{ij} \delta_{kl}$, \mathbf{I} is the symmetric fourth rank unit (isotropic) tensor, $I_{ijkl} = 1/2(\delta_{ik} \delta_{jl} + \delta_{jk} \delta_{il})$, δ_{ik} is Kronecker's delta, λ and μ are Lamé constants, and ν is Poisson's ratio. The tensors \mathbf{q} and \mathbf{m} unify two formulations of the Eshelby problem (see, e.g., [7]), which are the inclusion problem $\mathbf{C}_1 = 0$ and the inhomogeneity problem ($\boldsymbol{\varepsilon}_\pm^p = 0$).

Substituting (8)-(10) into (4) we express $[\mu_n]$ through stress on one side of the interface and the normal to the interface:

$$[\mu_n] = \gamma + \frac{1}{2} [\boldsymbol{\varepsilon}^p : \mathbf{C} : \boldsymbol{\varepsilon}^p] + \frac{1}{2} \boldsymbol{\varepsilon}_\pm : \mathbf{C}_1 : \boldsymbol{\varepsilon}_\pm - \boldsymbol{\varepsilon}_\pm : [\mathbf{C} : \boldsymbol{\varepsilon}^p] \pm \frac{1}{2} \mathbf{q}_\pm : \mathbf{K}_\mp(\mathbf{n}) : \mathbf{q}_\pm \quad (8)$$

$$[\mu_n] = \gamma - \frac{1}{2} \boldsymbol{\sigma}_\pm : \mathbf{C}_1 : \boldsymbol{\sigma}_\pm - \boldsymbol{\sigma}_\pm : [\boldsymbol{\varepsilon}^p] \pm \frac{1}{2} \mathbf{m}_\pm : \mathbf{S}_\mp(\mathbf{n}) : \mathbf{m}_\pm \quad (9)$$

where $\gamma(T) = [f_0]$ (see [5] or the recent papers [2,3] and reference therein).

Thus, the problem of finding the driving force $[\mu_n]$ acting on the interface is reduced to strain or stress calculations on one side of the interface. It seems to be reasonable to take the “+”-side. Then, if the interface is not far from the crack tip, the driving force acting on the interface is determined by the stress intensity factors as well as the Rice integral.

Let $\mathbf{C}_- = \mathbf{C}_+ = \mathbf{C}$ and $\boldsymbol{\varepsilon}_-^p = 0, \boldsymbol{\varepsilon}_+^p = \boldsymbol{\varepsilon}^p$. Then, by (9), on the interface

$$[\mu_n] = \gamma - \boldsymbol{\sigma}_+ : \boldsymbol{\varepsilon}^p + \frac{1}{2} \boldsymbol{\varepsilon}^p : \mathbf{S}(\mathbf{n}) : \boldsymbol{\varepsilon}^p \quad (10)$$

To illustrate a restrictive role of the dissipation inequality (3), let us assume that the loading is symmetric with respect to the crack line, transformations are localized at the transformation front Γ_* placed in front of crack tip, d_* is a characteristic size of the transformation front, x_* is a position of the front on the crack line and v_* is the front velocity. Let $\xi_* = x_* - l$ is a length of the segment occupied by the new phase, $\dot{\xi}_* = v_* - \dot{l}$. Then the expression of dissipation takes the form

$$TP[S] = d_* (K_*(l, \xi_*) - \gamma) \dot{\xi}_* - (2\gamma_\Sigma - K_l(l, \xi_*) - d_* (K_*(l, \xi_*) - \gamma)) \dot{l} \geq 0 \quad (11)$$

For brevity, we do not show here the dependencies $K_*(l, \xi_*)$ and $K_l(l, \xi_*)$. Furthermore, we assume that $2\gamma_\Sigma - K_l(l, \xi_*) > 0, K_*(l, \xi_*) - \gamma > 0$. Then

$$\dot{\xi}_* \geq \left(\frac{2\gamma_\Sigma - K_l(l, \xi_*)}{d_* (K_*(l, \xi_*) - \gamma)} - 1 \right) \dot{l} \quad (12)$$

If the crack grows (i.e. $\dot{l} > 0$), and

$$2\gamma_\Sigma - K_l(l, \xi_*) > d_* (K_*(l, \xi_*) - \gamma), \quad (13)$$

then $\dot{\xi}_* > 0$, the zone “+” grows, and the transformation front moves away from the crack tip.

If $\dot{l} > 0$ and $\dot{\xi}_* < 0$ then

$$2\gamma_\Sigma - K_l(l, \xi_*) < d_* (K_*(l, \xi_*) - \gamma) \quad (14)$$

If during subcritical crack growth $\xi_* \rightarrow 0$ and $d_* \sim \beta \xi_*$ then

$$P[S] \rightarrow - \left(2\gamma_\Sigma - \frac{K_l^2}{E} \right) \dot{l}, \quad \frac{K_l^2}{E} \leq 2\gamma_\Sigma$$

From the condition $P[S] \geq 0$ at $\dot{l} > 0$, it follows that

$$\frac{K_l^2}{E} \rightarrow 2\gamma_\Sigma \text{ if } \xi_* \rightarrow 0, \quad \dot{l} > 0 \quad (15)$$

Thus, the Griffiths crack length is reached for the material of the phase “+” if $\xi_* \rightarrow 0$. The relationships (12)-(15) demonstrate interconnections between the subcritical crack growth and the transformation front development.

The entropy inequality gives restrictions but does not determine the kinetics of the crack growth. Additional hypotheses are needed. Two ways have been discussed. One way is to formulate kinetic constitutive equations for a growing crack and advancing transformation front that do not contradict to the entropy inequality. Another way is to formulate a local fracture criterion and then derive the kinetic relation.

Chemical Reactions Front Propagation

We also consider an elastic solid in which chemical reactions of oxidizing type take place [9]. We suppose that the chemical reaction is localized at the chemical reaction front, and the reaction is sustained by the diffusion of an oxidizing gas constituent through the solid oxide. Based on introducing an intermediate configuration reflected chemical transformations of solid constituents we derive an expression of the potential energy release due to the reaction front propagation. As a result, we find the input of solid phases into a chemical affinity tensor as a combination of Eshelby stress tensors determined with respect to stress free configurations of the initial and chemically produced solid constituents and multiplied by chemical reaction parameters (stoichiometric coefficients and molar masses). Then we consider an input of a gas constituent and derive an expression of a chemical affinity tensor. For brevity, we do not present the relationships here. Finally, we formulate a simplest kinetic relation for the chemical reactions front propagation and consider interconnections between a growing crack and a chemical reaction front.

Conclusions

The energy balance is written down for a growing crack and moving interface based on the Eshelby stress concept. Based on the dissipation inequality, it is demonstrated that a moving interface as well as dissipation due to inelastic deformations can provide an opportunity of subcritical crack growth. The problem of finding the configuration force acting on the phase boundary is reduced to stress calculations at one side of the interface. This, in turn, allows calculating the configuration force in terms of the stress intensity factors, as well as the Rice integral. Inequalities are derived that must be satisfied in the case of the subcritical crack growth and kinetic relationships for crack and phase boundary propagation are formulated. Earlier results are presented related to a stress-assist chemical reaction front propagation.

Acknowledgements

This work is supported by the Sandia National Laboratories (USA). Sandia is a multi-program laboratory operated by Sandia Corporation, a Lockheed Martin Company, for the United States Department of Energy under Contract DEAC04-94AL85000.

References

- [1] R. Abeyaratne and J. K. Knowles, *Evolution of Phase Transitions. A Continuum Theory* (New York, Cambridge University Press, 2006).
- [2] A. B. Freidin and L. L. Sharipova, "On a model of heterogeneous deformation of elastic bodies by the mechanism of multiple appearances of new phase layers," *Meccanica* **41** 321-339 (2006).
- [3] A. B. Freidin and Z. Angew, "On new phase inclusions in elastic solids," *Math. Mech. (ZAMM)* **87** 2 102-116 (2007).
- [4] M. E. Gurtin, "On the energy release rate in quasi-static elastic crack propagation," *Journal of Elasticity* **9** 2 187-195 (1979).
- [5] L. B. Kublanov, A. B. Freidin, "Solid phase seeds in a deformable material," *Journal of Applied Mathematics and Mechanics (PMM)* **52** 382-389 (1988).
- [6] I. A. Kunin, *Elastic Media with Microstructure*, vol. 2 (New York, Springer-Verlag, 1983).
- [7] T. Mura, *Micromechanics of Defects in Solids*, 2nd edition (Dordrecht, Kluwer Academic, 1987).
- [8] A. A. Vakulenko, "The connections between stresses and strains in inelastic media. Studies on elasticity and plasticity," Leningrad State University No. 1 3-35 (1961).
- [9] C. L. Muhlstein, S. B. Brown, R. O. Ritchie, "High-cycle fatigue and durability of polycrystalline silicon thin films in ambient air," *Sensors and Actuators A94*, 177-188 (2001).

FEM SIMULATION OF FATIGUE DAMAGE, CRACK NUCLEATION, AND GROWTH IN A PRE-DAMAGED MATERIAL

I. K. Korolev,* S. V. Petinov,** A. B. Freidin*

* Institute of Problems in Mechanical Engineering, RAS, St. Petersburg, 199178, Russia

† St. Petersburg State Polytechnic University, St. Petersburg, 195251, Russia

Author Contact: i.korolev82@gmail.com

A finite-element method (FEM)-based procedure of fatigue crack growth simulation in the field of progressive damage is developed. A specific finite element grid is suggested that allows saving the information on accumulated damage and “natural” tracing of a growing crack; otherwise it is laborious to use the standard FEM-procedures. The basic principles of meshing are formulated, and following these principles, a two-level finite element grid is designed. Fatigue behavior of a notched plate with imbedded randomly distributed defects is analyzed. The damage evolution and the traces of growing cracks in the plate are assessed at different phases of fatigue life. The procedure developed is deemed an effective mechanism that allows both to model the crack formation from a defect and its further propagation accordingly the damage accumulation during all cyclic loading. It also provides a substantial reduction in influence of the mesh geometry on the progressive crack extensions.

Introduction

Simulation of fatigue crack growth in conjunction with the damage accumulation, based on coupled action of mechanisms of slip in material grains and the stress field has been attracting attention through the past decades (e.g., [1]). One of effective ways of modeling crack propagation is the use of finite-element method (FEM). Application of FEM for the analysis of crack propagation when the crack path may be affected by the inhomogeneous development of damage or by specifics of the stress field immediately assumes an operative reorganization of a finite element grid during the crack extensions. It helps to avoid the influence of the finite element grid topology on the crack trajectory. This is because the initial grid cannot adequately describe the redistribution of the stress and strain fields around the tip of the growing crack.

However, applicability of such an approach is limited by a class of problems where there is no correlation between the crack path and the previous history of damage accumulation in material. When dependence of the crack extensions on the prehistory of damage should be accounted for, the redesign of the FE mesh is unacceptable, since it leads to deleting the information on the progressive degradation of the material.

This work is focused on the design of finite element grid, which, on the one hand, would allow us naturally to save the information on the fatigue damage in material (finite elements) prior to failure and to model by this the whole process of fatigue crack development using the unique finite element mesh. On the other hand, it would minimize the influence of the mesh topology on the traces of fatigue cracks. Based on the formulated principles, the original structure of the FE grid is developed and verification of its consistency is presented.

Method

Basics of the Approach

Crack initiation and propagation are modeled based solely on assumption that the damage accumulation in material elements controls the process. As an example, the fatigue process is analyzed in a formally elastic plate with a central circular hole under cyclic zero-to-tension loading. First, the analysis is addressed to the homogeneous material modeled with the finite element mesh differing by topology. The fatigue process is modeled by the sequence of damage accumulation in FE's using the Palmgren-Miner rule [2]:

$$D = \sum_i \frac{n_i}{N_i} \quad (1)$$

where D is the accumulated damage in an element, $n_i = n(S_i)$ is the number of load cycles with the stress range S_i , $N_i = N(S_i)$, is the number of cycles prior to failure of the “ i ” element with the stress range S_i .

Values of $N(S_i)$ are obtained from the S-N curve for the plate material approximated by the Basquin equation [3]:

$$N(S) = C / S^m \quad (2)$$

where C and m – are the material empirical “constants” to be obtained from the experimental data, and S – is the stress range.

By substituting (2) into (1) the damage accumulated in every of the elements:

$$D = \sum_i \frac{n_i}{N_i} = (1/C) \sum_i n_i S_i^m \quad (3)$$

Successive failure of elements (i.e., when the damage in a sequential element becomes $D = 1$) is defined by decreased stiffness of the element by several decimal orders (“killing” of elements), and the succession of failures indicates the crack extension. Rapid acceleration of the progress of damage, characterized by the crack growth rate, was regarded as the indication of the plate failure. This scenario was realized in the case when the crack origination was assumed at the notch root, but at a certain distance from the axis of symmetry.

Development of the Specific Mesh Type

First, a standard regular finite element mesh is used. Figure 1 shows the initial stage of the crack extensions and the final state with well-developed cracking under cyclic loading (the cyclic load is applied far from the fragment shown, in “infinity”).

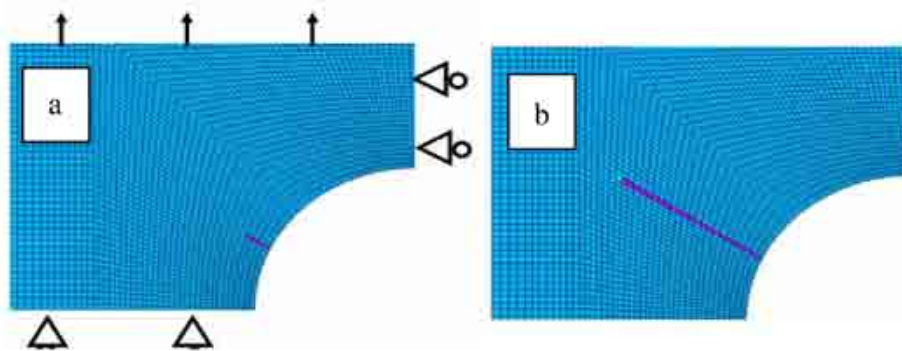


Figure 1. Crack growth simulation by the mechanism of the damage accumulation. Regular FE mesh.

Figure 1(a,b) shows that crack follows strictly the mesh nodal line, inclined to the direction of loading and direction of the maximum principal stress. Analysis (by using finer mesh at assumed crack tip) indicates that the most intensive damage at the crack increments develops in successive elements located directly ahead the crack tip (i.e., along the grid nodal line). It may be explained by modeling the crack extensions by successive “killing” of elements.

Keeping with the modeling of fatigue cracks by the damage accumulation principle, the following requirements for the meshing can be formulated to minimize the influence of the grid topology on the trajectory of a growing crack:

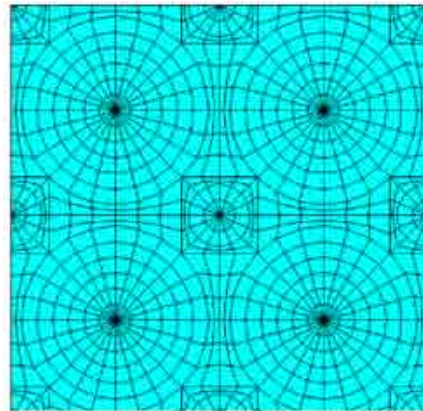
- (1) The crack tip should be provided “freedom” to turn under the influence of the local stress field, accompanied by the accumulated fatigue damage in successive elements.
- (2) The isotropy of the grid is desired. Any specified nodal lines in the mesh would control the crack extensions.

Respectively, a cell structure of the mesh was derived, meeting the above requirements. A cell of the mesh structure is shown in Figure 2.

The cell type has a two-level structure. The first level consists of “large blocks-circles;” in the center of these “circles” there are triangular elements that allow for trajectories of growing crack to deviate under influence of stress flow and accumulated damage in the part surrounding the crack tip. The second level consists of “small blocks-circles,” in the center of “circlets.” There are also located triangular elements. The second level allows the crack to turn if it would extend along the edge of a “large circle.”

By this, the proposed topology of the modified finite-element grid for modeling the crack propagation would allow a trajectory to turn according to the local stress flow; the less wavy deviations are also expected. The two-level cell structure has to be better suited for the modeling fatigue crack morphology when the damage summation procedure is applied.

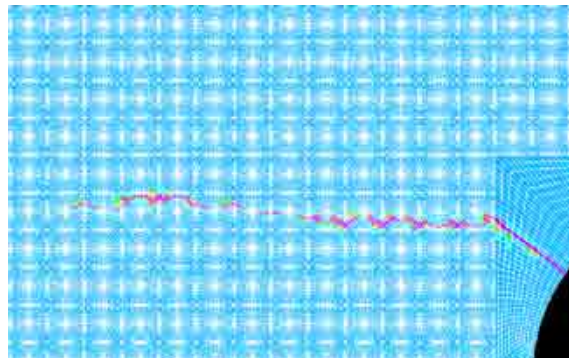
Figure 2. A cell of the proposed isotropic mesh type.



Verification of the Developed Grid Consistency

For the verification this mesh type was applied for the above crack growth analysis. Figure 3 presents the results of simulation of fatigue crack extensions under uniaxial cyclic loading for the same task as at Figure 1(a).

Figure 3. Fatigue crack growth simulation. Proposed mesh.



It is demonstrated that the simulated crack propagation in general satisfactorily follows orientation of the planes normal to the maximum principal stress flow, apart from the area where the mesh is oriented.

The accuracy of the proposed grid is checked with the help of comparison of stress intensity factors calculated in the cases:

- when the crack is simulated using the proposed approach
- when the regular mesh with singular elements is applied and
- SIFs obtained from the hand book sources (e.g., [4]).

A rectangular plate with symmetrical edge cracks loaded perpendicular to the crack planes is assumed. The plate dimensions are $2a = 2b = 7 \cdot 2l = 28$ mm, initial crack length is $2l = 4$ mm, the size of grid cells is 2 mm, and the plate is loaded by static stress $\sigma = 1$ MPa.

According to the handbook data [4], stress intensities (K_I^M) for the plate with symmetrical cracks at the edges are given by:

$$K_I^M = \sigma \sqrt{\pi l} \cdot F_I(\alpha), \quad \alpha = l/b, \quad F_I(\alpha) = (\sec(\alpha\pi / 2))^{1/2}$$

When the proposed modified meshing is applied, the stress intensities, K_I^{grid} , can be estimated by using the extrapolation to the crack tip technique [5]:

$$K_I^{grid} = \lim_{r \rightarrow 0} \sigma \sqrt{2\pi r},$$

where r is the distance of the reference point from the crack tip, $\sigma = \sigma(r)$ is the (maximum principal) stress at the reference point range.

When the plate with edge cracks is modeled by regular mesh with singular elements, stress intensities (K_I^{sin}) are calculated by means of a procedure built in a software based on the method of nodal displacements. Respectively, the SIF values are as follows:

- handbook [4] data: $K_I^M = 80.3 \text{ kPa} \cdot \text{m}^{1/2}$
- regular mesh with singular elements: $K_I^{sin} = 81.6 \text{ kPa} \cdot \text{m}^{1/2}$
- proposed modified meshing technique: $K_I^{grid} = 78.5 \text{ kPa} \cdot \text{m}^{1/2}$

The example shows that relative difference of the results does not exceed 2.5%, which can be regarded as favorable for the proposed approach together with the assumed isotropic meshing.

Results and Discussion

The modified mesh type was used to simulate behavior of initial micro-crack-like defects in material structures under cyclic loading. The defects and “fatigue properties” (coefficient C in (2)) of “material elements” (finite elements) were randomly distributed in a rectangular thin plate, as shown on the next page in Figure 4(a); cyclic load is applied in vertically (at “infinity”).

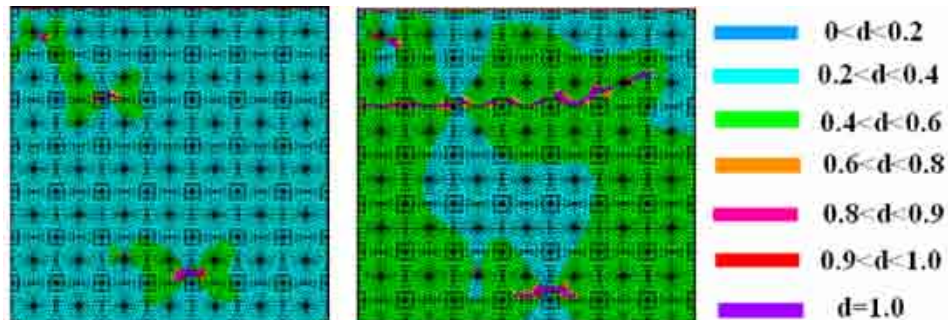


Figure 4. Development of defects in material structure into the propagating crack: (a) initial defects; (b) evolution of defects under cyclic loading; right hand – the damage intensity legend.

It is seen that a defect in the intensive damage area became an “active” one, which turned into the propagating crack; the other defects remained “dormant.”

The trajectory of crack initiated at the “active” defect, shown in Figure 4, is in general controlled by the stress flow; its deviation from the straight line perpendicular to the loading direction may be explained by the different (randomized) rate of the damage in “material” elements and, partly, by the sensitivity to the progress of damages induced by the defect in the lower part of the plate. In this example, the influence of grid topology on the crack trajectory can be essentially reduced. Also, the modified meshing provides better smoothness of the crack morphological features and makes it possible to trace the step-by-step damage accumulation and further formation of fracture nucleus near initial cracks/defects and their propagation.

Conclusions

A simple approach allowing for simulation of the fatigue crack initiation and growth in a nonuniform field of progressive fatigue damages is developed based on application of the principles of FE meshing, which provide realistic crack extensions independent of the mesh geometry.

Acknowledgements

This work is supported by Sandia National Laboratories, USA. Sandia is a multi-program laboratory operated by Sandia Corporation, a Lockheed Martin Company, for the United States Department of Energy under Contract DEAC04-94AL85000.

References

- [1] F. Ellyin, *Fatigue Damage, Crack Growth and Life Prediction* (London, Chapman & Hall, 1997).
- [2] M. Miner, “Cumulative damage in fatigue,” *Journal of Applied Mechanics* **12**, *Trans. ASME* **67** pp. A159-A164 (1945).
- [3] O. Basquin, “The exponential law of endurance tests,” *Proc. of ASTM* **10**, Part II, 625 (1910).
- [4] *Stress Intensity Factors Handbook*, ed. Y. Murakami, in 2 volumes (Pergamon Books Ltd, 1987).
- [5] B. Aamodt, “Application of the finite element to fracture mechanics,” *Dep. of Structural Mechanics* (Trondheim, NTH, 1974).



SOLID-STATE RAYLEIGH-TAYLOR EXPERIMENTS IN VANADIUM AT MBAR PRESSURES AT THE OMEGA LASER

B. A. Remington, H. S. Park, K. T. Lorenz, R. M. Cavallo, S. M. Pollaine, S. T. Prisbrey, R. E. Rudd, R. C. Becker, and J. V. Bernier

Lawrence Livermore National Laboratory, Livermore, CA 94550 USA

Author Contact: remington2@llnl.gov

We present experiments on the Rayleigh-Taylor (RT) instability in the plastic flow regime of solid-state vanadium (V) foils at ~1 Mbar pressure and strain rates of 10^6 - 10^8 s⁻¹, using a laser based, ramped-pressure acceleration technique. High-pressure material strength causes strong stabilization of the RT instability at short wavelengths. Comparisons with 2D simulations utilizing models of high-pressure strength show that the V strength increases by a factor of 3.5 at peak pressure, compared to its ambient strength. An effective lattice viscosity of ~400 poise would have a similar effect.

Introduction

The Rayleigh-Taylor (RT) instability in the presence of solid-state material strength is of considerable interest. High explosive (HE) driven experiments to study RT instability growth in solid state aluminum at peak pressures and strain rates of $P_{\text{max}} \sim 100$ kbar and $\dot{\epsilon} \sim 10^5$ s⁻¹ were developed in the 1970s and showed strong RT stabilization of short-wavelength perturbations[1]. More recently, HE-driven RT experiments have been done in several different metals (Al, Cu, V) at 300–700 kbar peak pressures in planar geometry, and at pressures reaching ~3 Mbar in convergent cylindrical geometry [2]. Using a newly developed, laser-based, ramped pressure drive, experiments have been performed at $P_{\text{max}} \sim 200$ kbar and $\dot{\epsilon} \sim 10^6$ s⁻¹ in Al [3]. We report here results from an RT experiment using a laser-generated ramped pressure drive, reaching $P_{\text{max}} \sim 1$ Mbar pressures at strain rates of 10^6 - 10^8 s⁻¹ in solid-state vanadium (V), a ductile body-centered cubic (BCC) metal. Strong RT stabilization is observed [4].

Method

We use six azimuthally symmetric laser beams at the Omega Laser [5], each with $E_L \sim 135$ J energy at laser wavelength of $\lambda_L = 351$ nm and 3.7 ns square pulse shape to generate our drive. The ~640 μm diameter flat-top spatial profile is achieved using continuous phase plates (CPP) on the drive beams, creating an average peak laser intensity of $I_L \sim 2.5 \times 10^{13}$ W/cm². This launches a strong shock into a reservoir consisting of 40 μm -thick polyimide, 125 μm thick polycarbonate, and 35 μm thick 2% brominated polystyrene, $\text{C}_{50}\text{H}_{48}\text{Br}_2$, all glued together. The CH(Br) layer absorbs low energy x-rays generated at the ablation front. When the shock breaks out the back of the reservoir, the plasma releases (unloads) across the 300 μm vacuum gap and stagnates on the V sample, creating a ~1 Mbar ramped pressure drive [6,7]. This causes the 35 μm thick V sample to accelerate at a peak value of $g \sim 5 \times 10^{13}$ cm/s². In order to insulate the rippled vanadium sample from the heat created by the initial stagnating plasma, we use a 6 μm thick, CH-based epoxy layer, conformal on the ripple side and machined flat on the gap side, as a heat shield. The accelerating rippled sample is RT unstable, and the ripple amplitude increases at a rate reduced due to material strength.

We measure the drive using a line VISAR velocity diagnostic [8] on separate targets consisting of a 10 μm thick Al foil backed by an LiF window for a range of laser energies. A streaked VISAR image from one of the drive shots is shown in the inset of Figure 1. We then use the radiation-hydrodynamics code LASNEX [9] to determine the plasma drive, which is a set of material density, velocity, and temperature profiles as a function of position from the unloading reservoir just prior to impacting the sample. The plasma drive applied to the V sample generates a ramped loading reaching $P_{\text{max}} \sim 900$ kbar, as shown in Figure 1, and compressions of $\rho/\rho_0 \sim 1.3$ -1.4. Figure 2 shows the corresponding equivalent plastic strain versus time in the V sample, from a 1D radiation-hydrodynamics simulation. The V sample is predicted to stay factors of three to five below the melt temperature, as shown in the inset in Figure 2. The 35 μm thick V sample was made with a $\lambda = 60$ μm wavelength, $\eta_0 = 0.6$ μm amplitude sinusoidal ripple on its surface by a sputtering technique. [10] The vanadium samples were full density, had an average grain size of ~ 1 μm in the lateral direction, 3–5 μm in the thickness (columnar) direction, and a measured tensile strength at ambient pressure and low strain rate of 715 MPa [10].

Results and Discussion

To measure the RT ripple growth, we used face-on radiography with a 5.2 keV laser driven vanadium He- α X-ray backlighter, either in an area backlighting or a point projection imaging configuration. The area backlighting technique uses a large-area X-ray source and a gated X-ray camera with 15 μm pinholes run at magnification of ~ 6 [3]. The point projection technique uses a ~ 15 μm diameter pinhole aperture just in front of the V backlighter foil to create point projection imaging at magnification ~ 19 , onto a gated X-ray camera. The inset in Figure 3 shows an example of a radiographic image of ripple growth at a delay time of 80 ns relative to the start of the drive laser. The RT-induced perturbation growth is written as a growth factor, $\text{GF}(t) = \Delta\text{OD}(t)/(\Delta\text{OD}_0 \cdot \text{MTF})$, where $\Delta\text{OD}(t)$ is the optical depth modulation due to the ripple at time t , $\Delta\text{OD}_0 = \eta_0/\lambda_{\text{mfp}}$ is the initial optical depth, $\lambda_{\text{mfp}} \sim 19.6$ μm is the mean free path length of the 5.2 keV backlighter X rays in vanadium, and MTF is the modulation transfer function, which quantifies the diagnostic spatial resolution. The $\Delta\text{OD}(t)$ is measured from the radiograph by Fourier analysis of the ripple lineouts. The self-consistent data set spanning several shot campaigns is shown by the red plotting symbols in Figure 3. Typical errors in the measured growth factors were $\delta\text{GF}/\text{GF} \sim 10\%$ or less. We estimate an average strain rate, $\dot{\epsilon}_{\text{av}} \sim 3 \times 10^7 \text{ s}^{-1}$, by fitting a linear slope to the simulated strain vs time (see Figure 2) over the interval of 25–40 ns. For $t > 40$ ns, this drops to $\dot{\epsilon}_{\text{av}} \sim 3 \times 10^6 \text{ s}^{-1}$.

We compare our ripple growth data to an analytic RT model that treats strength as an effective lattice viscosity.

In the linear regime, classical RT growth can be written as $\text{GF} \approx e^{\int \gamma_{\text{classical}} dt}$, where $\gamma_{\text{classical}} = [A \cdot \frac{2\pi}{\lambda} \cdot g(t)]^{1/2}$ gives the growth rate for inviscid fluids, and A , λ , and g are the Atwood number, perturbation wavelength, and foil acceleration, respectively. For viscous fluids, the RT growth rate is expressed in the dispersion relation, $\gamma_{\text{RT}}^2 + 2k^2\nu\gamma_{\text{RT}} - gkA = 0$ [12,13], where $\nu(\text{cm}^2/\text{s}) = \mu/\rho$ is the kinematic viscosity, $\mu(\text{dyne}\cdot\text{sec}/\text{cm}^2=\text{poise})$ is the dynamic viscosity, and ρ is density. We show these analytic results in Figure 3 for RT growth factors versus time. The analytic classical inviscid RT calculation for no strength is shown by the top curve, followed by the viscous model for (in order from the top) dynamic viscosities of 100, 200, 400, and 800 poise. The best fit viscosity was ~ 400 poise under these conditions. As a consistency check, we use a relationship equating strength with an effective lattice viscosity, $\nu = \mu/\rho \approx \sigma/(\sqrt{6}\rho\langle\dot{\epsilon}\rangle)$ [12], giving $\sigma \approx \sqrt{6}\langle\dot{\epsilon}\rangle\mu$. Using the average strain rate of $\langle\dot{\epsilon}\rangle \approx 3 \times 10^7 \text{ s}^{-1}$ over the interval of 25–40 ns from the 1D simulations (see Figure 2) and the fitted viscosity of 400 poise gives an estimated peak strength of 29 kbar. A rough approximation of strain rate can also be made from $\langle\dot{\epsilon}\rangle \approx \frac{1}{3}\dot{\rho}/\rho \approx \frac{1}{3}(\Delta\rho/\rho_0)/\Delta t_{\text{rise.time}}$ [6]. From the equation of state of V, an estimated compression of $\rho/\rho_0 \sim 1.4$ occurs over the measured rise time of ~ 6 ns, giving $\langle\dot{\epsilon}\rangle \approx 2 \times 10^7 \text{ s}^{-1}$, and hence, a rough peak strength estimate of 19 kbar.

The PTW model is a strain rate dependent strength model based on deformation by thermal activation for low strain rates and viscous phonon drag for high strain rates [13]. The dimensionless shear strength in the low-strain limit is expressed as

$$\hat{\tau}_y = \max \left\{ y_0 - (y_0 - y_\infty) \operatorname{erf}[\kappa \hat{T} \ln(\gamma \dot{\xi} / \dot{\epsilon})], s_0 (\dot{\epsilon} / \gamma \dot{\xi})^\beta \right\}, \quad (1)$$

where $\dot{\epsilon}$ is the strain rate, \hat{T} is the normalized temperature, $T_{\text{melt}} = T_{\text{melt}}(\rho)$ is the calculated melt temperature based on the Lindeman model [14], $\dot{\xi}$ is a reference inverse time scale, $\gamma \dot{\xi} = \dot{\epsilon}_{\text{crit}}$ is the critical strain rate above which the deformation switches from thermal activation to phonon drag, and y_0 , y_∞ , κ , γ , s_0 , and β are material dependent input parameters. The dimensionless shear strength, $\hat{\tau}_s$, in the (saturated) high-strain limit has a similar form, only with s_0 and s_∞ replacing y_0 and y_∞ . These are combined in a Voce work hardening prescription to give the predicted (dimensional) material strength. To fit our experimental data with 2D simulations using the PTW model, we lowered the critical strain rate for the transition from thermal activation to the phonon drag regime from the default value of $\gamma \dot{\xi} \sim 10^9 \text{ s}^{-1}$ to $\sim 10^6 \text{ s}^{-1}$. This was accomplished by multiplying the PTW input parameters γ , y_0 , and s_0 by 1/800, 0.60, and 0.69, respectively, as illustrated in Figure 4 [15]. These changes to the PTW input parameters leave the strength predictions at $\dot{\epsilon} < 10^6 \text{ s}^{-1}$ (thermal activation regime) unchanged, while increasing the strength for $\dot{\epsilon} > 10^6 \text{ s}^{-1}$ (phonon drag regime). The default PTW parameters for V in the high- regime were set by overdriven shock experiments in Ta, also a BCC metal [13]. Therefore, it is not surprising that substantial changes in these input parameters for ramp loaded V were required.

The 2D simulation results using this modified PTW strength model essentially goes through the experimental data (not shown). The calculated average peak flow stress (strength) is $\sim 25 \text{ kbar}$ based on these 2D simulations, corresponding to a peak pressure and strain rate of 900 kbar and $3 \times 10^7 \text{ s}^{-1}$. This is a factor of 3.5 higher than the measured ambient strength of 7.15 kbar [11]. We estimate the uncertainties in inferred strength from uncertainties in (1) the experimental growth factor measurements and (2) our drive model to each be $\sim 15\%$. Assuming that these are independent sources of error, this gives an overall estimated uncertainty in inferred peak strength of $\sim 20\%$.

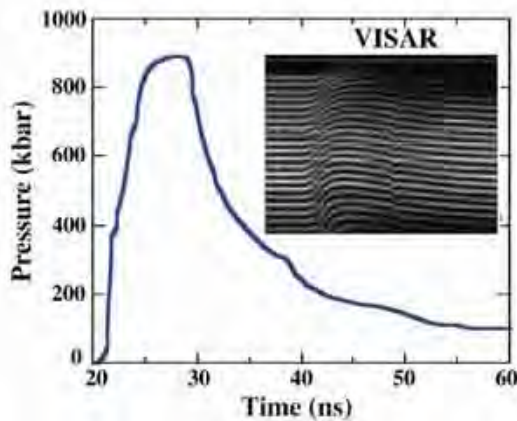


Figure 1. Pressure vs. time in the vanadium RT sample, as calculated from 1D radiation-hydrodynamics simulations, adjusted to reproduce the drive measured in the Al-LiF witness plates. The inset shows a raw line VISAR image for the Al-LiF drive shot.

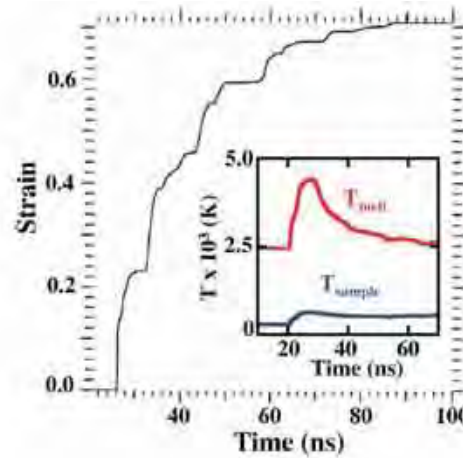


Figure 2. The simulation of plastic strain vs time in the V sample, from a 1D radiation-hydrodynamics simulation. The inset shows the melt temperature (from the Lindemann melt law) and sample temperature, both from the radiation-hydrodynamics simulations.

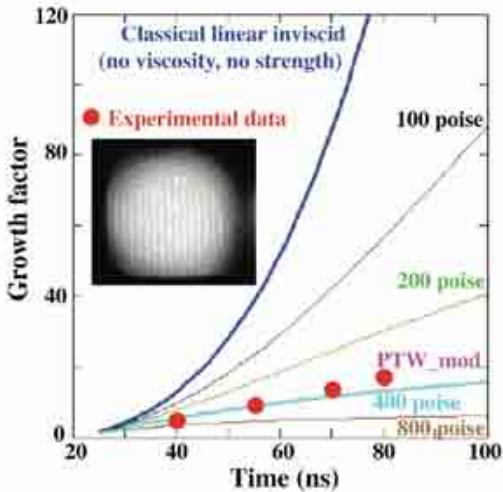


Figure 3. Calculated perturbation growth factor vs time from an analytic RT theory in a viscous medium corresponding to dynamic viscosities of (from the top) 0, 100, 200, 400, and 800 poise. The experimental data are given by the solid red circle plotting symbols; a raw experimental 2D X-ray radiograph at 80 ns is given in the inset.

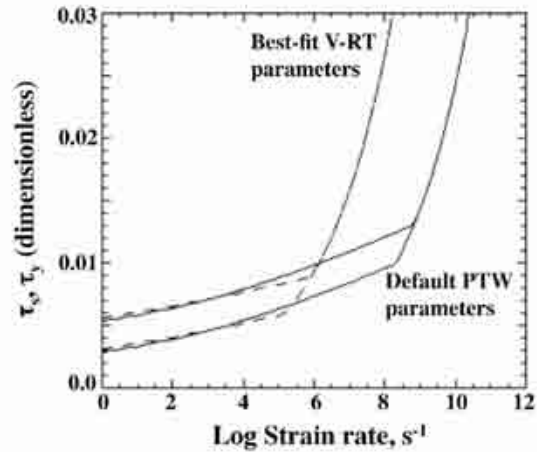


Figure 4. Dimensionless strength vs log(strain rate) for the PTW model using default input parameters for V (solid curves) and modified PTW input parameters to fit the experimental data (dashed curves). The upper curves are for work-hardened saturated strength, τ_s , and the lower curves correspond to the small strain limit, τ_y .

Conclusions

Our experiments show that (solid-state) vanadium strength is very effective at stabilizing RT instability growth at \sim Mbar pressures and very high (10^6 - 10^8 s^{-1}) strain rates. The deformation mechanism is suggested to be viscous phonon drag. A peak strength of vanadium at $P_{\text{max}} \sim 900$ kbar and 3×10^7 s^{-1} was estimated to be ~ 25 kbar, which is a factor of 3.5 higher than the ambient strength, with an estimated uncertainty of $\sim 20\%$. Analytic estimates show that an effective lattice viscosity of ~ 400 poise would have a similar stabilizing effect. Designs to extend these experiments to pressures $P \gg 1$ Mbar on NIF [16] have been developed [17].

Acknowledgements

This work was performed under the auspices of the Lawrence Livermore National Security, LLC (LLNS) under Contract No. DE-AC52-07NA27344.

References

- [1] J. F. Barnes, P. J. Blewett, R. G. McQueen, K. A. Meyer, D. Venable, "Taylor instability in solids," *Journal of Applied Physics* **45** 727-732 (1974).
J. F. Barnes, D. H. Janney, R. K. London, K. A. Meyer, D. H. Sharp, 1980 "Further experimentation on Taylor instability in solids," *Journal of Applied Physics* **51** 4678-4679 (1980).
- [2] A. I. Lebedev, O. N. Aprelkov, V. A. Arinin, A. S. Bulannikov, V. V. Burtsev, V. A. Golubev, N. B. Davydov, M. V. Zhernokletov, O. N. Ignatova, V. V. Igonin, Yu. M. Makarov, S. F. Manachkin, M. A. Mochalov, S. S. Nadezhin, P. N. Nizovtsev, V. A. Raevsky, S. N. Sinitsyna, V. P. Solov'ev, and L. A. Fadeev, "Perturbation Method for Study of Shear Strength of Materials at Pressures up to ~ 300 GPa," in *Shock Compression of Condensed Matter – 2005*, ed. M. D. Furnish, M. Elert, T. P. Russell, and C. T. White (AIP, 2006) pp. 745-748.
- [3] K. T. Lorenz, M. J. Edwards, S. G. Glendinning, A. F. Jankowski, J. McNaney, S. M. Pollaine, B. A. Remington, B. A., "Accessing ultrahigh-pressure, quasi-isentropic states of matter," *Physics of Plasmas* **12** 056309-1–056309-11 (2005).
- [4] H. S. Park et al., submitted, *Phys. Rev. Lett.* (2009).

- [5] T. R. Boehly, D. L. Brown, R. S. Craxton, R. L. Keck, J. P. Knauer, J. H. Kelly, T. J. Kessler, S. A. Kumpan, S. J. Loucks, S. A. Letzring, F. J. Marshall, R. L. McCrory, S. F. B. Morse, W. Seka, J. M. Soures, C. P. Verdon, "Initial performance results of the OMEGA laser system," *Optics Communications* **133** 495-506 (1997).
- [6] J. Edwards, K. T. Lorenz, B. A. Remington, S. Pollaine, J. Colvin, D. Braun, B. F. Lasinski, D. Reisman, J. M. McNaney, J. A. Greenough, R. Wallace, H. Louis, D. Kalantar, "Laser-driven plasma loader for shockless compression and acceleration of samples in the solid state," *Physical Review Letters* **92** 075002-1-075002-4 (2004).
- [7] K. T. Lorenz, M. J. Edwards, A. F. Jankowski, S. M. Pollaine, R. F. Smith, B. A. Remington, "High pressure, quasi-isentropic compression experiments on the Omega laser," *High Energy Density Physics* **2** 113-125 (2006).
- [8] P. M. Celliers, G. W. Collins, L. B. Da Silva, D. M. Gold, R. Cauble, "Accurate measurement of laser-driven shock trajectories with velocity interferometry," *Applied Physics Letters* **73** 1320-1322 (1998).
- [9] G. B. Zimmerman and W. L. Kruer, Numerical simulation of laser-initiated fusion, *Comments on Plasma Physics and Controlled Fusion* **2** 51-61 (1975).
- [10] A. F. Jankowski, J. Go, J. P. Hayes, "Thermal stability and mechanical behavior of ultra-fine bcc Ta and V coatings," *Surface & Coatings Technology* **202** 957-961 (2007).
- [11] K. O. Mikaelian, "Effect of viscosity on Rayleigh-Taylor and Richtmyer-Meshkov instabilities," *Phys. Rev. E* **47** 375-383 (1993).
- [12] J. D. Colvin, M. Legrand, B. A. Remington, G. Schurtz, S. V. Weber, "A model for instability growth in accelerated solid metals," *Journal of Applied Physics* **93** 5287-5301 (2003).
- [13] D. L. Preston, D. L. Tonks, and D. C. Wallace, Model of plastic deformation for extreme loading conditions," *Journal of Applied Physics* **93** 211-220 (2003).
- [14] D. J. Steinberg, S. G. Cochran, M. W. Guinan, "A constitutive model for metals applicable at high-strain rate," *J. Appl. Phys.* **51** 1498-1504 (1980).
- [15] B. A. Remington, P. Allen, E. M. Bringa, J. Hawreliak, D. Ho, K. T. Lorenz, H. Lorenzana, J. M. McNaney, M. A. Meyers, S. W. Pollaine, K. Rosolankova, B. Sadik, M. S. Schneider, D. Swift, J. Wark, B. Yaakobi, "Material dynamics under extreme conditions of pressure and strain rate," *Materials Science and Technology* **22** 474-488 (2006).
- [16] C. A. Haynam, P. J. Wegner, J. M. Auerbach, M. W. Bowers, S. N. Dixit, G. V. Erbert, G. M. Heestand, M. A. Hennesian, M. R. Hermann, K. S. Jancitis, K. R. Manes, C. D. Marshall, N. C. Mehta, J. Menapace, E. Moses, J. R. Murray, M. C. Nostrand, C. D. Orth, R. Patterson, R. A. Sacks, M. J. Shaw, M. Spaeth, S. B. Sutton, W. H. Williams, C. C. Widmayer, R. K. White, S. T. Yang, B. M. Van Wonterghem, "National Ignition Facility laser performance status," *Applied Optics* **46** 3276-3303 (2007).
- [17] H. Park, B. A. Remington, D. Braun, P. Celliers, G. W. Collins, J. Eggert, E. Giraldez, S. L. Pape, T. Lorenz, B. Maddox, A. Hamza, D. Ho, D. Hicks, P. Patel, S. Pollaine, S. Prisbrey, R. Smith, D. Swift, R. Wallace, "Quasi-isentropic material property studies at extreme pressures: from Omega to NIF," *Journal of Physics Conference Series* **112** 042024-1-042024-4 (2008).

INFLUENCE OF DYNAMIC PROPERTIES ON PERTURBATION GROWTH IN TANTALUM

V. V. Igonin,* O. N. Ignatova,* A. I. Lebedev,* S. S. Nadezhin,* A. M. Podurez,* B. A. Raevsky,*
V. P. Solov'ev,* M. A. Zocher,** D. Preston**

*All-Russia Research Institute of Experimental Physics (VNIIEF), Sarov 607190, Russia

**LANL, Los Alamos, USA

Author Contact: root@gdd.vniief.ru

Introduction

This work is devoted to experimental and numerical-theoretical study of peculiarities of plastic deformation of Ta at pressures of 10÷80 GPa and strain rates of $10^3\div10^9\text{ s}^{-1}$. Tantalum has a body-centered cubic lattice, and in the mentioned ranges of pressures and strain rates, tantalum behavior differs from those of aluminum and copper, which have a face-centered cubic lattice.

The studies were conducted by the perturbation method and the metallographic method with use of samples recovered after loading. Basic results are the following: in contrast to copper and aluminum, shock-wave softening was not revealed in tantalum, model of Ta strength was developed.

Experimental Procedure

Results of experimental and numerical investigations of the peculiarities of Ta plastic deformation under pressures $P\sim10\div80\text{ GPa}$ are presented. Tantalum has a body-centered cubic lattice (bcc lattice), and its behavior differs from that of aluminum and copper, which have a face-centered cubic lattice (fcc lattice) in the mentioned pressure range. For fcc metals (Al and Cu), the phenomenon of a temporal drop of strength behind a shock wave front is known. This time is $\tau\sim0.3\text{ }\mu\text{s}$ for Al and Cu. The reason of temporal drop of shear strength behind the front of shock wave is probably formation of a complicated two-periodical structure of microtwins, which causes temperature inhomogeneity at the mesoscale and violation of stability of plastic deformation. For today, there is no a comprehensive understanding of structural changes in tantalum, which occur behind the front of shock waves of rather high intensities ($\sigma_x>20\text{ GPa}$), and association of these changes and dynamic characteristics of substance, namely, shear strength and spall strength.

To obtain data on the shear strength of tantalum under high pressure, the X-ray radiography method of perturbations was used [1,2,3]. The essence of the “perturbation” method is recording of growth of periodical perturbations specified on surface of a liner made of studied material when loading and accelerating it by detonation products. The general scheme of liner loading is shown in Figure 1.

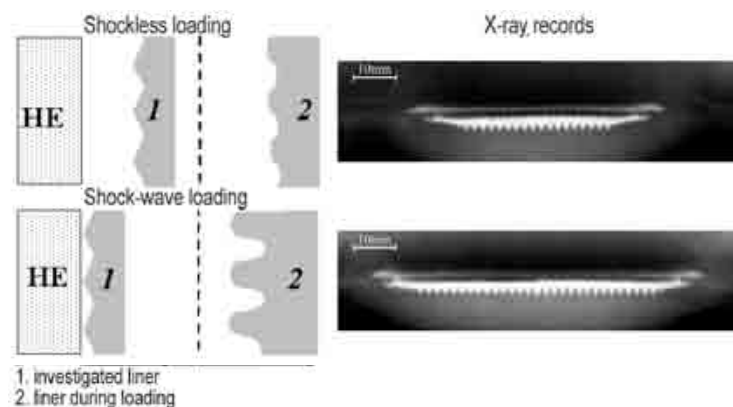


Figure1. Method for recording of perturbation growth.

When loading the liner by detonation products, a one-stage device is used, where pressure $P \sim 40$ GPa is reached. In this case, the Rayleigh-Taylor instability occurs at the HE-sample interface. Based on the experimental results, high sensitivity of perturbation growth to shear strength allows performing testing and parametric identification of phenomenological models of strength.

Figure 2 and Figure 3 show the experimental assembly. The gap between the HE surface and the investigated liner provides a shockless loading regime, and the absence of the gap provides a shock-wave regime. Calculated dependences of pressure at sample interface are presented in Figure 4. The scheme of X-ray radiography is presented in Figure 5.

The source of X-ray radiation was the facility “Eridan-3,” which had limiting energy of radiation of 1 MeV, pulse duration of ~ 0.15 μ s at half-height.

Information on growth of local perturbations was obtained from an X-ray image of the free surface of the investigated sample. In the tests, the X-ray image was recorded by the recording system based on ten screens ADC-CR. Typical X-ray images of liners in flight are shown in Figure 1.

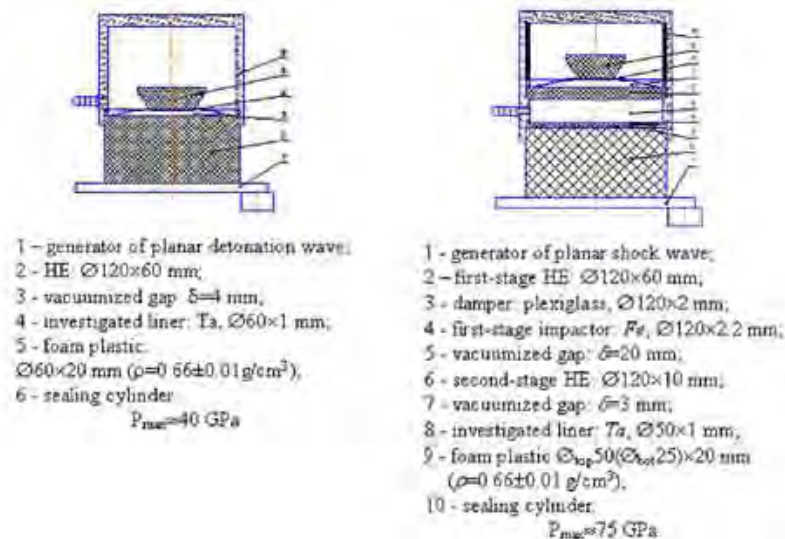


Figure 2. Experimental assemblies. Shockless loading.

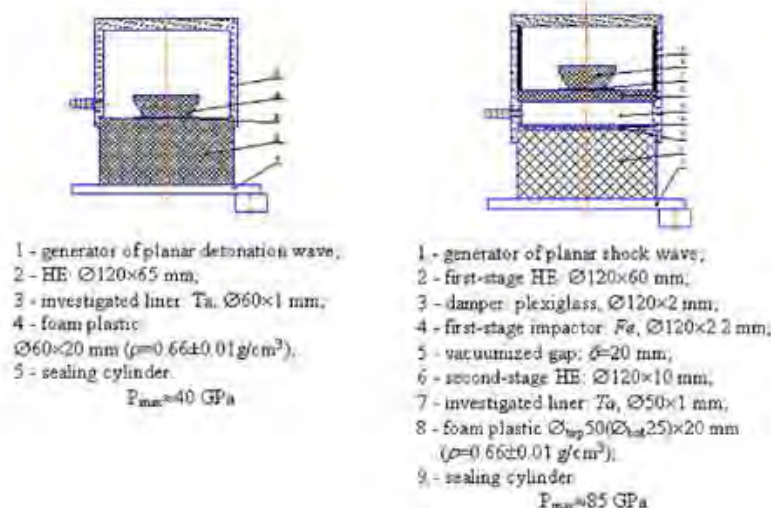


Figure 3. Experimental assemblies. Shock-wave loading.

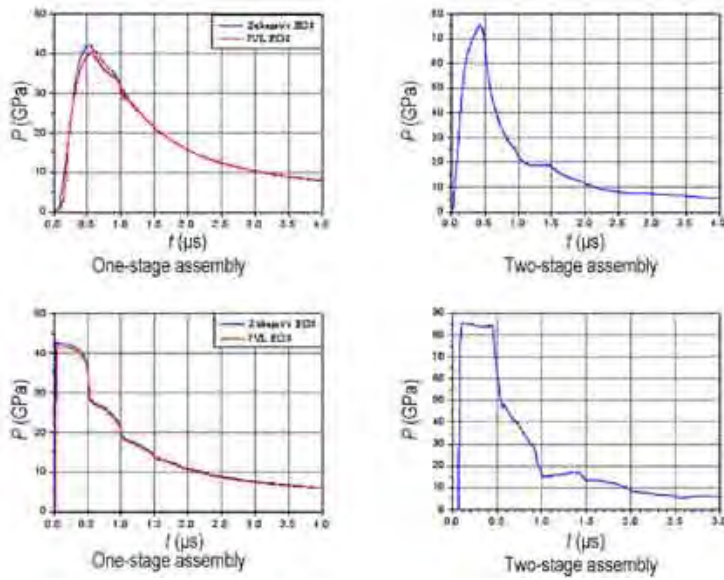


Figure 4. Pressure versus time. Shock-wave loading.

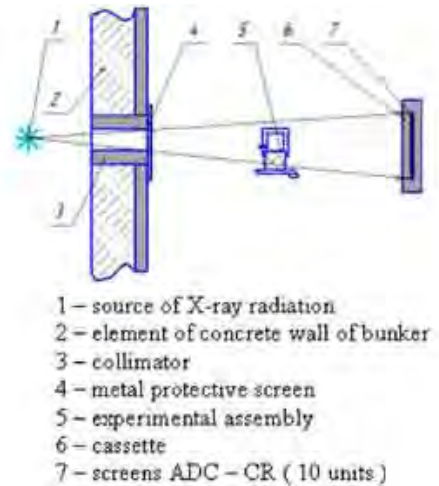


Figure 5. Scheme of X-ray radiography.

Numerical Simulation

Numerical simulation of perturbation growth was performed by the Lagrangian technique “Drakon” with use of the Steinberg-Glushak strength models [4,5,7]

$$Y_s = F(\epsilon_i^p, P, T), \quad (1)$$

where Y_s is yield strength and ϵ_i^p is strain intensity.

Figures 6 and 7 present results of tests and calculations of perturbation growth in tantalum samples under shockless loading and shock-wave loading.

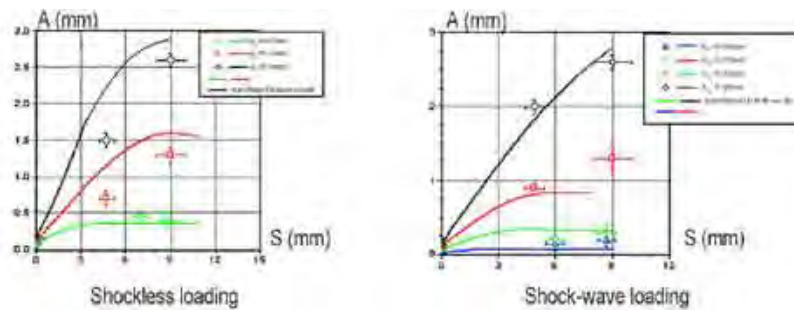


Figure 6. Results of tests and calculation of perturbation growth in tantalum. $P_{\max} \approx 40$ GPa.

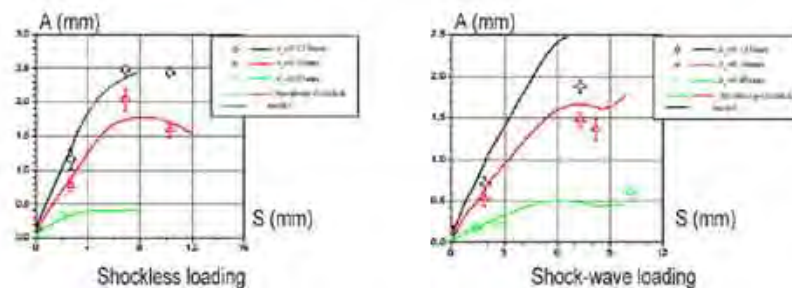


Figure 7. Results of tests and calculation of perturbation growth in tantalum. $P_{\max} \approx 75-85$ GPa.

The graphs reveal that the Steinberg-Glushak model, which is calibrated based on shockless tests, provides good description of results of the shock-wave tests. This fact can be considered as the absence or very insignificant effect of shock-wave softening. This is the distinctive feature of Ta as compared to the earlier investigated Al and Cu where shock-wave softening is significant. For comparison, Figure 8 presents similar results for copper and aluminum [7,8].

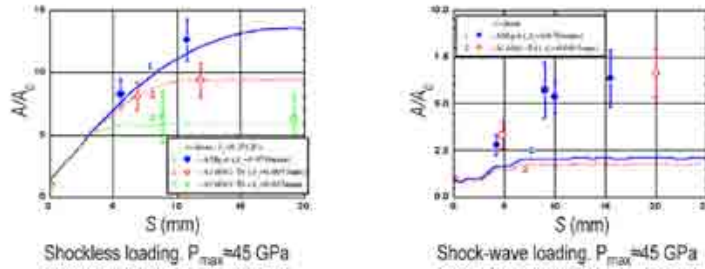


Figure 8. Results of tests and calculations of perturbation growth in aluminum.

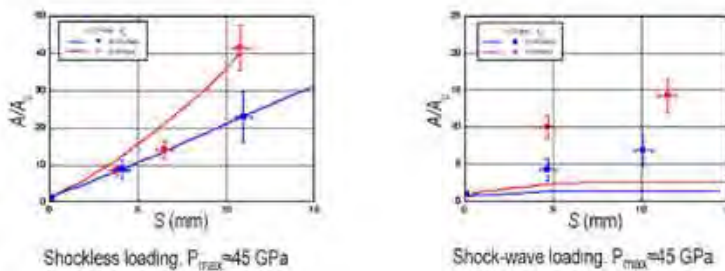


Figure 9. Results of tests and calculations of perturbation growth in copper.

Probably, these peculiarities can be explained by the difference in structures of the crystalline lattices. Al and Cu have fcc lattices, and Ta has a bcc lattice. The results of metallographic investigations of shock-loaded Ta, Cu, and Al correlate with this supposition. Density of shear bands of the twinning nature is by an order less in Ta than that in Cu and Al [9,10,11].

Figure 10 shows the dependences of the stationary yield strength on pressure behind the front of shock wave and shockless wave of compression. These dependences were obtained by the Steinberg-Glushak model (1) calibrated based on the experimental results. For comparison, the figure presents also the results obtained by J. R. Asay and L. C. Chhabildas with use of the self-consistency method [12].

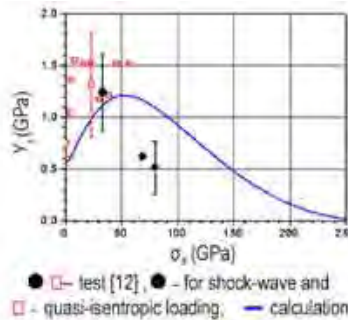


Figure 10. Yield strength versus pressure.

Acknowledgements

The authors thank the experts who participated in the work, namely, O. N. Aprelkov, A. V. Burenkov, V. V. Burtsev, V. V. Gorbunov, A. N. Cheraev, A. V. Tsibikov, V. N. Filyaev. The work has been carried out under the auspices of LANL Contract 37713-000-02-35 TO 022.

References

- [1] A. I. Lebedev, P. N. Nizovtsev, V. A. Rayevsky, V. P. Soloviev, "Rayleigh-Taylor instability in strong media, Experimental study," 5th International Workshop on the Physics of Compressible Turbulent Mixing, (New York, USA, 1995) pp. 231-236).
- [2] O. N. Aprelkov, V. V. Igonin, A. I. Lebedev, V. A. Rayevsky, P. N. Nizovtsev, V. P. Soloviev, "Study of Rayleigh-Taylor instability in copper and aluminum under pressures up to 45GPa and at strain rates of 10^5 - 10^8 ," *Proceedings of International Conference. V Khariton's Topical Scientific Readings* titled "Substances, materials and constructions under intensive dynamic loading". (Sarov, 2003).
- [3] A. I. Lebedev, O. N. Aprelkov, V. A. Arinin, V. V. Igonin, S. S. Nadezhin, P. N. Nizovtsev, V. A. Rayevsky, S. N. Sinitsyna, "Perturbation Method for Study of Shear Strength of Materials at Pressures up to ~300 Gpa," *Shock Compression of Condensed Matter* (Baltimore, Maryland, USA, 2005).
- [4] D. Steinberg, S. Cochran, M. Guinan, "A constitutive model for metals applicable at high -strain rate," *Journ. of Appl Phys* **51** 3 1496-1504 (1980).
- [5] Yu. V. Batkov, B. L. Glushak, S. A. Novikov. "Strengths of aluminum, copper and steel behind SW front," *FGV* No. 5 p. 126-132 (1989).
- [6] S. M. Bakhrakh, I. P. Bakumova, P. N. Nizovtsev, V. A. Rayevsky, E. V. Shuvalova, "Relaxation model of shear strength in Lagrangian-Euler setup," *RFNC-VNIIEF Proceedings*, Issue 5 (Sarov 2003) p. 44-53.
- [7] P. N. Nizovtsev, V. P. Soloviev, A. I. Lebedev, A. L. Mikhaylov, V. A. Rayevsky, V. A. Ogorodnikov, "Studies of Hydrodynamic Instabilities in Solids in Pressure Range of 40÷200 GPa, Final Report on Agreement #B345765 between LLNL and VNIIEF (1999).
- [8] V. A. Rayevsky, A. I. Lebedev, V. V. Igonin, O. N. Aprelkov, O. N. Ignatova, P. N. Nizovtsev et al. *Studies of Influence of Shear Strength on Perturbation Growth in Copper Under High Pressures*, Final Report on Agreement #B70040006-35, TO 51, Modification 12 between LANL and VNIIEF (2002).
- [9] V. A. Rayevsky, A. M. Podurets, V. G. Khanzhin et al., "Twin structures in copper after shock and shockless high-rate loading," *Proceedings of Abstracts for IX Topical Scientific Khariton's Readings* (Sarov, 2007) pp. 210-212.
- [10] O. N. Aprelkov, O. N. Ignatova, V. V. Igonin, A. I. Lebedev, V. A. Rayevsky, S. N. Sinitsyna, N. A. Yukina, "Heterogeneous deformation of Al and Cu under shock-wave and shockless loadings," *Proceedings of Conference "Shock waves in Condensed Matter"*, (St.-Petersburg, 2002).
- [11] V. A. Rayevsky, A. I. Lebedev, O. N. Aprelkov, V. V. Igonin, O. N. Ignatova, N. B. Davydov, A. M. Podurets, S. S. Nadezhin, V. P. Solov'ev et al., "Influence of Dynamic Material Properties on Perturbation Growth in Solid, Final Report of Agreement # 37713-000-02-35, Task Order # 022 between LANL and VNIIEF. (2007).
- [12] L.C. Chhabildas and J. R. Asay, "Dynamic yield strength and spall strength measurements under quasi-isentropic loading," *Shock-Wave and High -Strain-Rate Phenomena in Materials* (1992) p. 947-955.



CALCULATION OF SOUND SPEED BEHIND THE SHOCK WAVE FRONT FOR VARIOUS MATERIALS AND COMPARISON WITH EXPERIMENTAL DATA

B. A. Nadykto

All-Russia Research Institute of Experimental Physics (VNIIEF),
Sarov 607190, Russia

In this paper, the equation of state parameters for a number of materials are obtained on the basis of published experimental data on the shock-wave and static compression, and the bulk speed of sound in different pressure ranges is calculated. The calculated values are compared with published experimental data.

Introduction

Measurements of the speed of sound behind the shock front provide additional information on the response of shock-compressed material to high pressure. High pressure and heating of the material behind the shock front may lead to its melting. Availability of experimental data on the velocity of both longitudinal and bulk (plastic) waves makes it possible to detect melting behind the shock front. In a solid elasto-plastic body, the velocity of elastic longitudinal waves is higher than that of plastic waves. In liquids, there are no shear stresses, and the velocity of longitudinal waves is equal to that of plastic waves. The knowledge of only one velocity (elastic longitudinal or plastic waves) does not provide evidence of material melting. In addition to melting, the processes that may take place behind the shock front include phase transitions with changes in both crystalline and electron structure of the material. Such transitions may result in a sharp change in the slope of the $P(\rho)$ curve, which corresponds to the jump in the velocity of plastic waves.

Computational Technique

To calculate compressibility of materials, we use the technique described in detail in [1,2,3]. Energy and pressure are defined as a sum of the cold (elastic, potential) and thermal components:

$$E = E_c + E_T; P = P_c + P_T. \quad (1)$$

Elastic components of energy and pressure are defined as follows:

$$E_c(\sigma) = \frac{9B_0}{\rho_n} \left(\frac{\sigma^{2/3}}{2} - \sigma^{1/3} \right); P_c(\sigma) = 3B_0 (\sigma^{5/3} - \sigma^{4/3}), \quad (2)$$

where $\sigma = \rho/\rho_n$ is the compression ratio, and ρ_n is the equilibrium material density at $P=0$, $T=0$.

In the Mie-Grueneisen form, the thermal component of pressure is $P_T = \Gamma \rho E_T$. The Grueneisen factor Γ is calculated based on dependence (2). In the Dugdale-MacDonald approximation:

$$\Gamma = \frac{2\sigma^{1/3} - 1}{3\sigma^{1/3} - 2}. \quad (3)$$

The isothermal bulk compression modulus is defined as:

$$B_T = -V \left. \frac{\partial P}{\partial V} \right|_T = \rho \left. \frac{\partial P}{\partial \rho} \right|_T.$$

For $P=P_c + \Gamma \rho E_T$ the value of the isothermal bulk modulus equals:

$$B_T = B_c(\rho) + \Gamma \rho E_T + \rho^2 E_T \left. \frac{\partial \Gamma}{\partial \rho} \right|_T = B_c(\rho) + P_T \left(1 + \left. \frac{\partial \ln \Gamma}{\partial \ln \rho} \right|_T \right).$$

For elastic pressure defined by expression (2) and Γ from (3),

$$B_T = B_0(5\sigma^{5/3} - 4\sigma^{4/3}) + P_T \left(1 - \frac{\sigma^{1/3}}{3(3\sigma^{1/3} - 2)(2\sigma^{1/3} - 1)} \right).$$

The isentropic (adiabatic) bulk compression modulus equals

$$B_S = \frac{C_P}{C_V} B_T,$$

where C_P and C_V are heat capacities at constant pressure and constant volume, respectively. The speed of sound equals $c=(B/\rho)^{1/2}$.

Results and Discussion

Ref. [4] presents results of probably one of the first velocity measurements behind the shock front in aluminum, copper, lead, and iron. A number of experimental points were obtained for the velocity of both longitudinal elastic waves and – by the overtaking relief method – plastic sound waves. Our paper [5] presents calculated values of the bulk speed of sound in iron and copper and makes an attempt – based on the comparison with experimental data of Refs. [4], [6] – to determine the onset of melting in these materials behind the shock front. It turned out that melting in these materials is likely to occur simultaneously with the electron phase transformation.

Uranium

Shock-wave measurement data for natural uranium [7] display a change in the slope of both the $D(u)$ curve at $u \approx 1.1$ km/s, and the $P(\rho)$ curve at $P \approx 80$ GPa. Our calculations for natural uranium are in good agreement (see Figure 1(a)) with experimental points [7]. Using the derived equation of state, we calculated the bulk speed of sound in different phases of uranium and detected an increase in the speed of sound by 0.9 km/s at a pressure of about 80 GPa. Figure 1(b) shows the calculated curve of the bulk speed of sound versus pressure obtained using the chosen equation of state for uranium. Location of experimental points for the longitudinal velocity near the calculated curve for the bulk speed of sound may be indicative of the material being liquid.

Zinc

Major experimental data on the shock compression of zinc are presented in [7] for pressures up to 138 GPa and in [8] for pressures up to 800 GPa. For low pressures, there are data on static compression [10,11,12].

The equation of state for zinc was selected, as described above. Experimental data in the $D-u$, $P-\rho$, and $P-u$ coordinates point at a change in the slope of the $P(\rho)$ curves at $P=7.5$ GPa and $P=57$ GPa. This change in the slope can be explained by compression-induced change in the electron structure of zinc. Therefore, the equation of state for zinc was chosen in the form of three regions with different parameters for each phase:

$$\text{I} \quad \rho_0 = 7.2011 \text{ g/cm}^3, B_0 = 62.7 \text{ GPa. II} \quad \rho_0 = 7.50 \text{ g/cm}^3, B_0 = 114 \text{ GPa.}$$

$$\text{III} \quad \rho_0 = 9.18 \text{ g/cm}^3, B_0 = 337 \text{ GPa.}$$

$$\text{At } T = 293 \text{ K: } \rho_0 = 7.14 \text{ g/cm}^3, B_0 = 61 \text{ GPa, } E_0 = 0.0748 \text{ kJ/g; } T_D = 300 \text{ K.}$$



Comparison of the calculated $P(\rho)$ curves with experimental data is presented in Figure 2(a).

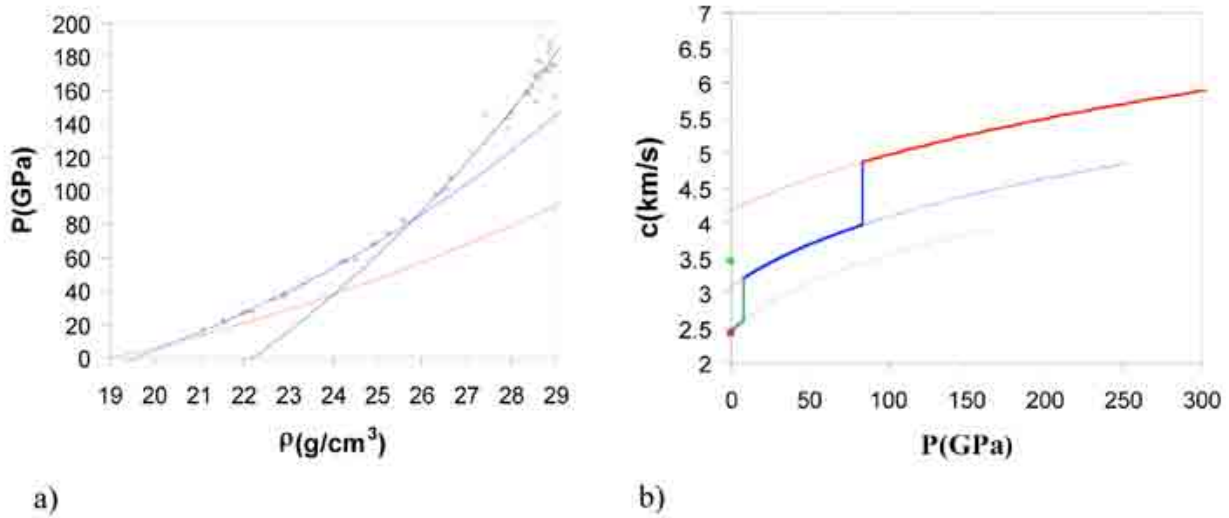


Figure 1. Dependencies behind the shock front in natural uranium. (a) $P(\rho)$. Experimental data from [7]. (b) Velocity of plastic sound waves behind the shock front as a function of pressure. The curves show our calculations for different phases of uranium.

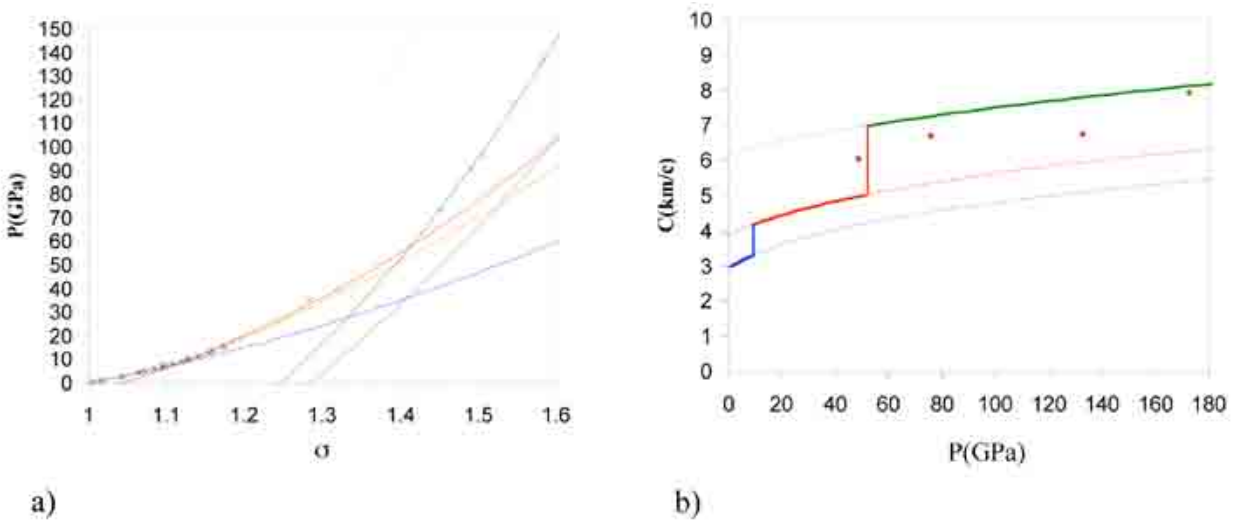


Figure 2. Dependencies behind the shock front in zinc. (a) $P(\rho)$. Experimental data: pluses – from [7], squares – from [8]. (b) Velocity of plastic sound waves behind the shock front as a function of pressure for zinc. Experimental data: squares – data from [9]. The curves show our calculations for different phases of zinc.

Calculations for the initial phase are in perfect agreement with data of Ref. [10] up to 4.5 GPa. The data for statically compressed Zn from [11, 12] coincide with the computational curve for the initial phase at low pressures and with the computational curve for the high-pressure intermediate phase at $P > 8$ GPa. Ref. [5] provides a computational analysis of phase transformations in zinc. Three phases of zinc presented there, apart from their difference in equilibrium density, show considerable differences in the energy of outer-shell electrons of the atomic cell in solid zinc. These energies are 26.5 eV, 46.5 eV and 112 eV for the initial, intermediate and next high-pressure phases, respectively. The data of [12] indicate that the hcp lattice of Zn remains stable up to 126 GPa. This allows us to state that the phase transformations observed in Zn are electron phase transitions without change in the crystalline structure. The energy of the atomic cell of initial Zn, 26.5 eV, is close to the energy of two outer-shell electrons of the free atom of Zn in the $3d^{10}4s^2$ state. The energy of three outer-shell electrons of the free atom of Zn equals 67 eV, and of four electrons, 129 eV.

The electron phase transition with preservation of the crystalline structure was experimentally observed in zinc [11] based on the measured dependence on V/V_0 of the c/a axis length ratio in the hcp structure of Zn, which displayed a clear non-monotone trend at a pressure of 9 GPa. The presence of the electron phase transition in Zn at $P=6.6$ GPa and $T=4.2$ K follows from Mössbauer spectroscopy [13], which displays drastic change in lattice dynamics at such a transition. Our analysis of Zn compressibility clearly points at the presence of this electron phase transition in Zn at $P=7.5$ GPa. Moreover, this analysis testifies for existence of another phase transition at $P=57$ GPa. Electron phase transitions similar to those in zinc can be observed in Cd, Tl, Pd, Ag, Sb, and other elements.

Using the selected equation of state parameters for zinc, we calculated the bulk speed of sound in zinc at different pressures. The computational data are shown in Figure 2b. The change in the equation of state parameters at phase transitions is accompanied by a sharp change (jump) in the bulk speed of sound. The calculations adequately reproduce the speed of sound at atmospheric pressure (2.9 km/s), obtained based on the experimental bulk compression modulus [14]. Figure 2b also shows measured values of the longitudinal speed of sound in zinc [9]. The closeness of the experimental velocity of longitudinal sound waves at pressures above 70 GPa to the calculated velocity of plastic waves may be indicative of zinc melting near the phase transition at 57 GPa. The experimental point at a pressure of 49 GPa may correspond to the solid state of zinc with Poisson's ratio of about 0.35.

Tin

Major experimental data on the shock compression of tin are presented in [7] for pressures up to 164 GPa and in [8] for pressures up to 750 GPa. For pressures below 4.5 GPa, there are data on static compression of white tin [10]. These data are in perfect agreement with the value of the bulk modulus given in [14].

Experimental data in the D-u, P- ρ , and P-u coordinates point at a change in the slope of the P(ρ) curves at $P=10$ GPa, 24 GPa, 80 GPa, and probably 250 GPa. This change in the slope can be explained by compression-induced change in the electron structure of tin. Therefore, the equation of state for tin was chosen in the form of four regions with different parameters for each phase:

$$\text{I} \quad \rho_0 = 7.355 \text{ g/cm}^3, B_0 = 56.3 \text{ GPa.} \quad \text{II} \quad \rho_0 = 7.755 \text{ g/cm}^3, B_0 = 81.8 \text{ GPa.}$$

$$\text{III} \quad \rho_0 = 8.3 \text{ g/cm}^3, B_0 = 130 \text{ GPa.} \quad \text{IV} \quad \rho_0 = 8.5 \text{ g/cm}^3, B_0 = 160 \text{ GPa.}$$

$$\text{At } T = 293 \text{ K: } \rho_0 = 7.31 \text{ g/cm}^3, B_0 = 55.25 \text{ GPa, } E_0 = 0.0466 \text{ kJ/g; } T_D = 210 \text{ K.}$$

Comparison of the calculated P(ρ) curves with experimental data is presented in Figure 3(a).

There is a phase transition in white tin with a volume jump of 1.1% at a pressure of 9.4 GPa and room temperature [15]. With this transition, the bulk compression modulus increases to 81.8 GPa. Each subsequent transformation at 24 GPa and 80 GPa is also accompanied by the growth of the bulk compression modulus to 130 and 160 GPa, respectively.

Using the selected equation of state parameters for tin, we calculated the bulk speed of sound in tin at different pressures. The computational data are shown in Figure 3(b). The change in the equation of state parameters at phase transitions is accompanied by a sharp change (jump) in the bulk speed of sound. The calculations adequately reproduce the speed of sound at atmospheric pressure (2.75 km/s), obtained based on the experimental bulk compression modulus [14]. Measurements of the speed of sound behind the shock front in tin by manganin and optical probes with indicator liquids were performed in [9].

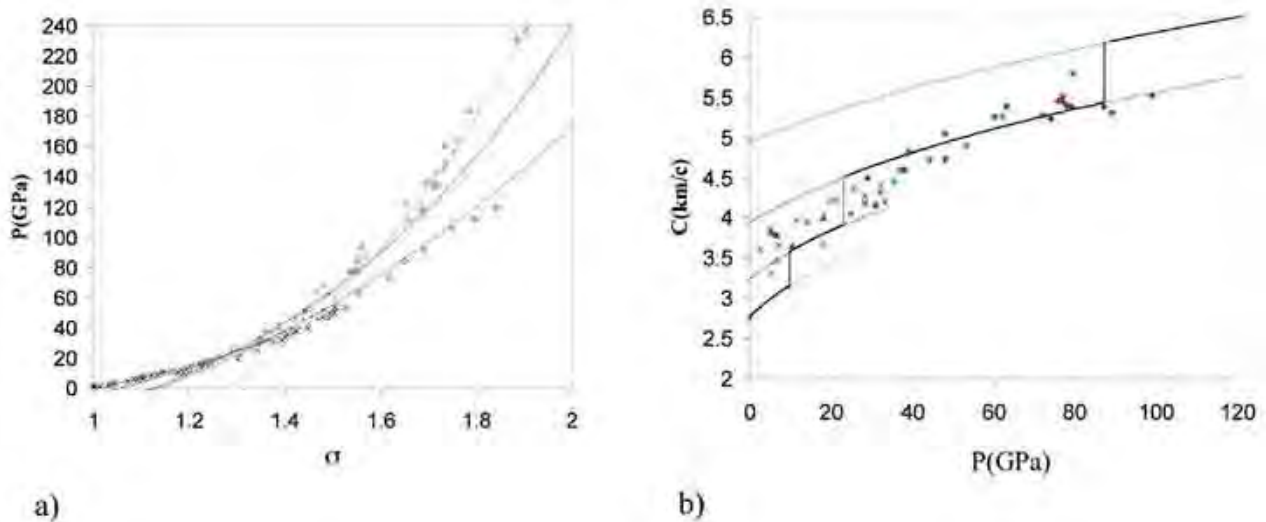


Figure 3. Dependencies on Hugoniot and normal isotherm in tin. (a) $P(p)$. Experimental data: squares – from [7], triangles – from [8], crosses, pluses and rhombs – data of static measurements [16]. (b) Velocity of plastic sound waves behind the shock front as a function of pressure for tin. Experimental data: rhombs and triangles – from [11], squares – from [17], crosses – from [18]. The curves show our calculations for different phases of tin.

Figure 3(b) shows the values of the sound speed in tin. The closeness of the experimental velocity of longitudinal sound waves [9] at pressures above 25 GPa to the calculated velocity of plastic waves may be indicative of the melted state of tin under such conditions. At a pressure of 100 GPa, a tin can be expected to undergo one more phase transition with an increase in the bulk speed of sound—apparently, in the liquid phase. Figure 3(b) also shows the data of Chinese researchers [17]. There are also data on the speed of sound in tin measured using Doppler laser interferometry [18] in the range of 2–33 GPa, which agree with data of [9] to within the measurement error ($\sigma = 5\%$). A multi-phase equation of state for tin is calculated in [19]. The jump-like increase in the bulk speed of sound occurs as a result of an electron phase transition in liquid tin. Available data of shock-wave experiments at pressures above 250 GPa may be indicative of recovery of the previous phase state. However, the small number of experimental points does not allow us to claim this for sure. If there is such a recovery, the bulk speed of sound should decrease at pressures above 250 GPa.

Cerium

Experimental data on the shock compression of cerium are presented in [7] for pressures up to 137 GPa and in [8] for pressures up to 560 GPa. Response of cerium to shock compression at low pressures (up to 16 GPa) has been studied in [21]. Static compression of cerium on diamond anvils has been studied in [20].

Cerium has a complex phase diagram comprising a $\gamma \rightarrow \alpha$ isomorphous electron phase transition with a high jump in volume. At normal temperature, the phase diagram [15] displays a $\text{CeIV} \rightarrow \text{CeV}$ phase transition at a pressure of 5.6 GPa. Data of static experiments on diamond anvils [20] for this pressure indicate a sharp change in the slope of the curve $P(p)$. Data of [7,8,20] show that the slope also changes around $P = 36$ GPa. This change in the slope can be explained by compression-induced change in the electron structure of cerium. Therefore, the equation of state for cerium was chosen in the form of three regions (apart from the initial γ -phase) with different parameters for each phase:

$$\text{I} \quad \rho_0 = 8.24 \text{ g/cm}^3, B_0 = 27 \text{ GPa.} \quad \text{II} \quad \rho_0 = 9.2 \text{ g/cm}^3, B_0 = 78 \text{ GPa.}$$

$$\text{III} \quad \rho_0 = 11.41 \text{ g/cm}^3, B_0 = 217 \text{ GPa.}$$

$$\text{At } T = 273 \text{ K: } B_0 = 26.7 \text{ GPa, } E_0 = 0.045 \text{ kJ/g; } T_D = 118 \text{ K.}$$

Comparison of the calculated $P(\rho)$ curves with experimental data is presented in Figure 4(a).

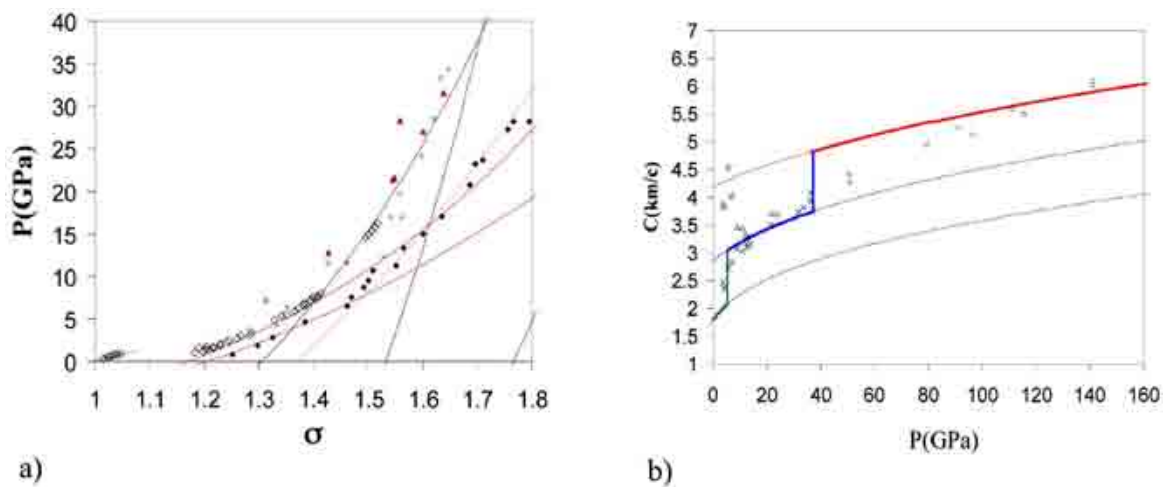


Figure 4. Dependencies on Hugoniot and normal isotherm in cerium. (a) $P(\rho)$. Experimental data: pluses – from [7], squares – from [8], open rhombs – from [21], solid rhombs – data of static measurements [20]. (b) Velocity of plastic sound waves behind the shock front as a function of pressure for cerium. Experimental data from [9] crosses – values of the bulk speed of sound, squares and triangles – velocities of longitudinal sound waves. The curves show our calculations for different phases of cerium.

Using the selected equation of state parameters for cerium, we calculated the bulk speed of sound in cerium at different pressures. The computational data are shown in Figure 4(b). The change in the equation of state parameters at phase transitions is accompanied by a sharp change (jump) in the bulk speed of sound.

Measurements of the speed of sound behind the shock front in cerium by manganin and optical probes with indicator liquids were performed in [9]. Squares and triangles in Figure 4(b) show the points measured in [9] for longitudinal sound waves in cerium, and crosses show the points for bulk (plastic) sound waves. In the range of pressures from 6 to 36 GPa, measured velocities of plastic sound waves are close to the calculated values. The comparison with measured velocities of longitudinal sound waves shows that cerium melting apparently ends at a pressure of 12 GPa [9].

Using the optical-lever technique, the authors of [21] detected a sharp decrease in the intensity of light reflected from the free surface of a sample at $\sigma_x \leq 16$ GPa. They attributed this decrease to the shock-driven melting of cerium.

The phase diagram in [15] suggests that melting of cerium behind the shock front proceeds from the CeV phase rather than from the α -phase (CeIV). According to [15], the melting point of CeV at a pressure of 6 GPa is 715°C. It might be illustrative to conduct an experiment to detect cerium melting behind the shock front with a starting sample of α -phase cerium (e.g., precompressed to the γ - α phase transition). One can expect in this case that the pressure of melting onset in cerium will be noticeably higher (a factor of 1.5-2).

The values of longitudinal speeds of sound measured in [11] at pressures above 36 GPa are located close to the calculated curve for the bulk speed of sound. This indicates that cerium is liquid at such pressures behind the shock front. However, its phase state differs from that at pressures between 6 and 36 GPa.

Conclusion

1. The comparison of calculated speeds of sound with published experimental data for longitudinal sound waves and, in some cases, plastic (bulk) waves allows us to establish the fact of material melting based on the coincidence of the measured velocity of longitudinal waves with the measured or calculated velocity of bulk waves.
2. Zinc can be expected to be in the liquid state behind the shock front at pressures above 60 GPa.



3. Measurement results suggest that tin can be expected to melt right after the structural (and at the same time electron) transformation at 10 GPa. The sharp increase in the calculated velocity of plastic sound waves at 24 GPa takes place already in the liquid phase. The calculations point at a sharp increase in the speed of sound in tin at a pressure of about 100 GPa.
4. Based on the published data on cerium compressibility, one can state that cerium melting behind the shock front proceeds not from the α -phase, but from the next high-pressure phase CeV.

References

- [1] B. A. Nadykto, "Semiempirical model for energy calculation of many-electron ions states," *Uspekhi Fizicheskikh Nauk* **163** 9 37 (1993).
- [2] B. A. Nadykto, *Theor. i Prikl. Fizika* Issue 3, 58 (Vopr. Atom. Nauki i Tech. 1996).
- [3] B. A. Nadykto *Khimicheskaya Fizika* **18** 11 87 (1999).
- [4] L. V. Al'tshuler, S. B. Kormer, M. I. Brazhnik, L. A. Vladimirov, M. P. Speranskaya, A. I. Funtikov, "The isentropic compressibility of aluminum, copper, lead, and iron at high pressures," *Zh. Eksp. Teor. Fiz.* **38** 4 1061 (1960) [*Sov. Phys.—JETP* **11**, 766 (1960)].
- [5] B. A. Nadykto, "Calculation of Electron Phase Parameters of Elements and Compounds Using Compressibility Data," in *New Models and Numerical Codes for Shock Wave Processes in Condensed Media*, ed., I. G. Cameron (Oxford: AWE Hunting BRAE, 1998) p. 205.
- [6] J. M. Brown and R. G. McQueen, "Phase transitions, Grüneisen parameters and elasticity for shocked iron between 77 GPa and 400 GPa," *J. Geophys. Res.* **91** 7485 (1986).
- [7] S. P. Marsch, ed., *LASL Shock Hugoniot Data* (Berkeley, CA, University of California Press 1980).
- [8] R. F. Trunin, L. F. Gudarenko, M. V. Zhernokletov, G. V. Simakov, "Experimental data of shock compression and adiabatic expansion of condensed materials" (in Russian), ed. R. F. Trunin (Sarov, Russian Federal Nuclear Center Academic Publication, 2001) p. 414.
- [9] M. V. Zhernokletov and A. E. Kovalev, "Measurements of speed of sound and analysis of phase transformations in cerium, tin and zinc," *IXth Fundamentals of Plutonium Workshop*, (Pleasanton, California, USA, 2009).
- [10] S. N. Vaidya and G. C. Kennedy, "Compressibility of 18 metals to 45 kbar," *Phys. Chem. Solids.* **31** 2329 (1970).
- [11] K. Takemura, "Zn under Pressure: A singularity in the hcp structure at $c/a = \sqrt{3}$," *Phys. Rev. Lett.* **75** 1807 (1995).
- [12] K. Takemura, "Structural study of Zn and Cd to ultrahigh pressures," *Phys. Rev. B* **56** 5170 (1997).
- [13] W. Potzel, M. Steiner, H. Karzel, W. Schiessl, M. Köfferlein, G. M. Kalvius, P. Blaha, "Electronically Driven Soft Modes in Zinc Metal," *Phys. Rev. Lett.* **74** 1139 (1995).
- [14] K. A. Gschneidner, "Physical properties and interrelationships of metallic and semimetallic elements," *Solid State Physics* **64** 275-426, ed. F. Seitz and D. Turnbull (New York, Academic Press, 1964).
- [15] E. Yu. Tonkov, "Phase diagrams of elements at high pressure," (in Russian) (Nauka, Moscow, 1979).
- [16] S. Desgreniers, Y. K. Vohra, A. L. Ruoff, "Tin at high pressure: An energy-dispersive x-ray-diffraction study to 120 GPa," *Phys. Rev. B* **39** 10359 (1989).
- [17] H. Jianbo, Z. Xianming, H. Tan, J. Li, C. Dai, "Successive phase transitions of tin under shock compression," *Applied Physics Letters.* **92** 111905 (2008).
- [18] M. E. Martinez and J. M. Servas, "Sound velocity Doppler laser interferometry measurements on TiN," *Shock Compression of Condensed Matter-2001*, eds. M. D. Furnish, N. N. Thadhani, and Y. Horie (Melville, New York, AIP, 2002) pp. 1200.
- [19] G. A. Cox, "A multiphase equation of state and strength model for tin," *Shock Compression of Condensed Matter-2005*, eds. M. D. Furnish, M. Elert, T. P. Russel, C. T. White *AIP Conference Proceedings* (Melville, New York, AIP, 2006) p. 208.
- [20] Y. K. Vohra, S. L. Beaver, J. Akella, C. Ruddle, S. Weir, "Ultrapressure equation of state of cerium metal to 208 GPa," *J. Appl. Phys.* **85** 4 2451 (1999).
- [21] V. I. Tarzhanov, E. A. Kozlov, Yu. N. Zuev, D. G. Pankratov et al., "Special features of compressibility and spall strength of explosively loaded cerium in the region of (α - γ) phase transformation," presented at the Fundamentals of Plutonium Workshop, Snezhinsk, Chelyabinsk region, September 8-12, 2008.

DEVIATORIC CONSTITUTIVE MODEL: DOMAIN OF STRAIN RATE VALIDITY

M. A. Zocher,* V. A. Raevsky,† O. N. Ignatova,†

*Los Alamos National Laboratory, Los Alamos, NM, 87545 USA

† All-Russia Research Institute of Experimental Physics (VNIIEF), Sarov 607190, Russia

Author Contact: zocher@lanl.gov

A case is made for using an enhanced methodology in determining the parameters that appear in a deviatoric constitutive model.

Introduction

Predictability rests on our ability to solve a properly posed initial boundary value problem (IBVP) that incorporates an accurate reflection of material constitutive behavior. That reflection is provided through the constitutive model. Moreover, the constitutive model is required for mathematical closure of the IBVP. Common practice in the shock physics community is to divide the Cauchy tensor into spherical and deviatoric parts and to develop separate models for spherical and deviatoric constitutive response. Our focus will be on the Cauchy deviator and deviatoric constitutive behavior. Discussions related to the spherical part of the Cauchy tensor are reserved for another time.

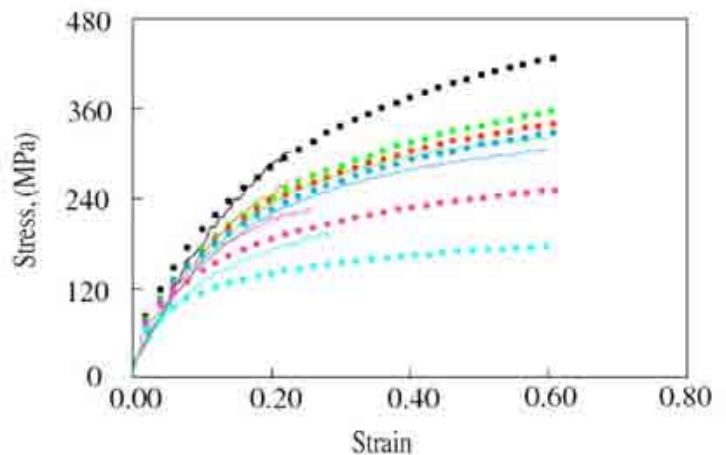
A number of deviatoric constitutive models have been developed for the solution of IBVPs that are of interest to those working in the field of shock physics (e.g., [1-4]). All these models are phenomenological and contain a number of parameters that must be determined in light of experimental data. The methodology employed in determining these parameters dictates the loading regime over which the model can be expected to be accurate.

The focus of this paper is the methodology employed in determining model parameters and the consequences of that methodology as it relates to the domain of strain rate validity. We begin by describing the methodology typically employed. We discuss limitations imposed upon predictive capability by the methodology typically employed, and we propose a modification to that methodology to significantly extend the domain of strain rate validity.

Typically Employed Methodology

The steps typically taken in determining the parameters that go into the constitutive model are outlined here. First quasistatic and Hopkinson bar tests are conducted. The Hopkinson bar provides data to strain rates of 10^3 s^{-1} . The constitutive model is fit to the quasistatic and Hopkinson bar data (Figure 1). Once this is done, nominal values of the parameters that go into the constitutive model are determined. Associated with each nominal value is a range of uncertainty.

Figure 1. Typical stress-strain curves used for fitting model parameters.



Small-scale experiments, such as the Taylor cylinder test [5] are used to validate the model and to tighten up on that uncertainty. The Taylor test provides an added benefit. Peak strain rates in the cylinder are on the order of 10^4 s^{-1} . By demanding that the model accurately predict Taylor cylinder deformation (Figure 2) without losing its ability to replicate the quasistatic and Hopkinson data, we effectively enlarge the strain rate domain over which we can be reasonably confident of the model's predictive capabilities.

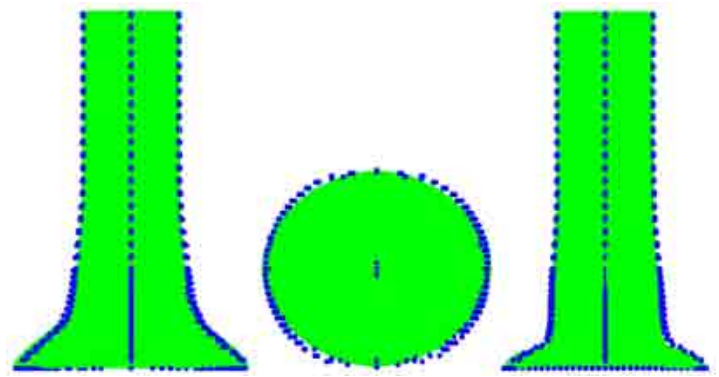


Figure 2. Typical Taylor Cylinder Result (green is predicted deformed shape, blue is actual deformed shape).

Enhanced Methodology

The typically employed methodology results in a model that is validated over strain rates from quasistatic to 10^4 s^{-1} . In use, however, these models are often applied to problems wherein peak strain rates exceed 10^4 s^{-1} . Such an application involves an extrapolation beyond the strain rate domain over which the model has been validated.

Extrapolation always involves risk, but unless the mechanisms/processes responsible for material flow fundamentally change, the model practitioner will likely “get by” with extrapolation, provided that he does not extrapolate “too far.” A number of recently conducted experimental studies have shown that for many materials, a threshold in strain rate exists (often in the vicinity of 10^6 s^{-1}), above which the fundamental nature of material flow suddenly changes, often involving localization of some kind. Aprelkov et al. [6] have shown that under conditions of moderately high strain rate ($\dot{\epsilon} \sim 10^6 - 10^7 \text{ s}^{-1}$) complex biperiodic twin structures form in copper, resulting in temporal softening (significant over a time period of about 0.2 to 0.4 μs). Temporal softening is followed by deformation hardening. Models that fail to account for such phenomena are likely to be rather poor predictors of macroscopic constitutive behavior, especially when applied to loading scenarios involving plastic flow occurring at strain rates $\sim 10^6 - 10^7 \text{ s}^{-1}$.

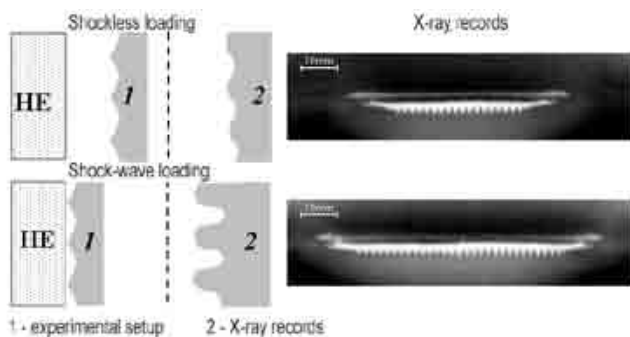


Figure 3. Perturbation growth method.

We propose extending the domain of strain rate validity by employing the perturbation method [7-11]. Using this method, a pre-perturbed plate is accelerated by detonation products. Experiments can be designed to produce either shock or quasi-isentropic loading. Rayleigh-Taylor instability ensues and the perturbations grow in time. Radiography (e.g., flash x-radiography or proton radiography) can be used to measure perturbation growth. Deviatoric constitutive behavior is by far the dominant factor determining the rate of perturbation growth. This being the case, the method provides an excellent tool for

validating deviatoric constitutive models. Moreover (and most importantly), since material in the vicinity of the perturbations flows at moderately high strain rates ($\dot{\epsilon} \geq 10^6 \text{ s}^{-1}$), the method focuses our attention on the extremely important strain rate regime over which deformation localization is all-important. Figure 3 illustrates the method.

Employing this enhanced methodology, we do everything that is done using the typically employed methodology. Namely, we demand that the model accurately predict Taylor cylinder deformation without losing its ability to replicate the quasistatic and Hopkinson data. But we supplement this with the requirement that the model also accurately predict perturbation growth. In the end, we produce a model that is validated over strain rates from quasistatic to $\sim 10^7 \text{ s}^{-1}$. Such a model will eliminate the need for extrapolation in the solution of a great many IBVPs that are of interest to us.

Results: Extrapolation versus Interpolation

We have said that extrapolation carries with it risk. We have also implied that interpolation is strongly to be preferred. In this section, we illustrate this point by showing comparisons of predicted perturbation growth in a typical experiment involving copper using deviatoric constitutive models validated using the typically employed methodology (Figure 4) versus the proposed enhanced methodology (Figure 5). Using the enhanced methodology clearly produces a better result.

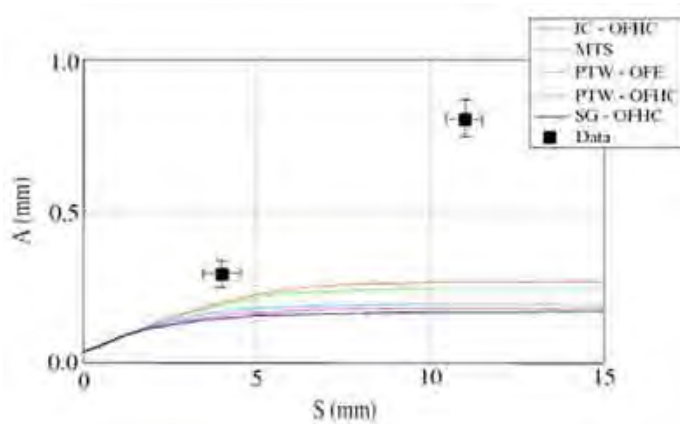


Figure 4. Prediction based on Typically Employed Methodology.

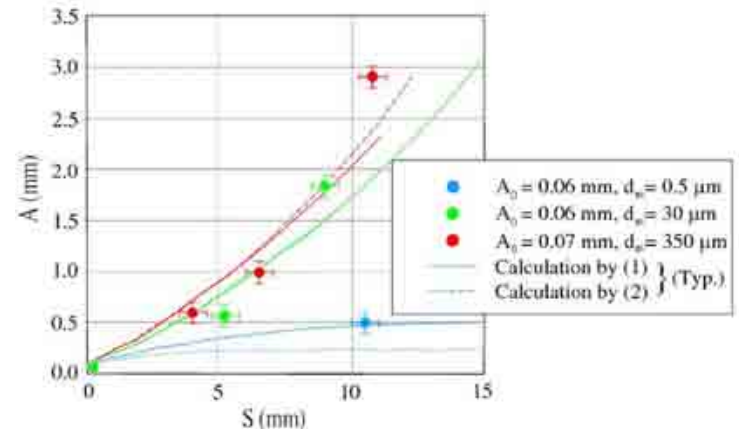


Figure 5. Prediction based on Enhanced Methodology.

Conclusions

The typically employed methodology for determining the parameters of a deviatoric constitutive model result in strain rate validity from quasistatic to 10^4 s^{-1} . Using such models in the solution of IBVPs wherein the material flows at strain rates above 10^4 s^{-1} requires extrapolation and that is risky. The proposed enhanced methodology produced models validated over strain rates from quasistatic to 10^6 s^{-1} (or even 10^7 s^{-1}). This eliminates the need for extrapolation in many cases.

Acknowledgements

This work was performed under the auspices of the U.S. Department of Energy by the University of California Los Alamos National Laboratory under contract No. W-7405-Eng-36.

References

- [1] D. Steinberg, S. Cochran, M. Guinan, "A constitutive model for metals applicable at high strain rate," *Journal of Applied Physics* **51** 3 1498-1504 (1980).
- [2] G. Johnson and W. Cook, "A Constitutive Model and Data for Metals Subjected to Large Strain Rates and High Temperatures," in *Proceedings: Seventh International Symposium on Ballistics* (2000) pp. 541-547.
- [3] P. S. Follansbee and U. F. Kocks, "A constitutive description of the deformation of copper based on the use of the mechanical threshold stress as an internal state variable," *Acta Metallica* **36** 1 82-93 (1988).
- [4] D. L. Preston, D. L. Tonks, D. C. Wallace, "Model of plastic deformation for extreme loading conditions," *Journal of Applied Physics* **93** 1 211-220 (2003).
- [5] M. A. Zocher, P. J. Maudlin, S. R. Chen, E. C. Flower-Maudlin, "An evaluation of several hardening models using taylor cylinder impact data," in *Proceedings: European Congress on Computational Methods in Applied Sciences and Engineering* (2000) pp. 1-20.
- [6] O. N. Aprelkov, O. N. Ignatova, V. V. Igonin, A. I. Lebedev, S. S. Nedezhin, A. M. Podurets, V. A. Raevsky, V. P. Solovyev, G. A. Salishchev, M. A. Zocher, A. M. Kaul, J. M. McNaney, B. A. Remington, "twinning and dynamic strength of copper during high-rate strain," in *Shock Compression of Condensed Matter – 2007*, ed. M. Elert, M.D. Furnish, R. Chau, N. Holmes, J. Nguyen (American Institute of Physics, 2007) pp. 619-622.
- [7] J. Barnes, P. Blewett, R. McQueen, K. Meyer, D. Venable, "Taylor instability in solids," *Journal of Applied Physics* **45** 2 727-732 (1974).
- [8] A. I. Lebedev, P. N. Nizovtsev, V. A. Raevsky, V. P. Solovyev, "Rayleigh-Taylor instability in strong media, Experimental study," in *Proceedings: 5th International Workshop on Compressible Turbulent Mixing*, ed. R. Young, J. Glimm, B. Boston (World Scientific 1996) pp. 231-236.
- [9] V. A. Raevsky, "Rayleigh-Taylor instability effects in acceleration of plane solid layer," in *Proceedings: 5th International Workshop on Compressible Turbulent Mixing*, R. Young, J. Glimm, B. Boston, eds. (World Scientific 1996) pp. 60-65.
- [10] V. A. Raevsky, A. I. Lebedev, A. L. Mikhailov, P. N. Nizovtsev, S. N. Sinitsyna, V. P. Solovyev, V. A. Ogorodnikov, "Research into RT instability in solids loaded to 70 GPa," in *Proceedings: 7th International Workshop on Compressible Turbulent Mixing*, ed. E. Meshkov, Y. Yanilkin, V. Zhmailo (VNIIEF Press 2001) pp. 178-184.
- [11] A. I. Lebedev, V. V. Ogonin, P. N. Nizovtsev, V. A. Raevsky, V. P. Solovyev, "Study of free surface instability in solids at shock loading," in *Proceedings: 7th International Workshop on Compressible Turbulent Mixing*, eds. E. Meshkov, Y. Yanilkin, V. Zhmailo (VNIIEF Press 2001) pp. 171-187.

MODELING AND SIMULATION OF THE THERMO-ACOUSTO-ELASTIC WAVES IN SOLIDS OF COMPLEX RHEOLOGY

D. A. Indeitsev, V. N. Naumov, B. N. Semenov, M. D. Sterlin

Institute of Problems of Mechanical Engineering of Russian Academy of Science,
St. Petersburg, 199178 Russia
Author Contact: ind@director.ipme.ru

Solutions of the system of differential equations of thermo-elasticity, heat-and-mass transfer-exchange between the components of a material of complex structure are derived and analyzed. Applications to the problems of change of mechanical properties of metals are given as a result of inflow of hydrogen. Features of the distribution of the thermo-elastic wave pulses in a two-component body with defects are investigated.

Introduction

The model of a two-component body allows one to describe the phenomena observable in experiments that are not explained from positions of classical continuous mechanics (e.g., hydrogen embrittlement) and feature propagation of thermal pulses in media with defects at low temperatures.

The primary structure of a material even in natural conditions unavoidably becomes complicated owing to absorption from surrounding space of atoms (e.g., gases and their binding by the skeleton of a material, in metals by crystal lattice).

Accumulation of hydrogen inside metal, as a rule, results in the embrittlement of a material. However, in laboratory conditions the same concentration of the dissolved hydrogen in titanium alloys resulted both in embrittlement and superplasticity. Therefore, the actual influence of the hydrogen factor on mechanical properties of metal cannot be predicted without the component-wise analysis of dynamics of each particular process of the inflow, redistribution (diffusion), binding, and release of hydrogen under the conditions of particular loadings and temperature changes. Mechanical loading on a surface of metal generates the waves of deformation, frequently accelerating processes of hydrogen binding inside a sample. The inflow of heat slows down the binding, but accelerates the diffusion processes. The inflow of warm mass increases the temperature. The present model allows one to take into account to some extent the properties of medium connected to a discrete atom-electronic structure of bodies as these components reflect the nonuniform scale of the physical processes proceeding in them. In addition, introduction of the second component in the model of a deformable body is induced with the fact that a crystal lattice and electronic component in a real sample react differently to action of such external factors as low temperatures both super short force and temperature loadings.

The objective of the present work is studying the dynamics of all specified phenomena on the basis of the uniform system of the equations completely describing all considered processes.

The Equations of Two-Component Model

Let us consider two material substances participating in the processes: a rather rigid skeleton (a crystal lattice of metal, for example) and one penetrating, capable substance to diffusion (hydrogen, for example). Eventually, the penetrating substance is divided into the parts: free, diffused, and connected to a skeleton. As the connected part carries out the same mechanical movement, as a skeleton, we shall consider them as the uniform component 1 and the free part of penetrated substances as the component 2.

In any vicinity of points of control volume, there can be points of both components 1 and 2, and between nearby points of the different components can go an exchange in weight (binding or release) or other interaction. Therefore, in continuous recording such points in different components have one Euler coordinate, and exchange processes go point-wise (as against the processes of carry going interpointly in the components).

Such an approach (though it contradicts a traditional principle of mechanics of a solid about indivisibility of a material point) lies in the essence of the exchange processes and will completely be coordinated to the general principles of mechanics if to take into account forces of interaction between components and sources of exchange weight. In the rest, physical laws can be written down component-wise.

The conservation law of the mass and the equations of dynamics for each of the components is

$$\frac{\partial \rho_k}{\partial t} + \nabla \cdot (\rho_k \mathbf{v}_k) = (-1)^k J \quad (1)$$

$$\nabla \cdot \boldsymbol{\sigma}_k = \rho_k \frac{d\mathbf{v}_k}{dt} + (-1)^k (J \mathbf{v}_k + \mathbf{R}) \quad (k = 1, 2) \quad (2)$$

Here ρ_k , \mathbf{v}_k , $\boldsymbol{\sigma}_k$ are mass density, velocities, and stress tensor of the component, k , J is a source term, \mathbf{R} is the force of interaction between components.

The equations of heat conductivity for components are ($k = 1, 2$)

$$\nabla \cdot (\lambda_k \nabla T_k) - c_k \rho_k \frac{\partial T_k}{\partial t} = K_k \alpha_k T_0 (\nabla \cdot \mathbf{v}_k) + (-1)^k \lambda_0 T_{12} \quad (3)$$

Here α_k is the factor of temperature expansion, K_k is the factor of volumetric deformation, T_k is temperature, λ_k is the factor of heat conductivity, C_k is the specific mass thermal capacity of the component k , T_0 is the reference temperature of a deformable body (sample), and λ_0 is the factor of heat exchange between components, $T_{12} = T_1 - T_2$.

Analysis of Hydrogen Influence on Dynamics of Phase-Structural Transformations

Having limited to one spatial measurement x , we shall present the system of the equations of thermo-elasticity, heat-and-mass transfer and exchange between components in the following sort:

$$\left\{ \begin{array}{l} \frac{\partial \sigma_1}{\partial x} = \rho_0 \frac{\partial^2 u_1}{\partial t^2}, \quad \sigma_1 = E_0 \varepsilon_1^m \frac{1}{1 + n^+ / \kappa}, \\ \varepsilon_1^m = \varepsilon_1 - \alpha_1 (T_1 - T_0), \quad \varepsilon_1 = \frac{\partial u_1}{\partial x}, \\ \frac{\partial n^-}{\partial t} = \frac{\partial}{\partial x} \left(D_n (T_2) (1 - b \varepsilon_1^m) \frac{\partial n^-}{\partial x} \right) + \frac{\partial}{\partial x} \left(D_r (n^-) (1 - b \varepsilon_1^m) \frac{\partial T_2}{\partial x} \right) - \\ \quad - \alpha (\varepsilon_1, T_1) n^- + \beta (\varepsilon_1, T_1) n^+, \\ \frac{\partial n^+}{\partial t} = \alpha (\varepsilon_1, T_1) n^- - \beta (\varepsilon_1, T_1) n^+ - \frac{\partial}{\partial x} \left(n^+ \frac{\partial u_1}{\partial t} \right), \\ c_1 \rho_0 \frac{\partial T_1}{\partial t} = \lambda_1 \frac{\partial^2 T_1}{\partial x^2} - E_0 \frac{1}{1 + n^+ / \kappa} \alpha_1 T_0 \frac{\partial \varepsilon_1}{\partial t} + \lambda_0 (T_1 - T_2), \\ c_2 m_2 n^- \frac{\partial T_2}{\partial t} = \lambda_2 \frac{\partial^2 T_2}{\partial x^2} + \lambda_n \frac{\partial}{\partial x} \left(D_n (T_2) (1 - b \varepsilon_1^m) \frac{\partial n^-}{\partial x} \right) - \lambda_0 (T_1 - T_2). \end{array} \right. \quad (4)$$

Here u_1 , ε_1 , σ_1 , T_1 , α_1 , c_1 , λ_1 are displacement, total strain, stress, temperature, factor of temperature expansion, specific thermal capacity, the factor of heat conductivity of the component 1; ρ_0 , E_0 are the density and the elastic modulus of the skeleton; T_2 , m_2 , c_2 , λ_2 , λ_n are the temperature, the mass of atoms, the specific thermal capacity, factor of heat conductivity, factor of the temperature diffusion of the component 2, κ is the factor, which is taking into account the ratio of the rigidities of a skeleton and of a penetrated substance, n^- , n^+ are relative concentration free and connected penetrated substances; D_n , D_T are the factors of diffusion and thermo-diffusion of penetrated substances; λ_0 is the factor of an heat transfer between components, α , β are the factors of a mass transfer between components.

Equation (4) enables us to solve a number of substantial problems of dynamics and to explain influence of embedding of an acting substance in a skeleton of a material on its mechanical properties, in particular, to clear influence of dynamics of process of hydrogen binding on metals embrittlement.

Some results for sample $0 \leq x \leq 1$ with initial conditions are $n^-(x, 0) \equiv n_0^-(x) \approx \text{const}$, $n^+(x, 0) \equiv n_0^+(x) \ll n_0^-(x)$. On the free end of the sample $x=0$ acts a short-term laser force pulse in a temperature equivalent $T_1(0, t) = T_2(0, t) \equiv \delta(t)$. At $x=1$ the sample is counted to be fixed ($u_1(1, t) \equiv 0$) and heat-weight-isolated at all $t > 0$. Figure 1 shows the characteristic dynamics of the hydrogen binding as a wave of sharp growth of n^+ .

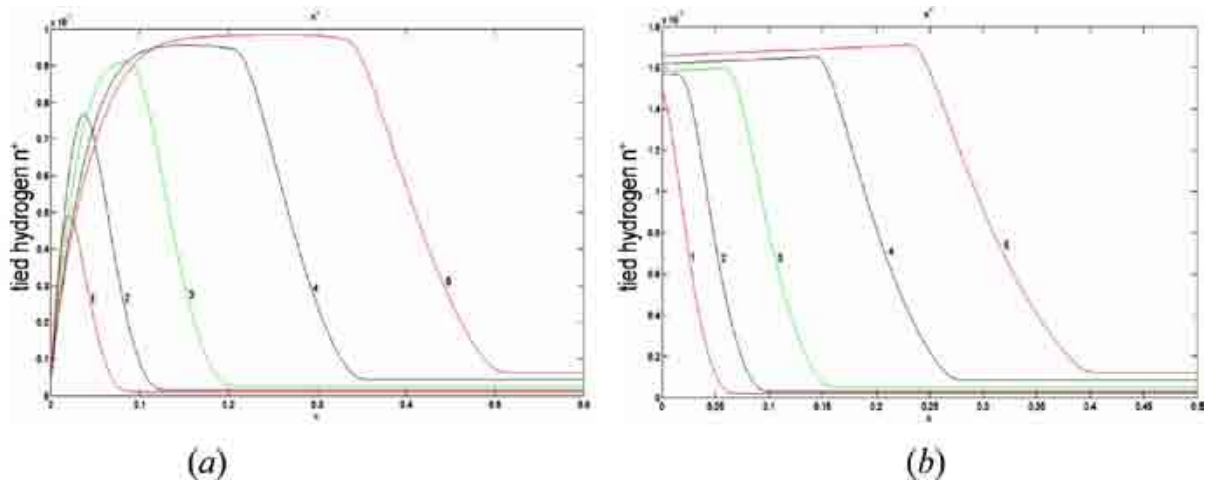


Figure 1. Distribution of the connected hydrogen on coordinate x during the increasing moments of time (1 – 5). (a) at strong dependence α on temperature, (b) at weak dependence α on temperature.

The recession of n^+ close to $x=0$ on Figure 1(a) is the consequence of heating of this area, opposed to binding. Dynamics of Figure 1(b) is characteristic also in solutions of a similar problem at mechanical influences on a material of a intensive short-time pulse, $\sigma_1(0, t) = \delta(t)$. However, in all cases a short-time pulse influence does not enter a material in a condition of a long instability and does not conduct to reorganization of its structure on distance from $x=0$. At the received $\sigma - \varepsilon$ diagrams, it is apparent that the material does not have time to be reconstructed, and fast recession of influence returns it to an initial condition. Thus, at short-term intensive influences, the wave of growth of hydrogen concentration does not result in a wave of reorganization of a material. If the loading is long, for example, linear, $\sigma_1(0, t) = a_1 t + a_0$, $a_1 > 0$, the wave of growth n^+ , going for a wave of deformation (Figure 2), conducts to reorganization of structure on $\sigma - \varepsilon$ the diagram the area of instability and final easing of metal is visible.

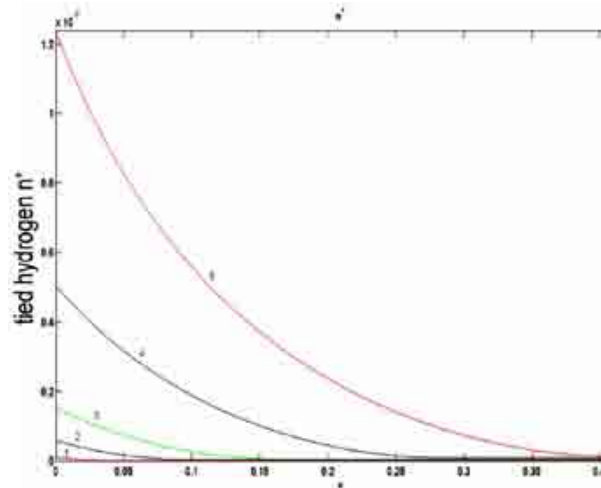


Figure 2. Dynamics of distribution on x at $\sigma_1(0, t) = a_1 t + a_0$.

Distribution of Thermoelastic Wave Pulses in a Two-Component Body with Defects

The equations of dynamics (1) with source term equal to zero ($J = 0$) and the equations of heat conductivity (2) take place for the one-dimensional two-component model of thermo-elastic body. In conditions of cryogenic temperatures and supershort pulse loadings the account of mutual influence of fields is of interest.

Let us consider a temperature shock loading at the end face $x = 0$. We understand as the first material component the crystal structure consisting of heavy atoms and ions and forming a skeleton of a sample. As the second material component, we understand set of light particles (electrons) freely (or it is not freely) penetrating into a crystal lattice. In many physical experiments, the samples loading is made by a short laser pulse. Thus first of all heating feels the light electronic component. By virtue of heat, the exchange between components and coherence of temperature and deformation processes in both components on a sample it will be propagated a thermo-elastic wave pulse. As defects, we understand the small located spatial areas in which some thermo-mechanical characteristics of a sample have the values which are distinct from nominal.

As the elementary (modeling) defect in a sample, we consider jump of the module of elasticity by the first material components (i.e., in the crystal lattice). Let on the section $1.8 \cdot 10^{-3} \leq x \leq 2.1 \cdot 10^{-3}$ the raised ten times modulus of elasticity E_1 takes place. Other parameters of considered model are chosen close to characteristics of a silicon crystal. According to the above, we consider that the short-time rectangular temperature pulse acts on the second component.

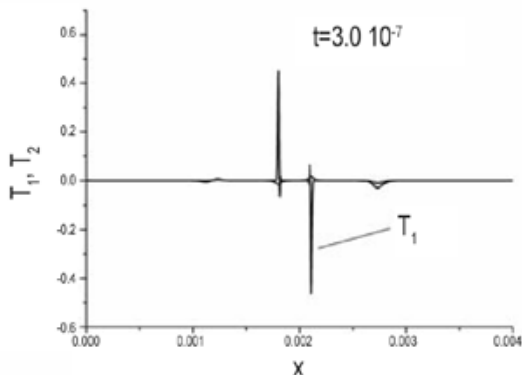


Figure 3. Temperature distribution at $t = 3 \cdot 10^{-7}$.

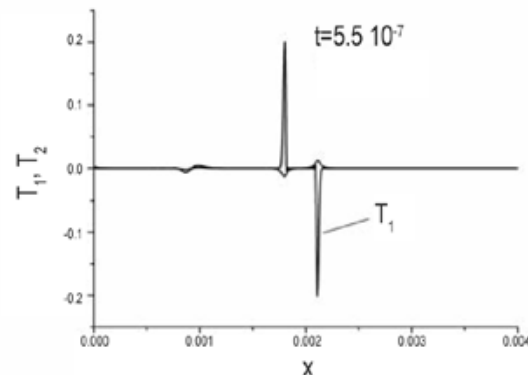


Figure 4. Temperature distribution at $t = 5.5 \cdot 10^{-7}$.

The plots in Figures 3 and 4 show spatial distribution of temperature of the first component during two corresponding moments of time. Formation of temperature maxima on the borders of the examined defect is distinctly visible. Eventually, these maxima decrease in size and are blurred on spatial coordinate x . The detailed analysis shows the absence of the evolution of the marked maxima at a very small factor of the heat conductivity of the first component, $\lambda_1 \approx 0$.

Further jump of factor of temperature expansion by the first material components, (i.e., a crystal lattice) is examined. The section $1.8 \cdot 10^{-3} \leq x \leq 2.1 \cdot 10^{-3}$ takes place the ten times raised factor of the temperature expansion α_1 . Other parameters of the considered model remain constant.

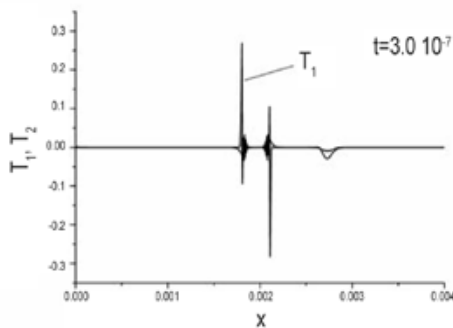


Figure 5. Dependence of temperature on time

$$t = 3 \cdot 10^{-7}.$$

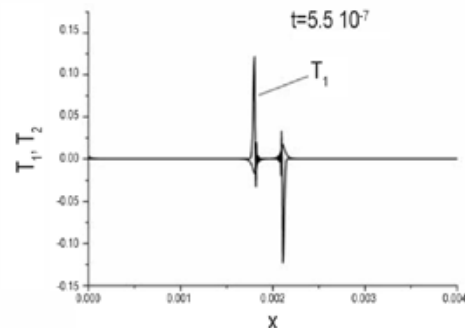


Figure 6. Dependence of temperature on time

$$t = 5 \cdot 10^{-7}.$$

The plots in Figures 5 and 6 in many respects are similar to results in Figures 3 and 4. We shall notice, however, that passage of a thermo-elastic disturbance through the forward border of the defect does not generate the reflected pulse, which would begin to propagate to section $x = 0$.

Conclusions

Within the framework of the theory of two-component medium are investigated the problem of influence of the dissolved in metals hydrogen on dynamics of structural transformations and propagation of a thermo-elastic pulse in bodies with defects.

The information on a level and distribution of the connected hydrogen in a material is not enough for the guaranteed forecast of the mechanical properties of a material. The knowledge of dynamics of the process resulting in hydrogen bonding is necessary. The methods stated in the paper allow the calculation of properties of a material with the complex structure, got by it as a result of the productions accompanying with temperature and mechanical influences.

In considered model of a thermo-elastic body a mutual influence of temperature and deformation fields takes place. Therefore, all features of propagation of temperature disturbance basically are connected to propagation of mechanical wave pulses. It follows from here, at passage of defects with abnormal values of the modulus of elasticity there are the reflections of a mechanical pulse and with it also of a temperature pulse from borders of these defects.

Acknowledgements

The financial support of the Sandia Corporation, contract 891095, and the Russian Foundation for Basic Research, grants 08-08-00737, 08-01-00691, 09-01-96500, 01-12017, is acknowledged. Sandia is a multi-program laboratory operated by Sandia Corporation, a Lockheed Martin Company, for the United States Department of Energy under Contract DEAC04-94AL85000.



ACCURATE DIRECT EULERIAN SIMULATION OF DYNAMIC ELASTIC-PLASTIC FLOW

J. R. Kamm, J. W. Walter

Los Alamos National Laboratory, Los Alamos, NM, 87545 USA

Author Contact : Kammj@lanl.gov

The simulation of dynamic, large strain deformation is an important, difficult, and unsolved computational challenge. Existing Eulerian schemes for dynamic material response are plagued by unresolved issues. We present a new scheme for the first-order system of elasto-plasticity equations in the Eulerian frame. This system has an intrinsic constraint on the inverse deformation gradient. Standard Godunov schemes do not satisfy this constraint. The method of Flux Distributions (FD) was devised to discretely enforce such constraints for numerical schemes with cell-centered variables. We describe a Flux Distribution approach that enforces the inverse deformation gradient constraint. As this approach is new and novel, we do not yet have numerical results to validate our claims. This paper is the first installment of our program to develop this new method.

Introduction

The accurate simulation of high-speed, shock-wave-driven flows involving solid materials is a rich computational material science subject as well as a critically important technical capability. A fundamental choice in the design of numerical algorithms for such simulations is the selection of the spatial reference frame in which the problem domain will be discretized. The earliest hydrodynamics codes, for both fluids and solids, employed the Lagrangian frame in which the computational mesh deforms with the material. This is an appropriate choice for flows with relatively small deformation, but it is of limited utility for complex, strongly shearing flows. One alternative is the Arbitrary Lagrangian Eulerian (ALE) approach, in which the mesh is allowed to deform independently of the material. ALE methods for solids are used for two purposes: (i) to avoid simulation failure due to mesh tangling in the Lagrangian phase or (ii) in the so-called Lagrange+remap style of Eulerian method, in which a Lagrangian update of the solution is mapped back onto the original mesh configuration every timestep. Almost all existing Eulerian methods for solids are of the Lagrange+remap variety.

Alternatively, one can discretize directly the Eulerian frame equations, for which the material moves through a space-fixed mesh that is immune to mesh distortion issues. Over the last 30 years, direct Eulerian methods have become the standard for almost all fluid dynamics simulations. We describe how to extend this approach with high accuracy to the Eulerian equations for solid dynamics in which *all* field variables are treated consistently with true conservation laws. We believe that the ultimate success of related computational techniques (such as adaptive mesh refinement, multi-material interface modeling, etc.) is held hostage to the physical fidelity, accuracy, and robustness of the underlying numerical method. The method we will describe forms the foundation for accurate simulations that can incorporate these sophisticated simulation techniques.

Background

Existing Lagrange+remap Eulerian schemes suffer from significant and unsolved difficulties for solid materials. Such schemes typically treat only the fluid variables (mass density, momentum, and fluid energy) in conservation form; often, even the fluid energy is treated nonconservatively. Inaccuracies result from using *hypoelastic* (stress-based)¹ constitutive models with nonconservative numerical algorithms for shock waves. In contrast, the Godunov-FD methodology we describe relies upon *hyperelastic* models, in which stress is

¹In hypoelastic models, the stress is treated as a fundamental variable that is governed by a non-conservative rate equation. In such models, fundamental principles (e.g., frame-indifference and conservation of energy) can be violated. It is impossible to cast a hypoelastic model in conservation form because stress is not a conserved quantity.

determined as a function of the current deformation and thermodynamic state. As discussed in the next section, the equations of dynamic hyperelasticity written in first-order conservation form in the Eulerian frame contain an *intrinsic constraint* involving the curl of the inverse deformation gradient. This constraint must be enforced in numerical solutions of this system. Very few papers on finite volume methods for this formulation, discussed by Kondaurov [4] and Godunov & Romenskii [2], have been published. The only (English language) published multi-dimensional implementation is by Miller & Colella [6]. In their scheme, this critically important constraint was not enforced; instead, the associated errors were diffused into the surrounding field. In contrast, the Godunov-FD method we describe will enforce the constraint *exactly*.

Subsequent to [4], these equations were considered by Plohr & Sharp [8,9], who obtained the governing equations for smooth and discontinuous solutions and for rate-dependent and rate-independent plasticity. The formulation we consider is based on their work. Trangenstein & Colella [14] analyzed the use of the gradient of the inverse flow map as a fundamental kinematic variable; they implemented a Godunov scheme for this formulation in 1D. Subsequently, Trangenstein and others published papers (see [15] and references therein) concerning various aspects of the conservative formulation. In [15], comparing a Lagrangian finite element method to a standard Godunov scheme, Trangenstein summarizes the difficulty presented by the curl constraint (our emphasis):

This constraint also goes to the heart of the difference between the Godunov approach and the finite element approach to the equations of solid mechanics... *In contrast...there is no discrete curl that annihilates the discrete Godunov gradient. As a result, there is no way to impose a discrete analogue of the curl condition in a way that is automatically consistent with the remainder of the Godunov difference scheme.*

The Flux Distribution Method overcomes this difficulty by expanding intercell fluxes to include *all* neighboring cells, not just those that share a face with the cell being updated.

Walter et al. [16] used a spatially unsplit, two-step Lax-Wendroff scheme together with front tracking of material interfaces. Although the two-step Lax-Wendroff scheme did not explicitly involve the quasi-linear form of the equations (see the next section), the front tracking algorithm did. In that work, plane-strain Cartesian-mesh computations of expanding and contracting shells clearly showed accumulation of a constraint-violating component in the inverse deformation gradient. Constraint-violation was most severe at the tracked fronts but also occurred in the interior of the shell. The inability to enforce the curl-free constraint led to the failure of this computational algorithm.

Method

The four main elements of the method are (i) the governing equations, (ii) the Flux Distribution approach for enforcing the intrinsic constraint, (iii) the Godunov scheme for the remainder of the numerical algorithm, and (iv) the constitutive model.

Governing Equations

The conservation laws for thermoelasticity can be written (see [5,9]):

$$\rho_{,t} + (\rho v^j)_{,j} = 0 \quad \text{mass} \quad (1)$$

$$(\rho v^i)_{,t} + (\rho v^i v^j - \sigma^{ij})_{,j} = 0 \quad \text{momentum} \quad (2)$$

$$(\rho e)_{,t} + (\rho e v^j - v_i \sigma^{ij})_{,j} = 0 \quad \text{total energy} \quad (3)$$

$$(g^\alpha_i)_{;t} + (g^\alpha_j v^j)_{;i} = 0 \quad \text{Eulerian continuity} \quad (4)$$

with the intrinsic constraint written

$$(\text{curl } \mathbf{g})^{\alpha\kappa} = g^\alpha_{i;t} \varepsilon^{ijk} / \sqrt{m} = 0 \quad \text{curl-free condition} \quad (5)$$

Here, $(\rho, e, v^i, \sigma^{ij}, g^\alpha_i)$ are the mass density, total energy ($e \equiv \varepsilon + (\mathbf{v} \cdot \mathbf{v})/2$, where ε is the specific internal energy), velocity, Cauchy stress, and inverse deformation gradient. Lagrangian (referential) and Eulerian (spatial) coordinate indices are Greek and Latin, respectively, $\varepsilon^{ij\alpha}$ is the usual permutation symbol, and $m = \det(m_{ij})$ is the metric determinant. Partial derivatives with respect to time and x^j are indicated by $()_{;t}$ and $()_{;j}$, respectively²; and heating and body force terms are neglected. The constitutive model that closes the system is described below. The constraint (5) is a consequence of using both v^i and g^α_i as independent variables, which is done to write the equations as a first-order system. Both v^i and g^α_i are related to the *motion*, χ , which maps the referential (Lagrangian) position of a material point \mathbf{X} to its current spatial (Eulerian) position \mathbf{x} : $x^i = \chi^i(\mathbf{X}, t)$, with $v^i \equiv \partial x^i / \partial t$ and $g^\alpha_i \equiv \partial X^\alpha / \partial x^i$.

As in [6], these governing equations (1)–(4) and (5) can be written as

$$\mathbf{W}_{;t} + \text{div } \mathbf{F}(\mathbf{W}) = \mathbf{0} \quad \text{and} \quad \mathbf{L}_C(\mathbf{W}) = \mathbf{0}, \quad (6a,b)$$

where \mathbf{W} and \mathbf{F} are the vectors of conserved variables and associated fluxes, and \mathbf{L}_C is the (linear) constraint operator. As noted in [6,14], (6a,b) has the form of an initial value constraint: if \mathbf{U} satisfies (6a) and (6b) holds at some initial t_0 , then (6b) holds for all $t > t_0$. Moreover, (6b) must be used to modify the quasi-linear form of the equations (which are obtained by expanding the divergence in (6a)) in order to obtain the correct Eulerian eigenstructure. This amounts to replacing (6a) with a modified system of the form

$$\mathbf{W}_{;t} + \text{div } \mathbf{F}(\mathbf{W}) = \xi(\mathbf{W}) \mathbf{L}_C(\mathbf{W}), \quad (7)$$

an idea that Miller & Colella [6] attribute to Godunov [2]. The new terms on the RHS of (7) are of the form $\mathbf{v} \times \mathbf{G}$ where the vector $\mathbf{G} \equiv \text{curl}(\mathbf{g}^T)$. In [6], system (7) is treated numerically as being *un-constrained*; instead, to control errors in (6b), Miller & Colella added diffusive terms proportional to $\text{curl}(\mathbf{G})$ to the RHS of (7). This approach had some success in controlling the maximum amplitude of \mathbf{G} . We believe that a Godunov-FD method can be constructed to satisfy (6b) (i.e., to satisfy (5)) *to machine precision*. The resulting scheme should be more accurate and simpler than the numerical method in [6], with *no* artificial diffusive terms.

Flux Distributions

The concept of Flux Distributions was introduced by Torrilhon & Fey [12] (see also [1,11,13]). They began with a generic transport equation, $\mathbf{u}_{;t} + \mathbf{F}(\mathbf{u}, \mathbf{x}) = \mathbf{0}$, which contains a generic *linear intrinsic* constraint C such that $C(\mathbf{F}(\mathbf{u}, \mathbf{x})) \equiv \mathbf{0}$. Consequently, $C(\mathbf{u})_{;t} \equiv \mathbf{0}$, which implies that $C(\mathbf{u}(\mathbf{x}, t)) \equiv \mathbf{0}$, for all \mathbf{x}, t , when this last equality is satisfied at the initial time. For (1)–(5), C is the spatial curl operator, so that $\text{curl}(\mathbf{g})_{;t} = \mathbf{0}$, which follows from taking the curl of (4). Let the vector field $\mathbf{u}: \mathcal{R}^D \rightarrow \mathcal{R}^D$ be approximated on a finite volume (FV) mesh, $\mathcal{T} = \{\kappa_k, k=1, \dots, \kappa\}$, by a cell-wise constant *grid function*, $\mathbf{U} \in V = \{\omega: \mathcal{T} \rightarrow \mathcal{R}^D\}$. The *flux distribution*, $\Phi_\kappa: V \rightarrow V$, attached to cell κ , maps $\mathbf{U} \rightarrow \Phi_\kappa(\mathbf{U})$ such that its support is given by $\text{supp}(\Phi_\kappa(\mathbf{U})) = \{\kappa\} \cup N(\kappa)$. Here, $N(\kappa)$ is the

² In curvilinear coordinates $()_{;j}$ indicates a covariant derivative and the form of (1)–(5) is unchanged.

complete neighborhood of cell κ ; that is, it contains *all* cells that share a vertex or edge (or, in 3D, a face) with cell κ . The flux from cell κ to cell λ is written: $\Phi_{\kappa}(U)|_{\lambda}$. Essentially any finite volume method can be written as:

$$U^{n+1}|_{\kappa} = U^n|_{\kappa} + \sum_{\lambda \in \text{supp}(\Phi_{\kappa})} \Phi_{\lambda}(U^n)|_{\kappa}. \quad (8)$$

Note that this cell update is a sum of fluxes over the *complete* neighborhood of cell κ . This is a generalization of the usual notion of intercell fluxes, which are considered only across shared co-dimension 1 entities of the given cell (e.g., across edges in 2D and across faces in 3D). For a linear constraint, one can decompose the flux distribution as:

$$\Phi_{\kappa}(U) = \sum_l \varphi^{(l)}_{\kappa}(U) \underline{\Phi}^{(l)}_{\kappa}, \quad (9)$$

where the $\varphi^{(l)}_{\kappa}$ are scalars (dependent on U) and the $\underline{\Phi}^{(l)}_{\kappa}$ are *shape functions* (independent of U). If a discretization of the constraint is written as $\underline{C}_{\kappa} \cdot U \approx C(u)|_{\kappa}$, then the discrete condition that is sufficient for local constraint preservation can be written as:

$$\underline{C}_{\kappa} \cdot \underline{\Phi}^{(l)}_{\lambda} = 0, \text{ for all } \kappa, \lambda \in \text{supp}(\Phi_{\kappa}), \text{ for all } l. \quad (10)$$

Evaluation of (10) over a neighborhood of cell κ yields a homogeneous linear system whose nullspace determines a set of linearly dependent, constraint-preserving shape functions, $\{\underline{\Phi}^{(l)}_{\kappa}\}$. A basis subset must be chosen from $\{\underline{\Phi}^{(l)}_{\kappa}\}$, and the coefficients $\varphi^{(l)}_{\kappa}(U)$ must be determined. These quantities are specified so that (8) and (9) define a stable, consistent difference scheme, which is of the desired order of accuracy. Torrilhon & Fey [12] state that non-trivial solutions to (10) exist whenever there exist fields u (that have compact support) for which the analytic constraint C vanishes. The discrete constraint \underline{C}_{κ} must be consistent with C in the sense of cell averages. The discretization for \underline{C}_{κ} will determine the nullspace of (10) and, ultimately, it will determine the set of constraint-preserving schemes that are available for the original equation. Thus, *the design of the appropriate discrete constraint \underline{C}_{κ} is a critical element of this process.*

Jeltsch & Torrilhon [3] consider the construction of a curl-preserving scheme for the momentum equation of the 2D non-linear wave system, $u_t + \text{grad } p(p) = 0$, where u is the momentum and p is the pressure. Here, the intrinsic constraint is: $\text{curl } u = 0$. The discretized constraint, \underline{C}_{κ} , that they specify is:

$$\text{curl}^{(*)}(u)|_{ij} = (1/2)(\{\zeta_{i+1,j}\}_y - \{\zeta_{i-1,j}\}_y)/\Delta x + (1/2)(\{\zeta_{i,j+1}\}_x - \{\zeta_{i,j-1}\}_x)/\Delta y, \quad (11)$$

where $\{\zeta_{ij}\}_y$, representing the y -directional average of quantity ζ_{ij} , is defined as $\{\zeta_{ij}\}_y \equiv (1/4)(\zeta_{i,j+1} + 2\zeta_{ij} + \zeta_{i,j-1})$; the x -directional average $\{\zeta_{ij}\}_x$ is defined similarly. The cell's index is $\kappa = (i,j)$ and its size is $\Delta x \Delta y$. The nullspace of $\text{curl}^{(*)}(u)|_{ij}$ determined by (10) is four-dimensional and, to within a constant factor, the first element $\underline{\Phi}^{(1)}_{\kappa}$ vanishes except in the upper right quadrant of the 3×3 stencil that is centered at cell κ :

$$\underline{\Phi}^{(1)}_{\kappa}|_{i+1,j+1} = (\Delta y, \Delta x)^T, \quad \underline{\Phi}^{(1)}_{\kappa}|_{i,j+1} = (-\Delta y, \Delta x)^T, \quad (12)$$

$$\underline{\Phi}^{(1)}_{\kappa}|_{i,j} = (-\Delta y, -\Delta x)^T, \quad \underline{\Phi}^{(1)}_{\kappa}|_{i+1,j} = (\Delta y, -\Delta x)^T. \quad (13)$$

The other three elements, $\underline{\Phi}^{(2)}_{\kappa}$, $\underline{\Phi}^{(3)}_{\kappa}$, $\underline{\Phi}^{(4)}_{\kappa}$, are obtained by shifting $\underline{\Phi}^{(1)}_{\kappa}$ around the cell. The nature of the cell flux distribution for the discrete constraint operator $\text{curl}^{(*)}$ together with $\underline{\Phi}^{(1)}_{\kappa}$ and $\underline{\Phi}^{(2)}_{\kappa}$ are sketched in Figure 1, where $h \equiv \max(\Delta x, \Delta y)$.

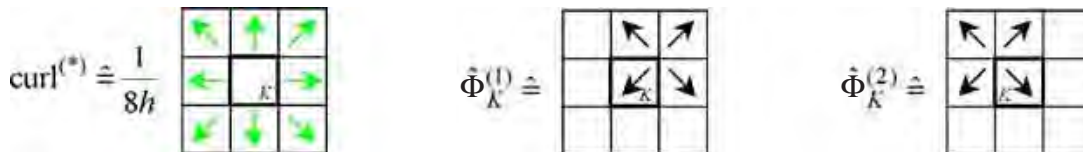


Figure 1. Discrete coefficients and corresponding flux distribution for curl preservation.

This approach differs from a classical finite volume scheme. In that case, the y -direction momentum update is written in terms of edge fluxes as $u_{i,j}^{y,n+1} = u_{i,j}^{y,n} + (\Delta t / \Delta y) (p_{i,j-(1/2)} - p_{i,j+(1/2)}) [0, 1]^T$, with edges at the half-integer indices. This can be cast in FD form of (8) by defining edge flux distributions (with similar terms at other edges) as:

$$\underline{\Phi}^{(\text{class})}_{i,j+(1/2)}|_{i,j} = (\Delta t / \Delta y) p_{i,j+(1/2)} [0, -1]^T, \quad \underline{\Phi}^{(\text{class})}_{i,j+(1/2)}|_{i,j+1} = (\Delta t / \Delta y) p_{i,j+(1/2)} [0, 1]^T. \quad (14)$$

These FDs are *not* curl-preserving because they are *not* linear combinations of those in Figure 1. In contrast, the curl-preserving, y -direction edge FD at $(i,j+1/2)$ is given by:

$$\underline{\Phi}^{(\text{curl-free})}_{i,j+(1/2)}|_{i,j} = (\Delta t / (\Delta x \Delta y)) p_{i,j+(1/2)} (\underline{\Phi}^{(1)}_{\kappa}|_{i,j} + \underline{\Phi}^{(2)}_{\kappa}|_{i,j}) / 8. \quad (15)$$

Schematics of the classical and curl-free FDs given in (14) and (15) are shown in Figure 2, where p is the edge flux at edge $(i,j+1/2)$ of the cell with index $\kappa = (i,j)$.

Godunov Scheme



Figure 2. Flux distributions for the y -momentum update in the wave equation system the indicated edge. Left: *classical* FV scheme. Right: *curl-free* FD approach.

For the system (1)–(5), a FD scheme would be used *only* in the update of the inverse deformation tensor \mathbf{g} , since this quantity must obey the constraint equation. In [6], Miller and Colella provide the foundation of the computational method used for aspects *other than* the constraint. A key part this Godunov scheme is the 1D Riemann problem, which requires a wave analysis of the quasi-linear form of (1)–(5). For a general 1D flow:

$$U_{,t} + \mathbf{D}(U) U_{,x} = 0, \quad (16)$$

where $x = x^1$ is the flow direction, $\mathbf{U} \equiv [g^1_1, g^2_1, g^3_1, v^1, v^2, v^3, \rho, \eta]^T$, with $g^2_2 \equiv g^3_3 = 1$, η is the entropy and $\mathbf{U} = \mathbf{U}(x,t)$. The array of conserved variables, $\mathbf{W} = \mathbf{H}(\mathbf{U})$, can be recovered by direct evaluation. The flux \mathbf{D} is decomposed as $\mathbf{D} = \mathbf{L}\mathbf{\Lambda}\mathbf{R}$, in which the diagonal matrix of eigenvalues $\mathbf{\Lambda}$ is flanked by the matrices of the left- and right-eigenvectors, \mathbf{L} and \mathbf{R} . Menikoff [5] gives a detailed wave analysis of (16). For a numerical solution, the domain is divided into space-time cells: $[x_{i-(1/2)}, x_{i+(1/2)}] \times [t^n, t^{n+1}]$. In the 1D case, the constraint is satisfied automatically. The 1D solution procedure is:

- Compute the required constitutive quantities using t^n data in each cell.
- Construct limited, high-order accurate slopes for \mathbf{U}_i^n in each cell.
- Use the eigenvalue decomposition of \mathbf{D} to obtain left (L) and right (R) upwind estimates of states at edges at the half-timestep, $\mathbf{U}_{L,i-(1/2)}^{n+(1/2)}$ and $\mathbf{U}_{R,i+(1/2)}^{n+(1/2)}$.
- Use a Riemann solver, with the states from step (c) and the corresponding conservative edge flux, to obtain a single half-timestep flux state at each edge. With $\mathcal{R}(\cdot, \cdot)$ denoting a Riemann solution based on two states, one writes

$$\mathbf{U}_{i+(1/2)}^* = \mathcal{R}(\mathbf{U}_{L,i-(1/2)}^{n+(1/2)}, \mathbf{U}_{R,i+(1/2)}^{n+(1/2)}), \quad \mathbf{F}_{i+(1/2)}^* = \mathbf{F}(\mathbf{H}(\mathbf{U}_{i+(1/2)}^*)), \quad (17)$$

where F is the 1D version of the flux function from (6a).

e) The final update is: $U_i^{n+1} = U_i^n - (\Delta t^n / \Delta x_i) (F_{i+(1/2)}^* - F_{i-(1/2)}^*)$.

In 2D (and 3D), a predictor-corrector approach gives a spatially-unsplit, corner-coupled scheme. An unsplit scheme is essential for a solid, due to directional coupling in a solid (unlike a fluid). Briefly, the 2D procedure (with flux vector $F \equiv [F_{(x)}, F_{(y)}]^T$) is:

- A) Compute the edge-centered *predictor* fluxes, $F_{(x) i+(1/2)j}^{(p)}$ and $F_{(y) ij+(1/2)}^{(p)}$, in each direction (as in 1D).
- B) *Correct* the predictor fluxes using the left (*L*) and right (*R*) edge states, U^* , evaluated at the half-timestep and augmented by a quasi-linear update (e.g., as in step (c) above) *in the transverse direction*. Notionally, for the *x*-direction (where U^* states include terms $v \times G$ from the RHS of (7)):

$$F_{(x) i+(1/2)j} = F_{(x)}(R(U_{(x_L) i+(1/2)j}^{*n+(1/2)}, U_{(x_R) i+(1/2)j}^{*n+(1/2)})), \text{ where, e.g.,} \quad (18)$$

$$U_{(x_L) i+(1/2)j}^{*n+(1/2)} = U_{(x_L) i+(1/2)j}^{n+(1/2)} - (\Delta t^n / \Delta y_j) (F_{(y) ij+(1/2)}^{(p)} - F_{(y) ij-(1/2)}^{(p)})/2. \quad (19)$$

There are several parts of this Godunov algorithm at which one must choose among different approaches. One such choice is that of the Riemann solver (RS). The RS must introduce sufficient dissipation into the overall scheme. This requirement, together with the computational expense of an exact RS, suggests that an approximate RS should be used. For the *fluid* Euler equations, solvers that are non-iterative or even fully linearized often perform adequately. The situation for solids is more difficult because (i) the equations have a more complex wave structure and (ii) material properties are often temperature dependent. The RS used in [6] was linearized; in subsequent work, Miller [7] published an exact solver applicable to (16). Under some conditions, he found errors in the linearized solutions related to incorrect partitioning of energy between thermal and compressional modes, which resulted in non-physical entropy and temperature. Between the extremes of exact and fully linearized solvers, various approximations can be made.

Constitutive Model

Equations (1)–(5) are supplemented with a thermoelastic constitutive model, which closes the system of equations. We restrict attention to homogeneous and isotropic models. Following [5,10], let the Helmholtz free energy be given by $\psi = \psi(E, \theta)$, where $E \equiv (1/2)(g^{-T}g^{-1} - I)$ is the Lagrangian large strain tensor and θ is the temperature. The exponents -1 and $-T$ indicate the inverse and transposed inverse, and I is the unit tensor. With this assumption, σ , η , and $\varepsilon \equiv \psi + \eta \theta$, are computed in standard manner after the free energy function ψ is specified. This model is thermodynamically consistent, properly frame indifferent, and sufficiently general to encompass a wide range of dynamic solid material behavior.³ Plohr & Plohr [10] analyze the quasi-linear form of (1)–(5) under the assumption that the Cauchy stress is written as a sum of volumetric (*V*) and deviatoric (*S*) parts: $\sigma = -pI + s$. The corresponding energy decomposition is:

$$\psi = \psi_V(\tau, \theta) + \psi_S(\tau, E^*, \theta), \quad (20)$$

where $\tau \equiv \rho^{-1}$, $E^* \equiv (1/2)(J^{-2/3}g^{-T}g^{-1} - I)$, $J \equiv 1/\det(g)$, and θ is the temperature. Exact decomposed expressions are obtained for p , s , and the elasticity tensors required for the solution of the Riemann problem. Exact expressions are also obtained under the additional assumptions of (i) *material isotropy*, for which $\psi_S = \psi_S(\tau, I_1^*, I_2^*, \theta)$, with I_1^* and I_2^* being the first two principal invariants of $I + 2E^*$; and (ii) *small elastic distortion*, for which $\|E^*\| \equiv [\text{tr}(E^{*T}E^*)]^{1/2} \ll 1$.³ Expressions accurate to $O(\|E^*\|^2)$ are derived for the elasticity tensors and the acoustic propagation matrix,

³ This is a valid approximation for the elasto-plastic response of metals.

\mathbf{a}_n (\mathbf{n} is the wave propagation direction). They compare their expressions for the convective time rates $\dot{\mathbf{p}}$ and $\dot{\mathbf{s}}$ with those commonly used in hypoelastic numerical schemes. In addition to recovering the terms by which the so-called Jaumann objective rate of \mathbf{s} differs from its convective rate,⁴ they identify three other terms of equal magnitude that cannot be obtained in a hypoelastic formulation because \mathbf{g} is not computed.

These findings demonstrate the need for accurate numerical methods that enforce the critical inverse deformation gradient constraint on the Eulerian thermoelastic equations. Our algorithm, using a Flux Distribution-based approach, provides such a method.

Conclusions

In this paper, we outlined a new method for the accurate integration of the Eulerian frame equations for hyperelastic material behavior, for which we provide the governing equations. We argued that the method of Flux Distributions can be used to exactly satisfy the critical zero-curl constraint on the inverse deformation gradient. We outlined a Godunov scheme to be used for the underlying numerical algorithm and described the hyperelastic constitutive model to be used. Although we do not yet have numerical results to validate our claims, we will present results of this program in future publications.

Acknowledgements

This work was performed under the auspices of the United States Department of Energy by Los Alamos National Security, LLC, at Los Alamos National Laboratory under contract DE-AC52-06NA25396. This paper is available as Los Alamos National Laboratory report LA-UR-09-03550.

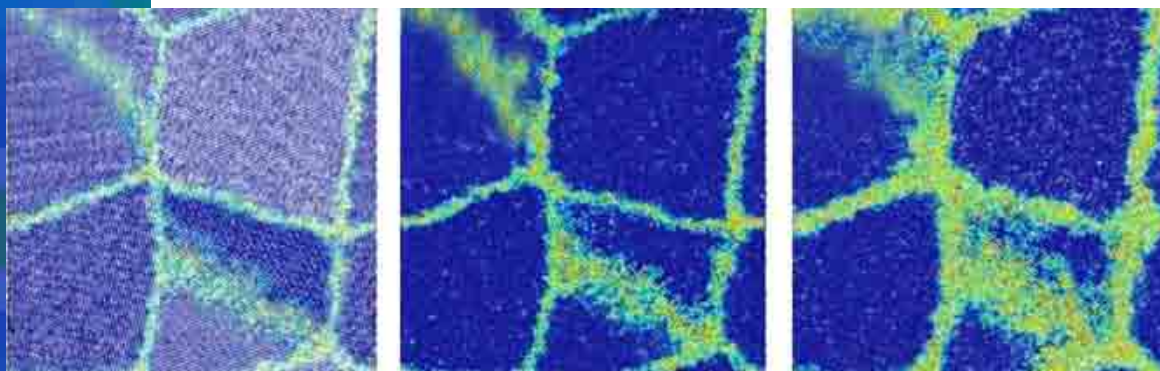
References

- [1] R. Artebrandt, M. Torrilhon, "Increasing the accuracy in locally divergence preserving finite volume schemes for MHD", *J. Comput. Phys.* **227** 3405-3427 (2008).
- [2] S. K. Godunov, E. I. Romenskii, *Elements of Continuum Mechanics and Conservation Laws* (New York, Kluwer Academic Plenum Publishers, 2003).
- [3] R. Jeltsch, M. Torrilhon, "On curl-preserving finite volume discretizations for shallow water equations," *BIT Numerical Mathematics* **46** S35-S53 (2006).
- [4] V. I. Kondaurov, "Conservation laws for an elastic-viscoplastic medium with finite deformations," *Mech. Solids* **17** 91-101, (1982).
- [5] R. Menikoff, *Notes on Elastic-Plastic Flow*, Los Alamos National Laboratory report LA-UR-03-0047-revised (2005).
- [6] G. Miller and P. Colella, "A high-order Godunov method for elastic/plastic flow in solids," *J. Comput. Phys.* **167** 131-176 (2002).
- [7] G. Miller, "An iterative Riemann solver for systems of hyperbolic conservation laws, with application to hyperelastic solid mechanics," *J. Comput. Phys.* **193** 198-225 (2003).
- [8] B. Plohr and D. Sharp, "A conservative Eulerian formulation of the equations for elastic flow," *Adv. Appl. Math.* **9** 481-499 (1989).
- [9] B. Plohr and D. Sharp, "A conservative formulation for plasticity," *Adv. Appl. Math.* **13** 462-493 (1992).
- [10] B. Plohr and J. Plohr, *Large Deformation Constitutive Laws for Isotropic Thermoelastic Materials*, Los Alamos National Laboratory report LA-UR-05-5471 (2005).
- [11] M. Torrilhon, *Zur Numerik der Idealen Magnetohydrodynamik*, ETH Dissertation N. 15353, ETH Zürich (2003).

⁴The terms yielding an objective stress rate are essential for accurate simulation at moderate to large strains.

- [12] M. Torrilhon and M. Fey, “Constraint-preserving upwind methods for multidimensional advection equations,” *SIAM J. Numer. Anal.* **42** 1694–1728 (2004).
- [13] M. Torrilhon, “Locally divergence-preserving upwind finite volume schemes for magnetohydrodynamic equations,” *SIAM J. Sci. Comput.* **26** 1166–1191 (2005).
- [14] J. Trangenstein and P. Colella, “A higher-order Godunov method for modeling finite deformation in elastic-plastic solids,” *Comm. Pure. Appl. Math.* **44** 41–100 (1991).
- [15] J. Trangenstein, “A second-order Godunov algorithm for two-dimensional solid mechanics,” *Comput. Mech.* **13** 343–359 (1995).
- [16] J. Walter, D. Yu, B. Plohr, J. Grove, J. Glimm, *An Algorithm for Eulerian Front Tracking for Solid Deformation*, Los Alamos National Laboratory Report, LA-UR-00-5370 (2001).

Materials Response to DYNAMIC LOADING III



The structure of grain boundaries in Al polycrystal in equilibrium at zero pressure and different temperatures T : a) 500 K; b) 700 K; c) 800 K.

Lacking a mathematical representation of material constitutive behavior, the field equations of continuum mechanics are an unclosed system. When subjected to dynamic loading, material constitutive behavior is often influenced by the initiation and evolution of damage. In turn, the initiation and evolution of damage are influenced by material constitutive behavior. Complicating matters further is that many materials undergo phase change under the influence of dynamic loading. Material response is typically nonlinear and path dependent, making the development of constitutive/damage models and the solution of the associated initial boundary value problem a nontrivial matter. Modeling the relationship between constitutive behavior, phase state, and damage remains an unsolved problem and an area of active research. Constitutive behavior is often framed within the context of plasticity (or viscoplasticity). Path dependence is often approximated through the inclusion of a number of internal state variables. Though explicit modeling of damage is possible, this approach is rarely employed. The approach more commonly appropriated is to approximate damage through phenomenological homogenization of its effect. Phase mechanics and the kinetics of phase change represent an area rich with opportunity for improving our predictive capability. The papers presented in this section focus on these issues. In particular, several papers are presented that deal with the constitutive behavior and the initiation and evolution of damage in cerium, a material that undergoes multiple phase changes under the influence of dynamic loading. Atomistic and molecular dynamics is used to gain a better understanding of the fundamental mechanisms and processes involved in damage formation. Issues of path dependence are explored through studies of the effect of preconditioning (by shock or quasi-isentropic loading) on constitutive behavior and damage formation/evolution, and through studies of damage followed by recompaction.

Marvin (Tony) Zocher, Los Alamos National Laboratory, Los Alamos, New Mexico, USA

Section VII:

- VII-2 Simulation of Ce Response to Dynamic Loading (VNIITF)
- VII-7 Predictions from the Equation of State of Cerium Yield Interesting Insights into Experimental Results (LANL)
- VII-11 Features of Cerium Compressibility and Spall Strength in the (γ - α) Phase-Transformation Region Under Explosive Loading (VNIITF)
- VII-16 Study of Phase Transitions in Cerium and Titanium by PVDF Gauge (VNIIEF)
- VII-20 Atomistic Modeling of Microstructure Influence on the Spall Strength (JIHT)
- VII-24 Effect of Shock Wave and Quasi-isentropic Loading on the Shear and Spalling Strength of Metals with Natural and Microcrystalline Structure (VNIIEF)
- VII-29 Spall Fracture and Compaction in Natural Uranium Under Shock-Wave Loading (VNIIEF)

SIMULATION OF Ce RESPONSE TO DYNAMIC LOADING

**A. Petrovtsev, A. Bychenkov, V. Dremov, V. Elkin, G. Kovalenko,
D. Shalkovsky, N. Sokolova, D. Varfolomeev**

All Russian Research Institute of Technical Physics (VNIITF), 456770, Snezhinsk, Chelyabinsk Region, Russia

We present the results of numerical simulations of experiments studying stress wave profiles in cerium, which were planned to be carried out in 2007 and 2008 at RFNC-VNIITF. Eight explosive experiments loading cerium with sliding and normal detonation of HE layers of different thickness and yield were to be conducted. The first stage of preparation to the experiments was to select the optimal setup with the help of numerical simulation. To validate the approach used in the numerical simulation of cerium behavior, several experiments conducted at Los Alamos National Laboratory (LANL) were simulated.

Introduction

Since Bridgman in 1927 discovered isostructural phase transition in cerium, it has been subjected to intense theoretical and experimental investigations. These efforts revealed a very complicated and curious phase diagram of cerium, which is still disputable. This is because of appearance of low-symmetric fcc- and hcp-like polymorphous modifications energies that are very close to each other. Complicated behavior of cerium is explained in part by 4f-electrons. Indeed, a number of theoretical models of 4-electron behavior in (γ - α) transition have been developed. Most of the models interpret the transition as Mott insulator-conductor transition and Kondo volume collapse. However, a generally recognized model of (γ - α) transition does not exist.

That is why theoretical and precise experimental data on cerium thermodynamic and mechanical properties, polymorphous modifications of crystal structures, kinetics of stresses relaxation and features of isomorphous and polymorphous transitions and melting during dynamic loading are of great mutual interest at LANL and RFNC-VNIITF. This interest was realized in laboratory-to-laboratory contract.

In compliance with the joint work plans, RFNC-VNIITF and LANL were to carry out experimental studies into shock-related properties of cerium by applying the techniques currently at use at RFNC-VNIITF. Eight explosive experiments loading cerium with sliding and normal detonation of HE of different thickness and yield were to be conducted. Stress-wave profiles were to be recorded with the optical lever method. For the purpose, wedge-like Ce samples meeting high requirements for purity, microstructure, and phase composition were produced in LANL and delivered to RFNC-VNIITF.

The first stage of preparing for the experiments was to select the optimal setup of the experiments with the help of numerical simulation. Calculation in 1D and 2D geometry was performed with VOLNA [5] and SPRUT [6] hydrodynamics codes respectively.

Adjusting Models in LANL Experiments Simulation

Several experiments conducted at LANL [1,2] to study shock-wave processes in cerium were numerically simulated using the EOS from [1,3] and models of elastic-plastic properties and phase transformations in cerium. This helped to assess acceptability of the developed approach for numerical simulations on the whole and, in particular, the implemented physics of plastic deformation and polymorphic γ - α transformation. Comparison of numerical simulations to the VISAR-recorded profiles of stress waves in the cerium samples shows (Figures 1 and 2) that cerium properties are sufficiently well described, and this proves applicability of the developed approach to the analysis of the strain characteristics of cerium to be expected in the experiments under preparation at RFNC-VNIITF.

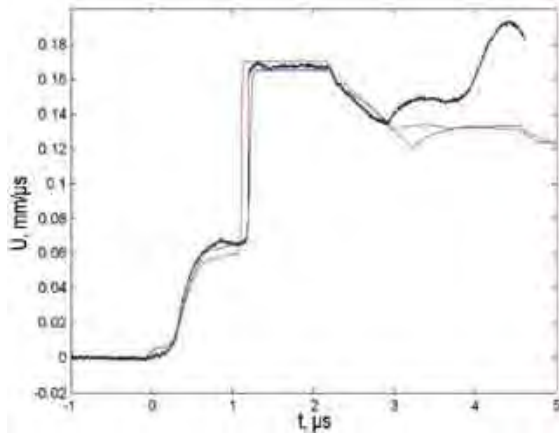


Figure 1. Stainless Steel Plate Impact Experiment. Speed of the sample-window interface vs time in experiment 56-05-27, simulations with EOS [3] (red curve) and with EOS [1] (blue curve) in comparison to the VISAR measurements [2]. The profiles are superposed at the arrival time of the elastic precursor.

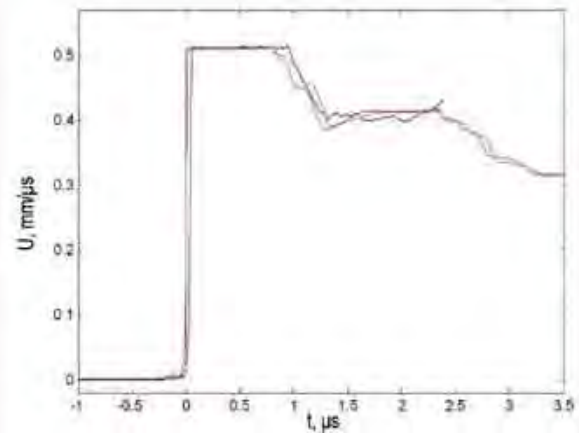


Figure 2. Tungsten Plate Impact Experiment. Speed of the sample-window interface versus time in experiment 56-04-23, simulation with EOS [3] (red curve) and with EOS [1] (blue curve) in comparison to the VISAR measurements [1,2]. The profiles are superposed at the arrival time of the elastic precursor.

Joint research into cerium properties includes experiments to be conducted by RFNC-VNIITF to measure stress wave profiles in the material within a wide range of wave amplitude. The first group of the experiments includes measurements of the wedge samples loaded with sliding detonation of HE layers having different thicknesses with the optical lever (OL) method. The second group of experiments includes similar experiments with samples loaded with normal detonation of HE layers. This group also includes experiments with samples loaded by a plate impact. The goal of the studies is to obtain information on kinetics of polymorphic γ - α and α - ϵ transformation in cerium and data on cerium strength within a wide strain range.

It should be noted that the research program implies sample recovery in a number of the above experiments for further material studies. Due to the high chemical activity of cerium, it is necessary to protect the samples from interaction with the environment and explosion products. For this purpose, the samples will be placed into air-tight capsules. Calculations will include the capsule components.

Loading with Sliding Detonation of the HE Layer

Problems of this type were considered in the 2-D planar geometry in the simplified statements shown in Figure 3. Simplified statement meant replacement of the actual wedge sample with a plane plate that significantly simplifies creation of a computational grid and increases simulation accuracy.

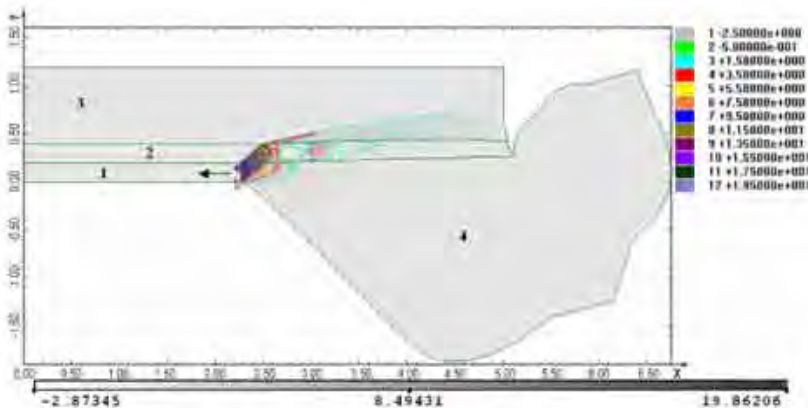


Figure 3. Statement of 2D problems for numerical simulation of the cerium samples loaded with sliding HE layer detonation. (1) HE, (2) a stainless steel lid of the air-tight capsule, (3) cerium, (4) detonation products. At the initial moment, normal detonation is initiated at the right boundary of the HE layer. Thicknesses of the lid h_c and HE layer h_{HE} varied. The sample in all simulations was $h_0 = 8$ mm thick. Cerium properties were modeled with EOS [3]. The figure shows system with $h_c = 2$ mm and $h_{HE} = 2$ mm at $t = 3.5$ μ s. Pressure in GPa is shown by different intensities of gray color (in the bottom of the figure) and pressure isolines (color scale in the right part of the figure).

A first series of simulations was carried out for the experiments with a thin layer of plastic HE. The simulated problems assumed the lid to be $h_c=2$ and 5 mm thick and HE layer $h_{HE}=0.5, 1, 2$, and 3 mm thick.

As shown in the Figure 3, the detonation wave creates a system of compression and rarefaction waves in the lid and sample that move along with the detonation wave front. The sliding nature of the lid loading leads to the “oblique” principal wave hitting the lid-sample interface and its traveling through the sample. Since cerium is less rigid than steel, a rarefaction wave is reflected inward the lid. Interaction with the HE detonation-induced rarefaction wave forms a tension area in the lid. The interaction between the reflected rarefaction wave with the HE detonation products causes reflection of the compression wave backwards into the lid. That compression wave moves into the sample and catches up the stress wave front in the sample affecting the character of attenuation. The sliding model of loading makes the above incident waves “oblique,” and therefore, areas of rarefaction and further compression in the lid are shifted in space. Analysis of the simulations shows that at small HE thicknesses, a “steady” mode of the stress wave propagation in the samples is quickly reached.

The second series of problems including the systems with cerium samples loaded with sliding detonation of thick ($h_{HE}=10\dots 20$ mm) layers of powerful HMX-containing HE. Unlike the previously considered systems with the thin HE layers, these problems show that there is not enough time for cerium particle loading to reach the steady mode. In the right part of the sample (which is closer to the detonation initiation area), wave amplitude is much lower than that in the remaining part due to its faster attenuation (loading pulse is shorter) and due to lateral unloading. Therefore, in addition to elastic precursor and principal plastic wave (in the main part of the sample), the wave structure includes a phase precursor.

Loading with Normal Detonation of HE Layer

This section discusses simulations of two groups of experiments differing by the energy of the HE layer. In the first group, loading is created with normal detonation of plastic HE of small thickness, $h_{HE}\approx 5$ mm. Lid thickness h_c of the air-tight capsule (made of stainless steel) varies in the experiments. To select optimal conditions of sample loading, other values of h_{HE} are considered close to the initial one.

In the second group of the experiments of this type, a capsule with a sample is loaded in a more intensive way with normal detonation of the thick layers of plastic and/or HMX-containing. Because of the more powerful loading, wave amplitudes in the samples correspond to the liquid phase in all cases, if melting curve data from [4] are used. However, taking into account possible uncertainties in the melting curve position, we performed simulation both within the hydrodynamic model and within the elastic-plastic one. Note that because of the small shear component of the stress tensor and lack of elastic precursor in the wave structure in the considered range of wave amplitudes, simulated effect of the shear component on the wave parameters proved to be small.

Loading with a Plate-Impactor

This type of loading is of interest, since it allows simultaneous study of two modes of stress wave propagation: steady, where the principal plastic wave front is followed by an area of constant flow (plateau), and nonsteady, when the pursuit wave of unloading is directly adjacent to the front. In the nonsteady mode, stress amplitude on the principal stress wave front attenuates. Problem parameters ($h_i=3.5$ mm, $W_i=0.8$ km/s, $W_i=1.1$ km/s) corresponded to the explosion-driven systems, creating minimum impactor velocity among other similar systems at RFNC-VNIITF.

Conclusion

Numerical simulations of a number of problems were carried out for the needs of the experiments with the cerium samples to be conducted at RFNC-VNIITF. Parameters of the loading systems and air-tight capsules were varied to obtain additional information to better define the optimal conditions for the experiments. The simulations show (see Figure 4) that the use of different ways of loading helps to “cover” the whole wave amplitude range of interest for the program of joint studies of cerium.

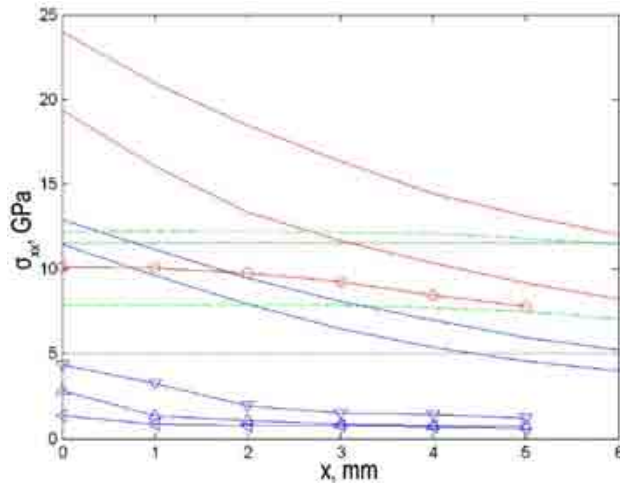


Figure 4. Summary data on the wave amplitude vs distance in the problems where samples are loaded in different ways. The lid is $h_c = 5$ mm thick. The EOS for cerium is [3]. Lines labeled with symbols correspond to the sliding detonation of powerful HE $h_{HE} = 10$ mm (circles) and of plastic HE $h_{HE} = 0.5, 1, \text{ or } 2$ mm (triangles). Solid lines correspond to the normal detonation of powerful HE $h_{HE} = 5$ or 10 mm (in red) and plastic HE $h_{HE} = 3$ or 5 mm (in blue). Green dashed lines correspond to the impact with a steel plate $h_l = 3.5$ mm moving at the velocity of $W_l = 0.8$ km/s or 1.1 km/s.

- Sliding detonation of a plastic HE $h_{HE} = 0.5$ mm. Deformation will run in the initial γ -cerium within the whole range of recording. Anomalous compressibility of the phase leads to an unusual two-wave (elastic precursor – principal plastic wave) structure of the stress wave with a smeared shock and a shock rarefaction wave within the unloading area.
- Sliding detonation of a plastic HE $h_{HE} = 1$ or 2 mm. Wave amplitudes will not exceed $\sigma_{max} = 5$ GPa. A three-wave (elastic precursor - phase precursor – principal plastic wave) structure of the stress wave will be observed within the whole measurement range.
- Normal detonation of a plastic HE layer $h_{HE} = 3$ or 5 mm. It will implement an intermediate range of wave amplitudes $\sigma_{max} = 5 \dots 12$ GPa. Cerium deformation will run in the solid phase. Parameters of the elastic precursor and principal plastic wave can be recorded. Note that our estimates of the melting region are based on the evaluated (with the use of EOS [3]) locations of the Hugoniot for cerium in the phase diagram and of the melting curve from [4].
- Normal detonation of a powerful HE $h_{HE} = 5$ or 10 mm. It will cover a range of maximum wave amplitudes $\sigma_{max} = 8 \dots 20$ GPa, which mainly fall into the liquid range.
- Sliding detonation of the thick ($h_{HE} = 10$ or 20 mm) layers of powerful HE and impact with the steel plates at the velocity of $W_l = 0.8$ km/s or $W_l = 1.1$ km/s implement conditions for cerium deformation that fall into the intermediate range of wave amplitudes $\sigma_{max} = 8 \dots 12$ GPa. Range of the wave amplitudes in these experiments actually reproduces the range of the wave amplitudes in the experiments with normal detonation of plastic HE layers. Simulations of the first of two types of experiments show the possible distortion of characteristics of the principal wave as it propagates in the sample because it is caught up by the perturbations resulting from the wave circulation in the capsule lid, perturbations being especially strong at $h_{HE} = 20$ mm. The experiments of the second type were of interest, since they can record both steady wave and transition to the nonsteady attenuating wave. This is important to “match” the results to be obtained at VNIITF with those recorded in LANL [1,2].

- The range of low wave amplitudes can be extended by adding the experiment with sliding detonation of the plastic HE layers having thickness of $h_{HE}=3$ mm for more reliable approach to the range of wave amplitudes created in the experiments with normal detonation of HE layers of the same yield. Another possibility for extending the range of wave amplitudes in the experiments of this type (sliding detonation of thin plastic HE layers) is related to the use of another material for the lid (for example, aluminum), the compressibility of which is closer to that of cerium. Such calculations were also performed.

Simulations show the possibility for the characteristics of the principal wave to be distorted because the wave is caught up by the perturbations formed in the lid. This perturbation, being a compression wave, is formed when the rarefaction wave, created when the principal wave passes through the lid-sample interface, reflects from the detonation products. The effect of catch-up is especially strong in the experiments with sliding detonation of powerful HE and with normal HE layer detonation, if the lid is thin. Numerical simulation of the experiments with sliding detonation of the plastic HE layers having a thickness of $h_{HE}=2$ mm at the lid thickness $h_c=5$ mm proves that the air-tight capsule lid can fracture. The areas of tensile stresses are created in the lid almost in all the considered experiments as a result of interaction of the rarefaction waves traveling from the detonation products and from the sample (cerium impedance is lower than that of steel). Simulations using EOS for cerium from [1] also indicate that the thick ($h_c=10$ mm) lid can fracture in the case of normal detonation of the HE layers. If EOS from [3] is used, intensity of the lid material tension decreases significantly and macroscopic fracture is not observed.

References

- [1] R. S. Hixson, D. L. Preston, W. W. Anderson, G. N. Chesnut, J. Cooley, G. T. Gray III, D. B. Hayes, V. I. Levitas, M. Manley, J. Smith, D. Thoma, J. E. Vorthman, *Report on Cerium Research for FY02*, LANL Report (2002).
- [2] F. J. Cherne, P. A. Rigg, W. W. Anderson, R. S. Hixson, Cerium windowed experiments. Private communication (see also Presentation LA-UR-06-4898).
- [3] V. M. Yelkin, E. A. Kozlov, E. V. Kakshina, and Yu. S. Moreva, "Two-phase (γ, α) equation of state for cerium and features of its dynamic compression," *AIP Conf. Proc.* **845** (2006) pp. 77-80.
- [4] B. Sitaud, J. Pere, and Th. Theverin, Melting curve determination for cerium up to 30 GPa, *AIP Conf. Proc.* **309** (1993) pp. 245-247.
- [5] V. F. Kuropatenko, G. V. Kovalenko et al., VOLNA code package and heterogeneous difference computational technique for non-steady flows of compressible continuous media," *Issues of Atomic Science and Technologies, series Mathematical Simulation of Physical Processes*, No. 2 (in Russian, 1989) pp.9-25.
- [6] V. A. Bychenkov and V. V. Gadjiyeva, "SPRUT computational technique for two-dimensional non-steady flows of decomposable media," *Issues of Atomic Science and Technologies, series Techniques and Codes for Numerical Solution of Problems in Mathematical Physics*, 2 No. 2 (in Russian, 1978).

PREDICTIONS FROM THE EQUATION OF STATE OF CERIUM YIELD INTERESTING INSIGHTS INTO EXPERIMENTAL RESULTS

F. J. Cherne,* B. J. Jensen,* P. A. Rigg,* and V. M. Elkin,†

*Los Alamos National Laboratory, Los Alamos, New Mexico, 87545 USA.

† Russian Federal Nuclear Center—All-Russia Research Institute of Technical Physics, Snezhinsk, Russia

Author Contact: Cherne@lanl.gov

There has been much interest in the past in understanding the dynamic properties of phase changing materials. In this paper, we begin to explore the dynamic properties of the complex material of cerium. Cerium metal is a good candidate material to explore capabilities in determining a dynamic phase diagram on account of its low dynamic phase boundaries, namely, the γ - α , and α -liquid phase boundaries. We present a combination of experimental results with calculated results to try to understand the dynamic behavior of the material. Using the front surface impact technique, we performed a series of experiments that displayed a rarefaction shock upon release. These experiments show that the reversion shock stresses occur at different magnitudes, allowing us to plot out the γ - α phase boundary. Applying a multi-phase equation of state a broader understanding of the experimental results will be discussed.

Introduction

Cerium is a complex material with an interesting phase diagram. Cerium exhibits anomalous melting at low pressure yet the dynamic melt boundary is somewhat uncertain at this time. There are seven known allotropic phases of cerium. The γ - α phase transition at room temperature shows an isomorphic volume collapse of 17% [1, 2]. This behavior has been shown to be an electronic transition [3]. It could be the only material that exhibits a solid-solid critical point where the isomorphic volume collapse decreases to 0%. It exhibits a complicated f-electron behavior. The material as it approaches the low-pressure solid-solid phase boundary exhibits a negative derivative of the bulk modulus with respect to pressure.

In studying cerium, we hope to validate a multi-phase equation of state with experimental evidence. It has been known that cerium as a result of the low pressure phase transition dynamically shows a two wave character indicative of the $\gamma \rightarrow \alpha$ phase transition [4]. One of the co-authors here presented the framework for a multi-phase equation of state that characterized the region between the γ and the α phases [5,6] based on some early thermodynamic work of Aptekar and Ponyatovskiy [7,8]. Therefore, in this paper, we show how use of the model combined with experiments yielded insights into this very interesting metal.

Model

The model is constructed based on the common Helmholtz free energy formation. The energy is written as a sum of three terms:

$$F(V,T) = F_c(V) + F_H(V, T) + F_{AE}(V, T) - S_{tr}T \quad (1)$$

where F_c is the “cold” energy given by a modified Vinet et al. equation of state [9,10]; F_H is the quasi-harmonic phonon free energy described by the Debye approximation; F_{AE} is the joint contribution to the free energy from the anharmonic lattice vibrations and the thermally excited electrons; and S_{tr} is an entropy component that allows for entropy changes during phase transitions. On account of the character of the low pressure phase transition of the γ - α phase boundary, namely. the material getting softer as one approaches the phase boundary, the Aptekar-

Ponyatovsky model was included. This model can be considered as a binary alloy model for the γ - α phases, and the Gibbs potential energy is written in the form:

$$G_{\gamma\alpha} = G_{\alpha} X_{\alpha} + G_{\gamma} X_{\gamma} + G_{\text{mix}} X_{\alpha} X_{\gamma} + TS_{\text{conf}} \quad (2)$$

Here G_{α} and G_{γ} are the thermodynamic potentials for the pure α and the γ phases; G_{mix} is a thermodynamic mixing potential; S_{conf} is the configurational entropy of the system; and T is temperature. The G_{mix} term is a function selected such that it is only dependent upon T and is given by the following:

$$G_{\text{mix}}(T) = G_{\text{mix}}^0 [1 + \theta_1/T + (\theta_2/T)^2] \quad (3)$$

where G_{mix}^0 , θ_1 , and θ_2 are adjustable parameters which are selected that the critical point is obtained. For a more thorough description of the model and the variables used we refer the reader to the paper by Elkin et al. [5,6].

Experimental Setup

We conducted a series of front-surface impact experiments. The experimental configuration consisted of a high-purity cerium sample backed by foam impacting an aluminum coated window. The windows were either lithium fluoride or z-cut sapphire. Particle velocity profiles were obtained at the cerium/window interface using the standard push-pull velocity interferometer system for any reflector (VISAR) system with a time resolution of approximately 1 ns. The wave profile data combined with measured projectile velocity and the known shock response of the window materials provided the stress history at the interface.

The VISAR optical windows were well-characterized, high-purity Hemlux grade z-cut sapphire samples obtained from Crystal Systems. Sapphire and LiF window materials were chosen as optical windows for this work because of the well-characterized optical and shock wave properties. All windows were polished on both sides and were flat and parallel to 0.0002 in. The nominal thicknesses of the windows were 19 mm. The nominal density of the lithium fluoride was 2.638 g/cc, and the sapphire was 3.985 g/cc.

The cerium used for these experiments were nominally 1 mm or less. The specimens were prepared from starting materials having a nominal purity of 99.99 % with respect to metals. The major nonmetal impurity was oxygen at the 1000 ppm level. The processing steps allowed for a final grain size of approximately 50 microns. The samples were lapped flat to the desired thickness and mounted into the projectile.

Results and Discussion

Four front surface impact shots were performed on cerium for this work. In Figure 1, we show two front-surface impact shots where we observe a rarefaction shock wave upon release. For illustration purposes, these are representative curves for the experiments performed. The wave profiles illustrate several features that we would like to point out: the initial shock at t_0 , a steady state, an isentropic release, and a rarefaction shock. The lower pressure shot shows a partial elastic release of the material as well.

Using the cerium multi-phase equation of state, we calculated the release isentropes for each of the experiments performed using the measured stress state as a starting point. Great care was taken when developing this multi-phase equation of state for cerium to replicate the measured bulk sound speed response of cerium through the γ - α phase transition. Using the Rankine-Hugoniot jump conditions and the model, we determined the temperature. Figure 2 shows the calculated release states for the two experiments shown in Figure 1. Following the calculated release isentrope, we determine the transition pressure to be the point where the minimum in the calculated bulk sound speed as a function of pressure occurs. The calculated temperature and pressure state where the minimum occurs is presented in Table 1 for all the experiments performed using the front-surface impact technique. In

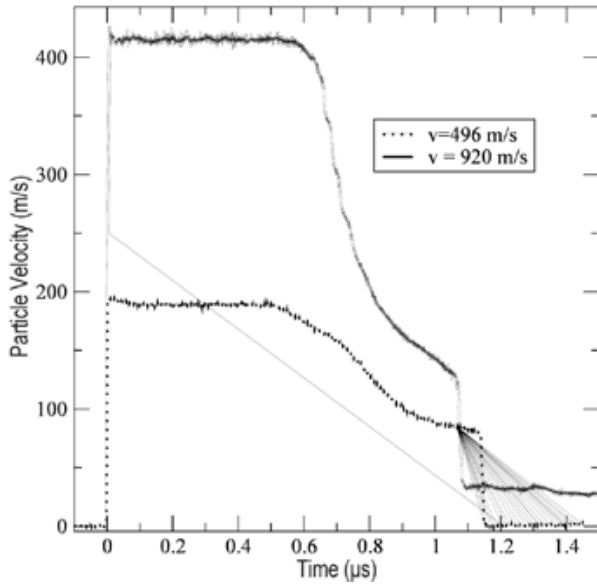


Figure 1. VISAR traces for two representative experiments using the front-surface impact technique at velocities of 498 m/s and 921 m/s.

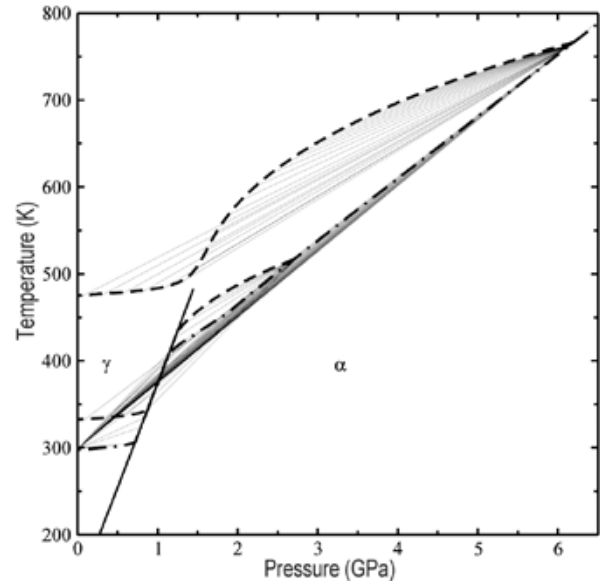


Figure 2. Calculated release isentropes for each of the experiments shown in Figure 1.

Table 1 and Figure 2, three of the four experiments have temperatures and pressures that fall above the solid-solid critical point in temperature.

Experiment 56-08-11 used sapphire as a window material, and the measured velocity at the transition was very low. This could account for measured reversion stress being lower than the reported room temperature phase transition stress upon shocking cerium using a transmission kind of geometry (known impactor material hitting a cerium sample glued to a window material) [4]. All the front surface impact shots performed below the melt transition in cerium show a rarefaction shock. Only one of the experiments falls into the region where we expect to observe a volume expansion or the first order phase transitions of $\alpha \rightarrow \gamma$. The difference in shock velocity and sound speed variation in the material whether the material undergoes a first order or a second order phase transition provides for the generation of a rarefaction shock wave to be observed. This observation confirms the condition that a rarefaction shock will form if $(d^2P/dV^2)_s < 0$ [11].

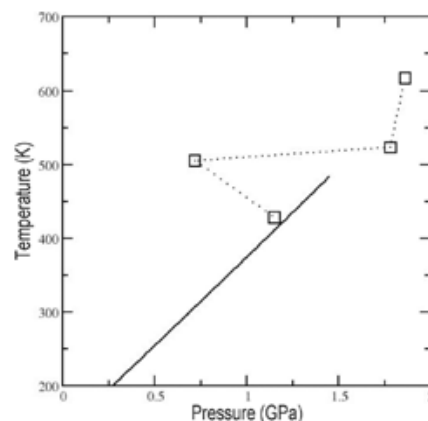
Table 1. Calculated transition pressure and measured transition pressure for all of the experiments performed.

| Experiment | Measured Impact Stress (GPa) | Measured reversion stress (GPa) | Calculated reversion stress (GPa) | Calculated reversion temperature (K) |
|------------|------------------------------|---------------------------------|-----------------------------------|--------------------------------------|
| 56-06-25 | 2.7 | 1.15 | 1.22 | 428 |
| 69ss-06-15 | 6.2 | 1.78 | 1.57 | 523 |
| 69ss-09-04 | 8.1 | 1.86 | 1.89 | 617 |
| 56-08-11 | 5.8 | 0.719 | 1.51 | 505 |

Examining the values of the measured versus predicted from the model reversion stresses, we see a remarkable agreement from the model and the experiment. On account of this agreement, we plot in Figure 3 a predicted phase diagram using the temperatures found from the calculations and the measured reversion stresses reported above. Future work to actually measure temperature on the phase boundary line using a transmission shot should be considered to better pin down the phase transition temperature. One could conceive of using a well-controlled heated cell over a finite temperature range experiment that would allow one to measure the transition stress

combined with the pyrometry, although for these low temperatures making such temperature measurements is very difficult. Therefore, we will have to accept a well-characterized multi-phase equation of state as the way to infer what the temperatures may be across phase boundaries.

Figure 3. Plot of the reversion stresses versus calculated temperature. The solid black line is the phase line between α and γ phases. The dashed lines and the symbols represent the measured reversion stress with the reversion temperature.



Conclusions

It has been long assumed that a volume expansion is necessary for the formation of a rarefaction wave. In the particular case of cerium where the change in volume across the phase boundary disappears although there is a marked minimum in the sound speed as a function of pressure, rarefaction shocks appear. Using the experimentally determined stresses and marching down the isentropic release, calculating sound speed shows a minimum. The stress state and temperature can be determined from the equation of state and, for three of the four experiments, shows an excellent agreement with the experimental reversion stress state. The fourth experiment, which used a sapphire window, has a lower reversion stress state than the measured phase transition stress starting from room temperature, which implies that this data point needs to be revisited.

Acknowledgements

This work was performed under the auspices of the U.S. Department of Energy by the University of California Los Alamos National Laboratory under contract No.DE-AC52-06NA25396.

References

- [1] A. R. Kutsar, "Position of the critical point of the isomorphous γ in equilibrium α phase transition in cerium," *Fiz. Metal. Metalloved.* **33** 1104-1108 (1972).
- [2] A. Schiwek, F. Porsch, and W. B. Holzapfel, "High temperature-high pressure structural studies of cerium," *International Journal of High Pressure Research* **22** 407-410 (2002).
- [3] A. Fujimori and J. H. Weaver, "4f-5d hybridization and the α - γ phase transition in cerium," *Phys. Rev. B* **32** 3422-3428 (1985).
- [4] M. N. Pavlovskii, V. V. Komissarov, A. R. Kutsar, "Isomorphic $\gamma \rightarrow \alpha$ phase transition of cerium under shock compression," *Combustion, Explosion, and Shock Waves* **35** 88-91 (1999).
- [5] V. M. Yelkin, E. A. Kozlov, E. V. Kakshina, Y. S. Moreva, "Two-phase (γ, α) equation of state for cerium and features of its dynamic compression," *Shock Compression of Condensed Matter-2005, AIP Conference Proceedings*, eds. M. D. Furnish, M. Elert, T. P. Russell, and C. T. White (Melville, NY, AIP, 2006) pp. 77-80.
- [6] V. M. El'kin, E. A. Kozlov, E. V. Kakshina, Y. S. Moreva, "Equation of state and the dynamic compression of cerium in the range of the γ - α phase transition," *Phys. of Met. and Metallogr. USSR* **101**, Issue 3, 208-217 (2006).
- [7] I. L. Aptekar. and E. G. Ponyatovskiy, *Phys. Met. Metall.-USSR* **25** 10-20 (in Russian, 1968).
- [8] I. L. Aptekar and E. G. Ponyatovskiy, *Phys. Met. Metall.-USSR* **25** 93-100 (in Russian, 1968).
- [9] P. Vinet, J. H. Rose, J. Ferrante, J. R. Smith, "Universal features of the equation of state of solids," *J. of Phys.: Condensed Matter* **1** 1941-1963 (1989).
- [10] J. H. Rose, J. R. Smith, F. Guinea, J. Ferrante, "Universal features of the equation of state of metals," *Phys. Rev. B* **29** 2963-2969 (1984).
- [11] Ya. B. Zeldovich and Yu. P. Raizer, *Physics of Shock Waves and High-Temperature Hydrodynamic Phenomena* (New York, Academic Press, 1966).

FEATURES OF CERIUM COMPRESSIBILITY AND SPALL STRENGTH IN THE (γ – α) PHASE–TRANSFORMATION REGION UNDER EXPLOSIVE LOADING

V. I. Tarzhanov,[†] E. A. Kozlov,[†] Yu. N. Zuev,[†] D. G. Pankratov,[†]
 I. V. Telichko,[†] A. N. Grachev,[†] D. M. Gorbachev,[†] A. V. Vorobyev,[†]
 Yu. S. Moreva,[†] E. V. Kakshina,[†] N. A. Tsepilov,[†] E. A. Shmakov,[†]
 N. V. Ivanova,[†] M. A. Zocher,[‡] G. T. Gray III,[‡] F. J. Cherne[‡]

[†]FSUE “RFNC-VNIITF”, Snezhinsk, Chelyabinsk Region, Russia

[‡]Los Alamos National Laboratory, Los Alamos, USA

Author Contact: V.I.Tarzhanov@vniitf.ru

The streak photography optical lever technique helped to obtain new data on the structure of stress waves in wedge samples of high-purity cerium. Data on amplitudes behind the wave front were used to construct cerium compressibility curves under high-rate deformation occurring in the initial γ -phase, as well as in the range of “ γ – α ” and “ α -liquid” phase transformations in cerium. Wave profiles for the free surface velocity of samples were used to determine the spall strength of cerium (0.2–0.4 GPa), which depends on the stress gradient in the tensile range.

Introduction

Cerium is an element that has a very complicated phase diagram [1,2]. Dynamic (shock-wave and explosive) experiments with the samples of metal cerium, and especially high-purity (99.99 %) cerium, are few [3-9].

The objectives of this work are as follows:

- refinement of data on compressibility of high-purity cerium under its explosive loading in the range of the γ – α - and α -liquid phase transformations;
- registration of wave profiles that demonstrate kinetics of high-rate deformation of cerium in the initial γ - phase and kinetics of the γ – α - electron phase transformation;
- determination of spall strength of cerium in the test range of longitudinal stress.

Material, Samples and Explosive Loading Conditions

For investigative purposes, one experiment used high-purity cerium (99.99%) with an initial density of 6.75 g/cm³. Eight wedge samples (30×40×6 mm³ with 12°00' angle) were made from special thermomechanically processed sheet blank with 6-mm thickness. The material had a single-phase initial structure and 100- μ m size of equiaxed grains. The free surface of wedge samples was ground and polished, and after ionic cleaning, a 10- μ m thin cooper layer was applied to it by the vacuum-deposition technique; then this layer was polished up to the required mirror state.

Four loading modes and two types of high explosives (HE) were used to create stress waves with 1 to 16 GPa amplitudes in the samples. Samples were loaded by sliding detonation of HE placed directly on the samples surface, as well as by normal detonation through the steel membrane (12Kh18N10T) with a thickness of 5 to 7 mm (Figure 1). In the case of the sliding loading, detonation propagated in the direction both from the “heel” and from “tip” of the sample. Plastic-bonded explosive based on PETN with a thickness of 0.7 to 5 mm, as well as HMX-based explosive with a thickness of 10 and 20 mm, were used.

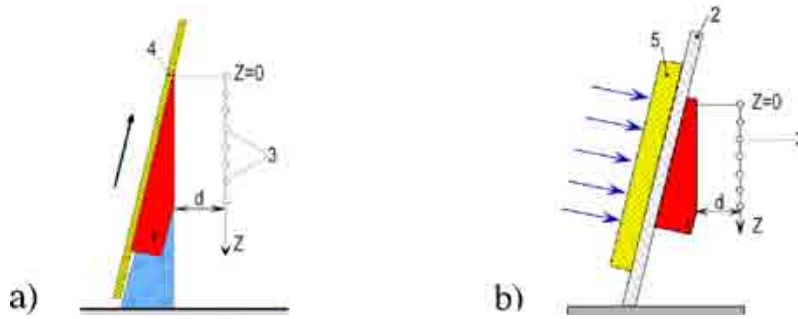


Figure 1. Schematic diagrams of experiments on loading of wedge samples with (a) sliding or (b) normal detonation of HE layers of different power and thickness. (1) tested sample, (2) driver plate, (3) slit aperture system (scan pattern) illuminated by explosive light source, (4) layer of plastic HE, which detonates in sliding mode, (5) PETN- or HMX-based HE layer, which detonates in a direction orthogonal to screen-cover surface.

Recording Technique and Streak Camera Records

Time profiles of free surface velocity for wedge samples and wave velocity in them were recorded by the photochronographic optical lever technique [10,11]. This technique supports in each experiment 5 to 10 analogous optical tracks with spatial and time resolution of 0.01 mm and 10 ns using an SFR-2M streak camera (Figures 1 and 2).

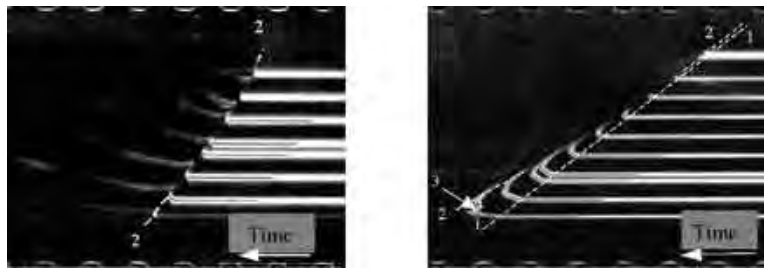


Figure 2. Streak camera records of experiment #638 and #646. Loading: (a) normal detonation of plastic HE layer, $h_{HE}=5.0$ mm, (b) sliding detonation of plastic HE from sample "tip", $h_{HE}=0.99$ mm. Optical lever – 30.0 mm. Film scanning rate is 3.75 mm/ μ s. 1-1 – elastophase precursor, 2-2 – principal plastic wave, 3 – "X"- wave.

Results and Discussion

Three-wave and single-wave structures of cerium compression were recorded in the realized range of samples loading.

Data on Cerium Compressibility

Cerium compression curves (Figures 3 and 4) presented in $D(u_p)$ - and $\sigma_{xx}/V/V_0$ -coordinates are typical for materials with phase transformation and elastic behavior at low σ_{xx} .

The rate of elastic precursor (EP) in cerium was 2.35 ± 0.02 km/s. Maximum and minimum rates of phase precursor (PP) were equal to 2.1 and 1.7 km/s at $\sigma_{xx}^{max} = 0.6$ and 0.8 GPa with wedge thickness of $x=2.2$ and 4.6 mm. The achieved minimum velocity of plastic wave was $D_3^{min}=1.0$ km/s (in laboratory coordinate system). In the coordinate system associated with PP, the velocity is 0.84 km/s. This velocity can be treated as an estimate of the space velocity of sound in heated and loose α -phase formed on the width of plastic wave front.

Dotted lines in Figure 3 present the boundaries of cerium regions, in which the single-wave, two-wave elastoplastic configurations, as well as three-wave configurations corresponding to the region of the mixture of γ - and α -phases should exist. The boundaries were determined on the condition that plastic wave velocity and velocity of elastic and phase precursors are equal, but in experiments, two-wave configurations were not recorded in region II. The reasons for their absence on the streak camera records are kinetic, and they will be discussed later.

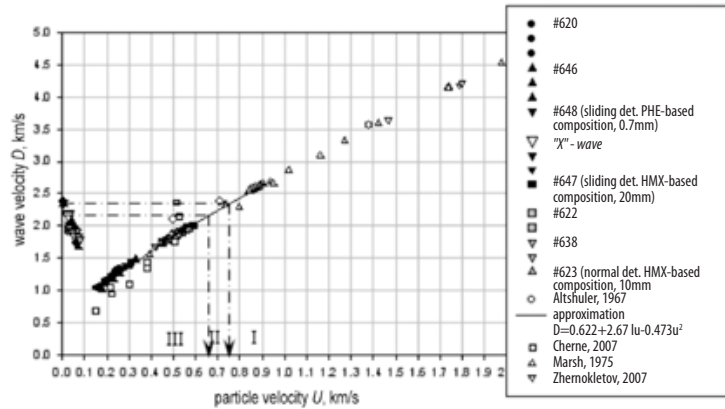


Figure 3. D-rates of propagation of axial stress amplitude values on fronts of the three-wave and single-wave configurations in cerium vs. mass velocities u .
(1, 2) states on elastic and phase precursors, (3) states on plastic wave.
(I, II, III) regions of single-wave, two-wave, and three-wave configurations.

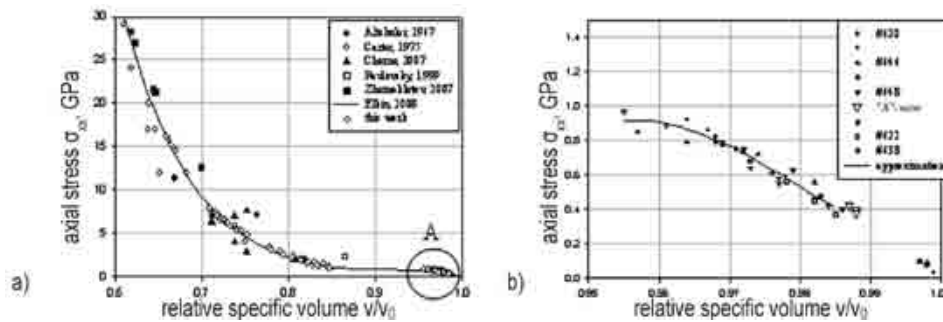


Figure 4. Amplitude values of axial stress σ_{xx} vs. relative specific volume V/V_0 .
(a) full measurement range (b) area A, enlarged.

The curve of cerium compression in coordinates $\sigma_{xx}, V/V_0$ in the region $\sigma_{xx} < 1$ GPa is convex upwards. Just this convexity provides an increase in amplitudes of phase precursor as σ_{xx} is decreasing in the plastic wave. The best separation between the phase precursor and plastic wave having similar wave velocities is achieved with the minimum loading amplitude realized in wedge samples on the maximum wedge thickness. The phase precursor is capable of maximum forward running and demonstration of its profile maximum.

The data on high-purity cerium compressibility obtained at VNIITF agree well with analogous laser-interferometric data obtained in Los-Alamos Laboratory for the metal of the same purity [7]. These data are characterized by a relatively small scatter of points. They agree well with the shock adiabat in the α -region and with isentropes in the region of the mixed γ - and α -phases from the multi-phase equation of state for cerium, which was derived by V. M. Elkin, et al. [8] using only static data.

The absence of specifics on the cerium-compression curve, which could be indicative of $(\alpha-\epsilon)$ transformation, confirms the theoretic prediction [8] that this curve has no intersection with the boundary of α - and ϵ -phases.

Experimental points at $\sigma_{xx}^{max} = 14-16$ GPa possibly lie near the boundary inside the cerium melting region on the shock adiabat and this is indirectly evidenced by sharp falloff in intensity of the light reflected from the sample free-surface.

Profiles of the Elastophase Precursors

All three-wave configurations recorded in experiments contain the principle plastic wave and the merging elastic and phase precursors characterized by smoothly growing stress.

Particle velocity profiles obtained from tracings of streak records for free surface velocity $W(t)$ bear information on kinetics of elastic precursor, as well as on kinetics of the $(\gamma - \alpha)$ transformation and relaxation of stresses in cerium (Figure 5).

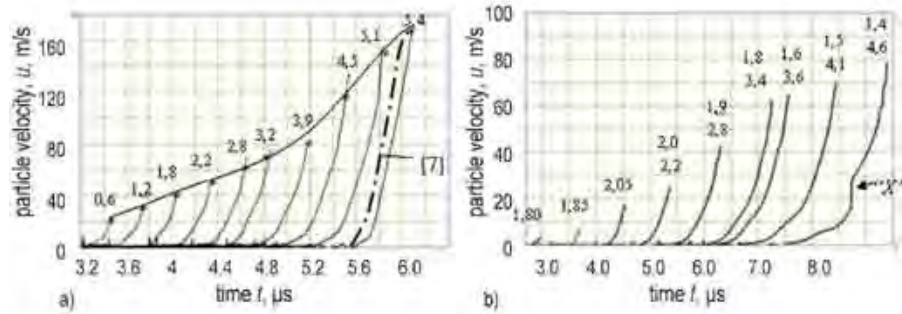


Figure 5. Mass velocity profiles for cerium sample in elastoplastic precursor, exp. #638(a), #636(b). The above curve is approximation of the maximum states on the phase precursor. Figures above curves show sample thickness in mm, the upper line of figures – is amplitude σ_{xx} in GPa.

The characteristic points correspondent to the maximum axial stresses in each wave of configuration are clearly seen as slope breaks on the profiles. The growth of phase precursor amplitude with the decrease of σ_{xx} in the plastic wave (also registered in [7-10]) is observed when the sample thickness increase.

The form of profiles $u_p(t)$ is qualitatively consistent with the form recorded earlier [7] by VISAR technique.

It is obvious that elastic precursor profile smoothly grows up to its maximum parameters $u_{pmax}^{EP} = 6$ m/s, $\sigma_{xx}^{EP} = 0.1$ GPa. In this work, absence of the two-wave elastoplastic structure of compression in streak camera records is associated with low growth of stresses. In the predicted region II of this structure (Figure 3), the stress growth in the elastic precursor turns out to be lower than in the optical lever method resolution even though the rate of the elastic precursor and plastic waves is almost the same and the run of the elastic wave is small.

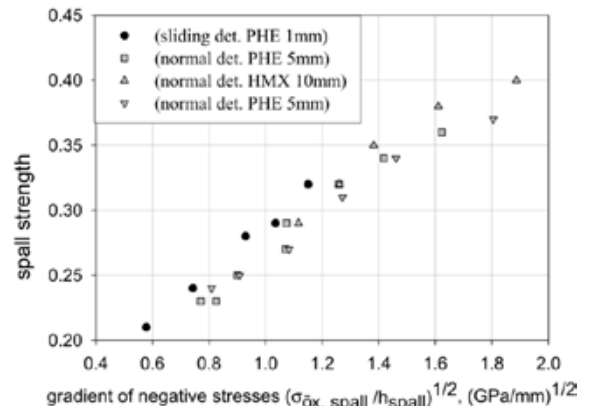
The merging of elastic and phase precursors is explained by kinetics slowness of stress growth in elastic precursor, as well as by the fact that their wave velocities are almost the same. However, we succeeded in recording the separation of the elastic and phase precursors in the bottom range of stresses at $\sigma_{xx} = 0.6 - 1.6$ GPa and wedge thickness of 3.5 to 5 mm. This separation is accompanied by extraction on the phase precursor tip of the shock front with $\sigma_{xx}^{max} = 0.4$ GPa (Figure 2(b)). The neighborhood of this shock front is referred to as the “X” wave. The reason for shock front extraction is the increase of the phase precursor amplitude and slope.

Spall Strength of Cerium

In the tested range of axial stresses, we determined that the spall strength of cerium σ_{xx}^* turned out to be rather low and variable in the range $\sigma_{xx}^* = 0.2-0.4$ GPa. The obtained values of spall strength agree with the data of [12]. Thickness of spall layers calculated from the streak camera records was 0.2 to 0.4 mm. The spall plates of the same thickness were found among the sample fragments recovered in the chamber.

Figure 6 illustrates a correlation between spall strength and the gradient of negative stress in the spall plane

Figure 6. Spall strength vs. gradient of negative stresses in spall plane.



Conclusions

1. The optical lever method was used to obtain new data on compressibility of high-purity cerium explosively loaded in the range $\sigma_{xx} = 0.6\text{--}16$ GPa with the high-rate deformation occurring in the initial γ -phase, as well as in the range of “ γ - α ” and “ α -liquid” phase transformations. These data are in good agreement with the published results and have smaller experimental scatter. The theoretical absence of intersection between the shock adiabat and the line of α - ϵ -phase equilibrium was experimentally confirmed. At $\sigma_{xx} = 14\text{--}16$ GPa, the optical lever method registered a sharp falloff in intensity of the light reflected from the free surface of the sample. This falloff can be conditioned by the shock-wave melting of cerium.
2. Registered profiles of stress waves in wedge samples of high-purity cerium demonstrate existence of one common elastophase precursor before the plastic wave front at $\sigma_{xx} \leq 7$ GPa. Amplitude of this common complex increases up to 0.9 to 1 GPa with the decrease of loading level down to 3 to 4 GPa. Separation of the α -phase and elastic precursors takes place at the bottom levels of loading ($\sigma_{xx} = 2\text{--}3$ ГПа) with the shock front extracted at the phase precursor tip.
3. Spall strength of cerium determined from wave profiles for the velocity of sample free surface is rather low (i.e., 0.2 to 0.4 GPa). It depends on the gradient of the longitudinal stress in the tensile region. Thickness of the first spall is 0.2 to 0.4 mm.

References

- [1] E. A. Kozlov, V. M. Elkin, A. V. Petrovtsev et al. *Behavior and Properties of Unalloyed High-Purity Cerium. Review of Experimental and Theoretic Information By Phase Diagram, Thermodynamic and Elastic Properties, and Phase Transformations Under Shock Loading, Shear Stresses, and Wave Profiles in Cerium*, RFNC-VNIITF Report, PS04.9179 (2004).
- [2] V. M. Elkin, E. A. Kozlov, E. V. Kakshina, Yu. S. Moreva, “Equation of state for cerium and features of its dynamic compression in γ -transition region,” *FMM*, **101** 2 (2006) [*Phys. Met. and Metall.* (Engl. transl.) **101** 3 208–217 (2006)].
- [3] L. V. Altshuler, A. A. Bakanova, I. P. Dudoladov, “The effect of electronic structure on metal compressibility at high pressures,” *ZHTF* **53** 6 1967 (1967).
- [4] W. J. Carter, J. N. Fritz, S. P. Marsh, and R. G. McQueen, “Hugoniot equation of state of the Lantanides,” *J. Chem. Phys. Solids* **36** 741–752 (1975).
- [5] M. N. Pavlovsky, V. V. Komissarov, A. R. Kutsar, “Isomorphic $\gamma \rightarrow$ phase transition of cerium under shock compression,” *Fizika Gorenia i Vzryva (Physics of Combustion and Explosion)* **35** 1 98–101 (1999).
- [6] M. V. Zhernokletov, A. E. Kovalev, V. V. Komissarov, M. G. Novikov, M. A. Zocher, F. J. Cherne, “Measurement of Sound Velocities and shear strength of cerium under shock compression,” *Proceedings of Joint 21st AIRAPT and 45th EHPRG International Conference on High Pressure Science and Technology*, ed G. G. N. Angilella, R. Pucci, F. Siringo (Catania, Italy, September 17–21, 2007, Abst. 0420) pp. 424–428.
- [7] F. J. Cherne, P. A. Rigg, B. J. Jensen, W. W. Anderson, G. N. Chesnut, D. B. Hayes, M. D. Knudson, “Experimental studies of Cerium,” in *IX Khariton Talks, March 12–16, 2007* (Sarov, RFNC-VNIIEF, 2007).
- [8] V. M. Elkin, V. N. Mikhaylov, T. Yu. Mikhaylova, “Multiphase (α, γ, ϵ , liquid) equation of state and features of cerium shock compression,” *VIII International Workshop Fundamental Plutonium Properties, September 8–12, 2008* (Snezhinsk, Russia, 2008).
- [9] V. A. Borisenok, V. G. Simakov, V. A. Volgin, V. M. Belsky, M. V. Zhernokletov, “Study of phase transitions in iron and cerium by PVDF gauge,” *Fizika Gorenia i Vzryva (Physics of Combustion and Explosion)* **43** 4 121–126 (2007).
- [10] G. R. Fowles, *J. Appl. Phys.* **32** 8 1475–1487 (1961).
- [11] E. A. Kozlov, “Shock adiabat features, phase transition macrokinetics and spall fracture of iron in different phase states,” *High Pressure Research* **10** 541–582 (1992).
- [12] V. A. Pushkov, V. A. Ogorodnikov, S. V. Erunov, “Crack resistance and spall strength of cerium at dynamic loading,” in *IX Khariton Talks, March 12–16, 2007* (Sarov, RFNC-VNIIEF, 2007) pp. 232–233.

STUDY OF PHASE TRANSITIONS IN CERIUM AND TITANIUM BY PVDF GAUGE

V. A. Borisenok,* V. G. Simakov,* M. V. Zhernokletov,*
M. A. Zocher,[†] and F. J. Cherne[†]

* All-Russia Research Institute of Experimental Physics (VNIIEF),
Sarov 607190, Russia

[†]Los Alamos National Laboratory, Los Alamos, NM 87545 USA

This paper examines phase transitions in cerium and titanium during shock compression using PVDF gauges. A two-wave structure was observed with loading pressures of $4 \text{ GPa} \leq P < 12 \text{ GPa}$. The wave structure consists of a leading isentropic compression wave followed by a shock wave. This wave structure was formed in cerium as a result of the isomorphic (γ - α) phase transition. Analysis of structures of shock wave and rarefaction wave in the range of $(0.6 \div 3.0) \text{ GPa}$ testifies to the fact that a shock wave of rarefaction is formed in the release phase in cerium. An anomaly was revealed in titanium under a loading pressure of $\sim 21 \text{ GPa}$ at the profile of plastic wave at a pressure of 11.5 GPa . The reason for the anomaly was the $\alpha \rightarrow \omega$ phase transition.

Introduction

For some solids, the propagation of shock waves of sufficient strength leads to phase transitions resulting in changes to the crystalline structure. Among the most interesting of challenges in shock wave physics is gaining a clear understanding of phase transitions on the short timescales ($\sim 10^{-7} \text{ s}$) of the experiment. It is of special interest to probe the kinetics of the phase transitions to obtain a realistic picture of the phenomenon.

In accordance with Contract #37713-000-02-35 (TO #23, #035) between VNIIEF (Russia) and Los Alamos National Laboratory (USA), VNIIEF researched pressure profiles, sound velocities, and temperatures for metals and organic and inorganic compositions, where phase transitions are possible at shock compression and release. This presentation includes results of the research with cerium and titanium.

Cerium has extraordinary properties in comparison with many other metals. Among the properties is existence of a critical point in a solid state in the isomorph transformation line (γ - α), abnormal behavior of compressibility, heat expansion, thermal capacity, etc. The specificity of cerium characteristics is associated with the peculiar changes of its electron structure at compression. A complicated phase diagram of cerium is responsible for formation of a multiline structure, realized both at its shock compression and at oncoming release [1].

One of the objectives of this work was experimental research of wave profiles in cerium during shock compression followed by release, including in the area of direct (γ - α) and reverse (α - γ) phase transitions.

The other objective of this contract is research of (α - ω) phase transition in titanium. This polymorphous transition was researched in the conditions of both static and dynamic pressures. Pressures of phase transition of titanium, which are obtained by an explosive loading method, are characterized by large scatter of experimental data from ~ 2 to $\sim 12 \text{ GPa}$. Concentration of impurities in material and the conditions of loading of it are believed to be the main reasons of this scatter.

Experimental Setup

Shock compression of cerium was performed by two methods. Shock compression experiments with cerium were performed in the pressure range of 3.8 to 12 GPa. In both cases, electrolytic cerium with a purity of 99.83% and densities of 6.75 g/cm^3 was used. Contents of the other elements (mass %) were La (0.07%), Nd (0.05%), Fe (0.02%).

In the pressure range of 3.8 to 12 GPa, HE-based generators of shock waves were used. The sample was placed between a multilayer screen and a disk made of fluoroplastic 10 mm thick, and it was loaded by a plane-wave device. A PVDF gauge (piezopolymer gauge of pressure) 20 μm thick and an operational zone area of 4 mm^2 was placed at the sample-fluoroplastic interface. A shock wave was formed in the screen by the action of TNT explosion products (loading was through an air gap of 5 mm). The gauge signal was recorded by digital oscilloscope TDS 5052. Electric charge density dependence generated by the gauge as a function of time was determined from current integration. Then, using the characteristic amplitude, we determined pressure as a function of time, $P(t)$.

At pressures lower than 3 GPa, the experiments with cerium were performed with use of a ballistic facility based on a light-gas gun. Helium is used as a working gas in the gun. The facility is equipped with a laser device intended for shell velocity measurement and an equipment complex intended for the technique of PVDF gauge.

Tests with shock compression of titanium were performed in pressure range of 10.5 to 26.2 GPa. Technically pure titanium of the type VT1-0 (99.3 weight% Ti) was used. To study wave structures in titanium samples, we used a set of explosive generators of shock waves.

The applicability of PVDF gauges in studying phase transitions in metals was proven by performing calibration experiments with samples of iron [2]. Using a similar experimental setup at a loading pressure ~ 28 GPa, the shock wave was measured in iron. The wave structure of this system and the profiles of the resultant shock waves were in agreement with data obtained using laser interferometry [3].

Experimental Results

Cerium

As an example, Figure 1 shows the results of explosive experiment with cerium at peak loading pressure of 3.8 GPa. From the figure, it is apparent that when loading a sample with a pressure profile that is approximately step function in nature (initial time dependence of the pressure (a) from zero to t_1 where t_1 is $\sim 1.5 \mu\text{s}$), a multi-wave pressure pulse is formed in the sample. This pulse consists of a gradually increasing “nose” followed by a shock wave. Several experiments conducted at different levels of pressure reveal that the nose duration decreases with increasing pressure. At shock wave pressures greater than ~ 12 GPa in cerium, the nose disappears.

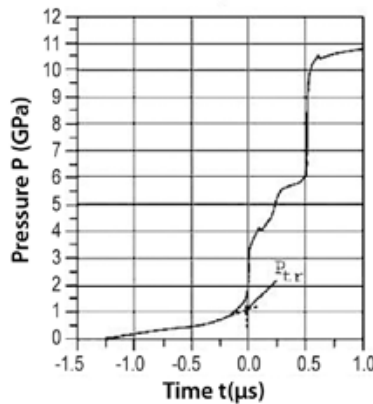


Figure 1. Results of experiment at pressure of 3.8 GPa is the pressure in the cerium sample.

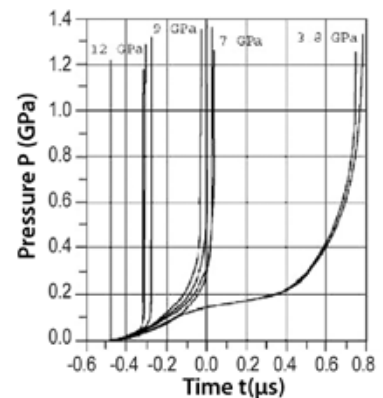


Figure 2. Initial parts of the pressure profile in cerium under various loading conditions ranging from 3.8 to 12 GPa.

Figure 2 shows the initial parts of the pressure-time dependencies recorded in all experiments, with tests conducted at a variety of loading pressures. Each curve is the result of a separate measurement.

The authors of [1] created a thermodynamically complete two-phase equation of state for cerium describing its dynamic compression. Using this equation of state, and accounting for the ($\gamma - \alpha$) phase transition, the authors of [1] analyzed possible wave structures that occur during the dynamic compression of cerium, the authors suggested that cerium compression occurs isentropically without the formation of a shock wave in the pressure regime up to the completion of the ($\gamma - \alpha$) transition. At greater pressures, a two-wave configuration is formed in cerium.

This configuration consists of a leading isentropic compression wave that is followed by a shock wave. The experiments presented here show similar behavior. It was also mentioned in [1] that the (α - ϵ) phase transition may occur at pressures of 6 to 10 GPa.

The pressure where the phase transition is completed and is determined as the “joint point” between the nose and the plastic wave as depicted in Figure 1.

In experiments with samples of various thicknesses and a minimum loading pressure of ~ 4 GPa, the phase transition pressure is found to be 1.0 to 1.2 GPa, which is in good agreement with static measurements [4]. With increasing loading intensity, the pressure of the “joint point” drops depending on its intensity.

Figure 3 presents pressure profiles recorded in the explosive experiments (at loading pressure of 3.8 to 4.1 GPa) and in the “gun” experiments. Comparison of them shows that the initial parts of the profiles are actually coinciding at impactor velocities $v \geq 170$ m/s (Figure 3).

It points to the fact that phase transition occurs at this loading, however, it has incomplete character at impactor velocities up to $v=480$ m/s, which are used in the experiments. As a result, the material is a mixture of the γ and α phases. It determines its anomalous properties. In particular, a shock wave of rarefaction is formed in the release phase.

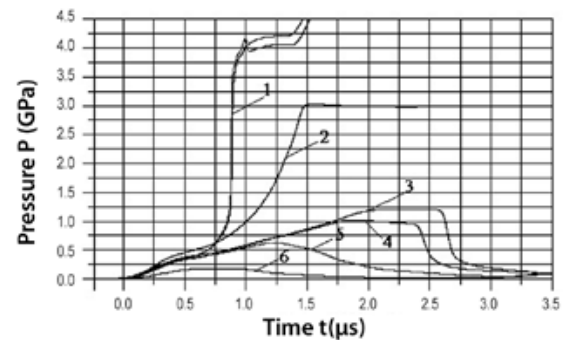


Figure 3. Pressure profiles recorded in explosive (1) and “gun” experiments with targets having thicknesses of 3 mm and various velocities of shell: (2) 480 m/c; (3) 319 m/c; (4) 260 m/c; (5) 169 m/c; (6) 44 m/c.

Titanium

Pressure profiles were measured by PVDF gauge in the range of 10 to 26.2 GPa. The $P(t)$ relations, which were obtained under loading pressure of 10 GPa, have no peculiarities testifying to phase transition. A five times increase of sample thickness (from 4 to 20 mm) only increases the duration of the front part of the $P(t)$ relation. Therefore, our results do not confirm the conclusions from [5] that phase transition occurs in VT1-0 at pressures of 6 to 10 GPa.

For clarity, results of the tests at various pressures are presented in Figure 4. The supposition can be made that a weak anomaly is formed at pressure profiles at $P \approx 21$ GPa due to the $\alpha \rightarrow \omega$ phase transition. In this case, the obtained result is in agreement with data from [6,7]. The reason for the weak anomaly is that the $\alpha \rightarrow \omega$ phase transition in titanium is accompanied by an insignificant reduction of volume ($\sim 1.2\%$).

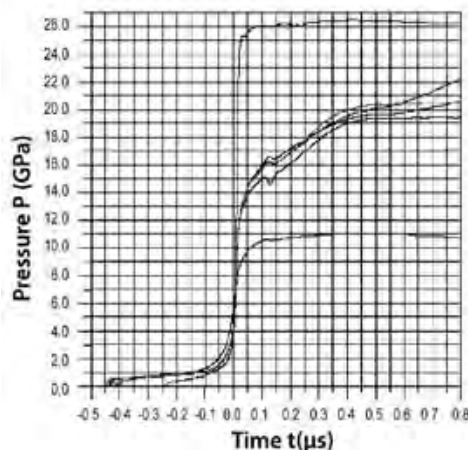


Figure 4. Results of tests with titanium.

Conclusions

In the researches of phase transitions in cerium by PVDF gauge, a two-wave structure was recorded. It consisted of the head wave of isentropic compression followed by a shock wave. This structure is formed as a result of isomorphic (γ - α) phase transition in the loading pressure range of $4 \text{ GPa} \leq p < 12 \text{ GPa}$. Analysis of pressure profiles in the range of (0.6 to 3.0) GPa testifies that the (γ - α) phase transition occurs in cerium. It is revealed that a shock wave of rarefaction is formed in the release phase in cerium.

In titanium, if loading pressure is $\sim 21 \text{ GPa}$, a weak anomaly takes place at the profile of plastic wave at a pressure of 11.5 GPa. The anomaly can be associated with the $\alpha \rightarrow \omega$ phase transition. This phenomenon is not observed at lower and higher loading pressures.

Acknowledgements

This work was performed under the auspices of the U.S. Department of Energy by the University of California Los Alamos National Laboratory under contract #37713-000-02-35 (TO #23, #035)

References

- [1] V. M. Yelkin, E. A. Kozlov, E. V. Kakshina, and Yu. S. Moreva. "Two-phase (α, γ) equation of state for cerium and features of its dynamic compression," *Proceeding of 2005 Conference of the Shock Compression of Condensed Matter – 2005*, eds. M. D. Furnish, M. Elert, T. P. Russell, and C. T. White (Melville, NY, 2006 AIP) pp. 77-80.
- [2] V. A. Borisenok, V. G. Simakov, V. A. Volgin et al., "Study of phase transitions in iron and cerium by PVDF gauge of pressure," *FGV* **43** 4 121-126 (2007).)
- [3] L. M. Barker and R. E. Hollenbach, "Shock wave study of the $\alpha \leftrightarrow \epsilon$ phase transition in iron," *J. Appl. Phys.* **45**, Issue 11, 4872 (1974).
- [4] A. R. Kutsar, "On location of critical point of isomorphous $\gamma \leftrightarrow \alpha$ phase transition in cerium," *FMM* **33**, Issue 5, 1104-1108 (1972).
- [5] A. N. Kiselev, A. A. Fal'kov, "Phase transition in titanium in shock waves," *FGV* **18** 1 115-120 (1982).
- [6] A. R. Kutsar, M. N. Pavlovsky, V. V. Komissarov. "Observation of two-wave configuration of shock wave in titanium," *Letters to ZhTF* **35**, Issue 3, 91-94. (1982)
- [7] C. W. Greeff, D. R. Trinkle, R. C. Albers "Shock-induced $\alpha \rightarrow \omega$ transition in titanium," *J. Appl. Phys.* **90** 2221 (2001).

ATOMISTIC MODELING OF MICROSTRUCTURE INFLUENCE ON THE SPALL STRENGTH

P. A. Zhilyaev, A. Yu. Kuksin, G. E. Norman, V. V. Stegailov, A. V. Yanilkin

Joint Institute for High Temperatures (JIHT), Russian Academy of Sciences, Moscow, 125412, Russia

Author Contact: Peter.Zhilyaev@gmail.com

The influence of crystal microstructure on nucleation kinetics of pores and the spall strength value is discussed. The comparison of molecular dynamics simulation data on single crystal Al without defects and with dislocation subsystem is presented. The influence of grain boundary amorphization at elevated temperatures on fracture of polycrystals is analyzed.

Introduction

The shock-wave experiments reveal different influences of temperature on spall strength, depending on material microstructure. The behavior of crystals near the melting temperature is especially interesting [1]. The melting curve can be crossed during unloading. One can expect a sharp decrease of tensile strength, since fast growth of the melted region should lead to plastic deformation and fracture of the surrounding crystal. As a result, the melting curve should describe melting thresholds that limit material strength at the high-temperature range. However, the experimental data [1] on polycrystalline aluminum revealed that reduction of the spall strength takes place substantially earlier melting line. Also, the reduction of strength is not observed for single crystals, and quite to the contrary, overheating of the crystals is possible.

The paper is devoted to the study of the effect in aluminum of using direct molecular dynamics. A single crystal with different defects (dislocations, stacking faults, voids) and a polycrystal are modeled. The main model is hydrostatic deformation with constant strain rate, corresponding to stretching in rarefaction waves. Hydrostatic tension is applied because of the presence of defects that provide relaxation of the deviator stresses due to the plastic deformation [2]. The tension (and the compression) is modeled by the scaling of atom coordinates on each computation step. Periodic boundary conditions are applied on the simulation box. Two different parameterizations of the embedded atom potential are used [3,4,5]. The number of atoms in the system varies from 200 thousand to 3 million. The modeling was done using LAMMPS package [6]. The centro-symmetry parameter [7] combined with calculation of the coordination number is used to analyze defects.

Dislocation Subsystem

Dislocation loops and stacking faults were produced in the system via a uniaxial compression and a subsequent relaxation to zero stresses and given temperature. It models a formation of defects of such kind during a propagation of a compression pulse and its reflection from free boundaries of a sample under shock wave loading. Several slip planes are activated during uniaxial compression and numerous intersecting dislocation loops arise. Similar

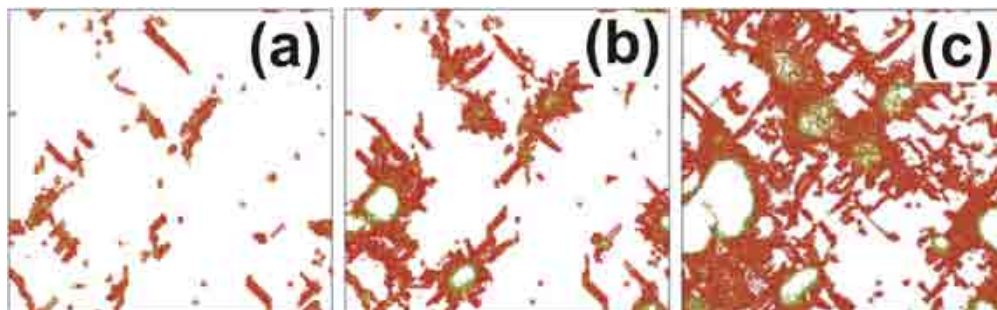


Figure 1. Uniform stretching of aluminum single crystal with dislocations. Strain rate equals to 10^8 s^{-1} . Only atoms of defects are shown.

dislocation structures are observed in molecular dynamic simulations of the shock wave loading with the use of “projectile-target” model [8,910]. The number and size of the defects decrease significantly during relaxation of the system to zero stresses. Remnant defects are vacancies, stacking faults, and dislocation loops (Figure 1a).

The spall strength of the system is determined as a maximal stress achieved in a process of uniform triaxial stretching. The computation time lies between 10^2 ps and 10^4 ps, depending on the stretching rate. The motion of dislocations and growth of the stacking fault regions are observed at the stage of a triaxial uniform tension, while the value of deviatoric stresses does not exceed 10 MPa in the simulations with both forms of the potential [3,4]. It is not enough for a dislocation motion, hence relatively large local stress is achieved in the crystal.

When a critical value of stress is achieved during stretching, the nucleation of voids starts near stacking faults and their intersections (Figure 1b, 1c). A certain amorphization is observed around voids, while the voids' shape is close to octahedron. Hence both mechanism of a void growth are manifested: viscous and dislocation-mediated. The void growth rate changes slightly with the strain rate. Values of the spall strength turn out to be similar for two parametrizations of the embedded atom potential [3,4].

Estimates of the spall strength for different strain rates are shown in Figure 2. The data on molecular dynamic simulations for a single crystal without defects (hydrostatic stretching of the system with 1 million atom, potential [4] is involved) are presented by point 3 on Figure 2. A constant temperature $T = 100$ K is kept in all the simulations performed. Considerable reduction of the spall strength is observed for crystal with dislocation subsystem in comparison with defect-less single crystal. It is also seen that the dependence of spall strength on strain rate is much stronger in case of crystal with defects and the slope of the corresponding curve is close to the experimental data (point 4 on Figure 2) from the shock wave tests [1]. Similar behavior is observed for polycrystals: voids nucleate on the defect structure of the grain boundaries, and the dependence of spall strength on strain rate is strong.

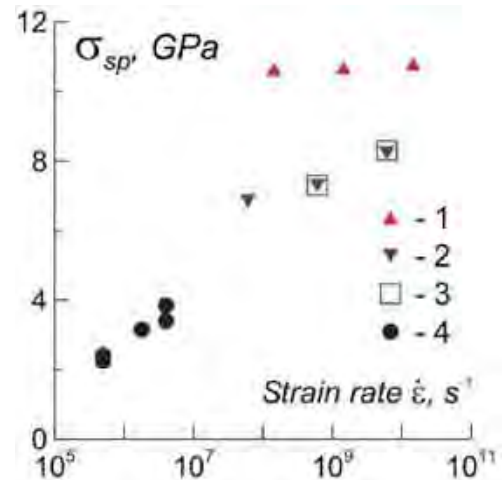


Figure 2. The dependence of spall strength on strain rate. Estimates from the molecular dynamics simulations of hydrostatic stretching at $T = 100$ K: (1) defect-less single crystal, potential [3]; (2,3) model with defects, potentials [3,4] respectively; (4) experimental results [1].

Polycrystals

Two models of polycrystal are studied: bicrystal and polycrystal (3D set of grains with different orientations). Polycrystal with many grains is created with the help of Voronoi constructions and subsequent relaxation. Bicrystal consisting of two grains is used for study of the fracture along grain boundaries.

Figure 3 shows a thermodynamic paths of deformation on the phase diagram of aluminum. There is a considerable difference between behavior of the single crystal and the polycrystal near melting curve. Considerable overheating is observed in the case of single crystal even in the presence of stacking faults, dislocations, and voids (Figure 3, lines 1 and 3). Although melting starts on the junctions of stacking faults before formation of voids, the fraction of melt is small. The growth of relatively large void under tension starts via emission of dislocation loops and melting takes place along with the growth. The volume of the melt in the latter case depends on the strain rate.

No superheating is reached in the case of hydrostatic stretching of polycrystal (Figure 3, line 2). The stress relaxation due to grain melting prevents from it. The melting curve is shifted considerably for small grains due to

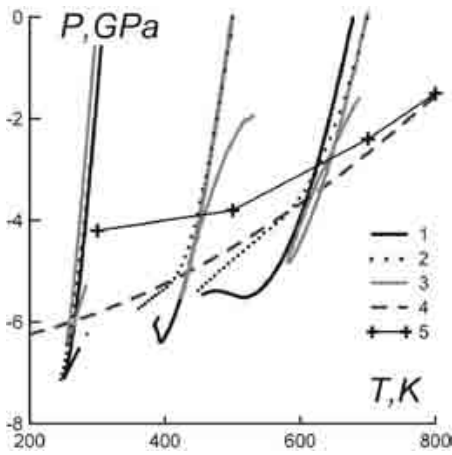


Figure 3. Phase diagram of Al and thermodynamic paths of stretching at constant strain rate 10^8 s^{-1} for three microstructures: a single crystal with dislocations (1), a polycrystal (2), and a single crystal with a void (3). The dashed line (4) is the melting curve for this potential. The crosses (5) are the critical stress values for crack propagation in the bicrystal model.

additional surface energy, but this effect is too small for the experimental samples (size of grains is about $1 \mu\text{m}$). Also, the amorphization of grain boundaries takes place due to their defect structure (Figure 4). The width of amorphous (intergranular) layer reaches 1.5 nm near the melting curve, the viscosity of substance in it is close to liquid. Such a behavior is size independent and has fast kinetics (~ 10 to 100 ps), so it is valid for experimental samples. However, large stresses are needed for spontaneous void nucleation formed in the liquid; hence, corresponding tensile strength is above the melting curve, contrary to the experimental data. The stability of polycrystals observed in MD simulations is connected to the stability of liquid under tension. It is unlikely that spontaneous nucleation of voids in the amorphous grain boundary layer takes place in experiments, since the volume of liquid is small and stresses are low.

Gaseous voids or microcracks can be supposed to exist in the initial polycrystal structure due to various impurities. The formation of the liquid layer in this case induces the void growth along grain boundaries and leads to a decrease of the spall strength.

Molecular dynamics simulations of bicrystal are carried out to demonstrate this effect (Figure 5). At first, bicrystal is relaxed at a fixed temperature and pressure. The microcrack along grain boundary is created by the removal of a number of atoms. The critical pressure for growth of a crack along grain boundary is relatively small and limits the tensile strength of polycrystal, as shown in Figure 3. One can see that the critical pressure drops when the state of the system crosses the melting line, similar to the experimental dependence.

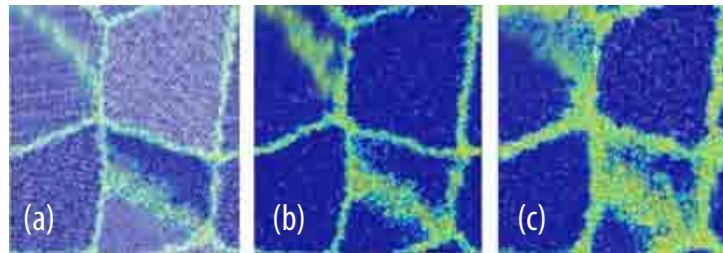


Figure 4. The structure of grain boundaries in Al polycrystal in equilibrium at zero pressure and different temperatures T : (a) 500 K ; (b) 700 K ; (c) 800 K .

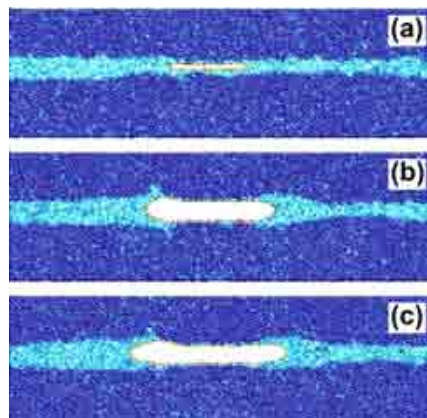


Figure 5. Void growth along grain boundary in Al bicrystal $T = 700 \text{ K}$, $P = -2.3 \text{ GPa}$. Several timesteps are presented: (a) 0 ps ; (b) 10 ps ; (c) 20 ps .

Conclusions

The following effects are observed for single crystal with defects:

- the spall strength decreases in comparison with defectless crystal,
- the dependence of spall strength on strain rate is stronger than in defectless crystal,
- spallation occurs when the state of the system lies beyond melting curve.

The following effects are observed for polycrystals:

- the grain boundaries amorphization takes place before melting and initiates the spallation and
- amorphization promotes void growth along grain boundaries.

Acknowledgements

We thank G. I. Kanel, V. E. Fortov, and J. B. Aidun for their interest in this study and useful discussion. This work was partially supported by the RFBR09-08-01116-a grant, RAS programs #11, 12 and Sandia National Laboratories under the U.S. DOE/NNSA Advanced Simulation and Computing program.

References

- [1] G. I. Kanel, S. V. Razorenov, V. Fortov, "Shock-wave compression and tension of solids at elevated temperatures: superheated crystal states, pre-melting, and anomalous growth of the yield strength," *J. Phys.: Condens. Matter* **16** 1 1007-1016 (2004).
- [2] E. M. Bringa, H. M. Zbib, J. M. McNaney, B. A. Remington, "Simulation of shock-induced plasticity including homogeneous and heterogeneous dislocation nucleations," *Applied Physics Letters* **89** 17 171918 (3 pp) (2006).
- [3] M. S. Daw, S. M. Foiles, M. I. Baskes. "The embedded-atom method: a review of theory and application," *Mater. Sci. Rep.* **9** 7-8 251-310 (1993).
- [4] Y. Mishin, M.J. Mehl, D.A. Papaconstantopoulos, A.F. Voter, J.D. Kress, "Interatomic potentials for monoatomic metals from experimental data and ab initio calculations," *Phys. Rev. B* **59** 5 3393-3407 (1999).
- [5] X.-Y. Liu, F. Ercolessi, J. B. Adams, "Aluminum interatomic potential from density functional theory calculations with improved stacking fault energy," *Modell. Simul. Mater. Sci. Eng.* **12** 4 665-670 (2004).
- [6] S. J. Plimpton., "Fast parallel algorithms for short-range molecular dynamics," *J. Comp. Phys.* **117** 1-19 (1995).
- [7] C. Kelchner, S. Plimpton, J. Hamilton, "Dislocation nucleation and defect structure during surface indentation," *Phys. Rev. B* **58** 17 11085-11088 (1998).
- [8] V. V. Stegailov, A. V. Yanilkin, "Structural transformations in single-crystal iron during shock-wave compression and tension: Molecular dynamics simulation," *JETP* **104** 6 928-935 (2007).
- [9] A. V. Yanilkin, A. Yu. Kuksin, G. E. Norman, V. V. Stegailov, "Atomistic simulation of high strain rate plasticity, spall damage and fracture of nanocrystalline Cu," *Shock Compression of Condensed Matter* **955**, ed. M. D. Furnish et al. (New York, American Institute of Physics, 2007) pp. 347-350.
- [10] B. Cao, E. M. Bringa, M. A. Meyers, "Shock compression of monocrystalline copper: Atomistic simulations," *Metallurgical and Materials Transactions A* **38A** 11 2681-2688 (2007).

EFFECT OF SHOCK WAVE AND QUASI-ISENTROPIC LOADING ON THE SHEAR AND SPALLING STRENGTH OF METALS WITH NATURAL AND MICROCRYSTALLINE STRUCTURE

O. N. Ignatova,* I. I. Kaganova,* A. B. Kal'manov,* A. N. Malyshev,* V. I. Skokov,* A. M. Podurez,*
B. A. Raevsky,* O. A. Tyupanova,* G. A. Salishev,† C. V. Razoryonov,‡ Marvin A. Zocher**

*All-Russia Research Institute of Experimental Physics (VNIIEF), Sarov 607190, Russia

†BelGU, 2a Korolyov St., Belgorod, 308015 Russia

‡IPHF RAN, 1 acad. Semenov pr., Chernogolovka, Moscow Region, 134432 Russia

**LANL, Los Alamos, USA

Author Contact: root@gdd.vniief.ru

Introduction

To develop a wide range models of shear and spalling strength for metals with varying crystalline structure, one has to know their mechanical properties in various stress-strain states. The response of metals to shear and tensile stress is governed by a number of parameters such as deformation ϵ_p , pressure P , temperature T , strain rate $\dot{\epsilon}_i$, deformation history, grain size, dislocation density, etc., the effect of which depend on the zone of stress-strain state.

In this paper, simulation and experimental studies on the effect of the preliminary loading on the response of materials to shear and tensile stress are presented. Metals are discussed that have two types of crystalline lattices and various initial grain size bcc (M1 annealed copper, grain size $\sim 110 \mu\text{m}$ and $\sim 0.5 \mu\text{m}$) and fcc (TVC tantalum, grain size $\sim 80 \mu\text{m}$ and $\sim 1 \mu\text{m}$).

Material and Experimental Procedure

The materials studied are M1 copper in the form of hot-rolled bars with a grain size of $d=110 \mu\text{m}$ and TVC tantalum with grain of $d=80 \mu\text{m}$. Fine grained (FG) copper and tantalum have been manufactured by a forging process [1].

The shock wave or quasi-isentropic loading of the samples is done either by impeding the freely flying plate, that is, a flyer made of the same materials (Figure 1a), or using an explosive charge (Figure 1b) at normal temperature or in liquid nitrogen. Loading parameters are as follow:

Shock wave loading: $P \sim 20\text{--}120 \text{ GPa}$, $\epsilon_f \sim 0.11\text{--}0.4$, $\dot{\epsilon}_i \sim 10^8 \div 10^{10} \text{ s}^{-1}$;
Quasi-isentropic loading: $P \sim 28\text{--}32 \text{ GPa}$, $\epsilon_f \sim 0.11\text{--}0.12$, $\dot{\epsilon}_i \sim 2 \cdot 10^6 \div 10^7 \text{ s}^{-1}$,

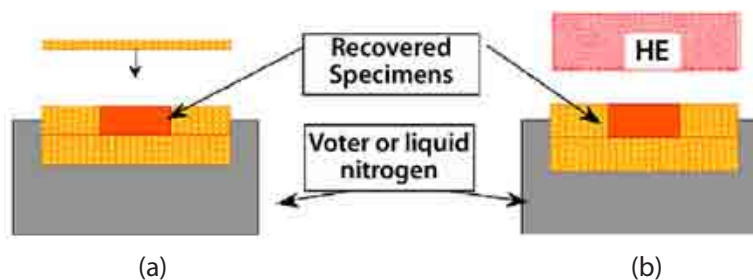


Figure 1. Sample loading by a flat shock wave (a) and a quasi-isentropic compression wave (b).

In all the experiments, the specimens are kept for further analysis and study of mechanical properties.

The microstructure of the deformed and recovered specimens is studied using optical, scanning electron (SEM), and transmission electron microscopy (TEM). The quantitative microstructure analysis is carried out using secants. The mechanical properties (shear and spall strength) of the samples preloaded are measured at static and dynamic stress using various techniques.

Results of Metallographic Studies

Typical pattern of twin structure in polycrystalline copper and tantalum are shown in Figure 2. The twins in copper with large grain size are found to form at a lower critical pressure in the shock wave. In copper, for instance, monocrystals are loaded perpendicular to the crystallographic plane (001), twins are formed in the shock wave at pressure $P > 20$ GPa, in polycrystalline copper with $d = 110 \mu\text{m}$ at $P > 27$ GPa, and with the grain size $d = 30 \mu\text{m}$ at $P > 40$ GPa. In FG copper with $d = 0.5 \mu\text{m}$, twins are not found in the shock wave at pressures up to 50 GPa [2].

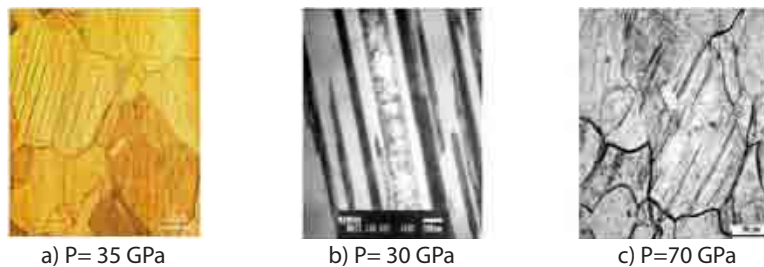


Figure 2. Twin structure in polycrystalline copper (a, b) and tantalum (c) formed after shock-wave loading at room temperature.

In the copper specimen, stripes viewed through an optic microscope after shock wave loading are shown as “twin packets” aligned parallel with thickness $\sim 0.1 \div 0.2 \mu\text{m}$, and a length of $50 \mu\text{m}$ (depending on the grain size) (Figure 2(a), (b)). When the twins are subjected to quasi-isentropic loading, and when the strain rate is low $\dot{\epsilon}_i \sim 10^6 \text{ s}^{-1}$, their density is rather $\geq 10\%$, and they do not group in wide “twin packets” [3]. With the increase in strain rate up to $\dot{\epsilon}_i \sim 10^7 \text{ s}^{-1}$, whether the twins are formation of “twin packets” at high strain rates is still unclear.

In a microcrystalline tantalum, at a given regime of loading, some stripes of localized shear of double behavior are observed. The volume share of the stripes as such is less than that in copper samples shocked under similar conditions. The liner dependence between the quantity of twins and shock wave (SW) time is observed in copper as well as in tantalum. As the initial temperature of the metals decreases to that of liquid nitrogen, the threshold value of the shock wave that induces the heterogeneous deformation on decreases.

Measurement of Dislocations

Application of various versions of X-ray diffraction methods has made it possible based on the profile of the diffraction lines to measure the change in dislocation density as a function of pressure for the samples recovered after shock wave loading. Initial dislocation density in FG copper is $\rho_0 = 1.8 \cdot 10^{11} \text{ sm}^{-2}$, being on the order of three times higher than that in the initial annealed microcrystalline state $\rho_0 \sim 10^8 \text{ sm}^{-2}$.

The experimental results are illustrated in Figure 3, where the dislocation density is plotted as deformation. Total deformation at SW loading is calculated based on the metal compressed.

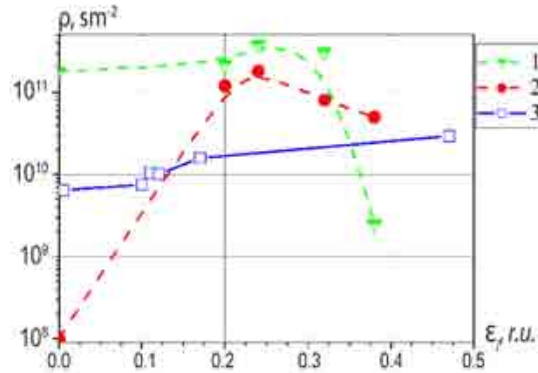


Figure 3. Dislocation density in copper (1, 2) and tantalum (3) with different grain size as function of deformation: (1) FG copper, (2) CG copper, (3) CG tantalum.

As Figure 3 shows, the SW loading generates in copper a higher dislocation density than it does on the quasi-static one. In FG copper with the highest initial dislocation density, the latter increases by a factor of two at the loading pressure of 30 to 50 GPa. Then the density drops up to the initial macrocrystalline state being most probably connected to the annealing of defects at adiabatic heating caused by SW compression. When tantalum is shock loaded at $P \approx 100$ GPa, the dislocation density increases from $6 \cdot 10^9 \text{ sm}^{-2}$ to $(2.5 \div 3) \cdot 10^{10} \text{ sm}^{-2}$, that is as low as 4÷5 time. The noticeable difference of the tantalum and copper microstructure response to shock wave loading as such is associated with the difference in their crystal structure.

Shear Strength before and after SW Loading

Static experiments with the samples at room temperature are performed at the standard testing machine «INSTRON» 1185 equipped with an A0706-II798 at strain rate $1.3 \cdot 10^{-3} \text{ s}^{-1}$. Figure 4(a), (b) illustrates σ - ϵ diagrams of static and dynamic compression for macrocrystalline and FG copper and tantalum in the initial state at room temperature and after SW loading with different intensity. The diagrams have been constructed in terms of the total deformation stored during the SW loading.

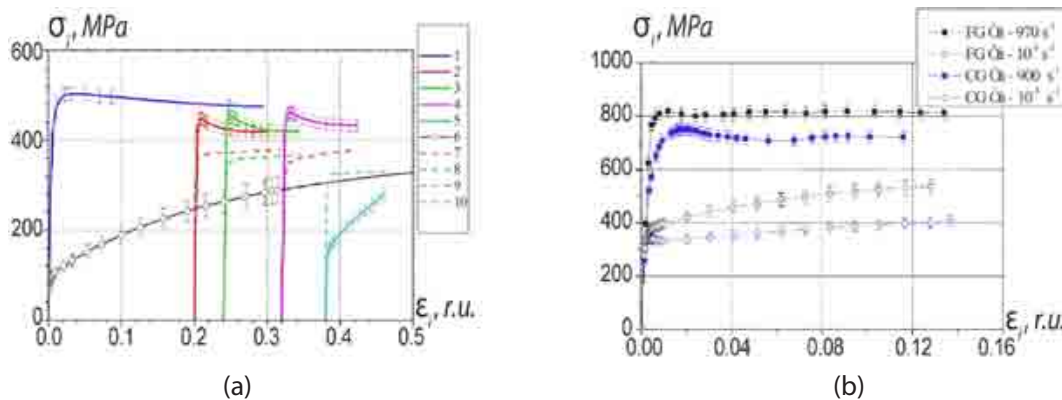


Figure 4. σ - ϵ diagrams of static compression of FG and CG copper (a) and tantalum (b) at normal temperature before and after SW loading with different intensity: (1) FG in initial state, (2-5) FG copper, $\sigma_X \sim 25$ to 75 GPa; (6) CG copper in initial state, (7-10) CG copper after SW loading 75 to 25 GPa.

Static diagrams suggest that the decrease in grain size in copper up to $0.5\ \mu\text{m}$ results increase of the nominal yield stress by a factor of five-six. Preliminary SW loading of FG copper up to pressure of ~ 25 to $55\ \text{GPa}$, within the experimental error, has caused no changes in strength. As the intensity of the shock wave increases up from ~ 55 to $75\ \text{GPa}$, the strength characteristics decrease to the state of a coarse scaled copper. Similar results have been obtained using Taylor method.

The decrease in the grain size in tantalum up to $\sim 1\ \mu\text{m}$ does not lead to a significant increase in the normal yield strength both in static and dynamic loading.

Continuous registration of the velocity traveling $W(t)$ of the free real surface of the specimens is done using VISAR (laser Doppler speedometer) with a time resolution of $\sim 1\ \text{ns}$ and space resolution of $\sim 0.1\ \text{mm}^2$. Shock wave pulses in copper samples are generated via impingement with flat aluminum (AD1) flyers accelerated by special explosive devises up to 550 to $790\ \text{m/s}$, for tantalum samples the flyer velocity, $1250\ \text{m/s}$. The relation between the thickness of the flyers and samples in the experiments performed is $\sim 1:5$, which allows to generated a triangular compression pulse on the sample end. Figure 5(a) shows the measured rate profiles for the free surface of copper in the initial CG state, FG state and after preliminary shock wave, and quasi-isentropic loading.

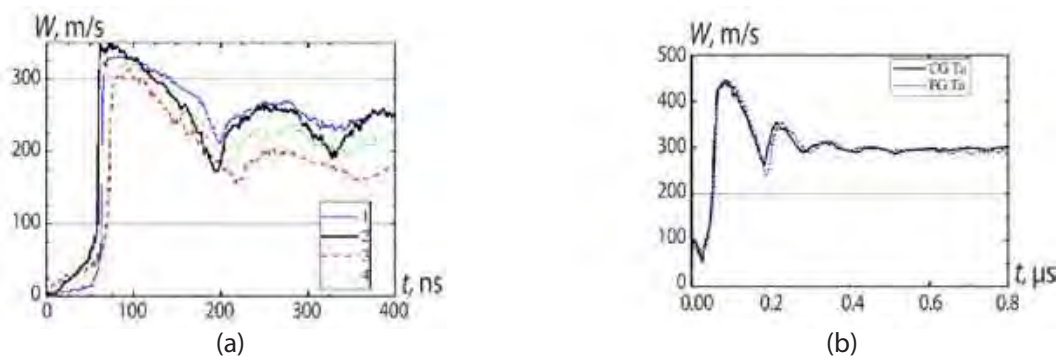


Figure 5. Velocity profiles for the free surface of copper (a) and tantalum (b) 1 initial sample, 2 FG copper, 3 after y QI loading, 4 after SW loading.

Thus, the preliminary exposure of copper to a shock or a quasi-isentropic compression wave leads to an increase in its elastic predecessor by a factor of about three. Figure 5(b) illustrates the measured profiles for the velocity of the free surface of the CG and FG tantalum. The decrease in the tantalum grain size up to $1\ \mu\text{m}$ has not resulted in the growth of the elastic predecessor.

Spallation in Copper

The process of generation and evaluation of failure (or spallation) has been studied using two methods:

- metallographic measurement of the spallation zone in recovered samples and finding the correlation between the damage amount and the loading history;
- examination of the unloading wave structure after the sample explosive to shock wave.

Loading pulses in the samples of interest ($h=4.5\ \text{mm}$) are generated by the impact of a plate of the same material (copper, $h=2\ \text{mm}$). Tensile stress and failure in the sample are formed when the sample is unloaded to a flouroplastic material. To determine the spallation parameters, a set of experiments at a gradual increase in the impact velocity $W=130\div 180\ \text{m/s}$ has been performed with three types of copper: in the initial state, after preliminary shock wave, and quasi-isentropic loading.

Following the experiments, the recovered samples were cross-sectioned and given microstructural analysis to evaluate the failure as a function of the flyer velocity. Figure 6 is images of the sample microstructure after loading and measure of damage. After exposure to shock wave with the intensity $\sim 32\ \text{GPa}$, the damage generation threshold in copper changes.

The other method to determine the spallation parameters is based on measuring the velocity profile of the free surface of the sample. The velocities of the free surface for all the copper versions exported to a shock wave with an intensity of 6 to 9 GPa have been measured using VISAR. The spallation of M1 copper for samples with different initial structure is shown to increase as the deformation rate grows in the range of 10^4 s^{-1} to 10^6 s^{-1} .

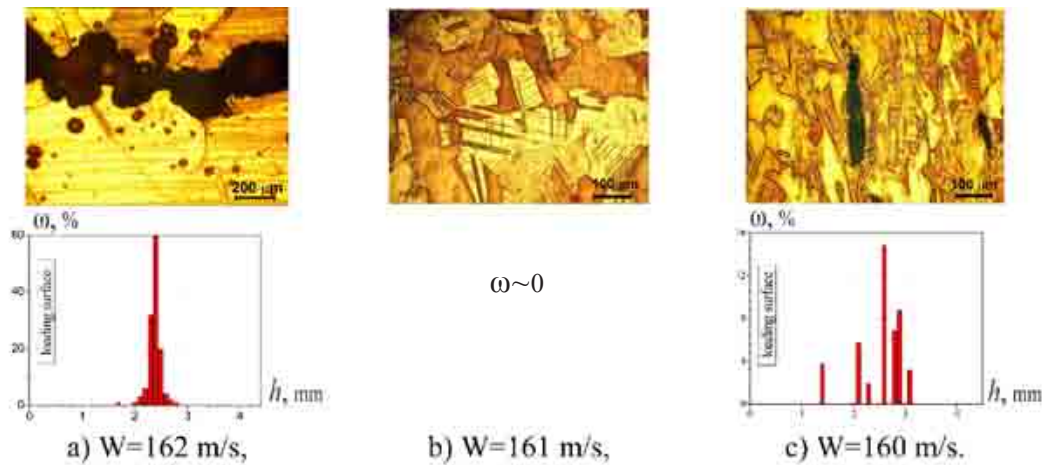


Figure 6. Microsection for copper loaded to initial state (a) after SW, (b) and QI, (c) loading.

Conclusion

The studies performed support the following conclusions. The preliminary SW and QI loading significantly affect the microstructure and mechanical properties in coarse scale bcc metals: one observes a large of microtwins, an increase in dislocation compactness by a factor of three, a five to six fold increase of the nominal yield stress, and the enhancement of $\sim 20\%$ of the metal response to tensile stress. Under the action of SW of more than 60 GPa, the copper sample undergoes annealing that results in recovery of mechanical properties to their original state. The preliminary SW loading of fcc metals slightly changes their internal microstructure and dislocation density. Variation in tantalum grain size up to $1 \mu\text{m}$ does not lead to the improvement of its mechanical properties. The data obtained are used to develop a wide range models of shear and spalling strength of bcc and fcc metals.

Acknowledgements

The work has been carried out under the auspices of the

- LANL: Contract 37713-000-02-35 TO 021;
- RFFI: Project 08-02-00087a.

References

- [1] S. V. Zharebtsov, R. N. Galeev, O. R. Valiakhmetov, S. P. Malysheva, G. A. Salishchev "Formation of subcrystalline structure in titanium alloys via intensive plastic deformation and their mechanical properties," *KSP No. 7* 17-22 (1999).
- [2] V. Raevsky, "Heterogeneous deformation of copper in shock waves at subgrain scale level," *14th APS Topical Conference on Shock Compression of Condensed Matter* (2005) pp. 221-229.
- [3] V. A. Raevsky, M. A. Podurets, V. G. Khanzhin et al., "Twin structures in copper after shock and shockless high-rate loading," in *IX Khariton's Topical Scientific Readings, Extreme states of substance, Detonation, Shock waves* (Sarov, 2007).

SPALL FRACTURE AND COMPACTION IN NATURAL URANIUM UNDER SHOCK-WAVE LOADING

O. A. Tyupanova, S. S. Nadezhin, A. N. Malyshev, O. N. Ignatova, V. I. Skokov, V. N. Knyazev, V. A. Raevsky, N. A. Yukina

All-Russia Research Institute of Experimental Physics (VNIIEF), Sarov 607190, Russia

Author Contact: root@gdd.vniief.ru

A series of experiments has been performed to study spall fracture and subsequent compaction in natural uranium under shock wave loading. The damage level of recovered samples has been estimated by metallographic analysis. Numerical simulation of these experiments has allowed verification of a simple compaction model.

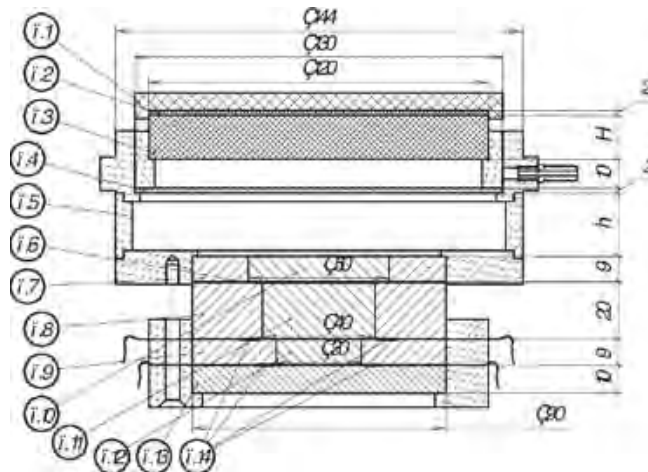
Introduction

Nucleation and growth of defects of different form and size inside a solid under pulse tensile stresses means disturbance of its solidity, and it is necessary to consider it as a damaged matter, respectively. A very limited number of works are devoted to studying the behavior of such matter, and most of them are of a theoretical character [1,2,3]. Experimental research in this area is concentrated on the study of compression of porous mediums, imitating the damaged matter as a first approximation, by weak shock waves [4,5]. The advantage of considering the damaged matter as porous (with matchable level of porosity α) and single-phase medium is a significant simplification of analytical expressions, used for its determining. At the same time, this approach could be inadequate, if take into account the complexity of damage growth process.

This work presents the experiments on spall fracture and subsequent compaction of damage in natural uranium, performed at IFV RFNC-VNIIEF, and results of compaction model verification, based on these data.

Tests and Simulation Set-ups

Test assembly for each experiment contained three samples of natural coarse-crystalline uranium. Shock wave loading has been made by uranium liner, accelerated by HE charge explosion to the velocity $W_{imp} \sim 1.2$ km/s (Figure 1).



1 – multipoint initiating system; 2 – plastic HE; 3 – main HE charge ($\Delta_{HE} = 10$ mm, $h = 24$ mm – test #1; $\Delta_{HE} = 13$ mm, $h = 14$ mm – test #2; $\Delta_{HE} = 14$ mm, $h = 10$ mm – test #3); 4 – liner; 5 – frame (PMMA); 6 – gap; 7-9 – saving rings; 10-12 – samples; 13 – support; 14 – manganin gauges (D1-D4).

Figure 1. Set-up of experiments.

After impact, the nonstationary shock wave with amplitude of $\sigma_H \sim 40 \text{ GPa}$ at the entrance of upper sample propagates into the assembly. There is a gap of $\sim 500 \text{ }\mu\text{m}$ thickness between upper and middle samples. When the nonstationary shock wave reflects from the rear free surface of the upper sample, tensile stresses arise in it, leading to the formation of a damaged zone [6]. Closing this gap results in propagation of a shock wave back to the upper sample affecting the zone of damage formed at this moment. Only a part of this damage zone is influenced by this wave due to its intensive attenuation.

The peculiarity of the experiments described is that the damage zone is subjected to compaction by two compression waves. The second wave arises due to prolonged action of explosion products onto the liner and, subsequently, onto the damage zone inside the upper sample from the loading surface side. The influence of this compaction wave onto the final state of damaged samples has been studied by variation of the liner flight distance ($h = 24, 14$, and 10 mm , see Figure 1), keeping the impact velocity constant. According to a specialized series of simulations, the pressure of explosion products onto the liner drops significantly while increasing this distance, and in the case of $h = 24 \text{ mm}$ the amplitude of second compression wave is not enough to recollect the damage. Calculated histories of pressure at the loading surface of the liner, obtained under numerical simulation of loading device and taken into account under simulation of experimental assembly to determine the compaction model's parameters, are presented in Figure 2.

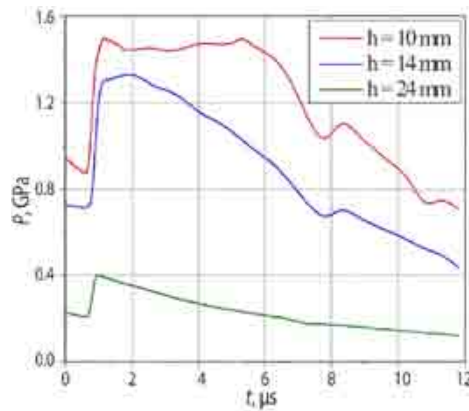


Figure 2. Calculated pressures on the liners' surface contacting with explosion products (time count is from impact moment).

Therefore, the post-shot state of upper samples in each test is the result of the consecutive effect of intensive shock wave, tensile stresses, which are enough for damage nucleation and growth, and two waves of compression (compaction). The amplitude of the first compression wave is adjusted by the gap thickness of the second one—by the distance between the liner and upper sample at the initial position. Manganin gauges have been used to check the stress-strain state in the assemblies. The samples were recovered and analyzed metallographically to reveal the microstructure, and the level and character of damage as well, using optical microscopes.¹

Numerical analysis of the described experiments has been performed by Lagrangian code UP [7]. All the materials of experimental assemblies (except fluoroplastic) have been considered as elastic-viscous-plastic mediums with spherical part of stress tensor in Mie-Gruneisen form with variable Gruneisen coefficient Γ_p . The phenomenological model of elastic-plastic deformation of relaxational medium (RING model [8]) has been used to simulate high-rate deformation. Fluoroplastic foam has been considered in hydrodynamic approximation.

¹ Threshold pressure of heterogeneous deformation of natural uranium has been determined in middle samples. The value of this threshold is determined as $\sim 20 \text{ GPa}$. Spall fracture of different levels has been studied in lower samples by placing “soft” supports of different matter (fluoroplastic foam, aluminum, copper). These results are the subject of separate research and are not presented here.

Kinetics of damage growth in materials under pulse tensile stresses has been simulated by two-stage kinetic model of NAG type, supposing viscous character of spall fracture [9,10].

The following model of damaged matter compaction has been verified here [11]:

$$\begin{cases} P = 0 & \text{if } \omega > \omega_0, \\ P = P_{comp} \left(1 - \left(\frac{\omega}{\omega_0} \right)^{1/2} \right) & \text{if } P < P_{comp} \text{ and } \omega < \omega_0, \\ \omega = 0 & \text{if } P > P_{comp}, \end{cases} \quad \text{or} \quad \omega = \omega_0 \cdot \left(1 - \frac{P}{P_{comp}} \right)^2 \quad \text{if } P < P_{comp} \text{ and } \omega < \omega_0 \quad (1)$$

where P_{comp} is the pressure of full compaction and ω_0 is the limit of damage, below which the damaged material begins to demonstrate strength for compression. It means that a cell is compressing without any resistance while the damage in it is over the value ω_0 . Model (1) is simple, but has a disadvantage: it does not take into account the compaction kinetics.

Results and Discussion

Manganin gauges have allowed verification of the adequacy of numerical codes, constitutive equations, and fracture models, and their parameters have also been used for numerical simulation. This is concluded from an adequate simulation of amplitude and time characteristics of $P(t)$ dependencies recorded in these experiments (Figure 3).

A photo of typical post-shot macrostructure of natural uranium is presented in Figure 4 (test #3, $h=10$ mm). Regions of changed structure, which can be seen even under low magnification (see Figure 4), are considered as zones of recollected (compacted) damage. The discreteness of these recollected damage zones along the diameter of the sample (X axis) is supposed to be caused by nonconstant thickness of the gap between samples (the gap was linear, $\Delta_{gap} = 360$ μm for $X=0$ mm and $\Delta_{gap} = 360$ μm for $X=50$ mm). Such nonmonotonic distribution of damage along the diameter has been also obtained for copper in [6] for the same test set-up. Figure 4 also shows the frame of axis X-Y, according to which a position of damage and compaction zones has been determined at the cross section. Figure 5 illustrates the peculiarities of sample microstructure in a specific section in the X axis from the loading surface ($Y=9$ mm) to the rear one ($Y=0$ mm). Such photos have been used to quantify the damage ω level in the samples, which is determined as the ratio of volume of defects to the whole volume of substance. Different levels of damage have been detected in the samples from 0 to $\omega \sim 0.10$.

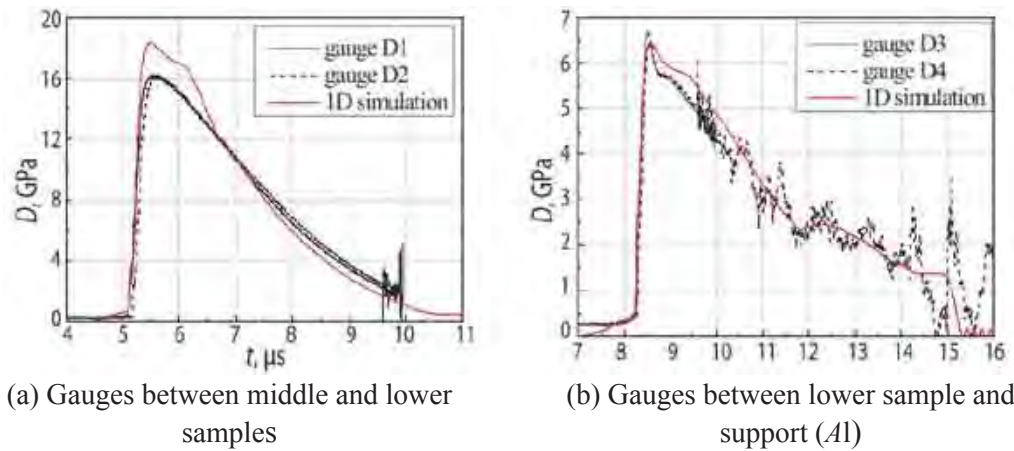


Figure 3. Comparison of experimental and calculated curves $P(t)$ (test #2).

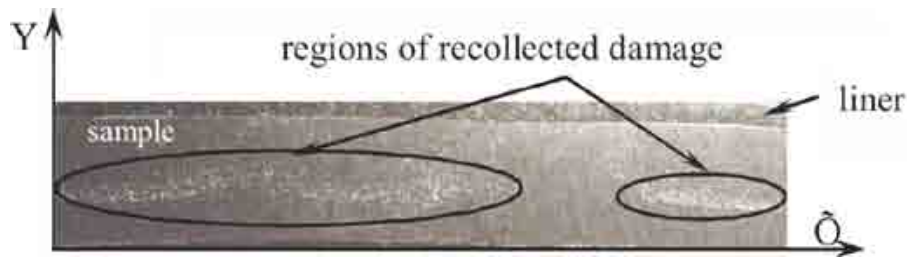


Figure 4. Macrostructure of cross-section for test #3 sample (loading was from upwards, magnification $\times 2.5$).

Analyzing the damage distributions along the sample thickness, obtained after metallographic analysis and presented in Figure 6, we can mark out two zones of material continuity disturbance. One of them with maximum ω , positioned near coordinate $Y \sim 4$ mm from the rear surface, is a result of the influence of a compaction wave from closing of the gap, onto the damage grown to this moment. As one can see from Figure 6, the level of final damage in this zone does not change in these tests and is a value of 4%.

The second zone with maximum damage, located in coordinate $Y \sim 3.1-3.2$ mm, is determined by amplitude of second compression wave, which recollets the damage from loading surface (due to explosion products effect). Figure 6 witnesses that the final level of damage in this zone increases from zero one (Figure 6c, $h=10$ mm) to up to $\omega \sim 10\%$ (Figure 6a, $h=24$ mm) while the liner flight distance increases and, consequently, explosion product pressure decreases.

The results of the present work gave an opportunity to verify the parameters of compaction model (1). Figure 6 shows the comparison of experimental and calculated distributions of damage ω obtained with the values of these parameters, which allow us to simulate the observed phenomena correctly: $P_{comp} = 3$ GPa, $\omega_0 = 0.256$. As a whole, one can see a satisfactory agreement between simulation and experiment by position of damage zones. At the same time, there is no quite correct quantitative description of ω distributions by simulation.

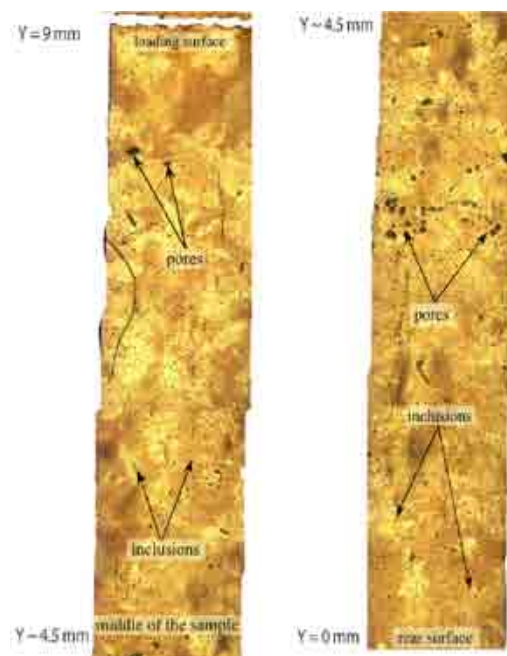


Figure 5. Photo of microstructure of test #1 sample from loading to rear surface ($X=25$ mm, $Y=9 \div 0$ mm) (without etching, the photo is sliced into two parts).

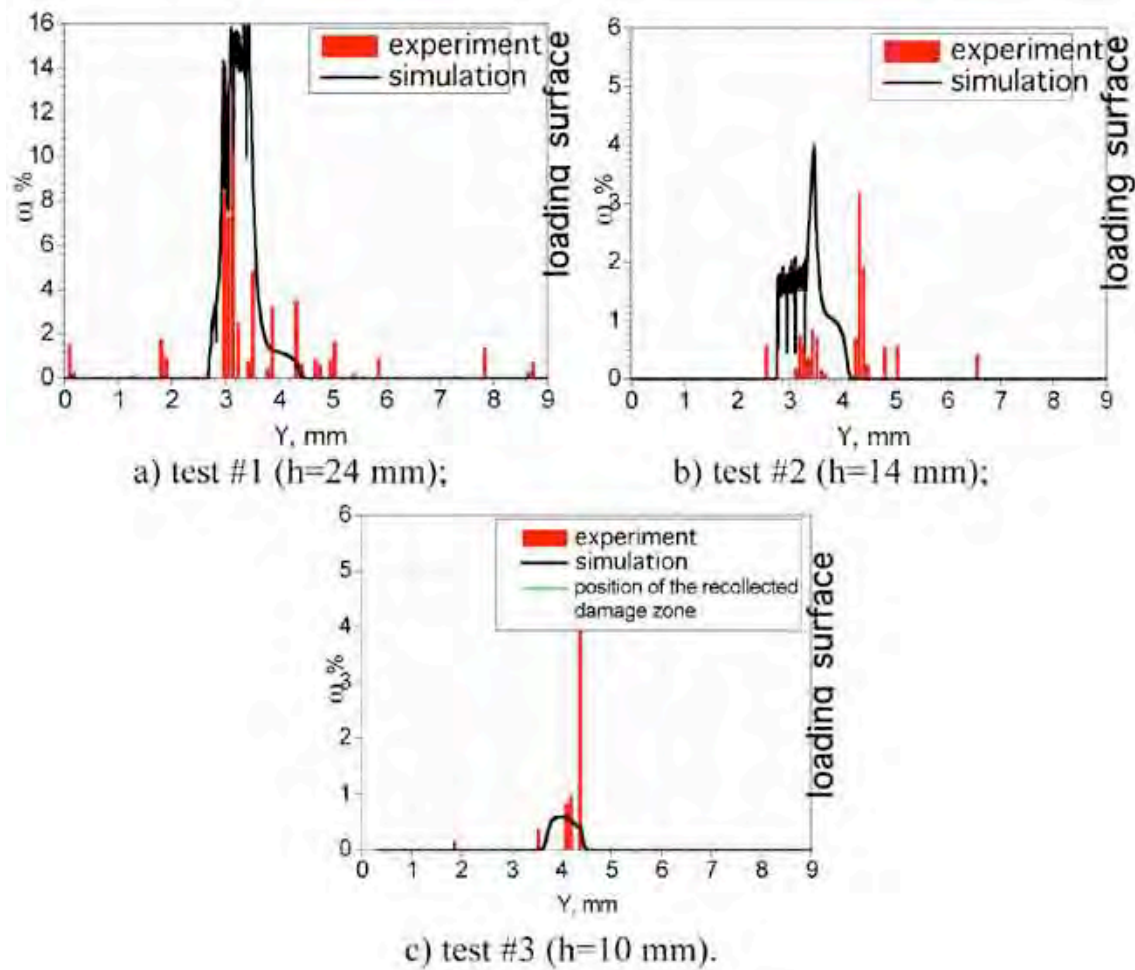


Figure 6. Comparison of calculated and experimental distributions of damage ω along the sample thickness in the central section ($X=25$ mm).

Conclusion

Numerical analysis of the performed series of experiments and metallographic study of the recovered samples allowed verification of the parameters for a model of damaged matter compaction developed at VNIIEF for natural uranium. At the same time, we did not achieve a full simulation of experimental results, namely, the amplitude of final damage distribution in the samples under study. The results indicate a significant complexity of the processes of growth and compaction of damage in heterogeneous materials, which are not subordinated to models developed for an isotropic medium.

References

- [1] N. Kh. Akhmadeev, "Study of spall fracture under shock deformation. Model of damaging medium" (in Russian), *PMTF* [4] 158-167 (1983).
- [2] K. H. Oh, P. V. Person, "A constitutive model for the shock Hugoniot of porous materials in the incomplete compaction regime," *J. Appl. Phys* **66** 15 4736-4742 (1989).
- [3] D. E. Grady, "Analytic solutions and constitutive relations for shock propagation in porous media," in *Shock Compression of Condensed Matter-2003*, eds. M. Furnish, Y. Gupta, J. Forbes (New York, 2004) pp. 205-208.
- [4] R. K. Linde, L. Seaman, D. N. Schmidt, "Shock response of porous copper, iron, tungsten, and polyurethane," *J. Appl. Phys.* **43** 8 3367-3375 (1972).
- [5] V. A. Ogorodnikov, M. V. Zhernokletov, S. V. Mikhailov et al, "Influence of strength, plasticity of the material and particle size of crumbeld medium onto the process of shock-wave deformation" (in Russian), *FGV* **41** 4 124-131 (2005).
- [6] O. N. Ignatova, A. N. Malyshev, O. A. Tyupanova et al., "Peculiarities of damage nucleation phase under intensive loading of copper" (in Russian), *Physics of Solids (Fizika tverdogo tela)* 2009 (to be published).
- [7] N. F. Gavrilov, G. G. Ivanova, V. N. Sofronov et al., "UP-OK code to solve 1D problems of continuum mechanics" (in Russian), *VANT* 11 11-14 (1982).
- [8] A. P. Bolshakov, B. L. Glushak, O. N. Ignatova et al., "Influence of intensive plastic strain and shock wave loading on strength of copper" (in Russian), in *VII Khariton's Readings*, ed. A. Mikhailov (Sarov, Russia, 2005) pp. 421-426.
- [9] T. W. Barbee, L. Seaman, R. Crewdsone, D. Curran, "Dynamic fracture criteria for ductile and brittle metals" *J. Materials* **7** [3] 393-401 (1972).
- [10] B. L. Glushak, I. R. Trunin et al., "Numerical simulation of spall fracture in metals" in *Fractals in Applied Physics*, ed. A. Dubinov (Arzamas-16, Russia, 1995) pp. 59-122.
- [11] V. A. Ogorodnikov and A. A. Sadovoy et al. "Kinetic model of plastic fracture subject to dissipative processes," (in Russian) *Chemical Physics*, **21** 9 104-109 (2002).

Appendix A



Obama, Medvedev release joint statement

By: **Politico Staff**

April 1, 2009 10:23 AM EST

Barack Obama and Dmitry Medvedev have released a (long) joint statement offering a readout of their Wednesday meeting:

"Reaffirming that the era when our countries viewed each other as enemies is long over, and recognizing our many common interests, we today established a substantive agenda for Russia and the United States to be developed over the coming months and years. We are resolved to work together to strengthen strategic stability, international security, and jointly meet contemporary global challenges, while also addressing disagreements openly and honestly in a spirit of mutual respect and acknowledgement of each other's perspective.

"We discussed measures to overcome the effects of the global economic crisis, strengthen the international monetary and financial system, restore economic growth, and advance regulatory efforts to ensure that such a crisis does not happen again.

"We also discussed nuclear arms control and reduction. As leaders of the two largest nuclear weapons states, we agreed to work together to fulfill our obligations under Article VI of the Treaty on Non-Proliferation of Nuclear Weapons (NPT) and demonstrate leadership in reducing the number of nuclear weapons in the world. We committed our two countries to achieving a nuclear free world, while recognizing that this long-term goal will require a new emphasis on arms control and conflict resolution measures, and their full implementation by all concerned nations. We agreed to pursue new and verifiable reductions in our strategic offensive arsenals in a step-by-step process, beginning by replacing the Strategic Arms Reduction Treaty with a new, legally-binding treaty. We are instructing our negotiators to start talks immediately on this new treaty and to report on results achieved in working out the new agreement by July.

"While acknowledging that differences remain over the purposes of deployment of missile defense assets in Europe, we discussed new possibilities for mutual international cooperation in the field of missile defense, taking into account joint assessments of missile challenges and threats, aimed at enhancing the security of our countries, and that of our allies and partners.

"The relationship between offensive and defensive arms will be discussed by the two governments.

"We intend to carry out joint efforts to strengthen the international regime for nonproliferation of weapons of mass destruction and their means of delivery. In this regard we strongly support the Treaty on the Non-Proliferation of Nuclear Weapons (NPT), and are committed to its further strengthening. Together, we seek to secure nuclear weapons and materials, while promoting the safe use of nuclear energy for peaceful purposes. We support the activities of the International Atomic Energy Agency (IAEA) and stress the importance of the IAEA Safeguards system. We seek universal adherence to IAEA comprehensive safeguards, as provided for in Article III of the NPT, and to the Additional Protocol and urge the ratification and implementation of these agreements. We will deepen cooperation to combat nuclear terrorism. We will seek to further promote the Global Initiative to Combat Nuclear Terrorism, which now unites 75 countries. We also support international negotiations for a verifiable treaty to end the production of fissile materials for nuclear weapons. As a key measure of nuclear nonproliferation and disarmament, we underscored the importance of the entering into force the Comprehensive Nuclear Test Ban Treaty. In this respect, President Obama confirmed his commitment to work for American ratification of this Treaty.

We applaud the achievements made through the Nuclear Security Initiative launched in Bratislava in 2005, including to minimize the civilian use of Highly Enriched Uranium, and we seek to continue bilateral collaboration to improve and sustain nuclear security. We agreed to examine possible new initiatives to promote international cooperation in the peaceful use of nuclear energy while strengthening the nuclear non-proliferation regime. We welcome the work of the IAEA on multilateral approaches to the nuclear fuel cycle and encourage efforts to develop mutually beneficial approaches with

states considering nuclear energy or considering expansion of existing nuclear energy programs in conformity with their rights and obligations under the NPT. To facilitate cooperation in the safe use of nuclear energy for peaceful purposes, both sides will work to bring into force the bilateral Agreement for Cooperation in the Field of Peaceful Uses of Nuclear Energy. To strengthen non-proliferation efforts, we also declare our intent to give new impetus to implementation of U.N. Security Council Resolution 1540 on preventing non-state actors from obtaining WMD-related materials and technologies.

"We agreed to work on a bilateral basis and at international forums to resolve regional conflicts.

"We agreed that al-Qaida and other terrorist and insurgent groups operating in Afghanistan and Pakistan pose a common threat to many nations, including the United States and Russia. We agreed to work toward and support a coordinated international response with the UN playing a key role. We also agreed that a similar coordinated and international approach should be applied to counter the flow of narcotics from Afghanistan, as well as illegal supplies of precursors to this country. Both sides agreed to work out new ways of cooperation to facilitate international efforts of stabilization, reconstruction and development in Afghanistan, including in the regional context.

"We support the continuation of the Six-Party Talks at an early date and agreed to continue to pursue the verifiable denuclearization of the Korean Peninsula in accordance with purposes and principles of the September 19, 2005 Joint Statement and subsequent consensus documents. We also expressed concern that a North Korean ballistic missile launch would be damaging to peace and stability in the region and agreed to urge the DPRK to exercise restraint and observe relevant UN Security Council resolutions.

"While we recognize that under the NPT Iran has the right to a civilian nuclear program, Iran needs to restore confidence in its exclusively peaceful nature. We underline that Iran, as any other Non-Nuclear Weapons State - Party to the NPT, has assumed the obligation under Article II of that Treaty in relation to its non-nuclear weapon status. We call on Iran to fully implement the relevant U.N. Security Council and the IAEA Board of Governors resolutions including provision of required cooperation with the IAEA. We reiterated their commitment to pursue a comprehensive diplomatic solution, including direct diplomacy and through P5+1 negotiations, and urged Iran to seize this opportunity to address the international community's concerns.

"We also started a dialogue on security and stability in Europe. Although we disagree about the causes and sequence of the military actions of last August, we agreed that we must continue efforts toward a peaceful and lasting solution to the unstable situation today. Bearing in mind that significant differences remain between us, we nonetheless stress the importance of last year's six-point accord of August 12, the September 8 agreement, and other relevant agreements, and pursuing effective cooperation in the Geneva discussions to bring stability to the region.

"We agreed that the resumption of activities of the NATO-Russia Council is a positive step. We welcomed the participation of an American delegation at the special Conference on Afghanistan convened under the auspices of Shanghai Cooperation Organization last month.

"We discussed our interest in exploring a comprehensive dialogue on strengthening Euro-Atlantic and European security, including existing commitments and President Medvedev's June 2008 proposals on these issues. The OSCE is one of the key multilateral venues for this dialogue, as is the NATO-Russia Council.

"We also agreed that our future meetings must include discussions of transnational threats such as terrorism, organized crime, corruption and narcotics, with the aim of enhancing our cooperation in countering these threats and strengthening international efforts in these fields, including through joint actions and initiatives.

"We will strive to give rise to a new dynamic in our economic links including the launch of an intergovernmental commission on trade and economic cooperation and the intensification of our business dialogue. Especially during these difficult economic times, our business leaders must pursue all opportunities for generating economic activity. We both pledged to instruct our governments to make efforts to finalize as soon as possible Russia's accession into the World Trade Organization and continue working towards the creation of favorable conditions for the development of Russia-U.S. economic ties.

"We also pledge to promote cooperation in implementing Global Energy Security Principles, adopted at the G-8 summit in Saint Petersburg in 2006, including improving energy efficiency and the development of clean energy technologies.

"Today we have outlined a comprehensive and ambitious work plan for our two governments. We both affirmed a mutual desire to organize contacts between our two governments in a more structured and regular way. Greater institutionalized interactions between our ministries and departments make success more likely in meeting the ambitious goals that we have established today.

"At the same time, we also discussed the desire for greater cooperation not only between our governments, but also between our societies — more scientific cooperation, more students studying in each other's country, more cultural exchanges, and more cooperation between our nongovernmental organizations. In our relations with each other, we also seek to be guided by the rule of law, respect for fundamental freedoms and human rights, and tolerance for different views.

"We, the leaders of Russia and the United States, are ready to move beyond Cold War mentalities and chart a fresh start in relations between our two countries. In just a few months we have worked hard to establish a new tone in our relations. Now it is time to get down to business and translate our warm words into actual achievements of benefit to Russia, the United States, and all those around the world interested in peace and prosperity."

© 2009 Capitol News Company, LLC

NOTICE: This report was prepared as an account of work sponsored by an agency of the United States Government. Neither the United States Government, nor any agency thereof, nor any of their employees, nor any of their contractors, subcontractors, or their employees, make any warranty, express or implied, or assume any legal liability or responsibility for the accuracy, completeness, or usefulness of any information, apparatus, product, or process disclosed, or represent that its use would not infringe privately owned rights. Reference herein to any specific commercial product, process, or service by trade name, trademark, manufacturer, or otherwise, does not necessarily constitute or imply its endorsement, recommendation, or favoring by the United States Government, any agency thereof, or any of their contractors or subcontractors. The views and opinions expressed herein do not necessarily state or reflect those of the United States Government, any agency thereof, or any of their contractors.

Printed in the United States of America. This report has been reproduced directly from the best available copy.

Available to DOE and DOE contractors from

U.S. Department of Energy
Office of Scientific and Technical Information
P.O. Box 62
Oak Ridge, TN 37831

Telephone: (865) 576-8401
Facsimile: (865) 576-5728
E-Mail: reports@adonis.osti.gov
Online ordering: <http://www.osti.gov/bridge>

Available to the public from

U.S. Department of Commerce
National Technical Information Service
5285 Port Royal Rd.
Springfield, VA 22161

Telephone: (800) 553-6847
Facsimile: (703) 605-6900
E-Mail: orders@ntis.fedworld.gov
Online order: <http://www.ntis.gov/help/ordermethods.asp?loc=7-4-0#online>



Institute of Problems of Mechanical Engineering (IPME)



Joint Institute for High Temperatures (JIHT)



All-Russia Research Institute of Automatics (VNIIA)

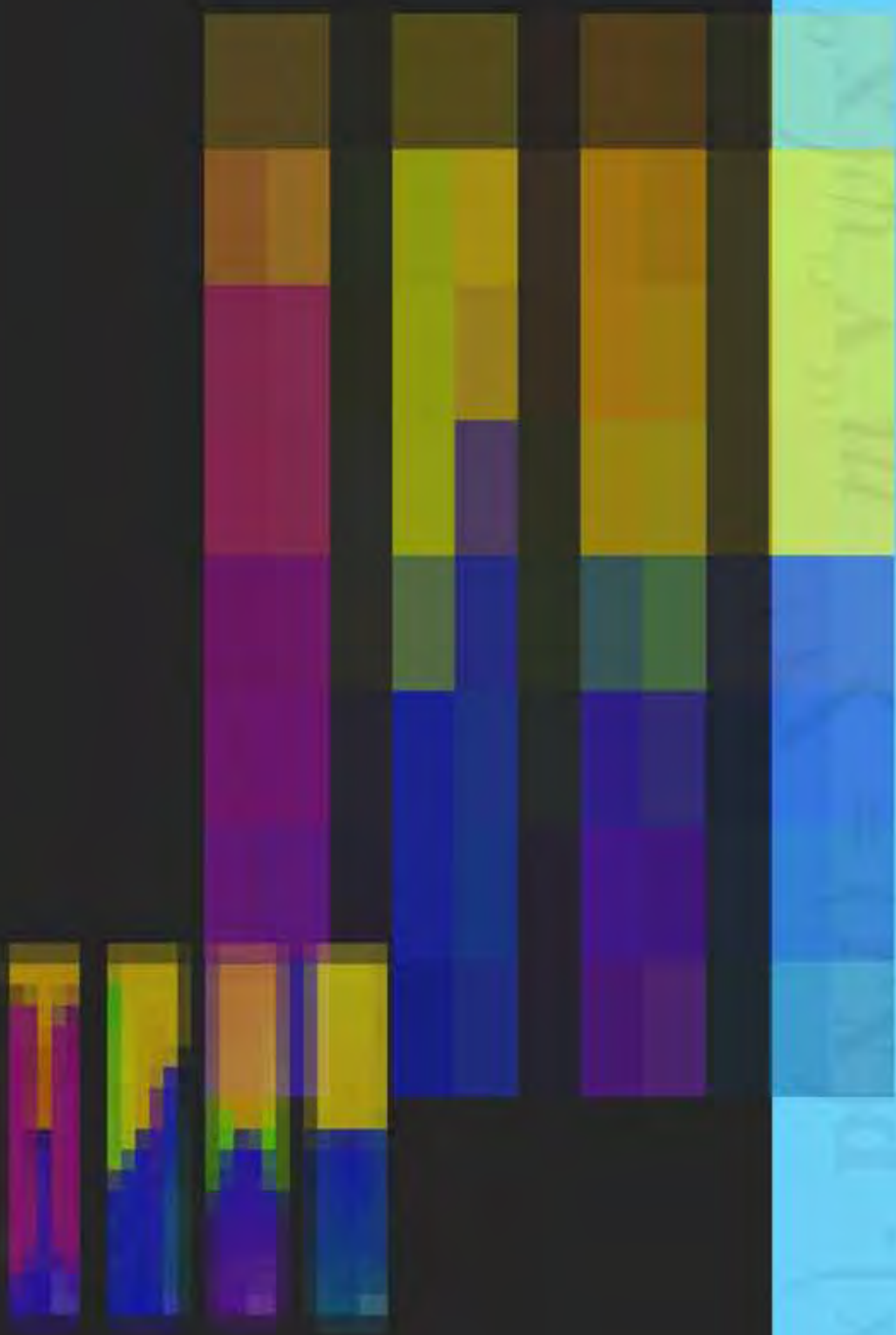


All-Russian Scientific Research Institute of Experimental Physics (VNIIEF)



All-Russian Scientific Research Institute of Technical Physics (VNIITF)





ISBN 978-1-61584-923-9

90000>



9 781615 849239



ISBN 978-1-61584-923-9

